applied sciences

Special Issue Reprint

Biomedical Imaging Technologies for Cardiovascular Disease

Volume II

Edited by
Julio Garcia Flores

mdpi.com/journal/applsci

MDPI

Biomedical Imaging Technologies for Cardiovascular Disease - Volume II

Biomedical Imaging Technologies for Cardiovascular Disease - Volume II

Editor

Julio Garcia Flores

MDPI

Basel • Beijing • Wuhan • Barcelona • Belgrade • Novi Sad • Cluj • Manchester

Editor
Julio Garcia Flores
University of Calgary
Calgary
Canada

Editorial Office
MDPI
St. Alban-Anlage 66
4052 Basel, Switzerland

This is a reprint of articles from the Special Issue published online in the open access journal *Applied Sciences* (ISSN 2076-3417) (available at: https://www.mdpi.com/journal/applsci/special_issues/Imaging_Cardiovascular2).

For citation purposes, cite each article independently as indicated on the article page online and as indicated below:

Lastname, A.A.; Lastname, B.B. Article Title. *Journal Name* **Year**, *Volume Number*, Page Range.

ISBN 978-3-7258-0503-7 (Hbk)
ISBN 978-3-7258-0504-4 (PDF)
doi.org/10.3390/books978-3-7258-0504-4

Contents

About the Editor

Julio Garcia Flores

Julio Garcia Flores, Ph.D. Assistant Professor in the Department of Radiology and Cardiac Sciences at the University of Calgary. His research focuses on cardiovascular imaging to assess heart valve disease, aortopathies, and congenital diseases. He leads the pre-clinical research program at the Stephenson Cardiac Imaging Centre, where he directs the larger 4D-Flow program in Canada. He is a Fellow of the Mexican National Researcher's System, a Junior Fellow of the International Society for Magnetic Resonance in Medicine, a Senior Member of the Institute of Electrical and Electronics Engineers, and a Fellow of the Society for Cardiovascular Magnetic Resonance. Dr. Garcia's publications include >200 works, including original articles and conferences with >2600 citations. He has performed over 60 international lectures and obtained over 40 international awards.

applied sciences

MDPI

Editorial

Biomedical Imaging Technologies for Cardiovascular Disease - Volume II

Julio Garcia [1,2,3,4,5]

[1] Department of Radiology, Cumming School of Medicine, University of Calgary, Calgary, AB T2N 1N4, Canada; julio.garciaflores@ucalgary.ca
[2] Department of Cardiac Sciences, Cumming School of Medicine, University of Calgary, Calgary, AB T2N 1N4, Canada
[3] Stephenson Cardiac Imaging Centre, University of Calgary, Calgary, AB T2N 1N4, Canada
[4] Libin Cardiovascular Institute, University of Calgary, Calgary, AB T2N 1N4, Canada
[5] Alberta Children's Hospital Research Institute, University of Calgary, Calgary, AB T2N 1N4, Canada

1. Introduction

Biomedical imaging innovation facilitates a better understanding of the heart's physiology, performance, function, and structure. Furthermore, each imaging technique provides specific benefits for the diagnosis, treatment, and follow-up of cardiovascular diseases. Technological progress improves the precision, sensitivity, and accuracy of the specialized measurements needed for the assessment of complex conditions. This Editorial refers to the Special Issue, "Biomedical Imaging Technologies for Cardiovascular Disease–Volume II". Seventeen manuscripts were taken into consideration for this Special Issue, all of which underwent a rigorous peer-review process. A total of eleven original articles and six reviews were published.

2. Overview of Original Articles

Transcatheter interventions have become a valuable therapeutic alternative for the treatment of valvular diseases and are often preferred over surgical replacement by patients with severe symptomatic valve disease. Transcatheter aortic valve replacement has emerged, has been widely assessed, and has become a well-established option [1]. As the procedure has gained maturity, it has been assessed for mitral and pulmonary valve replacement. In this Special Issue, Contribution #1 aimed to demonstrate the feasibility and accuracy of 4D cardiac computed tomography (CT) segmentations to conduct a landing zone analysis for the perioperative evaluation of transcatheter pulmonary valve replacement. Determining the optimal delivery is especially important for patients with a history of congenital heart defects, as their anatomy is often altered due to the multiple surgeries they undergo during infancy. One major innovation of transcatheter procedures was their minimally invasive nature. The surgical management of the mitral valve has also evolved into minimally invasive strategies. The authors of Contribution #2 aimed to analyze and report their experience in treating mitral annular calcification via minimally invasive mini-thoracotomy. This study also suggests widening the inclusion selection to include mild-to-severe mitral calcification patients, instead of only severe cases, given the low perioperative mortality reported. However, a recent study performed a risk analysis for this procedure on the mitral valve. The authors highlighted the need for safety surveillance during the learning curve of the surgery program [2]. CT angiography has also demonstrated success for peripherical arterial disease detection and diagnosis. Contribution #3 assessed this approach in 40 patients. The authors' findings demonstrated good reliability for the detection and diagnosis of peripherical arterial disease. Multi-imaging approaches have been demonstrated to facilitate complex cardiovascular surgical procedures. In many situations, previous animal testing is required to assess the effectiveness of the

Citation: Garcia, J. Biomedical Imaging Technologies for Cardiovascular Disease - Volume II. *Appl. Sci.* **2024**, *14*, 1688. https://doi.org/10.3390/app14051688

Received: 12 February 2024
Accepted: 19 February 2024
Published: 20 February 2024

procedure. Contribution #4 aimed to demonstrate the safety, reproducibility, and accuracy of a real-time cross-imaging fusion guide–image to minimize the risk of transjugular intrahepatic portosystemic shunts in an animal protocol. The authors suggested the potential usefulness of this approach in both emergency and non-emergency clinical contexts.

Cardiac magnetic resonance (CMR) is widely used for a more detailed assessment of cardiovascular diseases. Its non-ionizing nature facilitates the clinical follow-up of patients without radiation and can often overcome limitations of Doppler ultrasound. More recently, CMR has been used for the imaging of atrial fibrillation (AF) prior to cardiac ablation [3]. Several comorbidities have been associated with the redevelopment and persistence of AF after an ablation procedure. Obesity has been identified as a well-established risk factor for AF. Contribution #5 aimed to determine the factors influencing cardiac fat deposition and its impact on heart function and AF recurrence. Obesity was associated with increased cardiac fat deposition. Biological sex was a determinant of fat deposition locations in the heart, leading to reduced cardiac function. Several questions remained open regarding the association of obesity and cardiac fat deposition with electrical remodeling, left atrial scar location, and impaired hemodynamics. CMR allows for the comprehensive evaluation of blood hemodynamics using 4D flow MRI [4]. This advanced flow imaging technique is typically acquired using a single range of velocities, which is also referred to as single velocity encoding. Recently, dual- and multi-velocity encoding sequences were developed to increase the sampling accuracy range of 4D flow [5,6]. Contribution #6 aimed to investigate the feasibility and added value of dual-velocity 4D flow encoding to assess complex flow patterns in patients with type B aortic dissection. The authors recommended the use of highly accelerated approaches, using compressed sensing instead of accelerated parallel imaging, given the time cost of the acquisition. The usefulness of 4D flow MRI in congenital cases has been demonstrated in multiple studies. The 4D flow recommendations for congenital diseases highlight several of its applications [4]. Contribution #7 explored the capacity of 4D flow MRI for quantifying blood flow turbulence in Tetralogy of Fallot patients, a common congenital disease. The authors aimed to compare the level of turbulence in repaired Tetralogy of Fallot patients versus healthy controls. Turbulence was found to be abnormally elevated in these patients. However, the clinical value of this turbulence remains to be demonstrated.

Myocardial perfusion imaging has been proven useful in identifying coronary artery disease [7]. Contribution #8 proposed an attention-based feature-fusion VGG19 network for the detection of coronary artery disease using 486 patient records. This network demonstrated a high agreement with expert diagnosis and illustrated the potential of artificial intelligence tools in supporting clinical diagnosis. Similarly, Contribution #9 introduced a deep learning approach based on deep fuzzy cognitive maps to diagnose coronary artery disease. These innovative works illustrate the practical applications and the potential impact on daily clinical practice.

Doppler ultrasound is by far the most accessible imaging tool used in clinical practice. Contribution #10 used Doppler echocardiography to conduct a serial study monitoring the performance of dexamethasone therapy in premature neonates. Their findings demonstrated that the therapeutic strategy improved the respiratory status of patients as well as their heart function. Device innovation is also an important component of the health care system in improving patient management. Contribution #11 highlights a dedicated device development for arterial embolization. The caterpillar device was demonstrated to be safe and efficient in performing arterial occlusions in this pilot study.

3. Overview of Review Articles

Review articles effectively summarize and contextualize the state-of-the-art in a specialized topic. In this Special Issue, six review articles were included. Contribution #12 provides a comprehensive review for understanding the role of CT in the planning of transcatheter structural heart interventions. It highlights the most important benefits and drawbacks of CT for this procedure. Contribution #13 also provides an important overview

of the use of calcium scores obtained by CT. This manuscript also illustrates other useful aspects of CT for the assessment of cardiovascular risk. Animal models are often used to test multiple scenarios that cannot be tested in humans. Contribution #14 emphasizes the relevance of canine models to assess cardiac dysfunction. It also highlights the importance of translational research in both veterinary and human studies. Late gadolinium enhancement can facilitate the assessment of fibrosis in the left atrium. Contribution #15 provides a complete revision of the current strategies for the assessment of cardiac arrythmias and ablation procedures, along with fibrosis quantification. Takotsubo cardiomyopathy is a temporary heart condition that develops in response to an intense emotional or physical event. Contribution #16 revisits the strategies from cardiac nuclear imaging in identifying atypical variants of Takotsubo cardiomyopathy. Finally, Contribution #17 reviews the assessment of cardiovascular disease and progressive kidney failure.

Conflicts of Interest: The authors declare no conflicts of interest.

List of Contributions

1. Sun, X.; Hao, Y.; Steitz, M.; Breitenstein-Attach, A.; Kiekenap, J.F.S.; Emeis, J.; Khan, M.B.; Berger, F.; Schmitt, B. Straightened Segmentation in 4D Cardiac CT: A Practical Method for Multiparametric Characterization of the Landing Zone for Transcatheter Pulmonary Valve Replacement. *Appl. Sci.* **2022**, *12*, 12912. https://doi.org/10.3390/app122412912.
2. Barbero, C.; Spitaleri, A.; Pocar, M.; Parrella, B.; Santonocito, A.; Bozzo, E.; Depaoli, A.; Faletti, R.; Rinaldi, M. Handling Extensive Mitral Annular Calcification via a Minimally Invasive Right Mini-Thoracotomy Approach. *Appl. Sci.* **2023**, *13*, 2563. https://doi.org/10.3390/app13042563.
3. Floridi, C.; Cacioppa, L.M.; Agliata, G.; Cellina, M.; Rossini, N.; Valeri, T.; Curzi, M.; Felicioli, A.; Bruno, A.; Rosati, M.; et al. True Non-Contrast Phase versus Virtual-Non Contrast: "Lights and Shadows" of Dual Energy CT Angiography in Peripheral Arterial Disease. *Appl. Sci.* **2023**, *13*, 7134. https://doi.org/10.3390/app13127134.
4. Lee, E.W.; Shahrouki, P.; Saab, S.; Kaldas, F.; Eghbalieh, N.; McWilliams, J.; Ding, P.-X.; Kee, S.T. Single Puncture TIPS—A 3D Fusion Image-Guided Transjugular Intrahepatic Portosystemic Shunt (TIPS): An Experimental Study. *Appl. Sci.* **2022**, *12*, 5267. https://doi.org/10.3390/app12105267.
5. Peer-Zada, F.; Hamze, D.; Garcia, J. Characterization of Cardiac Fat in Atrial Fibrillation Patients Prior to Ablation Treatment. *Appl. Sci.* **2023**, *13*, 12005. https://doi.org/10.3390/app132112005.
6. Kilinc, O.; Baraboo, J.; Engel, J.; Giese, D.; Jin, N.; Weiss, E.K.; Maroun, A.; Chow, K.; Bi, X.; Davids, R.; et al. Aortic Hemodynamics with Accelerated Dual-Venc 4D Flow MRI in Type B Aortic Dissection. *Appl. Sci.* **2023**, *13*, 6202. https://doi.org/10.3390/app13106202.
7. Hudani, A.; White, J.A.; Greenway, S.C.; Garcia, J. Whole-Heart Assessment of Turbulent Kinetic Energy in the Repaired Tetralogy of Fallot. *Appl. Sci.* **2022**, *12*, 10946. https://doi.org/10.3390/app122110946.
8. Apostolopoulos, I.D.; Papathanasiou, N.D.; Papandrianos, N.; Papageorgiou, E.; Apostolopoulos, D.J. Innovative Attention-Based Explainable Feature-Fusion VGG19 Network for Characterising Myocardial Perfusion Imaging SPECT Polar Maps in Patients with Suspected Coronary Artery Disease. *Appl. Sci.* **2023**, *13*, 8839. https://doi.org/10.3390/app13158839.
9. Feleki, A.; Apostolopoulos, I.D.; Moustakidis, S.; Papageorgiou, E.I.; Papathanasiou, N.; Apostolopoulos, D.; Papandrianos, N. Explainable Deep Fuzzy Cognitive Map Diagnosis of Coronary Artery Disease: Integrating Myocardial Perfusion Imaging, Clinical Data, and Natural Language Insights. *Appl. Sci.* **2023**, *13*, 11953. https://doi.org/10.3390/app132111953.
10. Ladele, J.; Saker, A.; Altamimi, T.; De La Hoz, A.; Lalitha, R.; Miller, M.R.; Bhattacharya, S. Improved Cardiac Performance with Dexamethasone Therapy in Premature Neonates: Novel Insights Using Serial Echocardiographic Assessments. *Appl. Sci.* **2023**, *13*, 11380. https://doi.org/10.3390/app132011380.
11. Sue, M.J.; Luong, T.T.; Park, J.; Ding, P.-X.; Hao, F.; Eghbalieh, N.; Lee, E.W. A Multicenter, Retrospective, Matched, Comparison Study of Clinical Efficacy and Cost-Effectiveness of Caterpillar Arterial Embolization Device versus Fibered Coils in Arterial Embolization. *Appl. Sci.* **2022**, *12*, 5262. https://doi.org/10.3390/app12105262.

12. Circhetta, S.; Nobile, E.; De Filippis, A.; Vicchio, L.; Nusca, A.; De Stefano, D.; Piccirillo, F.; Cammalleri, V.; Mangiacapra, F.; Ricottini, E.; et al. Designing the Optimal Procedure: Role of CT Scan in the Planning of Transcatheter Structural Heart Interventions. *Appl. Sci.* **2023**, *13*, 1589. https://doi.org/10.3390/app13031589.
13. Bernardini, F.; Gelfusa, M.; Celeski, M.; Coletti, F.; Nusca, A.; De Stefano, D.; Piccirillo, F.; Mangiacapra, F.; Gallo, P.; Cammalleri, V.; et al. Beyond the Calcium Score: What Additional Information from a CT Scan Can Assist in Cardiovascular Risk Assessment? *Appl. Sci.* **2023**, *13*, 241. https://doi.org/10.3390/app13010241.
14. Flores Dueñas, C.A.; Cordero Yañez, I.A.; González, R.M.; Herrera Ramírez, J.C.; Montaño Gómez, M.F.; Gaxiola Camacho, S.M.; García Reynoso, I.C. Translational Echocardiography: The Dog as a Clinical Research Model of Cardiac Dysfunction. *Appl. Sci.* **2023**, *13*, 4437. https://doi.org/10.3390/app13074437.
15. Garre, P.; Vázquez-Calvo, S.; Ferro, E.; Althoff, T.; Roca-Luque, I. Impact of LGE-MRI in Arrhythmia Ablation. *Appl. Sci.* **2023**, *13*, 3862. https://doi.org/10.3390/app13063862.
16. De Feo, M.S.; Conte, M.; Frantellizzi, V.; Filippi, L.; Evangelista, L.; Ricci, M.; De Vincentis, G. Cardiac Nuclear Imaging Findings in Atypical Variants of Takotsubo Cardiomyopathy. *Appl. Sci.* **2024**, *14*, 487. https://doi.org/10.3390/app14020487.
17. Gigante, A.; Perrotta, A.M.; Tinti, F.; Assanto, E.; Muscaritoli, M.; Lai, S.; Cianci, R. Assessment of Cardiovascular Disease in Autosomal Dominant Polycystic Kidney Disease. *Appl. Sci.* **2023**, *13*, 7175. https://doi.org/10.3390/app13127175.

References

1. Joseph, J.; Naqvi, S.Y.; Giri, J.; Goldberg, S. Aortic Stenosis: Pathophysiology, Diagnosis, and Therapy. *Am. J. Med.* **2017**, *130*, 253–263. Available online: https://linkinghub.elsevier.com/retrieve/pii/S0002934316310737 (accessed on 12 February 2024). [CrossRef] [PubMed]
2. Papadopoulos, N.; Ntinopoulos, V.; Dushaj, S.; Häussler, A.; Odavic, D.; Biefer, H.R.C.; Dzemali, O. Navigating the challenges of minimally invasive mitral valve surgery: A risk analysis and learning curve evaluation. *J. Cardiothorac. Surg.* **2024**, *19*, 24. Available online: https://cardiothoracicsurgery.biomedcentral.com/articles/10.1186/s13019-024-02479-3 (accessed on 12 February 2024). [CrossRef]
3. Bisbal, F.; Baranchuk, A.; Braunwald, E.; de Luna, A.B.; Bayés-Genís, A. Atrial Failure as a Clinical Entity. *J. Am. Coll. Cardiol.* **2020**, *75*, 222–232. Available online: https://linkinghub.elsevier.com/retrieve/pii/S0735109719384530 (accessed on 12 February 2024). [CrossRef] [PubMed]
4. Zhong, L.; Schrauben, E.M.; Garcia, J.; Uribe, S.; Grieve, S.M.; Elbaz, M.S.; Barker, A.J.; Geiger, J.; Nordmeyer, S.; Marsden, A.; et al. Intracardiac 4D Flow MRI in Congenital Heart Disease: Recommendations on Behalf of the ISMRM Flow & Motion Study Group. *J. Magn. Reson. Imaging* **2019**, *50*, 677–687. [CrossRef] [PubMed]
5. Schnell, S.; Rose, M.J.; Wu, C.; Garcia, J.; Robinson, J.D.; Markl, M.; Rigsby, C.K. Improved assessment of aortic hemodynamics by K-T accelerated dual-venc 4D flow MRI in pediatric patients. *J. Cardiovasc. Magn. Reson.* **2016**, *18*, O96. [CrossRef]
6. Ha, H.; Kim, G.B.; Kweon, J.; Kim, Y.-H.; Kim, N.; Yang, D.H.; Lee, S.J. Multi-VENC acquisition of four-dimensional phase-contrast MRI to improve precision of velocity field measurement. *Magn. Reson. Med.* 2015. Available online: http://doi.wiley.com/10.1002/mrm.25715 (accessed on 12 February 2024).
7. Winzer, E.B.; Woitek, F.; Linke, A. Physical Activity in the Prevention and Treatment of Coronary Artery Disease. *J Am Heart Assoc.* **2018**, *7*, e007725. Available online: https://www.ahajournals.org/doi/10.1161/JAHA.117.007725 (accessed on 12 February 2024). [CrossRef] [PubMed]

applied sciences

MDPI

Article

Straightened Segmentation in 4D Cardiac CT: A Practical Method for Multiparametric Characterization of the Landing Zone for Transcatheter Pulmonary Valve Replacement

Xiaolin Sun [1,2,3,†], Yimeng Hao [1,2,†], Marvin Steitz [1,2], Alexander Breitenstein-Attach [1,2], Jonathan Frederik Sebastian Kiekenap [1], Jasper Emeis [1], Mahamuda Badhon Khan [1], Felix Berger [1,2] and Boris Schmitt [1,2,3,4,5,*]

1 Department of Pediatric Cardiology and Congenital Heart Disease, Charité University Medicine Berlin, Augustenburger Platz 1, 13353 Berlin, Germany
2 Department of Pediatric Cardiology and Congenital Heart Disease, Deutsches Herzzentrum Berlin, Augustenburger Platz 1, 13353 Berlin, Germany
3 DZHK (German Centre for Cardiovascular Research), Potsdamer Straße 58, 10785 Berlin, Germany
4 BIH (Berlin Institute of Health), Anna-Louisa-Karsch-Straße 2, 10178 Berlin, Germany
5 BCRT (BIH Center of Regenerative Therapies), Föhrer Straße 15, 13353 Berlin, Germany
* Correspondence: schmitt@dhzb.de; Tel.: +49-(0)30-4593-2875
† These authors have contributed equally to this work and share first authorship.

Featured Application: Four-dimensional cardiac straightened segmentation can be useful for the periprocedural evaluation of TPVR.

Citation: Sun, X.; Hao, Y.; Steitz, M.; Breitenstein-Attach, A.; Kiekenap, J.F.S.; Emeis, J.; Khan, M.B.; Berger, F.; Schmitt, B. Straightened Segmentation in 4D Cardiac CT: A Practical Method for Multiparametric Characterization of the Landing Zone for Transcatheter Pulmonary Valve Replacement. *Appl. Sci.* **2022**, *12*, 12912. https://doi.org/10.3390/app122412912

Academic Editor: Julio Garcia Flores

Received: 18 November 2022
Accepted: 14 December 2022
Published: 15 December 2022

Abstract: Cardiac computed tomography angiography (C-CTA) is crucial in assessing the right ventricular outflow tract (RVOT) prior to a transcatheter pulmonary valve replacement (TPVR), as an incorrect evaluation can make the procedure more challenging and can lead to device-related complications. This study aimed to evaluate the feasibility and accuracy of 4D straightened segmentation for a landing zone analysis over anatomical segmentation. Seven pre-operative CTAs and seven post-operative CTAs were used to measure the cross-sectional area, circumference, and diameters at five selected planes as the landing zone for TPVR and compared these to the 4D straightened model with the anatomical model. Furthermore, the right ventricular volume, stent volume, and 4D ellipticity index were calculated from the 4D straightened model. The 4D straightened segmentation had comparable accuracy and efficacy for the measurements at the landing zone. The cross-sectional area and the circumference varied greatly at the RVOT and the basal plane of the pulmonary valve compared with the other three planes of the 4D straightened models from the pre-operative CTAs; however, only the values at the RVOT were found to vary greatly from the post-operative CTAs. The 4D straightened model can provide accurate measurements and is thus a useful method for the periprocedural evaluation of TPVR.

Keywords: four-dimensional computed tomography; transcatheter pulmonary valve replacement; cardiac catheterization; 4D dynamic segmentation; landing zone

1. Introduction

Transcatheter pulmonary valve replacement (TPVR) is a well-established alternative therapeutic approach for patients with right ventricular outflow tract (RVOT) dysfunction, the majority of whom are young and suffer from congenital heart defects or have had multiple previous cardiac surgeries [1,2]. Recent studies show that, in terms of survival and freedom from reintervention or surgery, the outcomes of TPVR are comparable with those of surgical conduit/valve replacement to manage RVOT dysfunction across a wide age range [3,4]. Similar to transcatheter aortic valve replacement (TAVR), cardiac computed

tomography angiography (C-CTA) plays a crucial role in the characterization of the morphology, distensibility, and compliance of the RVOT prior to TPVR, since inaccurate sizing can complicate the procedure and cause device-related complications, such as embolization and paravalvular leak (PVL) [5,6].

Technological developments in three-dimensional (3D) and four-dimensional (4D) C CTA have opened the door to a novel method for the personalized planning of transcatheter heart valve implantation for patients with structural heart valve diseases [7–9]. Cross-sectional imaging with 3D and 4D C-CTA is critical to determine patients' suitability for TPVR; knowledge of RVOT anatomy, the proximity of the left coronary artery to the native pulmonary root, and the distensibility of the RVOT are indispensable for TPVR [10,11]. In addition to this, 3D and 4D C-CTA can support the identification of candidate percutaneous access routes, including the transfemoral, transjugular, and subclavian routes, and answer key anatomical questions. Furthermore, the landing zone—the ideal implantation site for TPVR—can protect the stented pulmonary valve (PV) from PVL, migration, and coronary compression. To create an accurate 4D segmentation of the landing zone anatomy at the RVOT, CT datasets should undergo segmentation where the personalized CT data are assigned to a region of interest to generate the 4D structures in synchronization with the heart rate. A previous study showed that the RVOT's morphology and size can vary significantly throughout the entire cardiac cycle, and so perimeter- and cross-sectional area-based measurements have proven more reliable than PV annulus diameters alone [12]. Additionally, the necessity of 4D C-CTA is emphasized by Gillespie and colleagues, who encourage taking measurements for the landing zone both during end-systole and end-diastole phases [13].

However, in current traditional clinical and preclinical settings, the resulting 4D CT data are frequently transformed into 3D data for manual quantification and visual evaluation, which can only show static information. Furthermore, anatomical 4D segmentations are unable to fully depict the characteristics of the RVOT adjacent to the aortic root during the course of the cardiac cycle, even with 4D information. Yet, the 4D dynamic volumes of the right ventricle, implanted stent, and landing zone, which are crucial for the quantitative interpretation of TPVR, are only partially illustrated by the available data. In addition to the 4D anatomical segmentation, the angle between the RVOT and the main pulmonary artery can cause the measuring lines to not fully align with the landing zone planes (e.g., the annular plane or sinotubular junction plane), which can result in incorrect landing zone measurements. The 2D properties of the STJ plane, the sinus plane and the pulmonary valve annular plane, are defined by three points at each level—the three commissures, the petaline peak of the sinuses, and the nadir of the pulmonary valve—instead of 3D properties, which could lead to inaccurate landing zone measurements. Multi-planar measurements are often employed in clinical practice to assess the RVOT before TPVR, but due to their 3D properties, planes may be positioned incorrectly in anatomical segmentations.

In this study, we exploited a practical approach to performing multiparametric analyses of pre- and post-interventional C-CTA for TPVR in a sheep model by straightening the 4D anatomical segmentations into a 4D straightened segmentation. Our primary objective was to evaluate the feasibility and accuracy of 4D straightened segmentation in comparison to traditional anatomical segmentation, identify its benefits, and explore its potential as a complementary planning tool in TPVR.

2. Materials and Methods

This study included seven adult sheep (Ovis aries), all of which received humane care in compliance with the guidelines of the European and German Societies of Laboratory Animal Science (FELASA, GV-SOLAS). The legal and ethical committee of the Regional Office for Health and Social Affairs in Berlin (LaGeSo) approved the GrOwnValve preclinical trial aiming to conduct transcatheter pulmonary valve replacement from autologous pericardium with a self-expandable stent in a sheep model (IC14-G 0062/18). The TPVRs were performed at Charité University Hospital of Berlin, Campus Virchow-Klinikum, Research

Institute for Experimental Medicine (FEM), while all 4D cardiac CTs were performed at the German Heart Center Berlin.

2.1. Scan Protocol and 4D Cardiac CT Processing

All cardiac CTAs were performed on a Siemens 64-slice dual-source multidetector CT scanner with ECG gating (SOMATOM Definition Flash, Siemens AG, Munchen, Germany). The sheep were scanned in the prone position with standard acquisition technical parameters: a gantry rotation time of 0.33 s, 100–320 mAs per rotation, a 120 kV tube voltage, matrix 256 with a 16-bit depth, a deviation effective X-ray dose of 15.5 $\pm$ 11.6 mSv, and a slice thickness of 0.75 mm. CT contrast enhancement was achieved by administering 2–2.5 mL/kg of an iodinated contrast agent at a rate of 5 mL/s. To achieve the ideal synchronization, a bolus tracking method was used for contrast bolus timing in the region of interest on the main pulmonary artery. The 4D cardiac CTA scanning protocol produced 10 continuous frames for the cardiac cycle, from 10% to 100%, with 10% of the RR interval covering the entire cardiac cycle.

2.2. Four-Dimensional Cardiac CT Analysis in 3D Slicer

2.2.1. Segmentations

The CT data of the seven sheep were processed offline using the open-source software 3D Slicer (https://www.slicer.org/ (accessed on 1 March 2022). The 4D anatomical right heart (from the superior vena cava to the end of the main pulmonary artery, without the inferior vena cava) blood pool was segmented using a certain threshold automatically and manually based on each C-CTA by two experienced doctors and optimized manually by a senior expert. The inferior vena cava was not included in this anatomical segmentation due to its low contrast (the contrast agent was administered via the cephalic vein) and the establishment of the subsequent straightened segmentation.

After creating the anatomical segmentation for each 10% of cardiac cycle, the straightened 4D right heart segmentations were created as follows. Two markup points were placed on the top plane of the superior vena cava and the end plane of the main pulmonary artery to construct a centerline for each anatomical segmentation, and then a centerline curve was generated by adding a new markup curve to the segmentation. An output straightened volume was created by executing the "Curved Planar Reformat" operation. This straightened volume was then used to construct a straightened segmentation both automatically and manually. The segmentation for each 10% of the cardiac cycle was obtained using the same methods. The ten 3D straightened segmentations were sequentially concatenated to create a 4D straightened right heart segmentation.

The straightened 4D right heart models were created by adding centerlines and curved planar reformatting to the corresponding anatomical model. Similar steps were used for all segmentations of both the pre-operative C-CTA (pre-CT) and post-operative C-CTA (post-CT). Comprehensive steps for the 4D cardiac CTA analysis were described previously [14].

2.2.2. Multiparametric Measurements of the Landing Zone

Dynamic landing zone measurements, which included cross-sectional area, circumference, maximum diameter, and minimum diameter in the pre-CTs, were taken in five planes at the landing zone: plane 1—RVOT (10 mm below plane 2), plane 2—BPV plane (three hinge points at the nadir of each of the attachments of the PV), plane 3—sinus plane, plane 4—sinotubular junction (STJ) plane, and plane 5—PA plane (10 mm above plane 4). The five planes in the post-CTs were defined as follows: plane 1—RVOT (10 mm below plane 2), plane 2—bottom plane of the stent (BPS) plane, plane 3—middle plane of the stent (MPS) plane, plane 4—top plane of the stent (TPS) plane, and plane 5—PA plane (10 mm above plane 4) (Figure 1). The RV volume was obtained by cutting the right heart segmentations at the tricuspid valve level and at the level of plane 4 both in the anatomical and the straightened segments. The right ventricular ejection fraction (RVEF) can be calculated using the minimum and maximum RV volume. The volume of the landing zone in the

pre- (PV volume) and post-CTs (stent volume, SV) was obtained by cutting the right heart segments from plane 1 to plane 5 both in the anatomical and the straightened segments. The rendered stent volume in the post-CTs was created by masking the right heart volume between plane 2 and 4 for the entire cardiac cycle. The ratio between the minimum and maximum diameter in each section was calculated to determine the grade of the elliptical shape (ellipticity index). The correlation between the anatomical model and straightened model was assessed using the Pearson correlation coefficient. We calculated the r value for the Pearson correlation coefficient using Formula (1),then obtained the t value using Formula (2). In the case where the degrees of freedom (d.f.) for r is $n - 2$, the p value can be obtained using the critical values of t for Pearson's r.

$$r = \frac{n\sum x_i y_i - \sum x_i \sum y_i}{\sqrt{n\sum x_i^2 - (\sum x_i)^2}\sqrt{n\sum y_i^2 - (\sum y_i)^2}} \tag{1}$$

$$t = \frac{r}{\sqrt{\frac{1-r^2}{n-2}}} \tag{2}$$

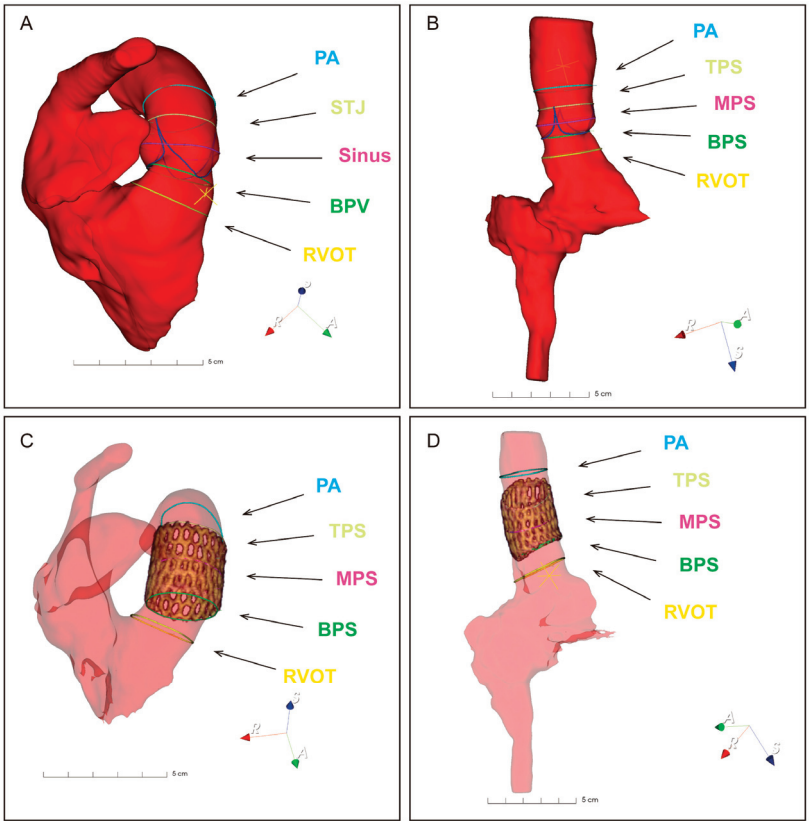

Figure 1. Five selected planes from different segmentations. (**A**) anatomical model from pre-operative CT, (**B**) straightened model from pre-operative CT, (**C**) anatomical model from post-CT, (**D**) straightened model from post-CT. PA pulmonary artery, STJ sinotubular junction, BPV basal plane of pulmonary valve, RVOT right ventricular outflow tract, TPS top plane of the stent, MPS middle plane of the stent, BPS bottom plane of the stent.

Bland–Altman analysis was conducted to further confirm the agreement between the two models.

2.3. TPVR Protocol

The sheep were tranquilized with an intramuscular injection of 0.4 mg/kg of midazolam, 0.4 mg/kg of butorphanol, and 0.011 mg/kg of glycopyrronium bromide. After administering intravenous anesthesia by injecting 1–2.5 mg/kg of propofol and 0.01 mg/kg of fentanyl, the sheep were intubated, and a gastric tube was placed into the stomach for gas and fluid evacuation during the preparation for CT and TPVR.

The sheep were ventilated under general anesthesia, which was maintained by isoflurane (1%) in oxygen (flow = 1 L/min, FiO2 = 75%), combined with a continuous rate infusion of fentanyl (5–15 mcg/kg/h) and midazolam (0.2–0.5 mg/kg/h) during the left mini-thoracotomy to harvest the autologous pericardium and perform the transjugular implantation of the autologous heart valve. GrOwnValve sizing was achieved according to the 4D measurements of the landing zone in the pre-CTs (Figure 1A). The autologous pericardium was harvested to manufacture a new PV by trimming and sewing it onto a Nitinol stent. The stented autologous PVs were loaded into the head of a self-designed delivery system and advanced via the left jugular vein under guidewire and fluoroscopy guidance. After confirmation of the deployment position in the right heart angiography, the GrOwnValve was deployed at the native PV position. The protocol for the GrOwnValve transjugular vein implantation was illustrated in detail previously [15].

2.4. Statistical Analysis

Statistics were analyzed using the GraphPad Prism 9 software (Graphpad Software, Biomatters, Ltd., NZ, and GSL Biotech, San Diego, CA, USA). Normal distribution was assessed with a Kolmogorov–Smirnov test. Continuous variables are presented as mean ± standard deviation (SD) for normal distribution or as median with interquartile ranges (IQRs) for non-normal distribution. The Pearson correlation coefficient was used to quantify the correlation between each plane of the anatomical model and the straightened model during the ten cardiac phases for each of the seven sheep. The agreement and bias between the two models were assessed with Bland–Altman analysis. A p value of <0.05 was considered statistically significant. All the test results are two-tailed.

3. Results

3.1. Four-Dimensional Cardiac CT Segmentation

Fourteen C-CTA datasets (a pre-CT and a post-CT from each of the seven sheep) were included in the study. Each CT was divided into ten cardiac phases. Furthermore, each CT was reconstructed into an anatomical model and a straightened model. In total, 28 anatomical models and straightened models were successfully segmented and reconstructed from the 14 CTs. The cross-sectional area, circumference, maximum diameter, and minimum diameter of the five planes were measured for each model. This resulted in a total of 350 paired datasets in each measurement that were acquired at the 10 different cardiac cycles between the anatomical model and the straightened model. In addition, the parameters for a single plane were compared as well.

3.2. Correlations between Anatomical Model and Straightened Model

In all pre-CT comparisons, there was a strong linear correlation between the anatomical model and the straightened model for the cross-sectional area and the circumference measurements at all five planes, with a Pearson correlation coefficient of 0.95 ($p < 0.0001$) for the cross-sectional area and 0.94 ($p < 0.0001$) for the circumference. The Bland–Altman analysis further confirmed a strong agreement between the two models (Figure 2).

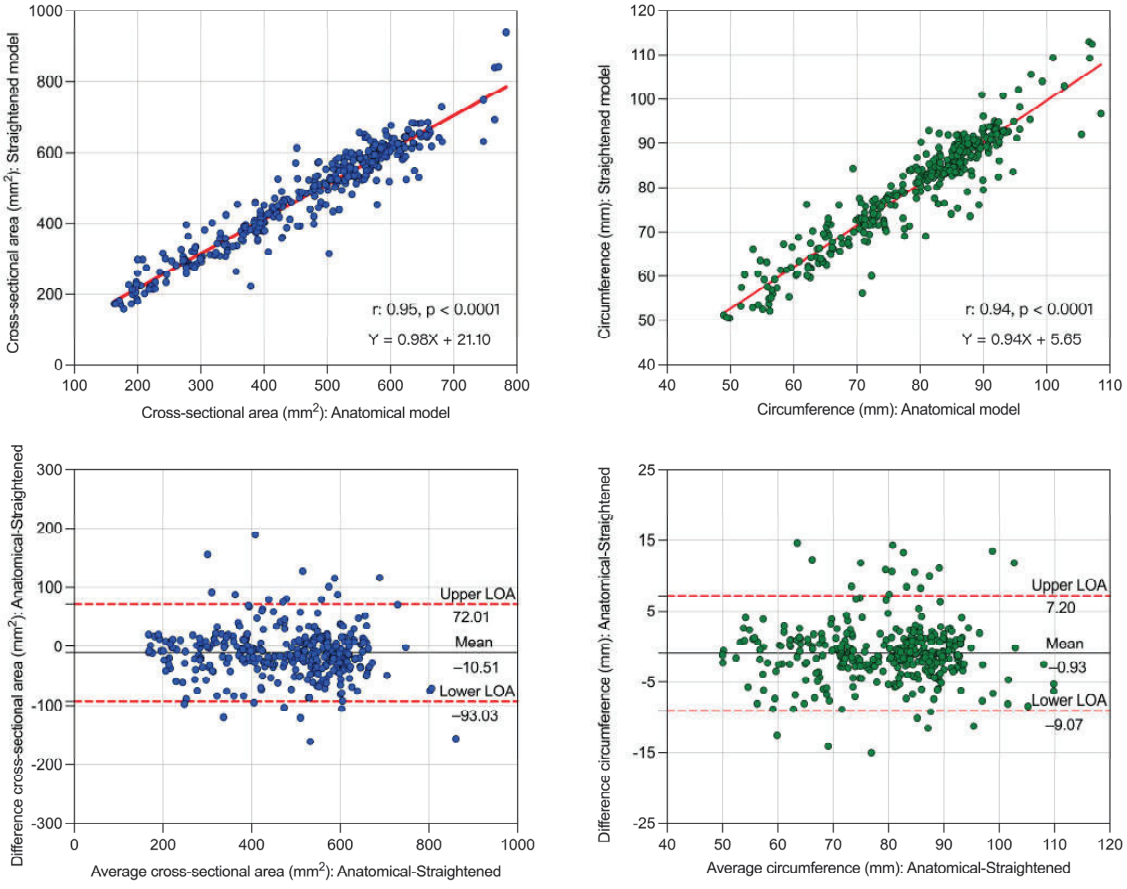

Figure 2. Pearson correlation scatterplot and Bland–Altman plot of cross-sectional area and circumference for the agreement between the anatomical model and straightened model from pre-CT. LOA—limit of agreement.

Similarly, the two pre-CT models for the minimum and maximum diameter were highly correlated, with a Pearson correlation coefficient of 0.96 ($p < 0.0001$) for the minimum diameter and 0.91 ($p < 0.0001$) for the maximum diameter. The limits of agreement between the anatomical model and the straightened model were in a good range for both the minimum diameter and maximum diameter (Figure 3).

There was also a statistically significant linear correlation between the cross-sectional area (r: 0.97, $p < 0.0001$) and the circumference (r: 0.97, $p < 0.0001$) of the two models for the post-CTs (Figure 4). The scatter plot of the Bland–Altman analysis also demonstrates good agreement for every paired dataset.

The post-CT anatomical model and straightened model for the minimum diameter and maximum diameter were highly correlated, with a Pearson correlation coefficient of 0.96 ($p < 0.0001$) for the minimum diameter and 0.91 ($p < 0.0001$) for the maximum diameter. The limits of agreement between the anatomical model and the straightened model were in a good range (Figure 5).

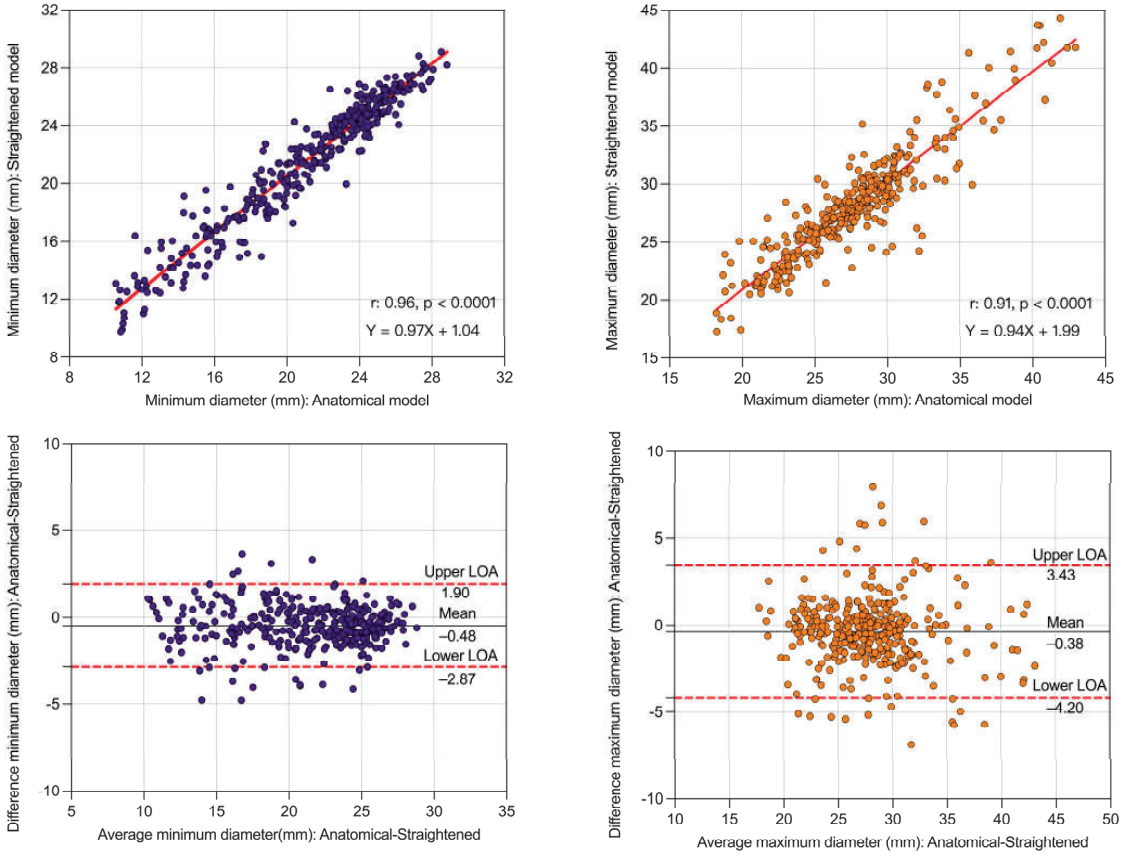

Figure 3. Pearson correlation scatterplot and Bland–Altman plot of minimum diameter and maximum diameter for the agreement between anatomical model and straightened model from pre-CT. LOA—limit of agreement.

The Pearson correlation coefficients and Bland–Altman agreements between the two model measurements of the annulus area, circumference, minimum diameter, and maximum diameter at each single plane are shown in Table 1. There was also an excellent correlation between every comparison. The results for the Pearson correlation coefficients and Bland–Altman analyses indicate a good accuracy of the straightened model.

3.3. Dynamic Variation of Landing Zone

The mean cross-sectional area and circumference dynamic variations of each plane during the whole cardiac cycle for the pre- and the post-CTs are shown in Figures 6 and 7. There was high variation in the RVOT and BPV cross-sectional area for the pre-CTs in the ten phases of the cardiac cycle, especially from 50% to 60% and 90% to 100%. For the straightened pre-CT model, the maximum and minimum mean annulus areas of the RVOT plane were 646 ± 149 mm^2 (90%) and 272 ± 122 mm^2 (50%), respectively, and the maximum and minimum cross-sectional area mean values of the BPV plane were 471 ± 48 mm^2 (100%) and 266 ± 101 mm^2 (60%), respectively. In addition, the post-CT RVOT annulus area differed greatly between 100% and 50% with areas of 1028 ± 210 mm^2 and 435 ± 144 mm^2, respectively. The dynamic variation trends for the circumference were similar to those for the cross-sectional area. The detailed mean differences (±standard deviation) of the cross-sectional area and the circumference are presented in Table S1.

However, the variation in the BPS plane area in the post-CTs was small because the radial force of the implanted stent fixed the stent on the annulus between the BPS and the PA plane, allowing the PA to expand fully, which also led to an increase in the annulus ellipticity of the BPS plane (Table 2). The annulus of the RVOT plane has a more notable elliptical geometry than the other planes. The detailed ellipticity indices of the five planes during the ten cardiac phases are presented in Table S2.

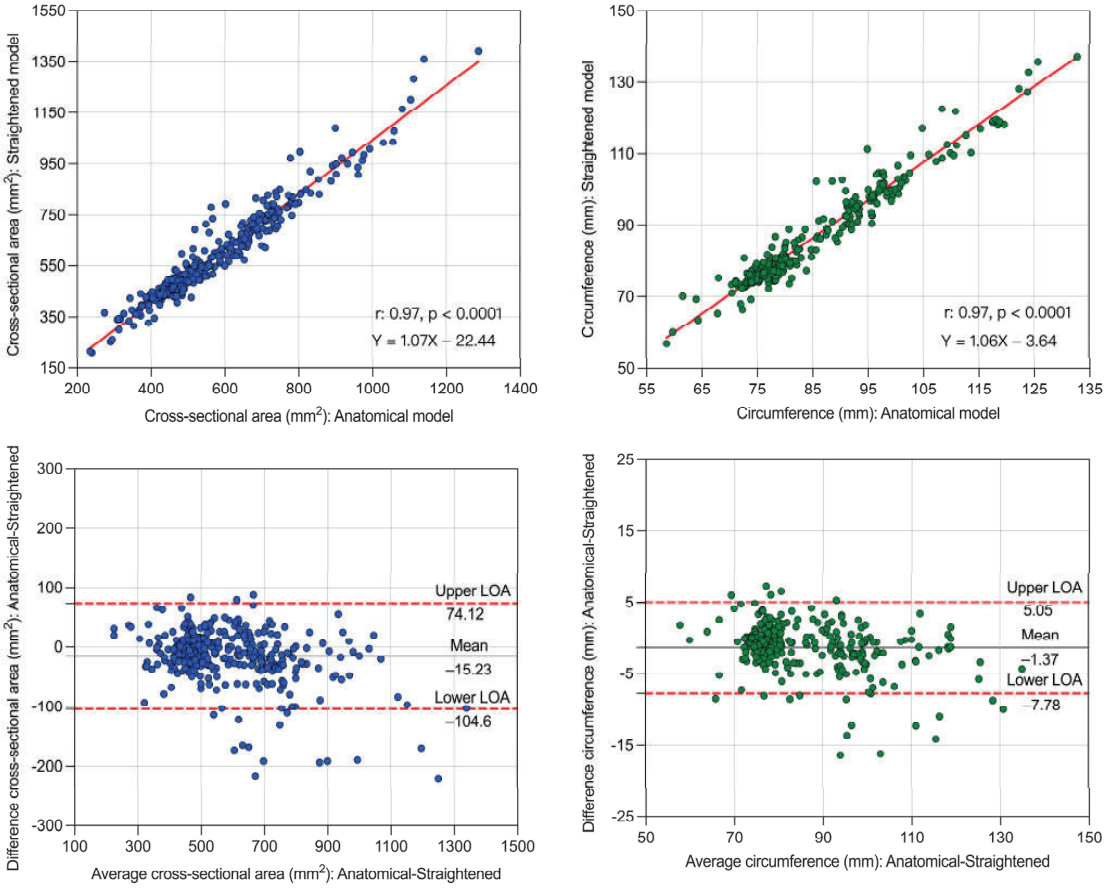

Figure 4. Pearson correlation scatterplot and Bland–Altman plot of cross-sectional area and circumference for the agreement between the anatomical model and straightened model from post-CT. LOA—limit of agreement.

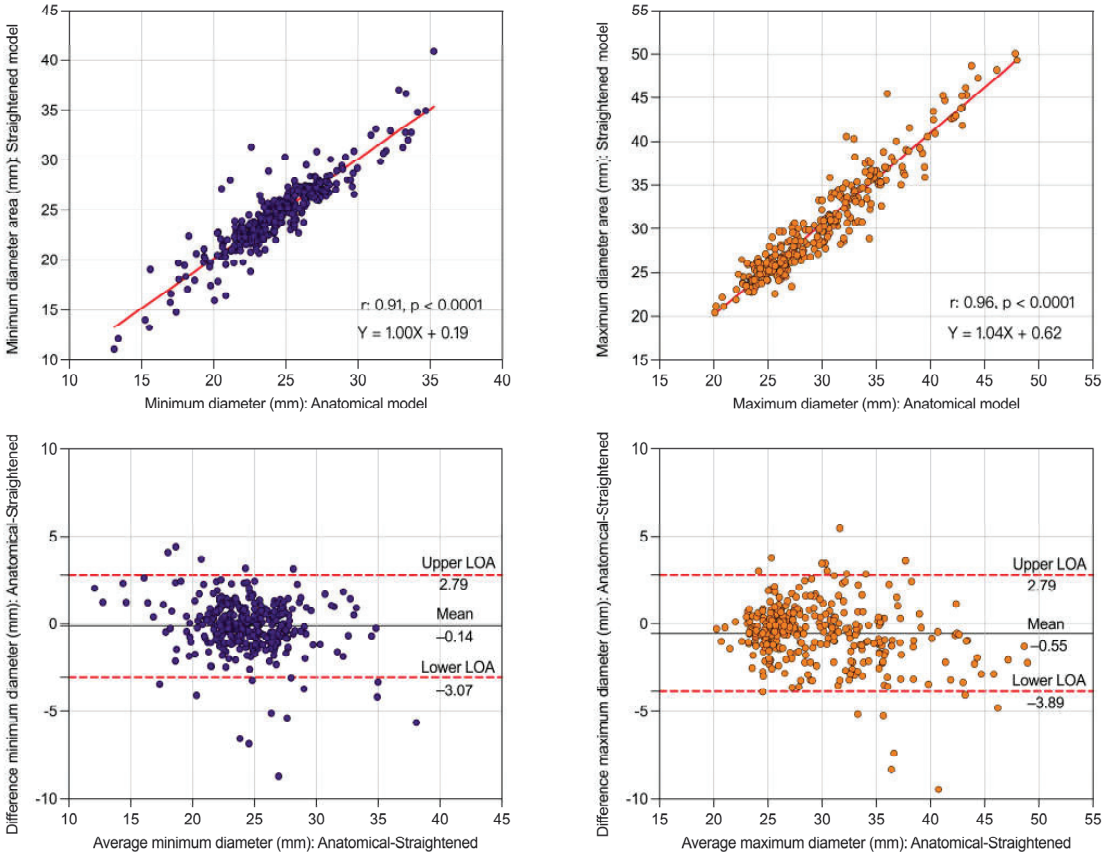

Figure 5. Pearson correlation scatterplot and Bland–Altman plot of minimum diameter and maximum diameter for the agreement between the anatomical model and straightened model from post-CT. LOA—limit of agreement.

Table 1. Pearson correlation coefficient and Bland–Altman analysis of cross-sectional area, circumference, minimum diameter, and maximum diameter for each single plane. CSA—cross-sectional area, C—circumference, LOA—limit of agreement, RVOT—right ventricular outflow tract, BPV—basal plane of pulmonary valve, STJ—sinotubular junction, PA—pulmonary artery, BPS—bottom plane of the stent, MPS—middle plane of the stent, TPS—top plane of the stent. * $p < 0.0001$.

Pre-CT		Pearson Correlation (r)	Bland–Altman Analysis		
			Mean Difference	Upper LOA	Lower LOA
RVOT	CSA (mm^2)	0.96 *	−7.43	95.24	−110.10
	C (mm)	0.95 *	−0.23	10.05	−10.51
	Minimum diameter (mm)	0.94 *	−0.49	2.32	−3.31
	Maximum diameter (mm)	0.94 *	−0.54	4.05	−5.13
BPV	CSA (mm^2)	0.87 *	−4.89	117.60	−127.40
	C (mm)	0.84 *	−0.89	12.23	−14.01
	Minimum diameter (mm)	0.88 *	−0.49	2.94	−3.92
	Maximum diameter (mm)	0.77 *	−0.18	6.03	−6.40
Sinus	CSA (mm^2)	0.93 *	−5.00	54.53	−64.53
	C (mm)	0.94 *	−0.87	4.03	−5.76
	Minimum diameter (mm)	0.92 *	−0.34	1.29	−1.98
	Maximum diameter (mm)	0.90 *	−0.13	1.79	−2.04
STJ	CSA (mm^2)	0.97 *	−14.30	30.54	−59.14
	C (mm)	0.97 *	−1.02	2.68	−4.72
	Minimum diameter (mm)	0.93 *	−0.61	1.15	−0.61
	Maximum diameter (mm)	0.94 *	−0.35	1.49	−2.18
PA	CSA (mm^2)	0.97 *	−20.94	29.80	−71.68
	C (mm)	0.97 *	−1.67	2.24	−5.57
	Minimum diameter (mm)	0.95 *	−0.48	1.29	−2.25
	Maximum diameter (mm)	0.92 *	−0.73	1.71	−3.17
RVOT	CSA (mm^2)	0.97 *	−37.39	110.10	−184.90
	C (mm)	0.97 *	−2.70	7.53	−12.92
	Minimum diameter (mm)	0.91 *	−0.40	4.94	−5.73
	Maximum diameter (mm)	0.93 *	−1.47	3.52	−6.46
BPS	CSA (mm^2)	0.95 *	0.96	67.47	−65.55
	C (mm)	0.95 *	0.13	5.44	−5.17
	Minimum diameter (mm)	0.84 *	0.05	2.11	−2.00
	Maximum diameter (mm)	0.93 *	0.06	2.73	−2.61
MPS	CSA (mm^2)	0.99 *	−10.36	23.76	−44.47
	C (mm)	0.99 *	−0.78	1.87	−3.43
	Minimum diameter (mm)	0.92 *	−0.19	1.29	−1.67
	Maximum diameter (mm)	0.96 *	−0.24	1.49	−1.96
TPS	CSA (mm^2)	0.97 *	−21.57	42.77	−85.91
	C (mm)	0.97 *	−1.74	3.26	−6.75
	Minimum diameter (mm)	0.93 *	0.11	1.92	−1.70
	Maximum diameter (mm)	0.97 *	−0.9	1.67	−3.47
PA	CSA (mm^2)	0.97 *	−7.77	66.30	−81.84
	C (mm)	0.97 *	−0.40	5.57	−6.38
	Minimum diameter (mm)	0.92 *	−0.27	1.85	−2.39
	Maximum diameter (mm)	0.94 *	−0.18	2.77	−3.13

Table 2. Annulus ellipticity index of five planes for pre-operative CT and post-operative CT. The ellipticity index was defined as minimum diameter/maximum diameter.

Ellipticity Index			
Pre-CT		Post-CT	
RVOT	0.55 ± 0.08	RVOT	0.69 ± 0.10
BPV	0.69 ± 0.12	BPS	0.88 ± 0.08
Sinus	0.89 ± 0.06	MPS	0.88 ± 0.09
STJ	0.90 ± 0.06	TPS	0.84 ± 0.10
PA	0.83 ± 0.06	PA	0.86 ± 0.09

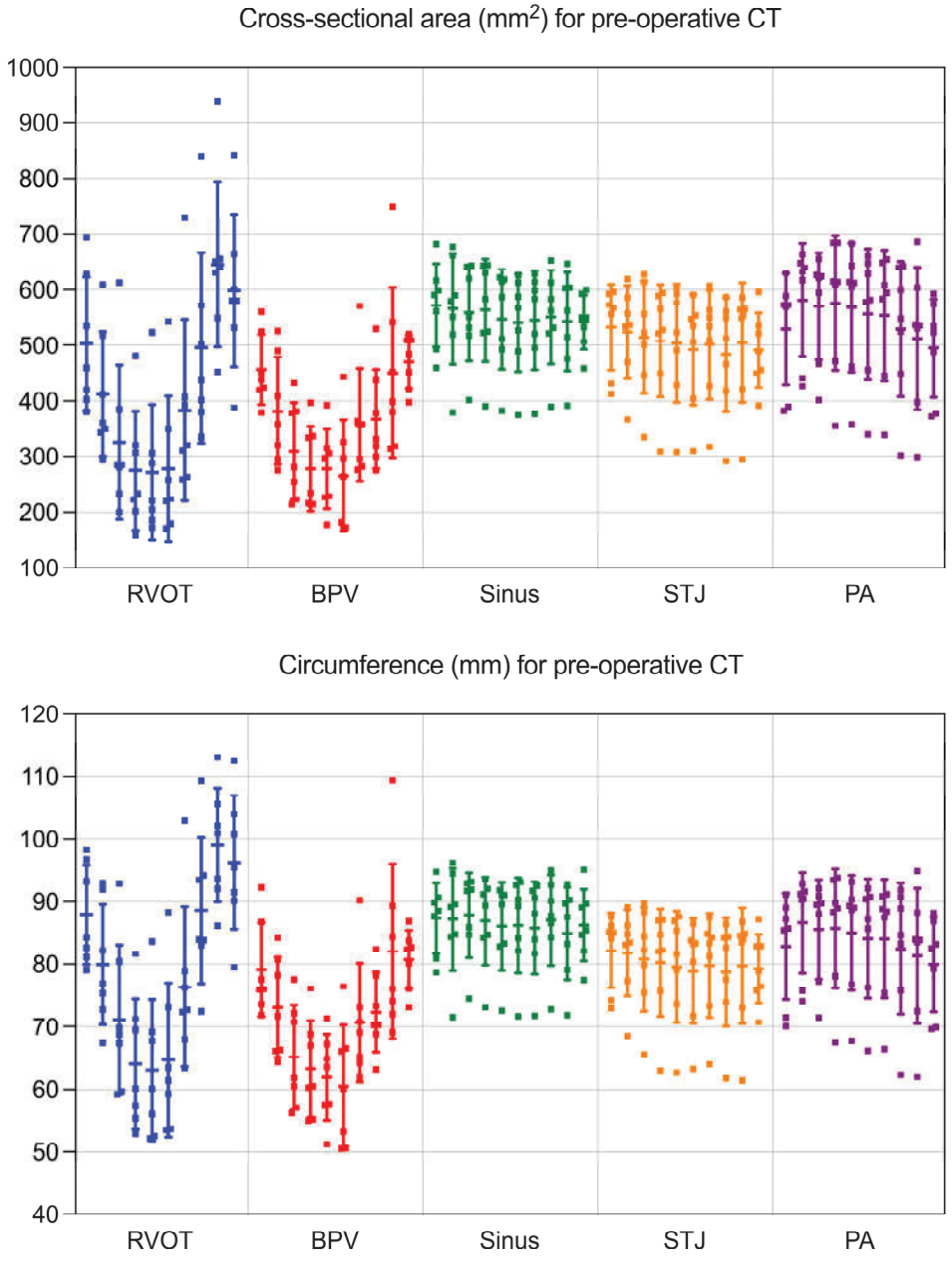

Figure 6. Dynamic variation in the cross-sectional area and circumference throughout the cardiac cycle at five planes from pre-operative CT. RVOT—right ventricular outflow tract, BPV—basal plane of pulmonary valve, STJ—sinotubular junction, PA—pulmonary artery. In each plane, one error bar indicates one frame (from 10% to 100%) in the cardiac cycle.

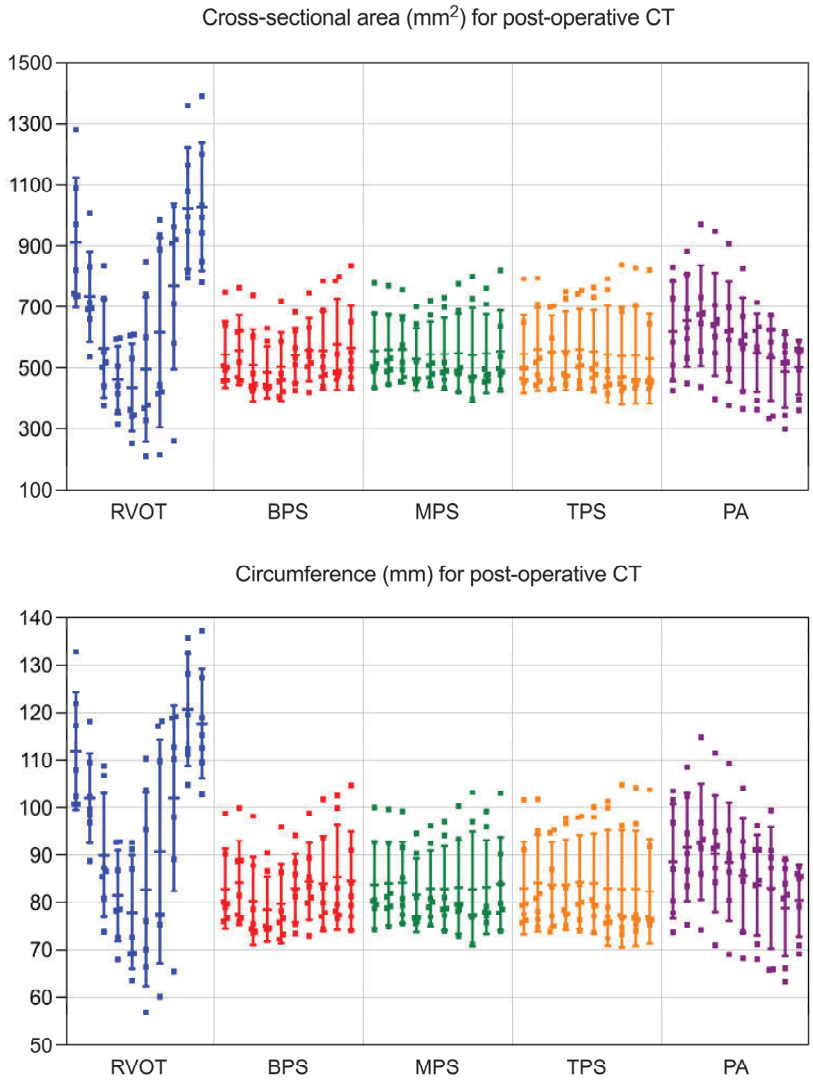

Figure 7. Dynamic variation in the cross-sectional area and circumference throughout the cardiac cycle at five planes from post-operative CT. RVOT—right ventricular outflow tract, BPS—bottom plane of the stent, MPS—middle plane of the stent, TPS—top plane of the stent, PA—pulmonary artery. In each plane, one error bar indicates one frame (from 10% to 100%) in the cardiac cycle.

4. Discussion

In this study, we illustrated the feasibility and accuracy of multiparametric analyses of the landing zone using 4D straightened segmentation generated from 4D C-CTA in sheep to measure and characterize the dynamic changes in the landing zone in pre-CTs and the implanted stent in post-CTs for TPVR at five selected planes. Furthermore, we used this methodology to obtain the 4D RV volume from all CTs, the landing zone volume from pre-CTs, the stent volume from post-CTs, and the ellipticity index at the selected planes, all of which could be used to estimate the right heart function, new heart valve selection, stent conditions following TPVR, and to help us gain a better understanding of the deformation of the landing zone at the native RVOT. Finally, we determined the

differences in the cross-sectional area and perimeter on the selected pulmonary artery plane and the RVOT plane by comparing the corresponding pre- and post-CTs, thus reflecting the structural changes after TPVR. Compared with anatomical 4D segmentation, this straightened model not only has the comparable accuracy of relative measurement, but it also aids in better understanding the deformation of the landing zone at the native RVOT and the implanted stent, while supporting the development of new TPVR devices that are not only morphologically appropriate for the majority of patients scheduled to undergo TPVR, but also achieve better mechanical performance in the long term. Additionally, this straightened 4D segmentation aids in determining proper valve sizing by measuring the parameters in the appropriate planes.

Methods involving 3D echocardiography, fluoroscopy imaging, and 3D C-CTA are usually employed to evaluate cross-sectional changes at the RVOT, which are based on 3D alignment and fixed-plane segmentation [16–18]. Currently, 4D C-CTA can measure and characterize the changes in heart morphology and size throughout the cardiac cycle [19]. However, the current method for 4D segmentation is based on anatomical right heart reconstruction, which can neither fully describe the features of the RVOT-PA nor reveal intuitive observations. Furthermore, there is no method to quantify the RVOT-PA using comprehensive 4D C-CTA analysis. Along with the 4D anatomical segmentation, the angle between the RVOT and the main pulmonary artery may prevent the measuring lines from perfectly aligning with the planes of the landing zone (such as the annular plane and the sinotubular junction plane, which are extremely important for TPVR), which could lead to inaccurate landing zone measurements. Additionally, as the landing zone for TPVR is not a straight conduit, this could increase the difficulty of placing the planes in the right position, as well as the measurements. In clinical practice, it is crucial to obtain the precise length of the TPVR landing zone to avoid right and/or left pulmonary artery occlusion when adapting a self-expandable stented heart valve. In addition, in the landing zone for TPVR, only the RVOT plane and main pulmonary artery plane are the "real 2D flat planes." The other three planes, STJ, sinus, and the basal plane of the pulmonary valve, are defined by three points (STJ—the three commissures; sinus—the three peaks of the sinuses; and the basal plane of the pulmonary valve—the nadir of the pulmonary valve). These three planes are virtual planes, or at least not 2D flat planes; they are characterized by 3D features. Even multi-planar measurements are widely used in clinical practice to evaluate the RVOT prior to TPVR, but planes could be placed inaccurately in anatomical segmentations due to their 3D features and the angle of observation. In this study, we applied a 4D straightened segmentation with comparable accuracy and efficacy for five planar measurements from seven pre-CTs and seven post-CTs, which not only illustrates and visualizes the right heart's total deformation throughout the cardiac cycle but also quantitatively characterizes the RVOT as a whole. All measurements at the necessary planes can be easily checked using this 4D straightened segmentation. The cross-sectional area, circumference, and max–min diameters measured from the 4D straightened models show a strong linear correlation and strong agreement with the 4D anatomical models. With the 4D straightened models from the pre-CTs, the cross-sectional area and circumference were found to vary greatly at the RVOT and the BPV compared with the other three planes, which is consistent with anatomical measurements from a previous study [12]; however, only the values at the RVOT were found to vary greatly from those derived from the post-CTs.

It is evident that single parameters alone are unable to reflect the features of the right heart clearly and comprehensively. Therefore, multiple parameters are needed to enable adequate pre- and post-TPVR evaluation of the right heart. Conventionally, cardiac function is assessed by 2D/3D echocardiography and cardiac magnetic resonance imaging (MRI) and is based mainly on the left ventricular ejection fraction (LVEF) and not the RVEF [20,21]. Furthermore, the RV volume cannot be evaluated precisely by echocardiography during clinical application due to the patient's complex anatomy after open-heart surgery and the influence of breathing. In order to address this issue and improve the evaluation, RV volume should be estimated by multiple parameters. In this context, 4D RV volume

measurements from 4D C-CTA could play an important role. We successfully segmented and calculated 4D RV volume from pre- and post-CT (Table S1) to measure the distance between the right ventricular inflow tract and the RVOT, which allowed for the innovation of the delivery system and the planning of the access route for TPVR according to the length of the delivery system from pre-CT, evaluating the RVEF perioperatively. In addition, for the pre- and post-TPVR evaluation, we defined volume among the five dynamic planes as our specific landing zone for our self-designed TPVR device and quantitatively measured the volume deformation throughout the entire cardiac cycle to obtain directly perceived motions, such as the dynamics of the landing zone volume, the implanted stent volume, and the native PV volume (Table S1). Two of the enrolled sheep (sheep F and J) were selected for a representative illustration of the 4D dynamic segmentation (Videos S1–S8). Additionally, calculating the 4D ellipticity index of the implanted stent allowed us to easily observe the stent deformations during the cardiac cycle and evaluate the stented valve size.

The morphology of the implanted stent after full deployment is crucial for the new heart valve to function. Improper morphology of the implanted stent could give rise to a paravalvular leak or new heart valve regurgitation and could result in an inefficient opening area, which could lead to poor long-term performance [9,11,22]. In order to prevent the improper morphology of the implanted stent, a better understanding of the anatomy and device innovation are critical. We calculated the 4D ellipticity index of the landing zone from pre- and post-CT, which showed a lower ellipticity index at the RVOT and the BPV planes compared with the three other planes from pre-CT, while only the RVOT had a lower ellipticity index in post-CT because of the fixation of the implanted stent. The oval geometry of the BPV is an indicator of whether patients will benefit from TPVR because the myocardium at the BPV level would squeeze the stent into an undesirable geometry during the systolic phase, which could lead to an inefficient opening area in the new heart valve. The changes in the cross-sectional area and circumference during the cardiac cycle should also be taken into account for proper valve sizing, which is conventionally performed within 3D C-CTA by selecting the end-diastolic phase. However, based on the results of our study, it may be more expedient to select the mid-systolic phase for valve sizing because the largest cross-sectional area and circumference at the BPV and the STJ could prevent an elliptical geometry in the implanted stent. Additionally, a comprehensive evaluation of the "neighborhood" surrounding the left coronary artery is required. This could also encourage medical engineers to develop elliptical stents and heart valves with new features.

This study has several limitations. First, the accuracy and feasibility of the 4D straightened model were only demonstrated with seven pre-CTs and seven post-CTs, and need to be further proven with a larger population. Additionally, all pre-CTs were obtained from healthy sheep without any congenital heart defects. For clinical application, especially in patients who have undergone transannular patch repair/Ross procedures or other open-heart surgeries, additional work would be required to reconstruct the heart's architecture due to artifacts from adhesions between the pericardium and the myocardium, the stent, and the distorted anatomy. To our knowledge, two major artefacts that significantly affect CT imaging accuracy are the blooming artefact and cardiac movement artefact [23,24]. With technical innovation, by reducing image noises and blooming artefacts, iterative reconstruction (IR) algorithms have the potential to enhance the quality of CT images. Compared to in vivo data, imaging data created from patient-specific models could provide accurate patient-specific geometry parameters without motion artefacts. However, in future studies, the acquisition times and contrast resolutions of scanners still need to be improved to obtain higher accuracy in CT imaging, which would improve the evaluation of TPVR outcomes.

5. Conclusions

Four-dimensional straightened segmentation can be a useful method for periprocedural evaluations for TPVR and could assist TPVR device innovation in the future.

6. Patents

There is no patent resulting from the work reported in this manuscript.

Supplementary Materials: The following supporting information can be downloaded at https://www.mdpi.com/article/10.3390/app122412912/s1, Table S1: The mean value of parameters for each plane during the cardiac cycle; Table S2: Ellipticity index for each plane during the cardiac cycle; Video S1: The deformation of 4D reconstructed anatomical segmentation from sheep F's pre-CT. Anterior view of the anatomical 4D segmentation with landing zone markers at the five selected planes, 1–6 s. Posterior view of the anatomical 4D segmentation with landing zone markers at the five selected planes, 6–13 s. Superior view of the anatomical 4D segmentation with landing zone markers at the five selected planes, 13–19 s; Video S2: The deformation of 4D reconstructed straightened segmentation from sheep F's pre-CT. Anterior view of the straightened 4D segmentation with landing zone markers at the five selected planes, 1–6 s. Posterior view of the straightened 4D segmentation with landing zone markers at the five selected planes, 6–13 s. Superior view of the straightened 4D segmentation with landing zone markers at the five selected planes, 13–19 s; Video S3: The deformation of 4D reconstructed anatomical segmentation from sheep F's post-CT. Anterior view of the anatomical 4D segmentation with landing zone markers at the five selected planes (with/without the implanted stent), 1–23 s. Posterior view of the anatomical 4D segmentation with landing zone markers at the five selected planes (with/without the implanted stent), 23–46 s. Superior view of the anatomical 4D segmentation with landing zone markers at the five selected planes (with/without the implanted stent), 46–69 s; Video S4: The deformation of 4D reconstructed straightened segmentation from sheep F's post-CT. Anterior view of the straightened 4D segmentation with landing zone markers at the five selected planes (with/without the implanted stent), 1–12 s. Posterior view of the straightened 4D segmentation with landing zone markers at the five selected planes (with/without the implanted stent), 12–24 s. Superior view of the straightened 4D segmentation with landing zone markers at the five selected planes (with/without the implanted stent), 24–37 s; Video S5: The deformation of 4D reconstructed anatomical segmentation from sheep J's pre-CT. Anterior view of the anatomical 4D segmentation with landing zone markers at the five selected planes, 1–6 s. Posterior view of the anatomical 4D segmentation with landing zone markers at the five selected planes, 6–13 s. Superior view of the anatomical 4D segmentation with landing zone markers at the five selected planes, 13–19 s; Video S6: The deformation of 4D reconstructed straightened segmentation from sheep J's pre-CT. Anterior view of the straightened 4D segmentation with landing zone markers at the five selected planes, 1–6 s. Posterior view of the straightened 4D segmentation with landing zone markers at the five selected planes, 6–13 s. Superior view of the straightened 4D segmentation with landing zone markers at the five selected planes, 13–20 s; Video S7: The deformation of 4D reconstructed anatomical segmentation from sheep J's post-CT. Anterior view of the anatomical 4D segmentation with landing zone markers at the five selected planes (with/without the implanted stent), 1–13 s. Posterior view of the anatomical 4D segmentation with landing zone markers at the five selected planes (with/without the implanted stent), 13–25 s. Superior view of the anatomical 4D segmentation with landing zone markers at the five selected planes (with/without the implanted stent), 25–38 s; Video S8: The deformation of 4D reconstructed straightened segmentation from sheep J's post-CT. Anterior view of the straightened 4D segmentation with landing zone markers at the five selected planes (with/without the implanted stent), 1–12 s. Posterior view of the straightened 4D segmentation with landing zone markers at the five selected planes (with/without the implanted stent), 12–24 s. Superior view of the straightened 4D segmentation with landing zone markers at the five selected planes (with/without the implanted stent), 24–37 s.

Author Contributions: Conceptualization, X.S., Y.H. and B.S.; methodology, X.S., Y.H. and B.S.; validation, X.S., Y.H. and B.S.; formal analysis, Y.H. and B.S.; investigation, X.S., Y.H., M.S., A.B.-A., J.F.S.K., J.E., M.B.K., F.B. and B.S.; resources, X.S., Y.H., M.S., A.B.-A., J.F.S.K., J.E., M.B.K., F.B. and B.S.; data curation, Y.H.; writing—original draft preparation, X.S., Y.H. and B.S.; writing—review and editing, Y.H., F.B. and B.S.; visualization, X.S., Y.H., M.S., A.B.-A., J.F.S.K., J.E., M.B.K., F.B. and B.S.; supervision, B.S. and F.B.; project administration, X.S., Y.H. and B.S.; funding acquisition, B.S. All authors have read and agreed to the published version of the manuscript.

Funding: This research was funded by from the German Federal Ministry for Economic Affairs and Energy, EXIST—Transfer of Research (03EFIBE103).Xiaolin Sun and Yimeng Hao are supported by the China Scholarship Council (Xiaolin Sun-CSC: 201908080063, Yimeng Hao-CSC: 202008450028). Xiaolin Sun is supported by a doctoral scholarship from Deutsches Zentrum für Herz-Kreislauf-Forschung (DZHK) e.V.

Institutional Review Board Statement: The animal study protocol, involving transcatheter pulmonary valve replacement from autologous pericardium with a self-expandable stent in a sheep model, was approved by the Ethics Committee of the Regional Office for Health and Social Affairs in Berlin (LaGeSo) (protocol code: IC14 g 0062/18, date of approval: 16 August 2018).

Informed Consent Statement: Not applicable.

Data Availability Statement: The data presented in this study are available in Supplementary Material.

Acknowledgments: We extend our heartfelt appreciation to all who contributed to this work, both past and present members. This work is supported by DZHK (German Center for Cardiovascular Research) and the grants from the German Federal Ministry for Economic Affairs and Energy, EXIST—Transfer of Research (03EFIBE103). Xiaolin Sun and Yimeng Hao are supported by the China Scholarship Council (Xiaolin Sun-CSC: 201908080063, Yimeng Hao-CSC: 202008450028). Xiaolin Sun is supported by a doctoral scholarship from DZHK (German Center for Cardiovascular Research).

Conflicts of Interest: The authors declare no conflict of interest.

References

1. Bonhoeffer, P.; Boudjemline, Y.; Saliba, Z.; Merckx, J.; Aggoun, Y.; Bonnet, D.; Acar, P.; Le Bidois, J.; Sidi, D.; Kachaner, J. Percutaneous replacement of pulmonary valve in a right-ventricle to pulmonary-artery prosthetic conduit with valve dysfunction. *Lancet* **2000**, *356*, 1403–1405. [CrossRef]
2. Georgiev, S.; Ewert, P.; Eicken, A.; Hager, A.; Hörer, J.; Cleuziou, J.; Meierhofer, C.; Tanase, D. Munich Comparative Study: Prospective Long-Term Outcome of the Transcatheter Melody Valve Versus Surgical Pulmonary Bioprosthesis With Up to 12 Years of Follow-Up. *Circ. Cardiovasc. Interv.* **2020**, *13*, e008963. [CrossRef] [PubMed]
3. McElhinney, D.B.; Zhang, Y.; Aboulhosn, J.A.; Morray, B.H.; Biernacka, E.K.; Qureshi, A.M.; Torres, A.J.; Shahanavaz, S.; Goldstein, B.H.; Cabalka, A.K.; et al. Multicenter Study of Endocarditis After Transcatheter Pulmonary Valve Replacement. *J. Am. Coll. Cardiol.* **2021**, *78*, 575–589. [CrossRef] [PubMed]
4. McElhinney, D.B.; Zhang, Y.; Levi, D.S.; Georgiev, S.; Biernacka, E.K.; Goldstein, B.H.; Shahanavaz, S.; Qureshi, A.M.; Cabalka, A.K.; Bauser-Heaton, H.; et al. Reintervention and Survival After Transcatheter Pulmonary Valve Replacement. *J. Am. Coll. Cardiol.* **2022**, *79*, 18–32. [CrossRef] [PubMed]
5. Chatterjee, A.; Bajaj, N.S.; McMahon, W.S.; Cribbs, M.G.; White, J.S.; Mukherjee, A.; Law, M.A. Transcatheter Pulmonary Valve Implantation: A Comprehensive Systematic Review and Meta-Analyses of Observational Studies. *J. Am. Heart Assoc.* **2017**, *6*, e006432. [CrossRef] [PubMed]
6. Rinaldi, E.; Sadeghi, S.; Rajpal, S.; Boe, B.A.; Daniels, C.; Cheatham, J.; Sinha, S.; Levi, D.S.; Aboulhosn, J. Utility of CT Angiography for the Prediction of Coronary Artery Compression in Patients Undergoing Transcatheter Pulmonary Valve Replacement. *World J. Pediatr. Congenit. Heart Surg.* **2020**, *11*, 295–303. [CrossRef]
7. Elattar, M.A.; Vink, L.W.; van Mourik, M.S.; Baan, J., Jr.; vanBavel, E.T.; Planken, R.N.; Marquering, H.A. Dynamics of the aortic annulus in 4D CT angiography for transcatheter aortic valve implantation patients. *PLoS ONE* **2017**, *12*, e0184133. [CrossRef]
8. Ooms, J.F.; Wang, D.D.; Rajani, R.; Redwood, S.; Little, S.H.; Chuang, M.L.; Popma, J.J.; Dahle, G.; Pfeiffer, M.; Kanda, B.; et al. Computed Tomography-Derived 3D Modeling to Guide Sizing and Planning of Transcatheter Mitral Valve Interventions. *JACC Cardiovasc. Imaging* **2021**, *14*, 1644–1658. [CrossRef]
9. Pluchinotta, F.R.; Sturla, F.; Caimi, A.; Giugno, L.; Chessa, M.; Giamberti, A.; Votta, E.; Redaelli, A.; Carminati, M. 3-Dimensional personalized planning for transcatheter pulmonary valve implantation in a dysfunctional right ventricular outflow tract. *Int. J. Cardiol.* **2020**, *309*, 33–39. [CrossRef]
10. Chung, R.; Taylor, A.M. Imaging for preintervention planning: Transcatheter pulmonary valve therapy. *Circ. Cardiovasc. Imaging* **2014**, *7*, 182–189. [CrossRef]
11. Curran, L.; Agrawal, H.; Kallianos, K.; Kheiwa, A.; Lin, S.; Ordovas, K.; Mahadevan, V.S. Computed tomography guided sizing for transcatheter pulmonary valve replacement. *Int. J. Cardiol. Heart Vasc.* **2020**, *29*, 100523. [CrossRef] [PubMed]
12. Schievano, S.; Capelli, C.; Young, C.; Lurz, P.; Nordmeyer, J.; Owens, C.; Bonhoeffer, P.; Taylor, A.M. Four-dimensional computed tomography: A method of assessing right ventricular outflow tract and pulmonary artery deformations throughout the cardiac cycle. *Eur. Radiol.* **2011**, *21*, 36–45. [CrossRef] [PubMed]
13. Gillespie, M.J.; Benson, L.N.; Bergersen, L.; Bacha, E.A.; Cheatham, S.L.; Crean, A.M.; Eicken, A.; Ewert, P.; Geva, T.; Hellenbrand, W.E.; et al. Patient Selection Process for the Harmony Transcatheter Pulmonary Valve Early Feasibility Study. *Am. J. Cardiol.* **2017**, *120*, 1387–1392. [CrossRef] [PubMed]

14. Sun, X.; Hao, Y.; Sebastian Kiekenap, J.F.; Emeis, J.; Steitz, M.; Breitenstein-Attach, A.; Berger, F.; Schmitt, B. Four-Dimensional Computed Tomography-Guided Valve Sizing for Transcatheter Pulmonary Valve Replacement. *Thorac. Cardiovasc. Surg.* **2022**, *70*, S67–S103. [CrossRef]
15. Hao, Y.; Sun, X.; Kiekenap, J.F.S.; Emeis, J.; Steitz, M.; Breitenstein-Attach, A.; Berger, F.; Schmitt, B. Transcatheter Pulmonary Valve Replacement from Autologous Pericardium with a Self-Expandable Nitinol Stent in an Adult Sheep Model. *J. Vis. Exp.* **2022**. [CrossRef]
16. Kang, S.L.; Benson, L. Recent advances in cardiac catheterization for congenital heart disease. *F1000Res* **2018**, *7*, 370. [CrossRef]
17. Kovács, A. 3D Echocardiography: Toward a Better Understanding of Cardiac Anatomy and Function. *J. Vis. Exp.* **2021**. [CrossRef]
18. Krishnaswamy, A.; Tuzcu, E.M.; Kapadia, S.R. Integration of MDCT and fluoroscopy using C-arm computed tomography to guide structural cardiac interventions in the cardiac catheterization laboratory. *Catheter. Cardiovasc. Interv.* **2015**, *85*, 139–147. [CrossRef]
19. Kidoh, M.; Utsunomiya, D.; Funama, Y.; Ashikaga, H.; Nakaura, T.; Oda, S.; Yuki, H.; Hirata, K.; Iyama, Y.; Nagayama, Y.; et al. Vectors through a cross-sectional image (VCI): A visualization method for four-dimensional motion analysis for cardiac computed tomography. *J. Cardiovasc. Comput. Tomogr.* **2017**, *11*, 468–473. [CrossRef]
20. Kucukseymen, S.; Arafati, A.; Al-Otaibi, T.; El-Rewaidy, H.; Fahmy, A.S.; Ngo, L.H.; Nezafat, R. Noncontrast Cardiac Magnetic Resonance Imaging Predictors of Heart Failure Hospitalization in Heart Failure With Preserved Ejection Fraction. *J. Magn. Reson. Imaging* **2022**, *55*, 1812–1825. [CrossRef]
21. Ostvik, A.; Salte, I.M.; Smistad, E.; Nguyen, T.M.; Melichova, D.; Brunvand, H.; Haugaa, K.; Edvardsen, T.; Grenne, B.; Lovstakken, L. Myocardial Function Imaging in Echocardiography Using Deep Learning. *IEEE Trans. Med. Imaging* **2021**, *40*, 1340–1351. [CrossRef] [PubMed]
22. Condado, J.F.; Corrigan, F.E., 3rd; Lerakis, S.; Parastatidis, I.; Stillman, A.E.; Binongo, J.N.; Stewart, J.; Mavromatis, K.; Devireddy, C.; Leshnower, B.; et al. Anatomical risk models for paravalvular leak and landing zone complications for balloon-expandable transcatheter aortic valve replacement. *Catheter. Cardiovasc. Interv.* **2017**, *90*, 690–700. [CrossRef] [PubMed]
23. De Ponti, E.; Morzenti, S.; Crivellaro, C.; Elisei, F.; Crespi, A.; Guerra, L. Motion Management in PET/CT: Technological Solutions. *Curr. Radiopharm.* **2018**, *11*, 79–85. [CrossRef] [PubMed]
24. Liu, H.; Wingert, A.; Wang, J.; Zhang, J.; Wang, X.; Sun, J.; Chen, F.; Khalid, S.G.; Jiang, J.; Zheng, D. Extraction of Coronary Atherosclerotic Plaques From Computed Tomography Imaging: A Review of Recent Methods. *Front. Cardiovasc. Med.* **2021**, *8*, 597568. [CrossRef]

applied sciences

MDPI

Article

Handling Extensive Mitral Annular Calcification via a Minimally Invasive Right Mini-Thoracotomy Approach

Cristina Barbero [1,*], Antonio Spitaleri [1], Marco Pocar [1,2], Barbara Parrella [1], Ambra Santonocito [3], Elena Bozzo [3], Alessandro Depaoli [3,4], Riccardo Faletti [3] and Mauro Rinaldi [1]

[1] Division of Cardiac Surgery, Città della Salute e della Scienza & Department of Surgical Sciences, University of Turin, Corso Dogliotti 14, 10126 Turin, Italy
[2] Department of Clinical Sciences and Community Health, University of Milan, 20122 Milan, Italy
[3] 1st Unit of Radiology, Department of Surgical Sciences, University of Turin, 10124 Turin, Italy
[4] Unit of Radiology, Diagnostic Area Department, Hospital of Ivrea ASL TO4, 10015 Ivrea, Italy
* Correspondence: cristina.barbero@unito.it; Tel.: +39-011-6335511; Fax: +39-011-6336130

Abstract: Mitral annular calcification is a chronic and degenerative process of the fibrous base of the mitral valve. Surgical management of mitral valve dysfunction with severe annular calcification remains technically demanding and, to date, the preferred approach is still a standard full sternotomy. We aimed to analyze and report our experience with mitral valve surgery addressing annular calcification via the minimally invasive approach through a right mini-thoracotomy. Data of patients with mitral valve disease and underlying annular calcification undergoing minimally invasive surgery from 2018 to 2022 were prospectively collected and retrospectively analyzed. The severity of mitral annular calcification was categorized with an angio-computerized tomography scan analysis as mild, moderate or severe according to calcium thickness, calcium distribution, and trigone and leaflet involvement using the Mitral Annular Calcification Computerized Tomography-score. During the study period, 27 patients with mitral valve disease and associated mitral annular calcification were enrolled. The most common etiology was advanced Barlow's disease, which was encountered in 18 cases (67%). Mitral valve replacement was performed in 21 patients (78%). No intraoperative death, atrioventricular disruption, or circumflex coronary artery injury occurred. Conversion to sternotomy was necessary in a single case. Residual moderate periprosthetic leak requiring early reoperation and permanent heart block mandating permanent pacemaker implantation were reported in one and in three patients, respectively. No cases of stroke were reported. Two patients died, accounting for a 7.4% perioperative mortality. At a median follow-up of 9 months, one patient had residual moderate mitral regurgitation, whereas two patients required short-term reoperation and prosthetic valve (re)replacement. Minimally invasive mitral valve surgery via right mini-thoracotomy should be considered an and effective approach to be indicated also in patients with mild-to-severe mitral annular calcification. Routine angio-computerized tomography scan during work-up is a mandatory step to stratify the anatomical extension and severity of the mitral annular calcification.

Keywords: mitral valve; minimally invasive cardiac surgery; mitral annular calcification; Barlow's disease; mitral valve repair; mitral valve replacement; mitral valve prolapse; cardiac rupture

Citation: Barbero, C.; Spitaleri, A.; Pocar, M.; Parrella, B.; Santonocito, A.; Bozzo, E.; Depaoli, A.; Faletti, R.; Rinaldi, M. Handling Extensive Mitral Annular Calcification via a Minimally Invasive Right Mini-Thoracotomy Approach. *Appl. Sci.* **2023**, *13*, 2563. https://doi.org/10.3390/app13042563

Academic Editor: Julio Garcia Flores

Received: 5 December 2022
Revised: 15 January 2023
Accepted: 30 January 2023
Published: 16 February 2023

1. Introduction

Mitral annular calcification (MAC) is a chronic and degenerative process of the fibrous base of the mitral valve (MV). Most commonly, MAC extends along the hinge of a variable portion of the posterior mitral annulus, but at times may extend to the body of the MV leaflets, to the anterior MV annulus, to one or more of the MV papillary muscles, to the posterior free wall of the left ventricle, and to the left atrium. The prevalence of MAC in the general population may reach 8 to 15% and it is associated with advanced age, female gender, risk factors for cardiovascular disease, atrial fibrillation, and variable degrees

of chronic kidney disease [1–3]. Overall, evidences in the literature depict an increased incidence of MV stenosis or regurgitation, or both, and arrhythmias in patients with MAC. Not surprisingly, the reported outcomes following MV surgery in patients with associated MAC are often less than satisfactory.

Since MAC may be viewed as a relative contraindication for surgery, the surgical management of MV dysfunction, particularly in the occurrence of severe MAC, remains a controversial issue and always implies one of the most technically demanding scenarios in contemporary adult cardiac surgery. MV operations in patients with MAC portend a higher risk of technical injury of perivalvular structures, namely, circumflex coronary injury, paravalvular leak, patient-prosthesis mismatch, and atrioventricular groove disruption [2,4,5].

In this anatomically challenging context, the preferred approach by the vast majority of cardiac surgeons is still a standard full sternotomy, and only few centers have reported limited experiences through a minimally invasive access. This is primarily dictated by the reluctance to approach the anatomical difficulties in suturing through heavily calcified annular or perivalvular tissues and effectively positioning prosthetic devices via a restricted and, at times, deep operative field. In recent years, however, institutions with long-standing experience with mini-thoracotomy MV operations have progressively extended indications also to include patients with MAC.

We aimed to analyze and report our experience with MV surgery addressing MAC via the minimally invasive approach through a right mini-thoracotomy.

2. Patients and Methods

2.1. Study Design

An observational study consisting of retrospective analysis on prospectically collected data related to patients with MAC undergoing minimally invasive MV operations since September 2018 was undertaken. Associated cardiac procedures were exclusion criteria, except for those accessible through one or more atrial incisions, most typically tricuspid valve repair or replacement, radiofrequency or cryoablation for atrial fibrillation, and atrial septal defect or patent foramen ovale closure. The study design was approved by our Institutional Review Board (protocol number 0095187). Clinical and echocardiographic follow-up was carried out through hospital outpatient controls, telephone interviews, or both. Median follow-up was 271 days (interquartile range, 102–671 days), and was 100% complete.

2.2. Echocardiographic Evaluation

Echocardiography is the preferred imaging tool to assess valvular disease. Although, traditionally, MAC may be suspected or diagnosed on chest radiographs or more clearly on cine angiograms, which also serve to define the anatomical relationships with the coronary circulation, echocardiography represents the first-line step to depict the diseased MV with MAC. More in particular, transesophageal imaging is mandatory to define leaflet involvement by the calcification and secondary restricted motion, along with the corresponding variable degree of stenosis or regurgitation, or more often both. Extension of the MAC deep into the posterior basal or, at times, mid portion of the left ventricular free must be mandatorily assessed to estimate the risk of disruption. Also the extension of the MAC to the subaortic curtain and eventual involvement of the aortic valve must be excluded when planning the feasibility of a minimally invasive MV operation. Some degree of mild or mild-to-moderate aortic insufficiency is common in this clinical setting and can safely be tolerated, whereas more severe aortic incompetence would jeopardize the effective delivery of cardioplegia in the aortic root. Three-dimensional transesophageal echocardiography is also useful to simulate the MV anatomy as viewed by the surgeon from the left atrial side. Whereas echocardiography well depicts the dynamics of the MV and MAC during the cardiac cycle, we now routinely indicate computed tomography (CT) scan to better define the density of the MAC.

2.3. Computed Tomography Imaging

The protocol included preoperative CT scan to assess and stratify the severity of the MAC in all patients. Imaging analysis was performed by two experienced radiologists. The DICOM "OsiriX MD" viewer was used for post-processing, whereby a short-axis view of the MV annulus was obtained by means of multiplanar reformatting (MPR). Mitral annular analysis was carried out through angio-CT scan with or without cardiac gating, or through basal CT scan (Figure 1). MAC severity was categorized as mild, moderate or severe according to calcium thickness, calcium distribution, and trigone and leaflet involvement using a MAC CT-score ranging from a minimum of 1 to a maximum of 10 (Figure 2). Each category was further divided into three subgroups of severity. Briefly, the MAC was considered mild with a score from 1 to 3 points, moderate from 4 to 6 and severe when the score reached or exceeded 7 points [6]. From a surgical standpoint the annular extension of the MAC is a crucial issue, with extreme circumferential 360° lesions being the most difficult to approach.

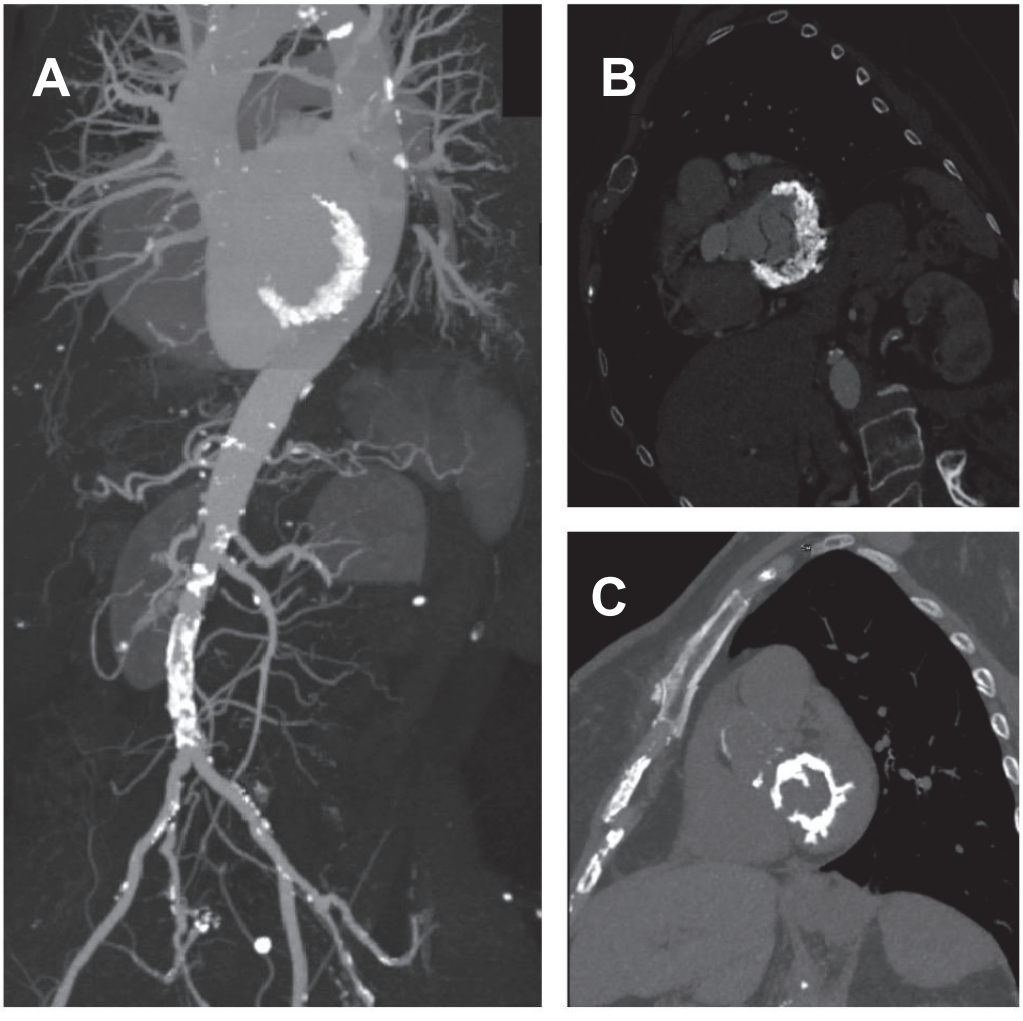

Figure 1. Severe MAC. (**A**,**B**): Heavily calcified annulus with a calcium thickness > 10 mm. (**C**): Calcium infiltration of the left ventricular free wall.

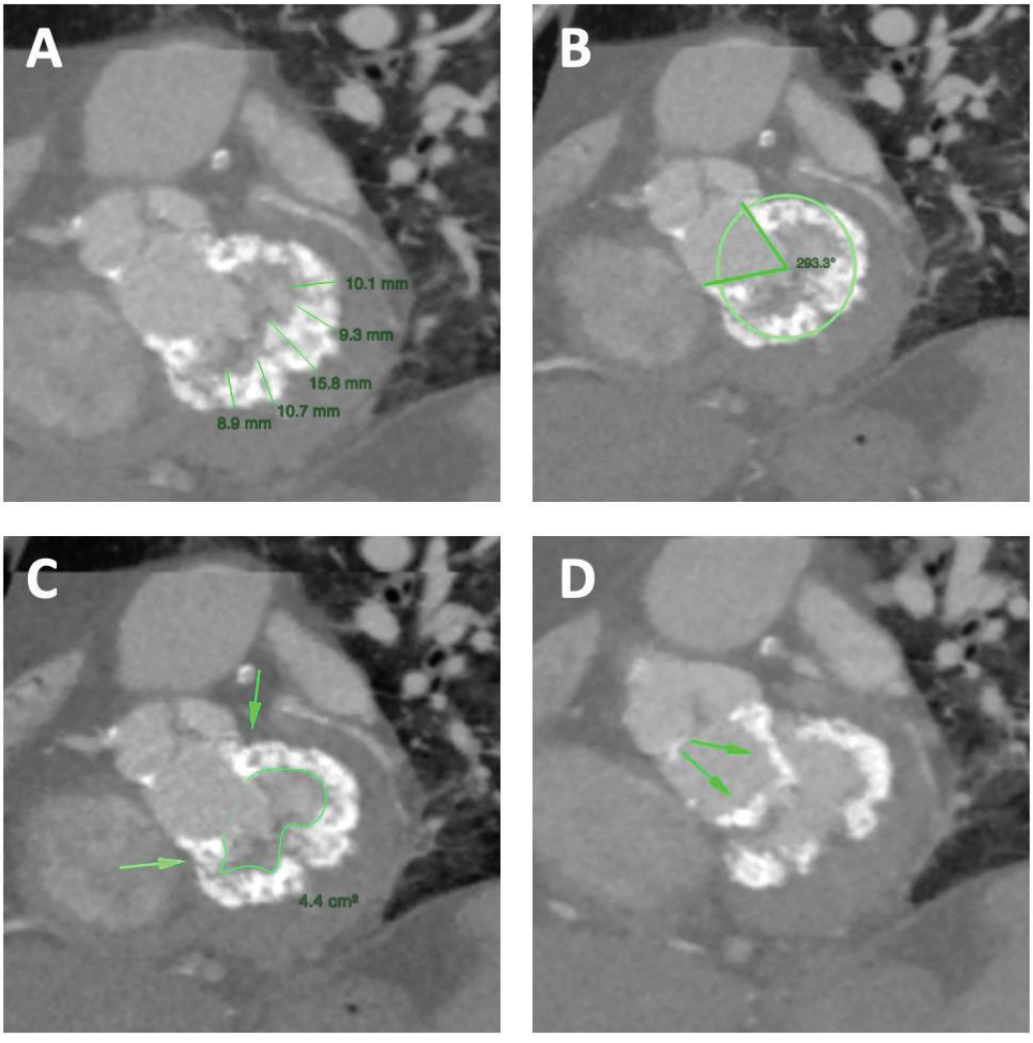

Figure 2. Cardiac computed tomography-based measurements of MAC using DICOM "OsiriX MD" viewer. (**A**) Calcium thickness measurement simulating a surgical short axis view. (**B**) Calcium distribution along the perimeter of the annulus. (**C**) Trigone involvement (arrows) and internal area of the annulus. (**D**) Leaflet involvement (arrows).

2.4. Surgical Technique

The right mini-thoracotomy approach, perfusion strategies and aortic clamping techniques adopted at our institution have been described previously [7–12]. Briefly, a double lumen endotracheal tube was positioned to allow single left lung ventilation. All patients underwent operation through a right anterolateral mini-thoracotomy in the fourth intercostal space. A soft-tissue retractor was used to expose the surgical port. No rib resection was performed in any of the patients. To improve the vision, an endoscope was inserted in an accessory port created below the working port, which also served for carbon dioxide insufflation to saturate the chest and minimize the hazards of air trapping and systemic embolism. An additional sixth intercostal space port was created for pump suction. After full heparinization, cardiopulmonary bypass was established with the patient cooled to

28–32 °C, depending on the anticipated complexity of the operation. Arterial perfusion was routinely gained with a peripheral femoral or axillary cannulation, while venous drainage was obtained via double femoral and percutaneous jugular cannulation. Axillary cannulation was indicated to provide antegrade systemic perfusion in the case of severe atherosclerotic burden [9].

Aortic clamping strategies adopted during the study period were the endoaortic clamping occlusion and the trans-thoracic clamp. In the endoaortic clamping setting, aortic occlusion and cardioplegia delivery were gained with a balloon catheter inserted through the sidearm of a 21–23F femoral arterial cannula (Intraclude®, Edwards Lifesciences, Irvine, CA, USA). In the trans-thoracic clamping setting the clamp was addressed towards the ascending aorta through the first intercostal space with a Chitwood clamp or through the main port with a Cygnet® flexible clamp. Cardioplegia was delivered through a 7F cardioplegia needle (CalMed Technologies, Santa Inez, CA, USA) placed into the proximal ascending aorta. Antegrade myocardial protection was provided with St. Thomas (Plegisol™, Hospira Inc., Lake Forest, IL, USA) or, more commonly, Custodiol (Bretschneider histidine, tryptophan, ketoglutarate solution, Köhler Chemie, Bensheim, Germany) cold crystalloid cardioplegia [12]. No additional topical cooling, nor retrograde cardioplegia through the coronary sinus, were used on any patient. Superior and inferior vena cava snaring was obtained by placing tourniquets around the vessels or by placing endovascular balloons (7F, 65 cm) (Meditech Boston Scientific Corporation, Natick, MA, USA) to provide a temporary mini right atriotomy to drain the cardioplegic solution and in patients requiring associated right atrial procedures.

The MV was exposed through a standard left atriotomy, parallel and posterior to the interatrial septum with minimal dissection of the interatrial groove. The extension of the calcification bar, leaflet involvement and the chances of valve repair were assessed. In case of valve replacement, the anterior leaflet was resected, while the posterior leaflet and corresponding chordae were left intact whenever possible to minimize the hazards of fragilization of the atrioventricular junction. In general, the least possible debridement was undertaken, primarily aimed to remove only protruding calcium which might interfere with the proper seating of the prosthesis. Nevertheless, a variable extension of posterior leaflet resection, possibly leaving in place the basal chordae, was unavoidable in some cases. Non-everting polyester 2-0 pledgetted mattress sutures were passed through the calcium just deep enough to encircle the annulus with the MAC itself, taking care to avoid injury to the circumflex artery and to the His bundle in proximity of the right trigone. In the case of caseous abscess collections, the cavity was debrided and excluded directly with the sutures used to secure the prosthetic valve. Extensive and aggressive annular decalcification was preferably avoided. Clamp release was obtained at the end of appropriate air venting at a core temperature above 33 °C.

Although we now consider this step unneccesary in younger and healthier patients undergoing minimally invasive MV operations, two epicardial temporary pacing wires were routinely placed on the right ventricle before unclamping, in relation to the hazards of atrioventricular conduction disturbances. Importantly, the latter may ensue at a later onset in the intensive care unit. This did not apply to patients with prior permanent pacemaker implantation.

Intraoperative transesophageal echocardiography was used in all the patients to guide the correct positioning of the cannulae before the onset of cardiopulmonary bypass and to analyze cardiac function, residual MV regurgitation, paravalvular leaks, and prosthetic valve gradients after the intracardiac phase of the operation.

2.5. Definitions of Adverse Events

Perioperative myocardial infarction is defined as cardiac troponin T value >10 times the 99th percentile of the upper reference limit during the first postoperative 48 h with associated electrocardiographic abnormalities and/or angiographic or imaging evidence of new onset myocardial ischemia and/or new loss of myocardial viability [13]. Low

cardiac output syndrome refers to a cardiac index lower than 2 L/min/m^2 and systolic blood pressure lower than 90 mmHg, in conjunction with signs of tissue hypoperfusion (cold periphery, clammy skin, confusion, oliguria, elevated lactate level) in the absence of hypovolemia [14]. Postoperative stroke refers to a new onset, permanent neurological disability or deficit [15]. Perioperative mortality includes all deaths occurring during hospitalization or within 30 days of the surgical procedure.

3. Results

During the study period 538 patients underwent minimally invasive MV surgery at our institution. MAC was diagnosed preoperatively and assessed with the CT scan protocol in 27 (5%). Baseline characteristics are reported in Table 1. Mean age was 71 years and the majority of patients were women (20/27, 74%). The most common etiology was advanced Barlow's disease or fibroelastic deficiency (18/27, 67%), whereas 4 cases were reoperations (15%). Long standing persistent atrial fibrillation was reported in 12 patients (44%).

Table 1. Preoperative characteristics (n = 27).

Age (Years)	71 ± 13
Female	20 (74)
BMI (kg/m^2)	23 ± 5
Euroscore II (%)	5 ± 6
Logistic Euroscore I (%)	10 ± 11
Diabetes	5 (19)
eGFR (mL/min/1.73 m^2)	53 ± 25
Previous cardiac surgery	4 (15)
LVEF (%)	62 ± 9
PAPs (mmHg)	45 ± 17
MV dysfunction	
Regurgitation	20 (74)
Regurgitation and stenosis	7 (26)
Moderate to severe tricuspid valve regurgitation	9 (33)
MV disease etiology	
Barlow/FED	18 (67)
Degenerative fibro-calcific	4 (15)
Rheumatic	3 (11)
Endocarditis	1 (4)
Failure of previous repair	1 (4)

SD: standard deviation; BMI: body mass index; eGFR: estimated glomerular filtration rate; LVEF: left ventricular ejection fraction; PAPs: pulmonary artery pressure, systolic; MV: mitral valve; FED: fibroelastic deficiency. Data are expressed as mean ± SD or as n (%).

All the patients enrolled underwent CT scan examination. Intravenous non-ionic contrast agents for cardiac gating were used in 16 patients (59%). In the latter, the analysis was performed with a Revolution CT (GE Healthcare, General Electric) scanner. Eight patients (30%) underwent standard angio CT examination, while 3 patients (11%) underwent basal CT examination. The degree of MAC severity is reported in Table 2.

Intraoperative data and postoperative outcomes are reported in Table 3. MV replacement was performed in 21 patients (78%), of whom 9 were diagnosed with severe MAC, whereas 12 showed a mild to moderate MAC. Bioprosthetic pericardial (Carpentier-Edwards Magna Ease, Edwards Lifesciences, Irvine, CA, USA) or porcine (Mosaic™, Medtronic Inc., Minneapolis, MN, USA) valves were used in almost all of the patients (20/21, 95%), confining mechanical MV replacement to a single case. The mean size in the implanted prosthetic valves was 27 ± 2.6. In the 6 patients undergoing MV repair, two patients had a severe degree of MAC, while four had mild to moderate MAC. Annuloplasty alone was sufficient in 3 patients (50%) whereas leaflet resection or artificial chordae in ePTFE (W. L. Gore & Associates Inc., Flagstaff, AZ, USA) were used in the remaining.

Table 2. Calcium distribution and MAC CT grading (n = 27).

Calcium thickness	
<5 mm	4 (15)
5–10 mm	11 (41)
>10 mm	12 (44)
Calcium distribution	
>180°	10 (37)
180°–270°	12 (44)
>270°	5 (19)
Trigones involved	
None	20 (74)
One	7 (26)
Two	–
Leaflets involved	
None	–
One	14 (52)
Two	13 (48)
MAC CT grading	
Mild	3 (11)
Moderate	13 (48)
Severe	11 (41)

MAC: mitral annular calcification; CT: computed tomography. Data are expressed as n (%).

Table 3. Intraoperative variables and postoperative outcomes (n = 27).

MV repair	6 (22)
Annuloplasty ring	6 (100)
Posterior leaflet resection	3 (50)
Artificial chords	2 (33)
MV replacement, prosthesis	21 (78)
Biological	20 (95)
Mechanical	1 (5)
Extensive annular decalcification	5 (19)
Concomitant TV Surgery	6 (22)
RAP	20 (74)
EAC	7 (26)
TTC	19 (70)
CPB (mins)	147 (127–173)
Cross-clamp (mins)	106 (84–119)
Conversion to sternotomy	1 (4)
Redo for early failure	1 (4)
Re-exploration for bleeding	2 (7)
Permanent PM implantation	3 (11)
Low cardiac output syndrome	4 (15)
Acute kidney injury	1 (4)
Dialysis	2 (7)
Vascular complication	1 (4)
Stroke	–
Perioperative myocardial infarction	–
Mechanical ventilation (hours)	15 (10–22)
ICU stay (days)	1 (1–1)
Hospital-stay (days)	7 (7–9)
30-day mortality	2 (7)
FU MV regurgitation, moderate or more	2 (7)
FU patient prosthesis mismatch (n=21)	
None or mild	19 (90)
Moderate	2 (10)
Severe	–

Table 3. *Cont.*

FU iEOA (cm^2/m^2)	1.44 ± 0.29
Follow-up (days)	271 (102–671)

MV: mitral valve; TV: tricuspid valve; RAP: retrograde arterial perfusion; EAC: endo-aortic clamp; TTC: transthoracic clamp; CPB: cardio-pulmonary bypass; IQR: interquartile range; SD: standard deviation; ICU: intensive care unit; FU: follow-up; iEOA: indexed effective orifice area. Data are expressed as median (IQR), mean ± SD, or n (%).

Extensive annular decalcification was unavoidable in 5 patients (18%) because of the impossibility to pass the sutures through the calcific bar in extremely severe MAC.

No cases of intraoperative death, atrioventricular disruption, or circumflex coronary artery injury occurred. Conversion to sternotomy was necessary in one case due to extremely unfavorable chest anatomy, with the impossibility to safely gain sufficient exposure of the ascending aorta to ensure adequate cross-clamp and safe myocardial protection.

Residual moderate periprosthetic leak requiring early reoperation on the first postoperative day, and permanent heart block requiring permanent pacemaker implantation were reported in one and in three patients, respectively. Importantly, stroke rate was zero. Two patients died, accounting for an operative mortality of 7.4%. The causes of death were multiorgan failure and septic shock on postoperative day 24 in the former, and multiorgan failure on postoperative day 14 in a patient with pre-existing severe chronic kidney disease and cirrhosis. Both displayed severe degree MAC and required MV replacement. Residual MV regurgitation at discharge was absent to mild in all patients. At follow-up, no death was observed. One patient developed moderate regurgitation following MV repair, and another patient required redo surgery for significant periprosthetic leak 14 months after surgery. Actually, this adverse event occurred in the same patient who had initially required redo surgery on postoperative day 1. At early reoperation the leak had been primarily closed through the right mini-thoracotomy with additional pledgetted sutures, but the later procedure was carried out via sternotomy and the patient underwent MV re-replacement.

4. Discussion

MAC requires technically demanding surgery, increases operative risk, and impairs the repair feasibility in patients with degenerative MV disease [16–18].

Several surgical techniques have been described to tackle this issue with varying results. These include isolated leaflet repair or resection, or implantation of artificial ePTFE chordae with or without annuloplasty [19,20], edge-to-edge MV repair [21], valve replacement with no annular calcium debridement securing the prosthesis inside the calcified annulus [22], intra-atrial insertion of a mitral prosthesis eventually with Dacron or pericardial patch interposition to form an external skirt or prosthetic neo-annulus [23,24], partial debridement of the calcific bar [25], en bloc decalcification and annular reconstruction with Dacron or pericardial patch [16], and ultrasonic debridement of the calcification [26]. Finally, extra-anatomical left atrial to left ventricular apex bypass with a valved conduit has been described by the Mayo Clinic team as an extra-anatomical solution in patients with extensive MAC [27], mimicking a technique originally performed during the Eighties at the Bambino Gesù Hospital in Rome to correct congenitally hypoplastic atrioventricular valve stenosis in children [28].

Clearly, the strategies that avoid altogether the manipulation of the MV annulus and that thus do directly address the MAC are technically more straightforward. Unfortunately, successful repair with no annuloplasty is applicable only in a minority of patients and, paradoxically, in those with less severe MACs and with minor leaflet involvement. Similarly, edge-to-edge procedures can be very easy and not time-consuming to perform, but almost invariably at the expense of some degree of residual MV regurgitation, in analogy to transcatheter edge-to-edge repair with MitraClip™ technology (Abbott Vascular, Abbott Park, IL, USA). Conversely, intra-atrial fixation of a MV prosthesis might appear a clever and appealing solution, but may not uniformly allow secure anchoring in an ectopic position and also often determines implantation of a smaller valve because the annular orifice

is blocked by the MAC, with consequently higher postoperative transvalvular gradients. Although successful off-label implantation of an upside down 23 mm or in extreme cases 21 mm St. Jude Regent (St. Jude Medical, Inc., St. Paul, MN, USA) aortic mechanical prosthesis in the mitral position has been reported, predominantly in smaller size women with MAC or prior mediastinal radiation therapy [29], gradients may be a critical issue and often imply clinically relevant patient-prosthesis mismatch with persistently elevated left atrial and pulmonary pressures and reduced long-term survival [30]. Mid- or long-term results with extra-anatomical bypass still await to be validated.

A somewhat more conservative approach to MAC with no or minimal annular debridement and a prosthesis secured to the near-intact calcium bar may offer reliable results, but should be balanced with the hazards of periprosthetic leak, circumflex artery injury and atrioventricular heart block, related to the sutures being driven through or around the calcified material, and with the difficulties in implanting a prosthesis of adequate size. Conversely, the risks related to more aggressive techniques with radical debridement and reconstruction of the annular anatomy are well recognized, with non-negligible mortality and major morbidity, i.e., heart block requiring permanent pacemaker insertion, perioperative myocardial infarction and hemorrhagic complications at the level of the atrioventricular junction or proximal left ventricular free wall, often uncontrollable and fatal [31–34].

The recent adoption of the so-called microinvasive options, such as transcatheter prosthetic MV implantation procedures may represent an appealing alternative, particularly in high-risk patients, but to date outcome is suboptimal and indications are anatomically stringent, particularly in case of a relatively small left ventricle and a narrow mitroaortic angle, which imply a hazard of left ventricular outflow tract obstruction. In this scenario, the earliest experience with severe MAC was collected from the MAC Global Registry and reported a 30-mortality rate of 25% [34]. In a systematic review by Alexis et al., on 354 patients with MAC disease undergoing trans-septal and trans-apical valve-in-valve, the risk of left ventricular outflow tract obstruction was 11.2%, the incidence of at least moderate post-procedural mitral regurgitation was 4.1%, the rate of device embolism was 3.7%, and the risk of reintervention was 16.7%. The reported 30-day and 1-year mortality rates were 23%, and 43% respectively [35].

Our surgical practice in patients with MV disease and MAC is, whenever possible, to prefer repair techniques, and this is usually feasible in cases of mild to moderate MAC without significant leaflet involvement. In our series, however, repair was feasible only in 6/27 patients (22%), always with implantation of a complete prosthetic ring, while posterior leaflet resection and artificial chordal positioning were performed in three and in two patients, respectively. In case of valve replacement our technique of choice includes the least debridement of annular calcifications in order to drive the sutures and to achieve a good seating of the prosthesis. Aggressive decalcification is seldom necessary, avoiding time-consuming annular reconstruction coupled by a reduced hazard of atrioventricular disruption, coronary injury and, ultimately, intraoperative death. Besides, minimally invasive techniques are more straightforward and less cumbersome with this approach.

The extent of the annular calcium bar impacts the feasibility of MV repair. In case of extensive or near-circumferential MAC or leaflet involvement, the MV flexibility is severely impaired and the chances of a durable repair are jeopardized. In our population, severe and moderate MAC grading was reported in 11 (41%) and 13 (49%) patients, respectively, whereas involvement of one or both MV leaflets was observed in 48% and 52% of the cases. Not surprisingly, as already stated, the repair rate was only 22% (6/27).

Traditionally, MAC has been primarily addressed through a conventional full sternotomy. Nevertheless, the promising results reported by minimally invasive cardiac surgical programs have drawn the attention toward more complex cases, including MV disease with MAC. The benefits of a minimally invasive approach are particularly evident in elderly or frail patients, as well as in case of prior cardiac operations with the inherent risks of re-sternotomy and coronary bypass graft injury, if present. Besides, MV exposure may be more favorable with a lateral approach in patents with a relatively small left atrium.

In our experience with minimally invasive MV surgery during the last two decades, this case series indicates the feasibility and effectiveness also in patients with MAC with low perioperative mortality and rate of complications.

Patients enrolled in the present report display a consistently high preoperative risk profile with multiple comorbidities, namely, chronic kidney disease in near-90%, diabetes in 19%, severe pulmonary hypertension in 22%, previous cardiac surgery in 15%, peripheral vascular disease in 15% of the patients, and complex MV anatomy with a MAC grade of 6 or more in 55%. Overall 30-day mortality was 7%. No case of intraoperative bleeding due to annular injury or perioperative myocardial infarction were observed. Notably, no perioperative stroke occurred. Periprosthetic leak was detected in two patients (one early failure, and one at follow-up).

In a case series by Feindel et al., MAC led to a 6-fold increase in the operative mortality of patients undergoing isolated MV surgery [17]. Other authors have reported early mortality after MV replacement in MAC as high as 28% [31]. The lower than expected mortality and morbidity in the present study can be justified by experience in minimally invasive MV surgery, with a tailored approach to each patient in our everyday practice [7–12], progressively extended to also include patients with mild-to-moderate and, more recently, severe MAC. The technique of choice in the latter has been, whenever feasible, MV replacement with minimal annular calcium debridement, allowing the surgeon to dramatically reduce the risk of heart rupture and coronary lesions.

Limitations

This was a retrospective, single-center study, and a control group of patients with MV disease and MAC undergoing surgery through standard sternotomy was not available. Moreover, not all the patients enrolled had a preoperative angio-CT scan with cardiac gating. Conversely, a strength of this report relates to the fact that perioperative mortality was stratified according to the EuroSCORE, which does not include specific variables related to MAC anatomy and thus underestimates the risks related to the complexity of the surgical procedure and to the fragility of the MV anulus in this specific population.

5. Conclusions

MAC increases the complexity of surgical procedure and operative mortality and morbidity. Results of the present study show that in experienced high-volume centers, the benefits of the minimally invasive approach can be safely extended to MAC patients as well. CT scans and, eventually, angiography are mandatory for total-body vascular assessment and decision-making in relation to perfusion and cardioplegia techniques. MV repair is preferred whenever possible, but more often, MAC precludes a durable result. When MV replacement is indicated, the technique of choice is minimal debridement of annular calcifications for the suturing and proper seating of the prosthesis.

Author Contributions: Conceptualization, C.B., A.S. (Antonio Spitaleri), M.P. and A.D.; methodology, C.B., M.P. and M.R.; software, A.S. (Antonio Spitaleri), A.S. (Ambra Santonocito), A.D. and R.F.; validation, C.B., M.P. and M.R.; formal analysis, C.B., A.S., M.P. and R.F.; investigation, A.S. (Antonio Spitaleri), B.P., A.S. (Ambra Santonocito) and E.B.; resources, C.B., A.S. (Antonio Spitaleri), M.P. and M.R.; data curation, C.B., A.S. (Antonio Spitaleri), B.P., A.S. (Ambra Santonocito) and E.B.; writing—original draft preparation, C.B., A.S. (Antonio Spitaleri) and A.S. (Ambra Santonocito); writing—review and editing, M.P.; visualization, C.B., A.S. (Antonio Spitaleri), B.P., A.S. (Ambra Santonocito) and E.B.; supervision, C.B., M.P., A.D. and R.F.; project administration, A.D., R.F. and M.R.; funding acquisition, R.F. and M.R. All authors have read and agreed to the published version of the manuscript.

Funding: This research received no external funding.

Institutional Review Board Statement: The study was conducted in accordance with the Declaration of Helsinki, and approved by the Institutional Review Board of the "AOU Città della Salute e della Scienza di Torino", Turin, Italy (protocol code 0095187; 9 October 2020).

Informed Consent Statement: Written informed consent has been obtained from the patients to publish this paper, when applicable.

Data Availability Statement: The data presented in this study are available upon request from the corresponding author.

Conflicts of Interest: The authors declare no conflict of interest.

References

1. Kanjanauthai, S.; Nasir, K.; Katz, R.; Rivera, J.J.; Takasu, J.; Blumenthal, R.S.; Eng, J.; Budoff, M.J. Relationships of mitral annular calcification to cardiovascular risk factors: The Multi-Ethnic Study of Atherosclerosis (MESA). *Atherosclerosis* **2010**, *213*, 558–562. [CrossRef] [PubMed]
2. O'Neal, W.T.; Efird, J.T.; Nazarian, S.; Alonso, A.; Heckbert, S.R.; Soliman, E.Z. Mitral annular calcification and incident atrial fibrillation in the Multi-Ethnic Study of Atherosclerosis. *Europace* **2014**, *17*, 358–363. [CrossRef] [PubMed]
3. Abramowitz, Y.; Hasan, J.; Tarun, C.; Michael, J.M.; Raj, R.M. Mitral annulus calcification. *J. Am. Coll. Cardiol.* **2015**, *66*, 1934–1941. [CrossRef] [PubMed]
4. Okada, Y. Surgical management of mitral annular calcification. *Gen. Thorac. Cardiovasc. Surg.* **2013**, *61*, 619–625. [CrossRef] [PubMed]
5. Di Stefano, S.; López, J.; Flórez, S.; Rey, J.; Arevalo, A.; Román, A.S. Building a new annulus: A technique for mitral valve replacement in heavily calcified annulus. *Ann. Thorac. Surg.* **2009**, *87*, 1625–1627. [CrossRef]
6. Guerrero, M.; Wang, D.D.; Pursnani, A.; Eleid, M.; Khalique, O.; Urena, M.; Salinger, M.; Kodali, S.; Kaptzan, T.; Lewis, B.; et al. A cardiac computed tomography–based score to categorize mitral annular calcification severity and predict valve embolization. *JACC Cardiovasc. Imaging* **2020**, *13*, 1945–1957. [CrossRef]
7. Barbero, C.; Marchetto, G.; Ricci, D.; El Qarra, S.; Attisani, M.; Filippini, C.; Boffini, M.; Rinaldi, M. Minimal access mitral valve surgery: Impact of tailored strategies on early outcome. *Ann. Thorac. Surg.* **2016**, *102*, 1989–1994. [CrossRef]
8. Barbero, C.; Marchetto, G.; Ricci, D.; Cura Stura, E.; Clerici, A.; El Qarra, S.; Filippini, C.; Boffini, M.; Rinaldi, M. Steps forward in minimally invasive cardiac surgery: 10-year experience. *Ann. Thor. Surg.* **2019**, *108*, 1822–1829. [CrossRef]
9. Barbero, C.; Pocar, M.; Marchetto, G.; Cura Stura, E.; Calia, C.; Boffini, M.; Rinaldi, M.; Ricci, D. Antegrade perfusion for mini-thoracotomy mitral valve surgery in patients with atherosclerotic burden. *Heart Lung Circ.* **2022**, *31*, 415–419. [CrossRef]
10. Barbero, C.; Rinaldi, M. Preoperative vascular screening: A novel breakthrough in minimally invasive mitral valve surgery. *Interact. Cardiovasc. Thorac. Surg.* **2017**, *24*, 368. [CrossRef]
11. Barbero, C.; Ricci, D.; El Qarra, S.; Marchetto, G.; Boffini, M.; Rinaldi, M. Aortic cannulation system for minimally invasive mitral valve surgery. *J. Thorac. Cardiovasc. Surg.* **2015**, *149*, 1669–1672. [CrossRef] [PubMed]
12. Barbero, C.; Pocar, M.; Marchetto, G.; Cura Stura, E.; Calia, C.; Dalbesio, B.; Filippini, C.; Salizzoni, S.; Boffini, M.; Rinaldi, M.; et al. Single-dose St. Thomas versus Custodiol® cardioplegia for right mini-thoracotomy mitral valve surgery. *J. Cardiovasc. Transl. Res.* **2022**. [CrossRef] [PubMed]
13. Thygesen, K.; Alpert, J.S.; Jaffe, A.S.; Chaitman, B.R.; Bax, J.J.; Morrow, D.A.; White, H.D. The Executive Group on behalf of the Joint European Society of Cardiology (ESC)/American College of Cardiology (ACC)/American Heart Association (AHA)/World Heart Federation (WHF) Task Force for the universal definition of myocardial infarction. Fourth universal definition of myocardial infarction. *Eur. Heart J.* **2019**, *40*, 237–269. [PubMed]
14. Lomivorotov, V.V.; Efremov, S.; Kirov, M.; Fominskiy, E.; Karaskov, A.M. Low-cardiac-output syndrome after cardiac surgery. *J. Cardiothorac. Vasc. Anesth.* **2017**, *31*, 291–308. [CrossRef]
15. Barbero, C.; Rinaldi, M.; Marchetto, G.; Valentini, M.C.; Cura Stura, E.; Bosco, G.; Pocar, M.; Filippini, C.; Boffini, M.; Ricci, D. Magnetic resonance imaging for cerebral micro-embolizations during minimally invasive mitral valve surgery. *J. Cardiovasc. Transl. Res.* **2022**, *15*, 828–833. [CrossRef]
16. Carpentier, A.F.; Pellerin, M.; Fuzellier, J.-F.; Relland, J.Y. Extensive calcification of the mitral valve anulus: Pathology and surgical management. *J. Thorac. Cardiovasc. Surg.* **1996**, *111*, 718–730. [CrossRef] [PubMed]
17. Feindel, C.M.; Tufail, Z.; E David, T.; Ivanov, J.; Armstrong, S. Mitral valve surgery in patients with extensive calcification of the mitral annulus. *J. Thorac. Cardiovasc. Surg.* **2003**, *126*, 777–782. [CrossRef]
18. Fusini, L.; Ali, S.G.; Tamborini, G.; Muratori, M.; Gripari, P.; Maffessanti, F.; Celeste, F.; Guglielmo, M.; Cefalù, C.; Alamanni, F.; et al. Prevalence of calcification of the mitral valve annulus in patients undergoing surgical repair of mitral valve prolapse. *Am. J. Cardiol.* **2014**, *113*, 1867–1873. [CrossRef]
19. Chan, V.; Ruel, M.; Hynes, M.; Chaudry, S.; Mesana, T.G. Impact of mitral annular calcification on early and late outcomes following mitral valve repair of myxomatous degeneration. *Interact. Cardiovasc. Thorac. Surg.* **2013**, *17*, 120–125. [CrossRef]
20. Morisaki, A.; Kato, Y.; Takahashi, Y.; Shibata, T. Mitral valve repair without mitral annuloplasty with extensive mitral annular calcification. *Interact. Cardiovasc. Thorac. Surg.* **2014**, *19*, 1080–1082. [CrossRef]
21. Maisano, F.; Caldarola, A.; Blasio, A.; De Bonis, M.; La Canna, G.; Alfieri, O. Midterm results of edge-to-edge mitral valve repair without annuloplasty. *J. Thorac. Cardiovasc. Surg.* **2003**, *126*, 1987–1997. [CrossRef] [PubMed]
22. Coselli, J.S.; Crawford, E.S. Calcified mitral valve annulus: Prosthesis insertion. *Ann. Thorac. Surg.* **1988**, *46*, 584–586. [CrossRef] [PubMed]

23. Nataf, P.; Pavie, A.; Jault, F.; Bors, V.; Cabrol, C.; Gandjbakhch, I. Intraatrial insertion of a mitral prosthesis in a destroyed or calcified mitral annulus. *Ann. Thorac. Surg.* **1994**, *58*, 163–167. [CrossRef] [PubMed]
24. Atoui, R.; Lash, V.; Mohammadi, S.; Cecere, R. Intra-atrial implantation of a mitral valve prosthesis in a heavily calcified mitral annulus. *Eur. J. Cardiothorac. Surg.* **2009**, *36*, 776–778. [CrossRef] [PubMed]
25. Iida, H.; Mochizuki, Y.; Matsushita, Y.; Mori, H.; Yamada, Y.; Miyoshi, S. A valve replacement technique for heavily calcified mitral valve and annulus. *J. Heart Valve Dis.* **2005**, *14*, 209–211. [PubMed]
26. Vander Salm, T.J.; Perras, M. As originally published in 1989: Mitral annular calcification: A new technique for valve replacement. *Ann. Thorac. Surg.* **1997**, *63*, 1819–1820. [PubMed]
27. Nguyen, A.; Schaff, H.V. Left atrial to left ventricle bypass for mitral valve stenosis. *J. Thorac. Cardiovasc. Surg.* **2019**, *157*, e361–e362. [CrossRef]
28. Amodeo, A.; Di Donato, R.; Corno, A.; Mazzera, E.; Giannico, S.; Nava, S.; Marcelletti, C. Systemic atrioventricular conduit for extracardiac bypass of hypoplastic systemic atrioventricular valve. *Eur. J. Cardiothorac. Surg.* **1990**, *4*, 601–603. [CrossRef]
29. Barac, Y.D.; Zwischeberger, B.; Schroder, J.N.; Daneshmand, M.A.; Haney, J.C.; Gaca, J.G.; Wang, A.; Milano, C.A.; Glower, D.D. Using a Regent aortic valve in a small annulus mitral position is a viable option. *Ann. Thorac. Surg.* **2018**, *105*, 1200–1204. [CrossRef]
30. Joury, A.; Duran, A.; Stewart, M.; Gilliland, Y.E.; Spindel, S.M.; Qamruddin, S. Prosthesis-patient mismatch following aortic and mitral valves replacement—A comprehensive review. *Prog. Cardiovasc. Dis.* **2022**, *72*, 84–92. [CrossRef]
31. D'Alessandro, C.; Vistarini, N.; Aubert, S.; Jault, F.; Acar, C.; Pavie, A.; Gandjbakhch, I. Mitral annulus calcification: Determinants of repair feasibility, early and late surgical outcome. *Eur. J. Cardiothorac. Surg.* **2007**, *32*, 596–603. [CrossRef] [PubMed]
32. Saran, N.; Greason, K.L.; Schaff, H.V.; Cicek, S.M.; Daly, R.C.; Maltais, S.; Stulak, J.M.; Pochettino, A.; King, K.S.; Dearani, J.A.; et al. Does mitral valve calcium in patients undergoing mitral valve replacement portend worse survival? *Ann. Thorac. Surg.* **2019**, *107*, 444–452. [CrossRef] [PubMed]
33. Bedeir, K.; Kaneko, T.; Aranki, S. Current and evolving strategies in the management of severe mitral annular calcification. *J. Thorac. Cardiovasc. Surg.* **2019**, *157*, 555–566. [CrossRef]
34. Guerrero, M.; Urena, M.; Himbert, D.; Wang, D.D.; Eleid, M.; Kodali, S.; George, I.; Chakravarty, T.; Mathur, M.; Holzhey, D.; et al. 1-Year outcomes of transcatheter mitral valve replacement in patients with severe mitral annular calcification. *J. Am. Coll. Cardiol.* **2018**, *71*, 1841–1853. [CrossRef] [PubMed]
35. Alexis, S.L.; Malik, A.H.; El-Eshmawi, A.; George, I.; Sengupta, A.; Kodali, S.K.; Hahn, R.T.; Khalique, O.K.; Zaid, S.; Guerrero, M.; et al. Surgical and transcatheter mitral valve replacement in mitral annular calcification: A systematic review. *J. Am. Heart Assoc.* **2021**, *10*, e018514. [CrossRef]

applied sciences

MDPI

Article

True Non-Contrast Phase versus Virtual-Non Contrast: "Lights and Shadows" of Dual Energy CT Angiography in Peripheral Arterial Disease

Chiara Floridi [1,2,3], Laura Maria Cacioppa [3], Giacomo Agliata [2], Michaela Cellina [4,*], Nicolo' Rossini [1], Tommaso Valeri [1], Martina Curzi [5], Alessandro Felicioli [3], Alessandra Bruno [1], Marzia Rosati [3], Roberto Candelari [3] and Andrea Giovagnoni [1,2]

[1] Department of Clinical, Special and Dental Sciences, University Politecnica delle Marche, 60126 Ancona, Italy
[2] Division of Radiology, Department of Radiological Sciences, University Hospital "Azienda Ospedaliera Universitaria delle Marche", 60126 Ancona, Italy
[3] Division of Interventional Radiology, Department of Radiological Sciences, University Hospital "Azienda Ospedaliera Universitaria delle Marche", 60126 Ancona, Italy
[4] Radiology Department, ASST Fatebenefratelli Sacco, 20121 Milan, Italy
[5] UOC Radiology, AST Fermo, Marche Region, 63900 Fermo, Italy
* Correspondence: michaela.cellina@asst-fbf-sacco.it

Abstract: (1) Background: The value of dual-energy CT angiography (DE-CTA) in the detection of peripheral arterial disease (PAD) has been widely recognized. We aim to evaluate the diagnostic accuracy of virtual non-contrast (VNC) imaging of DE-CTA compared to true non-contrast phase (TNC). (2) Methods: Our Internal Review Board (IRB) approved prospective study enrolled 40 patients (28 men, 12 women; median age 69 y, range 41–93 y) who underwent lower extremity DE-CTA for symptomatic PAD. Mean attenuation values of TNC and VNC were obtained by placing circular regions of interest (ROI) at five levels from the aortic to the popliteal arterial lumen, reported in Hounsfield units (HU), and compared using a two-sample *t*-test. The subjective quality of VNC images was assessed by two independent radiologists with 10 and 4 years of CTA-imaging experience according to a 4-point scale and verified by the intra-class correlation coefficient (ICC). Dose Length Product (DLP) values of each DE-CTA examination were also considered. (3) Results: Except for the external iliac artery, VNC attenuation values were significantly lower than the corresponding TNC values at all levels, with a mean difference ranging from 14.1 and 8.7 HU. At qualitative analysis, VNC images were considered excellent to diagnose in 40%, good in 50%, and sufficient in 10% of cases. No cases of non-diagnostic VNC imaging were reported. Avoiding the TNC phase, a mean reduction in DLP of 54% for each DE-CTA was estimated. (4) Conclusions: TNC and VNC images showed comparable reliability and diagnostic accuracy in the detection of PAD. VNC may be considered a promising substitute for TNC from the perspectives of dose reduction and workflow optimization.

Keywords: computed tomography angiography; peripheral arterial disease; dual-energy computed tomography; digital scanned projection radiography; dual energy; image reconstructions

Citation: Floridi, C.; Cacioppa, L.M.; Agliata, G.; Cellina, M.; Rossini, N.; Valeri, T.; Curzi, M.; Felicioli, A.; Bruno, A.; Rosati, M.; et al. True Non-Contrast Phase versus Virtual-Non Contrast: "Lights and Shadows" of Dual Energy CT Angiography in Peripheral Arterial Disease. *Appl. Sci.* **2023**, *13*, 7134. https://doi.org/10.3390/app13127134

Academic Editor: Julio Garcia Flores

Received: 20 April 2023
Revised: 10 June 2023
Accepted: 12 June 2023
Published: 14 June 2023

1. Introduction

Peripheral arterial disease (PAD) is characterized by arterial stenosis or occlusion anywhere from the aortoiliac axis to pedal arteries [1]. PAD has a high prevalence worldwide, occurring in up to 15% of the population over 70 years, and it is a prevalent cause of repeated hospitalizations and cardiovascular mortality [1–4].

After physical examination, imaging techniques such as Doppler ultrasound (DUS), computed tomography angiography (CTA), and digital subtraction angiography (DSA) are employed for PAD localization and definition [4]. DSA, historically the gold standard technique for PAD diagnosis, is nowadays limited to cases with a planned endovascular

therapeutic intervention due to its numerous limitations, such as radiation burden, contrast medium load, high costs, and access site complications [5,6]. For pure diagnostic purposes, DSA has been replaced by other non-invasive imaging techniques.

In current clinical practice, CTA, magnetic resonance angiography (MRA) and duplex sonography (DUS) are commonly employed to assess the extent and severity of PAD.

In particular, CTA of the lower extremity runoff is nowadays the preferred imaging modality [4,7] because of its large availability, its high resolution, the fast acquisition, and the suitability of multi-planar reconstructions (MPR) [5,8–10]. CTA is also highly accurate in assessing significant luminal lesions and evaluating arterial walls [8,11]. CTA principal drawbacks include the lack of hemodynamic information, the exposure to ionizing radiation, and the use of iodinated contrast agents. The occurrence of "blooming" artifacts caused by highly calcified atheromas resulting in an overestimation of stenosis severity and in false positive findings is also an important limitation [3–5,8,11–16].

Despite new generation CT scanners and protocols minimizing these issues [17], the increasing use of dual-energy computed tomography angiography (DE-CTA) in the diagnostic assessment of PAD may overcome CTA limitations. Specifically, DE-CTA improves the assessment of the vessel lumen lowering the employed contrast media volume [18].

As "dual-energy CT" refers to the use of two-photon spectra, DECT is frequently referred to as "spectral CT". In the DECT dataset, since X-ray attenuation depends on the atomic number (Z) of a material, low-Z, and high-Z materials can be differentiated if images are acquired at both high and X-ray spectra (low to high tube voltages) [16]. This process, known as material decomposition, can be obtained by a variety of methods depending on the type of DE-CT scanner (equipped with a double detector panel, two X-ray tubes, or a two-layered single detector panel). The acquisition of two imaging datasets with two different attenuation profiles is thus allowed [5]. In contrast to single-spectrum imaging, DECT imaging is also able to differentiate materials with similar attenuation coefficients based on chemical composition and atomic number [19–25]. Constituent materials characterized by high atomic numbers, such as iodine and calcium, can be easily differentiated by DECT processes, thus permitting the development of many clinical applications [26]. The DE technique has several applications for clinical imaging and can allow the reduction of the iodine contrast medium dose, as well as the radiation dose.

First, material decomposition algorithms may be applied for precise quantification of specific materials such as iodine uptake. They may also generate iodine maps from contrast-enhanced phases, which may be useful in the characterization of many clinical entities [26].

Moreover, post-processing algorithms allow the identification and removal of the calcium content of calcified plaques, obtaining a better evaluation of the contrast-enhanced vessel lumen, similar to DSA images [6,11,27–37]. Imaging of arteries may benefit greatly from these DECT reconstructions. Moreover, the algorithms applied for subtracting iodine content from acquisitions, called virtual non-contrast (VNC), can be used to evaluate unenhanced vessels instead of true non-contrast (TNC) acquisitions [24,38]. At present, several software tools and clinical applications of DECT have been developed. VNC algorithms may be applied to DECT images to identify the iodine content of every single voxel and to remove the iodine component of the CT number to create images lacking in contrast material enhancement. This analysis is based on a three-material decomposition including iodine, soft tissue, and another material in relation with the anatomical districted studied. The VNC algorithm is also able to quantify the iodine amount generating Iodine distribution maps. The selective removal of iodine content from post-contrast images, preserving calcium or other metallic devices is also performed with a good specificity. In vascular studies, this application may help to obtain a reconstruction of vessels without contrast from a post-contrast DE-CTA.

It has not been well established if the VNC is of acceptable quality to replace the TNC in arterial disease evaluation.

The purpose of our study is therefore to evaluate the diagnostic reliability of "virtual non-contrast" (VNC) images, obtained from the reprocessing of DE-CTA arterial scans acquired with third-generation scanners compared to baseline acquisition obtained without intravenous administration of iodinated contrast (TNC) in the study of PAD.

2. Materials and Methods

To evaluate the diagnostic reliability of VNC images obtained after DECT reconstructions, a suitable dataset was prepared. The data acquisition and elaboration is summarized in Figure 1 and described in detail in the following subsections.

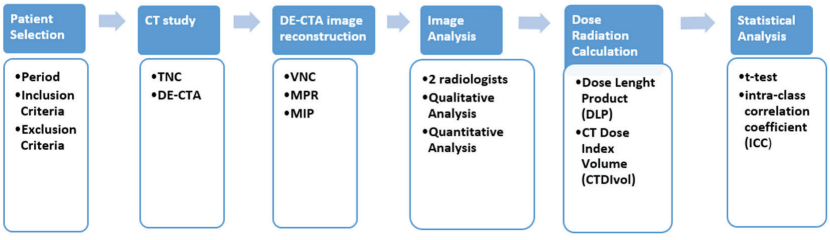

Figure 1. General diagram of methodology workflow. VNC = virtual non contrast; TNC = true non contrast; DE-CTA = dual-energy computed tomography angiography; MPR = multi-planar reformats; MIP = maximum-intensity projections.

2.1. Patient Population and Study Design

The present prospective single-center study obtained the Institutional Review Board approval of the University Politecnica delle Marche Internal Ethic Committee on 9 October 2021. Between September 2021 and May 2022, a total of 40 selected patients were enrolled. To be included, patients had to be previously submitted to a vascular evaluation for suspected chronic limb ischemia performed in the Vascular Surgery or Vascular Medicine Departments of our institution, consisting of clinical history record, physical examination, and measurement of ankle–brachial index (ABI). The clinical evaluation was also completed by a DUS examination and a laboratory test of renal function. All patients were then submitted to a CTA study of the lower limbs as required by the referring Vascular Surgeon for symptomatic PAD occurring with mild to severe claudication (Rutherford categories 1 to 3), rest pain, or non-healing minor or major ulcers (Rutherford categories 4 to 6). Patients previously submitted to stents intravascular placement, surgical revascularization, or primary amputations were excluded, as well as patients with symptoms consistent with acute limb ischemia [39].

Documented allergy to iodinated contrast medium, moderate or severe renal impairment (glomerular filtration rate < 45 mL/min), and congestive heart failure were also considered as exclusion criteria.

After the exclusion of previous allergic reactions to iodinated contrast medium, informed consent to the examination was obtained from all the participants.

Forty consecutive patients were examined for suspected PAD. Twenty-eight patients were males (median age 70 y, range, 45–85 y) and 12 patients were females (median age 69 y, range, 41–93 y). The median patient age was 69 years, ranging from 41 and 93 years. The calculated median body mass index (BMI) was 25.7 (range, 17–33.5).

Demographic and clinical characteristics of the study population were summarized in Table 1.

Table 1. Demographic and clinical characteristics of the study population.

Demographic	n (Range)
• Patients (n)	40
• Age (yrs)	69 (41–93)
• Weight (kg)	77 (53–126)
• Height (cm)	171 (158–193)
• BMI (kg/m^2)	25.7 (17–33.5)

2.2. CT Study Protocol

All studies were performed on a third-generation Dual Source Dual Energy CT scanner (Siemens Somatom Force, Siemens Healthcare, Forchheim, Germany).

All patients were positioned supine, feet first. Both feet were stabilized with adhesive tape to avoid any movements during the examination. Additionally, before the CT exam started, an 18-gauge cannula was placed into a superficial vein located in the antecubital fossa or forearm for intravenous (i.v.) contrast medium injection.

All image acquisitions were performed in the craniocaudal direction with a scan length ranging from the infrarenal abdominal aorta to the toes.

Before CT scan, patients were required to perform a deep inspiration and to hold on breath during the acquisition.

Firstly, a baseline, non-contrast, single energy acquisition was acquired with the parameters reported in Table 2.

Table 2. Single energy computed tomography (CT) and dual-energy computed tomography (DE-CT) scanning parameters.

Parameters	Single-Energy CT	DE-CT
Pitch	0.6	0.4
Slice collimation	3 mm (acquisition 192 × 0.6 mm^2)	1 mm (acquisition 192 × 0.6 mm^2)
Rotation time	0.5	0.5
Field of view (FOV)	300 mm	300 mm
Reconstruction slice thickness	3 mm	1 mm

Subsequently, DE-CTA was obtained. A 120-kVp bolus-tracking acquisition (CARE Bolus, Siemens) was used to determine scan initiation by placing a region-of-interest (ROI) in the infrarenal abdominal aorta with a trigger threshold of 300 Hounsfield units (HU) and 8-s delay. Tubes A and B were operated with 90 and 150 kVp. Image quality reference was setted to 120–67 mAs. The rest of DE-CT scanning parameters were summarized in Table 1.

These scanning parameters, both of single-energy non-contrast baseline acquisition and of DE-CTA acquisition, were chosen in relation with our clinical and diagnostic experience.

For each examination, a volume of 1 mL/kg of iodinated contrast medium followed by 40 mL of saline solution at a flow rate of 4 mL/and was intravenously administered. Automatic exposure control (CareDose 4D™, Siemens Healthcare, Forchheim, Germany) was used to adapt the tube current to variations in patient attenuation, both between different patients and within any given patient.

2.3. DE-CTA Image Reconstruction

Transverse low- and high-kVp DE-CTA imaging data were reconstructed using a medium sharp convolution kernel (Qr40). A specific dual-energy post-processing workstation with a patented algorithm (Syngo MMWP version VA 20; Siemens Healthcare, Forchheim, Germany) was used for image analysis, generating VNC images from DE-CTA images.

The algorithm is able to quantify the iodine amount of every single pixel generating an iodine distribution map. VNC images were then reconstructed to 3-mm thick axial images.

Multi-planar reformats (MPR; thickness, 1.5 mm; increment, 1.0 mm) and maximum-intensity projections (MIP; thickness, 10.0 mm; increment, 1.0 mm) in transverse, oblique coronal, and sagittal orientation were also obtained.

2.4. Image Analysis

All TNC and VNC images were reviewed by two radiologists with 12 (CF) and 9 (GA) years of experience in CTA on PACS workstations (Picture Archiving and Communication System; Centricity Radiology, GE Healthcare, Milwaukee). Only axial TNC and VNC images were assessed for qualitative and quantitative analysis.

Quantitative Analysis. The comparison of attenuation and noise between TNC and VNC images was made by drawing circular regions of interest (ROI) on both dataset images at the same level.

ROIs of approximately 0.5 cm^2, as large as possible for vessel caliber and avoiding vessel wall, vessel defects, plaques, and stent materials at five arterial segments, were drawn.

ROIs were positioned within the infra-renal abdominal aorta, common iliac artery, external iliac artery, femoral artery, and popliteal artery lumens.

Mean attenuation values in Hounsfield units (HU) and the corresponding standard deviation (SD) were measured as shown in Figure 2. Measurements were performed using transverse standard and MPR images and repeated three times to minimize sampling inaccuracies related to breath or movement artefacts.

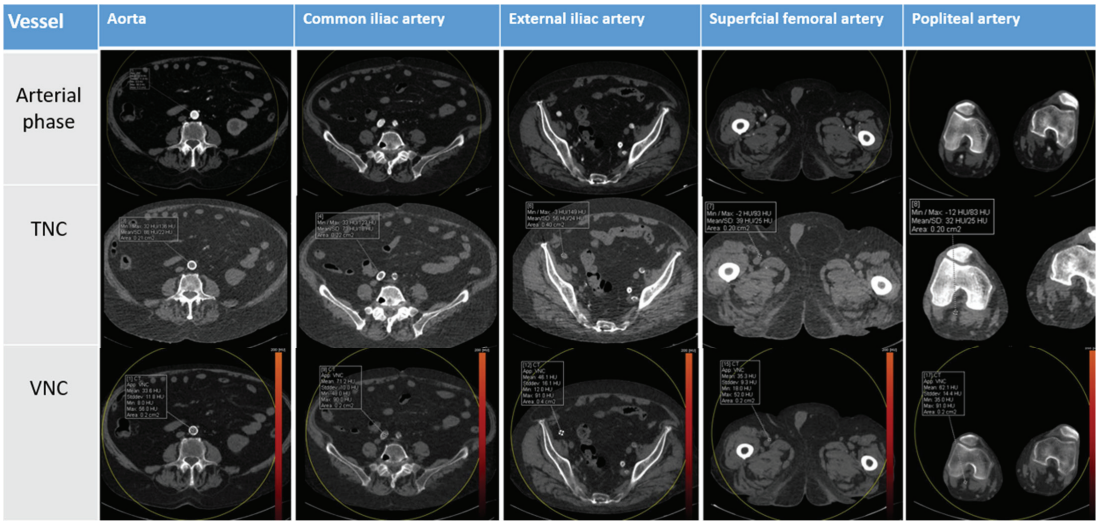

Figure 2. Arterial phase, true non-contrast (TNC) and virtual non-contrast (VNC) of dual-energy CTA run-off acquisition. In both TNC and VNC images, a circular region of interest (ROI) is placed at the level of the abdominal aorta, common iliac artery, external iliac artery, superficial femoral artery, and popliteal artery, avoiding vessel walls and plaques.

Qualitative Analysis. The two radiologists, blinded to clinical information and previous radiology reports of the examined patients, independently evaluated the quality of the CT images. The qualitative analysis was performed by using a 4-point Likert scale (4 = excellent, 3 = good, 2 = moderate but sufficient for diagnosis, and 1 = non-diagnostic) and included overall image quality, signs of residual contrast medium, possible subtracted calcifications, and stent structures.

The scores obtained with the two protocols were then compared and the inter-observer agreement was assessed, too. The specific artefacts were scored as yes/no.

2.5. Dose Radiation Calculation

Dose Length Product (DLP) and CT dose index volume (CTDIvol) values of each DE-CTA examination were also recorded from the automatically provided scan protocol to evaluate the absorbed radiation dose and its potentially harmful effects on the patient. DLP values were also standardized using gender-specific k coefficients (Kmale = 0.0056, kfemale = 0.0068) to obtain effective dose values (E). The effective dose values and estimated percentage of dose reduction were calculated.

2.6. Statistical Analysis

Data were analyzed using GraphPad Prism version 9.1.1 (GraphPad Software, Boston, MA, USA) statistical software. For all numerical values derived from multiple measurements, the mean value and SD were reported. The mean attenuation values of TNC and VNC images were compared using a paired measures test (*t*-test). A p-value < 0.05 was considered statistically significant.

The qualitative assessment was analyzed by the intra-class correlation coefficient (ICC) in the form of "Two-Way Random-Effects Model, absolute agreement, two raters/measurements", and interpreted as follows: for values <0.4, the agreement was poor; for values between 0.4–0.59, the agreement was fair; for values between 0.6–0.79, the agreement was good; and for values between 0.8–1, the agreement was excellent.

3. Results

All DE-CTA examinations were successfully performed without any adverse events. VNC images were compared to baseline TNC scan images. No significative motion or breath artifacts were registered. Intravascular attenuation measurements were performed using ROIs as previously described and reported as HU ± SD for TNC and VNC images. The data were subsequently compared using a test for paired measures.

At the level of the infrarenal abdominal aorta, the mean intravascular attenuation value in TNC images was 47.1 ± 6.6 HU and the corresponding value in VNC images was 33.0 ± 8.2 HU ($p < 0.00$). For common iliac artery, the mean intravascular attenuation values were 47.8 ± 8.9 HU in TNC and 34.1 ± 11.4 HU in VNC images ($p < 0.00$).

At the level of the superficial femoral artery, the mean intravascular attenuation value was 48.5 ± 9.0 HU in TNC images while the corresponding value in VNC images was 38.2 ± 10.4 HU ($p < 0.001$).

At the level of the popliteal artery, the mean intravascular attenuation values were 49.4 ± 7.8 HU in TNC and 40.7 ± 9.6 HU in VNC images ($p < 0.001$).

Finally, for the external iliac artery, the same values were 46.6 ± 9.4 HU in TNC images and 33.1 ± 6.4 HU in VNC images (p = ns).

The results of the attenuation comparison of TNC and VNC images at the examined levels have been summarized in Table 3.

In all the examined regions, TNC images showed significantly higher attenuation values ($p < 0.001$) than VNC images, with a mean difference of attenuation ranging from 14.1 and 8.7 HU, except for the level of the external iliac artery, where no statistically significant differences in terms of attenuation were registered ($p < 0.27$). In detail, a mean intravascular attenuation difference of 14.1 HU between TNC and VNC images at the level of the infrarenal aorta, a difference of 13.7 HU at the level of the common iliac artery, a difference of 13.5 HU at the level of the external iliac artery, a difference of 10.3 HU at the level of the superficial femoral artery, and a difference of 8.3 HU at level of popliteal artery were detected. The cumulative results of this analysis have been reported in Figure 3. Furthermore, the comparison of intravascular attenuation detected in TNC and VNC scans demonstrated less difference in HU value as the vessel caliber decreases, from the abdominal aorta to the popliteal segment, as shown in the diagram in Figure 4.

Table 3. Results of the comparison between true non-contrast (TNC) and virtual non-contrast (VNC) images in the different analyzed arterial segments: abdominal aorta, common iliac artery (AIC), external iliac artery (AIE), superficial femoral artery (AFS), popliteal artery (AP).

Anatomical Region	Contrast Phase	Mean Attenuation (HU)	Standard Deviation (DS)	*p*
Aorta	TNC	47.1	6.6	<0.000
	VNC	33.0	8.2	
AIC	TNC	47.8	8.9	<0.000
	VNC	34.1	11.4	
AIE	TNC	46.6	9.4	<0.27
	VNC	33.1	6.4	
AFS	TNC	48.5	9.0	<0.001
	VNC	38.2	10.4	
AP	TNC	49.4	7.8	<0.000
	VNC	40.7	9.6	

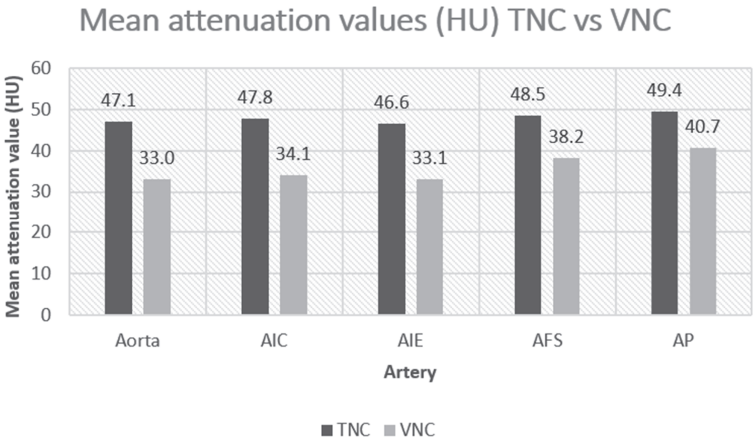

Figure 3. Bar graphs showing the comparison between mean attenuation values (HU) of true non-contrast (TNC) and virtual non-contrast (VNC) images in the different arterial segments analyzed: abdominal aorta, common iliac artery (AIC), external iliac artery (AIE), superficial femoral artery (AFS), popliteal artery (AP).

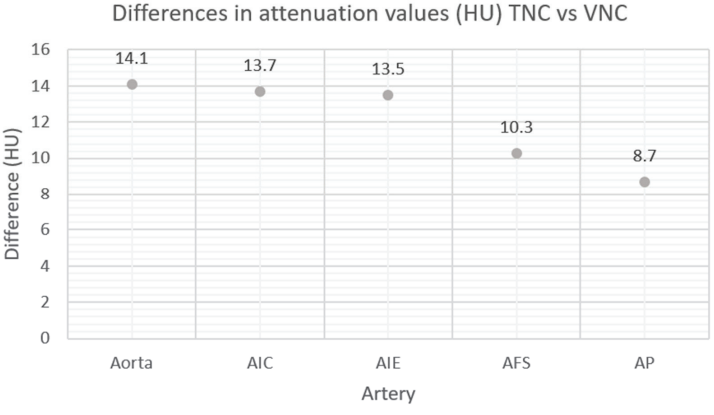

Figure 4. Differences in attenuation values (HU) between true non-contrast and virtual non-contrast images: the difference in HU value reduces as the vessel caliber decreases from the infrarenal aorta to the popliteal segment. AIC = common iliac artery; AIE = external iliac artery; AFS = superficial femoral artery; AP = popliteal artery.

Comprehensive results of the subjective qualitative analysis of VNC and TNC images performed by the two blinded observers were illustrated in Figure 5. All TNC images were rated as good in 10 (25%) cases and excellent in 30 (75%) cases (scores 3 and 4, respectively) while VNC images were rated as moderate in 4 (10%) cases, good in 20 (50%) cases, and excellent in 16 (40%) cases (scores 2, 3 and 4, respectively). All VNC images were judged sufficient for diagnosis. No cases of insufficiently diagnostic images were encountered by the two observers.

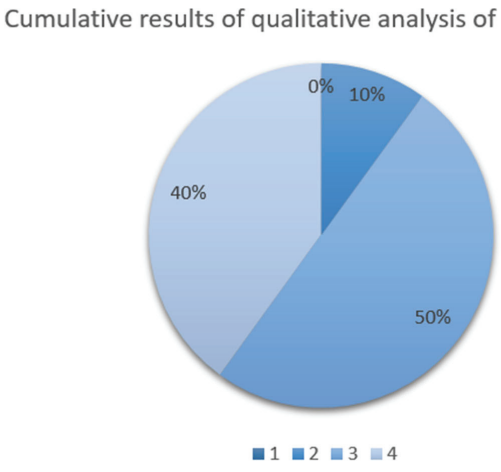

Figure 5. Cumulative results of qualitative analysis of virtual non-contrast images: 40% rated with a score of 4 (excellent); 50% with a score of 3 (good) and 10% with a score of 2 (moderate but sufficient for diagnosis). No virtual non-contrast reconstructions were considered non-diagnostic: 0% rated with a score of 1 in qualitative analysis.

The calculated ICC for the assessment of VNC images was good (0.6) while the ICC of TNC images resulted was excellent (0.9).

No cases of significative artefacts related to the permanence of iodine traces or due to the removal of stents or other devices were reported after the assessment of VNC images. Furthermore, in VNC reconstructions, highly calcified plaques were never improperly removed but, at most, were slightly attenuated.

The mean Dose Length Product (mGycm) for TNC acquisition was 546 mGycm while the mean DLP related to the DE-CTA arterial phase without the TNC acquisition was 463.5 mGycm. CT dose index volume (CTDIvol) measured values were 3.7 (2.4–9.4) for TNC acquisitions and 3.5 (1.1–6.6) for DE-CTA examinations without the TNC phase. The effective dose value of TNC acquisition was 3.25 (1.72–5.39) mSv while the effective dose value of contrast-enhanced acquisition alone was 2.76 (0.89–5.19) mSv.

The cumulative dosimetric data of TNC and arterial phases acquisitions of all DE-CTA examinations have been summarized in Table 4.

Table 4. Mean CT dose index volume (CTDIvol), mean Dose Length Product (DLP) and effective dose € values in true non-contrast and virtual non-contrast acquisitions.

Parameters	TNC	VNC
CTDI vol	3.7 (2.4–9.4)	3.5 (1.1–6.6)
DLP (mGyxcm)	546 (289–906)	463.5 (150–871)
E (mSv)	3.25 (1.72–5.39)	2.76 (0.89–5.19)

Therefore, a single DE-CTA scan with the lack of the TNC phase and completed by VNC reconstructed images may have resulted in a reduction of the administered mean effective dose.

4. Discussion

This prospective study based on 40 consecutive extremities DE-CTA scans was carried out to compare the image quality of TNC to VNC images, including attenuation and noise, as well as estimating the potential reduction in radiation dose. Based on the study results, firstly, VNC showed a good reliability in the detection of PAD in comparison to standard TNC phase; secondly, VNC reconstructions reported a high diagnostic quality at subjective analysis; and, thirdly, DE-CTA scans with the single VNC reconstructed images could result in a reduction of the administered mean effective dose.

The role of CTA in the assessment of the extent and severity of symptomatic PAD has been widely recognized by both the latest Guidelines from the American College of Cardiology/American Heart Association and the European Society of Cardiology [4,13]. Due to the recent advances in protocols and post-processing reconstructions and in lowering the amounts of radiation dose and contrast, CTA has therefore effectively replaced DSA as a first-line examination for diagnosing PAD.

As reported by previous studies, the advancement of third generation DECT and material decomposition algorithms may help in limiting blooming artifacts caused by dense calcifications and high iodine concentrations. DECT also enables a better assessment of the arterial lumen, avoiding stenosis overestimations [16]. With these assumptions, DECT imaging may be considered a valid alternative to conventional maximum intensity projection (MIP) standard reconstructions [16].

After a careful literature review, several studies were found to have attempted to account for VNC reconstructions as an alternative to standard non-contrast phases, all with controversial results [40–45]. Most of these studies were limited to the aorto-iliac attenuation values, except for one series, which has also been extended to the femoral axis [40]. Our study is one of the few to evaluate arterial lower limb vessels from the aortic axis to popliteal segments.

Since the anatomy and pathophysiology of femoropopliteal axis leads to specific challenges for both percutaneous and endovascular treatment, its non-invasive diagnosis is crucial to define the appropriate treatment strategy [2–4]. A great part of clinically significative PAD arises from femoropopliteal calcified lesions. Furthermore, endovascular treatments of this district are often challenging due to the important reactions to injuries of the thick arterial walls, which are prone to scar, proliferate, and thrombose. For these reasons, VNC reconstructions may significantly improve the evaluation of highly calcified steno-occlusive lesions of these segments [5].

Some authors reported a substantial agreement of intravascular attenuation values measured in the abdominal aorta between VNC reconstructions and TNC acquisitions [40,41]. Other studies have instead demonstrated a statistically significant difference in attenuation values at the same level, as confirmed by our series [40,43].

A greater difference in attenuation between the two CT protocols was detected in proximal vessels (aorto-iliac axis) and less pronounced in distal vessels (popliteal artery), except for the external iliac artery. This phenomenon could be explained by the different behavior of the homogeneous iodine distribution in parenchymatous tissues compared to laminar intravascular flow. The latter may lead to inaccuracies during VNC reconstructions due to blood motion artifacts. As proof of this, the greater accuracy in attenuation measurements at the level of the external iliac artery may be due to its anatomical characteristics and its lower flow [40–45].

The significatively lower attenuation values of VNC Images could be due to the very high concentration of iodine during the arterial phase. This phenomenon determinates, against the expectations, an excessive iodine removal during reconstructions, and consequent lower HU-values in VNC images [45]. As previously suggested by Sauter et al. [45],

this event may be reduced by the preference for contrast media with lower iodine concentrations, with the added advantage to reduce the iodine amount in older patients and those with chronic renal impairment. This interesting hypothesis is worth verifying in future studies.

Despite these considerations, the attenuation values measured in each arterial level have differed by 15 HU or less. The data provided by the vendor report a maximum average error of 10 HU in the performance of the reconstruction algorithm, which is better set for solid parenchyma rather than arterial vessels.

In the Sauter et al. [45] and Zhang et al. series [44], differences in attenuations between VNC and TNC images lower or equal to 10 HU were considered negligible, whereas differences between 10 and 15 HU were considered acceptable [44,45]. According to those results, our attenuation differences between TNC and VNC images were 10 HU or less in 40% of cases (superficial femoral artery and popliteal artery) and 10–15 HU in 60% (abdominal aorta, common iliac artery, and external iliac artery).

Even if a modified algorithm for calcium subtraction has been recently developed [5], allowing selective removal of calcified plaques, the arterial wall calcifications of the segments were included in VNC images by our post-processing algorithm. A slight attenuation, still enabling an accurate evaluation of the arterial wall and providing an improved luminal visualization, was only featured.

The results of the subjective analysis revealed a quality rated between good and excellent in 90% of VNC images examined. No reported non-diagnostic scores, no significative invalidating artifacts, and a good degree of concordance at inter-observer evaluation were found. These results are aligned with previous studies in demonstrating how subjective evaluation of image quality has not been significantly affected by VNC reconstruction [16,40].

The present study has several important limitations. Firstly, the single-center design was with a relatively small sample size. The second limitation is the heterogeneity of the study population in terms of demographic and clinical factors. In addition, the applicability of our results is limited to a DE-CTA dataset and to this vendor-specific Virtual Unenhanced analysis algorithm. As a last important limitation, the subjective scoring biases must be considered, regardless of the double-blinded and independent evaluations.

As future perspectives, given the limited size of the study group, our primary aim lies in enlarging the patient population in terms of size and indications. In addition to cases of clinically suspected PAD submitted to this study, in which DE-CTA with VNC reconstruction may help in establishing the degree of arterial stenoses, cases of treated PAD submitted to routinely follow-up DE-CTA should be further investigated. In such cases, DE-CTA imaging may contribute significantly to improve intravascular attenuation of stented arterial segments and in reducing prosthetic artifacts. The additional advantage of lowering radiation dose when repeated CT examinations are requested, as in post-operative follow-up, is also not insignificant.

Latest advanced DE-CTA technologies, such as rapid voltage-switching and energy-sensitive detector technology, should also be considered to obtain better results in terms of imaging quality and attenuation values.

In conclusion, despite the statistically significant difference in attenuation consisting in higher values of few HU in VNC compared to TNC, our quantitative analysis demonstrated the reliability of VNC images obtained by a third generation DECT scanner in the detection of PAD. A diagnostic quality ranging from good to excellent was also achieved. The further aim of reducing dose exposure with the introduction of VNC may be considered achieved with the finding of a 54% potential reduction of mean effective dose.

VNC reconstructions provided by DE-CTA, rather than being the current optimal alternative to standard baseline images, should be considered in a variety of selected cases. Routine multiphasic follow-up, when a reduction in radiation exposure is highly recommended or an overall acquisition time reduction is desirable, in cases of inaccurate

or inconclusive non-contrast images, and to avoid unnecessary DSA exams, are some of these situations.

The use of post-processing algorithms working on remote servers such as VNC offers the additional (and not secondary) advantage of avoiding unneeded acquisitions and reducing the high amount of generated CT images sent to the picture archiving and communication system (PACS).

Nevertheless, in daily clinical practice, where time gain, dose reduction, and data storage saving are crucial, the DE-CTA protocol with VNC reconstructions may be useful for PAD detection and for an accurate treatment planning.

Author Contributions: Conceptualization, C.F. and M.C. (Martina Curzi); methodology, G.A.; software, G.A. and M.C. (Michaela Cellina); validation, L.M.C., M.C. (Michaela Cellina) and A.F.; formal analysis, N.R.; investigation, T.V.; resources, A.B.; data curation, M.R.; writing—original draft preparation, L.M.C.; writing—review and editing, L.M.C.; visualization, M.R.; supervision, C.F.; project administration, R.C.; funding acquisition, A.G. All authors have read and agreed to the published version of the manuscript.

Funding: This research received no external funding.

Institutional Review Board Statement: The retrospective study conforms to the ethics guidelines of the Declaration of Helsinki and was approved by our Internal Review Board on 9 October 2021; patients provided their consent for the examination and use of their anonymized data.

Informed Consent Statement: Informed consent was obtained from all subjects involved in the study.

Data Availability Statement: Not applicable.

Conflicts of Interest: The authors declare no conflict of interest.

References

1. Aday, A.W.; Matsushita, K. Epidemiology of Peripheral Artery Disease and Polyvascular Disease. *Circ. Res.* **2021**, *128*, 1818–1832. [CrossRef]
2. Criqui, M.H.; Matsushita, K.; Aboyans, V.; Hess, C.N.; Hicks, C.W.; Kwan, T.W.; McDermott, M.M.; Misra, S.; Ujueta, F. Lower Extremity Peripheral Artery Disease: Contemporary Epidemiology, Management Gaps, and Future Directions: A Scientific Statement from the American Heart Association. *Circulation* **2021**, *144*, e171–e191. [CrossRef]
3. Fowkes, F.G.; Rudan, D.; Rudan, I.; Aboyans, V.; Denenberg, J.O.; McDermott, M.M.; Norman, P.E.; Sampson, U.K.; Williams, L.J.; Mensah, G.A.; et al. Comparison of global estimates of prevalence and risk factors for peripheral artery disease in 2000 and 2010: A systematic review and analysis. *Lancet* **2013**, *382*, 1329–1340. [CrossRef]
4. Aboyans, V.; Ricco, J.B.; Bartelink, M.E.L.; Björck, M.; Brodmann, M.; Cohnert, T.; Collet, J.P.; Czerny, M.; De Carlo, M.; Debus, S.; et al. 2017 ESC Guidelines on the Diagnosis and Treatment of Peripheral Arterial Diseases, in collaboration with the European Society for Vascular Surgery (ESVS): Document covering atherosclerotic disease of extracranial carotid and vertebral, mesenteric, renal, upper and lower extremity arteriesEndorsed by: The European Stroke Organization (ESO)The Task Force for the Diagnosis and Treatment of Peripheral Arterial Diseases of the European Society of Cardiology (ESC) and of the European Society for Vascular Surgery (ESVS). *Eur. Heart J.* **2018**, *39*, 763–816. [CrossRef] [PubMed]
5. Shwaiki, O.; Rashwan, B.; Fink, M.A.; Kirksey, L.; Gadani, S.; Karuppasamy, K.; Melzig, C.; Thompson, D.; D'Amico, G.; Rengier, F.; et al. Lower extremity CT angiography in peripheral arterial disease: From the established approach to evolving technical developments. *Int. J. Cardiovasc. Imaging* **2021**, *37*, 3101–3114. [CrossRef]
6. Yadav, V.; Khanduri, S.; Yadav, P.; Pandey, S.; Tyagi, E.; Yadav, H.; Krishnam, A.; Hamza, M. Diagnostic Accuracy of Color Doppler and Calcium Scoring versus Dual-Energy Computed Tomography Angiography in the Assessment of Peripheral Arterial Diseases of Lower Limb. *J. Clin. Imaging Sci.* **2020**, *10*, 45. [CrossRef] [PubMed]
7. Patel, M.C.; Levin, D.C.; Parker, L.; Rao, V.M. Have CT and MR angiography replaced catheter angiography in diagnosing peripheral arterial disease? *J. Am. Coll. Radiol.* **2015**, *12*, 909–914. [CrossRef]
8. Met, R.; Bipat, S.; Legemate, D.A.; Reekers, J.A.; Koelemay, M.J. Diagnostic performance of computed tomography angiography in peripheral arterial disease: A systematic review and meta-analysis. *JAMA* **2009**, *301*, 415–424. [CrossRef]
9. Napoli, A.; Anzidei, M.; Zaccagna, F.; Cavallo Marincola, B.; Zini, C.; Brachetti, G.; Cartocci, G.; Fanelli, F.; Catalano, C.; Passariello, R. Peripheral arterial occlusive disease: Diagnostic performance and effect on therapeutic management of 64-section CT angiography. *Radiology* **2011**, *261*, 976–986. [CrossRef]
10. Itoga, N.K.; Kim, T.; Sailer, A.M.; Fleischmann, D.; Mell, M.W. Lower extremity computed tomography angiography can help predict technical success of endovascular revascularization in the superficial femoral and popliteal artery. *J. Vasc. Surg.* **2017**, *66*, 835–843.e1. [CrossRef] [PubMed]

11. Meyersohn, N.M.; Walker, T.G.; Oliveira, G.R. Advances in axial imaging of peripheral vascular disease. *Curr. Cardiol. Rep.* **2015**, *17*, 87. [CrossRef] [PubMed]
12. Criqui, M.H.; Aboyans, V. Epidemiology of peripheral artery disease. *Circ. Res.* **2015**, *116*, 1509–1526. [CrossRef] [PubMed]
13. Gerhard-Herman, M.D.; Gornik, H.L.; Barrett, C.; Barshes, N.R.; Corriere, M.A.; Drachman, D.E.; Fleisher, L.A.; Fowkes, F.G.; Hamburg, N.M.; Kinlay, S.; et al. AHA/ACC Guideline on the Management of Patients with Lower Extremity Peripheral Artery Disease: Executive Summary: A Report of the American College of Cardiology/American Heart Association Task Force on Clinical Practice Guidelines. *Circulation* **2017**, *135*, e686–e725. [CrossRef] [PubMed]
14. Iezzi, R.; Santoro, M.; Marano, R.; Di Stasi, C.; Dattesi, R.; Kirchin, M.; Tinelli, G.; Snider, F.; Bonomo, L. Low-dose multidetector CT angiography in the evaluation of infrarenal aorta and peripheral arterial occlusive disease. *Radiology* **2012**, *263*, 287–298. [CrossRef]
15. Li, P.; Xu, L.; Yang, L.; Wang, R.; Hsieh, J.; Sun, Z.; Fan, Z.; Leipsic, J.A. Blooming Artifact Reduction in Coronary Artery Calcification by A New De-blooming Algorithm: Initial Study. *Sci. Rep.* **2018**, *8*, 6945. [CrossRef]
16. De Santis, D.; De Cecco, C.N.; Schoepf, U.J.; Nance, J.W.; Yamada, R.T.; Thomas, B.A.; Otani, K.; Jacobs, B.E.; Turner, D.A.; Wichmann, J.L.; et al. Modified calcium subtraction in dual-energy CT angiography of the lower extremity runoff: Impact on diagnostic accuracy for stenosis detection. *Eur. Radiol.* **2019**, *29*, 4783–4793. [CrossRef]
17. Schicchi, N.; Fogante, M.; Oliva, M.; Esposto Pirani, P.; Agliata, G.; Giuseppetti, G.M.; Giovagnoni, A. Radiation dose and image quality with new protocol in lower extremity computed tomography angiography. *Radiol. Med.* **2019**, *124*, 184–190. [CrossRef]
18. Aschof, A.J.; Catalano, C.; Kirchin, M.A.; Krix, M.; Albrecht, T. Low radiation dose in computed tomography: The role of iodine. *Br. J. Radiol.* **2017**, *90*, 20170079. [CrossRef]
19. Yang, L.; Sun, J.; Li, J.; Peng, Y. Dual-energy spectral CT imaging of pulmonary embolism with Mycoplasma pneumoniae pneumonia in children. *Radiol. Med.* **2022**, *127*, 154–161. [CrossRef]
20. Foti, G.; Mantovani, W.; Faccioli, N.; Crivellari, G.; Romano, L.; Zorzi, C.; Carbognin, G. Identification of bone marrow edema of the knee: Diagnostic accuracy of dual-energy CT in comparison with MRI. *Radiol. Med.* **2021**, *126*, 405–413. [CrossRef]
21. Foti, G.; Lombardo, F.; Guerriero, M.; Rodella, T.; Cicciò, C.; Faccioli, N.; Serra, G.; Manenti, G. Management of vertebral compression fractures: The role of dual-energy CT in clinical practice. *Radiol. Med.* **2022**, *127*, 627–636. [CrossRef]
22. Agostini, A.; Borgheresi, A.; Carotti, M.; Ottaviani, L.; Badaloni, M.; Floridi, C.; Giovagnoni, A. Third-generation iterative reconstruction on a dual-source, high-pitch, low-dose chest CT protocol with tin filter for spectral shaping at 100 kV: A study on a small series of COVID-19 patients. *Radiol. Med.* **2021**, *126*, 388–398. [CrossRef] [PubMed]
23. Tagliati, C.; Lanza, C.; Pieroni, G.; Amici, L.; Carotti, M.; Giuseppetti, G.M.; Giovagnoni, A. Ultra-low-dose chest CT in adult patients with cystic fibrosis using a third-generation dual-source CT scanner. *Radiol. Med.* **2021**, *126*, 544–552. [CrossRef] [PubMed]
24. Agostini, A.; Borgheresi, A.; Mari, A.; Floridi, C.; Bruno, F.; Carotti, M.; Schicchi, N.; Barile, A.; Maggi, S.; Giovagnoni, A. Dual-energy CT: Theoretical principles and clinical applications. *Med. Radiol.* **2019**, *124*, 1281–1295. [CrossRef] [PubMed]
25. Sanghavi, P.S.; Jankharia, B.G. Applications of dual energy CT in clinical practice: A pictorial essay. *Indian J. Radiol. Imaging* **2019**, *29*, 289–298. [CrossRef]
26. Javadi, S.; Elsherif, S.; Bhosale, P.; Jensen, C.T.; Layman, R.R.; Jacobsen, M.C.; Le, O.; Jia, S.; Parikh, R.J.; Tamm, E.P. Quantitative attenuation accuracy of virtual non-enhanced imaging compared to that of true non-enhanced imaging on dual-source dual-energy CT. *Abdom. Radiol.* **2020**, *45*, 1100–1109. [CrossRef]
27. Cicero, G.; Mazziotti, S.; Silipigni, S.; Blandino, A.; Cantisani, V.; Pergolizzi, S.; D'Angelo, T.; Stagno, A.; Maimone, S.; Squadrito, G.; et al. Dual-energy CT quantification of fractional extracellular space in cirrhotic patients: Comparison between early and delayed equilibrium phases and correlation with oesophageal varices. *Radiol. Med.* **2021**, *126*, 761–767. [CrossRef]
28. Garnett, R. A comprehensive review of dual-energy and multi-spectral computed tomography. *Clin. Imaging* **2020**, *67*, 160–169. [CrossRef]
29. Megibow, A.J.; Kambadakone, A.; Ananthakrishnan, L. Dual-Energy Computed Tomography: Image Acquisition, Processing, and Workflow. *Radiol. Clin. North Am.* **2018**, *56*, 507–520. [CrossRef]
30. Huang, S.Y.; Nelson, R.C.; Miller, M.J.; Kim, C.Y.; Lawson, J.H.; Husarik, D.B.; Boll, D.T. Assessment of vascular contrast and depiction of stenoses in abdominopelvic and lower extremity vasculature: Comparison of dual-energy MDCT with digital subtraction angiography. *Acad. Radiol.* **2012**, *19*, 1149–1157. [CrossRef]
31. Brockmann, C.; Jochum, S.; Sadick, M.; Huck, K.; Ziegler, P.; Fink, C.; Schoenberg, S.O.; Diehl, S.J. Dual-energy CT angiography in peripheral arterial occlusive disease. *Cardiovasc. Interv. Radiol.* **2009**, *32*, 630–637. [CrossRef] [PubMed]
32. Kim, J.S.; Park, S.H.; Park, S.; Hwang, J.H.; Kim, J.H.; Pak, S.Y.; Lee, K.; Schmidt, B. Imaging Findings of Peripheral Arterial Disease on Lower-Extremity CT Angiography Using a Virtual Monoenergetic Imaging Algorithm. *J. Korean Soc. Radiol.* **2022**, *83*, 1032–1045. [CrossRef]
33. Kau, T.; Eicher, W.; Reiterer, C.; Niedermayer, M.; Rabitsch, E.; Senft, B.; Hausegger, K.A. Dual-energy CT angiography in peripheral arterial occlusive disease-accuracy of maximum intensity projections in clinical routine and subgroup analysis. *Eur. Radiol.* **2011**, *21*, 1677–1686. [CrossRef] [PubMed]
34. Klink, T.; Wilhelm, T.; Roth, C.; Heverhagen, J.T. Dual-Energy CTA in Patients with Symptomatic Peripheral Arterial Occlusive Disease: Study of Diagnostic Accuracy and Impeding Factors. *Rofo* **2017**, *189*, 441–452. [CrossRef]

35. Koo, B.J.; Won, J.H.; Choi, H.C.; Na, J.B.; Kim, J.E.; Park, M.J.; Jo, S.H.; Park, H.O.; Lee, C.E.; Kim, M.J.; et al. Automatic Plaque Removal Using Dual-Energy Computed Tomography Angiography: Diagnostic Accuracy and Utility in Patients with Peripheral Artery Disease. *Medicina* **2022**, *58*, 1435. [CrossRef]
36. Almutairi, A.; Sun, Z.; Poovathumkadavi, A.; Assar, T. Dual Energy CT Angiography of Peripheral Arterial Disease: Feasibility of Using Lower Contrast Medium Volume. *PLoS ONE* **2015**, *10*, e0139275. [CrossRef]
37. Tanaka, R.; Yoshioka, K.; Takagi, H.; Schuijf, J.D.; Arakita, K. Novel developments in non-invasive imaging of peripheral arterial disease with CT: Experience with state-of-the-art, ultra-high-resolution CT and subtraction imaging. *Clin. Radiol.* **2019**, *74*, 51–58. [CrossRef]
38. Cicero, G.; Ascenti, G.; Albrecht, M.H.; Blandino, A.; Cavallaro, M.; D'Angelo, T.; Carerj, M.L.; Vogl, T.J.; Mazziotti, S. Extra-abdominal dual-energy CT applications: A comprehensive overview. *Radiol. Med.* **2020**, *125*, 384–397. [CrossRef]
39. Björck, M.; Earnshaw, J.J.; Acosta, S.; Bastos Gonçalves, F.; Cochennec, F.; Debus, E.S.; Hinchliffe, R.; Jongkind, V.; Koelemay, M.J.W.; Menyhei, G.; et al. Editor's Choice—European Society for Vascular Surgery (ESVS) 2020 Clinical Practice Guidelines on the Management of Acute Limb Ischaemia. *Eur. J. Vasc. Endovasc. Surg.* **2020**, *59*, 173–218. [CrossRef]
40. Lee, M.H.; Park, H.J.; Kim, J.N.; Kim, M.S.; Hong, S.W.; Park, J.H.; Kang, C.H. Virtual non-contrast images from dual-energy CT angiography of the abdominal aorta and femoral arteries: Comparison with true non-contrast CT images. *Br. J. Radiol.* **2022**, *95*, 20220378. [CrossRef] [PubMed]
41. Sommer, C.M.; Schwarzwaelder, C.B.; Stiller, W.; Schindera, S.T.; Stampfl, U.; Bellemann, N.; Holzschuh, M.; Schmidt, J.; Weitz, J.; Grenacher, L.; et al. Iodine removal in intravenous dual-energy CT-cholangiography: Is virtual non-enhanced imaging effective to replace true non-enhanced imaging? *Eur. J. Radiol.* **2012**, *81*, 692–699. [CrossRef]
42. Toepker, M.; Moritz, T.; Krauss, B.; Weber, M.; Euller, G.; Mang, T.; Wolf, F.; Herold, C.J.; Ringl, H. Virtual non-contrast in second-generation, dual-energy computed tomography: Reliability of attenuation values. *Eur. J. Radiol.* **2012**, *81*, e398–e405. [CrossRef] [PubMed]
43. Lehti, L.; Söderberg, M.; Höglund, P.; Nyman, U.; Gottsäter, A.; Wassélius, J. Reliability of virtual non-contrast computed tomography angiography: Comparing it with the real deal. *Acta Radiol. Open* **2018**, *7*, 205846011879011. [CrossRef] [PubMed]
44. Zhang, L.J.; Peng, J.; Wu, S.Y.; Wang, Z.J.; Wu, X.S.; Zhou, C.S.; Ji, X.M.; Lu, G.M. Liver virtual non-enhanced CT with dual-source, dual-energy CT: A preliminary study. *Eur. Radiol.* **2010**, *20*, 2257–2264. [CrossRef] [PubMed]
45. Sauter, A.P.; Muenzel, D.; Dangelmaier, J.; Braren, R.; Pfeiffer, F.; Rummeny, E.J.; Noël, P.B.; Fingerle, A.A. Dual-layer spectral computed tomography: Virtual non-contrast in comparison to true non-contrast images. *Eur. J. Radiol.* **2018**, *104*, 108–114. [CrossRef]

applied sciences

MDPI

Article

Single Puncture TIPS—A 3D Fusion Image-Guided Transjugular Intrahepatic Portosystemic Shunt (TIPS): An Experimental Study

Edward Wolfgang Lee [1,2,3,*], Puja Shahrouki [1], Sammy Saab [3,4], Fady Kaldas [2,3], Navid Eghbalieh [1], Justin McWilliams [1,3], Peng-Xu Ding [1] and Stephen T. Kee [1]

[1] Division of Interventional Radiology, Department of Radiology, UCLA Medical Center, David Geffen School of Medicine at UCLA, Los Angeles, CA 90095, USA; pshahrouki@mednet.ucla.edu (P.S.); navide123@yahoo.com (N.E.); jumcwilliams@mednet.ucla.edu (J.M.); jieru375@sina.com (P.-X.D.); stephentkee@gmail.com (S.T.K.)
[2] Division of Liver and Pancreas Transplantation, Department of Surgery, David Geffen School of Medicine at University of California, Los Angeles, CA 90095, USA; fkaldas@mednet.ucla.edu
[3] Dumont-UCLA Transplant Center, University of California, Los Angeles, CA 90095, USA; ssaab@mednet.ucla.edu
[4] Division of Hepatology, Department of Medicine, UCLA Medical Center, David Geffen School of Medicine at UCLA, Los Angeles, CA 90095, USA
* Correspondence: edwardlee@mednet.ucla.edu; Tel.: +1-310-267-8771

Abstract: Background: The use of a transjugular intrahepatic portosystemic shunt (TIPS) has been established as an effective treatment for portal hypertension. Despite the rapid development of this use, serious peri-procedural complications have been reported in over 10% of cases. This has largely been attributed to the access to the portal vein, also referred to as a "blind puncture", which often requires multiple attempts. The aim of this study was to demonstrate the safety, reproducibility and accuracy of the use of real-time 3D fusion image-guided (3DFIG) single puncture TIPS to minimize the complications that are related to the "blind puncture" of TIPS procedures. Methods: A 3DFIG TIPS approach was utilized on 22 pigs by combining pre-procedural cross-sectional imaging (CT, MR or CBCT) with intra-procedural cone beam CT or angiogram imaging, which allowed for the improved 3D visual spatial orientation of the portal vein and real-time tracking of the needle in 3D. Results: Thirty-five portosystemic shunts were successfully deployed in all 22 subjects without any peri-procedural complications. Overall, 91% (32/35) of the procedures were carried out using a single puncture. In addition, the mean fluoroscopy time in our study was more than 12 times lower than the proposed reference level that has previously been proposed for TIPS procedures. Conclusion: Multi-modality real-time 3DFIG TIPS can be performed safely using a single puncture, without complications, and can potentially be used in both emergency and non-emergency clinical situations.

Keywords: transjugular intrahepatic portosystemic shunt (TIPS); direct intrahepatic portosystemic shunt (DIPS); 3D fusion imaging; portal vein puncture; complications

Citation: Lee, E.W.; Shahrouki, P.; Saab, S.; Kaldas, F.; Eghbalieh, N.; McWilliams, J.; Ding, P.-X.; Kee, S.T. Single Puncture TIPS—A 3D Fusion Image-Guided Transjugular Intrahepatic Portosystemic Shunt (TIPS): An Experimental Study. *Appl. Sci.* **2022**, *12*, 5267. https://doi.org/10.3390/app12105267

Academic Editor: Julio Garcia Flores

Received: 12 April 2022
Accepted: 20 May 2022
Published: 23 May 2022

1. Introduction

The use of a transjugular intrahepatic portosystemic shunt (TIPS) is an effective treatment for portal hypertension and its associated complications, which has made it a widely used tool worldwide since the 1980s [1,2]. Multiple large clinical trials have confirmed that TIPS procedures play a major role in mitigating the severe consequences of portal hypertension, such as variceal bleeding and intractable ascites [3–8]. However, despite the numerous advantages of TIPS procedures, severe peri-procedural complications have been reported to occur in over 10% of cases, including transcapsular puncture, the accidental puncture of non-target structures and the puncture of the extrahepatic portal vein (PV) [9–12].

The primary source of procedure-related complications is associated with the most technically challenging step of the TIPS procedure: gaining access to the PV, which is often referred to as a "blind puncture" [9,13–15]. In this step, the operator has no visualization or real-time information of the spatial relationship between the systemic and portal venous systems. This "blind puncture" can make it more likely that the operator punctures areas other than the PV, such as the liver capsule, bile duct or hepatic artery and the extrahepatic PV, which may result in massive intraperitoneal hemorrhage or death. In rare cases, operators have been reported to make up to 50 attempts before successfully accessing the PV [16], which increases the risk of puncture-related complications. The difficult nature of this procedure can largely depend on the following factors: the malformation/transformation of a chronically diseased liver, the displacement of the liver due to ascites, thrombosed or cavernous portal/hepatic veins and the anatomic and pathologic variants of the portal architecture. In some of these cases, the selection of the correct PV may be critical for the effectiveness of the TIPS procedure [17,18], suggesting that the current standard technique of blind punctures may be inadequate. The use of a direct intrahepatic portosystemic shunt (DIPS), which is a technical variant of the TIPS procedure that relies on intravascular US, has been proposed as being preferable for certain patients, but has the same inherent limitations as current image-guided TIPS procedures [19].

In our study, we developed a new technique for targeting the portal vein during TIPS procedures. By fusing angiographic imaging (cone beam computed tomography; CBCT) and cross-sectional 2D images with CBCT, MR or computed tomography (CT), we aimed to evaluate the safety, reproducibility and accuracy of a real-time 3D fusion image-guided (FIG) TIPS procedure in vivo.

2. Materials and Methods

2.1. Animals

This retrospective study was approved by our institutional animal research committee (ARC#2006-054-33A). Twenty-two female Yorkshire pigs at a weight of 30–50 kg (~15 weeks old) were obtained and maintained by the Division of Laboratory Animal Medicine at our institution. The animals were maintained in group housing, either in pens or individual cages, and were fed a standard laboratory swine diet (LabDiet®, St. Louis, MO, USA). All animals received appropriate humane care from trained professional staff in compliance with the ARRIVE guidelines, the Principals of Laboratory Animal Care and the Guide for the Care and Use of Laboratory Animals, which was approved by the Animal Care and Use Committees of our institution and in accordance with NIH guidelines. All animals were fasted for at least 12 h before the procedure. Of 35 procedures on 22 animals: 10 procedures utilized TIPS with the use of CT-, CBCT- and angiogram-fused image guidance; 10 procedures used MR-, CBCT- and angiogram-fused image guidance; 7 animals underwent only CBCT- and angiogram-fused image guidance; and 8 animals underwent DIPS using pre-procedural CT-, CBCT- and angiogram-fused images.

2.2. General Anesthesia

General anesthesia was induced based on the National Institute of Health (NIH) guidelines for all TIPS procedures and pre-procedural MRI imaging. Each pig was placed in the supine position. For initial sedation, Telazol 4–8 mg/kg (Zoetis, Parisppanany, NJ, USA) was administered intramuscularly (IM). Anesthesia was then maintained by inhaled 1–3.5% isoflurane in oxygen. Pancuronium (0.1 mg/kg) was administered prior to all TIPS procedures to achieve reversible paralysis, which was monitored by evoked motor response. Blood pressure and EKG were also monitored continuously.

2.3. Pre-Procedural Imaging

2.3.1. CT

Pre-procedural contrast-enhanced CT images were taken using a 64-slice multi-detector CT (Somatom Sensation, Siemens, Forscheim, Germany). After the initial unenhanced

images of the abdomen were obtained, Iohexol 1.5 mL/kg (Omnipaque 300 mg/mL; GE, Princeton, NJ, USA) was power injected through a peripheral vein in the forelimb or another peripheral vein when a forelimb vein was inaccessible. This was followed by an injection of 40 mL of saline at a rate of 0.4 mL/s and images were subsequently acquired during both the arterial dominant phase (20 s after injection) and in the portal venous dominant phase (60 s after injection). The following CT parameters were used: 250 mA; 120 kVp; 3-mm collimation; and 2:1 pitch. The pigs were not maintained on anesthetic during the CT procedure as it took less than 5 min to complete the study.

2.3.2. MR Imaging

Pre-procedural MR imaging was performed using a 3T MR imaging unit (Siemens Healthcare, Malvern, PA, USA) and consisted of both unenhanced and contrast-enhanced dynamic (arterial and portal venous) fat-saturated T1-weighted gradient-echo imaging (repetition time msec/echo time msec, 257/2.32; thickness, 5 mm; acquisitions, two; field of view, 200 × 300 mm; and matrix, 256 × 256) and unenhanced T2-weighted fat-suppressed turbo spin-echo imaging (TR/TE, 4515/82; 5 mm; flip angle, 140; and field of view, 320 × 272 mm). The dynamic contrast-enhanced T1-weighted imaging was performed after the administration of an intravenous contrast agent (gadodiamide 0.1 mmol/kg, Omniscan; Nycomed, Zürich, Switzerland).

2.4. Cone Beam CT Imaging

Imaging was performed using commercially available flat-panel detectors (Artis Zeego, Siemens, Forcheim, Germany). The 2D and 3D images were acquired using CBCT technology (DynaCT, Siemens, Forcheim, Germany) and volumetric image reconstruction (modified Feldkamp back projection) was subsequently performed at a dedicated workstation. For each cone beam CT scan, 312 projection images (30 frames per second) were acquired, which covered a 200° clockwise arc at a rotation speed of 20° per second. As the images were being acquired, the projections were transferred to the reconstruction workstation. The two-dimensional projection images were reconstructed using modified Feldkamp back projection into three-dimensional volumetric images, which has an isotropic resolution of 0.98 mm for a 250 mm × 250 mm × 194 mm field of view (matrix size, 256 × 256 × 256).

2.5. TIPS and DIPS Creation Using 3D Image Guidance

Following the pre-procedural imaging, the animals were transported to the interventional imaging suite, which was equipped with rotational CBCT angiography and 3D reconstruction-rendered real-time angiography. All procedures were performed using an angiographic C-arm imaging system that utilized a flat-panel x-ray detector (Artis Zeego, Siemens, Forcheim, Germany). The animals were placed under the C-arm and general anesthesia was maintained with 1–3.5% isoflurane. All procedures were carried out by the same interventional radiologist who had 10 years of post-fellowship experience, including over 300 TIPS procedures. Next, the right internal jugular vein (RIJV) was accessed under US guidance. A 10F sheath was then advanced through the RIJV access point and either a glide catheter or multipurpose angiography (MPA) catheter was used to catheterize the right hepatic vein (HV). A Rösch-Uchida TIPS needle (Cook Inc., Bloomington, IN, USA) was then placed over the wire in place of the glide/MPA catheter. Once the Rösch-Ushida needle was placed in the right HV, a CBCT (DynaCT, Siemens, Forcheim, Germany) was obtained using the rotational angiography apparatus.

The pre-procedural CT or MR images were retrieved from a PACS system at the angiographic system workstation (Syngo X-Workplace, Siemens, Forcheim, Germany). The 3D-reconstructed CT or MR images were loaded into the InSpace® application (Siemens, Forcheim, Germany) and subsequently fused with the 3D-reconstructed CBCT images using the iGuide® software (Siemens, Forcheim, Germany). This fused 3D-reconstructed roadmap was overlaid onto the real-time fluoroscopic image. The tip of the Rösch-Ushida

needle and the target portal branch were identified on the images and the optimal path from the needle to the target puncture site of the PV was automatically mapped out by the iGuide® software. Under real-time 3D fluoroscopic guidance, the operator then advanced the TIPS needle into the PV following the determined path. Once the iGuide® PV puncture was made, venography was performed to confirm access to the portal system. For the DIPS procedures, the tip of the Rösch-Ushida needle was placed in the intrahepatic IVC instead of the right HV and the imaging fusion, 3D fluoroscopic guidance and portal puncture were performed as in the TIPS procedure.

2.6. Data Collection and Statistical Analysis

The procedural success and complication rates, time required to create the 3D fusion image guidance (3DFIG) images, total procedure time, total fluoroscopy radiation time and the number of PV puncture attempts were determined for all procedures. Continuous data are presented as the means and standard deviations (SDs) or medians and interquartile ranges (IQRs) whereas categorical data are presented as proportions and percentages. The data and statistical analyses were performed using SPSS software (SPSS v. 25.0, IBM, Chicago, IL, USA).

3. Results

3.1. Basic Assessment

Technically successful 3D-fused angiography-guided TIPS (n = 27) or DIPS (n = 8) procedures were performed in 35/35 (100%) cases (Figures 1–4). No immediate procedure-related complications were noted during or immediately after the TIPS or DIPS procedures in any of the 22 swine (0/35; 0%).

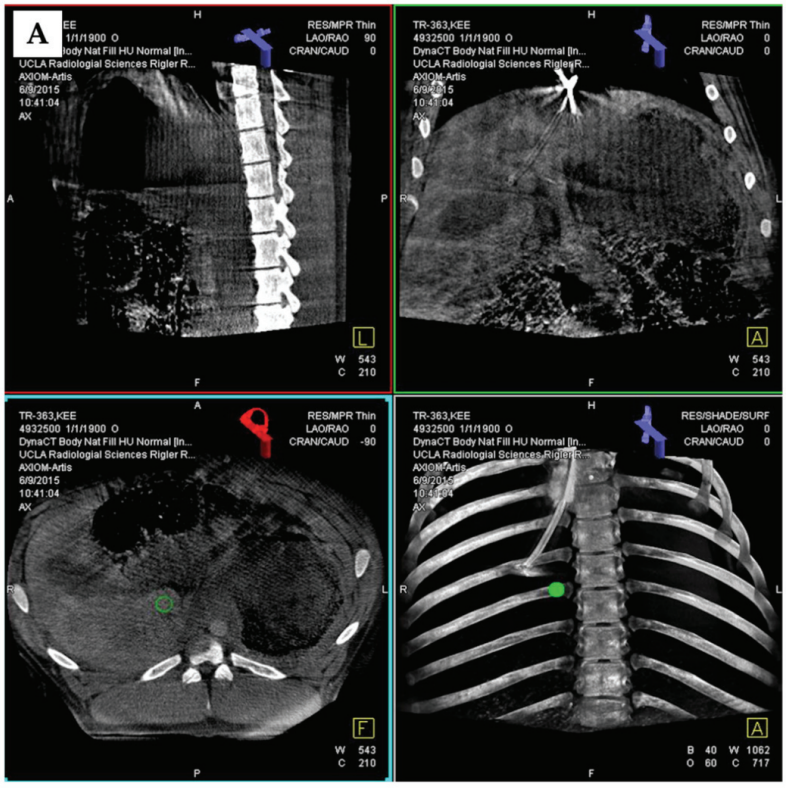

Figure 1. *Cont*.

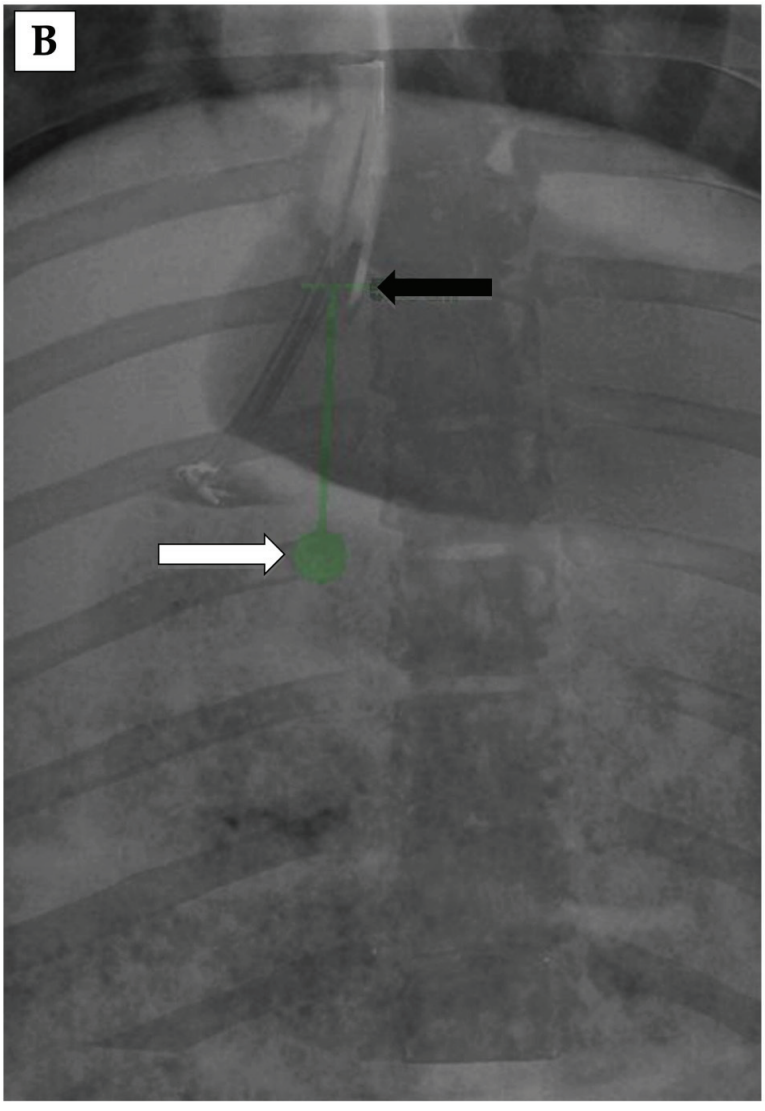

Figure 1. CBCT-guided TIPS: (**A**) procedure for the creation of a fusion image of CBCT, with the green dot (which was derived from CBCT reconstruction images) showing where the target (portal vein) was; (**B**) a fluoroscopic image of the pre-portal vein puncture for the 3DFIG TIPS procedure, demonstrating the virtual path (green) of the portal vein puncture, the location of the needle tip in the hepatic vein (black arrow) with the expected puncture distance and the expected location of the portal vein (white arrow).

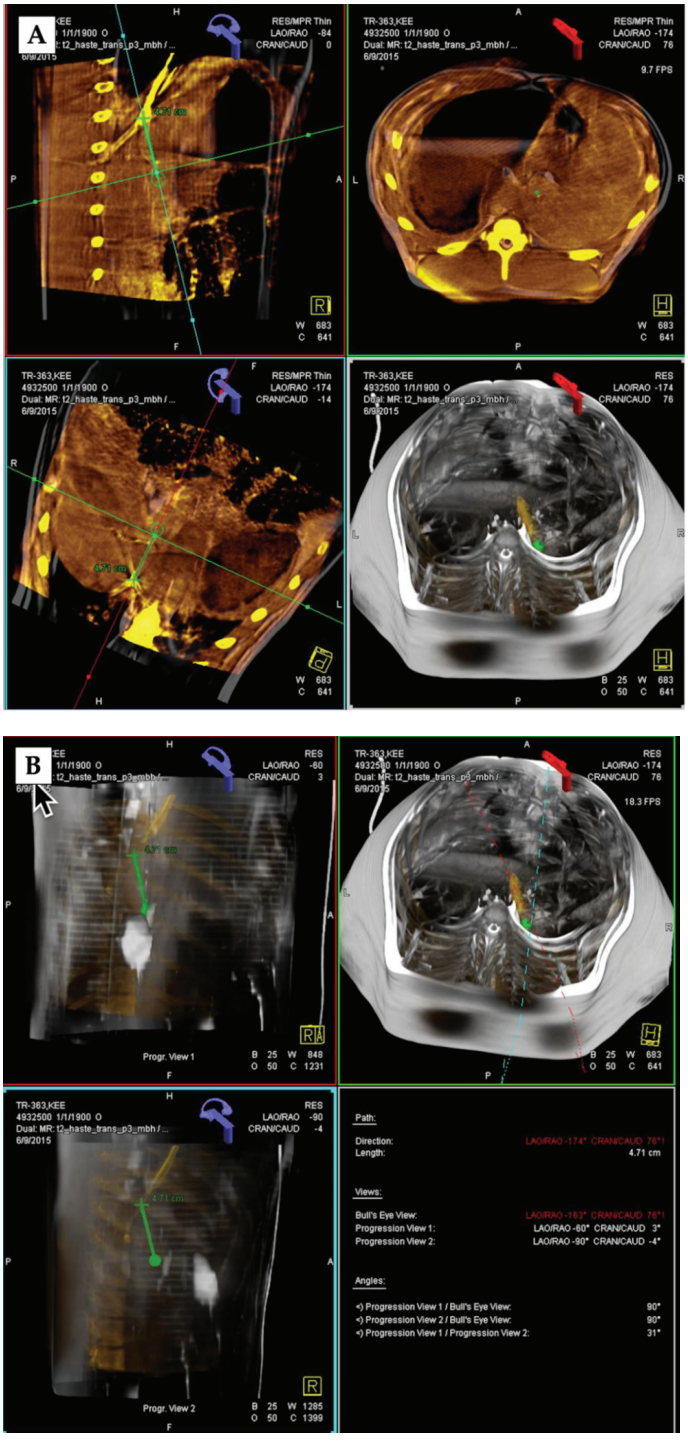

Figure 2. 3D Fusion Processing: (**A**) screenshots of the image software that was used to produce the three-dimensional fusion images of the pre-procedural MRs (yellow images) and peri-procedural

cone beam CTs and angiograms (grey images), including the virtual path (green) of the portal vein TIPS puncture and the direction and distance of the puncture; (**B**) visualized needle in the hepatic vein, which could be overlayed onto angiograms in real time for portal vein puncture guidance, with the green dot denoting the target (portal vein).

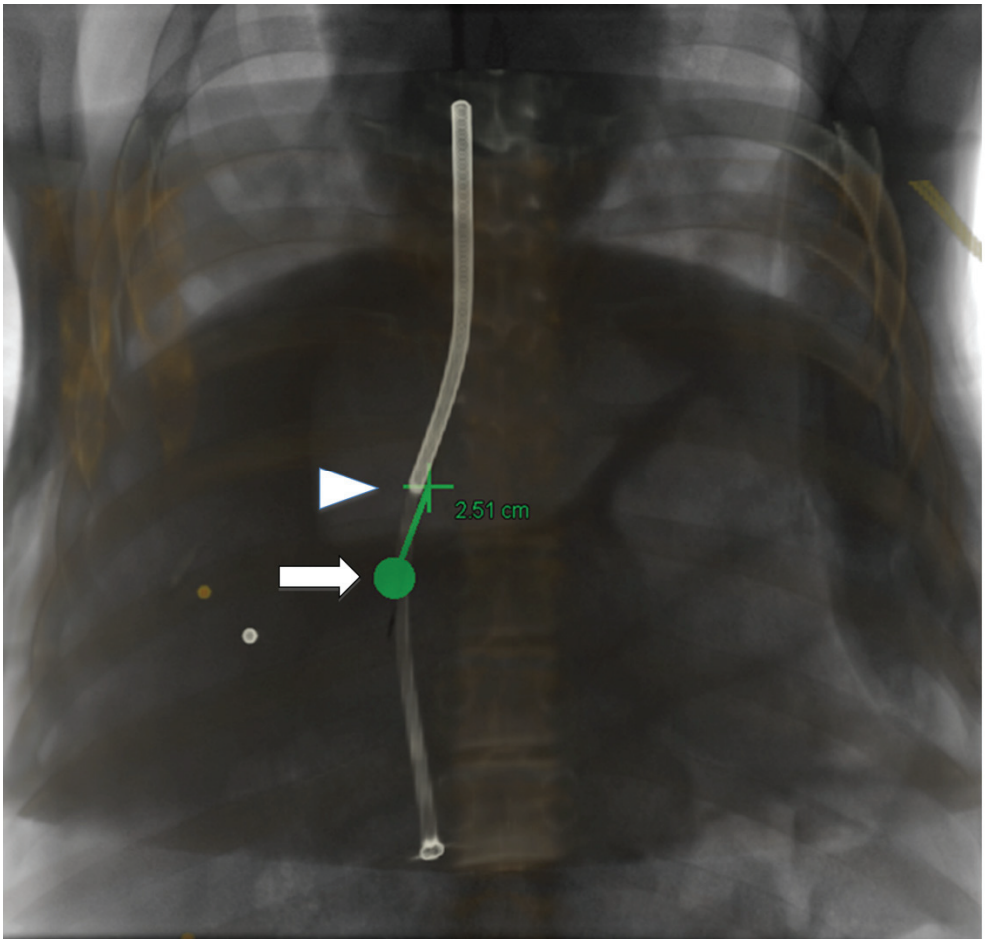

Figure 3. iGUIDE DIPS: a fluoroscopic image of the pre-portal vein puncture for the 3DFIG TIPS procedure using pre-procedural CT and peri-procedural cone beam CT images, demonstrating the virtual path (green) of the portal vein puncture, the location of the needle tip in the IVC (white arrowhead) with the expected distance of puncture and the expected location of the portal vein (white arrow). As expected, the expected distance from the IVC to the portal vein was very short for the DIPS procedure.

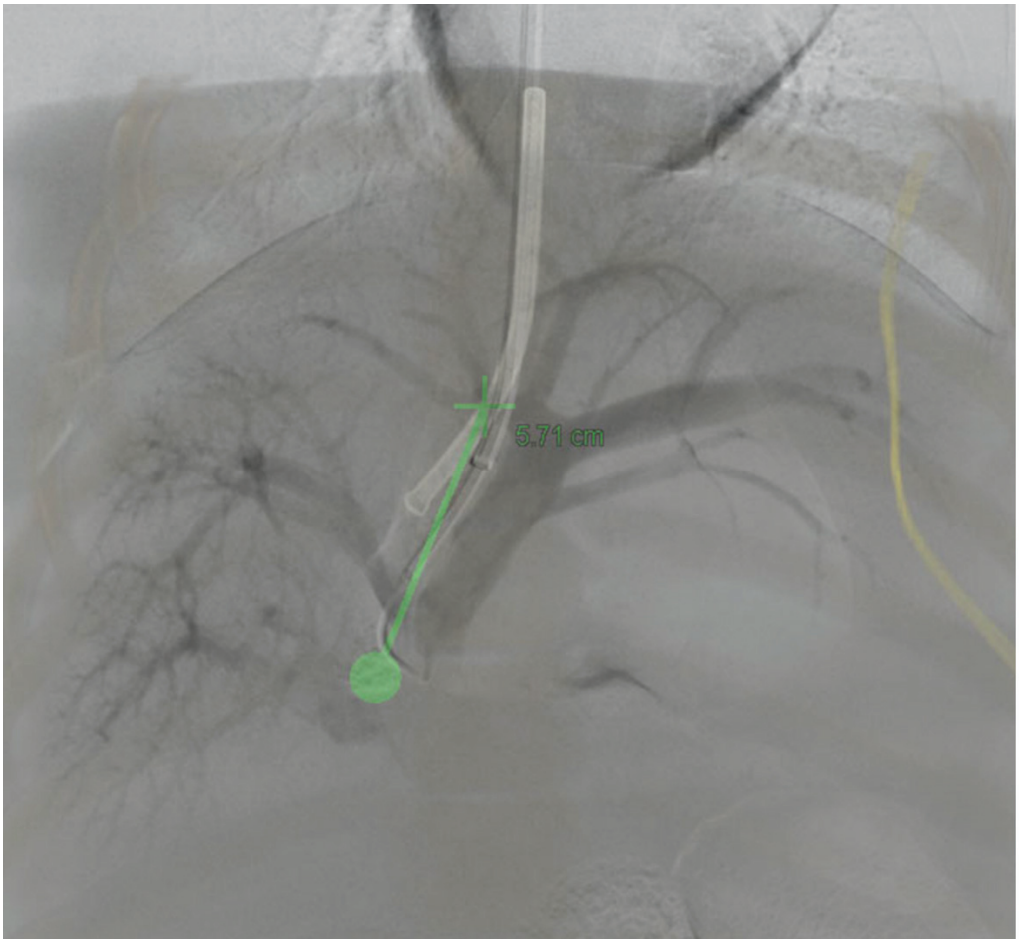

Figure 4. Portal Venogram: a 3DFIG TIPS procedural angiographic image that demonstrates the path of the needle from the hepatic vein to the portal vein (green) and the successful portal venogram after gaining access to the portal vein with TIPS needle.

3.2. 3D Angiography-Guided TIPS Procedure Using Pre-Procedural Cross-Sectional Imaging with CBCT/Angiography-Fused Images

The 3DFIG TIPS procedures that utilized CT and MR were successfully performed using a single PV puncture attempt in 90% (9/10) and 90% (9/10) of cases, respectively, and using two attempts in the remaining cases. The mean total procedure time (TPT: time from access to the right internal jugular vein (RIJV) to access to the PV) was 22.4 ± 5.1 and 18.7 ± 3.1 min for the CT and MR 3DFIG procedures, respectively. The median fluoroscopy time (MFT: fluoroscopy time between access to the RIJV to access to the PV) for both CT and MR 3DFIG procedures was 4.0 min (IQR, 3.0–5.3). The total time required to create the 3D images (TTC3D: time from importing images to 3D fusion to the creation of the iGuide® map) was 8.5 ± 3.4 and 7.5 ± 2.7 min for the CT and MR 3DFIG procedures, respectively (Table 1).

Table 1. Technical outcomes of the 3DFIG TIPS procedures.

	3DFIG TIPS with CBCT/Angio Alone	3DFIG TIPS with CT/CBCT/Angio	3DFIG TIPS with MR/CBCT/Angio	3DFIG DIPS with CT/CBCT/Angio
Technical Success	7/7	10/10	10/10	8/8
Complications	0	0	0	0
Single PV Puncture	7/7 (100%)	9/10 (90%)	9/10 (90%)	7/8 (88%)
TPT (min)	14.4 ± 1.0 *	22.4 ± 5.1	18.7 ± 3.1	14.1 ± 1.1
TTC3D (min)	3.0 ± 0.8 *	8.5 ± 3.4	7.5 ± 2.7	3.9 ± 0.7
MFT (min)	3.0 (IQR, 3.0–3.0) *	4.0 (IQR, 3.0–5.3)	4.0 (IQR, 3.0–5.3)	3.0 (IQR, 3.0–3.0)

TPT, total procedure time (mean ± SD); TTC3D, total time to create 3D fusion images (mean ± SD); MFT, median fluoroscopy time (median with IQRs). * denoted as $p < 0.05$ compared to CT/CBCT/Angiography or MR/CBCT/Angiography group

3.3. 3D Angiography-Guided TIPS Using CBCT/Angiography-Fused Images

To determine whether the procedure could be carried out without pre-procedural imaging, 3DFIG TIPS procedures were carried out using only CBCT/angiography-fused images. TIPS procedures were successfully carried out using a single stick in 100% (7/7) of cases. The TPT and TTC3D were 14.4 ± 1.0 and 3.0 ± 0.8 min, respectively. The median fluoroscopy time (MFT) was 3.0 min (IQR, 3.0–3.0). All three parameters (TPT, TTC3D and MFT) were significantly shorter during the 3DFIG TIPS procedures, with only CBCT/angiography being comparable to 3DFIG using CT/MR and CBCT/angiography ($p < 0.0001$).

3.4. 3D Angiography-Guided DIPS Using CT/CBCT/Angiography-Fused Images

DIPS procedures were successfully performed on the first attempt in 88% (7/8) of cases and after two attempts in the remaining case. The TPT and TTC3D were 14.1 ± 1.1 and 3.9 ± 0.7 min, respectively. The median fluoroscopy time was 3.0 min (IQR, 3.0–3.0).

4. Discussion

There is a major need for ancillary systems that are able to enhance the ability of operators to locate and enter the portal vein with relative ease. Many researchers have attempted to solve this problem by introducing various methods, such as guidance by perioperative ultrasound (US), magnetic resonance (MR) or intraprocedural carbon dioxide (CO_2) angiography, but no method has consistently been able to successfully produce single puncture PV access in large cohorts [11,13,20–22]. Furthermore, these methods can increase procedure length and the risk of other complications, with little benefit to streamlining the PV puncture step [23].

In this study, we demonstrated the feasibility of pre-procedural 3D fusion imaging for guiding TIPS and DIPS procedures. Specifically, we showed that the 3DFIG approach works by combining pre-procedural cross-sectional imaging (CBCT, CT or MR) with intraprocedural CBCT or angiogram imaging for real-time 3D-guided TIPS placement. The utility of this approach has been demonstrated using pre-procedural CT imaging in patients, in which the efficiency of placing the TIPS was clearly demonstrated [24–26]. The potential for the use of pre-procedural cross-sectional imaging for 3DFIG TIPS procedures is vast, as most non-emergency patients have imaging available prior to their planned TIPS procedure. Due to underlying chronic liver disease, these patients are mostly followed by their hepatologists or gastroenterologists and also undergo routine surveillance imaging.

Minimizing procedural times while maintaining accuracy is critical, especially in urgent and emergency TIPS procedures that are used to treat acute variceal bleeding. Although there was a limited number of subjects, we showed that 3DFIG TIPS procedures using CBCT/angiography-fused images alone produced similar outcomes but with significantly shorter procedural times, which has important clinical implications for patients who do not have pre-procedural CT or MR imaging available to them [27]. Finally, we demon-

strated the feasibility of using the 3DFIG DIPS procedure, which could prove to be especially relevant in patients for whom the traditional TIPS procedure is contraindicated [28].

The addition of 3DFIG to the TIPS and DIPS procedures led to a 100% success rate, with no complications and short fluoroscopy and procedure times. Most importantly, the number of needle puncture attempts that was required to gain PV access was low compared to the "blind" portosystemic needle punctures that are only guided by fluoroscopy [16,29]. Transvenous intrahepatic access to the PV is the most crucial and also most dangerous step of the TIPS procedure. The typical number of attempts that is required to access the PV has been reported to be between 3–5 attempts in the literature [16,29], although many more attempts may be needed in clinical practice, compared to the single pass success rate of 93% (25/27) for TIPS and 88% (7/8) for DIPS procedures in this study, with the remaining procedures requiring only two passes. Additionally, the mean fluoroscopy time in all procedures was shorter than 5 min, compared to the reference level of 60 min that has been proposed for TIPS procedures, which was derived from a RAD-IR study [30]. These benefits increase the safety profile and accuracy of the procedure and greatly reduce potential radiation exposure. Compared to other existing and proposed methods, the 3DFIG method provides users with the option to track the needle in real time, thereby facilitating the anatomical orientation by projecting fluoroscopic images onto 3D images to visualize the puncture target [11,13,20–22,31,32]. The planned puncture path can be adapted to different real-time projections, which allows the operator to make real-time reassessments of the path in 3D by simply adjusting the C-arm.

The 3DFIG method can enhance technical precision and accuracy during technically difficult TIPS procedures by providing: (1) improved 3D visual spatial orientation so the interventional radiologist can successfully puncture the portal vein; (2) 3D visualization of the patient's unique, and possibly distorted, anatomy; (3) the real-time tracking of the needle in 3D, in both the anteroposterior and lateral planes.

Some potential disadvantages of the 3DFIG method and limitations of our study were also identified. First, with the added steps of CBCT and fusion imaging processing, the procedure time may increase as CBCT and fusion imaging can be time-consuming. This may be especially true for centers that have minimal experience in CBCT and fusion imaging. However, using the current settings in our research angiography unit and an independent fusion imaging station, the process was significantly streamlined. With proper training and an effective protocol set-up, 3DFIG procedures can be easily adapted. Furthermore, the time that could be saved by limiting the number of attempts that is needed using our method could potentially balance out, or even shorten, the overall procedure time. Another limitation of this study was that the 3DFIG TIPS procedures were performed in normal porcine livers, which did not have cirrhosis or anatomical anomalies. Patients with difficult anatomies may produce lower success rates and may require more needle passes to achieve successful PV puncture [9,12,15,18]. Consequently, the risk of peri-procedural complications, morbidity rates, procedure and fluoroscopy times and exposure to radiation also increase. However, this was a feasibility study, which tested the reproducibility of 3DFIG portosystemic shunt placement. Even though the procedure was not performed in cirrhotic livers, it was performed in small porcine livers to mimic the size of a human cirrhotic liver. Potential future studies could employ the 3DFIG TIPS procedure in cirrhotic animal models or in patients with cirrhosis as a clinical safety study. Other potential anatomic and physiologic considerations also remain, however. For example, polycystic liver disease (PCLD) is often listed as a contraindication for TIPS procedures due to risk of cyst rupture and hemorrhage. However, a case of PCLD was reported to have undergone successful TIPS insertion with the aid of a hybrid 2D and 3D imaging system [33]. PV and HV thrombosis have historically been considered to be relative contraindications due to the technical difficulties in placing a shunt in abnormal anatomies of portal and hepatic veins, although recent evidence has suggested that a TIPS, when placed successfully, is in fact crucial for the management of these patients [34]. Future research should evaluate the feasibility of the 3DFIG TIPS procedure for these patients as it could play a particularly

useful role when the traditional TIPS procedure has been deemed too high a risk. Another potential limitation was that some of the pigs in this study underwent multiple procedures in order to increase the total number of procedures. In these cases, the knowledge of the previously placed shunts may have confounded any subsequent procedure attempts. For example, when a TIPS catheter was already in place before another was made, it would be revealed on the fluoroscopic images. However, this did not seem to affect the study results as the number of access attempts and the procedure time remained the same for the pigs that had prior procedures and those that did not.

In conclusion, our study showed that the 3DFIG TIPS (or iGuide® TIPS) procedure provides a more efficient and accurate way of performing the PV puncture step of the traditional procedure. The 3DFIG method is compatible with multiple imaging modalities and can potentially be used effectively in both emergency and non-emergency clinical situations. This hybrid technology provides the potential for the TIPS procedure to be used more widely as dependence on technical expertise may be less of a determining factor and it may be a suitable alternative for patients with underlying conditions who have traditionally been considered to be inappropriate candidates for TIPS placement. Regardless of the current limitations of the standard TIPS procedure, it continues to be a viable, and at times the only, method for treating and maintaining patients who are awaiting life-saving liver transplants.

Author Contributions: Conceptualization, E.W.L., S.S., P.-X.D. and S.T.K.; methodology, E.W.L., P.-X.D. and S.T.K.; validation, E.W.L., F.K., J.M. and S.T.K.; formal analysis, E.W.L., P.S. and N.E.; investigation, E.W.L., N.E. and P.-X.D.; writing—original draft preparation, E.W.L.; writing—review and editing, E.W.L., P.S., S.S., F.K., N.E., J.M., P.-X.D. and S.T.K.; supervision, E.W.L.; funding acquisition, E.W.L. All authors have read and agreed to the published version of the manuscript.

Funding: This research was funded by Siemens USA (grant number UCLA-2014-AX-Lee).

Institutional Review Board Statement: The animal study protocol was approved by the Institutional Review Board (or Ethics Committee) of University of California, Los Angeles (ARC#2006-054-33A: approved on 19 August 2014 and renewed on 16 November 2021).

Informed Consent Statement: Not applicable.

Data Availability Statement: Not applicable.

Conflicts of Interest: E.W.L. received research grant funding from Siemens USA. The authors declare no conflict of interest.

References

1. Rossle, M.; Richter, G.M.; Noldge, G.; Palmaz, J.C.; Wenz, W.; Gerok, W. New non-operative treatment for variceal haemorrhage. *Lancet* **1989**, *2*, 153. [CrossRef]
2. D'Amico, G.; Pagliaro, L.; Bosch, J. The treatment of portal hypertension: A meta-analytic review. *Hepatology* **1995**, *22*, 332–354. [CrossRef] [PubMed]
3. Coldwell, D.M.; Ring, E.J.; Rees, C.R.; Zemel, G.; Darcy, M.D.; Haskal, Z.J.; McKusick, M.A.; Greenfield, A.J. Multicenter investigation of the role of transjugular intrahepatic portosystemic shunt in management of portal hypertension. *Radiology* **1995**, *196*, 335–340. [CrossRef] [PubMed]
4. Ferral, H.; Bjarnason, H.; Wegryn, S.A.; Rengel, G.J.; Nazarian, G.K.; Rank, J.M.; Tadavarthy, S.M.; Hunter, D.W.; Castaneda-Zuniga, W.R. Refractory ascites: Early experience in treatment with transjugular intrahepatic portosystemic shunt. *Radiology* **1993**, *189*, 795–801. [CrossRef] [PubMed]
5. LaBerge, J.M.; Ring, E.J.; Gordon, R.L.; Lake, J.R.; Doherty, M.M.; Somberg, K.A.; Roberts, J.P.; Ascher, N.L. Creation of transjugular intrahepatic portosystemic shunts with the wallstent endoprosthesis: Results in 100 patients. *Radiology* **1993**, *187*, 413–420. [CrossRef]
6. LaBerge, J.M.; Somberg, K.A.; Lake, J.R.; Gordon, R.L.; Kerlan, R.K., Jr.; Ascher, N.L.; Roberts, J.P.; Simor, M.M.; Doherty, C.A.; Hahn, J.; et al. Two-year outcome following transjugular intrahepatic portosystemic shunt for variceal bleeding: Results in 90 patients. *Gastroenterology* **1995**, *108*, 1143–1151. [CrossRef]
7. Ochs, A.; Rossle, M.; Haag, K.; Hauenstein, K.H.; Deibert, P.; Siegerstetter, V.; Huonker, M.; Langer, M.; Blum, H.E. The transjugular intrahepatic portosystemic stent-shunt procedure for refractory ascites. *N. Engl. J. Med.* **1995**, *332*, 1192–1197. [CrossRef]

8. Rossle, M.; Haag, K.; Ochs, A.; Sellinger, M.; Noldge, G.; Perarnau, J.M.; Berger, E.; Blum, U.; Gabelmann, A.; Hauenstein, K.; et al. The transjugular intrahepatic portosystemic stent-shunt procedure for variceal bleeding. *N. Engl. J. Med.* **1994**, *330*, 165–171. [CrossRef]
9. Freedman, A.M.; Sanyal, A.J.; Tisnado, J.; Cole, P.E.; Shiffman, M.L.; Luketic, V.A.; Purdum, P.P.; Darcy, M.D.; Posner, M.P. Complications of transjugular intrahepatic portosystemic shunt: A comprehensive review. *Radiographics* **1993**, *13*, 1185–1210. [CrossRef]
10. Saxon, R.R.; Mendel-Hartvig, J.; Corless, C.L.; Rabkin, J.; Uchida, B.T.; Nishimine, K.; Keller, F.S. Bile duct injury as a major cause of stenosis and occlusion in transjugular intrahepatic portosystemic shunts: Comparative histopathologic analysis in humans and swine. *J. Vasc. Interv. Radiol.* **1996**, *7*, 487–497. [CrossRef]
11. Kee, S.T.; Ganguly, A.; Daniel, B.L.; Wen, Z.; Butts, K.; Shimikawa, A.; Pelc, N.J.; Fahrig, R.; Dake, M.D. MR-guided transjugular intrahepatic portosystemic shunt creation with use of a hybrid radiography/MR system. *J. Vasc. Interv. Radiol.* **2005**, *16*, 227–234. [CrossRef]
12. Gaba, R.C.; Khiatani, V.L.; Knuttinen, M.G.; Omene, B.O.; Carrillo, T.C.; Bui, J.T.; Owens, C.A. Comprehensive review of TIPS technical complications and how to avoid them. *AJR Am. J. Roentgenol.* **2011**, *196*, 675–685. [CrossRef]
13. Rose, S.C.; Pretorius, D.H.; Nelson, T.R.; Kinney, T.B.; Huynh, T.V.; Roberts, A.C.; Valji, K.; D'Agostino, H.R.; Oglevie, S.B.; James, G.M.; et al. Adjunctive 3D US for achieving portal vein access during transjugular intrahepatic portosystemic shunt procedures. *J. Vasc. Interv. Radiol.* **2000**, *11*, 611–621. [CrossRef]
14. Sanyal, A.J.; Shiffman, M.L. Transjugular intrahepatic portosystemic shunt: A medical perspective. *Dig. Dis.* **1995**, *13*, 153–162. [CrossRef]
15. Saxon, R.R.; Keller, F.S. Technical aspects of accessing the portal vein during the TIPS procedure. *J. Vasc. Interv. Radiol.* **1997**, *8*, 733–744. [CrossRef]
16. Funaki, B. Transjugular intrahepatic portosystemic shunt. *Semin. Interv. Radiol.* **2008**, *25*, 168–174. [CrossRef]
17. Walser, E.M.; Soloway, R.; Raza, S.A.; Gill, A. Transjugular portosystemic shunt in chronic portal vein occlusion: Importance of segmental portal hypertension in cavernous transformation of the portal vein. *J. Vasc. Interv. Radiol.* **2006**, *17*, 373–378. [CrossRef]
18. Jourabchi, N.; McWilliams, J.P.; Lee, E.W.; Sauk, S.; Kee, S.T. TIPS Placement via Combined Transjugular and Transhepatic Approach for Cavernous Portal Vein Occlusion: Targeted Approach. *Case Rep. Radiol.* **2013**, *2013*, 635391. [CrossRef]
19. Petersen, B.; Uchida, B.T.; Timmermans, H.; Keller, F.S.; Rosch, J. Intravascular US-guided direct intrahepatic portacaval shunt with a PTFE-covered stent-graft: Feasibility study in swine and initial clinical results. *J. Vasc. Interv. Radiol.* **2001**, *12*, 475–486. [CrossRef]
20. Adamus, R.; Pfister, M.; Loose, R.W. Enhancing transjugular intrahepatic portosystemic shunt puncture by using three-dimensional path planning based on the back projection of two two-dimensional portographs. *Radiology* **2009**, *251*, 543–547. [CrossRef]
21. Kew, J.; Davies, R.P. Intravascular ultrasound guidance for transjugular intrahepatic portosystemic shunt procedure in a swine model. *Cardiovasc. Interv. Radiol.* **2004**, *27*, 38–41. [CrossRef]
22. Roizental, M.; Kane, R.A.; Takahashi, J.; Kruskal, J.; Crenshaw, W.B.; Perry, L.; Stokes, K.; Clouse, M.E. Portal vein: US-guided localization prior to transjugular intrahepatic portosystemic shunt placement. *Radiology* **1995**, *196*, 868–870. [CrossRef]
23. Fanelli, F. The Evolution of Transjugular Intrahepatic Portosystemic Shunt: Tips. *ISRN Hepatol.* **2014**, *12*, 762096. [CrossRef]
24. Luo, X.; Wang, X.; Zhao, Y.; Ma, H.; Ye, L.; Yang, L.; Tsauo, J.; Jiang, M.; Li, X. Real-Time 3D CT Image Guidance for Transjugular Intrahepatic Portosystemic Shunt Creation Using Preoperative CT: A Prospective Feasibility Study of 20 Patients. *AJR Am. J. Roentgenol.* **2017**, *208*, W11–W16. [CrossRef]
25. Rouabah, K.; Varoquaux, A.; Caporossi, J.M.; Louis, G.; Jacquier, A.; Bartoli, J.M.; Moulin, G.; Vidal, V. Image fusion-guided portal vein puncture during transjugular intrahepatic portosystemic shunt placement. *Diagn. Interv. Imaging* **2016**, *97*, 1095–1102. [CrossRef]
26. Tacher, V.; Petit, A.; Derbel, H.; Novelli, L.; Vitellius, M.; Ridouani, F.; Luciani, A.; Rahmouni, A.; Duvoux, C.; Salloum, C.; et al. Three-dimensional Image Fusion Guidance for Transjugular Intrahepatic Portosystemic Shunt Placement. *Cardiovasc. Interv. Radiol.* **2017**, *40*, 1732–1739. [CrossRef]
27. Loffroy, R.; Estivalet, L.; Cherblanc, V.; Favelier, S.; Pottecher, P.; Hamza, S.; Minello, A.; Hillon, P.; Thouant, P.; Lefevre, P.H.; et al. Transjugular intrahepatic portosystemic shunt for the management of acute variceal hemorrhage. *World J. Gastroenterol.* **2013**, *19*, 6131–6143. [CrossRef]
28. Rossle, M. TIPS: 25 years later. *J. Hepatol.* **2013**, *59*, 1081–1093. [CrossRef]
29. Farsad, K.; Fuss, C.; Kolbeck, K.J.; Barton, R.E.; Lakin, P.C.; Keller, F.S.; Kaufman, J.A. Transjugular intrahepatic portosystemic shunt creation using intravascular ultrasound guidance. *J. Vasc. Interv. Radiol.* **2012**, *23*, 1594–1602. [CrossRef]
30. Miller, D.L.; Kwon, D.; Bonavia, G.H. Reference levels for patient radiation doses in interventional radiology: Proposed initial values for U.S. practice. *Radiology* **2009**, *253*, 753–764. [CrossRef]
31. Roeren, T.; Richter, G.M.; Limberg, B.; Jacoby, I.R.; Kauffmann, G.W. Ultrasound guided puncture of the portal vein in transjugular intrahepatic portasystemic stent shunt (TIPSS). *Radiologe* **1996**, *36*, 677–682. [CrossRef] [PubMed]
32. Rose, S.C.; Behling, C.; Roberts, A.C.; Pretorius, D.H.; Nelson, T.R.; Kinney, T.B.; Masliah, E.; Hassanein, T.I. Main portal vein access in transjugular intrahepatic portosystemic shunt procedures: Use of three-dimensional ultrasound to ensure safety. *J. Vasc. Interv. Radiol.* **2002**, *13*, 267–273. [CrossRef]

33. Sze, D.Y.; Strobel, N.; Fahrig, R.; Moore, T.; Busque, S.; Frisoli, J.K. Transjugular intrahepatic portosystemic shunt creation in a polycystic liver facilitated by hybrid cross-sectional/angiographic imaging. *J. Vasc. Interv. Radiol.* **2006**, *17*, 711–715. [CrossRef] [PubMed]
34. Riggio, O.; Ridola, L.; Lucidi, C.; Angeloni, S. Emerging issues in the use of transjugular intrahepatic portosystemic shunt (TIPS) for management of portal hypertension: Time to update the guidelines? *Dig. Liver Dis.* **2010**, *42*, 462–467. [CrossRef]

applied sciences

MDPI

Article

Characterization of Cardiac Fat in Atrial Fibrillation Patients Prior to Ablation Treatment

Feham Peer-Zada [1,†], Dima Hamze [1,†] and Julio Garcia [2,3,4,5,6,*]

[1] College of Medicine, Alfaisal University, Riyadh 11533, Saudi Arabia; fzada@alfaisal.edu (F.P.-Z.); dhamze@alfaisal.edu (D.H.)
[2] Department of Cardiac Sciences, University of Calgary, Calgary, AB T2N 2T9, Canada
[3] Department of Radiology, University of Calgary, Calgary, AB T2N 2T9, Canada
[4] Stephenson Cardiac Imaging Centre, University of Calgary, Calgary, AB T2N 2T9, Canada
[5] Libin Cardiovascular Institute, University of Calgary, Calgary, AB T2N 2T9, Canada
[6] Alberta Children's Hospital Research Institute, University of Calgary, Calgary, AB T3B 6A8, Canada
* Correspondence: julio.garciaflores@ucalgary.ca
† These authors contributed equally to this work.

Featured Application: This study demonstrated the impact that heart fat can have in atrial fibrillation patients and its association with fibrillation recurrence after ablation treatment.

Abstract: Epicardial adipose tissue (EAT) and pericardial adipose tissue (PAT) contribute to the development of left atrial fibrillation (AF). The purpose of this study is to determine the factors influencing cardiac fat, evaluate its impact on heart function, and evaluate its role in the recurrence of AF. Cardiac MRI exams of n = 198 patients with paroxysmal AF were retrospectively analyzed to quantify EAT and PAT. Body mass index (BMI) showed significant associations with increased EAT, PAT, and total cardiac fat, particularly with the total end-systolic area ($p < 0.001$). Males were associated with increased PAT ($r = -0.331$, $p < 0.001$) and EAT ($r = -0.168$, $p = 0.019$). Increased PAT end-diastolic volume was also associated with an increase in LV mass ($r = 0.249$, $p < 0.01$). An inverse relationship between EAT end-systolic area and cardiac index ($r = -0.220$, $p < 0.01$) was observed. Although BMI did not significantly affect AF recurrence, overweight patients (36%) experienced slightly more AF recurrence than obese patients (33%). Obesity is substantially associated with an increase in EAT and PAT, while sex appears to play a greater role in PAT than EAT and decreased cardiac function.

Keywords: epicardial adipose tissue; pericardial adipose tissue; cardiac magnetic resonance; atrial fibrillation; machine learning

Citation: Peer-Zada, F.; Hamze, D.; Garcia, J. Characterization of Cardiac Fat in Atrial Fibrillation Patients Prior to Ablation Treatment. *Appl. Sci.* **2023**, *13*, 12005. https://doi.org/10.3390/app132112005

Academic Editor: Zhonghua Sun

Received: 9 September 2023
Revised: 31 October 2023
Accepted: 31 October 2023
Published: 3 November 2023

1. Introduction

Atrial fibrillation (AF), as a sustained and growing epidemic, is the most common arrhythmia among adults, leading to an increase in mortality and morbidity [1]. The pathophysiology of AF is caused by asynchronous excitation of the atria, leading to irregularities in both the atrial and ventricular contractions [2]. Age [2] and various comorbidities including obesity [3], type 2 diabetes [4] obstructive sleep apnea [5], and alcohol consumption [6] are recognized as risk factors.

Obesity, which refers to the distribution of total body fat and is measured using body mass index (BMI), is a well-established risk factor for AF [7]. Excessive body fat, particularly metabolically active visceral fat, increases inflammatory and oxidative stress on the heart, leading to atrial enlargement and electrical instability, predisposing to AF [8–11]. Obesity-related expansion of epicardial adipose tissue (EAT), a visceral fat deposit located between the myocardium and epicardium, causes microvascular dysfunction and fibrosis of the underlying myocardium, resulting in atrial myopathy that can lead to AF [12]. Epicardial fat

thickness is associated with metabolic syndromes and an increased risk of cardiovascular diseases [13]. In-vivo and ex-vivo studies suggest that the accumulation of EAT can also potentially impact the left ventricle (LV) diastolic function [14–16]. Moreover, pericardial adipose tissue (PAT), which refers to fat deposits outside the epicardium, causes cardiovascular dysfunction [17]. An increment in PAT has been linked to a rise in the incidence, severity, and recurrence of AF seen in obesity [18]. The impact of the fat around the heart and AF remains unclear. Thus, quantifying EAT and PAT are important parameters that can help identify patients who may be at risk for cardiovascular events.

Different imaging modalities can measure cardiac fat deposits, such as cardiac computed tomography (CCT), which was proposed as a gold standard for quantifying the EAT volume. However, due to the significant amount of ionizing radiation, CCT poses a potential health risk to the patient [19]. This limitation was surmounted by the introduction of cardiac magnetic resonance imaging (MRI), which can measure cardiac function, morphology, perfusion, and myocardial tissue in a single exam with minimal, if any, impact on patients' health. In the current study, therefore, we aim to assess the factors that influence EAT and PAT fat in AF using cardiac MRI.

The study's hypotheses are: (1) an increase in BMI and subsequent obesity will be associated with increased cardiac fat deposition; (2) an increase in cardiac fat will have a functional impact on the heart, i.e., LV deterioration; and (3) there will be an increased incidence of AF recurrence in patients with higher cardiac fat deposits. The specific objectives of the study are: (1) to characterize parameters that influence cardiac fat; (2) to assess the effect of cardiac fat on the functional parameters of the heart; and (3) to assess the role of cardiac fat in AF recurrence.

2. Materials and Methods

2.1. Study Population

In this retrospective study, a total of 198 patients with a history of paroxysmal AF with normal systolic function, scanned between 2016 and 2021 with a standardized cardiac MRI exam, were retrospectively included from the Cardiovascular Imaging Registry of Calgary (CIROC) database. All patients were required to have a 1st referral for a cardiac MRI exam within 3 months prior to ablation procedure by their electrophysiologist. Patients with significant mitral or aortic valve disease, inappropriate/incomplete image quality (motion artifacts due to arrythmia event/incomplete acquisition), indication for re-ablation procedure, incomplete exams, or arrythmia events during the MRI examination were excluded. Those members of the study population that were found to have a normal BMI were used as the controls in this investigation, and the reference population to which the results strictly apply is therefore adults with a history of paroxysmal AF that were referred for ablation treatment and were found at the time of examination to have a normal BMI. The study utilized intakeDI^{TM} (Cohesic Inc., Calgary, AB, Canada), to coordinate and capture routine patient informed consent and self-reported health quality of life questionnaires and for standardized collection of MRI-related variables. CIROC provides access to medication prescription and usage, laboratory results, diagnostic and procedural information, device interrogation, 12-lead ECG and Holter data, vital statistics, and major cardiovascular outcomes. AF recurrence was assessed using 12-lead ECG and Holter monitoring following the ablation procedure. The most recent CIROC update output was obtained in October 2022. This study was approved by the University of Calgary's Conjoint Health Research Ethics Board, and all subjects gave written informed consent. All research activities were in accordance with the Declaration of Helsinki.

2.2. Cardiac Magnetic Resonace Imaging Acquisition

All subjects were required to exhibit sinus rhythm during the CMR examination. Patients underwent an identical standardized MRI protocol using 3T MRI scanners Skyra/Prisma (Siemens, Erlangen, Germany) inclusive of multiplanar steady-state free-precession (SSFP) cine imaging of the 4-chamber, 3-chamber, 2-chamber, and short axis of the LV at end-expiration.

Additionally, 3D magnetic resonance angiography (MRA) of the LA was performed using the administration of 0.2 mmol/kg gadolinium contrast (Gadovist®, Bayer Inc., Mississauga, ON, Canada) [20].

2.3. Standard Cardiac Magnetic Resonace Imaging Assessment

A commercial software (cvi42 v5.11, Circle Cardiovascular Imaging Inc., Calgary, AB, Canada) was used to analyze heart function from standard ECG-gated cine images. The short-axis cine images were used to measure LV end-diastolic volume (EDV), LV end-systolic volume (ESV), LV stroke volume (SV), LV mass, LV cardiac output (CO), LVEDV indexed to body surface area (BSA), LVESV indexed to BSA, LV mass indexed to BSA, and LV ejection fraction (LVEF). LA volume and LA volume indexed to BSA were measured using the bi-plane area-length method in 2- and 4-chamber views [20].

2.4. Epicardial and Pericardial Fat Assessment

An expert reader was provided with a complete series of 4-chamber images and performed blinded segmentation of the epicardial (EAT) and pericardial (PAT) adipose tissue. EAT was defined as the hyperintense signal within the pericardium surrounding the ventricles. PAT was defined as the fat adjacent but outside the pericardium. The segmentation was performed using an automate pipeline developed and validated by Daude et al. [19]. The end-systolic (ES) and end-diastolic (ED) frames were used for the quantification of EAT and PAT.

2.5. Statistical Analysis

The statistical analysis was performed using SPSS version 29.0 with statistical significance set to a p-value of 0.05. Normality of the data was assessed by the Kolmogorov–Smirnov test. If data were not normally distributed, non-parametric tests were used. The descriptive statistics of the study population and functional parameters of the heart were stratified by body mass index (BMI). Continuous variables were expressed as mean $\pm$ standard deviation (SD) and categorical variables as absolute numbers and percentages. Differences among BMI groups for the variables were assessed by one-way ANOVA or Kruskal–Wallis H test and corrected using Bonferroni adjustment. Intergroup comparisons were performed by T-tests for parametric data and Mann–Whitney U test for non-parametric data. Spearman's and Pearson's correlations were used to assess the correlation between the different cardiac fat parameters and functional parameters of the heart, as well as correlate cardiac fat to demographic variables like sex and age.

3. Results

3.1. Demographics

Table 1 compares the demographic and clinical features of the AF patients across normal (18.5 to 24.9 kg/m^2), overweight (25 to 29.9 kg/m^2), and obese (>30 kg/m^2) BMI categories. This study included 198 patients, ranging in age from 22 to 83 years. Obese patients were generally younger (57.4 $\pm$ 10.4 years) than overweight patients (60.0 $\pm$ 9.5 years), despite having a higher BMI and body surface area (34.0 $\pm$ 3.2 kg/m^2, 2.3 $\pm$ 0.2 m^2) relative to overweight patients (27.2 $\pm$ 1.5 kg/m^2, 2.1 $\pm$ 0.2 m^2). Comorbid conditions such as diabetes (75% and 25%), hypertension (34.6% and 49.1%), and hypercholesterolemia (42.3% and 50%) were more common in overweight and obese patients, respectively. Interestingly, there was no significant difference in stroke risk (p = 0.059) between BMI groups, with the most prevalent CHA_2DS_2-VASc score of 1 indicating moderate risk for all BMI categories. Obese patients were more likely to be using anticoagulants (30%), beta blockers (21.5%), and antiarrhythmic drugs (21.5%), but overall medication consumption was highest in overweight patients.

Table 1. Demographic and clinical characteristics of atrial fibrillation patients in relation to BMI.

BMI	Normal (n = 45)	Overweight (n = 79)	Obese (n = 74)	*p*-Value
Demographics				
Age (years)	56.1 (±12.1)	60.0 (±9.5)	57.4 (±10.4)	0.071
Sex n (% men)	31 (15.5%)	56 (28.0%)	57 (28.5%)	0.187
Sex n (% women)	14 (7.0%)	23 (11.5%)	17 (8.5%)	
Height (cm)	178.6 (±8.5)	177.3 (±10.2)	177.4 (±9.8)	0.265
Weight (Kg)	73.4 (±8.1) †	85.9 (±10.7) ‡	107.1 (±15.3) #	<0.001 **
Body Mass Index, BMI (kg/m^2)	23.0 (±1.4) †	27.2 (±1.5) ‡	34.0 (±3.2) #	<0.001 **
Body Surface Area, BSA (m^2) [a]	1.9 (±0.1) †	2.1 (±0.2) ‡	2.3 (±0.2) #	<0.001 **
Smoke [b]	1 (±1)	1 (±1)	2 (±1)	0.327
Caffeine [c]	3 (±1)	4 (±1)	4 (±1)	0.111
Alcohol [d]	3 (±1)	3 (±1)	3 (±1)	0.069
Comorbidities				
Diabetes	0	3 (75%)	1 (25%)	0.333
Hypertension [e]	3 (5.5%	19 (34.6%)	27 (49.1%)	0.086
Hypercholesteremia	1 (3.9%) †	11 (42.3%)	13 (50%) #	0.001 *
Stroke Risk Score				
CHA_2DS_2-VASc Score	1.4 (±0.9)	1.7 (±1.0)	1.8 (±1.01)	0.059
Score 0 (n)	6	6	6	
Score 1 (n)	20	29	29	
Score 2 (n)	14	27	22	
Score 3 (n)	4	12	11	
Score 4 (n)	1	4	5	
Score 5 (n)	0	1	1	
Medications				
Anti-arrhythmic	15 (7.5%) †	47 (23.5%)	43 (21.5%) #	0.004 *
Anti-coagulant	37 (18.5%)	69 (34.5%)	60 (30%)	0.182
Beta-blocker	26 (13%)	47 (23.5%)	45 (22.5%)	0.316
ACE inhibitor or ARB	7 (3.5%)	20 (10%)	29 (14.5%) #	0.005 *
Statins	8 (4%)	22 (11%)	19 (9.5%)	0.149
Non-dihydropyridine calcium channel blocker	5 (2.5%)	20 (10%) ‡	7 (3.5%)	0.006 *
Lab results				
Total cholesterol (mmol/L)	4.5 (±0.9)	4.7 (±1.3)	4.6 (±1.1)	0.314
Low-density lipoprotein, LDL (mmol/L)	2.4 (±0.6)	2.7 (±1.0)	2.7 (±0.9)	0.233
High-density lipoprotein, HDL (mmol/L)	1.5 (±0.4)	1.3 (±0.5)	1.2 (±0.3) #	0.038 *
Triglycerides, TG (mmol/L)	1.3 (±0.6)	1.7 (±0.8)	1.6 (±0.7)	0.129

Continuous variables are expressed as mean ± SD and categorical variables as absolute numbers and percentages. Percentages are of each BMI group. * p-value < 0.05 assessed by Kruskal–Wallis H test and adjusted using Bonferroni adjustment for multiple comparisons; ** $p < 0.001$; [a] measured by Mosteller equation; [b] Smoked or vaped nicotine products within the past 10 years, 1, no products; 2, ≤1 products per day; 3, 1–10 products per day; 4, >10 per day; [c] Past 3-months (on average) caffeine (coffee, tea, or other caffeinated drinks), 1, none; 2, 1 cup per month; 3, 1–2 cups per week; 4, 1–2 per day; [d] Past 3-months (on average) alcohol, 1, none; 2, 1–3 per month; 3, 1–2 per week; 4, 1–2 per day; [e] both treated and untreated hypertension were considered; †, difference between group 1 and 2, $p < 0.05$; ‡, difference between group 2 and 3, $p < 0.05$; #, difference between group 1 and 3, $p < 0.05$. Intergroup comparisons were performed by T-tests for parametric data and Mann–Whitney U test for non-parametric data.

3.2. Factors Influencing Different Cardiac Fat Parameters

Table 2 highlights a significant increase in both the end-systolic and end-diastolic phases of all EAT, PAT, and total cardiac fat areas with obesity. The end-diastolic fat area was found to be less than the end-systolic area in all cardiac fat parameters, which can be attributed to the compression effect of the myocardium on the fat during ventricular diastole. BMI, age, and sex's correlation with EAT, PAT, and total cardiac fat areas is demonstrated in Table 3. BMI exhibited a significant association with all parameters, particularly with total end-systolic area (r = 0.458, $p < 0.001$). Male sex had a higher

association to PAT and total cardiac fat area, most notably with PAT area in 4-chamber view ($r = -0.331$, $p < 0.001$). Age weakly correlated with EAT end-systolic ($r = 0.172$, $p = 0.016$) and EAT end-diastolic ($r = 0.19$, $p = 0.008$) areas, but not with PAT. A higher PAT area in end-systolic and end-diastolic phases in males than females was observed across all BMI groups (see green brackets in Figure 1c–e). However, a larger total cardiac fat area was observed in males than females only across overweight and obese patients but not in normal-weight patients (see green bracket in Figure 1f,g). In normal-weight patients (yellow box plot in Figure 2), the area of EAT, PAT, and total cardiac fat in end-systolic phase is significantly higher in >60 years age group than 40 to 50 years age group (see green brackets in Figure 2a,c,f, $p < 0.05$). Similar results were obtained with the areas of EAT and PAT in end-diastolic phase (top upper green bracket in Figure 2b,d) but not with total cardiac fat (Figure 2g). This may suggest that cardiac fat parameters increase with age in normal weighted patients with paroxysmal AF. In overweight patients, there were larger EAT areas in end-diastolic phase in the age group 50 to 60 years compared with age group 40 to 50 years (see lower green bracket Figure 2b, $p < 0.05$). In obese patients, we observed an apparent trend of the EAT areas in the end-systolic and end-diastolic phases increasing with age until 60 years, at which point there showed a slight drop, although not statistically significant (Figure 2a,b). Notably, EAT and PAT were not associated with CHA_2DS_2-VASc stroke-risk score, suggesting that cardiac fat may be an independent marker of AF.

Table 2. Cardiac fat parameters in relation to BMI.

	Normal (n = 45)	Overweight (n = 79)	Obese (n = 74)	*p*-Value
Epicardial Adipose Tissue (EAT)				
EAT End-systolic area (cm^2)	10.8 (±4.5) †	14.7 (±5.7) ‡	17.6 (±5.1) #	<0.001 **
EAT End-diastolic area (cm^2)	10.4 (±4.8) †	13.9 (±5.7) ‡	16.5 (±4.9) #	<0.001 **
Pericardial Adipose Tissue (PAT)				
PAT Area in 4-Chamber view (cm^2)	24.9 (±17.6) †	35.2 (±16.6) ‡	48.1 (±21.7) #	<0.001 **
PAT End-systolic area (cm^2)	12.8 (±9.8) †	18.9 (±10.7) ‡	25.6 (±12.2) #	<0.001 **
PAT End-diastolic area (cm^2)	11.8 (±9.8) †	17.7 (±9.6) ‡	24.5 (±11.5) #	<0.001 **
Total cardiac fat (EAT + PAT)				
Total end-systolic area (cm^2)	23.6 (±13.8) †	33.6 (±15.6) ‡	43.1 (±16.2) #	<0.001 **
Total end-diastolic area (cm^2)	22.1 (±14.12) †	31.6 (±14.5) ‡	40.9 (±15.2) #	<0.001 **

Variables are expressed as mean ± SD. ** $p < 0.001$ assessed by Kruskal–Wallis H test and adjusted using Bonferroni adjustment for multiple comparisons; †, difference between group 1 and 2, $p < 0.05$; ‡, difference between group 2 and 3, $p < 0.05$; and #, difference between group 1 and 3, $p < 0.05$.

Table 3. Correlation between cardiac fat parameters and demographic characteristics.

	BMI	Age Ranges [a]	Sex [b]
Epicardial Adipose Tissue (EAT)			
EAT End-systolic area (cm^2)	0.389 **, <0.001	0.172 *, 0.016	−0.167 *, 0.20
EAT End-diastolic area (cm^2)	0.429 **, <0.001	0.190 **, 0.008	−0.168 *, 0.019
Pericardial Adipose Tissue (PAT)			
PAT Area in 4-Chamber view (cm^2)	0.434 **, <0.001	NS	−0.331 **, <0.001
PAT End-systolic area (cm^2)	0.434 **, <0.001	NS	−0.296 **, <0.001
PAT End-diastolic area (cm^2)	0.432 **, <0.001	NS	−0.282 **, <0.001
Total cardiac fat (EAT + PAT)			
Total end-systolic area (cm^2)	0.458 **, <0.001	NS	−0.267 **, <0.001
Total end-diastolic area (cm^2)	0.443 **, <0.001	0.145 *, 0.043	−0.258 **, <0.001

Pearson's correlation was performed for parametric data, and Spearman's correlation was conducted for non-parametric data. All variables are expressed as correlation coefficient r, *p*-value. * Correlation is significant at the 0.05 level (2-tailed); ** Correlation is significant at the 0.01 level (2-tailed). [a] 5 age ranges were considered: less than 30, between 30 and 40, between 40 and 50, between 50 and 60, and older than 60; [b] male sex was assigned a value of 1 and female of 2. Age ranges were considered a continuous variable. A negative correlation indicates tendency towards males. BMI, Body mass index; NS, Not significant $p > 0.05$.

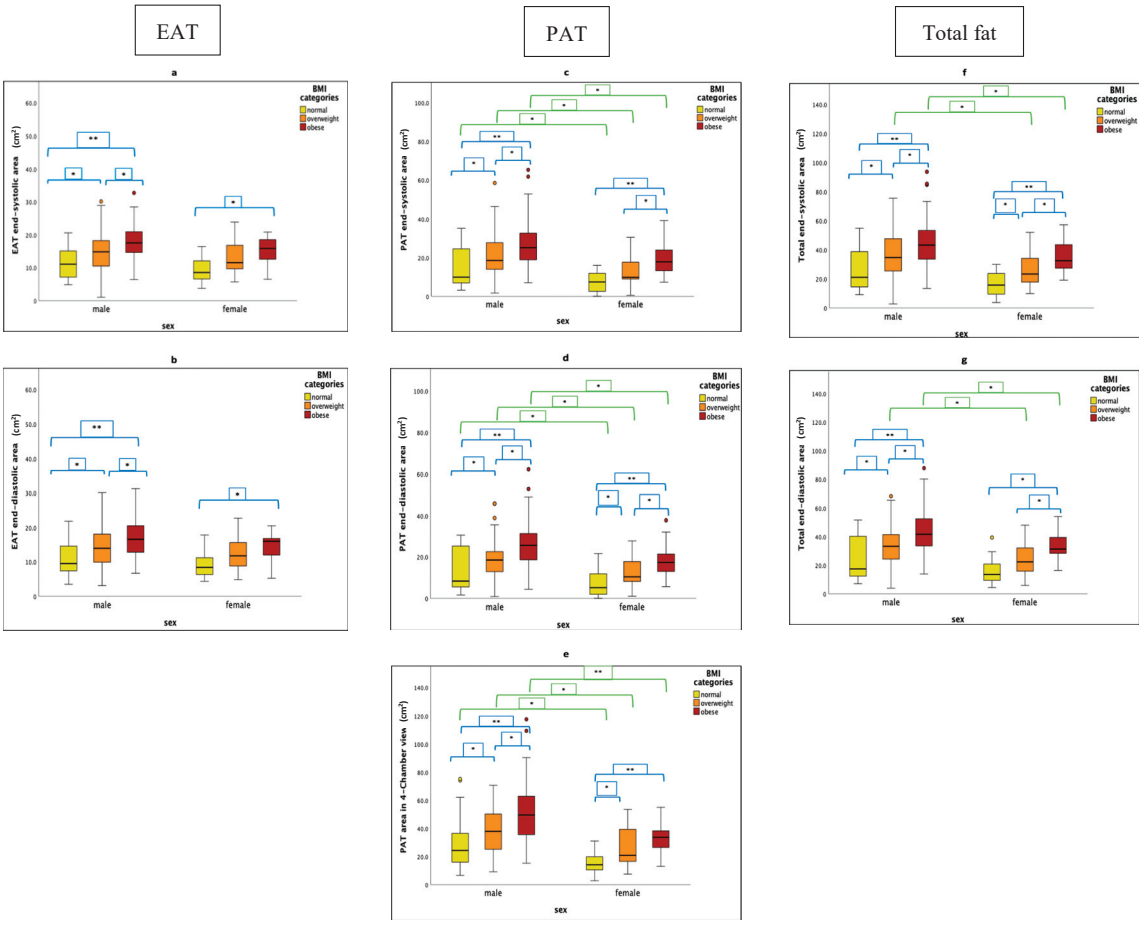

Figure 1. Area of EAT, PAT, and total cardiac fat stratified by sex and BMI, suggesting that sex may play more of a role in PAT than EAT, with higher deposition in males across all BMI groups. (**a**,**c**,**f**) illustrates the respective fat parameter within end-systolic phase, and (**b**,**d**,**g**) within end-diastolic phase. (**e**) illustrates PAT area in 4-chamber view. The box plots were generated by SPSS using the areas for EAT, PAT, and total cardiac fat with respect to sex and BMI. Within each sex group (male and female), box plots are colored according to BMI categories (normal, overweight, and obese, as shown in the top-left legend). Blue brackets on top of the box plots represent differences in EAT, PAT, and total cardiac fat within BMI categories in each sex group, whereas the green brackets represent differences in cardiac fat across sex within the same BMI group. * within the box represents $p < 0.05$ as measured by one-way ANOVA, independent samples T-test or Mann–Whitney U test; ** indicates $p < 0.001$; EAT, Epicardial adipose tissue; and PAT, pericardial adipose tissue.

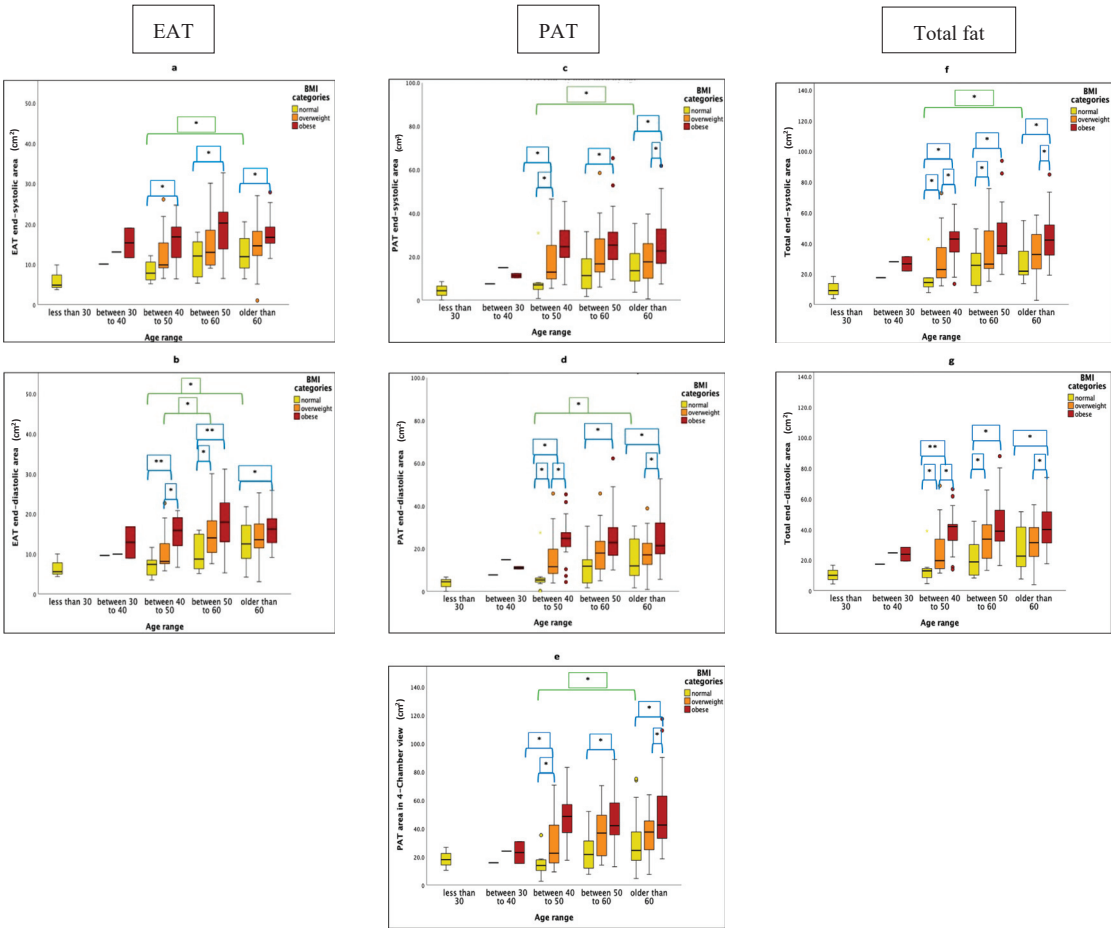

Figure 2. Area of EAT, PAT, and total cardiac fat stratified by age groups and BMI. Cardiac fat parameters may increase with age in normal-weight patients with paroxysmal AF. (**a**,**c**,**f**) illustrates the respective fat parameter within the end-systolic phase, and (**b**,**d**,**g**) within the end-diastolic phase. (**e**) illustrates PAT area in 4-chamber view. The box plots were generated by SPSS using the areas for EAT, PAT, and total cardiac fat with respect to five age groups (<30, 30–40, 40–50, 50–60, and >60 years) and BMI. Within each age group, box plots are colored according to BMI categories. Blue brackets on top of the box plots represent differences in EAT, PAT, and total cardiac fat within BMI categories in each age group, whereas the green brackets represent differences in cardiac fat across different ages within the same BMI group. * within the box represents $p < 0.05$ as measured by one-way ANOVA or Mann–Whitney U test; ** indicates $p < 0.001$; EAT, Epicardial adipose tissue; PAT, pericardial adipose tissue; and BMI, body mass index.

3.3. Functional Parameters and Cardiac Fat

Table 4 summarizes the anatomical and functional characteristics of the heart in our patient population in relation to BMI groups. The LA volume increased with BMI for both patient and indexed values. In the left and right ventricles, patient EDV and ESV also increased with BMI. However, when indexed to account for BSA, ventricular volumes decreased, indicating reduced heart functionality with increased body fat. Similarly, patients' LV mass significantly increased with obesity (126.2 ± 32.6 g); however, indexed values revealed a decrease in mass in obese patients (55.1 ± 11.8 g/m^2) compared to nor-

mal patients (56.0 ± 9.8 g/m^2). Obese patients exhibited a significantly reduced cardiac index (2.9 ± 0.6 L/min/m^2) compared to normal patients (3.2 ± 0.6 L/min/m^2), but no significant decrease in left and right ventricular ejection fraction (EF) across BMI was noted. Table 5 illustrates the association between cardiac fat and functional parameters. A positive correlation between LV mass and PAT areas was evident, with the PAT area in 4-chamber view displaying the highest association (r = 0.279, $p < 0.01$). Conversely, a negative correlation was observed between EAT end-systolic area and cardiac index (r = −0.220, $p < 0.01$), suggesting that an increase in EAT may be associated with a decreased functional capacity of the heart. Scatter plots for these correlations are shown in Figure 3.

Table 4. Anatomical and functional characteristics of the heart in atrial fibrillation patients in relation to BMI.

BMI	Normal (n = 45)	Overweight (n = 79)	Obese (n = 74)	*p*-Value
Left Ventricle (LV)				
LV-EDV (mL)	161.7 (±31.8)	161.7 (±30.5) ‡	177.4 (±38.0) #	<0.001 **
LV-ESV (mL)	62.9 (±17.8)	65.2 (±18.7) ‡	71.8 (±20.5) #	0.01 *
LV-Mass (g)	107.0 (±21.8)	107.6 (±26.6) ‡	126.2 (±32.6) #	<0.001 **
LV-EF (%)	61.0 (±8.3)	59.9 (±7.1)	59.5 (±8.0)	0.14
Indexed LV-EDV (mL/m^2) [a]	84.5 (±14.0) †	78.3 (±11.9)	77.3 (±12.9) #	<0.001 **
Indexed LV-ESV (mL/m^2) [a]	32.8 (±8.3)	31.5 (±7.8)	31.3 (±8.0)	0.21
Indexed LV-Mass (g/m^2) [a]	56.0 (±9.8) †	51.8 (±10.3)	55.1 (±11.8)	0.03 *
LV-Cardiac Index (L/min/m^2) [a]	3.2 (±0.6) †	2.7 (±0.4)	2.9 (±0.6) #	<0.001 **
Left Atrium (LA)				
LA-Volume (mL)	73.0 (±20.8) †	88.2 (±32.4) ‡	100.1 (±30.7) #	<0.001 **
Indexed LA-Volume (mL/m^2) [a]	38.3 (±11.4)	43.1 (±16.5)	43.9 (±13.1) #	0.04 *
Right Ventricle (RV)				
Patient RV-EDV (mL)	178.5 (±47.0)	174.6 (±41.3) ‡	191.0 (±48.6)	0.03 *
Patient RV-ESV (mL)	80.1 (±26.5)	78.9 (±26.4)	86.3 (±27.5)	0.09
RV-EF (%)	55.3 (±7.7)	55.5 (±7.5)	55.1 (±6.6)	0.32
Indexed RV-EDV (mL/m^2) [a]	92.9 (±20.4) †	84.3 (±16.4)	83.0 (±17.4) #	0.01 *
Indexed RV-ESV (mL/m^2) [a]	41.6 (±11.8)	37.9 (±11.1)	37.4 (±10.2) #	0.04 *

All variables are expressed as mean ± SD. * *p*-value < 0.05 assessed by Kruskal–Wallis H test and adjusted using Bonferroni adjustment for multiple comparisons; ** $p < 0.001$; [a] parameter was indexed by body surface area (BSA); EDV: End-diastolic volume; ESV: End-systolic volume; EF: Ejection Fraction. †, difference between group 1 and 2, $p < 0.05$; ‡, difference between group 2 and 3, $p < 0.05$; and #, difference between group 1 and 3, $p < 0.05$.

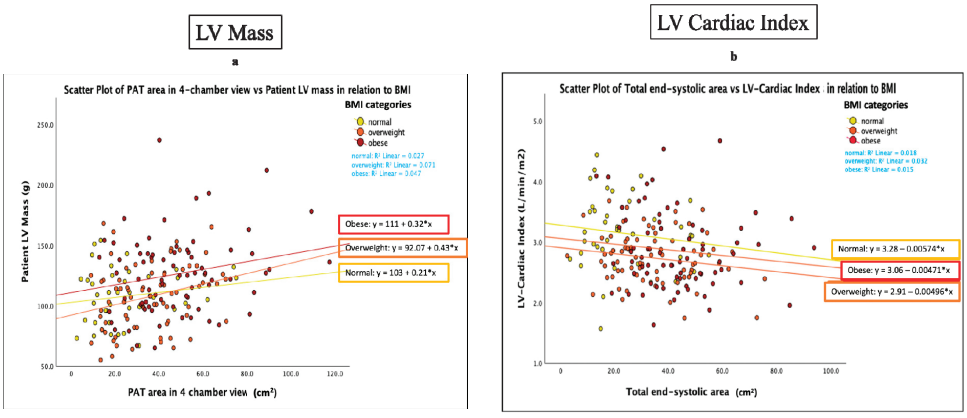

Figure 3. Scatter plots of cardiac fat vs cardiac function stratified by BMI. (**a**) An increase in PAT area in 4-chamber view is associated with an increase in LV mass, particularly in overweight and obese patients. (**b**) An increase in total fat area is correlated to a decrease in cardiac index, most notably in overweight patients. PAT: pericardial adipose tissue; LV: Left ventricle; and BMI: body mass index.

Table 5. Correlation of cardiac fat parameters with structural and functional characteristics of the heart.

	Indexed LV-EDV [a]	LV-EDV	LV-ESV	LV-Cardiac Index [a]	LV-Mass	Indexed RV-EDV [a]	LA-Volume
Epicardial Adipose Tissue (EAT)							
EAT End-systolic area (cm^2)	−0.166 *, 0.02	NS	NS	−0.220 **, <0.01	0.188 **, 0.01	−0.173 *, 0.02	NS
EAT End-diastolic area (cm^2)	−0.183 *, 0.01	NS	NS	−0.211 **, <0.01	0.157 *, 0.03	−0.168 *, 0.02	NS
Pericardial Adipose Tissue (PAT)							
PAT Area in 4 Chamber view (cm^2)	NS	0.159 *, 0.03	0.179 *, 0.01	NS	0.279 **, <0.01	NS	0.156 *, 0.04
PAT End-systolic area (cm^2)	−0.146 *, 0.04	NS	0.164 *, 0.02	−0.207 **, <0.01	0.224 **, <0.01	NS	NS
PAT End-diastolic area (cm^2)	NS	0.176 *, 0.02	0.194 **, 0.01	−0.163 *, 0.03	0.249 **, <0.01	NS	0.174 *, 0.02
Total cardiac fat (EAT + PAT)							
Total end-systolic area (cm^2)	−0.174 *, 0.02	NS	NS	−0.213 **, <0.01	0.217 **, <0.01	−0.154 *, 0.03	NS
Total end-diastolic area (cm^2)	NS	NS	0.156 *, 0.03	−0.184 *, 0.01	0.224 **, 0.01	NS	0.164 *, 0.03

Pearson's correlation was performed for parametric data, and Spearman's Correlation was conducted for non-parametric data. All variables are expressed as correlation coefficient r, *p*-value. * Correlation is significant at the 0.05 level (2-tailed); ** Correlation is significant at the 0.01 level (2-tailed). [a] parameter was indexed by body surface area (BSA). LV: Left Ventricle; EDV: End-diastolic volume; ESV: End-systolic volume; and NS: Not significant $p > 0.05$.

3.4. Obesity and AF Reccurrence

Table 6 demonstrates that the frequency of AF recurrence was highest in overweight patients (36.4%), followed by obese (33.3%) and normal-weight patients (20.2%). However, there was no significant difference in AF recurrence rates among the groups ($p = 0.298$). Obese patients had the longest days until recurrence (80.1 ± 131.1 days), followed by normal-weight (69.0 ± 86.7 days) and overweight patients (53.3 ± 59.3 days). The Kaplan–Meier graph in Figure 4 also illustrates this concept, showing a trend of longer time to AF recurrence in obese patients compared to normal and overweight patients. Subjects with recurrence demonstrated increased, but not significant, EAT (EAT end-systolic: 14.94 ± 5.61 cm^2 vs. 14.84 ± 7.42 cm^2, $p = 0.945$; EAT end-diastolic: 14.22 ± 5.64 cm^2 vs. 12.9 ± 5.86 cm^2, $p = 0.337$).

Table 6. Atrial fibrillation recurrence in relation to BMI.

BMI	Normal (n = 45)	Overweight (n = 79)	Obese (n = 74)	*p*-Value *
Frequency of recurrence n(%)	40 (20.2%)	72 (36.4%)	66 (33.3%)	0.298
Days until recurrence	69.0 (±86.7)	53.3 (±59.3)	80.1 (±131.1)	0.321

Continuous variables are expressed as mean ± SD and categorical variables as absolute number and percentage. * *p*-value was assessed by Kruskal–Wallis H test and adjusted using Bonferroni adjustment for multiple comparisons.

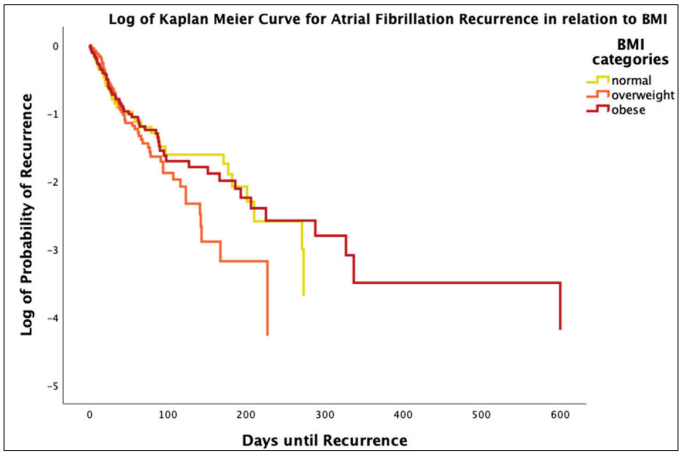

Figure 4. Kaplan–Meier survival analysis curve for atrial fibrillation recurrence in relation to BMI. The Log Rank (Mantel-Cox) *p*-value for overall comparison is 0.552.

4. Discussion

Our findings indicate that obesity and its subsequent deposition of cardiac fat significantly impacts both the anatomical and functional characteristics of the heart, predisposing to atrial fibrillation. All cardiac fat parameters, including EAT, PAT, and total cardiac fat area, are substantially associated with an increase in BMI. Moreover, an increase in BMI was also associated with a decrease in functionality, as indicated by reduced cardiac indices in obese patients.

Our findings demonstrate that BMI is significantly associated with EAT, PAT, and total cardiac fat area, making obesity pivotal in atrial fibrillation. In the context of cardiovascular diseases, including AF, EAT has been shown to have a direct relationship with obesity and BMI [21,22]. The relationship stems from the shared embryological origin of EAT with the epicardial layer of the myocardium, resulting in no connective tissue layer separating the two [22]. Therefore, excessive deposition of EAT causes direct fibrofatty infiltration and the release of inflammatory mediators such as interleukin-1-beta, interleukin-6, tumor necrosis factor-alpha, and monocyte chemoattractant protein-1 that, via paracrine mechanism, cause atrial fibrosis and AF [21].

Furthermore, EAT contains abundant ganglionated plexi that might contribute to the recurrence of AF [23–26]. In our study, overweight and obese AF patients showed higher recurrence compared to normal. EAT inflammatory activity has been reported as being higher in patients with AF than in controls, and it was shown to be greater in the left main artery than in the subcutaneous or visceral thoracic tissue [23]. An increased EAT could affect the ganglia function and impact the atrial substrate remodeling, and thereby, the maintenance of AF [25]. The association of the regional distribution of fat was not evaluated in the current study. However, regional EAT increment may be associated with AF nesting [25]. The latter remains an important question to address in future studies.

Our study also reveals an association between PAT and BMI in the setting of paroxysmal AF. On the other hand, Wong et al. demonstrated significant associations of PAT with AF presence, severity, and post-ablation outcomes, independent of systemic adiposity measures like BMI and BSA, suggesting that PAT may be a possible independent biomarker of AF [27]. However, this might be attributable to the use of volume measurements compared to area measurements in our study.

Sex and age also impact cardiac fat and AF. Our findings reveal slight sex differences for EAT and PAT deposition, with male sex having a stronger correlation to PAT area than EAT. In fact, across all BMI groups, males had significantly higher PAT areas compared to females. Men tend to have higher visceral fat deposition, which includes EAT and PAT,

whereas women have more subcutaneous fat deposits [28]. Gill et al. also illustrated that PAT volume is positively associated with BMI and is significantly higher in men than in women. However, in the context of metabolic syndrome and other cardiometabolic risk measures that are similar for various cardiovascular diseases including AF, the association of PAT was found to be stronger in women compared to men [29]. Nonetheless, sex seems to play less of a role in EAT than PAT, as in our study, there was no significant difference between the area of EAT in the hearts of normal, overweight, or obese males and their female counterparts. Conversely, Zhu et al. demonstrated higher total EAT volume in male AF patients and higher peri-atrial/total EAT ratio in post-menopausal females, alongside a greater rate of post-ablation AF recurrence [30]. Further exploration into sex differences in cardiac fat deposition is needed.

Advancing age, a well-established AF risk factor, may affect cardiac fat dynamics [2]. Our results demonstrate significant EAT and PAT area differences in normal-weight patients between age groups 40 and 50 years and over 60 years, suggesting that epicardial fat naturally increases with age. Indeed, previous studies have found EAT to be 22% thicker in patients aged 65 years and older, corroborating the notion of age-related increase [22,31]. This could be partially attributed to the hormonal changes that come with aging or to medications that manage comorbid conditions.

With respect to anatomical and functional parameters, we observed that patients' LV mass significantly increased with obesity and was positively correlated with EAT and PAT. However, when indexed by BSA, LV mass was reduced among obese patients and had no association with cardiac fat. Our data suggest eccentric and not concentric LV changes, indicating increased preload rather than afterload, which might be consistent with increased BMI. This implies that the relationship between LV mass and cardiac fat is influenced by body size adjustment, suggesting that LV mass may be linked to larger body size rather than solely cardiac hypertrophy. This aligns with findings by Nerker et al. and Fox et al., who propose that in the context of CAD, the influence of obesity on cardiac remodeling may overcome the local consequences of both EAT and PAT [32,33]. The central obesity and visceral adipose tissue may raise LV afterload, eventually resulting in LV remodeling as a compensatory mechanism, which comprises an increase in LV diameter, volume, and mass [32]. Thus, it seems that obesity's impact on LV mass and cardiac structure may extend beyond local cardiac fat deposits.

EAT and PAT in our patient population also exhibited negative correlations with functional aspects such as LV-Cardiac Index (CI), which reflects cardiac output (CO) adjusted by BSA [34]. Although, to our knowledge, no clear EAT/PAT-CI relationship in the setting of AF has been established, it is recognized that higher BMI is associated with an enlarged left atrium, subsequently increasing stroke volume and CO [3]. Prolonged elevated output leads to LV enlargement and hypertrophy, eventually resulting in diastolic dysfunction and systolic impairment [3]. Indeed, AF is known to increase the risk of heart failure along with EAT [15,16,35].

Obese patients with AF tend to be younger than patients with a normal BMI, which was also the case in our patient population. The impact of age may explain our findings, given that age is a key predictor of all-cause mortality in AF [3]. Moreover, obese patients tend to have more comorbidities, warranting stricter treatment strategies for rhythm control and anticoagulation, potentially influencing their outcomes [3]. Thus, the roots of the obesity paradox likely stem from the complex interactions of several contributing factors, requiring further exploration in future studies. In our study, EAT did not show an association with AF recurrence. However, other studies have demonstrated that EAT can be associated with AF recurrence [36].

Our study has certain limitations that warrant consideration. Firstly, this was a single-center investigation, and our findings may not fully represent broader populations. We were limited to the records captured by our local registry. The normal BMI group served as a control group and reference for other BMI groups. An appropriate control match was not conducted. We focused solely on area measurements of EAT and PAT and did not consider

volume measurements. The automate machine learning model is only able to quantify EAT and PAT following similar patterns to those used in the training dataset. The latter limited our capacity to define and quantify regions not included in the model. Additionally, due to the constraints of our available data, we were unable to analyze the potential effects of underweight individuals (BMI < 18.5). Although BMI is acknowledged as a significant cardiovascular risk indicator, it must be noted that it is limited in predicting total adiposity due to the contribution of subcutaneous adipose mass [37].

5. Conclusions

Our findings indicate that obesity, and its subsequent cardiac fat deposition, has a significant impact on the anatomical and functional characteristics of the heart, predisposing to AF. Significant correlations were found between cardiac fat parameters EAT, PAT, and total cardiac fat area, and higher BMI levels. An increased BMI was also associated with a decrease in functionality, as indicated by reduced cardiac indices in obese patients.

Author Contributions: Conceptualization, J.G.; methodology, F.P.-Z., D.H. and J.G.; software, J.G.; validation, F.P.-Z., D.H. and J.G.; formal analysis, F.P.-Z. and D.H.; investigation, F.P.-Z., D.H. and J.G.; resources, J.G.; data curation, F.P.-Z., D.H. and J.G.; writing—original draft preparation, F.P.-Z. and D.H.; writing—review and editing, J.G.; visualization, F.P.-Z. and D.H.; supervision, J.G.; project administration, J.G.; funding acquisition, J.G. All authors have read and agreed to the published version of the manuscript.

Funding: This research was funded by The University of Calgary, URGC SEM #1054341; J.G. start-up funding. Unrestricted research funding was provided by Siemens Healthineers and the Stephenson Cardiac Imaging Centre. We acknowledge the support of the Natural Science and Engineering Research Council of Canada/Conseil de recherche en science naturelles et en génie du Canada, RGPIN-2020-04549 and DGECR-2020-00204.

Institutional Review Board Statement: The study was conducted according to the guidelines of the Declaration of Helsinki and approved by the Conjoint Health Research Ethics Board of the University of Calgary (REB13-0902 was approved on 18 June 2014).

Informed Consent Statement: Written informed consent was obtained from all subjects involved in the study.

Data Availability Statement: The anonymized data presented in this study are available upon request from the corresponding author. The data are not publicly available due to privacy and ethical restrictions.

Conflicts of Interest: The authors declare no conflict of interest.

References

1. Magnussen, C.; Niiranen, T.J.; Ojeda, F.M.; Gianfagna, F.; Blankenberg, S.; Njølstad, I.; Vartiainen, E.; Sans, S.; Pasterkamp, G.; Hughes, M.; et al. Sex Differences and Similarities in Atrial Fibrillation Epidemiology, Risk Factors, and Mortality in Community Cohorts: Results From the BiomarCaRE Consortium (Biomarker for Cardiovascular Risk Assessment in Europe). *Circulation* **2017**, *136*, 1588–1597. [CrossRef] [PubMed]
2. Staerk, L.; Sherer, J.A.; Ko, D.; Benjamin, E.J.; Helm, R.H. Atrial Fibrillation Epidemiology, Pathophysiology, and Clinical Outcomes. *Circ. Res.* **2017**, *120*, 1501–1517. [CrossRef]
3. Vyas, V.; Lambiase, P. Obesity and Atrial Fibrillation: Epidemiology, Pathophysiology and Novel Therapeutic Opportunities. *Arrhythmia Electrophysiol. Rev.* **2019**, *8*, 28. [CrossRef] [PubMed]
4. Matsumoto, C.; Ogawa, H.; Saito, Y.; Okada, S.; Soejima, H.; Sakuma, M.; Masuda, I.; Nakayama, M.; Doi, N.; Jinnouchi, H.; et al. Incidence of atrial fibrillation in elderly patients with type 2 diabetes mellitus. *BMJ Open Diabetes Res. Care* **2022**, *10*, e002745. [CrossRef]
5. Lindsay, B.D.; Nalliah, C.J.; Sanders, P.; Kalman, J.M. Clinical Review Obstructive Sleep Apnea Treatment and Atrial Fibrillation: A Need for Definitive Evidence. *J. Cardiovasc. Electrophysiol.* **2016**, *27*, 1001–1010.
6. Larsson, S.C.; Drca, N.; Wolk, A. Alcohol consumption and risk of atrial fibrillation: A prospective study and dose-response meta-analysis. *J. Am. Coll. Cardiol.* **2014**, *64*, 281–289. [CrossRef]
7. Neefs, J.; Boekholdt, S.M.; Khaw, K.T.; Luben, R.; Pfister, R.; Wareham, N.J.; Meulendijks, E.R.; Sanders, P.; de Groot, J.R. Body Mass Index and Body Fat Distribution and New-Onset Atrial Fibrillation. Sub study of The European Prospective Investigation Into Cancer and Nutrition in Norfolk (EPIC-Norfolk) Study. *Nutr. Metab. Cardiovasc. Dis.* **2019**, *29*, 692. [CrossRef] [PubMed]

8. Greif, M.; von Ziegler, F.; Wakili, R.; Tittus, J.; Becker, C.; Helbig, S.; Laubender, R.P.; Schwarz, W.; D'anastasi, M.; Schenzle, J.; et al. Increased pericardial adipose tissue is correlated with atrial fibrillation and left atrial dilatation. *Clin. Res. Cardiol.* **2013**, *102*, 555–562. [CrossRef] [PubMed]
9. Verhagen, S.N.; Vink, A.; van der Graaf, Y.; Visseren, F.L.J. Coronary perivascular adipose tissue characteristics are related to atherosclerotic plaque size and composition. A post-mortem study. *Atherosclerosis* **2012**, *225*, 99–104. [CrossRef]
10. Sequeira, D.I.; Ebert, L.C.; Flach, P.M.; Ruder, T.D.; Thali, M.J.; Ampanozi, G. The correlation of epicardial adipose tissue on postmortem CT with coronary artery stenosis as determined by autopsy. *Forensic Sci. Med. Pathol.* **2015**, *11*, 186–192. [CrossRef] [PubMed]
11. Farias-Itao, D.S.; Pasqualucci, C.A.; Nishizawa, A.; da Silva, L.F.F.; Campos, F.M.; Bittencourt, M.S.; da Silva, K.C.S.; Leite, R.E.P.; Grinberg, L.T.; Ferretti-Rebustini, R.E.d.L.; et al. B Lymphocytes and Macrophages in the Perivascular Adipose Tissue Are Associated with Coronary Atherosclerosis: An Autopsy Study. *J. Am. Heart Assoc.* **2019**, *8*, e013793. [CrossRef] [PubMed]
12. Willar, B.; Van Tran, K.; Fitzgibbons, T.P. Epicardial adipocytes in the pathogenesis of atrial fibrillation: An update on basic and translational studies. *Front. Endocrinol.* **2023**, *14*, 1154824. [CrossRef]
13. Bornachea, O.; Vea, A.; Llorente-Cortes, V. Interplay between epicardial adipose tissue, metabolic and cardiovascular diseases. *Clin. Investig. Arterioscler.* **2018**, *30*, 230–239. [PubMed]
14. Nakanishi, K.; Fukuda, S.; Tanaka, A.; Otsuka, K.; Taguchi, H.; Shimada, K. Relationships between Periventricular Epicardial Adipose Tissue Accumulation, Coronary Microcirculation, and Left Ventricular Diastolic Dysfunction. *Can. J. Cardiol.* **2017**, *33*, 1489–1497. [CrossRef]
15. Hogea, T.; Noemi, N.; Suciu, B.A.; Brinzaniuc, K.; Chinezu, L.; Arbănași, E.M.; Kaller, R.; Carașca, C.; Arbănași, E.M.; Vunvulea, V.; et al. Increased Epicardial Adipose Tissue and Heart Characteristics Are Correlated with BMI and Predict Silent Myocardial Infarction in Sudden Cardiac Death Subjects: An Autopsy Study. *Diagnostics* **2023**, *13*, 2157. [CrossRef] [PubMed]
16. Hogea, T.; Suciu, B.A.; Ivănescu, A.D.; Carașca, C.; Chinezu, L.; Arbănași, E.M.; Eliza, R.; Kaller, R.; Arbănași, E.M.; Muresan, A.V.; et al. Increased Epicardial Adipose Tissue (EAT), Left Coronary Artery Plaque Morphology, and Valvular Atherosclerosis as Risks Factors for Sudden Cardiac Death from a Forensic Perspective. *Diagnostics* **2023**, *13*, 142. [CrossRef]
17. Shah, R.V.; Anderson, A.; Ding, J.; Budoff, M.; Rider, O.; Petersen, S.E.; Jensen, M.K.; Koch, M.; Allison, M.; Kawel-Boehm, N.; et al. Pericardial, But Not Hepatic, Fat by CT Is Associated with CV Outcomes and Structure: The Multi-Ethnic Study of Atherosclerosis. *JACC Cardiovasc. Imaging* **2017**, *10*, 1016–1027. [CrossRef]
18. Al-Rawahi, M.; Proietti, R.; Thanassoulis, G. Pericardial fat and atrial fibrillation: Epidemiology, mechanisms and interventions. *Int. J. Cardiol.* **2015**, *195*, 98–103. [CrossRef]
19. Daudé, P.; Ancel, P.; Gouny, S.C.; Jacquier, A.; Kober, F.; Dutour, A.; Bernard, M.; Gaborit, B.; Rapacchi, S. Deep-Learning Segmentation of Epicardial Adipose Tissue Using Four-Chamber Cardiac Magnetic Resonance Imaging. *Diagnostics* **2022**, *12*, 126. [CrossRef]
20. Kramer, C.M.; Barkhausen, J.; Bucciarelli-Ducci, C.; Flamm, S.D.; Kim, R.J.; Nagel, E. Standardized cardiovascular magnetic resonance imaging (CMR) protocols: 2020 update. *J. Cardiovasc. Magn. Reason.* **2020**, *22*, 17. [CrossRef]
21. Batal, O.; Schoenhagen, P.; Shao, M.; Ayyad, A.E.; Van Wagoner, D.R.; Halliburton, S.S.; Tchou, P.J.; Chung, M.K. Left atrial epicardial adiposity and atrial fibrillation. *Circ. Arrhythm. Electrophysiol.* **2010**, *3*, 230–236. [CrossRef] [PubMed]
22. Wu, Y.; Zhang, A.; Hamilton, D.J.; Deng, T. Epicardial Fat in the Maintenance of Cardiovascular Health. *Methodist Debakey Cardiovasc. J.* **2017**, *13*, 20. [CrossRef]
23. Mazurek, T.; Kiliszek, M.; Kobylecka, M.; Skubisz-Głuchowska, J.; Kochman, J.; Filipiak, K.; Królicki, L.; Opolski, G. Relation of Proinflammatory Activity of Epicardial Adipose Tissue to the Occurrence of Atrial Fibrillation. *Am. J. Cardiol.* **2014**, *113*, 1505–1508. [CrossRef] [PubMed]
24. Couselo-Seijas, M.; Rodríguez-Mañero, M.; González-Juanatey, J.R.; Eiras, S. Updates on epicardial adipose tissue mechanisms on atrial fibrillation. *Obes. Rev.* **2021**, *22*, e13277. [CrossRef]
25. Singhal, R.; Lo, L.-W.; Lin, Y.-J.L.; Chang, S.-L.; Hu, Y.-F.; Chao, T.-F.; Chung, F.-P.; Chiou, C.-W.; Tsao, H.-M.; Chen, S.-A. Intrinsic Cardiac Autonomic Ganglionated Plexi within Epicardial Fats Modulate the Atrial Substrate Remodeling: Experiences with Atrial Fibrillation Patients Receiving Catheter Ablation. *Acta Cardiol. Sin.* **2016**, *32*, 174–184. Available online: http://www.ncbi.nlm.nih.gov/pubmed/4816916 (accessed on 30 October 2023).
26. Avazzadeh, S.; McBride, S.; O'brien, B.; Coffey, K.; Elahi, A.; O'halloran, M.; Soo, A.; Quinlan, L. Ganglionated Plexi Ablation for the Treatment of Atrial Fibrillation. *J. Clin. Med.* **2020**, *9*, 3081. [CrossRef] [PubMed]
27. Wong, C.X.; Abed, H.S.; Molaee, P.; Nelson, A.J.; Brooks, A.G.; Sharma, G.; Leong, D.P.; Lau, D.H.; Middeldorp, M.E.; Roberts-Thomson, K.C.; et al. Pericardial Fat Is Associated with Atrial Fibrillation Severity and Ablation Outcome. *J. Am. Coll. Cardiol.* **2011**, *57*, 1745–1751. [CrossRef]
28. Camhi, S.M.; Bray, G.A.; Bouchard, C.; Greenway, F.L.; Johnson, W.D.; Newton, R.L.; Ravussin, E.; Ryan, D.H.; Smith, S.R.; Katzmarzyk, P.T. The Relationship of Waist Circumference and BMI to Visceral, Subcutaneous, and Total Body Fat: Sex and Race Differences. *Obesity* **2011**, *19*, 402. [CrossRef]
29. Gill, C.M.; Azevedo, D.C.; Oliveira, A.L.; Martinez-Salazar, E.L.; Torriani, M.; Bredella, M.A. Sex differences in pericardial adipose tissue assessed by PET/CT and association with cardiometabolic risk. *Acta Radiol.* **2018**, *59*, 1203–1209. [CrossRef]
30. Zhu, J.; Zhuo, K.; Zhang, B.; Xie, Z.; Li, W. Sex Differences in Epicardial Adipose Tissue: Association with Atrial Fibrillation Ablation Outcomes. *Front. Cardiovasc. Med.* **2022**, *9*, 905351. [CrossRef]

31. Conte, M.; Petraglia, L.; Poggio, P.; Valerio, V.; Cabaro, S.; Campana, P.; Comentale, G.; Attena, E.; Russo, V.; Pilato, E.; et al. Inflammation and Cardiovascular Diseases in the Elderly: The Role of Epicardial Adipose Tissue. *Front. Med.* **2022**, *9*, 844266. [CrossRef]
32. Nerlekar, N.; Muthalaly, R.G.; Wong, N.; Thakur, U.; Wong, D.T.L.; Brown, A.J.; Marwick, T.H. Association of volumetric epicardial adipose tissue quantification and cardiac structure and function. *J. Am. Heart Assoc.* **2018**, *7*, e009975. [CrossRef]
33. Fox, C.S.; Gona, P.; Hoffmann, U.; Porter, S.A.; Salton, C.J.; Massaro, J.M.; Levy, D.; Larson, M.G.; D'Agostino, R.B.; O'Donnell, C.J.; et al. Pericardial Fat, Intrathoracic Fat, and Measures of Left Ventricular Structure and Function. *Circulation* **2009**, *119*, 1586–1591. [CrossRef]
34. Patel, N.; Durland, J.; Makaryus, A.N. *Physiology, Cardiac Index*; StatPearls: St. Petersburg, FL, USA, 2022.
35. Iacobellis, G. Epicardial adipose tissue in contemporary cardiology. *Nat. Rev. Cardiol.* **2022**, *19*, 593–606. [CrossRef] [PubMed]
36. Conte, M.; Petraglia, L.; Cabaro, S.; Valerio, V.; Poggio, P.; Pilato, E.; Attena, E.; Russo, V.; Ferro, A.; Formisano, P.; et al. Epicardial Adipose Tissue and Cardiac Arrhythmias: Focus on Atrial Fibrillation. *Front. Cardiovasc. Med.* **2022**, *9*, 932262. [CrossRef] [PubMed]
37. Bakkum, M.J.; Danad, I.; Romijn, M.A.J.; Stuijfzand, W.J.A.; Leonora, R.M.; Tulevski, I.I.; Somsen, G.A.; Lammertsma, A.A.; van Kuijk, C.; van Rossum, A.C.; et al. The impact of obesity on the relationship between epicardial adipose tissue, left ventricular mass and coronary microvascular function. *Eur. J. Nucl. Med. Mol. Imaging* **2015**, *42*, 1562. [CrossRef] [PubMed]

applied sciences

MDPI

Article

Aortic Hemodynamics with Accelerated Dual-Venc 4D Flow MRI in Type B Aortic Dissection

Ozden Kilinc [1], Justin Baraboo [1,2], Joshua Engel [1], Daniel Giese [3,4], Ning Jin [5], Elizabeth K. Weiss [1,2], Anthony Maroun [1], Kelvin Chow [1,6], Xiaoming Bi [6], Rachel Davids [6], Christopher Mehta [7], S. Chris Malaisrie [7], Andrew Hoel [8], James Carr [1], Michael Markl [1,2] and Bradley D. Allen [1,*]

[1] Department of Radiology, Northwestern University, Chicago, IL 60611, USA
[2] Department of Biomedical Engineering, Northwestern University, Chicago, IL 60611, USA
[3] Magnetic Resonance, Siemens Healthcare GmbH, 91052 Erlangen, Germany
[4] Institute of Radiology, University Hospital Erlangen, Friedrich-Alexander-Universität Erlangen-Nürnberg (FAU), 91054 Erlangen, Germany
[5] Cardiovascular MR R&D, Siemens Medical Solutions USA, Inc., Cleveland, OH 44139, USA
[6] Cardiovascular MR R&D, Siemens Medical Solutions USA, Inc., Chicago, IL 60611, USA
[7] Department of Surgery (Cardiac Surgery), Northwestern University, Chicago, IL 60611, USA
[8] Department of Surgery (Vascular Surgery), Northwestern University, Chicago, IL 60611, USA
* Correspondence: bdallen@northwestern.edu

Abstract: The aim of this study is to investigate the applicability of the dual-venc (DV) 4D flow magnetic resonance imaging (MRI) to quantify the complex flow patterns in type B aortic dissection (TBAD). One GRAPPA-accelerated single-venc (SV) and one compressed-sensing (CS) accelerated DV 4D flow MRI sequences are used to scan all subjects, including twelve chronic TBAD patients and two volunteers. The scans are performed twice for the reproducibility assessment of the scan protocols. Voxelwise quantitative flow parameters including kinetic energy (KE), peak velocity (PV), forward and reverse flows (FF, RF) and stasis are calculated. High-venc (HV) data from the DV acquisition are separately analyzed. The scan time reduction by the CS-accelerated DV 4D flow MRI acquisition is 46.4% compared with the SV acquisition. The DV velocity-to-noise ratio (VNR) is higher compared with HV ($p = 0.000$). No true lumen (TL) parameter shows a significant difference among the acquisition types ($p > 0.05$). The false lumen (FL) RF is higher in SV compared with the DV acquisition ($p = 0.009$). The KE is higher ($p = 0.038$) and stasis is lower ($p = 0.01$) in HV compared with SV acquisition. All FL parameters except stasis are higher and stasis is lower in HV compared with DV acquisition ($p < 0.05$). Positive Pearson correlations among the acquisition types in TL and high agreements between the two scans for all acquisition types are observed except HV RF in the FL, which demonstrates a moderate agreement. The CS-accelerated DV 4D flow MRI may have utility in the clinical daily routine with shortened scan times and improved velocity measurements while providing high VNR in TBAD. The observed hemodynamic flow trends are similar between GRAPPA-accelerated SV and CS-accelerated DV 4D flow MRI acquisitions; however, parameters are more impacted by CS-accelerated HV protocol in FL, which may be secondary to the CS regularization effects.

Keywords: dissection; 4D flow MRI; flow; aorta; type B aortic dissection; imaging; quantitative imaging

Citation: Kilinc, O.; Baraboo, J.; Engel, J.; Giese, D.; Jin, N.; Weiss, E.K.; Maroun, A.; Chow, K.; Bi, X.; Davids, R.; et al. Aortic Hemodynamics with Accelerated Dual-Venc 4D Flow MRI in Type B Aortic Dissection. *Appl. Sci.* **2023**, *13*, 6202. https://doi.org/10.3390/app13106202

Academic Editor: Laura Cercenelli

Received: 18 April 2023
Revised: 12 May 2023
Accepted: 15 May 2023
Published: 18 May 2023

1. Introduction

Aortic dissection is a serious vascular injury where high blood pressure flow between the layers of the aorta caused by an intimal tear results in the formation of true (TL) and false lumen (FL) separated by an intimal flap [1–3]. Stanford type A aortic dissection (TAAD) occurs in the ascending aorta, whereas Stanford type B aortic dissection (TBAD) originates distal to the left subclavian artery and extends into the descending aorta [4]. Descending

aorta dissections may occur in isolation (de novo TBAD [dnTBAD]), or secondary to the TAAD repairs, where patients may have chronic residual descending aorta dissection (rTAAD) after the surgical procedure for TAAD. TBAD can be medically managed with anti-impulse therapy if there are no signs of complicated dissection such as end-organ ischemia or rupture [2,4–7]. Even though the anti-impulse therapy is an effective strategy for stable TBAD treatment, a significant percentage of these patients need surgical intervention during the follow-up period secondary to the progressive FL expansion and therefore increased risk of aortic rupture [1,2]. Rapid diagnostic imaging with computed tomography angiography (CTA) or magnetic resonance angiography (MRA) is crucial for the clinical management of TBAD; however, traditional image-based management and risk-stratification have been primarily based on morphologic features of the aorta [8].

Time-resolved 3D phase contrast magnetic resonance imaging (MRI) with 3-directional velocity encoding (4D flow MRI) has been a widely accepted, useful investigational tool in evaluating several cardiovascular pathologies, including aortic dissection [1,5,9–13]. In vivo blood-flow characterization with 4D flow MRI has potential utility in identifying TBAD patients with enlarging aortas by the quantitative flow pattern assessment at the entry tear and in the FL [1,6,9–19]. Despite its benefits, long scan times associated with the multidimensional imaging and single velocity encoding (venc) level potentially limit the clinical adoption of the traditional 4D flow MRI. There are several potential consequences of single-venc (SV) 4D flow MRI acquisitions as velocity noise is directly proportional to the venc. The velocity (v) aliasing may occur for unpredictable high blood flow velocities (v > venc) such as in TL in TBAD and additionally, increased noise for slow flow regions (v < venc) may also be observed such as in FL in TBAD.

The venc used in the SV 4D flow MRI acquisitions is usually adjusted to the estimated peak velocity (PV) to avoid velocity aliasing, limiting the evaluation of the slow flow velocities [20–22]. However, there is a direct positive correlation between the velocity-noise-ratio (VNR) and the measured velocity and inverse relationship between the VNR and the venc; consequentially, the higher the venc, the lower VNR. This is especially important in regions with a slow flow such as in FL in TBAD [23]. Ideal hemodynamic evaluation of cardiovascular diseases should be performed by a technique that maintains high VNR across the encountered range of velocities. However, this range is very broad in TBAD as there are large differences in TL and FL velocities. It is also likely that poor VNR will lead to reduced accuracy of more advanced hemodynamic parameters such as flow stasis and kinetic energy (KE) which may be important markers of adverse outcome risk in TBAD [18]. To address this problem, low-venc (LV) and high-venc (HV) images are being acquired in the same scan with dual-velocity encoded (dual-venc—DV) 4D flow MRI using methods such as Bayesian analysis where the aliased data can be recovered using the HV data while preserving the favorable VNR of the LV data [24–26]. Combining DV 4D flow MRI method with compressed sensing (CS) acceleration technique may provide additional critically important benefits for TBAD management such as shorter scan times, as CS can significantly accelerate MRI acquisitions utilizing the inherent sparsity of MRI data [27–30].

In our previous study, we investigated the applicability of the CS-accelerated SV 4D flow MRI in TBAD with no impact by the DV methodology [31]. Here, in this study, we aim to systematically evaluate the potential utility of CS-accelerated DV 4D flow MRI with an acceleration level of 7.7 (R = 7.7) in aortic hemodynamics, including KE, PV, forward flow (FF), reverse flow (RF) and flow stasis in a cohort of chronic TBAD patients and volunteers. We have provided the detailed comparisons of the quantitative flow parameters in TBAD between the SV GRAPPA-accelerated 4D flow MRI and CS-accelerated DV 4D flow MRI acquisitions and discuss our results, taking into account the results from the previously published studies available in the literature. We hypothesize that DV 4D flow MRI acquisition improves the characterization of flow hemodynamics relative to SV 4D flow MRI acquisition by better capturing the full dynamic range of velocities in TBAD while maintaining a high VNR.

2. Materials and Methods

Study Cohort

This study was approved by the Institutional Review Board and written informed consent was obtained from all subjects. As described in our previous study [31], the prospectively recruited cohort included twelve type B aortic dissection (TBAD) patients (57.75 ± 7.04 years old; 5-female, 7-male) including 6 medically managed de novo TBAD (dnTBAD) and 6 residual descending aorta dissection (rTAAD) cases and two healthy volunteers (a 28-year-old male and a 21-year-old female). The scans were performed for all subjects twice with the same scan protocol 5 to 10 days apart to evaluate the reliability of the acquisitions. The overall cohort included both the baseline and follow-up scans to be used for the groupwise comparisons of the quantitative hemodynamic parameters and for the correlations among the acquisition types. The volunteer data (entire aorta) was added to the true lumen (TL) analysis of the patients whereas the false lumen (FL) analysis was performed in the patient group only.

Image Acquisition

All 4D flow magnetic resonance imaging (MRI) scans were performed on a 1.5T MRI system (MAGNETOM Sola, Siemens Healthcare, Erlangen, Germany). The volumetric coverage of the whole heart and entire aorta during the free-breathing non-contrast scan was provided and retrospective ECG gating was used. Respiratory navigator gating was used only for sagittally acquired dual-venc (DV) acquisitions as single-venc (SV) scans were acquired in coronal orientation with phase encoding left to right, which is less sensitive to respiratory motion artifacts. The DV scans were sagittally performed to reduce the scan time, as coronal 4D flow MRI scans take longer time. The scan protocol included one conventional GRAPPA-accelerated (R = 2) acquisition SV and one compressed sensing (CS) (R = 7.7) accelerated DV 4D flow MRI scans. The same scans were repeated five to ten days after the initial scan in all subjects for interscan reliability assessment. The flip angle was the same (7°) for all scan types. The velocity encoding (venc) value was 160 cm/s for GRAPPA-accelerated SV acquisitions, whereas both low (80 cm/s) and HV (160 cm/s) were used for the DV acquisitions. The venc strategy was symmetric for the SV scans whereas an asymmetric strategy was used for the DV scans. High-venc (HV) (160 cm/s) data from the DV acquisitions were separately analyzed and the results were compared with the other scan types as well. Table 1 summarizes the rest of the scan parameters for each acquisition type. The field of view and in-plane spatial resolution were not constant between the SV and DV acquisitions as low-venc (LV) scan (part of DV) needs stronger gradients for the velocity encoding. Automatic reconstructions on the scanner were performed before the analysis and phase images from the LV and HV data were jointly processed using the Bayesian method to derive velocity for the DV 4D flow MRI acquisitions [24–26]. The HV was calculated as the phase difference between velocity compensated reference set and high velocity encoded set.

Image Processing and Segmentation

The offline post-processing steps of the 4D flow MRI data were identical for all acquisition types using an in-house tool programmed in Matlab (MATLAB; The MathWorks, Natick, MA) to correct eddy currents, aliasing and noise of the areas outside of the flow regions as described previously [31–33]. Time-averaged magnitude and 3D phase-contrast angiogram (PC-MRA) images were utilized to perform the manual segmentations using the designated software (Mimics Innovation Suite; Materialise, Leuven, Belgium). The entire aorta, excluding aortic arch branch vessels, was manually segmented on the time-averaged 4D flow MRI magnitude images and PC-MRA images were used to segment the TL by an observer (OK) with 3 years of experience in imaging research. The entire aorta was segmented on the PC-MRA images in volunteers and used to mask the 4D flow MRI data. The volunteer data covering the entire aorta were combined with the TL data of the patient group for the TL analysis. The LV and HV data were combined into DV data on the scanner without any additional preprocessing steps. Post-acquisition processing steps, DV

acquisition volumetric map examples and the HV data for several TL and FL parameters in one dnTBAD case are displayed in Figure 1.

Table 1. 4D flow magnetic resonance imaging (MRI) scan parameters and mean and standard deviation of the scan time for each acquisition type (scan time was not applicable to high-venc 4D flow MRI data as it was derived from the dual-venc 4D flow MRI acquisition).

Acquisition Type	Single-Venc 4D Flow MRI	Dual-Venc 4D Flow MRI	High-Venc 4D Flow MRI
Scanner	1.5T MRI	1.5T MRI	1.5T MRI
Contrast	No	No	No
Scan Time (min)	11.12 +/− 2.64	5.96 +/− 1.33	n/a
Acceleration Factor (R)	2	7.7	7.7
Field of View (mm^2)	365–459 × 459–499	306–399 × 380–399	306–399 × 380–399
Slice Thickness (mm)	2.8–3.5	2.5–2.8	2.5–2.8
Repetition Time (ms)	4.5–6.2	4.5–5.2	4.5–5.2
Echo Time (ms)	2.18	3	3
Spatial Resolution (mm^3)	2.6 × 2.6 × 2.8–3.5	2.1–2.2 × 2.1–2.2 × 2.5–2.8	2.1–2.2 × 2.1–2.2 × 2.5–2.8
Temporal Resolution (ms)	26.7–52.8	36.5–41.8	36.5–41.8
Flip Angle (°)	7	7	7
Velocity Encoding (cm/s)	160	80 and 160	160

Parametric Hemodynamic Maps

The 3D parametric maps for each flow parameter were obtained using in-house analysis tools (MATLAB; The MathWorks, Natick, MA, USA) according to a previously described approach [6,18]. The 4D flow velocity data were interpolated to 1 mm^3 voxels using spline interpolation. The 3D aortic centerline was calculated automatically based on the TL, and orthogonal planes were automatically placed every millimeter along the centerline. In the next step, each voxel was matched to the closest plane to determine the flow direction along the centerline compared with the normal vector, i.e., forward (ascending aorta to descending aorta) and reverse (descending aorta to ascending aorta). The kinetic energy (KE), forward flow (FF) and 5th percentile peak velocity (PV) were calculated inside the TL and FL for each voxel in the patient group and in the entire aorta of the volunteers. Voxel-wise reverse flow (RF) and stasis were separately calculated in the FL of the patient group, as described in our previous study [31].

Forward Flow and Reverse Flow: The FF and RF were calculated in each voxel through the cardiac cycle and summed. The mean FF and mean RF were reported averaging these sums over the entire volume.

Kinetic Energy: The voxel-wise KE was calculated using the following equation: $KE = 0.5 \times \rho \times dV \times v(t)^2$, where the assumed blood density (ρ) was 1060 kg/m^3, dV the unit voxel volume (i.e., 1 mm^3) and the velocity magnitude for each voxel at each cardiac timeframe [i.e., v(t)]. The reported KE was calculated as total KE by summing the values in each voxel over the cardiac cycle and then over the entire luminal volume.

Peak Velocity: The 3D PV volumetric maps were determined using the time point with the maximum 95th percentile voxel-wise PV. The mean of the top 5% of velocities was reported as PV for the TL and FL.

Stasis: The voxel-wise flow stasis was defined as the percentage of the cardiac timeframes that the velocity in that voxel is <0.1 m/s. These percentages were averaged over the entire FL volume and reported as mean stasis.

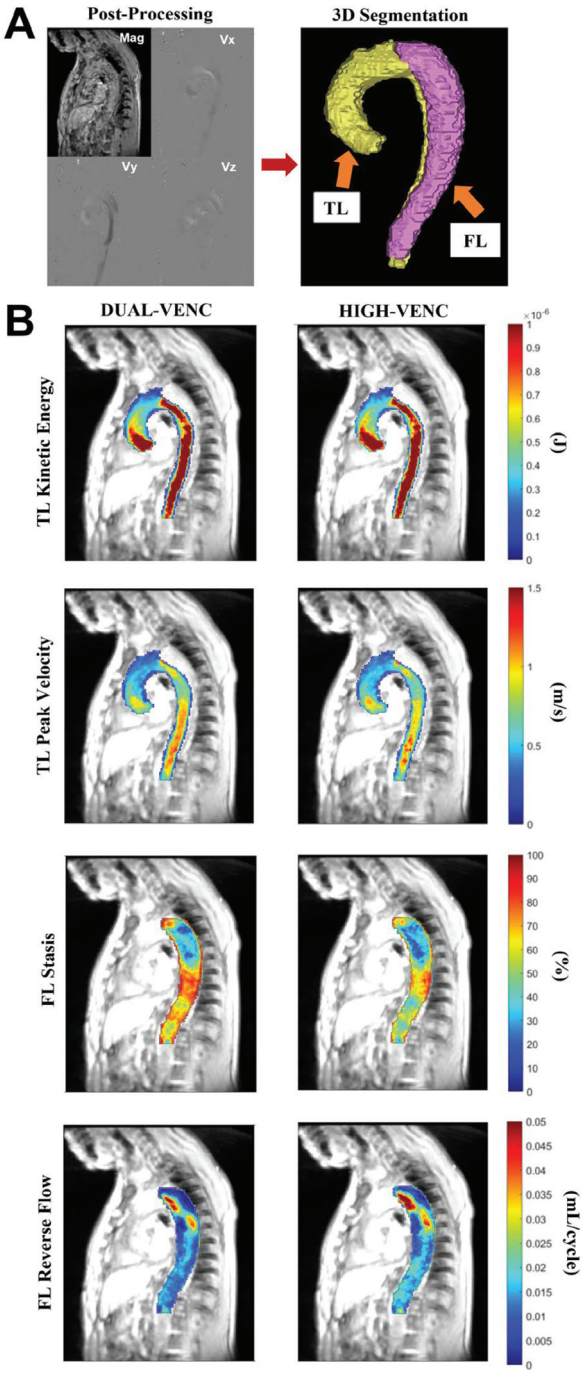

Figure 1. (**A**) Postprocessing of the 4D flow magnetic resonance imaging (MRI) data on MATLAB and manual true (TL) and false lumen (FL) 3D segmentations. (**B**) The volumetric maps of peak velocity and kinetic energy in TL and reverse flow and stasis in FL from the dual-venc (DV) acquisition and high-venc data extracted from the DV acquisition in one subject with de novo type B aortic dissection.

Statistical Analysis

The repeated measures analysis of variance (ANOVA) method and Pearson correlation coefficients (r) were used to perform groupwise comparisons between the acquisition types. The velocity-noise-ratio (VNR) in the TL in the patient group was calculated by dividing the mean velocity over the entire cardiac cycle in the TL by the velocity noise estimated by the standard deviation (SD) of measured velocities in the static spine. The obtained VNR values were compared pairwise among the acquisition types by the repeated measures ANOVA method. Intraclass correlation coefficients (ICC) were calculated between the baseline and follow-up scans for the interscan reliability assessment of each sequence type using the following reliability levels: <0.5 indicates poor reliability, between 0.5 and 0.75 indicates moderate reliability, between 0.75 and 0.9 indicates good reliability, and any value >0.9 is indicative of excellent reliability [34]. A p-value < 0.05 is considered statistically significant. The average scan time and their SDs of the entire cohort consisting of both baseline and follow-up scans were also reported for each acquisition type.

3. Results

Scan Times

The average scan time for GRAPPA-accelerated acquisition is 11.12 +/− 2.64 min and 5.96 +/− 1.33 min for the dual-venc (DV) acquisition in the entire cohort. The scan time reduction by the DV 4D flow magnetic resonance imaging (MRI) acquisition is 46.4% compared with the conventional GRAPPA 4D flow MRI acquisition.

Hemodynamic 4D Flow MRI Parameters: True Lumen

The mean and standard deviations (SD) of all parameters for all three acquisition types, groupwise comparisons and Pearson correlation coefficients in the true lumen (TL) are summarized in Table 2. Notably, no TL parameters are significantly different among the acquisition types (all $p > 0.05$). The Pearson correlation coefficient analysis demonstrates high correlation (all r > 0.92, all $p < 0.05$) in the TL for all parameters for all pairwise comparisons among the three acquisition types.

Hemodynamic 4D Flow MRI Parameters: False Lumen

The kinetic energy (KE), peak velocity (PV), forward flow (FF) and stasis are not significantly different between the single-venc (SV) and dual-venc (DV) acquisitions in the false lumen (FL) ($p > 0.05$ for all). The mean reverse flow (RF) is significantly higher in SV acquisition compared with DV acquisition ($p = 0.009$) with a 25% increase of the value in SV acquisition. The KE is significantly higher ($p = 0.038$), and stasis is significantly lower ($p = 0.01$) in high-venc (HV) data compared with SV acquisition. All FL parameters except stasis are significantly higher in HV data compared with DV acquisition ($p < 0.05$ for all) and stasis is significantly lower in HV data compared with DV acquisition ($p = 0.000$).

The Pearson correlation coefficient levels in the FL are as follows: r = 0.859, 0.768, 0.751, 0.422 and 0.822 for KE, PV, FF, RF and stasis, respectively, between GRAPPA and DV 4D flow MRI acquisitions ($p < 0.05$ for all); r = 0.636, 0.577, 0.473 and 0.516 for KE, FF, RF and stasis, respectively, between GRAPPA-accelerated 4D flow MRI data and HV data from the DV acquisition with p values less than 0.05 for all four correlation levels. On the other hand, r is 0.390 and for PV between GRAPPA and HV data without statistical significance ($p = 0.590$). Pearson correlation coefficient levels between DV and HV data are 0.884, 0.818, 0.869, 0.474 and 0.845 for KE, PV, FF, RF and stasis, respectively ($p < 0.05$ for all parameters). Mean and SDs of all parameters for all three acquisition types, groupwise comparison results and Pearson correlation coefficient levels in the FL are also summarized in Table 2. The values for each parameter and the trend of their distribution among the three acquisition types in TL and FL are represented in Figure 2 boxplots.

Table 2. Each true and false lumen parameter for single-venc and dual-venc (DV) acquisitions and high-venc data results separately from the DV acquisition, groupwise comparison results and Pearson correlation coefficient levels (* indicates statistical significance).

True Lumen		SINGLE-VENC vs. DUAL-VENC		SINGLE-VENC vs. HIGH-VENC		DUAL-VENC vs. HIGH-VENC	
		SINGLE-VENC	DUAL-VENC	SINGLE-VENC	HIGH-VENC	DUAL-VENC	HICH-VENC
Total Kinetic Energy (J)	Mean ± SD	0.188 ± 0.079	0.186 ± 0.078	0.188 ± 0.079	0.195 ± 0.083	0.186 ± 0.078	0.195 ± 0.083
	p value	0.053					
	Correlation	0.955 *		0.953 *		0.989 *	
%5 Peak Velocity (m/s)	Mean ± SD	1.267 ± 0.261	1.256 ± 0.267	1.267 ± 0.261	1.240 ± 0.260	1.256 ± 0.267	1.240 ± 0.260
	p value	0.189					
	Correlation	0.951 *		0.939 *		0.992 *	
Mean Fonward Flow (mL/cycle)	Mean ± SD	0.121 ± 0.030	0.126 ± 0.034	0.121 ± 0.030	0.125 ± 0.029	0.126 ± 0.034	0.125 ± 0.029
	p value	0.302					
	Correlation	0.919 *		0.935 *		0.975 *	
False Lumen		**SINGLE-VENC vs. DUAL-VENC**		**SINCLE-VENC vs. HIGH-VENC**		**DUAL-VENC vs. HIGH-VENC**	
		SINGLE-VENC	**DUAL-VENC**	**SINGLE-VENC**	**HIGH-VENC**	**DUAL-VENC**	**HIGH-VENC**
Total Kinetic Enengy (J)	Mean ± SD	0.021 ± 0.013	0.020 ± 0.013	0.021 ± 0.013	0.038 ± 0.028	0.020 ± 0.013	0.038 ± 0.028
	p value	0.566		0.038 *		0.008 *	
	Correlation	0.859 *		0.636 *		0.884 *	
%5 Peak Velocity (m/s)	Mean ± SD	0.371 ± 0.148	0.381 ± 0.152	0.371 ± 0.148	0.488 ± 0.140	0.381 ± 0.152	0.488 ± 0.140
	p value	0.626		0.076		0.003 *	
	Correlation	0.768 *		0.390		0.818 *	
Mean Forward Flow (mL/cycle)	Mean ± SD	0.019 ± 0.008	0.017 ± 0.007	0.019 ± 0.008	0.021 ± 0.006	0.017 ± 0.007	0.021 ± 0.006
	p value	0.363		0.388		0.004 *	
	Correlation	0.751 *		0.577 *		0.869 *	
Mean Reverse Flow (mL/cycle)	Mean ± SD	0.016 ± 0.003	0.012 ± 0.002	0.016 ± 0.003	0.016 ± 0.005	0.012 ± 0.002	0.016 ± 0.005
	p value	0.009 *		0.908		0.014 *	
	Correlation	0.422 *		0.473 *		0.474 *	
Mean Stasis (%)	Mean ± SD	80.13 ± 10.39	80.48 ± 10.46	80.13 ± 10.39	64.46 ± 10.99	80.48 ± 10.46	64.46 ± 10.99
	p value	0.784		0.001 *		<0.001 *	
	Correlation	0.822 *		0.516 *		0.845 *	

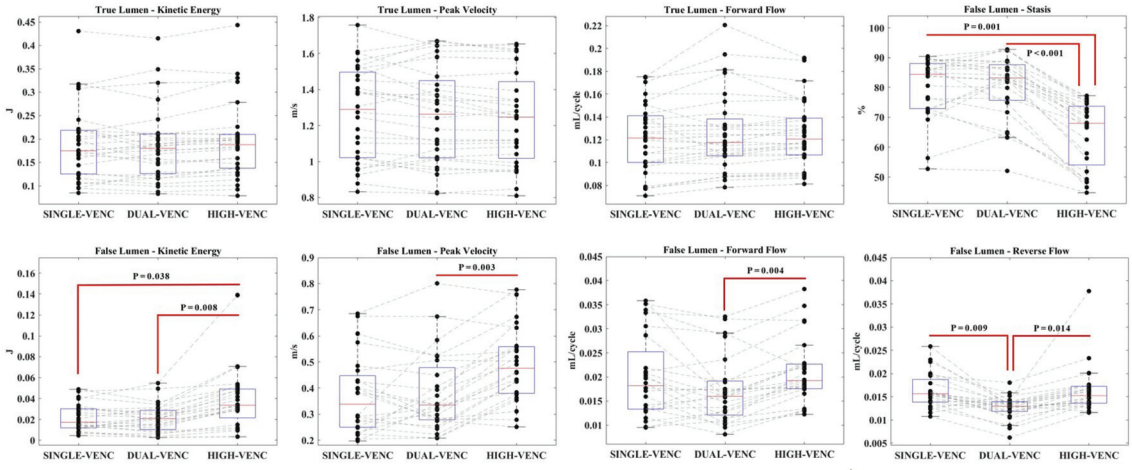

Figure 2. The values for each parameter and their distribution trend are shown in boxplots.

Interscan Reliability Assessment

An excellent level of reliability is observed between baseline and follow-up scans for all three acquisition types for all TL parameters including KE, PV and FF in intraclass correlation coefficient (ICC) analysis with more than 0.931 agreement level for all parameters ($p < 0.01$ for all). The agreement levels in FL are also significantly high for all parameters for SV and DV acquisitions and for KE, stasis, PV and FF in the HV data, (ICC level > 0.800 and $p < 0.01$ for all). The mean RF shows a moderate level of agreement between the first and second scan results in HV data in the FL with a correlation level of 0.640 ($p = 0.043$). The ICC levels between the first and second scans for each dataset are summarized in Table 3.

Table 3. Intraclass correlations between the baseline and follow-up scans for each acquisition type. Correlation levels for all true lumen and false lumen parameters show statistical significance ($p < 0.05$).

True Lumen		**SINGLE-VENC Scan 1 vs. Scan 2**	**DUAL-VENC Sean 1 vs. Sean 2**	**HIGH-VENC Scan 1 vs. Scan 2**
Intraclass Correlation levels	**Kinetic Energy (J)**	0.948	0.931	0.949
	Peak Velocity (m/s)	0.957	0.965	0.958
	Forward Flow (mL/cycle)	0.973	0.945	0.935
False Lumen		**SINGLE-VENC Scan 1 vs. Scan 2**	**DUAL-VENC Scan 1 vs. Scan 2**	**HIGH-VENC Scan 1 vs. Scan 2**
Intraclass Correlation Levels	**Kinetic Energy (J)**	0.983	0.890	0.805
	Reverse Flow (mL/cycle)	0.907	0.851	0.640
	Peak Velocity (m/s)	0.989	0.926	0.925
	Forward Flow (mL/cycle)	0.975	0.970	0.882
	Stasis (%)	0.974	0.924	0.851

Velocity-to-Noise Ratio

The TL velocity-noise-ratio (VNR) value in the patient group for GRAPPA-accelerated acquisition is 3.17 +/− 0.63, 2.82 +/− 1.20 for HV data of the DV 4D flow MRI acquisition and 3.80 +/− 1.39 for the DV 4D flow MRI acquisition. The difference is only significant between the HV and DV acquisitions (HV was 25.7% lower than DV, $p < 0.001$).

4. Discussion

In this study we investigate the performance and reliability of compressed-sensing (CS)-accelerated dual-venc (DV) 4D flow magnetic resonance imaging (MRI) in type B aortic dissection (TBAD) compared with the traditional GRAPPA-accelerated 4D flow MRI. Key results include (1) significantly shorter scan times in CS-accelerated DV acquisition, (2) except for the false lumen (FL) reverse flow (RF), there is no significant difference for the true lumen (TL) or FL hemodynamic parameters between DV and single-venc (SV) acquisitions, (3) superior velocity-noise-ratio (VNR) with improved FL hemodynamic quantification using the DV protocol with CS acceleration relative to CS-accelerated high-venc (HV) alone and (4) excellent reproducibility of all three approaches. Our key takeaway is that the VNR gains with CS-accelerated DV acquisitions seem to improve the performance of CS-accelerated DV 4D flow MRI, especially for advanced hemodynamic characterization in regions more predisposed to effects of low VNR such as the FL in TBAD. This feature, combined with the substantial reduction in scan time makes CS-accelerated DV 4D flow MRI an attractive alternative to traditional and standard CS-accelerated 4D flow MRI in disease states with a high dynamic range of velocities such as aortic dissection.

Hemodynamic parameters in the true lumen and false lumen

It is interesting to note that our results demonstrate no significant difference in any of the hemodynamic TL parameters among three datasets including the conventional GRAPPA-accelerated 4D flow MRI and CS-accelerated DV 4D flow MRI and HV data acquired as a part of the DV acquisition. CS-based reconstruction has been previously used in various studies and underestimation of several 4D flow MRI-derived flow parameters has commonly been observed [13,28–30,35], differently from our study as we do not observe an underestimation of the PV in TL. In their study, Pathrose et al. use three acceleration levels (R = 5.7, 7.7, and 10.2) of CS-accelerated 4D flow MRI protocol in a heterogenous cohort of patients with several aortic disease types and demonstrate an underestimation of several quantitative parameters by all CS based acquisitions. However, the number of TBAD cases is limited to four in their study and the FL analysis results in the dissection cases are not reported separately [13].

On the other hand, FL results demonstrate an overestimation of kinetic energy (KE) and flow parameters peak velocity (PV), forward flow (FF) and RF, and lower estimations of low flow parameter stasis in HV dataset compared with the DV acquisition. As the HV data is a subset of the DV acquisition, these effects are likely secondary to the higher VNR obtained in the DV reconstruction method. Among these hemodynamic parameters quantified, KE is the most unsteady parameter between two datasets with a 90% increase of the mean value from DV data to HV data. The percent change of the PV, FF, RF and stasis are 28.8, 23.5, 33.3 and 19.9%, respectively, which are relatively lower compared with KE. However, these results may still be considered as clinically significant. As KE calculation is directly proportional to the velocity squared, a small number of noisy voxels with a high velocity may be causing the higher average KE values and CS acceleration may be further contributing to the observed higher estimations by increasing the noise in the images. A similar trend for KE and stasis is also observed in the comparison between SV and HV datasets, which is likely secondary to the effects of the CS acceleration. Furthermore, these significant differences in KE and stasis support the idea of the impacts of the KE calculation method besides the impacts of the CS acceleration technique on the image noise. Additionally, the velocities are lower in FL compared with TL which leads to more susceptibility to image noise and velocity encoding (venc)-induced image noise limits the dynamic range of the measurable velocities, making the use of a DV approach in 4D flow MRI acquisitions more important.

Comparison to previously published dual-venc studies

Schnell et al. use the k-t GRAPPA-accelerated DV 4D flow MRI sequence in sixteen volunteers to evaluate its utility to assess intracranial hemodynamics including net flow and PV. The regional flow quantification in their study demonstrates a similar PV at all arterial locations, as seen in both TL and FL analyses in our study. Net flow analysis demonstrates

significantly higher values in both arterial and venous systems in the DV data compared with the HV data. Our results indicate similar FF results between SV and DV acquisitions in both TL and FL, and RF is relatively lower in DV acquisition compared with the SV. The phantom experiments in their study demonstrate 51.4% noise reduction in DV acquisitions compared with HV and the volunteer data shows decreased noise in DV compared with HV [22].

In another study, Schnell et al. acquire k-t GRAPPA-accelerated DV 4D flow MRI with ascending and descending aorta coverage in four Marfan syndrome patients and one bicuspid aortic valve patient and demonstrate an improved VNR in the DV 4D flow MRI data compared with the HV scan and significantly correlated PV results between DV and HV in ascending aorta and arch, as seen in our TL analysis results [20]. The TL VNR results in our patient group maintain the high VNR values in DV acquisition without any significant change compared with SV acquisition. However, as expected, HV data results demonstrate a VNR reduction compared with both DV and SV acquisitions reaching to the significance level only in comparison with DV acquisition. Our results confirm that DV acquisition preserves the favorable VNR of the low-venc (LV) data and the reduction in the VNR in HV data might be related to the CS acceleration which is neutralized by using both LV and HV reconstruction in the DV acquisition. Additionally, descending aorta dissection is the unique pathology in our study, distinctly from the above studies, and CS-acceleration and DV reconstruction methods are investigated in both high- and low-flow environments.

The scan-time reduction by DV 4D flow MRI acquisition is 46.4% compared with the conventional 4D flow MRI in our study, supporting the potential of the CS-accelerated DV 4D flow MRI for clinical translation with significantly shorter scan times, entire velocity dynamic range coverage in the TL and FL avoiding the velocity aliasing and improved VNR relative to the HV acquisition alone. Shorter scan times increase the imaging efficiency and improve patient comfort, which is desirable in critically ill TBAD cases along with the importance of faster imaging for clinicians to take accurate steps in treatment management.

The rigidly set velocity encoding value has been a common issue in 4D flow MRI in various pathologies including aortic dissection. In TBAD, this problem specifically lies in the substantial differences in the blood velocity of TL and FL. However, the measurement of high and low flows in the vessel can be effectively achieved by the advanced Bayesian multipoint velocity encoding method [24–26]. The DV 4D flow MRI technique has been used in various studies representing the dynamic velocity range more accurately in brain and cardiac vessels [22,26,36–38]. However, the effects resulting from the combination of the CS acceleration and DV technique on 4D flow MRI based hemodynamic flow quantifications in TBAD have not been reported in TL and FL separately. Additionally, these 4D flow MRI-derived hemodynamic parameters have not been implemented in diagnostic and/or prognostic criteria in TBAD and neither any gold standard hemodynamic flow quantification method nor any 4D flow MRI based hemodynamic parameter value has been validated as a reference for TBAD patients. Moreover, the fact that no difference is observed between the three datasets in the TL and the same trend is also observed for most parameters in the comparison between SV and DV acquisitions in the FL is promising for future applications of this technique in clinical settings with additional benefits of the CS acceleration scan time savings compared with conventional 4D flow MRI, reliable results as seen in our study between the baseline and follow-up scans with high interscan agreements and high-level image quality similar to the conventional 4D flow MRI. The observed differences in comparisons of the parameters between HV data and both DV and SV acquisitions are likely associated with CS acceleration as similar results were previously observed in comparison between GRAPPA-accelerated and CS-accelerated SV 4D flow MRI acquisitions in the same cohort of patients [31].

Our study has several limitations. The first is the small size of the cohort. Further investigation of the DV acquisition in TBAD in larger cohorts needs to be performed in future studies to establish reference normal values for each hemodynamic parameter with this technique. Even though an increase in the VNR is observed with the DV acquisition

compared with the SV acquisition, the observed marginal increase is not statistically significant and may be secondary to the small number of the subjects. The increase in the VNR with the DV acquisition may be better observed in studies with larger cohorts which may better help to assess the clinical correlations and accuracy and precision of the PV and flow measurements. Secondly, the TL and FL segmentations are challenging, especially on non-contrast images. The utilization of the high blood-tissue contrast anatomical imaging registered to flow data or machine-learning based methods may address this issue. Additionally, in cases of actively moving FL, static masks used in the methodology may have impacted the capture of the entire FL through the cardiac time point. Our study is also limited in that we investigate only one LV, HV pairing. However, the HV was chosen so to prevent aliasing while still maximizing the VNR within the aorta. While reducing the LV may increase the VNR in DV 4D flow MRI reconstruction, increasing the gap between the LV and HV may reduce the ability to correctly unwrap the aliased data. Further investigation of the DV acquisition remains needed in future studies to address this problem. Several differences between the acquisition parameters between GRAPPA-accelerated SV acquisitions and CS-accelerated DV acquisitions such as temporal resolution, image orientation and the need for navigator gating in sagittally-acquired DV images, higher signal-to-noise ratio for larger field-of-view in coronally acquired SV images and potential breathing/fat artefacts in the sagittal views may also be the factors behind the reasons of the differences seen. Specifically, temporal resolution of the SV scan vary greatly and more than the DV scan (26–52 ms vs. 36.48 ms) and inferior temporal resolution could be the cause of the surprisingly similar PV estimations. Therefore, future studies matching all scan parameters between the acquisition types may address this limitation. The CS acceleration in the DV acquisition and comparisons of the results with the traditional GRAPPA acceleration and using only a single acceleration level are the other limitations of our study in addition to the scan parameter differences between the acquisition types. Ideally, the only difference between the DV and SV acquisitions would be the venc selections, however the CS acceleration is needed to shorten the scan times in DV acquisitions where the scanner reconstruction times are already longer secondary to the unwrapping. Different CS acceleration levels should also be investigated in future studies.

5. Conclusions

In conclusion, our study highlights the potential of dual-venc (DV) acquisitions to substantially reduce scan times and improve the velocity-noise-ratio (VNR), velocity measurements and the quantification of advanced hemodynamic parameters in true lumen (TL) and false lumen (FL) of type B aortic dissection (TBAD) cases with a single 4D flow magnetic resonance imaging (MRI) acquisition in spite of the significant dynamic range of velocities encountered in these patients. Further investigations in larger cohort cohorts are necessary to validate our results and establish reference normal values for quantitative flow parameters with this method.

Author Contributions: Conception and design: All authors contributed to the conception and design of the study. Data collection: O.K. and J.E. Analysis and interpretation: All authors contributed to the analysis and interpretation of the data. Manuscript preparation: All authors also contributed to the drafting of this manuscript. All authors have read and agreed to the published version of the manuscript.

Funding: Funding for this study was provided by the American Heart Association (20CDA35310687) and the National Institutes of Health—National Institute of Biomedical Imaging & Bioengineering (T32EB025766).

Institutional Review Board Statement: This study uses data collected by protocols approved by Northwestern University IRB and all subjects provided written informed consent to participate as outlined in the manuscript.

Informed Consent Statement: Informed consent was obtained from all subjects involved in the study.

Data Availability Statement: The data that support the findings of this study are available on request from the corresponding author, O.K. The data are not publicly available due to data sets containing information that could compromise research participant privacy.

Acknowledgments: The authors would like to thank Beth Whippo and Donny Nieto for their support in recruiting and scanning patients in this study.

Conflicts of Interest: J.C. has received institutional research grants from Siemens, Bayer and Guerbet, speaker honoraria from Bayer, Guerbet, Siemens and is on the advisory boards of Siemens, Bayer, and Bracco. B.D.A. has received consultant fees from Circle Cardiovascular Imaging and research grant from American Heart Association. J.B. has received research grants from National Institute of Biomedical Imaging & Bioengineering. M.M. has received grant support from Siemens and Circle Cardiovascular imaging.

Abbreviations

ANOVA	Analysis of variance
CS	Compressed sensing
CTA	Computed tomography angiography
dnTBAD	De novo Type B aortic dissection
DV	Dual-venc
FF	Forward flow
FL	False lumen
HV	High-venc
ICC	Intraclass correlation coefficient
KE	Kinetic energy
MRA	Magnetic resonance angiography
MRI	Magnetic resonance imaging
PC-MRA	Time-averaged 3D phase contrast magnetic resonance angiogram
PV	Peak velocity
R	Acceleration factor
RF	Reverse flow
rTAAD	repaired TAAD with residual TBAD
SD	Standard deviation
SV	Single-venc
TAAD	Type A aortic dissection
TBAD	Type B aortic dissection
TL	True lumen
v	velocity
Venc	Velocity encoding
VNR	Velocity-to-noise ratio

References

1. Zilber, Z.A.; Boddu, A.; Malaisrie, S.C.; Hoel, A.W.; Metha, C.K.; Vassallo, P.; Burris, N.S.; Roldán-Alzate, A.; Collins, J.D.; François, C.J.; et al. Noninvasive Morphologic and Hemodynamic Evaluation of Type B Aortic Dissection: State of the Art and Future Perspectives. *Radiol. Cardiothorac. Imaging* **2021**, *3*, e200456. [CrossRef] [PubMed]
2. Malaisrie, S.C.; Mehta, C.K. Updates on Indications for TEVAR in Type B Aortic Dissection. *Innovations* **2020**, *15*, 495–501. [CrossRef] [PubMed]
3. Malaisrie, S.C.; Szeto, W.Y.; Halas, M.; Girardi, L.N.; Coselli, J.S.; Sundt, T.M., 3rd; Chen, E.P.; Fischbein, M.P.; Gleason, T.G.; Okita, Y.; et al. 2021 The American association for thoracic surgery expert consensus document: Surgical treatment of acute type A aortic dissection. *J. Thorac. Cardiovasc. Surg.* **2021**, *162*, 735–758. [CrossRef] [PubMed]
4. Akin, I.; Nienaber, C.A. Prediction of aortic dissection. *Heart* **2020**, *106*, 870–871. [CrossRef] [PubMed]
5. Fattori, R.; Cao, P.; De Rango, P.; Czerny, M.; Evangelista, A.; Nienaber, C.; Rousseau, H.; Schepens, M. Interdisciplinary expert consensus document on management of type B aortic dissection. *J. Am. Coll. Cardiol.* **2013**, *61*, 1661–1678. [CrossRef]
6. Jarvis, K.; Pruijssen, J.T.; Son, A.Y.; Allen, B.D.; Soulat, G.; Vali, A.; Barker, A.J.; Hoel, A.W.; Eskandari, M.K.; Malaisrie, S.C.; et al. Parametric Hemodynamic 4D Flow MRI Maps for the Characterization of Chronic Thoracic Descending Aortic Dissection. *J. Magn. Reson. Imaging* **2020**, *51*, 1357–1368. [CrossRef]
7. Rohlffs, F.; Tsilimparis, N.; Diener, H.; Larena-Avellaneda, A.; Von Kodolitsch, Y.; Wipper, S.; Debus, E.S.; Kölbel, T. Chronic type B aortic dissection: Indications and strategies for treatment. *J. Cardiovasc. Surg.* **2015**, *56*, 231–238.

8. Elsayed, R.S.; Cohen, R.G.; Fleischman, F.; Bowdish, M.E. Acute Type A Aortic Dissection. *Cardiol. Clin.* **2017**, *35*, 331–345. [CrossRef]
9. Burris, N.S.; Hope, M.D. 4D flow MRI applications for aortic disease. *Magn. Reson. Imaging Clin. N. Am.* **2015**, *23*, 15–23. [CrossRef]
10. Garcia, J.; Barker, A.J.; Markl, M. The role of imaging of flow patterns by 4D flow MRI in aortic stenosis. *JACC Cardiovasc. Imaging* **2019**, *12*, 252–266. [CrossRef]
11. Hope, M.D.; Meadows, A.K.; Hope, T.A.; Ordovas, K.G.; Saloner, D.; Reddy, G.P.; Alley, M.T.; Higgins, C.B. Clinical evaluation of aortic coarctation with 4D flow MR imaging. *J. Magn. Reson. Imaging* **2010**, *31*, 711–718. [CrossRef]
12. Bissell, M.M.; Loudon, M.; Hess, A.T.; Stoll, V.; Orchard, E.; Neubauer, S.; Myerson, S.G. Differential flow improvements after valve replacements in bicuspid aortic valve disease: A cardiovascular magnetic resonance assessment. *J. Cardiovasc. Magn. Reson.* **2018**, *20*, 10. [CrossRef]
13. Pathrose, A.; Ma, L.; Berhane, H.; Scott, M.B.; Chow, K.; Forman, C.; Jin, N.; Serhal, A.; Avery, R.; Carr, J.; et al. Highly accelerated aortic 4D flow MRI using compressed sensing: Performance at different acceleration factors in patients with aortic disease. *Magn. Reson. Med.* **2021**, *85*, 2174–2187. [CrossRef]
14. Marlevi, D.; Sotelo, J.A.; Grogan-Kaylor, R.; Ahmed, Y.; Uribe, S.; Patel, H.J.; Edelman, E.R.; Nordsletten, D.A.; Burris, N.S. False lumen pressure estimation in type B aortic dissection using 4D flow cardiovascular magnetic resonance: Comparisons with aortic growth. *J. Cardiovasc. Magn. Reson.* **2021**, *23*, 51. [CrossRef]
15. Burris, N.S.; Nordsletten, D.A.; Sotelo, J.A.; Grogan-Kaylor, R.; Houben, I.B.; Figueroa, C.A.; Uribe, S.; Patel, H.J. False lumen ejection fraction predicts growth in type B aortic dissection: Preliminary results. *Eur. J. Cardiothorac. Surg.* **2020**, *57*, 896–903. [CrossRef]
16. Stankovic, Z.; Allen, B.D.; Garcia, J.; Jarvis, K.B.; Markl, M. 4D flow imaging with MRI. *Cardiovasc. Diagn. Ther.* **2014**, *4*, 173–192.
17. Allen, B.D.; Aouad, P.J.; Burris, N.S.; Rahsepar, A.A.; Jarvis, K.B.; Francois, C.J.; Barker, A.J.; Malaisrie, S.C.; Carr, J.C.; Collins, J.D.; et al. Detection and Hemodynamic Evaluation of Flap Fenestrations in Type B Aortic Dissection with 4D Flow MRI: Comparison with Conventional MRI and CTA. *Radiol. Cardiothorac. Imaging* **2019**, *1*, e180009. [CrossRef]
18. Chu, S.; Kilinc, O.; Pradella, M.; Weiss, E.; Baraboo, J.; Maroun, A.; Jarvis, K.; Mehta, C.K.; Malaisrie, S.C.; Hoel, A.W.; et al. Baseline 4D Flow-Derived in vivo Hemodynamic Parameters Stratify Descending Aortic Dissection Patients with Enlarging Aortas. *Front. Cardiovasc. Med.* **2022**, *9*, 905718. [CrossRef]
19. Clough, R.E.; Waltham, M.; Giese, D.; Taylor, P.R.; Schaeffter, T. A new imaging method for assessment of aortic dissection using four-dimensional phase contrast magnetic resonance imaging. *J. Vasc. Surg.* **2012**, *55*, 914–923. [CrossRef]
20. Schnell, S.; Rose, M.J.; Wu, C.; Garcia, J.; Robinson, J.D.; Markl, M.; Rigsby, C.K. Improved assessment of aortic hemodynamics by *k-t* accelerated dual-VENC 4D flow MRI in pediatric patients. *J. Cardiovasc. Magn. Reson.* **2016**, *18*, O96. [CrossRef]
21. Ma, L.E.; Markl, M.; Chow, K.; Vali, A.; Wu, C.; Schnell, S. Efficient triple-VENC phase-contrast MRI for improved velocity dynamic range. *Magn. Reson. Med.* **2020**, *83*, 505–520. [CrossRef] [PubMed]
22. Schnell, S.; Ansari, S.A.; Wu, C.; Garcia, J.; Murphy, I.G.; Rahman, O.A.; Rahsepar, A.A.; Aristova, M.; Collins, J.D.; Carr, J.C.; et al. Accelerated dual-venc 4D flow MRI for neurovascular applications. *J. Magn. Reson. Imaging* **2017**, *46*, 102–114. [CrossRef] [PubMed]
23. Lee, A.T.; Pike, G.B.; Pelc, N.J. Three-point phase-contrast velocity measurements with increased velocity-to-noise ratio. *Magn. Reson. Med.* **1995**, *33*, 122–126. [CrossRef] [PubMed]
24. Binter, C.; Knobloch, V.; Manka, R.; Sigfridsson, A.; Kozerke, S. Bayesian multipoint velocity encoding for concurrent flow and turbulence mapping. *Magn. Reson. Med.* **2013**, *69*, 1337–1345. [CrossRef]
25. Moersdorf, R.; Treutlein, M.; Kroeger, J.R.; Ruijsink, B.; Wong, J.; Maintz, D.; Weiss, K.; Bunck, A.C.; Baeßler, B.; Giese, D. Precision, reproducibility and applicability of an undersampled multi-venc 4D flow MRI sequence for the assessment of cardiac hemodynamics. *Magn. Reson. Imaging* **2019**, *61*, 73–82. [CrossRef]
26. Kroeger, J.R.; Pavesio, F.C.; Mörsdorf, R.; Weiss, K.; Bunck, A.C.; Baeßler, B.; Maintz, D.; Giese, D. Velocity quantification in 44 healthy volunteers using accelerated multi-VENC 4D flow CMR. *Eur. J. Radiol.* **2021**, *137*, 109570. [CrossRef]
27. Cheng, J.Y.; Hanneman, K.; Zhang, T.; Alley, M.T.; Lai, P.; Tamir, J.I.; Uecker, M.; Pauly, J.M.; Lustig, M.; Vasanawala, S.S. Comprehensive motion-compensated highly accelerated 4D flow MRI with ferumoxytol enhancement for pediatric congenital heart disease. *J. Magn. Reson. Imaging* **2016**, *43*, 1355–1368. [CrossRef]
28. Dyvorne, H.; Knight-Greenfield, A.; Jajamovich, G.; Besa, C.; Cui, Y.; Stalder, A.; Markl, M.; Taouli, B. Abdominal 4D flow MR imaging in a breath hold: Combination of spiral sampling and dynamic compressed sensing for highly accelerated acquisition. *Radiology* **2015**, *275*, 245–254. [CrossRef]
29. Neuhaus, E.; Weiss, K.; Bastkowski, R.; Koopmann, J.; Maintz, D.; Giese, D. Accelerated aortic 4D flow cardiovascular magnetic resonance using compressed sensing: Applicability, validation and clinical integration. *J. Cardiovasc. Magn. Reson.* **2019**, *21*, 65. [CrossRef]
30. Ma, L.E.; Markl, M.; Chow, K.; Huh, H.; Forman, C.; Vali, A.; Greiser, A.; Carr, J.; Schnell, S.; Barker, A.J.; et al. Aortic 4D flow MRI in 2 minutes using compressed sensing, respiratory controlled adaptive k-space reordering, and inline reconstruction. *Magn. Reson. Med.* **2019**, *81*, 3675–3690. [CrossRef]

31. Kilinc, O.; Chu, S.; Baraboo, J.; Weiss, E.K.; Engel, J.; Maroun, A.; Giese, D.; Jin, N.; Chow, K.; Bi, X.; et al. Hemodynamic evaluation of type B aortic dissection using compressed sensing accelerated 4D flow MRI. *J. Magn. Reson. Imaging* **2022**, *7*, 1752–1763. [CrossRef]
32. Bernstein, M.A.; Zhou, X.J.; Polzin, J.A.; King, K.F.; Ganin, A.; Pelc, N.J.; Glover, G.H. Concomitant gradient terms in phase contrast MR: Analysis and correction. *Magn. Reson. Med.* **1998**, *39*, 300–308. [CrossRef]
33. Walker, P.G.; Cranney, G.B.; Scheidegger, M.B.; Waseleski, G.; Pohost, G.M.; Yoganathan, A.P. Semiautomated method for noise reduction and background phase error correction in MR phase velocity data. *J. Magn. Reson. Imaging* **1993**, *3*, 521–530. [CrossRef]
34. Bobak, C.A.; Barr, P.J.; O'Malley, A.J. Estimation of an inter-rater intra-class correlation coefficient that overcomes common assumption violations in the assessment of health measurement scales. *BMC Med. Res. Methodol.* **2018**, *1218*, 93. [CrossRef]
35. Hsiao, A.; Lustig, M.; Alley, M.T.; Murphy, M.J.; Vasanawala, S.S. Evaluation of valvular insufficiency and shunts with parallel-imaging compressed-sensing 4D phase-contrast MR imaging with stereoscopic 3D velocity-fusion volume-rendered visualization. *Radiology* **2012**, *265*, 87–95. [CrossRef]
36. Vali, A.; Aristova, M.; Vakil, P.; Abdalla, R.; Prabhakaran, S.; Markl, M.; Ansari, S.A.; Schnell, S. Semi-automated analysis of 4D flow MRI to assess the hemodynamic impact of intracranial atherosclerotic disease. *Magn. Reson. Med.* **2019**, *82*, 749–762. [CrossRef]
37. Aristova, M.; Vali, A.; Ansari, S.A.; Shaibani, A.; Alden, T.D.; Hurley, M.C.; Jahromi, B.S.; Potts, M.B.; Markl, M.; Schnell, S. Standardized evaluation of cerebral arteriovenous malformations using flow distribution network graphs and dual-venc 4D flow MRI. *J. Magn. Reson. Imaging* **2019**, *50*, 1718–1730. [CrossRef]
38. Shiina, Y.; Kawakubo, M.; Inai, K.; Asagai, S.; Nagao, M. Dual VENC 4D flow magnetic resonance imaging demonstrates arterial-pulmonary collaterals in an adult with tetralogy of Fallot. *Eur. Heart J. Cardiovasc. Imaging* **2021**, *22*, e95. [CrossRef]

applied sciences

MDPI

Article

Whole-Heart Assessment of Turbulent Kinetic Energy in the Repaired Tetralogy of Fallot

Ashifa Hudani [1,2], James A. White [2,3,4], Steven C. Greenway [3,4,5,6] and Julio Garcia [2,3,4,7,*]

1 Department of Biomedical Engineering, University of Calgary, Calgary, AB T2N 1N4, Canada
2 Stephenson Cardiac Imaging Centre, University of Calgary, Calgary, AB T2N 1N4, Canada
3 Department of Cardiac Sciences, Cumming School of Medicine, University of Calgary, Calgary, AB T2N 1N4, Canada
4 Libin Cardiovascular Institute, University of Calgary, Calgary, AB T2N 1N4, Canada
5 Alberta Children's Hospital Research Institute, University of Calgary, Calgary, AB T2N 1N4, Canada
6 Department of Biochemistry and Molecular Biology, Cumming School of Medicine, University of Calgary, Calgary, AB T2N 1N4, Canada
7 Department of Radiology, Cumming School of Medicine, University of Calgary, Calgary, AB T2N 1N4, Canada
* Correspondence: julio.garciaflores@ucalgary.ca

Featured Application: Turbulence kinetic energy can be useful to characterize repair of Tetralogy of Fallot hemodynamic abnormalities.

Abstract: Approximately 10% of congenital heart diseases (CHDs) include Tetralogy of Fallot (TOF). Fortunately, due to advanced surgical techniques, most patients survive until adulthood. However, these patients require frequent monitoring for postoperative complications leading to heart hemodynamic alterations. Turbulent kinetic energy (TKE), as derived from 4D-flow magnetic resonance imaging (4D-flow MRI), has been used to characterize abnormal heart hemodynamics in CHD. Hence, this study aimed to assess the difference in TKE between patients with repaired TOF (rTOF) and healthy volunteers. A total of 35 subjects, 17 rTOF patients and 18 controls, underwent standard-of-care cardiac MRI and research 4D-flow MRI using a clinical 3T scanner. Heart chambers and great vessels were segmented using 3D angiograms derived from 4D-flow MRI. The TKE was quantified within segmented volumes. TKE was compared to standard cardiac MRI metrics. Controls demonstrated higher TKE in the left atria and left ventricle. However, patients demonstrated higher TKE in the right atria, right ventricle ($p < 0.05$), and pulmonary artery. Lastly, no correlation was observed between TKE and standard clinical measurements. TKE can be a key indicator of the abnormal hemodynamics present in patients with rTOF and can assist future interventions and help monitor long-term outcomes.

Keywords: repaired tetralogy of fallot; magnetic resonance imaging; 4D-flow MRI; heart hemodynamics; turbulent kinetic energy

Citation: Hudani, A.; White, J.A.; Greenway, S.C.; Garcia, J. Whole-Heart Assessment of Turbulent Kinetic Energy in the Repaired Tetralogy of Fallot. *Appl. Sci.* **2022**, *12*, 10946. https://doi.org/10.3390/app122110946

Academic Editor: Qi-Huang Zheng

Received: 30 September 2022
Accepted: 24 October 2022
Published: 28 October 2022

1. Introduction

In the cardiovascular system, blood flow is maintained with high efficiency to obtain laminar flow between heart chambers and vessels [1]. However, nonlaminar flow (transitional and turbulent) is observed in many congenital heart diseases; in particular, patients with repaired Tetralogy of Fallot (rTOF) can develop changes in turbulent kinetic energy (TKE) [2]. Tetralogy of Fallot (TOF) is a common cyanotic congenital heart defect which is a combination of four defects including right ventricular hypertrophy (RVH), pulmonary stenosis (PS), ventricular septal defect (VSD), and overriding aortic root [3]. Luckily, due to advancements in cardiovascular surgical techniques that aim to increase flow to the pulmonary circulation, a 40% reduction in death outcomes has been achieved in specialized hospitals [4]. Long-term survival can reach 90% after 20 years of surgical repair. Despite

patients now surviving into adulthood, these patients still require frequent and long-term monitoring for many postoperative complications that still arise over time, including right ventricle (RV) dilation and hypertrophy, left or right ventricular dysfunction, RV outflow tract obstruction, and pulmonary regurgitation (PR) [4]. These complications are due to the adverse effects faced within the hemodynamics of the cardiovascular system, contributing to poor long-term outcomes including sudden cardiac death, progressive exercise intolerance, and ventricular arrhythmia [5–7]. Surgical and percutaneous pulmonary valve replacements could prevent some of these long-term complications. Unfortunately, guideline indications are not well-supported for these procedures since a better understanding of heart (dys)function and hemodynamics in rTOF is needed.

Transthoracic echocardiography is the first line imaging modality for assessing cardiovascular diseases given its easy accessibility, low cost, and safety [8,9]. However, it may be limited by poor acoustic windows, beam alignments, operator dependence, and inaccuracy for quantifying regurgitant lesions [10–12]. Currently, standard cardiac magnetic resonance (CMR) is the gold standard for monitoring heart functions and remodeling in patients with rTOF [13]. CMR is able to identify rTOF complications based on morphological and simplified functional parameters including ejection fraction, ventricular volume, etc. [14]. However, these measurements provide a late expression of the physiological changes that occur, resulting in an inaccurate prediction of the true outcome [15,16]. Flow is usually evaluated using 2D phase contrast, which can provide unidirectional velocity measurements perpendicular to the acquisition plane in the vessel of interest. In addition, these measurements do not provide us with an accurate representation of the 3D complexity of the blood flow due to its 2D nature, hence limiting access to flow information in all directions [17]. Furthermore, due to this restriction, it does not provide detailed information or a complete picture regarding alterations in the hemodynamic patterns within the entire heart. In addition, noninvasive Doppler methods allow us to measure adverse velocity fluctuations, but they are also limited in one direction due to the restriction of the ultrasound beam and have an elevated user variability [18,19]. Hence, advanced imaging modalities and more sensitive markers need to be developed, evaluated, and assessed in order to help guide therapy and improve future outcomes within this patient cohort.

A promising noninvasive approach is 4D-flow magnetic resonance imaging (MRI), which provides advanced hemodynamic information enabling the quantification of advanced fluid dynamic metrics, including Turbulent Kinetic Energy (TKE), pressure difference maps, and viscous energy loss [5,20]. As blood flow velocities are measured in all three spatial directions with 4D-flow MRI, it facilitates the volumetric analysis of congenital diseases, such as TOF. In particular, 4D-flow-derived TKE describes the kinetic energy of the fluctuating velocity field and quantifies the inefficiencies of the energetic transfer in the blood flow [21]. This metric can help provide a functional outcome for patients with rTOF [22]. Therefore, the objective of this study is to use 4D-flow MRI to quantify TKE on the entire heart of patients with rTOF and compare it to standard clinical parameters.

2. Materials and Methods

2.1. Study Population

A single-center retrospective case study was performed to compare patients with rTOF with health controls. A total of 17 patients with rTOF (age: 28 ± 8, 5 females) and 18 controls (36 ± 12, 7 females) were recruited from our local observational Cardiovascular Imaging Registry of Calgary (CIROC). The University of Calgary Research Ethics Board approved the study and all subjects provided written consent at the time of the scan's examination. Research activities were performed in accordance with the Declaration of Helsinki. Informed consent from both cohorts was captured using health questionnaires and a dedicated software was used for the collection of standard MRI-related parameters (CardioDI^{TM}, Cohesic Inc., Calgary, AB, Canada). Inclusion criteria for the controls were the following: All participants had no history of cardiovascular diseases or diabetes; they were all older than 18 years of age and had no history of uncontrolled hyperten-

sion, as confirmed by a certified nurse. Moreover, the inclusion criteria for the patients were the following: All patients had a history of a TOF repair, and all were older than 18 years of age at the time of examination. However, the exclusion criteria for the controls included the following if they were unable to complete the MRI scan, while the exclusion criteria for the patients were the following: if the patient had severe renal impairments (eGFR < 30 mL/min/1.73 m^2) and if they were unable to complete the MRI scans due to implantable devices or any other contra-indications for MRI [23]. Prior to scanning, basic demographic measurements were collected, including age, sex, weight, and heart rate. The body surface area was calculated using the Mosteller formula.

2.2. Cardiac Magnetic Resonance Imaging Protocol

A standardized cardiac imaging protocol for congenital heart diseases was performed on all participants using 3T MRI scanners (Skyra and Prisma, Siemens, Erlangen, Germany) in accordance with published recommendations [23]. Imaging of the entire heart was achieved via standard routine electrocardiographic (ECG) gating, balanced time-resolved steady-state free precision (SSFP) cine imaging in short-axis, 3-chamber, 2-chamber, and 4-chamber views. Moreover, a 3D contrast-enhanced magnetic resonance angiography (CEMRA) of the entire heart was also performed by administering 0.2 mmol/kg of gadolinium contrast (Gadovist®, Bayer Inc., Mississauga, ON, Canada). For volumetric blood flow assessments, a time-resolved 3D phase-contrast MRI with three-directional velocity encoding was obtained using a 4D-flow MRI WIP from Siemens (WIP 845A). The entire heart was covered using sagittal slices. The acquisition was performed for 5–10 min followed by the administration of the contrast agent, using retrospective ECG gating and free-breathing supported by a diaphragmatic motion navigator. The following parameters were used for the 4D-flow acquisition: bandwidth = 455–495 Hz/Pixel; pulse repetition time = 4.53–5.07 ms; echo time = 2.01–2.35 ms; flip angle = 15 degrees; spatial resolution = 2.0–3.6 × 2.0–3.0 × 2.5–3.5 mm^3; Venc = 150–250 cm/s; phases = 30; and temporal resolution = 25–35 ms. The total acquisition time varied depending on the patient's heart rate and respiratory navigator efficiency.

2.3. Standard Cardiac Imaging Analysis

Standard cardiac images were analyzed by a blinded observer on the same day of the acquisition using a dedicated clinical software cvi[42] version 5.11.5 (Circle Cardiovascular Imaging Inc, Calgary, AB, Canada) to determine left and right end-diastolic volume (LVEDV; RVEDV), LV and RV end-systolic volume (LVESV; RVESV), and LV and RV ejection fraction (LVEF; RVEF), as part of standard clinical reading.

2.4. 4D-Flow Data Analysis

As shown in Figure 1, after acquisition, 4D-flow data were corrected for eddy currents, i.e., linear phase drift according to static tissues, noise masking, and velocity aliasing using "Velomap_tool", a Matlab tool developed by Bock et al. in 2007 and that is broadly used by the flow MRI community [24]. Our in-house tool "4D-Flow Analysis Tool" was developed in MATLAB 2020b (Mathworks, Natick, MA, USA) and integrates the Velomap tool for data pre-processing. After data correction, an individual phase-contrast magnetic resonance angiogram (PC-MRA) throughout the entire cardiac cycle was used to segment the following vessels: Aorta, Pulmonary Artery (PA), Left Atria (LA), Left Ventricle (LV), Right Atria (RA), and Right Ventricle (RV). The PC-MRA is given by $I_i^{PC-MRA}(\vec{r}) = I_i^{Mag}(\vec{r})\sqrt{\sum_{j=x,y,z} v_{j,i}^2(\vec{r})}$, where I_i^{Mag} is the magnitude image, $\vec{r}$ is the spatial location within the volume, v is the velocity-encoded image with j representing the velocity encoding direction in image coordinates (x, y, z), and i is the measured time frame in the cardiac cycle. This segmentation approach has been previously reported [25,26]. Furthermore, each vessel was divided into several regional volumes for facilitating data analysis. The Aorta was divided into the following 4 segments: aortic root, arch, ascending aorta, and descending aorta. The PA was divided into the following 3 segments: left pulmonary artery

(LPA), right pulmonary artery (RPA), and mid pulmonary artery (MPA). Lastly, the LA, LV, RA, and RV were divided into the following 2 segments: inferior and superior.

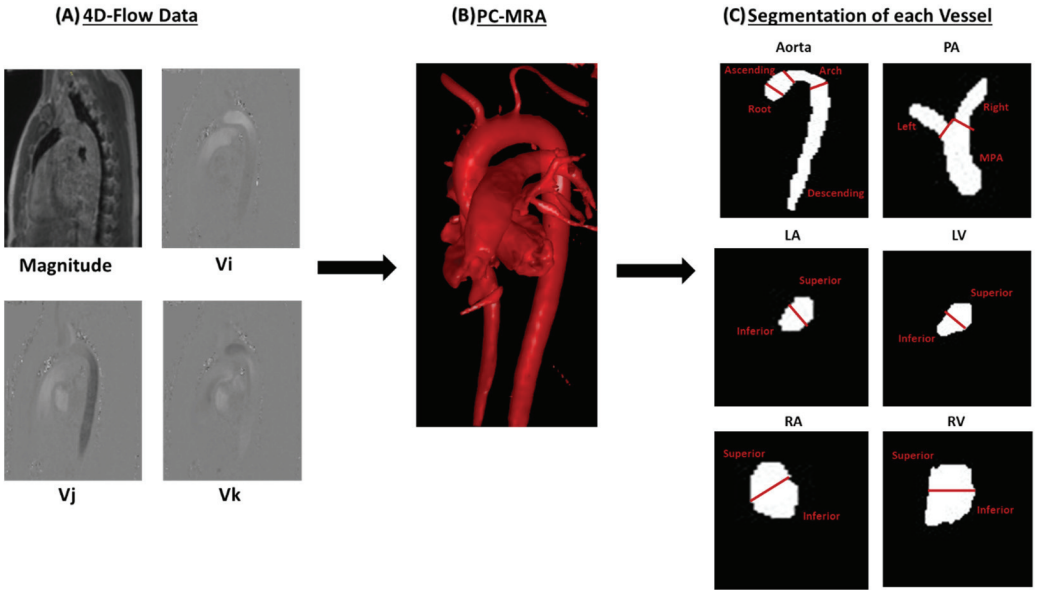

Figure 1. Postprocessing of 4D-flow data. First, 4D-flow velocity data in each direction (Vi, Vj, and Vk) were corrected for eddy currents, noise, and aliasing (Panel (**A**)). Followed by correcting the data, a phase contrast-magnetic resonance angiogram (PC-MRA) was created (Panel (**B**)) and was used to isolate the following vessels (Panel (**C**)): Aorta, Pulmonary Artery (PA), Left Atria (LA), Left Ventricle (LV), Right Atria (RA), and Right Ventricle (RV). After segmentation, each vessel was subdivided into various sections. The Aorta is subdivided into the root, ascending, arch, and descending. The PA is divided into the left pulmonary artery, right pulmonary artery, and main pulmonary artery (MPA). The LA, LV, RA, and RV are all divided in the same way, splitting it into its superior and inferior components.

After segmentation, an in-house Matlab tool "YYC 4D Flow TKE Tool" was used to calculate TKE throughout the entire cardiac cycle for each segmentation, as demonstrated in Figure 2. The magnitude of the individual velocity-encoding directions was reconstructed to compute TKE. TKE is defined as $TKE = \frac{1}{2}\rho \sum_{i=1}^{3} \sigma_i^2$, where ρ is the fluid density, and σ_i is the fluctuation intensity in the three orthogonal directions [21]. TKE has been validated in vitro and in vivo by several groups [21,27–30]. Our implementation is based on the original code from Dyverfeldt et al. [21]. Our TKE tool facilitates the integration of individual segmentations and TKE calculation to generate standardized analysis reports using regions of interest and templates.

TKE is calculated using the magnitude information from the 4D-flow dataset and taking the intervoxel velocity standard deviation in all 3 spatial directions throughout the cardiac cycle [27]. A variety of hemodynamic parameters were computed for the entire segmentation along with each volumetric segment for each vessel, including maximum TKE (TKEmax), minimum TKE (TKEmin), mean TKE (TKEmean), and standard deviation TKE (TKEstdv). TKEmax was defined as the maximum TKE in any voxel in each region. Similarly, TKEmin was defined as the minimum TKE in any voxel in each region. While TKEmean was defined as the mean TKE in each region. Lastly, TKEstdv was defined as the standard deviation in each region. In addition, simplified standardized templates were created to compare TKE between the two cohorts.

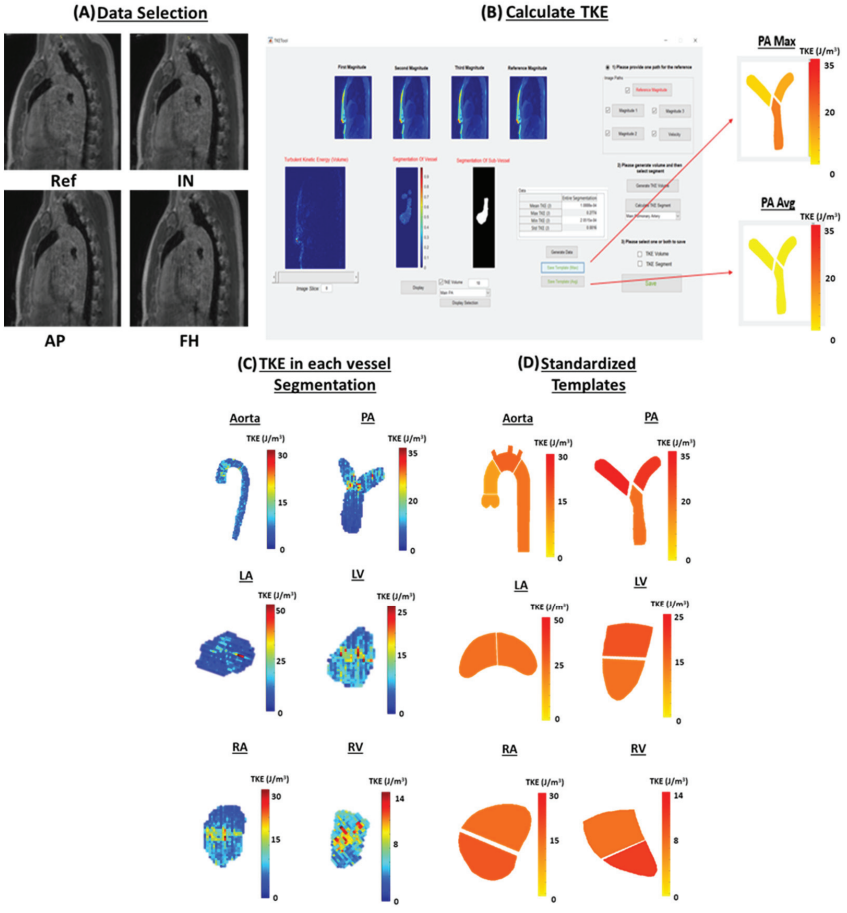

Figure 2. Calculation and analysis of turbulent kinetic energy (TKE). Panel (**A**) shows samples of the magnitude in each direction, including the reference velocity magnitude, in-plane velocity magnitude (IN), anterior–posterior velocity magnitude (AP), and foot head velocity magnitude (FH). This is followed by the calculation of TKE using the YYC 4D Flow TKE Tool that was built in-house (ρ is the fluid density, and σ_i indicates the standard deviation of the component of velocity vector at the i-direction, Panel (**B**)). In Panel (**C**), TKE is shown for a healthy control at phase 5 in the Aorta, Pulmonary Artery (PA), Left Atria (LA), Left Ventricle (LV), Right Atria (RA), and Right Ventricle (RV). Similarly, standardized templates were also computed for each vessel (Panel (**D**)).

2.5. Statistical Analysis

Statistical analyses were performed using SPSS 25 (SPSS, Chicago, IL, USA). Normality was assessed using the Shapiro–Wilk test and the Kolmogorov–Smirnov test. Due to the data not following a normal distribution, a Mann–Whitney-U test was performed for both study demographics along with the TKE comparison between the two groups. Results are provided as the group mean $\pm$ standard deviation and a p-value < 0.05 was used to consider the statistical significance. Furthermore, Pearson's correlation was used to analyze the relationship between TKE and the left ventricular ejection fraction (LVEF), right ventricular ejection fraction (RVEF), indexed left ventricular end-diastolic volume (LVEDVi), indexed left ventricular systolic volume (LVESVi), indexed right ventricular end-diastolic volume (RVEDVi), and indexed right ventricular end-systolic volume (RVESVi). The body surface area was used for indexation. A p-value < 0.01 was considered statistically significant.

3. Results

Patient Characteristics

Table 1 demonstrates the clinical parameters along with the demographic data acquired for the 17 controls and 18 patients that were enrolled in the study. The age at scan was higher in the controls compared with patients (26 ± 13 years vs. 29 ± 9 years, $p = 0.05$). As seen in Table 1, LVEF (58 ± 9% vs. 64 ± 7%, $p = 0.04$), LVEDV (138 ± 32 mL vs. 168 ± 38 mL, $p = 0.02$), LVEDVi (76 ± 12 mL/m^2 vs. 88 ± 16 mL/m^2, $p = 0.02$), RVESV (117 ± 56 mL vs. 78 ± 27 mL, $p = 0.04$), RVEF (48 ± 8 % vs. 56 ± 6 %, $p = 0.01$), RVESVi (65 ± 30 mL/m^2 vs. 40 ± 12 mL/m^2, $p = 0.01$), and RVEDVi (121 ± 39 mL/m^2 vs. 91 ± 19 mL/m^2, $p = 0.02$) were statistically different between patients and controls.

Table 1. Subject baseline characteristics.

Characteristic	Patients (n = 17)	Controls (n = 18)	*p*-Value
Age at scan (year)	29 ± 9	36 ± 13	0.05
Sex (f/m)	5/12	7/11	0.56
BSA (m^2)	1.80 ± 0.21	1.91 ± 0.29	0.18
HR (bpm)	73 ± 13	65 ± 12	0.08
BP systolic (mmHg)	107 ± 8	113 ± 17	0.15
BP diastolic (mmHg)	60 ± 10	66 ± 16	0.20
LVEF (%)	58 ± 9	64 ± 7	0.04
LVEDV (mL)	138 ± 32	168 ± 38	0.02
LVEDVi (mL/m^2)	76 ± 12	88 ± 16	0.02
LVESV (mL)	59 ± 22	62 ± 19	0.60
LVESVi (mL/m^2)	32 ± 11	33 ± 9	0.90
LVMASS (g)	93 ± 24	104 ± 31	0.23
LVMASSi (g/m^2)	51 ± 11	53 ± 10	0.52
RVEF (%)	48 ± 8	56 ± 6	0.01
RVEDV (mL)	220 ± 80	177 ± 46	0.11
RVEDVi (mL/m^2)	121 ± 39	91 ± 19	0.02
RVESV (mL)	117 ± 56	78 ± 27	0.04
RVESVi (mL/m^2)	65 ± 30	40 ± 12	0.01

BSA: Body surface area; HR: heart rate; BP: blood pressure; LVEDVi: Indexed Left Ventricular End Diastolic Volume; LVESVi: Indexed Left Ventricular End Systolic Volume; LVEF: Left Ventricular Ejection Fraction; LVMASSi: Indexed Left Ventricular Mass (LVEF); LVEDV: Left Ventricular End Diastolic Volume; LVESV: Left Ventricular End Diastolic Volume; LVMASS: Left Ventricular Mass (LVEF); RVEDVi: Indexed Right Ventricular End Diastolic Volume; RVESVi: Indexed Right Ventricular End Systolic Volume; RVEF: Right Ventricular Ejection Fraction; RVEDV: Right Ventricular End Diastolic Volume; RVESV: Right Ventricular End Systolic Volume.

Hemodynamic parameters of the aorta and PA for both cohorts are seen in Figure 3. Controls demonstrated a higher TKEmean in the aorta than patients during all phases of the cardiac cycle, including peak systole (PS), average systole (avg systole), average diastole (avg diastole), and total cardiac cycle (TCC). However, patients demonstrated a higher TKEmax in the aorta than controls at avg systole, avg diastole, and TCC. In addition, patients demonstrated a higher TKEmax in PA compared to the controls throughout the entire cardiac cycle. TKEmean in the PA was only higher in patients compared to controls at PS. Yet, no statistical significance was observed between the two cohorts for both TKEmean and TKEmax in the aorta and PA.

Furthermore, Figure 4 demonstrates the hemodynamic parameters observed in the LA and RA for both cohorts. TKEmean was observed to be higher in controls compared to patients throughout the cardiac cycle in the LA. Similarly, TKEmax was also observed to be higher in controls compared to patients throughout the cardiac cycle in the LA. Although, TKEmean was observed to be higher in patients compared to controls in the RA throughout the cardiac cycle. Similarly, patients also demonstrated a higher TKEmax compared to controls throughout the cardiac cycle in the RA. No statistical significance was observed between the two cohorts in either the LA or the RA.

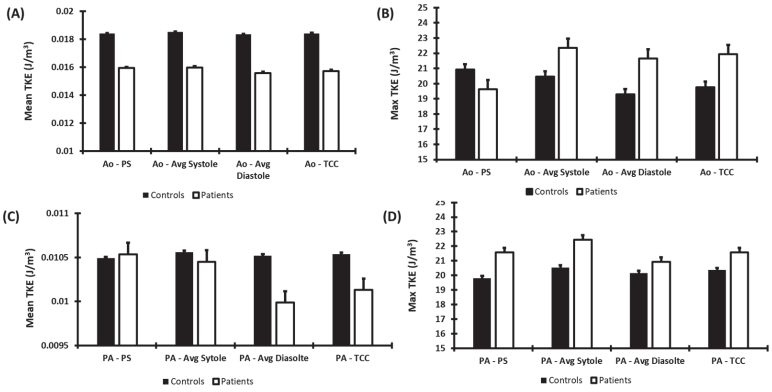

Figure 3. Turbulent kinetic energy in the aorta and pulmonary artery. Mean turbulent kinetic energy (TKE) and max TKE were calculated throughout the entire cardiac cycle, including peak systole (PS), average systole (avg systole), average diastole (avg diastole), and total cardiac cycle (TCC) in the Aorta (Ao) and Pulmonary Artery (PA) for both patients and controls. Panel (**A**) shows mean TKE in the Ao. Panel (**B**) shows max TKE in the Ao. Panel (**C**) shows mean TKE in the PA, and Panel (**D**) shows max TKE in the PA. No statistical significance was observed between the two cohorts in either the Ao or the PA.

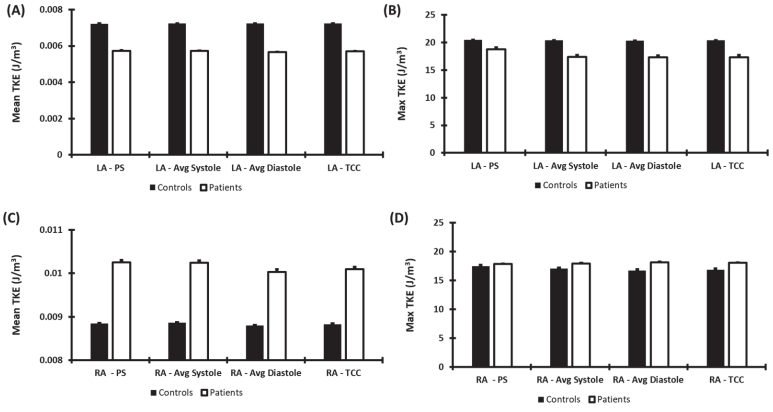

Figure 4. Turbulent kinetic energy in the left atria and right atria. Mean turbulent kinetic energy (TKE) and max TKE were calculated throughout the entire cardiac cycle, including peak systole (PS), average systole (avg systole), average diastole (avg diastole), and total cardiac cycle (TCC) in the Left Atria (LA) and Right Atria (RA) for both patients and controls. Panels (**A**,**B**) show the mean TKE and the max TKE in the LA for both controls and patients. Panels (**C**,**D**) show the mean TKE and max TKE in the RA. No statistical significance was observed between the two cohorts in the LA and RA.

Moreover, Figure 5 demonstrates the hemodynamic parameters observed in the LV and RV for both cohorts. TKEmean was observed to be higher in controls compared to patients in the LV throughout the cardiac cycle. Controls also demonstrated higher TKEmax in the LV compared to patients throughout the cardiac cycle. However, no statistical significance was observed in the LV. Similarly, patients also demonstrated a higher TKEmax and TKEmean at the RV throughout the cardiac cycle. Statistical significance between the two cohorts was observed for TKEmean at PS (0.015 ± 0.009 J/m^3 vs. 0.009 ± 0.005 J/m^3, $p < 0.05$), avg systole (0.015 ± 0.007 J/m^3 vs. 0.009 ± 0.005 J/m^3, $p < 0.05$), and avg diastole (0.014 ± 0.007 J/m^3 vs. 0.009 ± 0.005 J/m^3, $p < 0.05$). Pearson's correlation was also

computed between standard clinical measurements and TKE. However, no significant or strong correlation was found between the two.

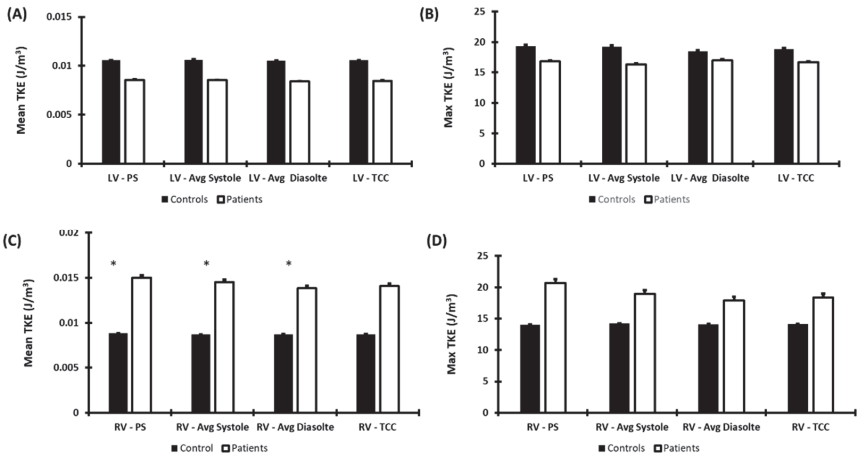

Figure 5. Turbulent kinetic energy in the left ventricle and right ventricle. Mean turbulent kinetic energy (TKE) and max TKE were calculated throughout the entire cardiac cycle, including peak systole (PS), average systole (avg systole), average diastole (avg diastole), and total cardiac cycle (TCC) in the Left Ventricle (LV) and Right Ventricle (RV) for both patients and controls. Panels (**A**,**B**) show the mean TKE and the max TKE in the LV throughout the entire cardiac cycle for controls and patients. Panels (**C**,**D**) show the mean TKE and the max TKE in the RA throughout the entire cardiac cycle for controls and patients. Statistical significance between the two cohorts was only observed in the RV at PS, avg systole, and avg diastole (*: $p < 0.05$).

4. Discussion

This study demonstrated that TKE may impact the entire heart throughout the cardiac cycle. Patients with rTOF showed abnormal TKE changes in all chambers, providing further insight into the hemodynamic alterations of the entire heart for this patient cohort. Our main findings showed that controls exhibit higher TKEmean and TKEmax in both the LA and LV compared to patients. This may be due to defects that are mostly observed on the right side of the heart. In addition, we may observe this difference because patients with rTOF may also exhibit slower velocities in these vessels compared to controls. Hence, this may have led to lower values of TKE, as observed in this study. Furthermore, this study did observe higher values of both TKEmean and TKEmax in the RV in patients compared to controls. These results were similar to previously reported findings in energetic changes on rTOF, as compared with controls [2]. Therefore, this may suggest that patients with rTOF may have an imbalance of velocities between left- and right-sided chambers of the heart, leading to higher velocities on the right and resulting in elevated TKE values in the RV.

In the current study, we derived TKE from a whole-heart 4D-flow MRI acquisition in adult patients. It is important to remark that this type of acquisition can also be performed in pediatric patients by adjusting the spatial resolution and velocity-encoding parameters [5]. In adults, a spatial resolution of 2.5–3.0 mm^3 is recommended; in pediatric populations, 1.5 mm^3 is recommended, and 0.75–1.0 mm^3 is recommended in neonates. The advantages of 4D-flow MRI in neonatal and pediatric populations over standard 2D phase-contrast are well-documented [31,32]. The advances in acceleration techniques reached clinically acceptable scan times, and the possibility of free-breathing protocols and the use of feed and wrap have become more practical for diminishing emotional stress [33]. However, the use of sedation and anesthesia is still clinical routine for facilitating the exam [34,35]. In both adult and pediatric patients, motion artifacts can impact the accuracy of the 4D-flow acquisition. Respiratory motion is usually well managed by using a respiratory navigator,

as we used in our study cohort. Novel free-breathing methods manage motion effects within the image acquisition framework [36,37]. However, large motion effects cannot be effectively corrected.

TKEmax was also shown to be elevated in the PA within patients compared to controls throughout the entire cardiac cycle. This may be due to the fact that PR is observed within this patient cohort [38]. This relates to how we observed elevated TKE in the RV, as previous studies demonstrated that PR significantly impacts the flow in the RV [39]. Unfortunately, not many studies evaluated TKE in patients with rTOF, but some studies demonstrated elevated KE in the RV and PA compared to controls [40]. In particular, Fredriksson et al. highlighted the potential clinical value of TKE in the development of late complications after TOF repair and the importance of follow-up [22]. TKE comes to provide additional information beyond the heart function and strain characterization that can be achieved with a standard-of-care ultrasound and MRI. It is reasonable to consider that these basic metrics can support decision making, but there could be other factors besides RV volume and deformation rate that can contribute to an adverse outcome. Flow-derived metrics, as TKE, could provide a major understanding on 3D intra-cardiac hemodynamics and local alterations within the blood flow. It is important to remark that 3D hemodynamics are not fully characterized using standard ultrasound or MRI. Furthermore, studies also demonstrated the alteration of flow patterns by overserving higher retrograde flow and pathological vortices within the right side of the heart in patients with rTOF compared to controls [41,42]. The observation of retrograde flow and vortices may explain the elevated TKE measured in the PA and RV throughout the cardiac cycle, as an expenditure of energy occurs during vortex formation and dissipation. Right-sided vortices may represent energy loss and poor efficient circulation, which can potentially be harmful for the RV in TOF with impaired contractile capacity and could indicate an early intervention. However, in the current study, the vortex formation was not evaluated or investigated in association with TKE.

Moreover, this study also evaluated the comparison between TKE with standard clinical measurements including LVEF, RVEF, LVEDVi, LVESVi, RVEDVi, and RVESVi. As no significant or strong correlation was observed between TKE and standard clinical measurements evaluated, this suggests that TKE is an independent local measurement providing further insight into the abnormal flow seen in this patient cohort. A previous study performed by Dyverfeldt et al. also demonstrated similar results. This study also found that the total TKE was not related to global flow patterns that are evaluated by magnetic-resonance-measured velocity fields [30].

As the current work was an exploratory pilot study, the recruitment of more patients and healthy controls is highly recommended in further understanding how TKE may play a role in various vessels within this patient cohort. Moreover, the evaluation of other irregular flow parameters should be conducted and correlated for each vessel for a better understanding of hemodynamic differences between patients and controls. In the current study, we developed simple reporting templates for the visual assessment of individuals and cohorts. The latter could simplify the TKE interpretation and could be used for a visual follow-up assessment. However, not all templates respected current clinical guidelines. In particular, ventricular templates could use the American Heart Association's (AHA) standard reporting procedures when reporting to clinicians. Our simplified approach aimed to provide a quick snapshot of TKE. The latter highlights the need for well-defined reporting for TKE and 4D-flow measurements, which can be substantially complex given the large amount of data. This aspect explains why a single time point is frequently reported (e.g., peak systole) or simplified using time-average values or maximum intensity projections. Furthermore, in future, TKE measurements could be indexed to the volume of each vessel for both controls and patients, which may provide further insight into the difference observed between the right and left chambers. The association of TKE with the onset of any rTOF complications must be investigated to understand the TKE role in adverse outcomes. Lastly, intra-observer and inter-observer variabilities should be evaluated to validate this technique.

Our study only considered rTOF patients for the investigation of TKE. However, other congenital diseases could benefit from the characterization of abnormal TKE. A recent numerical study demonstrated that lower vortex formation and lower TKE can identify deteriorated intra-cardiac performance in Fontan patients, while the ejection fraction did not, whereas the latter still needs to be demonstrated in vivo [43]. The use of computational fluid dynamics (CFD) to complement and/or validate 4D-flow-derived calculations is not new. TKE, as it is calculated our study, has been validated using experimental models, and CFD reported a good agreement between MRIs, models, and simulations [44]. Some CFD studies evaluated the influence of the pulmonary artery bifurcation angle, pressure distribution, and flow patterns [45,46]. In particular, Loke et al. reported a framework for computational modeling using cardiac MRI images and 4D-flow MRI in rTOF patients and included the calculation of kinetic energy, vorticity, and TKE in rTOF [47]. However, these studies were mostly exploratory with a limited number of subjects. Furthermore, CFD has also been used to improve the calculation of wall shear stress, as 4D-flow spatial and temporal resolutions can underestimate this measurement [48–50]. Casas et al. used CFD to assess the impact of spatial resolutions and reported that TKE estimates were accurate and minorly impacted by resolution, while viscous energy dissipation was underestimated and showed resolution dependance [48]. However, 4D-flow in vivo acquisition mostly reflects the macro-scale of turbulence, as data are acquired with a 2–3 mm^3 resolution [49]. CFD can facilitate the TKE understanding of the turbulence cascade at the Kolmogorov micro-scale, which is something that cannot be achieve in-vivo. Exploring hemodynamic data with CFD in such scales can be computationally demanding and time consuming. Some level of feasibility can be achieved using novel 3D Lattice Boltzmann methods, which have proved to be more efficient for clinical applications [50].

Some additional limitations of this study include a small sample size as not many patients and controls were enrolled in this study. The patient's sample size also limited the ability to investigate specific complications (e.g., pulmonary regurgitation). Age and sex matching or propensity score matching could also improve that study design for TKE assessments. In the current study, controls were on average 7 years older than patients, and no personalized analysis was performed. Long acquisition (>10 min) can be an important limitation in clinical settings. In the current study, the 4D-flow acquisition in all subjects was inferior to 10 min. Acceleration techniques such as compressed sensing can reduce up to 50% of the acquisition time, but the effect on TKE accuracy is still unknown. Another limitation of this study may include variability in the segmentations, as each patient has a different characteristic and morphology of vessels. It must be remarked that segmentations were static and were not adjusted to the dynamic motion of the heart. Heart motion can be significant and affect the averaged TKE calculation in ventricles. A future alternative could be the use of automated segmentation using machine learning methods.

Similarly to flow-derived parameters, the accuracy of TKE is greatly dependent upon spatial and temporal resolution. The latter must be particularly considered when scanning children. As reported by Dillinger et al., the level of intra-voxel underestimation will depend on the turbulence level and velocity encoding strategy [51]. Single encoding gradient can vary by 20%. A Lagrangian velocity spectrum on a voxel-by-voxel basis may correct the latter. Although the approach used for this study to calculate TKE has been validated, more larger and longitudinal studies would be beneficial for understanding the observed hemodynamic fluctuations.

5. Conclusions

In conclusion, this study demonstrated that TKE can be evaluated in the whole heart of patients with rTOF. TKEs in the RV, RA, and PA were higher in rTOF patients compared to the controls. These results suggest that TKE could potentially serve as an independent biomarker for the monitoring of rTOF. Further validation and longitudinal studies may provide further insight into the hemodynamics of rTOF patients for improving patient management and clinical decision making.

Author Contributions: Conceptualization, A.H. and J.G.; methodology, J.G.; software, A.H. and J.G.; validation, A.H., J.A.W., S.C.G. and J.G.; formal analysis, A.H.; investigation, A.H., S.C.G. and J.G.; resources, S.C.G. and J.G.; data curation, A.H.; writing—original draft preparation, A.H. and J.G.; writing—review and editing, S.C.G., J.A.W. and J.G.; visualization, A.H. and J.G.; supervision, J.G.; project administration, J.G.; funding acquisition, S.C.G. and J.G. All authors have read and agreed to the published version of the manuscript.

Funding: This research was funded by The University of Calgary, URGC SEM #1054341; J.G. start-up funding. We acknowledge the support of the Natural Science and Engineering Research Council of Canada/Conseil de recherche en science naturelles et en génie du Canada, RGPIN-2020-04549, and DGECR-2020-00204.

Institutional Review Board Statement: The study was conducted according to the guidelines of the Declaration of Helsinki and approved by the Conjoint Health Research Ethics Board of University of Calgary (REB13-0902 approved on 6/18/2014 and currently active).

Informed Consent Statement: Written informed consent was obtained from all subjects involved in the study.

Data Availability Statement: The anonymized data presented in this study are available upon request from the corresponding author. The data are not publicly available due to privacy and ethical restrictions.

Conflicts of Interest: The authors declare no conflict of interest.

References

1. Richter, Y.; Edelman, E.R. Cardiology Is Flow. *Circulation* **2006**, *113*, 2679–2682. [CrossRef] [PubMed]
2. Fredriksson, A.G.; Svalbring, E.; Eriksson, J.; Dyverfeldt, P.; Alehagen, U.; Engvall, J.E.; Ebbers, T.; Carlhall, C.J. 4D flow CMR can detect subtle right ventricular dysfunction in primary left ventricular disease. *J. Cardiovasc. Magn. Reson.* **2015**, *17* (Suppl. 1), Q4. [CrossRef]
3. Lloyd-Jones, D.; Adams, R.J.; Brown, T.M.; Carnethon, M.; Dai, S.; De Simone, G.; Ferguson, T.B.; Ford, E.; Furie, K.; Gillespie, C.; et al. Heart Disease and Stroke Statistics—2010 Update. *Circulation* **2010**, *121*, e46–e215. [CrossRef] [PubMed]
4. Hu, L.; Ouyang, R.; Sun, A.; Wang, Q.; Guo, C.; Peng, Y.; Qin, Y.; Zhang, Y.; Xiang, Y.; Zhong, Y. Pulmonary artery hemodynamic assessment of blood flow characteristics in repaired tetralogy of Fallot patients versus healthy child volunteers. *Quant. Imaging Med. Surg.* **2020**, *10*, 921–933. [CrossRef]
5. Zhong, L.; Schrauben, E.M.; Garcia, J.; Uribe, S.; Grieve, S.M.; Elbaz, M.S.M.; Barker, A.J.; Geiger, J.; Nordmeyer, S.; Marsden, A.; et al. Intracardiac 4D Flow MRI in Congenital Heart Disease: Recommendations on Behalf of the ISMRM Flow & Motion Study Group. *J. Magn. Reson. Imaging* **2019**, *50*, 677–681. [CrossRef] [PubMed]
6. Adamson, L.; Vohra, H.A.; Haw, M.P. Does pulmonary valve replacement post repair of tetralogy of Fallot improve right ventricular function? *Interact. Cardiovasc. Thorac. Surg.* **2009**, *9*, 520–527. [CrossRef]
7. Khalaf, A.; Tani, D.; Tadros, S.; Madan, S. Right- and Left-Ventricular Strain Evaluation in Repaired Pediatric Tetralogy of Fallot Patients Using Magnetic Resonance Tagging. *Pediatr. Cardiol.* **2013**, *34*, 1206–1211. [CrossRef]
8. Baumgartner, H.; Falk, V.; Bax, J.J.; De Bonis, M.; Hamm, C.; Holm, P.J.; Iung, B.; Lancellotti, P.; Lansac, E.; Rodriguez Muñoz, D.; et al. 2017 ESC/EACTS Guidelines for the management of valvular heart disease. *Eur. Heart J.* **2017**, *38*, 2739–2791. [CrossRef]
9. Otto, C.M.; Nishimura, R.A.; Bonow, R.O.; Carabello, B.A.; Erwin, J.P.; Gentile, F.; Jneid, H.; Krieger, E.V.; Mack, M.; McLeod, C.; et al. 2020 ACC/AHA Guideline for the Management of Patients With Valvular Heart Disease: A Report of the American College of Cardiology/American Heart Association Joint Committee on Clinical Practice Guidelines. *Circulation* **2021**, *143*. [CrossRef]
10. Myerson, S.G. CMR in Evaluating Valvular Heart Disease. *JACC Cardiovasc. Imaging* **2021**, *14*, 2020–2032. [CrossRef]
11. Malik, S.B.; Chen, N.; Parker, R.A.; Hsu, J.Y. Transthoracic Echocardiography: Pitfalls and Limitations as Delineated at Cardiac CT and MR Imaging. *Radio Graph.* **2017**, *37*, 383–406. [CrossRef]
12. Grant, M.D.; Mann, R.D.; Kristenson, S.D.; Buck, R.M.; Mendoza, J.D.; Reese, J.M.; Grant, D.W.; Roberge, E.A. Transthoracic Echocardiography: Beginner's Guide with Emphasis on Blind Spots as Identified with CT and MRI. *Radio Graph.* **2021**, *41*, E1022–E1042. [CrossRef] [PubMed]
13. Therrien, J.; Provost, Y.; Merchant, N.; Williams, W.; Colman, J.; Webb, G. Optimal timing for pulmonary valve replacement in adults after tetralogy of Fallot repair. *Am. J. Cardiol.* **2005**, *95*, 779–782. [CrossRef] [PubMed]
14. Robinson, J.D.; Rose, M.J.; Joh, M.; Jarvis, K.; Schnell, S.; Barker, A.J.; Rigsby, C.K.; Markl, M. 4-D flow magnetic-resonance-imaging-derived energetic biomarkers are abnormal in children with repaired tetralogy of Fallot and associated with disease severity. *Pediatr. Radiol.* **2019**, *49*, 308–317. [CrossRef] [PubMed]
15. Knauth, A.L.; Gauvreau, K.; Powell, A.J.; Landzberg, M.J.; Walsh, E.P.; Lock, J.E.; del Nido, P.J.; Geva, T. Ventricular size and function assessed by cardiac MRI predict major adverse clinical outcomes late after tetralogy of Fallot repair. *Heart* **2008**, *94*, 211–216. [CrossRef] [PubMed]

16. Valente, A.M.; Gauvreau, K.; Assenza, G.E.; Babu-Narayan, S.V.; Schreier, J.; Gatzoulis, M.A.; Groenink, M.; Inuzuka, R.; Kilner, P.J.; Koyak, Z.; et al. Contemporary predictors of death and sustained ventricular tachycardia in patients with repaired tetralogy of Fallot enrolled in the INDICATOR cohort. *Heart* **2014**, *100*, 247–253. [CrossRef]
17. Dyverfeldt, P.; Bissell, M.; Barker, A.J.; Bolger, A.F.; Carlhäll, C.-J.; Ebbers, T.; Francios, C.J.; Frydrychowicz, A.; Geiger, J.; Giese, D.; et al. 4D flow cardiovascular magnetic resonance consensus statement. *J. Cardiovasc. Magn. Reson.* **2015**, *17*, 72. [CrossRef]
18. Grigioni, M.; Daniele, C.; D'Avenio, G.; Barbaro, V. On the monodimensional approach to the estimation of the highest Reynolds shear stress in a turbulent flow. *J. Biomech.* **2000**, *33*, 701–708. [CrossRef]
19. Isaaz, K.; Bruntz, J.F.; Costa, A.D.; Winninger, D.; Cerisier, A.; de Chillou, C.; Sadoul, N.; Lamaud, M.; Ethevenot, G.; Aliot, E. Noninvasive quantitation of blood flow turbulence in patients with aortic valve disease using online digital computer analysis of Doppler velocity data. *J. Am. Soc. Echocardiogr.* **2003**, *16*, 965–974. [CrossRef]
20. Garcia, J.; Barker, A.J.; Markl, M. The Role of Imaging of Flow Patterns by 4D Flow MRI in Aortic Stenosis. *JACC Cardiovasc. Imaging* **2019**, *12*, 252–266. [CrossRef]
21. Dyverfeldt, P.; Kvitting, J.-P.E.; Sigfridsson, A.; Engvall, J.; Bolger, A.F.; Ebbers, T. Assessment of fluctuating velocities in disturbed cardiovascular blood flow: In vivo feasibility of generalized phase-contrast MRI. *J. Magn. Reson. Imaging* **2008**, *28*, 655–663. [CrossRef] [PubMed]
22. Fredriksson, A.; Trzebiatowska-Krzynska, A.; Dyverfeldt, P.; Engvall, J.; Ebbers, T.; Carlhäll, C.-J. Turbulent kinetic energy in the right ventricle: Potential MR marker for risk stratification of adults with repaired Tetralogy of Fallot. *J. Magn. Reson. Imaging* **2018**, *47*, 1043–1053. [CrossRef] [PubMed]
23. Kramer, C.M.; Barkhausen, J.; Bucciarelli-Ducci, C.; Flamm, S.D.; Kim, R.J.; Nagel, E. Standardized cardiovascular magnetic resonance imaging (CMR) protocols: 2020 update. *J. Cardiovasc. Magn. Reson.* **2020**, *22*, 17. [CrossRef] [PubMed]
24. Bock, J.; Kreher, B.; Hennig, J.; Markl, M. Optimized Pre-Processing of Time-Resolved 2 D and 3 D Phase Contrast MRI Data. In Proceedings of the 15th Annual Meeting of ISMRM, Berlin, Germany, 19–25 May 2007.
25. Geeraert, P.; Jamalidinan, F.; Burns, F.; Jarvis, K.; Bristow, M.S.; Lydell, C.; Hidalgo Tobon, S.S.; de Celis Alonso, B.; Fedak, P.W.M.; White, J.A.; et al. Hemodynamic Assessment in Bicuspid Aortic Valve Disease and Aortic Dilation: New Insights From Voxel-By-Voxel Analysis of Reverse Flow, Stasis, and Energetics. *Front. Bioeng. Biotechnol. 2022, 9, 725113.* Available online: https://www.frontiersin.org/articles/10.3389/fbioe.2021.725113 (accessed on 11 August 2022).
26. Fatehi Hassanabad, A.; Burns, F.; Bristow, M.S.; Lydell, C.; Howarth, A.G.; Heydari, B.; Gao, X.; Fedak, P.W.M.; White, J.A.; Garcia, J. Pressure drop mapping using 4D flow MRI in patients with bicuspid aortic valve disease: A novel marker of valvular obstruction. *Magn. Reson. Imaging* **2020**, *65*, 175–182. [CrossRef]
27. Sundin, J.; Bustamante, M.; Ebbers, T.; Dyverfeldt, P.; Carlhäll, C.-J. Turbulent Intensity of Blood Flow in the Healthy Aorta Increases with Dobutamine Stress and is Related to Cardiac Output. *Front. Physiol.* **2022**, *13*, 869701. [CrossRef]
28. Ha, H.; Ziegler, M.; Welander, M.; Bjarnegård, N.; Carlhäll, C.-J.; Lindenberger, M.; Länne, T.; Ebbers, T.; Dyverfeldt, P. Age-Related Vascular Changes Affect Turbulence in Aortic Blood Flow. *Front. Physiol.* **2018**, *9*, 36. [CrossRef]
29. Binter, C.; Gotschy, A.; Sündermann, S.H.; Frank, M.; Tanner, F.C.; Lüscher, T.F.; Manka, R.; Kozerke, S. Turbulent Kinetic Energy Assessed by Multipoint 4-Dimensional Flow Magnetic Resonance Imaging Provides Additional Information Relative to Echocardiography for the Determination of Aortic Stenosis Severity. *Circ. Cardiovasc. Imaging* **2017**, *10*, e005486. [CrossRef]
30. Ha, H.; Lantz, J.; Ziegler, M.; Casas, B.; Karlsson, M.; Dyverfeldt, P.; Ebbers, T. Estimating the irreversible pressure drop across a stenosis by quantifying turbulence production using 4D Flow MRI. *Sci. Rep.* **2017**, *7*, 46618. [CrossRef]
31. Geiger, J.; Callaghan, F.M.; Burkhardt, B.E.U.; Valsangiacomo Buechel, E.R.; Kellenberger, C.J. Additional value and new insights by four-dimensional flow magnetic resonance imaging in congenital heart disease: Application in neonates and young children. *Pediatr. Radiol.* **2021**, *51*, 1503–1517. [CrossRef]
32. Panayiotou, H.R.; Mills, L.K.; Broadbent, D.A.; Shelley, D.; Scheffczik, J.; Olaru, A.M.; Jin, N.; Greenwood, J.P.; Michael, H.; Plein, S.; et al. Comprehensive Neonatal Cardiac, Feed and Wrap, Non-contrast, Non-sedated, Free-breathing Compressed Sensing 4D Flow MRI Assessment. *J. Magn. Reson. Imaging* **2022**. [CrossRef]
33. Cheng, J.Y.; Hanneman, K.; Zhang, T.; Alley, M.T.; Lai, P.; Tamir, J.I.; Uecker, M.; Pauly, J.M.; Lustig, M.; Vasanawala, S.S. Comprehensive motion-compensated highly accelerated 4D flow MRI with ferumoxytol enhancement for pediatric congenital heart disease: Motion-Compensated Accelerated 4D Flow. *J. Magn. Reson. Imaging* **2016**, *43*, 1355–1368. [CrossRef] [PubMed]
34. Hanneman, K.; Kino, A.; Cheng, J.Y.; Alley, M.T.; Vasanawala, S.S. Assessment of the precision and reproducibility of ventricular volume, function, and mass measurements with ferumoxytol-enhanced 4D flow MRI: 4D Flow MRI Assessment of Ventricular Mass. *J. Magn. Reson. Imaging* **2016**, *44*, 383–392. [CrossRef] [PubMed]
35. Moghari, M.H.; van der Geest, R.J.; Brighenti, M.; Powell, A.J. Cardiac magnetic resonance using fused 3D cine and 4D flow sequences:Validation of ventricular and blood flow measurements. *Magn. Reson. Imaging* **2020**, *74*, 203–212. [CrossRef]
36. Ma, L.E.; Yerly, J.; Piccini, D.; Di Sopra, L.; Roy, C.W.; Carr, J.C.; Rigsby, C.K.; Kim, D.; Stuber, M.; Markl, M. 5D Flow MRI: A Fully Self-gated, Free-running Framework for Cardiac and Respiratory Motion–resolved 3D Hemodynamics. *Radiol. Cardiothorac. Imaging* **2020**, *2*, e200219. [CrossRef] [PubMed]
37. Dimov, I.P.; Tous, C.; Li, N.; Barat, M.; Bomberna, T.; Debbaut, C.; Jin, N.; Moran, G.; Tang, A.; Soulez, G. Assessment of hepatic arterial hemodynamics with 4D flow MRI: In vitro analysis of motion and spatial resolution related error and in vivo feasibility study in 20 volunteers. *Eur. Radiol.* **2022**. [CrossRef] [PubMed]

38. Valente, A.M.; Cook, S.; Festa, P.; Ko, H.H.; Krishnamurthy, R.; Taylor, A.M.; Warnes, C.A.; Kreutzer, J.; Geva, T. Multimodality Imaging Guidelines for Patients with Repaired Tetralogy of Fallot: A Report from the American Society of Echocardiography: Developed in Collaboration with the Society for Cardiovascular Magnetic Resonance and the Society for Pediatric Radiology. *J. Am. Soc. Echocardiogr.* **2014**, *27*, 111–141. [CrossRef]
39. Mikhail, A.; Labbio, G.D.; Darwish, A.; Kadem, L. How pulmonary valve regurgitation after tetralogy of fallot repair changes the flow dynamics in the right ventricle: An in vitro study. *Med. Eng. Phys.* **2020**, *83*, 48–55. [CrossRef]
40. Tsuchiya, N.; Nagao, M.; Shiina, Y.; Miyazaki, S.; Inai, K.; Murayama, S.; Sakai, S. Circulation derived from 4D flow MRI correlates with right ventricular dysfunction in patients with tetralogy of Fallot. *Sci. Rep.* **2021**, *11*, 11623. [CrossRef]
41. Geiger, J.; Markl, M.; Jung, B.; Grohmann, J.; Stiller, B.; Langer, M.; Arnold, R. 4D-MR flow analysis in patients after repair for tetralogy of Fallot. *Eur. Radiol.* **2011**, *21*, 1651–1657. [CrossRef]
42. Hirtler, D.; Garcia, J.; Barker, A.J.; Geiger, J. Assessment of intracardiac flow and vorticity in the right heart of patients after repair of tetralogy of Fallot by flow-sensitive 4D-MRI. *Eur. Radiol.* **2016**, *26*, 3598–3607. [CrossRef]
43. Grünwald, A.; Korte, J.; Wilmanns, N.; Winkler, C.; Linden, K.; Herberg, U.; Groß-Hardt, S.; Steinseifer, U.; Neidlin, M. Intraventricular Flow Simulations in Singular Right Ventricles Reveal Deteriorated Washout and Low Vortex Formation. *Cardiovasc. Eng. Technol.* **2022**, *13*, 495–503. [CrossRef] [PubMed]
44. Petersson, S.; Dyverfeldt, P.; Sigfridsson, A.; Lantz, J.; Carlhäll, C.; Ebbers, T. Quantification of turbulence and velocity in stenotic flow using spiral three-dimensional phase-contrast MRI. *Magn. Reson. Med.* **2016**, *75*, 1249–1255. [CrossRef] [PubMed]
45. Chern, M.-J.; Wu, M.-T.; Her, S.-W. Numerical Study for Blood Flow in Pulmonary Arteries after Repair of Tetralogy of Fallot. *Comput. Math. Methods Med.* **2012**, *2012*, 1–18. [CrossRef] [PubMed]
46. Boumpouli, M.; Danton, M.H.D.; Gourlay, T.; Kazakidi, A. Blood flow simulations in the pulmonary bifurcation in relation to adult patients with repaired tetralogy of Fallot. *Med. Eng. Phys.* **2020**, *85*, 123–138. [CrossRef] [PubMed]
47. Loke, Y.-H.; Capuano, F.; Balaras, E.; Olivieri, L.J. Computational Modeling of Right Ventricular Motion and Intracardiac Flow in Repaired Tetralogy of Fallot. *Cardiovasc. Eng. Technol.* **2022**, *13*, 41–54. [CrossRef] [PubMed]
48. Manchester, E.L.; Pirola, S.; Salmasi, M.Y.; O'Regan, D.P.; Athanasiou, T.; Xu, X.Y. Evaluation of Computational Methodologies for Accurate Prediction of Wall Shear Stress and Turbulence Parameters in a Patient-Specific Aorta. *Front. Bioeng. Biotechnol.* **2022**, *10*, 836611. [CrossRef]
49. Garcia, J.; Sheitt, H.; Bristow, M.S.; Lydell, C.; Howarth, A.G.; Heydari, B.; Prato, F.S.; Drangova, M.; Thornhill, R.E.; Nery, P.; et al. Left atrial vortex size and velocity distributions by 4D flow MRI in patients with paroxysmal atrial fibrillation: Associations with age and CHA_2DS_2-VASc risk score. *J. Magn. Reson. Imaging* **2020**, *51*, 871–884. [CrossRef]
50. Sadeghi, R.; Gasner, N.; Khodaei, S.; Garcia, J.; Keshavarz-Motamed, Z. Impact of mixed valvular disease on coarctation hemodynamics using patient-specific lumped parameter and Lattice Boltzmann modeling. *Int. J. Mech. Sci.* **2022**, *217*, 107038. [CrossRef]
51. Dillinger, H.; McGrath, C.; Guenthner, C.; Kozerke, S. Fundamentals of turbulent flow spectrum imaging. *Magn. Reson. Med.* **2022**, *87*, 1231–1249. [CrossRef]

applied sciences

MDPI

Article

Innovative Attention-Based Explainable Feature-Fusion VGG19 Network for Characterising Myocardial Perfusion Imaging SPECT Polar Maps in Patients with Suspected Coronary Artery Disease

Ioannis D. Apostolopoulos [1,*], Nikolaos D. Papathanasiou [2], Nikolaos Papandrianos [1], Elpiniki Papageorgiou [1] and Dimitris J. Apostolopoulos [2]

[1] Department of Energy Systems, University of Thessaly, 41500 Larissa, Greece
[2] Department of Nuclear Medicine, School of Medicine, University General Hospital of Patras, University of Patras, 26500 Patras, Greece
* Correspondence: ece7216@upnet.gr

Abstract: Greece is among the European Union members topping the list of deaths related to coronary artery disease. Myocardial Perfusion Imaging (MPI) with Single-Photon Emission Computed Tomography (SPECT) is a non-invasive test used to detect abnormalities in CAD screening. The study proposes an explainable deep learning (DL) method for characterising MPI SPECT Polar Map images in patients with suspected CAD. Patient data were recorded at the Department of Nuclear Medicine of the University Hospital of Patras from 16 February 2018 to 28 February 2022. The final study population included 486 patients. An attention-based feature-fusion network (AFF-VGG19) was proposed to perform the diagnosis, and the Grad-CAM++ algorithm was employed to reveal potentially significant regions. AFF-VGG19's agreement with the medical experts was found to be 89.92%. When training and assessing using the ICA findings as a reference, AFF-VGG19 achieved good diagnostic strength (accuracy of 0.789) similar to that of the human expert (0.784) and with more balanced sensitivity and specificity rates (0.873 and 0.722, respectively) compared to the human expert (0.958 and 0.648, respectively). The visual inspection of the Grad-CAM++ regions showed that the model produced 77 meaningful explanations over the 100 selected samples, resulting in a slight accuracy decrease (0.77). In conclusion, this research introduced a novel and interpretable DL approach for characterising MPI SPECT Polar Map images in patients with suspected CAD. The high agreement with medical experts, robust diagnostic performance, and meaningful interpretability of the model support the notion that attention-based networks hold significant promise in CAD screening and may revolutionise medical decision-making in the near future.

Keywords: explainable artificial intelligence; coronary artery disease; Myocardial Perfusion Imaging; Polar Maps; deep learning

Citation: Apostolopoulos, I.D.; Papathanasiou, N.D.; Papandrianos, N.; Papageorgiou, E.; Apostolopoulos, D.J. Innovative Attention-Based Explainable Feature-Fusion VGG19 Network for Characterising Myocardial Perfusion Imaging SPECT Polar Maps in Patients with Suspected Coronary Artery Disease. *Appl. Sci.* **2023**, *13*, 8839. https://doi.org/10.3390/app13158839

Academic Editor: Julio Garcia Flores

Received: 27 June 2023
Revised: 27 July 2023
Accepted: 28 July 2023
Published: 31 July 2023

1. Introduction

Coronary artery disease (CAD) is a leading cause of death worldwide. Greece is among the European Union members topping the deaths related to CAD [1]. It is a common cardiovascular disorder that results from the accumulation of plaques in the coronary arteries, which supply blood and oxygen to the heart muscle [2]. These plaques are composed of cholesterol, fat, and other substances and can cause narrowing or blockage of the coronary arteries, leading to reduced blood flow to the heart [2]. This reduced blood flow can cause chest pain, shortness of breath, or even a heart attack. CAD is a multifactorial disease, with risk factors including high blood pressure, high cholesterol, smoking, diabetes, and a family history of heart disease [3]. Preventative measures such as early detection, healthy lifestyle choices, and proper management of risk factors are essential for reducing the incidence and severity of CAD and promoting cardiovascular health [4].

The ultimate diagnosis and remedy of CAD involve invasive coronary angiography (ICA) and, subsequently [5], percutaneous coronary angioplasty (PCI) [6] or coronary artery bypass grafting (CABG) [7] in selected cases. Conservative treatment with appropriate medication opts for patients not eligible for PCI or CABG. Early diagnostic tests and clinical factors are employed to assess the CAD risk with low moderate predicting strength due to ambiguous results and the subjectivity of human experts. Myocardial Perfusion Imaging (MPI) with Single-Photon Emission Computed Tomography (SPECT) is a test used to evaluate the blood flow [8] to the heart muscle and to detect any abnormalities in CAD screening. The test is performed by injecting a small amount of radioactive material into the bloodstream and using a special camera to take pictures of the heart as it beats. This helps to determine if the heart muscle is receiving enough blood and oxygen.

Deep learning (DL) [9] is a type of artificial intelligence that has rapidly become a powerful tool in medical imaging analysis. In recent years, it has shown remarkable results in detecting, classifying, and segmenting images in various medical applications, including radiology, pathology, and ophthalmology [10–12]. DL algorithms are particularly suited to medical imaging, because they can automatically learn from large datasets and recognise complex patterns that might not be easily detectable by human experts [13]. DL algorithms have been used in various applications in medical imaging, including image classification, object detection, segmentation, and registration. In image classification, DL algorithms can recognise different types of images, such as X-rays or MRI scans, and classify them into specific categories [14].

One of the main benefits of DL in medical imaging is its ability to analyse large amounts of data quickly and accurately. Medical imaging produces large amounts of data, and DL algorithms can analyse these data more efficiently than human experts. For example, a DL algorithm can analyse thousands of mammography images in minutes, detecting subtle changes indicative of breast cancer.

Another benefit of DL in medical imaging is its ability to detect subtle changes that human experts might overlook. In some cases, radiologists may miss early signs of disease or fail to identify specific patterns in medical images, especially when analysing large volumes of data. On the other hand, DL algorithms can learn from large datasets and recognise complex patterns that humans may not detect easily. This ability to detect subtle changes early can lead to an earlier diagnosis and more effective treatment, improving patient outcomes.

DL in medical imaging also has the potential to improve the workflow and reduce costs. With the ability to analyse large volumes of data quickly and accurately, DL algorithms can automate many routine tasks currently performed manually by human experts. This can free up radiologists and other medical professionals to focus on more complex tasks and cases, reducing the workload and improving the efficiency. DL algorithms can also help reduce costs by reducing the need for expensive and invasive diagnostic tests and procedures.

In this study, a DL method is proposed for CAD diagnosis. The input of the proposed system is the four associated Polar Maps that aggregate the information of the MPI SPECT scan. Though MPI SPECT is not a definite diagnostic test, it is a reliable non-invasive method. The study's methodology lies in an innovative attention-based network that performs hierarchical and non-hierarchical feature extraction and classification. The contributions of the present study can be clarified as follows:

- A novel attention-based modification of the VGG19 network is proposed that improves the identification of essential areas of the Polar Map and performs feature-fusion via concatenation.
- The network is evaluated with reference to the invasive coronary angiography (ICA) test results and shows high classification accuracy, sensitivity, and specificity.
- The network agrees with the medical experts, who visually inspected the Polar Maps and delivered their diagnostic yields.

- The post hoc explainability algorithm reveals the crucial areas of the Polar Map, which the medical experts assessed to verify the correctness of the model.

The rest of the paper is organized as follows. The literature review is presented in Section 1.1. The materials and methods of the study are introduced in Section 2. More specifically, Section 2.1 describes the DL method of the study, i.e., the Attention-based Feature-Fusion VGG19 network, Section 2.2 discusses about the explainability-enhancing method, Section 2.3 presents the dataset of the study, Section 2.4 the image preprocessing methodology, and Section 2.5 presents an overview of the experiments. The results are presented in Section 3, where the model is assessed based on its agreement with the human expert (Section 3.1) and its diagnostic efficiency (Section 3.2). Various comparisons are held in Sections 3.3–3.5. A discussion is held in Section 4, with the major remarks in Section 5.

1.1. Related Work

Papandrianos et al. [15] developed an RGB-CNN model to classify SPECT images as normal or ischemic, addressing a data scarcity issue with data augmentation. The model achieved impressive results, with 90.2% accuracy and a 93.77% AUC value, outperforming human reader interpretation as the ground truth. Despite the limited dataset, the model demonstrated remarkable predictive capabilities.

The same research team [13] aimed to diagnose ischemia and/or infarction using CNNs with a dataset comprising 224 patients who underwent stress and rest SPECT tests, followed by invasive coronary angiography (ICA) 40 days later. They explored two deep learning techniques: implementing an RGB-CNN from scratch and employing transfer learning with pretrained models like VGG16, DenseNet, MobileNet, and InceptionV3 to classify images as normal or abnormal. Comparing the results to visual assessments by medical experts, the proposed CNN demonstrated significant abilities, achieving an overall accuracy of 93.48% $\pm$ 2.81%. Once again, the CNN model showcased its potential in accurately diagnosing ischemia and infarction, even with a relatively limited dataset. This accuracy is significantly improved compared to the 90.2% initially obtained in [15].

Narges Zahiri et al. [16] investigated the capabilities of deep CNNs in distinguishing between normal and abnormal Polar Maps, using physician diagnoses as the reference. The dataset consisted of 3318 stress and rest Polar Maps, and data augmentation techniques were applied to expand the training dataset. The proposed deep learning model underwent thorough validation through a five-fold cross-validation procedure, achieving an AUC (Area Under the Curve) of 0.845. Notably, including rest perfusion, the maps led to a significant improvement in the DL model's AUC (0.845) compared to using only stress polar maps (0.827).

Papandrianos et al. [17] aimed to explore the feasibility of automatically classifying polar maps as normal or abnormal using a custom RGB-CNN. The dataset comprised 314 polar maps in stress and rest representations, with AC (attenuation correction) and NAC (non-attenuation correction) formats. The RGB-CNN was trained using physician interpretations as the ground truth and was compared to the performance of the pre-trained VGG-16 network. The results showed that the RGB-CNN achieved an accuracy of 92.07%, while VGG-16 achieved 95.83%. Although the RGB-CNN's performance was slightly lower, it still competed effectively against robust state-of-the-art methods for polar map classification.

In some research, deep learning-based results are compared against quantifiable metrics recommended by medical guidelines. These metrics provide objective and standardised measures to evaluate the performances of deep learning models in various medical tasks. By comparing the DL-based results with these established metrics, researchers can assess the effectiveness and reliability of the proposed models in clinical settings, ensuring they align with the best practices and recommendations provided by medical experts.

For example, Yuka Otaki et al. [12] developed a DL model to identify CAD and evaluated its performance by comparing it with the total perfusion deficit (TPD) method. The dataset comprised 1160 patients and included raw upright and supine stress Myocardial

Perfusion Imaging (MPI) polar maps. Both MPI and invasive coronary angiography (ICA) were conducted within a 6-month interval. The researchers employed a leave-one-centre-out approach with four different models for external validation. This validation method allowed them to assess the DL model's generalisation and performance across various medical centres, enhancing the reliability of the results.

Julian Betancur et al. [18] developed a CNN to identify CAD. The study included 1160 participants, and the data comprised semi-upright and supine stress Polar Map representations. Obstructive disease classification was evaluated using the leave-one-centre-out cross-validation technique with four centres. All validated predictions were combined to avoid single-centre bias. Notably, the CNN model diagnosed without relying on predefined coronary territories. The CNN's performance was compared against the combined perfusion quantification using TPD, achieving a sensitivity of 84.8%, surpassing the 82.6% sensitivity obtained with clinical reading.

In a subsequent study, Julian Betancur et al. [19] compared the automatic diagnosis of CAD using SPECT image inputs with a deep CNN against the TPD method. They examined 1638 patients without known CAD who underwent invasive coronary angiography within six months of MPI. The dataset included raw and quantitative polar maps in stress representations only. To evaluate their proposed deep learning model, they employed a stratified 10-fold cross-validation procedure. The AUC score for disease prediction using the DL model was superior to TPD (per patient: 0.80 vs. 0.78; per vessel: 0.76 vs. 0.73). When the DL threshold was set to the same specificity as TPD, the per-patient sensitivity improved from 79.8% (TPD) to 82.3%, and the per-vessel sensitivity improved from 64.4% (TPD) to 69.8%.

In addition to differentiating between normal and abnormal subjects, certain studies focused on region-based classification. Instead of considering the overall classification of the entire image, region-based classification involves identifying and classifying specific regions or regions of interest within the image. This approach allows researchers to gain more detailed insights into the particular areas or regions that may be affected by certain conditions or diseases.

Arvidsson et al. [20] developed a CNN to predict obstructive coronary artery disease in the left anterior artery, left circumflex artery, and right coronary artery using SPECT Polar Maps. The research involved 588 patients, and clinical data, including angina symptoms and age, were incorporated into the analysis. The proposed CNN framework demonstrated promising results, achieving an average AUC of 0.89 per vessel and an impressive 0.95 per patient, with the invasive coronary angiography (ICA) findings used as the reference standard. To provide visual insights into the basis of the predictions, the researchers employed gradient-weighted class activation mapping (Grad-CAM) to highlight the regions influencing the model's output. Notably, the authors identified sex differences in the diagnostic performance of the deep learning model for predicting obstructive CAD from D-SPECT, with the CNN outperforming the visual and TPD methods in men but not in women. This finding underscores the importance of considering potential sex-specific variations when employing DL models for a CAD diagnosis.

There is a growing trend in research towards proposing explainable deep learning (DL)-based methods that perform image classification and provide insights into the suggested areas of interest, where the model bases its predictions. These methods aim to enhance the interpretability and transparency of DL models, addressing the "black box" nature of traditional deep learning algorithms. By incorporating explainable techniques, researchers seek to inform users about the specific regions or features in the input images that contribute to the model's decision-making process. This builds trust in the model's predictions and allows domain experts, such as doctors in medical imaging applications, to better understand and validate the results. Explainable DL methods are becoming increasingly important in various fields, including healthcare, where accurate and interpretable predictions are critical for decision-making and patient care.

Miller et al. [21] developed a DL model to enhance the diagnostic accuracy of CAD and aid in physical interpretation. The dataset consisted of 240 patients who underwent MPI examinations, with invasive coronary angiography used as the reference standard. The results showed that, when human readers used the DL's predictions, they achieved an AUC of 0.779, whereas their interpretation without DL assistance reached an AUC of 0.747. It is worth noting that the DL model, when used independently, achieved an AUC of 0.793, showcasing its potential in improving the diagnostic performance for CAD. Incorporating the explainable DL model provided higher accuracy and facilitated the interpretation of the results, making it a valuable tool for assisting medical professionals in CAD diagnosis and decision-making.

Yuka Otaki et al. [22,23] introduced an explainable DL model to detect obstructive CAD. Their study included a large dataset of 3578 patients with suspected CAD from nine different centres. The authors proposed a hand-crafted CNN to process SPECT Polar Maps acquired under stress conditions. In the fully connected layer of the CNN, they incorporated additional features such as the patient's sex and age to augment the model's input. When evaluated against the invasive coronary angiography findings, this method achieved an impressive AUC score of 0.83 through a 10-fold cross-validation procedure, outperforming the quantitative analysis results by expert readers (AUC = 0.8). Moreover, attention maps were generated to highlight the regions and segments that contributed the most to the per-vessel predictions, providing insights into the model's decision-making process and making it more interpretable for clinical application.

Singh et al. [24] developed an explainable deep learning model for predicting nonfatal myocardial infarction (MI) or death, highlighting image regions relevant to obstructive CAD. The study included 20,401 patients who underwent SPECT MPI procedures for training and internal testing, and an additional 9019 patients were included in the external testing group from two different sites to assess the generalisability. The dataset comprised stress and rest polar maps, age, sex, and cardiac volumes, which were added at the first fully connected layer. To enhance the explainability, the researchers developed Grad-CAM. For comparison, a logistic regression model was also developed using age, sex, stress TPD, rest TPD, stress left ventricular ejection fraction, and stress left ventricular end-systolic volume as the input features. The developed deep learning model achieved an impressive AUC of 0.76, outperforming stress TPD with an AUC of 0.63 and ischemic TPD with an AUC of 0.6. Moreover, it also improved upon the logistic regression model, which achieved an AUC of 0.72. The explainable deep learning model provided enhanced accuracy compared to traditional quantitative approaches and exhibited good calibration and robust results. These findings indicated the potential of the developed model for improved risk prediction and decision-making in the context of myocardial infarction and CAD.

Jui-Jen Chen et al. [25] examined 979 SPECT subjects from a local hospital for diagnosis; however, it was not specified whether the images were labelled based on experts' visual inspections or ICA findings. A three-dimensional CNN was employed to classify the SPECT slices, and Grad-CAM heat maps were generated to identify myocardial defects in the images. The proposed model achieved impressive accuracy, sensitivity, and specificity metrics of 87.64%, 81.58%, and 92.16% in distinguishing between normal and abnormal images using a test set of 89 samples. These results demonstrated the model's promising capabilities for the accurate and reliable classification of SPECT images to diagnose cardiovascular conditions.

Nathalia Spier et al. [26] explored using Graph Convolutional Neural Networks (Graph CNNs) for diagnosing CAD. They included 946 polar map images representing the stress and rest conditions of the heart and labelled them based on human observer interpretations. Heatmaps were generated to highlight the pathological segments of the heart. The results demonstrated the model's strong performance in classifying unseen data during a four-fold cross-validation procedure, outperforming the clinical visual analysis, with 92.8% specificity for the rest data and 95.9% for the stress data. The proposed model agreed 89.3% with the human observer for rest test polar maps and 91.1% for the stress

test polar maps. For localisation performed on a fine 17-segment division of the polar map, the agreement was 83.1% with the human observer. These findings indicate the model's potential in aiding CAD diagnosis and its ability to accurately identify pathological segments in cardiac images.

Selcan Kaplan Berkaya et al. [27] developed a classification model for SPECT images to identify perfusion abnormalities, such as ischemia and infarction. The researchers investigated two different models. The first model was a deep learning (DL)-based approach that utilised state-of-the-art CNNs and fully connected support vector machine (SVM) layers to classify the deep-extracted image features. The second model involved image processing techniques, including segmentation, feature extraction, and colour thresholding, applied to the segmented parts of each SPECT slice. This method extracted five predefined image features that were classified using a rule-based algorithm. In terms of performance, the integrated CNN-SVM model achieved 92% accuracy, 84% sensitivity, and 100% specificity, based on the visual assessments conducted by experts.

On the other hand, the knowledge-based classification attained 93% accuracy, 100% sensitivity, and 86% specificity. These metrics were reported on a test dataset that included 17% of the total samples. The results demonstrated the potential of both DL-based and knowledge-based approaches in accurately classifying SPECT images and detecting perfusion abnormalities, with each model showing strengths in different performance aspects.

Hui Liu et al. [28] demonstrated a DL approach for automatically diagnosing myocardial perfusion abnormalities using stress MPI profile maps as the input, considering both abnormal and normal cases. The study included a substantial dataset of 37,243 patients who underwent stress-only and stress/rest SPECT MPI examinations using three SPECT/CT cameras. The DL model utilised the ResNet-34 architecture for feature extraction. In addition to the MPI data, six extra features, including gender, BMI, length, stress type, radiotracer, and the option of including or not including the attenuation correction, were incorporated into the model. The results were compared against the conventional quantitative perfusion defect size (DS) method. The DL model achieved an impressive AUC of 0.87, outperforming the DS method. Furthermore, the proposed network demonstrated robustness to variations in image acquisition devices, achieving 82% and 84% accuracy across all scanners. Notably, the model exhibited even greater performance in female participants, reaching an accuracy of 87%. These findings highlight the effectiveness and generalisability of the DL-based approach for diagnosing myocardial perfusion abnormalities, presenting a promising tool for improving cardiovascular diagnosis and patient care.

Apostolopoulos et al. [29] acquired Polar Maps under stress, and rest conditions were used to diagnose CAD by employing the pretrained VGG16 model. The research involved 216 participants, and both attenuation correction (AC) and non-attenuation correction (NAC) Polar Map images were merged into a single image per patient. With reference to the findings from invasive coronary angiography, the VGG16 model achieved an accuracy of 74.53%, a sensitivity of 75.00%, and a specificity of 73.43%. In comparison, experienced nuclear medicine physicians' interpretations of the MPI yielded an accuracy of 75.00%, a sensitivity of 76.97%, and a specificity of 70.31%. The accuracy of a semi-quantitative polar map analysis using AC and NAC techniques was comparatively lower at 66.20% and 64.81%, respectively. Additionally, the VGG16 model demonstrated a robustness to variations in image acquisition devices. These results suggest the potential of the DL-based approach for CAD diagnosis, showing comparable performances to experienced physicians' interpretations and outperforming the traditional semi-quantitative methods.

The same author team extended their study [30] by presenting a hybrid CNN–Random Forest approach proposed for classifying Polar Map images and clinical attributes into normal and abnormal classes, with ICA findings as the reference for CAD disease. The research involved 566 patient cases. The InceptionV3 pretrained model was used to predict the class of the input Polar Maps. The model's output was combined with 22 clinical factors, including gender and age, and fed into the Random Forest classifier for outcome prediction.

With reference to the ICA results, the model achieved an accuracy of 78.44%, sensitivity of 77.36%, and specificity of 79.25%.

Interestingly, the overall accuracy of the human cognitive process reached 79.15%, approximately 1% higher than the automatic model's accuracy (78.43%). Furthermore, the overall agreement rating between the human experts and the model was 86% (Cohen's Kappa = 72.24), indicating a strong level of agreement. The model was also tested on unseen data from a different SPECT scanner and achieved consistent results with an accuracy of 76.53%. These findings demonstrated the effectiveness of the hybrid approach for CAD diagnosis and its potential for practical clinical use.

Trung et al. [31] utilised polar maps and SPECT slices as the input data. The dataset consisted of 1413 heart SPECT images, which a nuclear expert labelled as either CAD or non-CAD. The performance of the CNN network, specifically using the VGG-16 architecture, was evaluated using a five-fold cross-validation procedure. The results revealed that SPECT images provided a better diagnosis than polar maps. The precision achieved using SPECT images was 86.14 $\pm$ 2.14%, while polar maps achieved a precision of 82.57 $\pm$ 2.33%. These findings demonstrated the potential superiority of SPECT images over polar maps in CAD diagnosis using the proposed CNN model.

2. Materials and Methods

2.1. Attention-Based Feature-Fusion VGG19

This section presents the major components of the Attention-based Feature-Fusion VGG19 (AFF-VGG19), which can be summarised as follows:

1. Baseline VGG19 [32] network.
2. Feature-fusion blocks [33,34].
3. Attention modules [35–37].

2.1.1. Baseline VGG Network

VGG19 is a deep neural network architecture that researchers developed from the Visual Geometry Group (VGG) at the University of Oxford in 2014 [32].

The VGG19 architecture is a deep convolutional neural network with 19 layers, hence the name VGG19. The VGG19 architecture has 19 layers, including 16 convolutional layers and 3 fully connected layers. The first 13 layers are convolutional, and the remaining 6 are fully connected. The convolutional layers have a fixed kernel size of 3 $\times$ 3, and they use a stride of 1 and 0 padding to keep the spatial resolution of the feature maps the same. The max-pooling layers have a fixed kernel size of 2x2 and a stride of 2, which reduces the spatial resolution by half.

The VGG19 architecture has been used for many image recognition and classification tasks, including object recognition, scene classification, and image segmentation. It has achieved state-of-the-art performances on several benchmark datasets, including the ImageNet Large Scale Visual Recognition Challenge (ILSVRC) [38] and the CIFAR-10 [39] and CIFAR-100 [40] datasets.

When fine-tuning with the VGG19 architecture, the first few convolutional layers are typically frozen, while the later ones are fine-tuned. The intuition behind this approach is that the earlier layers learn lower-level features that are more general. In contrast, the later layers learn higher-level features that are more specific to the task.

The present study employs VGG19 and allows for domain adaption via retraining some of the model's layers. In this way, the model retains sound feature-extracting knowledge from the ImageNet database domain and can extract powerful low-level features common in every image domain. Higher medical-specific features are expected to be mined by the deep convolutional layers of the network, which are trainable. With this conception, the total trainable parameters of the network are approximately 5 million.

2.1.2. Feature-Fusion Modification

Feature-fusion [34] is a technique used in CNNs to combine features learned from different layers or branches of the network. The goal is to improve the network's performance by taking advantage of complementary information learned at different stages of the network.

Technically, feature-fusion is implemented by concatenating or adding the feature maps from different layers or branches of the network. The resulting feature maps are then passed through a nonlinear activation function and used as the input to the next network layer. The choice of fusion operation (concatenation or addition) and the specific layers to be fused can be designed based on the problem being solved.

Figure 1 illustrates the feature-fusion blocks connected to the final three max-pooling layers of the baseline VGG19. A feature-fusion block tracks the output of the max-pooling layer, performs a batch normalisation and a random 50% dropout, and connects the product directly to the concatenation layer.

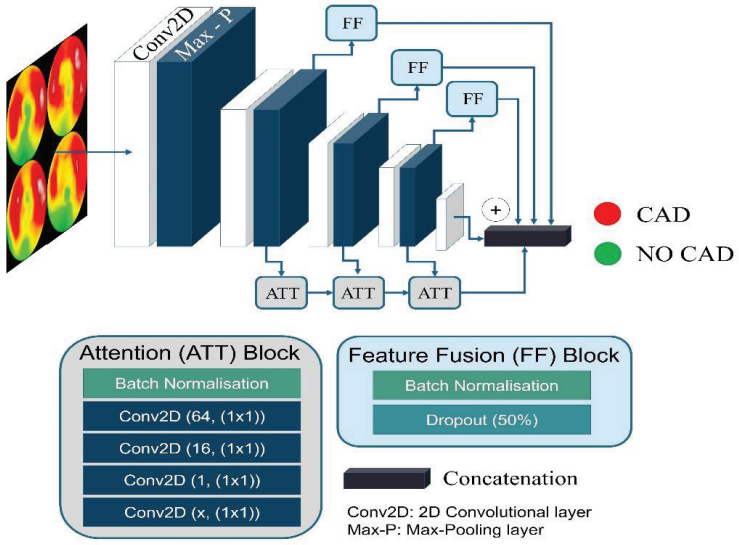

Figure 1. Attention-based Feature-Fusion VGG19 architecture.

The concatenation layer consists of two components: (i) the global average pooling layer and (ii) the densely connected layer, which flattens the extracted features.

In this way, the low-level features are retained and not refiltered due to the hierarchical nature of the VGG19 network.

2.1.3. Attention Module

The attention module [37] is a critical component of CNNs that has gained widespread popularity recently, particularly in natural language processing (NLP). The attention mechanism is designed to help the network focus on the most relevant parts of the input data when making predictions. The attention mechanism is a method for selectively focusing on different parts of the input data when making predictions. In CNNs, this is typically accomplished by assigning weights to different regions of the input data. These weights are then used to compute a weighted sum of the input features, which is used to make the final prediction.

There are several ways to implement the attention mechanism in CNNs. One common approach is to use a soft attention mechanism, which involves computing a set of attention weights for each input feature. These attention weights are typically computed using a

neural network, which takes the input feature and outputs a scalar value between 0 and 1 representing the attention weight.

Once the attention weights have been computed, they compute a weighted sum of the input features. The weights are applied to the input features using element-wise multiplication, and the resulting products are summed to produce the final output.

The attention module of the proposed network is presented in Figure 1. It consists of 4 convolutional blocks. We propose using five-layered attention modules located after the second, third, and fourth convolutional groups and connected to the output of the following max pooling layers. The first layer is a batch normalisation layer. The second, third, fourth, and fifth layers are convolutional operations utilising 64, 16, 1, and x filters of 1×1 kernel size. The x number depends on the convolution group to which the attention module belongs. The attention module in the second group has an x of 128. Accordingly, the third and fourth groups have an x of 256 and 512, respectively. The extracted features are multiplied with the output of the convolutional group and connected to the network's top.

2.1.4. Training Parameters

The following parameters are selected for the specific task. Their selection require fine-tuning, performed before network training and evaluation.

1. The dense layer at the top connects each of the neurons from the previous layers and allows the network to extract features from the input data. AF-VGG19 consists of one dense layer of 512 nodes.
2. Loss function: The categorical cross-entropy loss function is commonly used in supervised learning tasks with multiple classes. It is used to measure the dissimilarity between the predicted probabilities of a model and the true class labels.
3. Optimiser: An optimiser plays a crucial role in training a CNN [9]. It updates the model weights based on the gradients calculated during the forward and backward passes. The present version of our network uses the Adam optimiser.
4. Early Stopping: We implemented two early stopping rules. Suppose the validation accuracy reaches 0.91 and does not improve for ten epochs, while the training accuracy remains above 0.91. In that case, the training stops, and the weights of the best epoch are restored.
5. Data Augmentation: Data augmentation is an essential training technique, even when a large amount of data are available. Data augmentation aids in overfitting reduction when the model's performance on the training data is substantially better than on unseen data. Data augmentation creates new data points by transforming existing data points to preserve the original data information. The latter helps improve the model's generalisation ability and performance on unseen data. As advised by similar studies [27–29], slight data augmentations are applied for particular classification tasks. These include slight height and width shifts (by 10 pixels), random rotations (by a maximum of 10 degrees), and Gaussian noise injections.

2.2. Explainability-Enhancing Algorithm

Grad-CAM++ [41] is a visualisation technique for understanding the decision-making process of CNNs. It provides a heatmap highlighting the important regions in an image that the network used to make a prediction. As a result, the way the network is processing the input image and diagnosing any potential issues with the model is better understood.

Grad-CAM++ operates by computing the gradient of the target class with respect to the feature maps in the final convolutional layer of the network. These gradients represent each feature map's importance in the network's final decision.

The final step of Grad-CAM++ is to compute a weighted sum of the feature maps using the computed gradients. The result is a heatmap highlighting the important regions in the input image for the network's prediction. The heatmap can be computed for any target class, providing insight into which regions of the input image the network uses to make its predictions.

2.3. Dataset

Patient data were recorded at the Department of Nuclear Medicine of the University Hospital of Patras from 16 February 2018 to 28 February 2022. Over this period, 2036 consecutive patients underwent gated-SPECT MPI with 99mTc-tetrofosmin. Two-hybrid SPECT/CT gamma camera systems (Varicam, Hawkeye and Infinia, Hawkey-4, GE Healthcare, Chicago, IL, USA) were employed for MPI imaging. Computed tomography-based attenuation correction (AC) was applied to stress and rest images in all subjects. Five hundred and six participants were subsequently subjected to ICA within sixty days from MPI for further investigation. Twenty patients were excluded from the dataset due to inconclusive MPI results or missing ICA reports. The final study population included 486 patients (CAD-positive cases refer to 43.82% of the total). Data collection was approved by the ethical committee of the University General Hospital of Patras (Ethical & Research Committee of University Hospital of Patras—protocol number 108/10-3-2022). The study's retrospective nature waived the requirement to obtain informed consent from the participants. All data-related processes were performed anonymously. All procedures in this study followed the Declaration of Helsinki. Three experienced nuclear medicine physicians provided the diagnostic results of MPI SPECT by inspecting the study retrospectively and, independently, the Polar Maps. Between-reader inconsistencies were resolved by consensus.

Tomographic reconstruction of raw image data on a dedicated workstation (Xeleris 3, GE Healthcare) by the OSEM (ordered subset expectation maximisation) algorithm using two iterations and ten subsets. After reconstruction, a low-pass filter (Butterworth, with power of ten and a cut-off value of 0.40 for stress and 0.45 for rest images) was applied. Apart from 3-plane tomographic slices (in short, vertically long and horizontally long axes), the software automatically created polar maps. A polar map is an image that summarises the results of 3D tomographic slices into a single 2D circular presentation. Polar maps were extracted from the workstation in DICOM (Digital Imaging and Communications in Medicine) format for further processing.

2.4. Image Preprocessing

Image preprocessing is an essential step in medical image analysis. To process the extracted DICOM images, reading them into memory and applying some initial transformations were necessary. One such transformation was the application of colour maps (Figure 2). Colour maps are used to convert a grayscale image into a colour image. This can help visualise the different structures in the image, such as bones and soft tissue, with different colours. This can be particularly useful in medical imaging, where it is vital to identify and differentiate different structures. We used a library such as Matplotlib to apply a colour map, which provided several colour maps.

For each patient, we extracted four Polar Maps as follows:

1. Polar map (with attenuation correction) in rest conditions.
2. Polar map (with attenuation correction) in stress conditions.
3. Polar map (without attenuation correction) in rest conditions.
4. Polar map (without attenuation correction) in stress conditions.

The four Polar Maps were merged into a single image (Figure 2) in JPEG format for feeding AFF-VGG19.

Once the image was transformed with a colour map, it could be converted into a numerical array. This allowed us to perform numerical operations on the image, such as filtering, segmentation, and registration. Normalisation is a common preprocessing step that helps ensure that image data are in a consistent range. This can be particularly important for DL models, which are sensitive to the scale of the input data. Normalisation can be performed by dividing the image values by the maximum value or by subtracting the mean and dividing by the standard deviation.

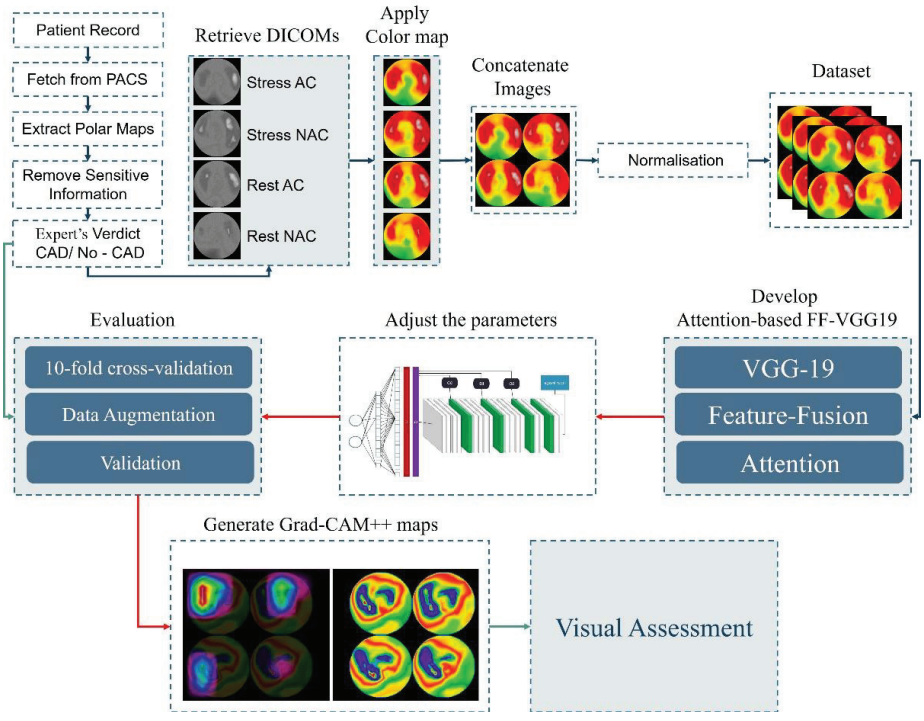

Figure 2. Experiment design.

2.5. Experiment Design

Figure 2 illustrates the experiment pipeline.

The experiments were performed using a workstation of the following properties: 11th Gen Intel® Core™ i9-11900KF @3.50GHz processor, equipped with an NVIDIA GeForce RTX 3080 Ti GPU and a 64-GB RAM for a 64-bit operating system. The Python 3.9 libraries TensorFlow 2.9.0 and Sklearn 1.0.2 were used.

The assessment of the models was done under a 10-fold cross-validation scheme. During each fold, the accuracy, sensitivity (or recall), specificity, positive predictive value (*PPV*) or precision, negative predictive value (*NPV*), false-positive rate (*FPR*), and F-1 score of the run were derived from the recorded true positives (*TP*), false positives (*FP*), true negatives (*TN*), and false negatives (*FN*) of each class. We used the following formulas to compute the metrics:

$$Sensitivity = \frac{TP}{(TP + FN)}$$

$$Specificity = \frac{TN}{(TN + FP)}$$

$$PPV = \frac{TP}{(TP + FP)}$$

$$NPV = \frac{TN}{(TN + FN)}$$

$$FPR = \frac{FP}{(FP + TN)}$$

$$F-1 = \frac{2 \times PPV \times Sensitivity}{PPV + Sensitivity}$$

3. Results

3.1. Assessing the Agreement between the Model and the Human Expert

The model was trained using the nuclear medicine expert diagnostic yield as a reference. Therefore, the model was trained to mimic how the human reader reads and interprets the image. As a result, this experiment measured the agreement between the expert and the model and was irrelevant to the presence of CAD. The model strongly agreed with the expert (0.8992 accuracy, Table 1). The model exhibited 198 true-positive cases, 239 true-negative cases, 34 false positives, and 15 false negatives. The high F-1 score indicated no subjective class-related biases in the model.

Table 1. AFF-VGG19 and human expert diagnostic efficiency.

Metric	With Reference to ICA Findings		With Reference to Human Reader
	AFF-VGG19 (Model)	Nuclear Medicine Expert	AFF-VGG19 (Model)
True Positives	186	204	198
True Negatives	197	177	239
False Positives	76	96	34
False Negatives	27	9	15
Accuracy	0.78881	0.7840	0.8992
Sensitivity	0.8732	0.9577	0.9296
Specificity	0.7216	0.6484	0.8755
PPV	0.7099	0.68	0.8534
NPV	0.8795	0.9516	0.9409
FPR	0.2784	0.3516	0.1245
F-1 score	0.7832	0.7953	0.8899

3.2. Assessing the Model's Robustness in CAD Diagnosis Based on ICA Findings

AFF-VGG19 was retrained using the ICA findings as the reference. Therefore, the model aimed to identify the presence of significant ischemic vessels related to CAD. The reader should note that the MPI test was an inherently weak predictor for CAD and often exhibited false-positive and false-negative findings [28–30,42].

The model attained a slightly better accuracy (0.7888) than the human expert (0.7840). The human expert was more biased towards the CAD class, exhibiting 96 false-positive cases, much higher than the model (76). As a result, the human expert had higher sensitivity (0.9577 versus 0.8732) and lower specificity (0.6484 versus 0.7216) rates. It is worth noticing that the human reader yielded a slightly higher F-1 score (0.7953 versus 0.7832) (Figure 3).

In conclusion, the results demonstrated an acceptable agreement rate between the model and the expert and similar diagnostic strength when evaluated based on the ICA findings. The model was less subjective, i.e., less biased towards the CAD class. This was an expected behaviour, because the human reader may overestimate ambiguous cases and suggest a patient undergo an invasive test (ICA) that serves as both a diagnostic examination and a remedy.

3.3. Comparison with Other VGG Approaches

The efficiency of AFF-VGG19 has also been assessed against other VGG approaches. More specifically, we employed the baseline VGG16 and VGG19 models, the Feature-Fusion VGG19 model [10], and an attention-based VGG19 model containing only the described attention module. AFF-VGG19 was superior to the other approaches. It improved the diagnostic accuracy of the baseline VGG19 by 9% (Table 2) and was better than the baseline FF-VGG19 (0.7881 accuracy versus 0.7119). These results highlighted that the feature-fusion and attention modules work well in cooperation and improve the performance.

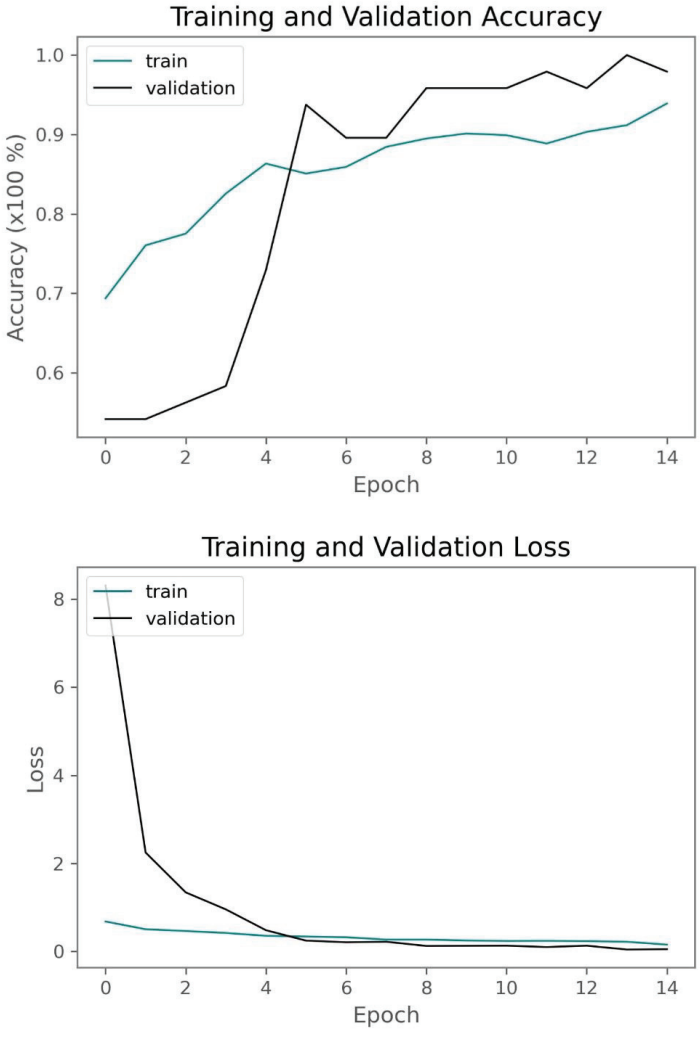

Figure 3. Training and validation accuracy and loss of AFF-VGG19 when trained with the ICA findings as reference.

Table 2. Performance metrics of VGG approaches with reference to ICA findings.

Network	Accuracy	Sensitivity	Specificity	F-1 Score
Baseline VGG16	0.6770	0.7606	0.6117	0.6736
Baseline VGG19	0.6955	0.7700	0.6374	0.6891
FF-VGG19 [10]	0.7119	0.7840	0.6557	0.7046
Attention VGG19	0.7469	0.8498	0.6667	0.7464
Attention FF-VGG19	0.7881	0.8732	0.7216	0.7832

3.4. Comparison with Pretrained State-of-the-Art

The selection of the VGG19 network as the baseline for integrating the feature-fusion block and the attention module was based on the recent literature [17,29] and the experi-

ments provided in Table 3. Several baseline state-of-the-art pretrained models were trained using the ICA findings to determine the best-performing one.

Table 3. Performance metrics of CNN approaches with reference to ICA findings.

Network	Accuracy	Sensitivity	Specificity	F-1 Score
VGG16	0.6770	0.7606	0.6117	0.6736
VGG19	0.6955	0.7700	0.6374	0.6891
ResNet152	0.6605	0.7465	0.5934	0.6584
ResNet152V2	0.6605	0.7512	0.5897	0.6598
InceptionV3	0.6543	0.7793	0.5568	0.6640
InceptionResNetV2	0.6646	0.7793	0.5751	0.6707
MobileNet	0.6564	0.7653	0.5714	0.6613
MobileNetV2	0.6584	0.7606	0.5788	0.6612
DenseNet169	0.6091	0.7277	0.5165	0.6200
DenseNet201	0.6296	0.7418	0.5421	0.6371
NASNetMobile	0.6379	0.7465	0.5531	0.6437
EfficientNetB6	0.6667	0.7559	0.5971	0.6653
EfficientNetB7	0.6564	0.7465	0.5861	0.6557
EfficientNetV2B3	0.6111	0.6714	0.5641	0.6021
ConvNeXtLarge	0.6276	0.6526	0.6081	0.6057
ConvNeXtXLarge	0.6214	0.6479	0.6007	0.6000
Xception	0.6605	0.7465	0.5934	0.6584

VGG16, VGG19, Xception, and EfficientNetB6 provided the top four accuracies. The minor differences in the accuracy of the four best models were not investigated for statistical significance. Instead, the most uniform network was chosen (VGG).

3.5. Comparison with the Literature

Table 4 presents the related literature employing Polar Map images and DL methods for diagnosing CAD or measuring the agreement with human readers.

The results of the study were consistent with the literature. There were studies reporting a similar or higher diagnostic efficiency. This discrepancy was caused by training data variations related to scale and class distribution.

Table 4. Performance metrics of the literature approaches.

Study	Input	Reference	Explainability	Results
[26]	Polar Maps	Human reader	✓	**Agreement:** 0.83 **Sensitivity:** 0.47 **Specificity:** 0.70
[43]	Polar maps + cardiac risk factors	ICA		**Accuracy:** 0.857
[22]	Polar Maps	ICA	✓	**Sensitivity:** DL (0.82), SSS (0.75), U-TPD (0.77), and S-TPD (0.73) in men DL (0.71), SSS (0.71), U-TPD (0.7), and S-TPD (0.65) in women
[29]	Polar Maps	ICA	-	DL **Accuracy:** 0.74 **Sensitivity:** 0.75. **Specificity:** 0.73. Similar results with the experts Semi-Quantitative Analysis **Accuracy**: 0.66.

Table 4. *Cont.*

Study	Input	Reference	Explainability	Results
[30]	Polar Maps + Clinical	ICA	-	Expert **Accuracy**: 0.7 **Sensitivity**: 0.89 **Specificity**: 0.71 Model **Accuracy**: 0.78 **Sensitivity**: 0.77 **Specificity**: 0.79
[20]	Polar maps + angina symptoms and age	I.C.A.		Per vessel **AUC**: 0.89 Per patient **AUC**: 0.95
[16]	Polar maps	Human reader		**Accuracy:** 0.7562 **Sensitivity:** 0.7856 **Specificity:** 0.7434 **F1 score:** 0.6646 **AUC**: 0.8450
[43]	Polar maps	Human reader		**Accuracy**: 0.92
[24]	Stress rest polar maps combined with age, sex, and cardiac volumes	ICA	✓	**AUC**: 0.76 **AUC**: 0.73 (external dataset)
This study	Stress and rest Polar Maps (AC and NAC.)	Human reader	✓	**Accuracy:** 0.8992 **Sensitivity:** 0.8992 **Specificity:** 0.8755
This study	Stress and rest Polar Maps (AC and NAC.)	I.C.A.	✓	**Accuracy:** 0.78881 **Sensitivity:** 0.8732 **Specificity:** 0.7216

3.6. Visual Assessment

Grad-CAM++ was implemented to visualise important areas on the Polar Maps, as suggested by the AFF-VGG19 network. The nuclear medicine specialists of the authors group performed a visual assessment regarding the highlighted areas on the Polar Maps.

Based on the visual inspection, the model was reassessed. Figure 4 illustrates a sample of true-positive findings. Figure 5 illustrates true-negative, false-positive, and false-negative samples.

The model revealed and highlighted important segments of the Polar Maps correctly. The suggested regions were relevant to the evidence of artery stenosis but of a greater spatial extent than the extent of the positive findings. Also, some maps were quite vague about the exact locations they dictated in the images and were considered incorrect. The inspection of 100 Polar Maps and the suggested regions of interest (the produced Grad-CAM++ heat maps) indicated a slight performance decrease, as Table 5 suggests.

The 100 samples included 45 *TP* cases, 35 *TN* cases, 12 *FP* cases, and 8 *FN* cases. These metrics corresponded to a 0.8 accuracy in CAD identification. Of the 45 *TP* cases, 43 had meaningful suggested regions, 1 had an ambiguous region (too large), and 1 had an irrelevant suggested region.

Of the 35 *TN* cases, 34 generated a meaningful heat map, and 1 an ambiguous (too large area). For the 12 *FP* cases, 4 heat maps located the suspected artery correctly, but the classification was wrong. In addition, eight of the twelve irrelevant suggestions were in the right locations, but the suggested class was not expected. The eight *FN* cases did not contain any highlighted areas. Therefore, these cases were considered to be irrelevant. Considering the number of meaningful explanations, the model's accuracy reached 77%, 3% less than the obtained accuracy without inspecting the suggested areas.

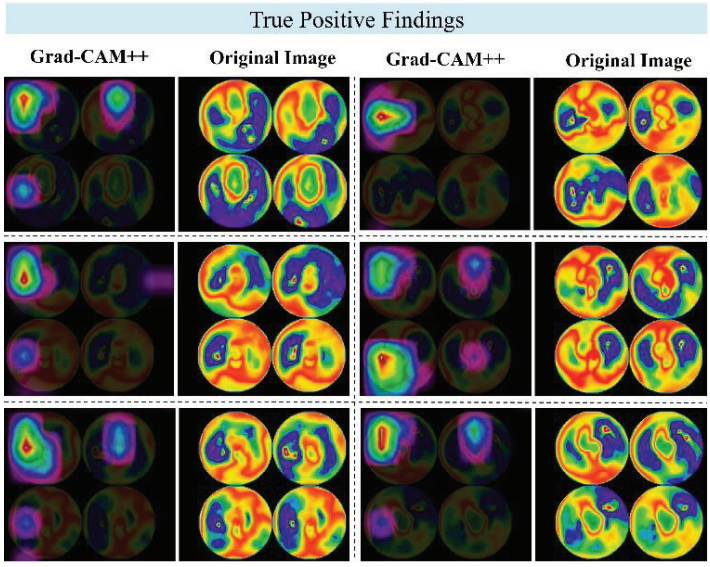

Figure 4. Grad-CAM++ examples of true-positive findings. Each row represents a different patient case, and each image pair represents the original image (**right**) and the Grad-CAM++ map (**right**).

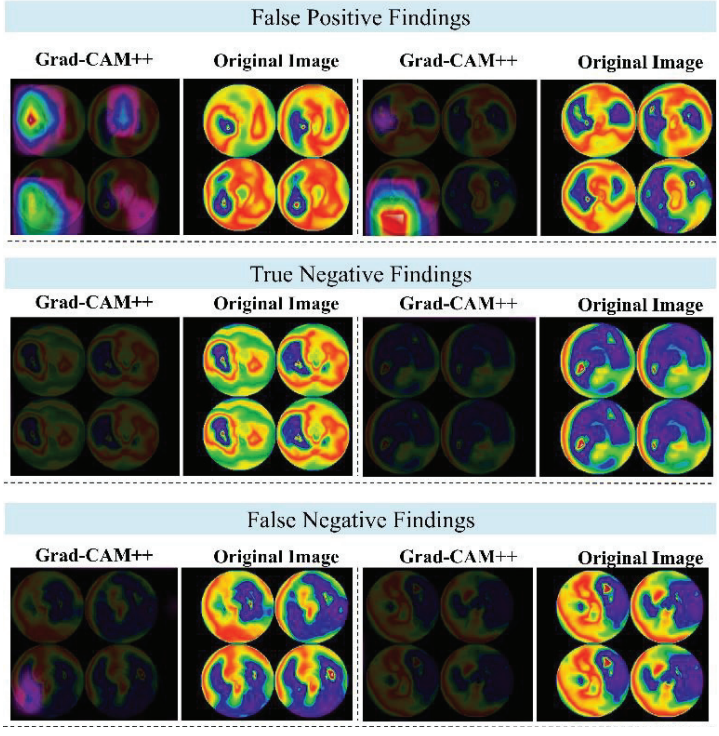

Figure 5. Grad-CAM++ examples of false-positive, true-negative, and false-negative findings. Each row represents a different patient case, and each image pair represents the original image (**right**) and the Grad-CAM++ map (**right**).

Table 5. Results of the examination of the produced Grad-CAM++ heatmaps. An asterisk (*) indicates that, though the image classification yielded a false positive, the produced heatmap correctly pointed to the location of interest.

Polar Maps	Number of Examined	Number of Adequate Explanations	Number of Ambiguous Explanations	Number of Irrelevant Explanations
TP cases	45	43	1	1
TN cases	35	34	1	0
FP cases	12	0 (4 *)	0	12 (8 *)
FN cases	8	0	0	8
Total	100	77	2	21

4. Discussion

DL can substantially contribute to medical image processing and medical image analysis for diagnostic purposes. In the case of CAD, the significance of DL in the analysis of MPI SPECT scans and MPI SPECT Polar Maps is already highlighted [13,17,22,26,29,30].

In this study, we proposed an advanced deep learning (DL) methodology that incorporated feature-fusion and attention modules to enhance the localisation abilities of the baseline VGG19 network. Additionally, we implemented the Grad-CAM++ algorithm to enable a visual assessment of the regions where VGG19 focused on its most critical features.

We initiated our discussion by examining the agreement between AFF-VGG19 and the medical experts. We trained the model using the human reader's diagnostic yield as a reference to achieve this. The results demonstrated a high level of agreement, with an impressive 89.92% alignment between the model's predictions and the classifications assigned by the human reader to the images. This finding underscored the model's capacity to capture relevant features and make clinically meaningful predictions, providing valuable insights for medical practitioners.

Furthermore, we performed training and assessment using the ICA findings as a reference, simulating real-world diagnostic scenarios. AFF-VGG19 displayed a robust diagnostic strength, boasting an accuracy of 0.78881, closely mirroring the performance of the human expert (0.7840). Notably, the model exhibited more balanced sensitivity (0.8732) and specificity (0.7216) rates, outperforming the human expert in this regard (0.9577 and 0.6484, respectively). Human readers, particularly nuclear medicine physicians, may exhibit bias towards the positive class of CAD due to several reasons. First, they may encounter cases with ambiguous diagnostic test results, where the findings are not definitive, leading them to err on the side of caution and lean towards diagnosing CAD to avoid missing potential cases, even if the evidence is inconclusive. Second, there may be a preference for false-positive results, because they allow for follow-up with invasive procedures like invasive coronary angiography (ICA) to confirm the presence of CAD. Missing CAD cases (false negatives) can be risky for patients, and this preference for false positives may contribute to the bias towards the CAD class.

Additionally, the bias can be related to the dataset used, as nuclear medicine physicians typically select symptomatic patients for SPECT/MPI testing in clinical practice. As a result, the dataset used for training and validation may have a higher proportion of patients with CAD, reflecting the real-world scenario where doctors encounter more patients with cardiac symptoms. To mitigate the impact of bias, training the machine learning model on a balanced dataset during the training and validation phases is essential. A balanced dataset allows the model to handle both positive and negative cases effectively without becoming skewed towards the majority class. Nevertheless, despite using a balanced dataset, the model may still face challenges in real-world scenarios due to inherent biases in data collection and human decision-making. Therefore, evaluating the model on diverse and unbiased datasets is crucial to ensure its generalisability and reliability. Moreover, raising awareness among human experts about potential biases and encouraging them to

be mindful of their decision-making process can contribute to the improved performance and fairness of AI models in real-world applications.

These results indicate that AFF-VGG19 has the potential to be a valuable tool in assisting medical experts in making more reliable and accurate diagnoses.

However, it is essential to consider the interpretability of the model's predictions. We visually inspected the Grad-CAM++ regions to gain insights into the decision-making process of AFF-VGG19. Among the 100 selected samples, the model produced 77 meaningful explanations, offering valuable information on the regions it focused on for classification. While this interpretability was advantageous, it came with a slight trade-off in accuracy, resulting in a marginal decrease of 0.77. We attributed this reduction to the presence of irrelevant region suggestions even when the model correctly classified the image. Therefore, future research may further refine the model's interpretability while maintaining its diagnostic performance.

Our study contributes to the growing body of research on DL applications in CAD screening. The combination of feature-fusion and attention mechanisms in AFF-VGG19 demonstrates the potential for improving localisation abilities, making it a promising candidate for CAD diagnosis. Moreover, the high level of agreement with medical experts and competitive diagnostic strength compared to human experts indicate that the model could be a valuable asset in clinical practice. The study results are consistent with the literature compared to studies employing similar datasets for the same purpose (Table 4).

However, we acknowledge some limitations in our study. The dataset was collected from a single institution, and future investigations should include multi-centre data to enhance the generalisability. Additionally, addressing the issue of irrelevant region suggestions in the Grad-CAM++ analysis could further enhance the model's interpretability without compromising the accuracy. Substantial performance improvements may be achieved by experimenting with more sophisticated attention and feature-fusion modules or by substituting the baseline CNN model with more problem-specific approaches, such as the RBG-CNN network [17]. More state-of-the-art pretrained networks can be benchmarked for fine-tuning. However, such experiments would be reasonable, providing that a larger-scale dataset was collected. The study needs to perform external validation to inspect the robustness of the models to acquisition device variations and variations regarding the acquisition parameters. More precise localisation outcomes may also be obtained using alternative post hoc explainability-enhancing methods besides Grad-CAM++. The 17-segment Polar Map can constrain the region of interest for the model and force it to seek important features in reasonable areas. Former studies have suggested this methodology [26]. Finally, the integration of clinical factors is expected to have a significant contribution [30]. Feature selection algorithms can highlight the most vital clinical factors to be combined with the CNN output and provide a more precise diagnosis.

5. Conclusions

In this study, we proposed an innovative and explainable DL method aimed at characterising MPI SPECT Polar Map images in patients with suspected CAD. The cornerstone of our method was an attention-based feature-fusion network (AFF-VGG19) designed to perform accurate diagnoses. To unveil potentially significant regions, we employed the Grad-CAM++ algorithm, contributing to the interpretability of our model. We were pleased to find that AFF-VGG19 demonstrated substantial agreement (89.92%) with medical experts, showcasing its competence in CAD diagnosis. Upon evaluating the model's performance using the ICA findings as a reference, we observed that AFF-VGG19 achieved strong diagnostic capabilities. Our findings validated the utility of DL methodologies, particularly attention-based networks, in the context of CAD screening. The results aligned with the existing literature and offered promising evidence that such models are likely to play a pivotal role in future CAD diagnosis and screening practices.

Author Contributions: Conceptualisation, I.D.A.; Data curation, N.D.P.; Formal analysis, N.D.P., N.P., E.P. and D.J.A.; Investigation, E.P.; Methodology, I.D.A., N.D.P., N.P. and D.J.A.; Project administration, E.P.; Resources, N.P.; Software, I.D.A.; Supervision, E.P. and D.J.A.; Validation, N.D.P.; Visualisation, N.P.; and Writing—original draft, I.D.A. All authors have read and agreed to the published version of the manuscript.

Funding: This research project was supported by the Hellenic Foundation for Research and Innovation (HFRI) under "2nd Call for HFRI Research Projects to support Faculty Members & Researchers" (Project Number: 3656).

Institutional Review Board Statement: Data collection was approved by the ethical committee of the University General Hospital of Patras (Ethical & Research Committee of University Hospital of Patras—protocol number 108/10-3-2022).

Informed Consent Statement: The retrospective nature of the study waived the requirement to obtain informed consent from the participants.

Data Availability Statement: The data of the study are not publicly available due to ethical reasons. However, they can be communicated upon reasonable request.

Conflicts of Interest: The authors declare no conflict of interest.

References

1. Michas, G.; Karvelas, G.; Trikas, A. Cardiovascular disease in Greece; the latest evidence on risk factors. *Hell. J. Cardiol.* **2019**, *60*, 271–275. [CrossRef] [PubMed]
2. Malakar, A.K.; Choudhury, D.; Halder, B.; Paul, P.; Uddin, A.; Chakraborty, S. A Review on Coronary Artery Disease, Its Risk Factors, and Therapeutics. *J. Cell. Physiol.* **2019**, *234*, 16812–16823. [CrossRef] [PubMed]
3. Hajar, R. Risk Factors for Coronary Artery Disease: Historical Perspectives. *Heart Views* **2017**, *18*, 109. [CrossRef] [PubMed]
4. Winzer, E.B.; Woitek, F.; Linke, A. Physical Activity in the Prevention and Treatment of Coronary Artery Disease. *J. Am. Heart Assoc.* **2018**, *7*, e007725. [CrossRef]
5. Takx, R.A.; Blomberg, B.A.; Aidi, H.E.; Habets, J.; de Jong, P.A.; Nagel, E.; Hoffmann, U.; Leiner, T. Diagnostic accuracy of stress myocardial perfusion imaging compared to invasive coronary angiography with fractional flow reserve meta-analysis. *Circ. Cardiovasc. Imaging* **2015**, *8*, e002666. [CrossRef]
6. Canfield, J.; Totary-Jain, H. 40 Years of Percutaneous Coronary Intervention: History and Future Directions. *J. Pers. Med.* **2018**, *8*, 33. [CrossRef]
7. Alexander, J.H.; Smith, P.K. Coronary-Artery Bypass Grafting. *N. Engl. J. Med.* **2016**, *374*, 1954–1964. [CrossRef]
8. Dorbala, S.; Ananthasubramaniam, K.; Armstrong, I.S.; Chareonthaitawee, P.; DePuey, E.G.; Einstein, A.J.; Gropler, R.J.; Holly, T.A.; Mahmarian, J.J.; Park, M.-A.; et al. Single Photon Emission Computed Tomography (SPECT) Myocardial Perfusion Imaging Guidelines: Instrumentation, Acquisition, Processing, and Interpretation. *J. Nucl. Cardiol.* **2018**, *25*, 1784–1846. [CrossRef]
9. Goodfellow, I.; Bengio, Y.; Courville, A. *Deep Learning*; MIT Press: Cambridge, MA, USA, 2016.
10. Apostolopoulos, I.D.; Papathanasiou, N.D. Classification of lung nodule malignancy in computed tomography imaging utilising generative adversarial networks and semi-supervised transfer learning. *Biocybern. Biomed. Eng.* **2021**, *41*, 1243–1257. [CrossRef]
11. Apostolopoulos, I.D.; Papathanasiou, N.D.; Apostolopoulos, D.J. A Deep Learning Methodology for the Detection of Abnormal Parathyroid Glands via Scintigraphy with 99mTc-Sestamibi. *Diseases* **2022**, *10*, 56. [CrossRef]
12. Otaki, Y.; Singh, A.; Kavanagh, P.; Miller, R.J.H.; Parekh, T.; Tamarappoo, B.K.; Sharir, T.; Einstein, A.J.; Fish, M.B.; Ruddy, T.D.; et al. Clinical Deployment of Explainable Artificial Intelligence of SPECT for Diagnosis of Coronary Artery Disease. *JACC Cardiovasc. Imaging* **2022**, *15*, 1091–1102. [CrossRef]
13. Papandrianos, N.; Papageorgiou, E. Automatic Diagnosis of Coronary Artery Disease in SPECT Myocardial Perfusion Imaging Employing Deep Learning. *Appl. Sci.* **2021**, *11*, 6362. [CrossRef]
14. Cheng, J.-Z.; Ni, D.; Chou, Y.-H.; Qin, J.; Tiu, C.-M.; Chang, Y.-C.; Huang, C.-S.; Shen, D.; Chen, C.-M. Computer-Aided Diagnosis with Deep Learning Architecture: Applications to Breast Lesions in US Images and Pulmonary Nodules in CT Scans. *Sci. Rep.* **2016**, *6*, 24454. [CrossRef]
15. Papandrianos, N.; Feleki, A.; Papageorgiou, E. Exploring Classification of SPECT MPI Images Applying Convolutional Neural Networks. In Proceedings of the 25th Pan-Hellenic Conference on Informatics; ACM, Volos, Greece, 26 November 2021; pp. 483–489.
16. Zahiri, N.; Asgari, R.; Razavi-Ratki, S.-K.; Parach, A.-A. Deep Learning Analysis of Polar Maps from SPECT Myocardial Perfusion Imaging for Prediction of Coronary Artery Disease. In Review, 2021. Available online: https://www.researchsquare.com/article/rs-1153347/v1 (accessed on 1 June 2023).
17. Papandrianos, N.I.; Apostolopoulos, I.D.; Feleki, A.; Apostolopoulos, D.J.; Papageorgiou, E.I. Deep Learning Exploration for SPECT MPI Polar Map Images Classification in Coronary Artery Disease. *Ann. Nucl. Med.* **2022**, *36*, 823–833. [CrossRef]

18. Betancur, J.; Hu, L.-H.; Commandeur, F.; Sharir, T.; Einstein, A.J.; Fish, M.B.; Ruddy, T.D.; Kaufmann, P.A.; Sinusas, A.J.; Miller, E.J.; et al. Deep Learning Analysis of Upright-Supine High-Efficiency SPECT Myocardial Perfusion Imaging for Prediction of Obstructive Coronary Artery Disease: A Multicenter Study. *J. Nucl. Med.* **2019**, *60*, 664–670. [CrossRef]
19. Betancur, J.; Commandeur, F.; Motlagh, M.; Sharir, T.; Einstein, A.J.; Bokhari, S.; Fish, M.B.; Ruddy, T.D.; Kaufmann, P.; Sinusas, A.J.; et al. Deep learning for prediction of obstructive disease from fast myocardial perfusion SPECT: A multicenter study. *JACC Cardiovasc. Imaging* **2018**, *11*, 1654–1663. [CrossRef]
20. Arvidsson, I.; Overgaard, N.C.; Astrom, K.; Heyden, A.; Figueroa, M.O.; Rose, J.F.; Davidsson, A. Prediction of Obstructive Coronary Artery Disease from Myocardial Perfusion Scintigraphy Using Deep Neural Networks. In Proceedings of the 2020 25th International Conference on Pattern Recognition (ICPR), Milan, Italy, 10 January 2021; IEEE: London, UK, 2021; pp. 4442–4449.
21. Miller, R.J.H.; Kuronuma, K.; Singh, A.; Otaki, Y.; Hayes, S.; Chareonthaitawee, P.; Kavanagh, P.; Parekh, T.; Tamarappoo, B.K.; Sharir, T.; et al. Explainable Deep Learning Improves Physician Interpretation of Myocardial Perfusion Imaging. *J. Nucl. Med.* **2022**, *63*, 1768–1774. [CrossRef] [PubMed]
22. Otaki, Y.; Tamarappoo, B.; Singh, A.; Sharir, T.; Hu, L.-H.; Gransar, H.; Einstein, A.; Fish, M.; Ruddy, T.; Kaufmann, P.; et al. Diagnostic Accuracy of Deep Learning for Myocardial Perfusion Imaging in Men and Women with a High-Efficiency Parallel-Hole-Collimated Cadmium-Zinc-Telluride Camera: Multicenter Study. *J. Nucl. Med.* **2020**, *61*, 92.
23. Miller, R.J.H.; Singh, A.; Otaki, Y.; Tamarappoo, B.K.; Kavanagh, P.; Parekh, T.; Hu, L.-H.; Gransar, H.; Sharir, T.; Einstein, A.J.; et al. Mitigating Bias in Deep Learning for Diagnosis of Coronary Artery Disease from Myocardial Perfusion SPECT Images. *Eur. J. Nucl. Med. Mol. Imaging* **2022**, *50*, 387–397. [CrossRef] [PubMed]
24. Singh, A.; Miller, R.J.H.; Otaki, Y.; Kavanagh, P.; Hauser, M.T.; Tzolos, E.; Kwiecinski, J.; Van Kriekinge, S.; Wei, C.-C.; Sharir, T.; et al. Direct Risk Assessment From Myocardial Perfusion Imaging Using Explainable Deep Learning. *JACC Cardiovasc. Imaging* **2022**, *16*, 209–220. [CrossRef]
25. Chen, J.-J.; Su, T.-Y.; Chen, W.-S.; Chang, Y.-H.; Lu, H.H.-S. Convolutional Neural Network in the Evaluation of Myocardial Ischemia from CZT SPECT Myocardial Perfusion Imaging: Comparison to Automated Quantification. *Appl. Sci.* **2021**, *11*, 514. [CrossRef]
26. Spier, N.; Nekolla, S.; Rupprecht, C.; Mustafa, M.; Navab, N.; Baust, M. Classification of Polar Maps from Cardiac Perfusion Imaging with Graph-Convolutional Neural Networks. *Sci. Rep.* **2019**, *9*, 7569. [CrossRef]
27. Kaplan Berkaya, S.; Ak Sivrikoz, I.; Gunal, S. Classification Models for SPECT Myocardial Perfusion Imaging. *Comput. Biol. Med.* **2020**, *123*, 103893. [CrossRef] [PubMed]
28. Liu, H.; Wu, J.; Miller, E.J.; Liu, C.; Yaqiang, L.; Liu, Y.-H. Diagnostic Accuracy of Stress-Only Myocardial Perfusion SPECT Improved by Deep Learning. *Eur. J. Nucl. Med. Mol. Imaging* **2021**, *48*, 2793–2800. [CrossRef] [PubMed]
29. Apostolopoulos, I.D.; Papathanasiou, N.D.; Spyridonidis, T.; Apostolopoulos, D.J. Automatic characterisation of myocardial perfusion imaging polar maps employing deep learning and data augmentation. *Hell. J. Nucl. Med.* **2020**, *23*, 125–132.
30. Apostolopoulos, I.D.; Apostolopoulos, D.I.; Spyridonidis, T.I.; Papathanasiou, N.D.; Panayiotakis, G.S. Multi-input deep learning approach for Cardiovascular Disease diagnosis using Myocardial Perfusion Imaging and clinical data. *Phys. Med.* **2021**, *84*, 168–177. [CrossRef]
31. Trung, N.T.; Ha, N.T.; Thuan, N.D.; Minh, D.H. A Deeplearning Method for Diagnosing Coronary Artery Disease Using SPECT Images of Heart. *J. Sci. Technol.* **2020**, *144*, 022–027.
32. Simonyan, K.; Zisserman, A. Very Deep Convolutional Networks for Large-Scale Image Recognition. *arXiv* **2015**, arXiv:1409.1556.
33. Haq, I.U.; Ali, H.; Wang, H.Y.; Lei, C.; Ali, H. Feature Fusion and Ensemble Learning-Based CNN Model for Mammographic Image Classification. *J. King Saud Univ.-Comput. Inf. Sci.* **2022**, *34*, 3310–3318. [CrossRef]
34. Amin, S.U.; Muhammad, G.; Abdul, W.; Bencherif, M.; Alsulaiman, M. Multi-CNN Feature Fusion for Efficient EEG Classification. In Proceedings of the 2020 IEEE International Conference on Multimedia & Expo Workshops (ICMEW), London, UK, 6–10 July 2020; IEEE: London, UK, 2020; pp. 1–6.
35. Tian, C.; Xu, Y.; Li, Z.; Zuo, W.; Fei, L.; Liu, H. Attention-Guided CNN for Image Denoising. *Neural Netw.* **2020**, *124*, 117–129. [CrossRef]
36. Mou, L.; Zhu, X.X. Learning to Pay Attention on Spectral Domain: A Spectral Attention Module-Based Convolutional Network for Hyperspectral Image Classification. *IEEE Trans. Geosci. Remote Sens.* **2020**, *58*, 110–122. [CrossRef]
37. Jetley, S.; Lord, N.A.; Lee, N.; Torr, P.H.S. Learn To Pay Attention. *arXiv* **2018**, arXiv:1804.02391. [CrossRef]
38. Deng, J.; Dong, W.; Socher, R.; Li, L.-J.; Li, K.; Fei-Fei, L. Imagenet: A large-scale hierarchical image database. In Proceedings of the 2009 IEEE Conference on Computer Vision and Pattern Recognition, Miami, FL, USA, 20–25 June 2009; IEEE: London, UK, 2009; pp. 248–255.
39. Krizhevsky, A.; Nair, V.; Hinton, G. The CIFAR-10 Dataset. 2014, 55. Available online: http://www.cs.toronto.edu/kriz/cifar.Html (accessed on 1 June 2023).
40. Krizhevsky, A.; Nair, V.; Hinton, G. CIFAR-100 (Canadian Institute for Advanced Research). Available online: http://www.cs.toronto.edu/kriz/cifar.html (accessed on 1 June 2023).
41. Chattopadhyay, A.; Sarkar, A.; Howlader, P.; Balasubramanian, V.N. Grad-CAM++: Improved Visual Explanations for Deep Convolutional Networks. In Proceedings of the 2018 IEEE Winter Conference on Applications of Computer Vision (WACV), Lake Tahoe, NV, USA, 12–15 March 2018; pp. 839–847.

42. Betancur, J.; Otaki, Y.; Motwani, M.; Fish, M.B.; Lemley, M.; Dey, D.; Gransar, H.; Tamarappoo, B.; Germano, G.; Sharir, T.; et al. Prognostic Value of Combined Clinical and Myocardial Perfusion Imaging Data Using Machine Learning. *JACC Cardiovasc. Imaging* **2018**, *11*, 1000–1009. [CrossRef] [PubMed]
43. Rahmani, R.; Niazi, P.; Naseri, M.; Neishabouri, M.; Farzanefar, S.; Eftekhari, M.; Derakhshan, F.; Mollazadeh, R.; Meysami, A.; Abbasi, M. Precisión diagnóstica mejorada para la imagen de perfusión miocárdica usando redes neuronales artificiales en diferentes variables de entrada incluyendo datos clínicos y de cuantificación. *Rev. Esp. Med. Nucl. E Imagen Mol.* **2019**, *38*, 275–279. [CrossRef] [PubMed]

applied sciences

MDPI

Article

Explainable Deep Fuzzy Cognitive Map Diagnosis of Coronary Artery Disease: Integrating Myocardial Perfusion Imaging, Clinical Data, and Natural Language Insights

Anna Feleki [1], Ioannis D. Apostolopoulos [1], Serafeim Moustakidis [1,2,*], Elpiniki I. Papageorgiou [1], Nikolaos Papathanasiou [3], Dimitrios Apostolopoulos [3] and Nikolaos Papandrianos [1]

[1] Department of Energy Systems, University of Thessaly, Gaiopolis Campus, 41500 Larisa, Greece; annafele1@uth.gr (A.F.); apostolopoulos.john.dim@gmail.com (I.D.A.); elpinikipapageorgiou@uth.gr (E.I.P.); npapandrianos@uth.gr (N.P.)
[2] AIDEAS OÜ, Narva mnt 5, 10117 Tallinn, Estonia
[3] Department of Nuclear Medicine, University Hospital of Patras, 26504 Rio, Greece; nikopapath@upatras.gr (N.P.); dimap@med.upatras.gr (D.A.)
* Correspondence: s.moustakidis@aideas.eu

Abstract: Myocardial Perfusion Imaging (MPI) has played a central role in the non-invasive identification of patients with Coronary Artery Disease (CAD). Clinical factors, such as recurrent diseases, predisposing factors, and diagnostic tests, also play a vital role. However, none of these factors offer a straightforward and reliable indication, making the diagnosis of CAD a non-trivial task for nuclear medicine experts. While Machine Learning (ML) and Deep Learning (DL) techniques have shown promise in this domain, their "black-box" nature remains a significant barrier to clinical adoption, a challenge that the existing literature has not yet fully addressed. This study introduces the Deep Fuzzy Cognitive Map (DeepFCM), a novel, transparent, and explainable model designed to diagnose CAD using imaging and clinical data. DeepFCM employs an inner Convolutional Neural Network (CNN) to classify MPI polar map images. The CNN's prediction is combined with clinical data by the FCM-based classifier to reach an outcome regarding the presence of CAD. For the initialization of interconnections among DeepFCM concepts, expert knowledge is provided. Particle Swarm Optimization (PSO) is utilized to adjust the weight values to the correlated dataset and expert knowledge. The model's key advantage lies in its explainability, provided through three main functionalities. First, DeepFCM integrates a Gradient Class Activation Mapping (Grad-CAM) algorithm to highlight significant regions on the polar maps. Second, DeepFCM discloses its internal weights and their impact on the diagnostic outcome. Third, the model employs the Generative Pre-trained Transformer (GPT) version 3.5 model to generate meaningful explanations for medical staff. Our dataset comprises 594 patients, who underwent invasive coronary angiography (ICA) at the department of Nuclear Medicine of the University Hospital of Patras in Greece. As far as the classification results are concerned, DeepFCM achieved an accuracy of 83.07%, a sensitivity of 86.21%, and a specificity of 79.99%. The explainability-enhancing methods were assessed by the medical experts on the authors' team and are presented within. The proposed framework can have immediate application in daily routines and can also serve educational purposes.

Keywords: fuzzy cognitive maps; particle swarm optimization; convolutional neural networks; classification; feature selection; Grad-CAM; coronary artery disease; natural language processing

Citation: Feleki, A.; Apostolopoulos, I.D.; Moustakidis, S.; Papageorgiou, E.I.; Papathanasiou, N.; Apostolopoulos, D.; Papandrianos, N. Explainable Deep Fuzzy Cognitive Map Diagnosis of Coronary Artery Disease: Integrating Myocardial Perfusion Imaging, Clinical Data, and Natural Language Insights. *Appl. Sci.* **2023**, *13*, 11953. https://doi.org/10.3390/app132111953

Academic Editor: Julio Garcia Flores

Received: 24 September 2023
Revised: 28 October 2023
Accepted: 30 October 2023
Published: 1 November 2023

1. Introduction

1.1. Backdrop

In recent years, ML and DL techniques have achieved unprecedented success in diverse applications, ranging from image recognition to natural language processing (NLP). These powerful algorithms have the potential to revolutionize medical practice, driving

innovation in diagnostics, treatment, and patient care [1]. In particular, the intersection of ML and medicine holds great promise for improving the accuracy and efficiency of diagnosis in complex diseases, such as CAD [2], which is the main problem this paper deals with.

Despite the remarkable strides made by ML and DL in medical applications, their success comes with an inherent drawback—the "black–box" nature of these models [3]. Black–box models are characterized by their complex, high–dimensional architectures, where the relationship between inputs and outputs becomes increasingly inscrutable [4]. While these models demonstrate outstanding predictive capabilities, their lack of explainability poses significant challenges in critical domains, especially healthcare [5]. The opacity of black–box models not only hampers the acceptance of artificial intelligence (AI) solutions in medical practice but also raises concerns related to safety, ethics, and regulatory compliance [3]. Explainability, in the context of ML and DL, refers to the ability to comprehend and interpret the decision–making process of a model [6]. Traditionally, simpler models, such as linear regression and decision trees, offered transparent and understandable insights into their predictions [6]. However, the advent of more sophisticated algorithms, such as deep neural networks, has shifted the focus towards performance optimization at the expense of interpretability [7].

The field of medical diagnosis, and especially CAD diagnosis, heavily relies on the expertise of healthcare professionals, who meticulously analyze medical data, patient history, and other relevant factors to arrive at accurate diagnoses [8]. As AI algorithms are integrated into the diagnostic process, ensuring the transparency of their predictions becomes paramount. Physicians and clinicians demand an understanding of why an AI model arrives at a specific diagnosis to instill confidence in its use and facilitate better–informed clinical decisions [9]. Explainability bridges the gap between AI models' predictive capabilities and human comprehension, fostering trust and facilitating AI adoption in healthcare [5,7]. Moreover, from an ethical perspective, explainability enhances transparency and accountability. The "right to explanation" is an emerging ethical principle, particularly in the context of AI deployment [9]. This principle asserts that individuals have the right to understand the rationale behind AI–driven decisions concerning their health and well–being. In medical practice, this principle not only aligns with regulatory requirements but also safeguards patients' autonomy and informed consent [3].

Amid the growing concern over the black–box nature of AI models, researchers have explored alternative techniques that offer boosted interpretability. Fuzzy Cognitive Maps [10,11], an established method in the realm of soft computing, have emerged as a promising paradigm to address the challenge of explainability in ML and DL applications. FCMs are graph–based models that excel in capturing complex causal relationships in a dynamic system [11]. Comprising a collection of interconnected concepts represented as nodes, FCMs leverage fuzzy logic to model imprecise relationships between these concepts [10,11]. The strengths and directions of connections, represented by weighted edges, enable the representation of expert knowledge and domain expertise, making FCMs particularly suitable for medical applications [12–14]. Recent publications, such as those by Sovatzidi et al. [15–17], have further advanced the field by enabling the processing of images within the FCM framework. They achieved this using transfer learning and K–means clustering, thereby opening new avenues for more transparent and explainable models in medical domains, including CAD.

1.2. Related Studies

The referenced literature encompasses a diverse array of medical cases specifically related to CAD. These cases have been successfully addressed through the application of DL and FCM methodologies. These studies serve as foundational works, illustrating both the capabilities and limitations of existing techniques in CAD diagnostics and treatment planning.

1.2.1. CAD Diagnosis Using CNNs

Papandrianos et al. [7] aimed to develop an explainable DL methodology for the automatic 3–class CAD classification problem (infarction, ischemia, normal) with Single Photon Emission Computed Tomography (SPECT) images. The dataset included 625 patients in stress and rest representation. Data augmentation was utilized to expand the dataset and achieve generalization. The model presented efficient results with 93.3% accuracy and 94.58% AUC, where k–fold cross–validation was used to ensure the model's reliability. Grad–CAM was also utilized as an explainable tool for the classification outcomes of the proposed model.

Papandrianos et al. [18] developed RGB–CNN for two–class CAD classification with SPECT MPI images. A total of 224 patients were included in this study, and they were in stress and rest representation. Transfer learning was employed for comparison reasons against RGB–CNN with benchmark CNN models, like VGG–16, MobileNet, and InceptionV3. RGB–CNN outperformed these, with a 93.47 $\pm$ 2.81% accuracy. Papandrianos et al. [19] explored three CNN architectures for 3–class CAD classification: RGB–CNN, VGG–16, and DenseNet–121. The dataset contained 647 CAD instances in SPECT–MPI format, and data augmentation was performed to increase the number of available instances. RGB–CNN, VGG–16, and DenseNet–121 achieved an accuracy of 91.86%, 88.54%, and 86.11%, respectively. Ten–fold cross–validation was also utilized.

Apostolopoulos et al. [20] explored CNN to classify polar maps into normal and abnormal. The study consisted of 216 patient cases in stress and rest demonstrations, where the polar maps were in both attenuation–corrected (AC) and non–corrected (NAC) formats. VGG–16 was implemented with transfer learning, and 10–fold cross–validation was applied to estimate VGG–16′s performance. Data augmentation was utilized as well. For comparison reasons, semi–quantitative methodologies were used and experts' analyses were performed, and VGG–16 performed best, with accuracy, sensitivity, and specificity values of 74.53%, 75%, and 3.43%, respectively. Semi–quantitative techniques attained 66.20% accuracy. Spier et al. [21] proposed Graph CNN for the automatic classification of myocardial polar maps into normal and abnormal. A total of 946 instances were included in the dataset in stress and rest representations. For further evaluation of the model's performance, a 4–fold cross–validation was developed. Regarding the interpretability of the results, heatmaps were generated that illustrate the region of abnormality in each instance. The proposed model attained 89.9% on rest polar maps and 91.1% on stress polar maps.

Otaki et al. [22] constructed a DL model for the accurate diagnosis of CAD in polar maps. For this research, 1160 patients without known CAD were included in upright and supine positions and only in stress demonstrations. Gender and BMI were also inserted into the dataset as clinical characteristics of patients. For the provision of explainability, Grad–CAM was applied to demonstrate the accountable regions for pathology. Concerning the result, the DL model achieved 82% sensitivity in men and 71% in women. For comparison reasons, the standard SSS (Summed Stress Score) was evaluated, yielding the following values: 75% and 71% for the upright Total Perfusion Deficit (U–TPD), 77% and 70% for the supine (S–TPD), and 73% and 65% in men and women, respectively. Based on the presented results, the study demonstrated significant variations in the diagnostic performance of DL compared to D–SPECT in predicting CAD in men and women. These differences may be attributed to the fact that men and women have different cardiac sizes, and certain factors differ between the genders. For the evaluation of results, leave–one–center–out external validation was applied.

Otaki et al. [23] constructed an explainable DL network from scratch to diagnose obstructive CAD in SPECT MPI images. A total of 3578 patients were included with suspected CAD only in stress representation. Age, gender, and cardiac volumes were fused in the final fully connected layer to enhance the patient's representation of CAD. The DL model performed well with 0.83% AUC against the readers' diagnosis, which produced 0.71% AUC. Ten–fold repeated testing was applied to ensure the reliability of DL's results.

Grad–CAM was applied for the generation of attention maps, highlighting the regions that correspond to the output.

Chen et al. [24] developed a three–dimensional CNN to classify MPI scans into normal and abnormal. A total of 979 instances were included in this study in Cadmium Zinc Telluride (CZT) format and a grayscale model. Grad–CAM was applied to detect the parts contributing to the corresponding prediction. The 3D model attained 87.64% accuracy, where a five–fold cross–validation technique was applied.

1.2.2. CAD Diagnosis Using FCMs

Khodadadi et al. [12] developed an FCM for the diagnosis of the risk of ischemic stroke. A non–linear Hebbian learning method was applied for FCM training to enhance its efficiency. The dataset included a total of 100 cases. The model achieved an overall accuracy of $93.6 \pm 4.5\%$ when using 10–fold cross–validation. The performance of the model was significantly improved with the incorporation of expert knowledge and fuzzy logic. For comparison reasons, Support Vector Machine (SVM) and K–nearest neighbors were developed, attaining accuracies of 86% and 80.2%, respectively.

Apostolopoulos et al. [13] employed a State Space Advanced FCM (AFCM) model and incorporated a rule–based mechanism to enhance the knowledge of the system and its interpretability for the automatic, non–invasive diagnosis of CAD. The authors enhanced AFCM by utilizing advanced state equations, applied SigmoidN as an activation function, which has been applied in different studies [24], and constructed the proposed model RE–AFCM. A total of 303 patient cases were included in this study, consisting of 116 healthy cases and 187 pathological cases. The authors decided to integrate thirty input concepts that best demonstrate patient status concerning CAD diagnosis along with one output concept. The dataset attributes correspond to the factors influencing the diagnosis of CAD. They concluded that the advanced methodologies increased the performance of the model by 7%. RE–AFCM outperformed traditional FCM and ML algorithms, and SigmoidN performs better than Sigmoid. Regarding the results, RE–AFCM attained 85.47% accuracy, with 89.3% sensitivity, 79.3% specificity, and 87.43% and 82.14% for PPV and NPV, respectively.

Apostolopoulos et al. [14] developed an Medical Decision Support System (MDSS), where FCM was applied for the prediction of CAD. This study was an enhancement of previous work, and a total of 303 patient cases were included, including 116 healthy cases and 187 pathological cases. The stenosis of the coronary artery was the only criterion for the labeling of instances. The authors decided to include thirty input concepts that represent patients regarding CAD diagnosis, along with one output concept. The proposed model achieved 78.2% accuracy, 83.96% sensitivity, 68.97% specificity, 81.34% Positive Predictive Value (PPV), and 72.73% Negative Predictive Value (NPV) and outperformed traditional classification algorithms by at least 2%. Based on the fact that the MDSS was not trained on the corresponding dataset, the extracted results are efficient.

1.3. Contribution of this Study

The existing body of literature in the realm of CAD diagnosis through Machine Learning (ML) techniques, particularly CNNs and FCMs, has made noteworthy advancements. However, these contributions often fall short of addressing the critical issue of explainability, thereby limiting their practical utility in clinical settings. The "black–box" nature of such models poses a significant barrier to their adoption by healthcare professionals who require transparent decision–making processes for ethical and practical reasons.

In light of these limitations, the present study introduces a groundbreaking methodology, termed DeepFCM, which aims to bridge this gap by offering a truly transparent and explainable model for CAD diagnosis. Unlike existing models, DeepFCM is designed to integrate both imaging data, specifically MPI polar maps, and tabular clinical data. This multi–modal approach not only enhances the model's diagnostic accuracy but also its interpretability. The cornerstone of DeepFCM's transparency lies in its three–pronged approach to explainability: (i) Visual explainability: The model incorporates an integrated

Gradient Class Activation Mapping (Grad–CAM) algorithm, which illuminates the significant regions within the MPI polar maps. This feature provides clinicians with a visual guide to the areas of interest that influenced the model's decision, thereby enhancing its transparency. (ii) Weight disclosure: DeepFCM goes a step further by revealing the internal weights and their corresponding influence on the diagnostic outcome. This level of transparency is instrumental in fostering trust and facilitating the model's adoption in clinical practice. (iii) Textual explanation: To bridge the gap between machine–based reasoning and human comprehension, the model employs the state–of–the–art Generative Pre–trained Transformer (GPT) 3.5 to generate coherent, meaningful, and human–readable explanations. This feature serves as a valuable tool for medical professionals, aiding them in making well–informed clinical decisions.

2. Materials and Methods

2.1. Coronary Artery Disease Dataset

2.1.1. Data Acquisition

Between 16 February 2018 and 28 February 2022, the Department of Nuclear Medicine at the University Hospital of Patras conducted a study involving 2036 consecutive patients who underwent gated–SPECT MPI using 99mTc–tetrofosmin. They employed two–hybrid SPECT/CT gamma–camera systems (Varicam, Hawkeye, Infinia, Hawkey–4, GE Healthcare) for MPI. Attenuation correction (AC) based on computed tomography was applied to stress and rest images for all patients. Among these patients, 506 individuals underwent ICA within sixty days of MPI for further examination. After excluding twenty patients due to inconclusive MPI results or missing ICA reports, the final study population consisted of 594 patients, with 43.82% showing CAD–positive results.

The ethical committee of the University General Hospital of Patras approved the data collection process (Ethical and Research Committee of the University Hospital of Patras, protocol number 108/10–3–2022). As this study was retrospective in nature, informed consent from the participants was not required. All data–related procedures were conducted anonymously and in accordance with the Declaration of Helsinki. The diagnostic results of MPI SPECT were provided by three experienced nuclear medicine physicians, who independently inspected the polar maps and resolved any discrepancies through consensus.

The raw image data were tomographically reconstructed on a dedicated workstation (Xeleris 3, GE Healthcare, Chicago, IL, USA) using the Ordered Subset Expectation–Maximization (OSEM) algorithm with two iterations and ten subsets. Subsequently, a low–pass filter (Butterworth) was applied with specific parameters for stress and rest images. The dedicated software (Xeleris 3.0513) automatically generated polar maps, which are 2D circular representations summarizing the results of the 3D tomographic slices. These polar maps were saved in Digital Imaging and Communications in Medicine (DICOM) format for further processing.

2.1.2. Image Data Preprocessing

In the domain of medical image analysis, image preprocessing holds immense significance as it serves to enhance the quality of DICOM images before embarking on further analysis [25]. Among the essential transformations applied, the utilization of color maps stands out as a key technique to convert grayscale images into visually informative colored representations. This enables the visualization of distinct structures within the image, such as bones and soft tissue, by assigning different colors to various anatomical elements. In the realm of medical imaging, where accurate identification and differentiation of structures are paramount, color maps prove to be an invaluable aid [7].

To execute the application of color maps, widely used libraries like Matplotlib offer a diverse selection of color maps to suit specific requirements. In the context of this study, each patient's data yield four polar maps, each corresponding to different conditions, capturing information with and without attenuation correction during rest and stress states. These four polar maps are then thoughtfully consolidated into a single Joint Photographic

Experts Group (JPEG) image format, preparing them for input into the model, enabling more in–depth analysis and interpretation. The transformation of the image via color maps serves an additional purpose, converting the visual representation into a numerical array format. This numerical representation unlocks the potential for conducting various numerical operations, such as filtering, segmentation, and registration, on the image data. It facilitates advanced analytical techniques and computational methodologies to extract meaningful insights from medical images [7].

In light of DL models' prevalence in modern medical image analysis, proper normalization of the image data becomes paramount. This step ensures that the image data are brought within a consistent range, avoiding issues arising from variations in scales and intensity. Given that DL models are highly sensitive to the input data's scale, normalization becomes an indispensable preprocessing step [18]. Two commonly employed normalization techniques include dividing the image values by their maximum value or performing subtraction of the mean and division by the standard deviation [2].

2.1.3. Clinical Data Preprocessing

High–dimensional data analysis is a challenge for researchers and engineers in the fields of ML and data mining algorithms. Feature selection provides an efficient approach to dealing with this problem by removing redundant features, which uses less computation time, enhances learning accuracy, and provides a more comprehensive dataset [26]. In feature selection, a subset of an original dataset is acquired that includes the most relevant features of the dataset [27].

Feature selection was conducted in this paper based on a previous study of the research team at EMERALD [26], where it was applied for CAD classification using clinical data and expert diagnosis. More specifically, five ML algorithms were applied to the dataset, and each ML algorithm generated a subset. This procedure was conducted both with input from expert assessments and doctors and without. To determine the optimal feature set for each algorithm, three feature selection algorithms have been developed: forward sequential feature selection, backward sequential feature selection, and genetic algorithms. An assessment of performance was conducted using standard metrics to detect the most effective feature set. In our study, the subset with the best performance metrics from the research study [26] was utilized and was named the optimal subset.

2.2. Deep Fuzzy Cognitive Map Model

Our proposed DeepFCM model includes the combination of the FCM, CNN, PSO, Grad–CAM, and NLP, along with expert knowledge. The FCM handles the clinical data, and PSO is responsible for the calculation of the weight matrix, which includes the interconnections among concepts. The CNN's role involves handling image data by extracting predictions for each case study and providing extra input to the FCM model. Grad–CAM interprets CNN predictions, and NLP evaluates the total process. The DeepFCM model combines the clinical data with the CNN's output, and the whole process is demonstrated in Figure 1.

2.2.1. Fuzzy Cognitive Maps

FCMs are soft computing tools that are a combination of fuzzy logic and neural networks [13]. FCMs were introduced by Kosko [10] as an advanced version of cognitive maps with the application of fuzzy casual functions with real numbers to the connections. The FCM is a fuzzy diagram that transforms a system into concepts, where each concept represents a variable, a state, or a characteristic of a system. Between concepts, there are weight values/interconnections that demonstrate how the concepts interact with each other. There are three types of weight values. More specifically, $w_{ij} = 0$ means that there is no causality between concepts, $w_{ij} > 0$ indicates a positive relationship, and $w_{ij} < 0$ determines a negative causality. Expert knowledge defines the number of nodes and the initial values of the interconnections among concepts. An FCM can be described by a weight matrix that

includes all the interconnections among concepts and the state vector, which has the values of concepts [10]. The value of each concept is influenced by the values of the connected concepts with the corresponding causal weights and by its previous state. The sum of the concept values of nodes together demonstrates the state vector of the system.

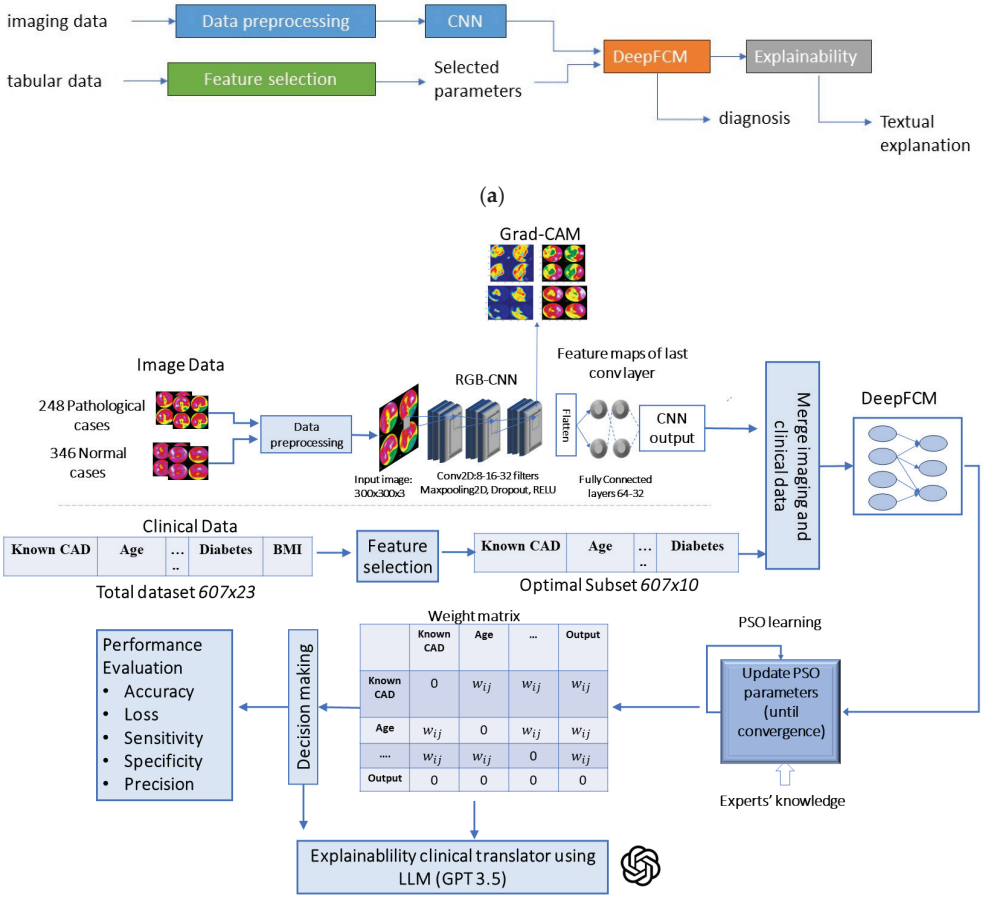

Figure 1. Figure of proposed methodology for DeepFCM: (**a**) high–level flowchart and (**b**) detailed flowchart.

Regarding the FCM inference and the evolution of the system, FCM calculates iteratively the state of concepts until it reaches the equilibrium point by multiplying the vector of concepts' values with the weight matrix [14,28,29]. To normalize the FCM–predicted values of concepts into a specific range after multiplication, a transfer function is used, where a sigmoid, bivalent, or trivalent function is applied. The sigmoid function is demonstrated in type (2). The equation is presented below.

$$A_i^{(K+1)} = f\left(A_i^{(K)} + \sum_{i,j}^{N} w_{ij} A_j^{(K)}\right) \quad (1)$$

where $A_i^{(K+1)}$ is the value of the concept iteration $(K+1)$, $A_j^{(K)}$ is the concept at the iteration (K), and f is the transfer function.

$$f(x) = \frac{1}{1+e^{-x}} \tag{2}$$

In the generated weight matrix, the diagonal has zero values since every concept influences other concepts but not itself [14].

After multiple iterations, the FCM could lead to one of the following scenarios:

i. The equilibrium point is where the current states of the FCM have converged to steady values.
ii. Limit cycle behavior, where the final state of the FCM, which indicates the outputs, in each iteration takes specific values.
iii. Chaotic behavior, where each concept takes random and unstable values.

2.2.2. RGB–CNN

A CNN indicates an algorithm that mimics humans' decision making. A CNN consists of input, hidden, and output layers. The hidden layer incorporates convolutional, pooling, dropout, and fully connected layers and aims to extract patterns from image data. A CNN can automatically extract features by employing a variety of filters on the input images, and via an advanced learning process, the most significant pixel values are retained. CNNs have extracted remarkable results from previous medical studies [2,7,18,19].

The convolutional layer is the first layer of a CNN, and its primary functionality is the creation of a feature map, which contains an abstract representation of the input image [2]. Pooling layers are applied after every convolutional layer to down–sample the data and reduce the computational complexity of the network. Pooling layers select the maximum or average value within a local window to retain the most important features [2]. Concerning the dropout layer, it helps to reduce unnecessary pixels and prevents overfitting. The dropout layer nullifies random pixel values to decrease the computational time of the training process. A flattening layer is applied next to convert multi–dimensional data into a vector. The last layer of the CNN is a sequence of fully connected layers, where each node is connected to the preceding one leading to the network's final prediction [7]. In most CNN models, the Rectified Linear Unit (ReLU) is utilized in convolutional and fully connected layers as an activation function, and sigmoid or softmax are used for output layers for binary and multiclass classification problems, respectively [7,30,31].

After a thorough exploration process, we concluded with the ideal combination of parameters regarding pixel values, batch size, dropout rate, and number of nodes and layers of convolutional and fully connected layers. The proposed RGB–CNN rescales the input images to 300×300 pixels and consists of three convolutional layers with 8,16, and 32 filters (kernels) accordingly. After each convolutional layer, there is a max pooling with a 2×2 kernel size and a dropout layer with a drop rate of 0.2. Next, the flattening layer transforms multi–dimensional data into vectors to prepare data for fully connected layers. Regarding the fully connected layers, we selected two layers with 64 and 32 nodes, accordingly. The output layer is a single–node layer with a sigmoid activation function since we dealt with a two–class classification problem. Data augmentation was also utilized to increase the dataset size by generating altered versions of the original images. In our research, we applied rescaling to all images as a normalization technique, and regarding data augmentation, we employed width_shift_range = 0.1, height_shift_range = 0.1, shear_range = 0.1, and zoom_range = 0.1 to prevent overfitting and develop a generalizable model [2,7,32].

2.2.3. Integration of CNN Predictions and Clinical Data to Construct the DeepFCM Model

The FCM was initially designed using clinical characteristics as the input, regarding patient status. We strengthened the FCM's performance by introducing CNN predictions

as additional input and exploiting the automatic feature extraction process. This hybrid approach leverages the strengths of the clinical data, where feature selection was employed to preserve the most important features and CNN—-derived insights from medical images while extracting high—-dimensional features. This integration constructs an innovative approach that provides a more comprehensive and accurate CAD diagnosis and provides a holistic view of patients' conditions to nuclear experts. DeepFCM is more likely to detect risk factors at an early stage and reduce diagnostic errors.

2.2.4. Initialization of DeepFCM Weights by Experts

Regarding the initialization among interconnections of concepts in an FCM, linguistic values can be provided by nuclear experts in a fuzzy set format. In general, fuzzy sets deliver uncertainty and mimic human knowledge. Traditionally, in binary logic, a statement can be true or false, and in set theory, an element can belong to only one set [32]. Fuzzy sets introduce partial truth, which is defined by human language and decisions. Fuzzy sets were defined by Zadeh [33], and they have been useful in pattern recognition and medical diagnosis.

Membership functions (MFs) are the building blocks of fuzzy set theory since they introduce the degree of fuzziness in a fuzzy set [34]. MFs can be developed in various shapes and should be compatible with the problem since it affects a fuzzy inference system. The different shapes could be triangular, trapezoidal, Gaussian, etc. The membership values, regardless of the shape, should depend on the range [0, 1]. The membership function which represents a fuzzy set is defined as μA, and for an element x of set X, the term $\mu A(x)$ is the membership degree of element x in set X [35]. In Figure 2, we can see a demonstration of a fuzzy set with a triangular membership function. The triangular membership function is characterized by a set of three parameters, denoted as $\{a, b, c\}$, where c represents the base of the triangle and a and b determine the height [35]. These parameter values are established based on experts' knowledge.

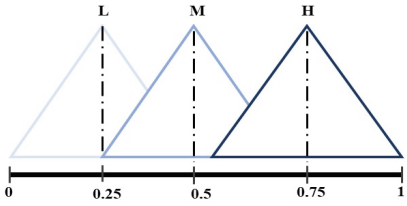

Figure 2. Demonstration of three fuzzy sets: low, medium, and high.

In this research study, the linguistic values provided by nuclear experts were as follows: Very Weak (VW) with a range [0, 0.3], Weak (W) with a range [0.15, 0.5], Medium (M) with a range [0.35, 0.65], Strong (S) with a range [0.5, 0.85], and Very Strong (VS) with a spectrum [0.7, 1]. The linguistic values were transformed into numerical ranges to be utilized in the algorithm.

2.2.5. DeepFCM Learning, Weight Initialization, and Update of Weights with PSO

In FCMs, the weight matrix includes all the interconnections among concepts [10]. The initial values of the weight matrix are randomly initialized or are based on linguistic values suggested by nuclear experts. In our case, the relationship values among meaningful concepts were initialized based on expert knowledge, as displayed in Table 1. The initial values of the rest of the interconnections were randomly selected from the range $[-1, 1]$.

Table 1. Representation of the suggested weights between meaningful input–input concepts and input–output concepts obtained from nuclear experts.

Relationship among Concepts	Linguistic Value Provided by Experts
Known CAD→Output	S
Previous PCI→Output	W
Diabetes→Output	S
Chronic Kidney Disease→Output	W
Angina Like→Output	S
ECG→Output	M
Male→ECG	W
Expert Diagnosis→Output	VS
CNN→Output	S

Particle Swarm Optimization (PSO) is a population–based algorithm that includes a collection of individuals to search for optimal regions in the search space. PSO utilizes a small number of parameters [36]. The population is called a swarm, and the individuals are called particles. Every particle in the system can move with a defined velocity within a search space, and it preserves the best position that has been encountered. Once the global best position has been calculated, it is shared with all the particles in the group [37].

In the present study, PSO was employed to handle the computation of the weight matrix and adapt the interconnections among concepts by minimizing the error of the objective function. For every particle, a weight matrix is generated, and the one that produces the minimum error when comparing the actual output with the predicted is forwarded to the testing phase. The weight matrix is critical for the FCM's performance, and the desirable characteristics of the weight matrix include stability and alignment with the dataset's characteristics while producing minimal error.

2.2.6. DeepFCM Inference—Natural Language

The concluding weight matrix, along with the concept vector and the clinical characteristics along with RGB–CNN's prediction, were inserted into a robust NLP system (GPT–3.5) to discuss the results and verbalize them in natural language. Grad–CAM was also employed in this research to interpret the RGB–CNN predictions and transform them from a black–box model to a more comprehensive model with transparent inner computations related to CAD diagnosis in polar map images.

GPT–3.5, as a Large Language Model, is trained with neural network methodologies on billions of words derived from articles, books, and internet content, and it learns the relationship between words and generates text by following patterns observed in sentences from its training data. In the context of inference, when a user inserts a prompt, GPT–3.5, drawing from its existing knowledge and the patterns that it has extracted, generates a response in human–like language [38–40].

2.3. Explainability–Enhancing Methods

2.3.1. Self–Explainable Aspects of DeepFCM

At the core of an FCM lies the weight table [10], a fundamental component that defines the strength of relationships between interconnected concepts. The weight table serves as a quantitative representation of domain knowledge and expertise, either contributed by domain experts or inferred from historical data [14]. Each element in the weight table specifies the degree of impact that one concept exerts on another, reflecting the causal influence in the cognitive mapping.

The weight table's explainable nature stems from its intuitive and comprehensible structure. Domain experts can easily comprehend the impact of each concept on others, as the weight values are interpretable and can be expressed in linguistic terms, such as "strong", "weak", "positive", or "negative". This transparency facilitates expert involvement in model development and validation, providing a valuable opportunity to refine and

fine–tune the model based on domain–specific insights. Furthermore, the weight table's transparency fosters the detection of influential concepts, as high weights indicate strong causal connections. This feature becomes particularly relevant in critical applications such as medical diagnosis, where identifying significant factors affecting the outcome is essential for effective decision making.

Another critical aspect contributing to the inherent explainable nature of FCMs lies in their representation of interconnections between concepts. The directed edges between nodes in an FCM indicate the causal relationships and the direction of influence from one concept to another. These connections represent the cause–and–effect dependencies that govern the dynamics of the system under consideration. By visually examining the graph structure of the FCM, domain experts can identify complex causal pathways, feedback loops, and interdependencies between concepts. This understanding not only enhances the model's transparency but also facilitates the identification of potential bottlenecks, vulnerabilities, or reinforcing factors within the system. Moreover, the causal relationships depicted by the interconnections in FCMs allow for "what–if" analyses, where experts can assess the impact of hypothetical changes to specific concepts on the overall system behavior. Such analyses promote risk assessment and strategic decision making in various applications, including policy planning, environmental management, and healthcare interventions.

In comparison to other complex ML models, FCMs offer several distinct advantages in terms of interpretability [28]. Neural networks, for example, are notorious for their black–box nature, as the intricate relationships within their hidden layers are challenging to unravel. In contrast, FCMs' explicit representation of causal connections fosters a holistic understanding of the decision–making process, enabling domain experts to assess model predictions with confidence and identify any potential biases or anomalies. Similarly, decision trees, although interpretable, may lack the expressive power to capture complex and uncertain relationships among variables. FCMs, however, excel at dealing with such complexities through the use of fuzzy logic, allowing for continuous and gradable influence between concepts [10].

2.3.2. Natural Language Processing Models

While FCMs offer transparency in the form of weight tables and concept interconnections, translating these numerical outputs into easily understandable language can be a formidable task for domain experts, especially in the medical domain. GPT–3.5 is a language model developed by OpenAI [40]. It is designed for natural language understanding and generation tasks. The model has been trained on a wide range of internet text to be able to provide informative and contextually relevant responses to user prompts [41]. GPT–3.5 is capable of understanding and generating human–like text, making it a versatile tool for various applications, including answering questions, assisting with writing, tutoring, and more [38,42].

To use GPT–3.5 for generating medical diagnoses from classification models, we integrated it into the DeepFCM framework, which incorporates both GPT–3.5 and the classification model. The process involves the following steps [38]:

- Train the classification model: Firstly, we developed a specialized classification model specifically for medical diagnosis, as explained. This model is trained on medical data with labeled diagnoses to accurately classify patients' conditions based on their symptoms and other relevant information.
- Integrate GPT–3.5: After training the classification model, we integrated GPT–3.5 into the medical information system. OpenAI provides an API that allows developers to access GPT–3.5 programmatically and send prompts for generating responses.
- Prompt generation: When a user enters medical information, such as symptoms or test results, into the system, the classification model generates a diagnosis that involves the final classification output, the final output vector, and the final weights of the DeepFCM model. These components are used as a prompt for GPT–3.5.

- Obtain response: GPT–3.5 will process the prompt and generate a response in natural language. This response could be a human–readable explanation of the diagnosis provided by the classification model, additional information about the condition, potential treatment options, or other relevant insights.
- Present results to users: We displayed the generated response to the user, helping healthcare professionals understand the reasoning behind the diagnosis and make informed decisions regarding patient care.

2.3.3. Gradient Class Activation Mapping (Grad–CAM)

Grad–CAM was introduced by Selvaraju et al. [43,44]. It is an interpretation method that provides insights into the decision–making process of CNNs by visualizing the important regions of an input image that contribute most significantly to a specific classification decision. In Grad–CAM, the gradients of the target class score with respect to the feature maps of the final convolutional layer are used to determine the importance of each spatial location within the feature maps [43]. These gradients are averaged to obtain the final class activation map, highlighting the regions that strongly influence the CNN's decision for a particular class. Although Grad–CAM provides valuable localization information, it has limitations when dealing with multiclass tasks, i.e., distinguishing between different object categories in a single image. It tends to emphasize only the most dominant object category, failing to capture intricate details in other classes [45,46]. In the present study, Grad-CAM was adapted to provide visual explanations of polar map images.

2.4. Experiment Setup

In terms of hardware and software specifications, the experiments were conducted on a Dell G15-5515 laptop with an AMD Ryzen™ 7 5800H Mobile (20 MB total cache, 8 cores, 16 threads), with an operating system Windows 11 Home Edition. The available laptop consists of 16 GB RAM with 2 x 8 GB, DDR4, 3200 MHz, and an NVIDIA GeForce RTX™ 3060, 6 GB GDDR6, 3 DP card. Regarding the coding process, we employed Python 3.9.0, utilizing TensorFlow 2.10.1 and Keras 2.10. To handle our dataset, the OpenCV library was employed, and for dataset splitting and result computation, scikit–learn was utilized. An investigation was applied through a series of experiments to conclude the suggested architectures. This involved evaluating various architectures for FCM and PSO parameters.

Commonly employed performance metrics were utilized in this study, like accuracy, loss, sensitivity, specificity, and precision, to assess the effectiveness of the proposed DeepFCM architecture. Accuracy denotes the ratio of correctly classified instances to the total number of instances. Loss indicates the error between predicted and actual values. Sensitivity and specificity indicate the true positives (TP) and true negatives (TN) accordingly. Precision is the ratio of the number of true positives to the total number of positive predictions. These metrics offer a well–rounded assessment of the model's capabilities, addressing both the classification accuracy and its ability to correctly identify CAD–positive and CAD–negative cases [2,19].

Regarding ensuring our model's robustness, k–fold cross–validation was performed, where k represents the number of partitions into which the dataset is divided [47]. In our case, we divided the dataset into 10 partitions, of which 9 were utilized as training and 1 as testing. This process was repeated until each partition had been utilized for testing. With the application of k–fold cross–validation, overfitting can be avoided and generalization can be ensured [47]. To reduce redundant training iterations, early stopping was applied. Early stopping is a regularization technique that is utilized in the CNN training process to prevent overfitting and improve generalization error and overall accuracy as well. Early stopping enhances the training process and minimizes computation time. Moreover, it inspects the generalization error that is calculated during the training process and stops the training [48].

3. Results

3.1. Classification Results

The DeepFCM methodology achieved an accuracy of 83.07%, with a sensitivity of 86.21% and a specificity of 79.99% (refer to Table 2). For the sake of comparison, we also provide the results of the standalone RBG–CNN model, which solely processes the images. Additionally, we showcase the performance of DeepFCM when it utilizes the full feature set, rather than just the selected features. We further present the diagnostic yield of doctors, which is based on their visual inspection of the polar maps and consideration of the clinical data. Readers need to note that the benchmarks for all these comparisons are the results from invasive coronary angiography.

Table 2. Comparison of results among expert diagnosis, RGB–CNN applied to images only, and DeepFCM applied to the optimal subset and total dataset.

Run	Accuracy	Loss	Sensitivity	Specificity	Precision
Expert diagnosis	78.91	0.21	77.9	79.7	75.09
RGB–CNN	75.42 ± 4.54	0.47	80.53	66.38	66.39
DeepFCM optimal subset	83.07 ± 4.72	0.17	86.21	79.99	81.78
DeepFCM all features	76.1 ± 5.52	0.24	77.79	72.78	71.67

It is demonstrated that DeepFCM applied to the optimal subset performed remarkably and achieved higher performance metrics. The integration of both imaging and clinical data surpassed the RGB–CNN model and expert diagnosis. Furthermore, feature selection enhanced the results by leading to a more effective representation of the dataset, as we can see by comparing the 83.07% accuracy with the optimal subset and 76.1% with the total dataset. The results showcase the promising potential of the hybrid DeepFCM model. The proposed model, DeepFCM, applied to the optimal subset attained average accuracy, with a mean of 83.07% and a small standard deviation of ±4.72%. The low loss value of 0.17 reflects the model's robust convergence during training. The sensitivity of 86.21% and specificity of 79.99% signify its competence in identifying CAD–positive and CAD–negative case studies, respectively. Moreover, a precision of 81.78% highlights the model's capability to accurately classify true positive cases.

In Table 3, we demonstrate the interconnection among concepts in the first column, the range of values provided by experts for the initialization of interconnection to be randomly selected in the second column, and the weight value that was produced from DeepFCM for the according interconnection in the third column. We can observe that the DeepFCM applied to the optimal subset generated efficient results that are close to the initial range with small deviations.

Table 3. Presentation of extracted ranges for the relationship between concepts produced from the DeepFCM model applied to the optimal subset and comparison with expert knowledge.

Relationship of Concepts	Transformed Linguistic Values to Ranges	Produced Values from DeepFCM
Known CAD→Output	[0.5, 0.85]	0.68 ± 0.08
Previous PCI→Output	[0.15, 0.5]	0.34 ± 0.09
Diabetes→Output	[0.5, 0.85]	0.63 ± 0.1
Chronic Kidney Disease→Output	[0.15, 0.5]	0.32 ± 0.009
Angina Like→Output	[0.5, 0.85]	0.67 ± 0.12
ECG→Output	[0.35, 0.65]	0.43 ± 0.08
Male→ECG	[0.15, 0.5]	0.17 ± 0.1
Expert Diagnosis→Output	[0.7, 1]	0.88 ± 0.1
CNN→Output	[0.5, 0.85]	0.75 ± 0.09

3.2. Interpretation Results

3.2.1. Grad–CAM

Regarding explainability, Grad–CAM was utilized in this research to provide interpretability to the RGB–CNN predictions. The Grad–CAM results were evaluated by a nuclear medicine specialist to strengthen the reliability of the results. For the implementation of Grad–CAM, the feature maps were extracted from the last convolutional layer of the RGB–CNN model and inserted into the Grad–CAM for the generation of heatmaps. The heatmaps demonstrate the impact of each pixel on the final prediction of RGB–CNN. In this study, the colormap entitled Jet was utilized, obtained from the OpenCV library, where low–impact pixel values are colored in blue and high–impact values are colored in red, as seen in Figure 3. Based on nuclear medicine experts, the Grad–CAM results offer interpretability and transparency of RGB–CNN's inner computations, regarding CAD diagnosis.

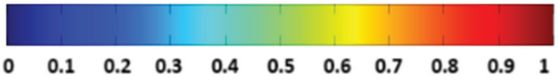

Figure 3. Jet colormap color range demonstration.

In Figure 4, we demonstrate the Grad-CAM application to four pathological case studies, and in Figure 5, four normal case studies, related to CAD diagnosis. Regarding examples a and b, they correspond to correctly predicted instances, while c and d refer to cases that were falsely predicted. The different colors specify the importance of pixels, demonstrating the impact of the CNN classifier on individual pixels. Grad–CAM identifies the regions of interest and colors them in red. We observe that the Grad–CAM has provided exceptional and comprehensive results, where it correctly highlighted and detected the regions of interest.

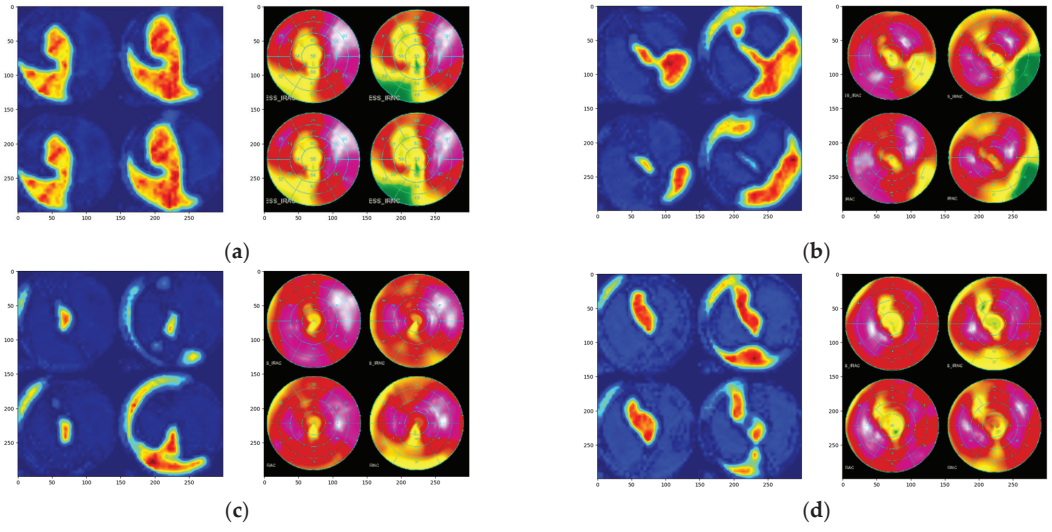

Figure 4. Representation of Grad–CAM application to pathological polar maps: (**a**) first TP case study, (**b**) second TP case study, (**c**) first False Positive (FP) case study, (**d**) second FP case study.

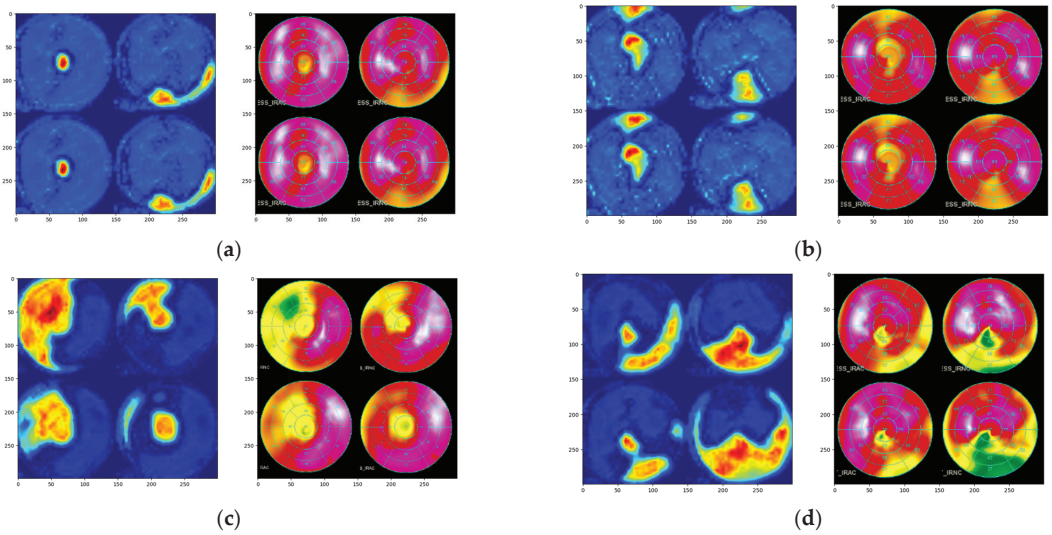

Figure 5. Representation of Grad–CAM application to normal polar maps: (**a**) first TN case study, (**b**) second TN case study, (**c**) first False Negative (FN) case study, (**d**) second FN case study.

3.2.2. NLP

In relation to NLP processing, we present two case studies with the following clinical characteristics. In the first case, the patient has no documented history of CAD, diabetes, or chronic kidney disease. There is no record of the patient having undergone Percutaneous Coronary Intervention (PCI), and the Electrocardiogram (ECG) results are normal. However, the patient exhibits symptoms related to angina. The patient is a male over 40. Both medical experts and the trained RGB–CNN correctly classified this instance as pathological. In the second case, the patient does not have any known history of chronic kidney disease or angina and has no record of having undergone an ECG procedure. Nevertheless, the patient displays symptoms associated with previous CAD, PCI, and diabetes. Additionally, the patient is a male over the age of 40. Both medical professionals and RGB–CNN accurately diagnosed the patient with CAD. The authors introduced the case studies into GPT–3.5 by creating a text prompt, as shown in Figure 6. This prompt includes a description of our proposed system and allows NLP to evaluate the DeepFCM's performance, the produced concept vector, and the clinical characteristics, regarding the first case study.

> *You are a Fuzzy Cognitive Map explainability-enhancing AI tool. Your task is to make doctor-friendly interpretations of FCM outputs. (Analysis of input concepts). Here is the final weight matrix, which shows the weights between each input concept and the output: 0.82, 0.57, 0.59, 0, 0.44, 0.43, −0.12, −0.42, 0.93, 0.91. A user will give you the initial values of each concept and the predicted class. You must give them a meaningful and informative explanation of the decision, based on the values of the input concepts and the weight matrix. Focus more on the concepts that have non-zero values. Avoid using the weight values in numbers.*

Figure 6. Representation of text prompt applied to GPT–3.5 regarding the first case study.

In Figures 7 and 8, we present the texts generated by GPT–3.5 for the two case studies accordingly, where GPT–3.5 provided a detailed analysis of the relationship of each clinical characteristic with the output. We can observe that the produced texts offer nuclear experts an interpretable and thorough demonstration of patient status and provide the logic behind DeepFCM's predictive capabilities. GPT–3.5 facilitates the transformation of DeepFCM into a transparent and trustworthy tool suitable for integration into the decision–making process for CAD diagnosis.

Based on the input concept values you provided, it seems that the patient does not have a history of CAD or PCI. The patient does not have diabetes or chronic kidney disease. However, they do experience angina-like pain, which could be a symptom of CAD. The patient's ECG result is not mentioned, so we cannot determine its impact on the diagnosis. The patient is male, and their age is not specified to be below 40 years. The expert diagnosis and the polar map classification are both positive, indicating that the human expert and the CNN model predict the presence of CAD. This aligns with the output class of 1, which suggests that the patient is indeed suffering from CAD. It is important to note that the weight matrix values indicate the strength of the relationships between the input concepts and the output class, but they are not directly interpretable in verbal language. Instead, we focus on the presence or absence of certain input concepts and their overall impact on the diagnosis. In this case, the presence of angina-like pain, positive expert diagnosis, and positive polar map classification contribute to the diagnosis of CAD.

Figure 7. Demonstration of GPT–3.5 results regarding the first case study.

Based on the given input concept values and the weight matrix, the FCM predicts that the patient is suffering from CAD. Let's analyze the contributing factors. The presence of Known_CAD, Previous_PCI, and Diabetes all have positive weights, indicating that these factors increase the likelihood of CAD. Known_CAD suggests that the patient has a history of CAD, while Previous_PCI suggests they have undergone a Percutaneous Coronary Intervention. The presence of Diabetes is also known to be a risk factor for CAD. On the other hand, Chronic_kidney_disease and Angina_like have zero weights, implying that they do not significantly influence the prediction. Chronic_kidney_disease is not considered a strong indicator of CAD in this model, and Angina_like, although related to angina symptoms, does not have a strong impact on the prediction. The absence of ECG, Male concept, and Age < 40 also have zero weights, suggesting that they do not play a significant role in determining the presence of CAD in this particular case. The Expert_diagnosis and Polar Map classification are both positively weighted, indicating that they contribute to the prediction of CAD. The Expert_diagnosis provided by the human expert and the Polar Map classification from the CNN-based analysis of the Myocardial Perfusion Imaging test are both valuable inputs for identifying CAD. In summary, based on the input concept values and the weight matrix, the FCM predicts that the patient is suffering from CAD due to the presence of Known_CAD, Previous_PCI, Diabetes, Expert_diagnosis, and Polar Map classification. It is important to note that this interpretation is based on the specific weights and input values provided, and further analysis and medical evaluation may be necessary for a comprehensive diagnosis.

Figure 8. Demonstration of GPT–3.5 results regarding the second case study.

4. Discussion

In this research study, we developed an automatic FCM–based model to detect CAD in patients. The dataset included 346 normal and 248 pathological cases, which nuclear experts had initially characterized for classification purposes. Clinical and imaging data (polar maps) were included. Feature selection was applied to improve the results by retaining the features with a higher impact on the final diagnosis and discarding the features that introduced noise and redundancy into the model. For further enhancement of the FCM, we developed RGB–CNN, a lightweight model for CAD diagnosis exploiting CNN abilities in extracting high–dimensional features from the available images. This incorporation of CNN predictions along with historical data constructed the proposed model, DeepFCM, which demonstrated considerable promise in enhancing accuracy and interpretability to healthcare professionals.

The proposed model achieved $83.07 \pm 4.72\%$ accuracy, 0.17 loss, and 86.21%, 79.99%, and 81.78% for sensitivity, specificity, and precision, respectively. With the application Grad–CAM, RGB–CNN's computations became interpretable and transparent, enhancing the model's explainability for research applications. Furthermore, the results obtained from DeepFCM were integrated into the NLP model (GPT–3.5) to enhance the interpretability of the findings.

DeepFCM can elucidate intricate cause–and–effect relationships among symptoms, diseases, and treatments inherently. The key to understanding these relationships lies in the interpretation of the weight matrix within the FCM. The weight matrix captures the strength and direction of influences between different nodes or concepts, offering doctors a transparent and interpretable framework to analyze how various factors contribute to a patient's condition. For example, DeepFCM learned that the diagnosis of the expert, which was an integrated feature of the model, should affect the output by a weight of 0.88, which is the largest observed weight in Table 3. This fact indicates that DeepFCM distinguishes the human expert as the most vital contributor to the result, thereby maintaining the doctor–in–the–loop approach. The weight matrix implied an inner relationship between the ECG outcome and the gender of the patient. More specifically, it was found that when the patient is male, the weight of the ECG should be slightly strengthened (Table 3). This connection is indeed documented in the literature [49], where it was found that men exhibit higher sensitivity in the ECG test. Finally, an interesting observation is that the CNN's prediction on the polar maps strongly affects the output (0.75). To summarize, DeepFCM suggests that the following four factors constitute essential predictors: the human expert's diagnostic yield, the characterization of the polar maps, as provided by the RGB–CNN of the framework, the patient's history regarding CAD, and the presence of angina–like symptoms.

Grad–CAM provided insights into the decision–making process of RGB–CNN by highlighting the regions of the polar maps that are most influential in making a particular classification or diagnosis. It was observed that, in most of the cases, the produced heatmaps indicated decisive features in areas where the polar map was initially green, which is considered acceptable. In healthy subjects, Grad–CAM produced mainly blue heatmaps, which implies no decisive features toward the positive class. However, there were some cases where the produced heatmap pointed out irrelevant areas. Although such cases undermine the performance of DeepFCM, they can be exploited by the medical staff to guess a potential mistake in the framework. For example, a DeepFCM prediction that was based on an inconclusive heatmap can be considered non–reliable by human experts. On the other hand, a meaningful heatmap indicates that DeepFCM has discovered important features and may be considered more reliable.

The integration of the NLP model improved the informativeness of the system. It provided a verbal interpretation of the results. It went beyond raw numerical data and transformed them into meaningful and human–readable descriptions. By providing a verbal interpretation of the results, the NLP model bridges the gap between data and understanding. It offers clinicians or users the ability to grasp the significance of the numbers, translating statistical findings into comprehensible narratives or descriptions. However, the reader can observe its inherent limitations in performing an in–depth analysis of the provided data. For example, the model failed to analyze and discuss the effect of the patient's gender on the ECG concept.

In Table 4, we have gathered all the DL medical–related state–of–the–art studies for comparison reasons. We can observe that the rest of the studies have reached efficient results with only image data as input, where CAD is demonstrated in SPECT–MPI format or in polar map images, where CNN training was applied. However, our proposed DeepFCM framework, although it did not exceed the performance of the previous literature studies in terms of accuracy, offers explainability and transparency of results, with the application of the FCM and the integration of clinical and imaging data, along with expert knowledge. By incorporating both imaging and clinical data, we demonstrate a holistic view of a patient's status, taking into account not only the image but also the medical history. The proposed model, DeepFCM, leverages expert knowledge as well, which enhances reliability.

Table 4. Comparison of previous related studies with the proposed framework DeepFCM.

Study	Input Data	DL Methods	Classification Problem	Results
Proposed DeepFCM	Polar maps + clinical	DeepFCM	CAD\No–CAD	Accuracy: 0.83
Papandrianos et al. [18]	SPECT	RGB–CNN (hand–crafted)	CAD\No–CAD	Accuracy: 0.93 $\pm$ 0.28 AUC: 0.936
Papandrianos et al. [2]	Polar maps	RGB–CNN (hand–crafted)	CAD\No–CAD	Accuracy: 0.92
Apostolopoulos et al. [20]	Polar maps	VGG–16	CAD\No–CAD	Accuracy:0.74 Sensitivity 0.75 Specificity: 0.73
Apostolopoulos et al. [50]	Polar maps + clinical	CNN (Inception V3) + Random Forest	CAD\No–CAD	Accuracy:0.78 Sensitivity:0.77 Specificity:0.79
Spier et al. [21]	Polar maps	Graph CNN (hand–crafted)	CAD\No–CAD	Agreement rating (Segment–by–segment): 0.83, Sensitivity: 0.47, Specificity: 0.7
Berkaya et al. [51]	SPECT	VGG–19	CAD\No–CAD	Accuracy: 0.93 Sensitivity: 1.0 Specificity: 0.86
Jui–Jen Chen et al. [24]	Gray SPECT images	3D–CNN (hand–crafted)	CAD\No–CAD	Accuracy: 0.87 Sensitivity: 0.81 Specificity: 0.92
Liu et al. [52]	Stress–only SPECT	ResNet–34	CAD\No–CAD	AUC: 0.872 $\pm$ 0.002
Zahiri et al. [47]	Polar maps	CNN	CAD\No–CAD	Accuracy: 0.7562 Sensitivity: 0.7856 Specificity: 0.7434 F1 score: 0.6646 AUC: 0.8450
Arvidsson et al. [53]	Polar maps + clinical (angina symptoms, age)	CNN	Probability of CAD in the left anterior artery, left circumflex artery, and right coronary artery	Per–vessel AUC: 0.89 Per–patient AUC: 0.95

The research presents some noteworthy limitations that warrant discussion. First and foremost, this study's dataset, while sufficiently large to facilitate the experiments conducted, is derived exclusively from a single hospital. This mono–centric data source inherently introduces limitations in terms of its representativeness and generalizability. The healthcare landscape can exhibit considerable regional variations in patient demographics, treatment protocols, and disease prevalence. Consequently, relying solely on data from one hospital can potentially skew the findings and limit their applicability to a broader population.

Another critical aspect that warrants further investigation pertains to the efficiency and effectiveness of the CNN model, a pivotal component of the DeepFCM framework. While the integration of CNNs in FCMs holds promise for a wide range of applications, including medical image analysis and decision support systems, there remains a need for in–depth research to assess and optimize the performance of this fusion.

The DeepFCM framework presents immediate potential for revolutionizing the routine diagnosis of CAD in clinical practice. Its unique combination of explainability and commendable classification accuracy makes it a compelling tool for healthcare professionals. DeepFCM not only offers robust classification accuracy but also provides transparent and understandable insights into its decision–making process, which is vital for building trust and facilitating the adoption of AI–driven solutions in healthcare. With the ability to pinpoint the critical factors contributing to CAD diagnosis, doctors can make more informed decisions and tailor treatment plans more effectively. This immediate potential signifies a

transformative step forward in enhancing the accuracy and reliability of CAD diagnosis, ultimately improving patient outcomes and streamlining everyday clinical routines.

5. Conclusions

Our research introduced the DeepFCM model, a pioneering approach that seamlessly integrates imaging and clinical data to enhance the diagnosis of CAD. Beyond its diagnostic capabilities, a defining feature of DeepFCM is its emphasis on explainability and transparency. By incorporating feature selection, we ensured that only the most pertinent clinical data influenced the outcomes. Additionally, the development of the RGB–CNN model showcased the potential of CNNs in this domain, with the integration of Grad–CAM further boosting the interpretability of these networks. In terms of quantitative results, DeepFCM achieved an accuracy of 83.07%, a sensitivity of 86.21%, and a specificity of 79.99%. These metrics not only matched but exceeded the diagnostic accuracy of expert evaluations and the standalone RGB–CNN model. Recognizing the importance of clear communication in healthcare, we incorporated the GPT–3.5 NLP model to translate DeepFCM's predictions into comprehensible explanations for medical professionals. This step is crucial in fostering trust and understanding between computational models and the medical community. This work represents a significant stride forward in CAD diagnosis, merging clinical and imaging data with advanced computational techniques. The added layer of explainability serves to bridge the gap between complex algorithms and clinical practice, enhancing trust among nuclear medicine experts.

Author Contributions: Conceptualization, A.F., I.D.A., S.M., and N.P. (Nikolaos Papathanasiou); methodology, I.D.A., A.F., N.P. (Nikolaos Papandrianos), S.M., and E.I.P.; software, A.F. and I.D.A.; validation, N.P. (Nikolaos Papathanasiou), D.A., and N.P. (Nikolaos Papandrianos); formal analysis, N.P. (Nikolaos Papandrianos) and A.F.; investigation, I.D.A. and A.F.; resources, I.D.A., N.P. (Nikolaos Papathanasiou), and N.P. (Nikolaos Papathanasiou); data curation, I.D.A., N.P. (Nikolaos Papathanasiou), and N.P.(Nikolaos Papandrianos); writing—original draft preparation, A.F. and I.D.A.; writing—review and editing, N.P. (Nikolaos Papathanasiou), E.I.P., and S.M.; visualization, A.F.; supervision, N.P. (Nikolaos Papandrianos), E.I.P. and S.M.; project administration, E.I.P. All authors have read and agreed to the published version of the manuscript.

Funding: The research project was supported by the Hellenic Foundation for Research and Innovation (H.F.R.I.) under the "2nd Call for H.F.R.I. Research Projects to support Faculty Members & Researchers" (Project Number: 3656).

Institutional Review Board Statement: This research does not report human experimentation; it does not involve human participants following experimentation. All procedures in this study were in accordance with the Declaration of Helsinki.

Informed Consent Statement: This study was approved on the 3rd of March 2022 by the ethical committee of the Universi-ty General Hospital of Patras (Ethical & Research Committee of University Hospital of Patras—protocol number 108/10–3–2022). The requirement to obtain informed consent was waived by the director of the diagnostic center due to its retrospective nature.

Data Availability Statement: The datasets analyzed during the current study are available from the nuclear medicine physician upon reasonable request.

Conflicts of Interest: The authors declare no conflict of interest.

References

1. Domingues, I.; Pereira, G.; Martins, P.; Duarte, H.; Santos, J.; Abreu, P.H. Using Deep Learning Techniques in Medical Imaging: A Systematic Review of Applications on CT and PET. *Artif. Intell. Rev.* **2020**, *53*, 4093–4160. [CrossRef]
2. Papandrianos, N.I.; Apostolopoulos, I.D.; Feleki, A.; Apostolopoulos, D.J.; Papageorgiou, E.I. Deep Learning Exploration for SPECT MPI Polar Map Images Classification in Coronary Artery Disease. *Ann. Nucl. Med.* **2022**, *36*, 823–833. [CrossRef] [PubMed]
3. Poon, A.I.F.; Sung, J.J.Y. Opening the Black Box of AI-Medicine. *J. Gastroenterol. Hepatol.* **2021**, *36*, 581–584. [CrossRef] [PubMed]
4. Barredo Arrieta, A.; Díaz-Rodríguez, N.; Del Ser, J.; Bennetot, A.; Tabik, S.; Barbado, A.; Garcia, S.; Gil-Lopez, S.; Molina, D.; Benjamins, R.; et al. Explainable Artificial Intelligence (XAI): Concepts, taxonomies, opportunities and challenges toward responsible AI. *Inf. Fusion* **2020**, *58*, 82–115. [CrossRef]

5. Dwivedi, R.; Dave, D.; Naik, H.; Singhal, S.; Omer, R.; Patel, P.; Qian, B.; Wen, Z.; Shah, T.; Morgan, G.; et al. Explainable AI (XAI): Core Ideas, Techniques, and Solutions. *ACM Comput. Surv.* **2023**, *55*, 1–33. [CrossRef]
6. Linardatos, P.; Papastefanopoulos, V.; Kotsiantis, S. Explainable AI: A Review of Machine Learning Interpretability Methods. *Entropy* **2020**, *23*, 18. [CrossRef]
7. Papandrianos, N.I.; Feleki, A.; Moustakidis, S.; Papageorgiou, E.I.; Apostolopoulos, I.D.; Apostolopoulos, D.J. An Explainable Classification Method of SPECT Myocardial Perfusion Images in Nuclear Cardiology Using Deep Learning and Grad-CAM. *Appl. Sci.* **2022**, *12*, 7592. [CrossRef]
8. Akella, A.; Akella, S. Machine Learning Algorithms for Predicting Coronary Artery Disease: Efforts toward an Open Source Solution. *Future Sci. OA* **2021**, *7*, FSO698. [CrossRef] [PubMed]
9. Teng, Q.; Liu, Z.; Song, Y.; Han, K.; Lu, Y. A Survey on the Interpretability of Deep Learning in Medical Diagnosis. *Multimed. Syst.* **2022**, *28*, 2335–2355. [CrossRef]
10. Kosko, B. Fuzzy Cognitive Maps. *Int. J. Man-Mach. Stud.* **1986**, *24*, 65–75. [CrossRef]
11. Kosko, B. *Neural Networks and Fuzzy Systems: A Dynamical Systems Approach to Machine Intelligence*, Prentice-Hall International editions; Prentice-Hall: Englewood Ciffs, NJ, USA, 1992; ISBN 978-0-13-612334-7.
12. Khodadadi, M.; Shayanfar, H.; Maghooli, K.; Hooshang Mazinan, A. Fuzzy Cognitive Map Based Approach for Determining the Risk of Ischemic Stroke. *IET Syst. Biol.* **2019**, *13*, 297–304. [CrossRef] [PubMed]
13. Apostolopoulos, I.D.; Groumpos, P.P.; Apostolopoulos, D.I. State Space Advanced Fuzzy Cognitive Map Approach for Automatic and Non Invasive Diagnosis of Coronary Artery Disease. *Biomed. Phys. Eng. Express* **2021**, *7*, 045007. [CrossRef]
14. Apostolopoulos, I.D.; Groumpos, P.P. Non—Invasive Modelling Methodology for the Diagnosis of Coronary Artery Disease Using Fuzzy Cognitive Maps. *Comput. Methods Biomech. Biomed. Engin.* **2020**, *23*, 879–887. [CrossRef] [PubMed]
15. Sovatzidi, G.; Vasilakakis, M.D.; Iakovidis, D.K. Fuzzy Cognitive Maps for Interpretable Image-Based Classification. In Proceedings of the 2022 IEEE International Conference on Fuzzy Systems (FUZZ-IEEE), Padua, Italy, 18–23 July 2022; pp. 1–6.
16. Sovatzidi, G.; Vasilakakis, M.D.; Iakovidis, D.K. IF3: An Interpretable Feature Fusion Framework for Lesion Risk Assessment Based on Auto-Constructed Fuzzy Cognitive Maps. In *Cancer Prevention Through Early Detection*; Ali, S., van der Sommen, F., Papież, B.W., van Eijnatten, M., Jin, Y., Kolenbrander, I., Eds.; Springer Nature Switzerland: Cham, Switzerland, 2022; pp. 77–86.
17. Sovatzidi, G.; Vasilakakis, M.D.; Iakovidis, D.K. Automatic Fuzzy Graph Construction For Interpretable Image Classification. In Proceedings of the 2022 IEEE International Conference on Image Processing (ICIP), Bordeaux, France, 16–19 October 2022; pp. 3743–3747.
18. Papandrianos, N.; Papageorgiou, E. Automatic Diagnosis of Coronary Artery Disease in SPECT Myocardial Perfusion Imaging Employing Deep Learning. *Appl. Sci.* **2021**, *11*, 6362. [CrossRef]
19. Papandrianos, N.I.; Feleki, A.; Papageorgiou, E.I.; Martini, C. Deep Learning-Based Automated Diagnosis for Coronary Artery Disease Using SPECT-MPI Images. *J. Clin. Med.* **2022**, *11*, 3918. [CrossRef]
20. Apostolopoulos, I.D.; Papathanasiou, N.D.; Spyridonidis, T.; Apostolopoulos, D.J. Automatic Characterization of Myocardial Perfusion Imaging Polar Maps Employing Deep Learning and Data Augmentation. *Hell. J. Nucl. Med.* **2020**, *23*, 125–132. [CrossRef]
21. Spier, N.; Nekolla, S.; Rupprecht, C.; Mustafa, M.; Navab, N.; Baust, M. Classification of Polar Maps from Cardiac Perfusion Imaging with Graph-Convolutional Neural Networks. *Sci. Rep.* **2019**, *9*, 7569. [CrossRef] [PubMed]
22. Otaki, Y.; Tamarappoo, B.; Singh, A.; Sharir, T.; Hu, L.-H.; Gransar, H. Diagnostic accuracy of deep learning for myocardial perfusion imaging in men and women with a high-efficiency parallel-hole-collimated cadmium-zinc-telluride camera: Multicenter study. *J. Nucl. Med. Soc. Nucl. Med.* **2020**, *61*, 92.
23. Otaki, Y.; Singh, A.; Kavanagh, P.; Miller, R.J.H.; Parekh, T.; Tamarappoo, B.K.; Sharir, T.; Einstein, A.J.; Fish, M.B.; Ruddy, T.D.; et al. Clinical Deployment of Explainable Artificial Intelligence of SPECT for Diagnosis of Coronary Artery Disease. *JACC Cardiovasc. Imaging* **2022**, *15*, 1091–1102. [CrossRef] [PubMed]
24. Chen, J.J.; Su, T.Y.; Chen, W.S.; Chang, Y.H.; Lu, H.H.S. Convolutional Neural Network in the Evaluation of Myocardial Ischemia from Czt Spect Myocardial Perfusion Imaging: Comparison to Automated Quantification. *Appl. Sci. Switz.* **2021**, *11*, 514. [CrossRef]
25. Suganyadevi, S.; Seethalakshmi, V.; Balasamy, K. A Review on Deep Learning in Medical Image Analysis. *Int. J. Multimed. Inf. Retr.* **2022**, *11*, 19–38. [CrossRef]
26. Samaras, A.-D.; Moustakidis, S.; Apostolopoulos, I.D.; Papandrianos, N.; Papageorgiou, E. Classification Models for Assessing Coronary Artery Disease Instances Using Clinical and Biometric Data: An Explainable Man-in-the-Loop Approach. *Sci. Rep.* **2023**, *13*, 6668. [CrossRef]
27. Ghosh, P.; Azam, S.; Jonkman, M.; Karim, A.; Shamrat, F.M.; Ignatious, E.; Shultana, S.; Beeravolu, A.; De Boer, F. Efficient Prediction of Cardiovascular Disease Using Machine Learning Algorithms With Relief and LASSO Feature Selection Techniques. *IEEE Access* **2021**, *9*, 19304–19326. [CrossRef]
28. Nápoles, G.; Ranković, N.; Salgueiro, Y. On the Interpretability of Fuzzy Cognitive Maps. *Knowl.-Based Syst.* **2023**, *281*, 111078. [CrossRef]
29. Jastrzebska, A.; Napoles, G.; Homenda, W.; Vanhoof, K. Fuzzy Cognitive Map-Driven Comprehensive Time-Series Classification. *IEEE Trans. Cybern.* **2023**, *53*, 1348–1359. [CrossRef]

30. Manimegalai, P.; Suresh Kumar, R.; Valsalan, P.; Dhanagopal, R.; Vasanth Raj, P.T.; Christhudass, J. 3D Convolutional Neural Network Framework with Deep Learning for Nuclear Medicine. *Scanning* **2022**, *2022*, 9640177. [CrossRef] [PubMed]
31. Wang, P.; Qiao, J.; Liu, N. An Improved Convolutional Neural Network-Based Scene Image Recognition Method. *Comput. Intell. Neurosci.* **2022**, *2022*, 3464984. [CrossRef] [PubMed]
32. Oh, J.W.; Jeong, J. Data Augmentation for Bearing Fault Detection with a Light Weight CNN. *Procedia Comput. Sci.* **2020**, *175*, 72–79. [CrossRef]
33. Zadeh, L.A. Fuzzy Sets. *Inf. Control* **1965**, *8*, 338–353. [CrossRef]
34. Raharja, M.A.; Darmawan, I.D.M.B.A.; Nilakusumawati, D.P.E.; Supriana, I.W. Analysis of Membership Function in Implementation of Adaptive Neuro Fuzzy Inference System (ANFIS) Method for Inflation Prediction. *J. Phys. Conf. Ser.* **2021**, *1722*, 012005. [CrossRef]
35. Kreinovich, V.; Kosheleva, O.; Shahbazova, S. Why Triangular and Trapezoid Membership Functions: A Simple Explanation. In *Recent Developments in Fuzzy Logic and Fuzzy Sets: Dedicated to Lotfi A*; Springer: Vienna, Austria, 2020; pp. 25–31. ISBN 978-3-030-38892-8.
36. Han, F.; Chen, W.-T.; Ling, Q.-H.; Han, H. Multi-Objective Particle Swarm Optimization with Adaptive Strategies for Feature Selection. *Swarm Evol. Comput.* **2021**, *62*, 100847. [CrossRef]
37. Yi, J.; Ran, Y.; Yang, G. Particle Swarm Optimization-Based Approach for Optic Disc Segmentation. *Entropy Basel Switz.* **2022**, *24*, 796. [CrossRef]
38. Liu, P.; Yuan, W.; Fu, J.; Jiang, Z.; Hayashi, H.; Neubig, G. Pre-Train, Prompt, and Predict: A Systematic Survey of Prompting Methods in Natural Language Processing. *ACM Comput. Surv.* **2023**, *55*, 1–35. [CrossRef]
39. Thirunavukarasu, A.J.; Ting, D.S.J.; Elangovan, K.; Gutierrez, L.; Tan, T.F.; Ting, D.S.W. Large Language Models in Medicine. *Nat. Med.* **2023**, *29*, 1930–1940. [CrossRef] [PubMed]
40. van Dis, E.A.M.; Bollen, J.; Zuidema, W.; van Rooij, R.; Bockting, C.L. ChatGPT: Five Priorities for Research. *Nature* **2023**, *614*, 224–226. [CrossRef] [PubMed]
41. Nath, S.; Marie, A.; Ellershaw, S.; Korot, E.; Keane, P.A. New Meaning for NLP: The Trials and Tribulations of Natural Language Processing with GPT-3 in Ophthalmology. *Br. J. Ophthalmol.* **2022**, *106*, 889–892. [CrossRef]
42. Currie, G.; Robbie, S.; Tually, P. ChatGPT and Patient Information in Nuclear Medicine: GPT-3.5 Versus GPT-4. *J. Nucl. Med. Technol.* **2023**, *51*, 165–166. [CrossRef] [PubMed]
43. Selvaraju, R.R.; Cogswell, M.; Das, A.; Vedantam, R.; Parikh, D.; Batra, D. Grad-CAM: Visual Explanations from Deep Networks via Gradient-Based Localization. *Int. J. Comput. Vis.* **2020**, *128*, 336–359. [CrossRef]
44. Chattopadhyay, A.; Sarkar, A.; Howlader, P.; Balasubramanian, V.N. Grad-CAM++: Improved Visual Explanations for Deep Convolutional Networks. In Proceedings of the 2018 IEEE Winter Conference on Applications of Computer Vision (WACV), Lake Tahoe, NV, USA, 12–15 March 2018; pp. 839–847.
45. Zhang, Y.; Hong, D.; McClement, D.; Oladosu, O.; Pridham, G.; Slaney, G. Grad-CAM Helps Interpret the Deep Learning Models Trained to Classify Multiple Sclerosis Types Using Clinical Brain Magnetic Resonance Imaging. *J. Neurosci. Methods* **2021**, *353*, 109098. [CrossRef] [PubMed]
46. Jahmunah, V.; Ng, E.Y.K.; Tan, R.-S.; Oh, S.L.; Acharya, U.R. Explainable Detection of Myocardial Infarction Using Deep Learning Models with Grad-CAM Technique on ECG Signals. *Comput. Biol. Med.* **2022**, *146*, 105550. [CrossRef] [PubMed]
47. Zahiri, N.; Asgari, R.; Razavi-Ratki, S.-K.; Parach, A.-A. Deep Learning Analysis of Polar Maps from SPECT Myocardial Perfusion Imaging for Prediction of Coronary Artery Diseas. *Res. Sq.* **2021**, preprint. [CrossRef]
48. Heckel, R.; Yilmaz, F.F. Early Stopping in Deep Networks: Double Descent and How to Eliminate It. *arXiv* **2020**, arXiv:2007.10099.
49. Nguyen, P.K.; Nag, D.; Wu, J.C. Sex Differences in the Diagnostic Evaluation of Coronary Artery Disease. *J. Nucl. Cardiol. Off. Publ. Am. Soc. Nucl. Cardiol.* **2011**, *18*, 144–152. [CrossRef] [PubMed]
50. Apostolopoulos, I.D.; Apostolopoulos, D.I.; Spyridonidis, T.I.; Papathanasiou, N.D.; Panayiotakis, G.S. Multi-Input Deep Learning Approach for Cardiovascular Disease Diagnosis Using Myocardial Perfusion Imaging and Clinical Data. *Phys. Medica PM Int. J. Devoted Appl. Phys. Med. Biol. Off. J. Ital. Assoc. Biomed. Phys. AIFB* **2021**, *84*, 168–177. [CrossRef] [PubMed]
51. Kaplan Berkaya, S.; Ak Sivrikoz, I.; Gunal, S. Classification Models for SPECT Myocardial Perfusion Imaging. *Comput. Biol. Med.* **2020**, *123*, 103893. [CrossRef]
52. Liu, H.; Wu, J.; Miller, E.J.; Liu, C.; Liu, Y.; Liu, C.; Liu, Y.-H. Diagnostic Accuracy of Stress-Only Myocardial Perfusion SPECT Improved by Deep Learning. *Eur. J. Nucl. Med. Mol. Imaging* **2021**, *48*, 2793–2800. [CrossRef] [PubMed]
53. Arvidsson, I.; Overgaard, N.C.; Aström, K.; Heyden, A.; Figueroa, M.O.; Rose, J.F.; Davidsson, A. Prediction of Obstructive Coronary Artery Disease from Myocardial Perfusion Scintigraphy Using Deep Neural Networks. In Proceedings of the 2020 25th International Conference on Pattern Recognition (ICPR), Milan, Italy, 10–15 January 2021; pp. 4442–4449. [CrossRef]

applied sciences

MDPI

Article

Improved Cardiac Performance with Dexamethasone Therapy in Premature Neonates: Novel Insights Using Serial Echocardiographic Assessments

Jejelola Ladele [1,2], Ayman Saker [1,3], Talal Altamimi [1,4], Andrea De La Hoz [5], Renjini Lalitha [1], Michael R. Miller [1,5] and Soume Bhattacharya [1,*]

[1] Department of Pediatrics, Division of Neonatal Perinatal Medicine, Western University, London, ON N6A 3K7, Canada; jejelola.ladele@tehn.ca (J.L.); asaker@cheo.on.ca (A.S.); taaltamimi@iau.edu.sa (T.A.); renjini.lalitha@lhsc.on.ca (R.L.); michael.miller@lhsc.on.ca (M.R.M.)
[2] Department of Pediatrics, Division of Neonatal Perinatal Medicine, University of Toronto, Toronto, ON M5S 1A1, Canada
[3] Department of Pediatrics, Division of Neonatal Perinatal Medicine, University of Ottawa, Ottawa, ON K1N 5Y3, Canada
[4] Department of Pediatrics, Division of Neonatal Intensive Care, College of Medicine, Imam Abdulrahman Bin Faisal University, Dammam 31113, Saudi Arabia
[5] Department of Lawson Research—Medicine, London Health Sciences Centre, London, ON N6A 5W, Canada; andrea.delahoz@lhsc.on.ca
* Correspondence: soume.bhattacharya@lhsc.on.ca

Abstract: (1) Background: dexamethasone is used for the prevention and treatment of chronic lung disease (CLD) in premature neonates, and its impact on cardiac performance and pulmonary vascular resistance has not been well studied. (2) Methods: eligible neonates of <30 weeks gestational age (GA) had echocardiograms performed on them at three time points—before the initiation of dexamethasone (Echo-1), 24–48 h post the completion of dexamethasone therapy (Echo-2), and 7–14 days after course completion (Echo-3). (3) Results: 28 neonates with a 25.2 week mean GA and 652.9 g birthweight were included. The mean cumulative dose of dexamethasone was 0.98 mg/kg, given over 8–10 days. Echo-1 and Echo-2 showed a significant improvement in the right ventricular fractional area change (RV FAC 44.88 vs. 49.71, $p = 0.025$), tricuspid annular plane systolic excursion (TAPSE 0.65 cm vs. 0.70 cm, $p = 0.013$), and RV S′ (7.18 vs. 8.56, $p = 0.05$). The left ventricular (LV) ejection fraction was similar but with a significant increase in the LV S′ (4.77 vs. 6.01, $p = 0.006$). A longitudinal analysis at three time points showed a significant increase in RV FAC (0.02 units 95% CI (0.00–0.04), $p = 0.037$), TAPSE (0.09 units 95% CI (0.06–0.13), $p < 0.001$), RV S′ (0.97 units (95% CI = 0.11–1.84), $p = 0.028$), a reduction in the eccentricity index (0.07 units 95% CI (−0.14–−0.01), $p = 0.030$), and an increase in the LV S′ (0.56 units (95% CI = 0.18–0.94)). (4) Conclusion: The use of postnatal dexamethasone for the prevention/treatment of CLD in premature neonates resulted in an expected improvement in respiratory status along with a significant improvement in the echocardiographic measures of biventricular heart performance.

Keywords: preterm neonates; dexamethasone; echocardiograms; chronic lung disease; cardiac performance; pulmonary vascular resistance

Citation: Ladele, J.; Saker, A.; Altamimi, T.; De La Hoz, A.; Lalitha, R.; Miller, M.R.; Bhattacharya, S. Improved Cardiac Performance with Dexamethasone Therapy in Premature Neonates: Novel Insights Using Serial Echocardiographic Assessments. *Appl. Sci.* **2023**, *13*, 11380. https://doi.org/10.3390/app132011380

Academic Editor: Julio Garcia Flores

Received: 20 September 2023
Revised: 13 October 2023
Accepted: 16 October 2023
Published: 17 October 2023

1. Introduction

Chronic lung disease (CLD) is a major morbidity in preterm neonates that is largely driven by the imbalance between pro- and anti-inflammatory mediators and is influenced by several factors, including sepsis, ventilation-induced trauma, free radical production, and pulmonary edema in an immature lung [1]. The use of the steroid dexamethasone in the prevention and treatment of CLD has been extensively explored [2–6]. Dexamethasone

induces lung maturational changes, promotes antioxidant activities, and helps with surfactant synthesis in the neonatal population [7]. Steroids were liberally used in the past in preterm neonates to treat and prevent CLD. However, due to concerns about adverse effects mainly on neuro-developmental outcomes, its use is now restricted for newborns at high risk for developing CLD or those who are ventilator dependent for prolonged periods in order to facilitate extubation. The current recommendation by the Canadian Pediatric Society (CPS) is that clinicians can consider a short course of low-dose dexamethasone in neonates at high risk for CLD or those with severe CLD [8].

Dexamethasone is known to have a broad range of effects on multiple organ systems, in addition to the lungs. The heart, in particular, is one such organ that has been postulated to be both directly impacted by steroid use as well as indirectly through possible changes in lung compliance. The effects of dexamethasone on left heart function are well documented and include myocardial thickening, hypertrophic cardiomyopathy involving the inter-ventricular septum and the left ventricle, and left ventricular outflow tract obstruction [9–12]. Some authors have described these effects as transient [10,13,14]. An increase in blood pressure has also been reported after dexamethasone use, with speculation on its ability to increase systemic vascular resistance and enhance responsiveness to catecholamines [15]. However, not much is known about its effects on the right ventricle and pulmonary vascular resistance (PVR). Pulmonary vascular remodeling with a resultant increase in PVR is an integral factor in the pathogenesis of CLD. Pulmonary hypertension (with resultant right ventricular dilatation and dysfunction) is now increasingly being recognized as a complication of CLD, significantly contributing to the morbidity and mortality in children with CLD [16–18].

As our understanding of CLD evolves, the interplay between lungs, PVR, right heart function, and steroids warrants careful attention. Echocardiography provides a safe and easy method to investigate cardiac function in preterm neonates. With the evolution of advanced echocardiographic techniques, such as tissue Doppler imaging, cardiac performance can be assessed in greater detail, which allows us to gain novel insights into the cardiopulmonary physiology of the preterm population. Hence, we designed this study to determine the longitudinal effects of low-dose dexamethasone therapy on echocardiographic parameters that measure PVR and cardiac performance in preterm neonates at risk of CLD.

2. Materials and Methods

This prospective cohort study was conducted at a level-three neonatal intensive care unit between April 2019 and July 2022. This center is a high-risk fetal–maternal center and is one of the largest tertiary perinatal centers in Canada, with around 5700 newborn deliveries per year and admitting an average of 1000 neonates per year. Ethical approval was obtained from our local Institutional Research Ethics Board (The Western University Health Science Research Ethics Board; REB 113654). Neonates with gestational age (GA) below 30 weeks who were being started on low-dose dexamethasone therapy for the prevention and treatment of CLD by the clinical care team were eligible for inclusion. Neonates with known structural congenital heart defects (except for atrial septal defect (ASD), ventricular septal defect (VSD), and patent ductus arteriosus (PDA)), lung malformations, genetic or chromosomal anomalies, and those who received steroids for any other indication (e.g., post-extubation stridor, adrenal insufficiency, capillary leak syndrome) were excluded.

2.1. Dexamethasone Protocol

Preterm neonates at high risk of CLD received dexamethasone treatment orally or through intravenous (IV) injection over 8 to 10 days. Patient selection for this therapy was as per physician discretion until December 2021, after which patients were treated based on a standardized unit policy that specified dosage, postnatal days of use, and provided high-level guidance surrounding patient selection. Prior to the development of the policy, the cumulative dose of dexamethasone used was 0.35 mg/kg, which was then subsequently

changed to 1.05 mg/kg (postnatal days 7–14) or 1.925 mg/kg (postnatal day 14 onwards), administered over 8–10 days.

2.2. Data Collection

We conducted echocardiograms at three time points on all neonates recruited into the study: the first was completed immediately prior to initiation of dexamethasone (Echo 1), the second was completed within 24–48 h of completing the dexamethasone course (Echo 2), and the third was completed 7–14 days after completion of the dexamethasone course (Echo 3). Relevant clinical information, including GA, weight at time of echocardiogram, mode of ventilation, pressure parameters on the ventilator (mean airway pressure (MAP), positive end-expiratory pressure (PEEP), peak inspiratory pressure (PIP), fractional inspired oxygen (FiO_2), use of inotropic/vasoactive medications and diuretics, oxygen requirement, and blood gas, were obtained and recorded. Other data retrieved from an infant's chart included maternal age and obstetric history, namely use of antenatal steroids, mode of delivery, maternal infection, chorioamnionitis, Apgar scores at the 5th and 10th minutes of life, resuscitative needs at birth, and surfactant therapy. Data regarding neonatal course and outcomes such as survival, duration of invasive and non-invasive respiratory support, intraventricular hemorrhage (IVH), periventricular leukomalacia (PVL), PDA requiring treatment, pulmonary hemorrhage, necrotizing enterocolitis (NEC), retinopathy of prematurity (ROP), and culture-positive sepsis were also collected.

2.3. Echocardiographic Measurements

Echocardiographic images were obtained using the Philips ultrasound machine with a 12 MHz/8 MHz cardiology probe, as appropriate. This was carried out by four experienced sonographers according to standard protocol using 2D, color, and Doppler imaging in parasternal, suprasternal, apical, and subcostal views. All measurements were conducted by experienced sonographers.

PVR was measured by the ratio of pulmonary artery acceleration time (PAAT) to right ventricular ejection time (PAAT: RVET), and right heart performance was measured using tricuspid annular plane systolic excursion (TAPSE), RV S' (Right Ventricle Lateral Wall Systolic Myocardial Velocity) by tissue Doppler imaging (TDI), right ventricular fractional area change (RV FAC), and right ventricular output (RVO) in mL/kg/min. The RVET and PAAT were measured via pulse wave (PW) Doppler imaging of the main pulmonary artery from the parasternal long-axis or short-axis view of the right ventricular (RV) outflow tract. We calculated PAAT as the time interval between the onset of systolic pulmonary arterial flow (onset of ejection) and peak flow velocity. To obtain the RVO, pulsed Doppler recordings of the flow at the level of the pulmonary valve were made from the parasternal long-axis or short-axis view, with care taken to minimize the angle of insonation. An average velocity time integral was derived by tracing the doppler waveform of three consecutive cardiac cycles using the incorporated cardiac software. The heart rate was measured from the peak-to-peak intervals of the Doppler velocity time signals. The diameter of the pulmonary valve insertion was measured at end-systole from a frame-by-frame videotape analysis of the 2D parasternal long-axis image and was averaged over three cardiac cycles.

Interventricular septal motion at end-systole (IVSs) was assessed by visual inspection of the interventricular septum from a 2D short-axis view acquired at the level of the papillary muscle. IVSs were considered 'flat' if there was complete absence of concavity towards the left ventricle. The eccentricity index (EI) was measured at end-systole, with EI defined as the ratio of D2/D1, where D1 is the left ventricle short-axis diameter perpendicular to the septum and D2 is the left ventricle short-axis diameter parallel to the septum. The TAPSE is the downward vertical distance the tricuspid annulus moves during systole, and we measured this using M-mode echocardiography in an apical 4-chamber view. From the apical window, an RV-focused apical 3-chamber (RV3C) view was acquired by rotating the transducer counterclockwise from the standard RV-4C view while maintaining a slight

rightward tilt to keep the right ventricle in view. The probe was rotated until the left side of the heart was completely out of view, the aortic valve was in the center of the image, and simultaneous visualization of RV inflow, outflow, and the inferior wall was achieved. Precaution was taken to avoid visualizing the anterior wall of the right ventricle. Our aim was to capture the maximum RV cavity while keeping these anatomic landmarks in view. Using this view, we measured the three-chamber RV FAC by manually tracing the endocardial borders at end-diastole and end-systole. The RV FAC (%) was calculated using the formula RV FAC (%) = (2-chamber RV area at end-diastole − 3-chamber RV area at end-systole)/3-chamber RV area at end-diastole) × 100%.

The presence or absence of PDA and patent foramen ovale (PFO) was also recorded. Left ventricular (LV) chamber dimensions, ejection fraction (EF), left ventricular output (LVO), LV S′ (Left Ventricular Lateral Wall Systolic Myocardial Velocity) with TDI, septal thickness, and LV posterior wall thickness in M mode were measured as per ASE recommendations [19]. Relative wall thickness (RWT) was calculated based on the formula RWT = (LV Posterior wall + Septal thickness)/LVIDd. All measurements were averaged over three consecutive cardiac cycles.

2.4. Outcome Measures

Our primary outcome was defined as a change in PVR and right heart performance. PVR was measured via the PAAT: RVET ratio. Right heart performance was measured via RV FAC, RVO, TAPSE and TDI RV S′. Our secondary outcome was the change in LV size (measured by septal thickness, posterior wall thickness, RWT) and function (measured by EF, LVO, TDI LV S′).

2.5. Sample Size

A sample size of N = 30 was based on a PVR mean (SD) of 0.35 (0.14) for Echo 1 and to detect a 25% change at Echo 2, using a dependent t-test with 5% alpha, 80% power, and an attrition rate of 10–20%.

2.6. Statistical Analysis

Continuous variables were summarized with means and standard deviations (or medians and interquartile ranges for non-normal distributions); paired and unpaired group differences were examined with dependent and independent *t*-tests, respectively. A repeated measures analysis of variance was used to examine the relationship between drug dosing groups and echo parameters between patients' first and second echo events. Relationships between continuous variables were examined with Pearson correlations. Categorical variables were summarized with frequencies and percentages, and paired group differences were examined with McNemar tests (or McNemar–Bowker tests, as appropriate). Logistic regression models were used to examine predictors of successful extubation. Trends over time were examined with linear, mixed models with maximum likelihood estimation, including echo events as fixed effects and patients as random effects using a scaled identity covariance structure with a random intercept. SPSS v.29 (IBM Corp., Armonk, NY, USA) was used for all analyses, and p-values < 0.05 were considered statistically significant.

3. Results

Thirty neonates were recruited for the study. Two withdrew consent, three patients were transferred out prior to study completion, two patients died during the study period, and one patient was clinically unstable (study flow diagram, Figure 1). The mean (SD) gestational age in the cohort was 25.2 (1.2) weeks, with a mean (SD) birthweight of 652.9 (156.3) grams. Dexamethasone administration was started at a mean (SD) age of 19.6 (9.2) days, with a mean (SD) cumulative dose of 0.98 (0.6) mg/kg given over 8–10 days. The baseline demographic and clinical characteristics are summarized in Table 1.

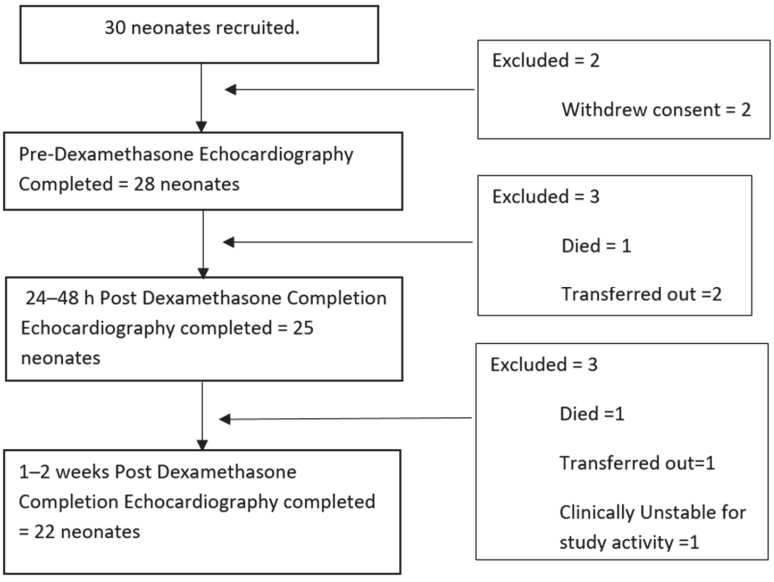

Figure 1. Study flow diagram.

Table 1. Baseline clinical and demographic characteristics (*n* = 28).

Variables		
Gestation age in weeks, mean (SD)		25.2 (1.2)
Birth weight in grams, mean (SD)		652.9 (156.3)
Male sex, *n* (%)		15 (53.6)
Antenatal steroids, *n* (%)	• Complete	18 (64.3)
	• Incomplete	8 (28.6)
	• None	2 (7.1)
C/section delivery, *n* (%)		15 (53.6)
Apgar score, median (IQR)	5 min	6 (3.25–8)
	10 min	7 (6–9)
Maternal chorioamnionitis, *n* (%)		3 (10.7)
Postnatal surfactant, *n* (%)		25 (89.3)
Cumulative dexamethasone in mg/kg, mean (SD)		0.98(0.6)
Cumulative dexamethasone dosage, *n* (%)	<1 mg/kg	16 (57.1)
	>1 mg/kg	12 (42.9)
Duration of dexamethasone course (days), mean (SD)		8.7 (1.5)
Postnatal age in days at dexamethasone course, mean (SD)		19.6 (9.2)

Abbreviations: C/section—cesarean section; SD—standard deviation; IQR—Interquartile range.

We compared the respiratory and echocardiographic parameters prior to the start of dexamethasone treatment and at the completion of the course (see Table 2). At the time of initiation of dexamethasone (Echo 1), 96.4% of the study neonates were intubated and ventilated. Immediately post dexamethasone course completion (Echo 2), the need for invasive ventilation had decreased to 52%. However, due to small cell sizes, we could not adequately test the differences in respiratory support between these two time points. In all

infants, the respiratory parameters showed significant improvement during the treatment course. The results showed that the MAP, PIP, and FiO_2 all significantly decreased post dexamethasone course (all $p < 0.05$).

Table 2. Echocardiographic parameters prior to dexamethasone (Echo1) and immediately after completion of dexamethasone course (Echo 2).

Parameter Type	Parameters		Prior to Dexamethasone, N = 28	Immediately after Completion of Dexamethasone, N = 25	*p* Value
Respiratory Parameters	Type of ventilatory support (%)	CMV	7 (25)	10 (40)	^
		HFOV	4 (14.3)	2 (8)	
		HFJV	16 (57.1)	1 (4)	
		Non-Invasive	1 (3.6)	12 (48)	
	Mean airway pressure in cm H_2O, mean (SD)		12.8 (2.46)	11.38 (2.51)	0.017
	FiO_2 in %, mean (SD)		48.52 (16.71)	37.52 (14.88)	0.003
	PIP in cm H_2O, mean (SD)		28.93 (6.38)	21.33 (4.71)	<0.001
	PEEP, cm H_2O, mean (SD)		10.17 (2.18)	9.15 (1.40)	0.065
Echocardiographic Parameters, Mean (SD)	LV FS (%)		41.36 (6.96)	47.8 (14.72)	0.062
	LV EF (%)		69.54 (9.82)	70.33 (11.58)	0.779
	LVO (mL/kg/min)		271.45 (87.45)	303.01 (135.11)	0.137
	LV VTI (cm)		10.5 (2.5)	11.32 (4.12)	0.196
	LVIDd (cm)		1.28 (0.28)	1.31 (0.33)	0.395
	LVIDs (cm)		0.76 (0.16)	0.73 (0.19)	0.381
	LV posterior wall (cm)		0.24 (0.05)	0.26 (0.04)	0.166
	Septal thickness (cm)		0.26 (0.07)	0.27 (0.07)	0.695
	Relative wall thickness		0.41 (0.72)	0.43 (0.11)	0.667
	LV S′ (cm/s)		4.77 (0.97)	6.013 (1.41)	0.006 *
	RV S′ (cm/s)		7.18 (2.10)	8.56 (2.24)	0.05
	Septum S′ (cm/s)		4.74 (1.01)	5.57 (0.75)	0.032 *
	RVET (s)		0.18 (0.04)	0.17 (0.03)	0.672
	PAAT (s)		0.06 (0.02)	0.07 (0.02)	0.152
	PAAT: RVET ratio		0.36 (0.11)	0.41 (0.13)	0.106
	RV VTI (cm)		9.81 (2.53)	10.60 (3.58)	0.358
	RV FAC in %, mean (SD)		44.88 (5.85)	49.71 (8.90)	0.025 *
	TAPSE (cm)		0.65 (0.12)	0.73 (0.17)	0.013 *
	PDA, n (%)		17 (60.7)	11 (39.3)	0.453
	Eccentricity index in %, mean (SD)		1.24 (0.31)	1.09 (0.16)	0.067

* $p < 0.05$; ^ Due to small cell sizes, we could not adequately test differences between respiratory support at Echo 1 vs. Echo 2 (i.e., chi-square test would not run); Abbreviations: CMV—Conventional Mechanical Ventilation; HFOV—High-Frequency Oscillatory ventilation; HFJV—High-Frequency Jet Ventilation; FiO_2—Fractional inspired oxygen; H_2O—water; PEEP—Peak End-Expiratory Pressure; LV FS—Left Ventricular Fractional Shortening; LV EF—left ventricular ejection fraction; LVO—left ventricular output; LV VTI—left ventricular velocity time integral; LVIDd—left ventricle internal diameter in diastole; LVIDs—left ventricle internal diameter in systole; LV S′—left ventricle systole prime; RV S′—right ventricle systolic prime; RVET—right ventricular ejection time; PAAT—pulmonary artery acceleration time; RV VTI—right ventricle velocity time integral; TAPSE—tricuspid annular plane systolic excursion; PDA—patent ductus arteriosus; SD—standard deviation.

3.1. Longitudinal Analysis of Respiratory and Echocardiographic Changes

Upon examining the change in respiratory parameters and echocardiographic parameters at all three echocardiogram time points—prior to course, immediately at steroid completion, and 7–14 days post steroid course completion—we found that, for each additional echocardiogram, the MAP significantly decreased, on average by 0.78 units ((95% CI = −1.39–−0.16), $p = 0.015$); the FiO_2 significantly decreased, on average by 4.54 units ((95% CI = −8.36–−0.71), $p = 0.021$); and the PIP significantly decreased, on average by 2.50 units ((95% CI = −4.77–−0.22), $p = 0.032$). The PEEP did not show a significant change over time ($p = 0.496$). Figure 2.

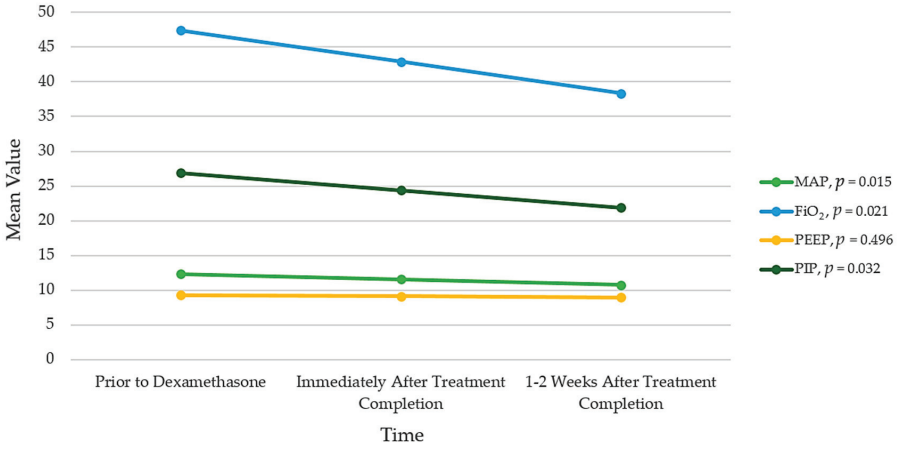

Figure 2. Changes in respiratory parameters at three time points: prior to dexamethasone, immediately after dexamethasone completion and 7–14 days after dexamethasone completion.

The echocardiographic parameters for each additional echocardiograph RV FAC significantly increased, on average by 0.02 units ((95% CI = 0.00–0.04), $p = 0.037$). In addition, the TAPSE significantly increased, on average by 0.09 cm ((95% CI = 0.06–0.13), $p < 0.001$); The eccentricity index significantly decreased, on average by 0.07 units (95% CI = −0.14–−0.01), $p = 0.030$. These findings are represented in Figure 3. The PAAT and PAAT:RVET ratio did not show significant change over time. From the LV perspective, the LV S′ significantly increased on average for each additional echocardiography by 0.56 units ((95% CI = 0.18–0.94), $p = 0.005$). The septal S′ increased by an average of 0.61 units per additional echocardiography ((95% CI = 0.23–1.00), $p = 0.003$). The RVS′ significantly increased on average per echocardiography by 0.97 units (95% CI = 0.11–1.84), $p = 0.028$. No significant changes were noted in the posterior wall thickness, relative wall thickness, LV chamber dimensions, or LV EF, or in the presence or absence of PDA.

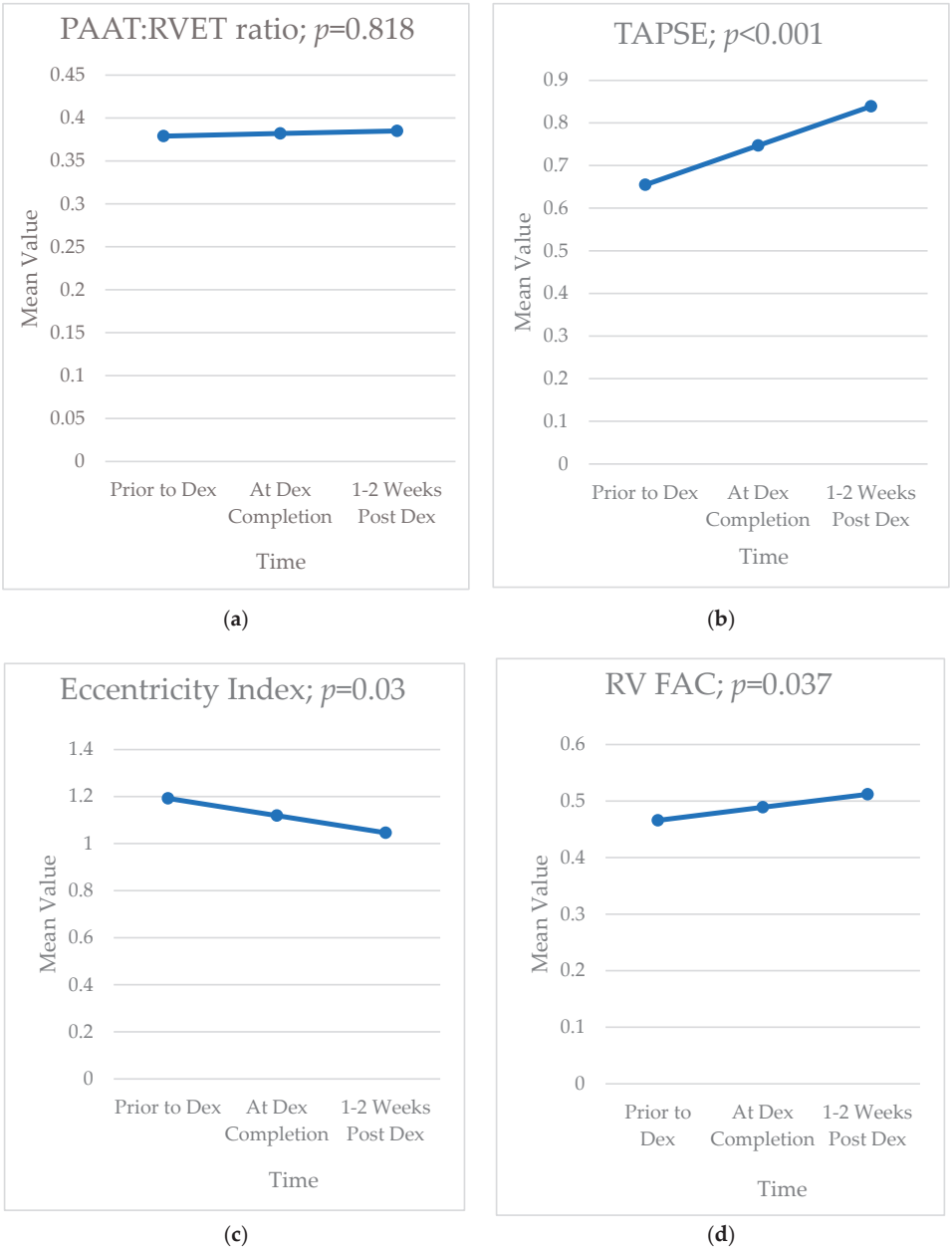

Figure 3. Changes in echocardiographic parameters at three time points; prior to dexamethasone (referred to as the "Prior to Dex" timepoint), immediately after dexamethasone completion (referred to as the "At Dex Completion" timepoint), and 7–14 days after dexamethasone completion (referred to as the "1–2 Weeks Post Dex" timepoint. Parameters include (**a**) PAAT:RVET (ratio, mean), (**b**) TAPSE (cm, mean), (**c**) eccentricity index (%, mean), and (**d**) RV FAC (%, mean).

3.2. Exploratory Analysis

We explored the extubation success (defined as successful extubation after dexamethasone initiation without need of re-intubation within the next 72 h) in this cohort. The rate of extubation success was 44.4% (12 out of 27). We ran a regression analysis to assess the clinical and echocardiographic variables that may predict the chances of a successful extubation. The baseline echo parameters showed no significant association with the outcome variable. The only significant predictor was a cumulative dexamethasone dose >1 mg/kg, with the odds of success increasing by 5.5 (95% CI = 1.05–28.88) when the cumulative dose was higher >1 mg/kg ($p = 0.044$). The change in RV function parameters (FAC and TAPSE) before and after the dexamethasone course did not have a significant correlation with cardiorespiratory outcomes such as days on mechanical ventilation, days on oxygen, and the development of chronic pulmonary hypertension. Using the oxygen saturation index (OSI) as a surrogate of the respiratory parameters, we examined the correlation between echocardiographic parameters and respiratory changes. We found no significant correlation between the OSI change and an RV FAC change ($r = -0.04$, $p = 0.887$) or TAPSE change ($r = 0.19$, $p = 0.399$). We examined whether there was a relationship between the dose of dexamethasone and the change in right ventricular function (TAPSE and RV FAC) and did not find a significant interaction.

3.3. Neonatal Outcomes

In this cohort, of the 25 patients who completed their follow-up, 23 (82.1%) were diagnosed to have BPD at 36 weeks corrected gestational age. Fourteen (50%) were discharged home on oxygen, 24 (85.7%) of the original cohort survived to discharge, and 4 (14.3%) received a diagnosis of chronic pulmonary hypertension.

4. Discussion

Our present study evaluated the effects of low-dose dexamethasone therapy in premature neonates on cardiorespiratory function and physiology. Using standard and advanced echocardiographic techniques, we investigated the effects of steroids on cardiac performance and pulmonary vascular resistance. Our results show that there was a significant improvement in respiratory parameters with dexamethasone therapy, along with an improvement in right heart systolic performance. The longitudinal systolic function of the LV also improved, as indicated by increases in the LV S' and Septal S'. There was no significant reduction seen in the echocardiographic measures of PVR, and no change was seen in the LV wall thickness with the range of dexamethasone doses used in this cohort. Using echocardiography, we demonstrate the positive longitudinal changes to the markers of biventricular systolic heart function in extreme preterm neonates with dexamethasone therapy. Unlike previous studies, this is the first study to show an improvement in LV systolic function with dexamethasone therapy using load-independent technology such as TDI.

The use of dexamethasone therapy in the management of CLD is based on the beneficial effects of steroids on the lungs. Steroids have been shown to improve lung function, reduce inflammation, increase antioxidant activity, and increase surfactant synthesis. In this study, we saw an improvement in the respiratory parameters of infants with the initiation of dexamethasone. This improvement was sustained 1–2 weeks post dexamethasone completion and was mainly seen in the form of reduced inflation pressure and oxygen requirements, subsequently suggesting an overall improvement in compliance and gas exchange. These findings are in keeping with other studies [2–6,20]. Around 44% of the cohort was successfully extubated; however, the majority received a diagnosis of BPD. During the study period, two different dose regimes were used: a very-low-dose regime of a 0.35 mg/kg cumulative dose and a comparatively higher regimen of a 1.02 mg/kg cumulative dose. The latter dose was associated with a higher chance of extubation success. The latter dose is in keeping with the current recommendation by the CPS [8] and in line with the recently published network meta-analysis [5].

On examination of the RV indices, we found that dexamethasone therapy had a significant positive effect on right heart systolic performance, as measured by the RV FAC, TAPSE, and RV S′ through TDI. There was a longitudinal reduction in the eccentricity index, suggesting a favorable transition from a pulmonary to systemic pressure relationship. Interestingly, we did not see any significant changes in the PAAT and PAAT: RVET ratio—a surrogate measure of PVR. With the improvement in PVR, we expect the PAAT: RVET ratio to increase. In our study, the PAAT: RVET ratio increased from 0.30 to 0.41 post dexamethasone therapy but was not statistically significant. Evan et al. in 1994 [21] and more recently Sehgal et al. in 2022 [22] demonstrated a reduction in PVR with the use of steroids. In the Evan et al. study, 20 neonates who received dexamethasone therapy were observed to undergo an increase in the PAAT: RVET ratio after the initiation of dexamethasone, suggesting a decrease in pulmonary artery pressure; however, this change was not sustained and did not show a correlation with the improvement noted in the respiratory status. On the contrary, we did see a significant unit decrease in the eccentric index over time, which reflects a longitudinal reduction in pulmonary artery pressure. The lack of significant change in the PAAT: RVET ratio in our study could be due to the small sample size, two different dosing regimens making the assessment difficult, the inherent limitations of the measure to accurately reflect the actual state of PVR, technical limitations in the extreme preterm population, and/or shortcomings of the measurement, especially in the presence of a PDA.

Interestingly, an improvement in RV performance was consistently demonstrated at all study time periods. Sehgal et al. also reported an improvement in RV systolic performance [22]. Such improvement could be due to a concurrent improvement in pulmonary compliance and a reduction in inflation pressures. To explore this further, we looked at the correlation of OSI and RV performance and did not find a significant relation. As such, our findings suggest that the improvement in RV performance could be independent of respiratory changes and intrinsically related to dexamethasone. Such improvement may be linked to improved ventriculo–arterial coupling and reduced RV afterload, as suggested by the longitudinal decrease in the eccentricity index.

The parameters reflective of LV longitudinal systolic function in TDI were found to increase over time without changes in the LV EF or LVO. Such improvement in LV function could be driven by the RV itself based on the principles of biventricular interdependence and shared myocardial fibers, especially in the septal wall, as well as by the application of advanced imaging techniques such as TDI, which is load-independent. Both the LV EF and LVO are influenced by the loading conditions of the LV. Dexamethasone is known to increase systemic vascular resistance, thereby increasing the afterload on the LV, which could possibly explain the lack of a significant increase in the LV EF and LVO within our cohort. Alternatively, it could be a reflection of physiological maturation or a direct effect of steroids on both right and left ventricular myocytes. Animal model studies have demonstrated that dexamethasone can stimulate angiotensin-converting enzyme (ACE) activity in cardiac myocytes, potentially influencing cardiac remodeling [23]. Low-dose dexamethasone in hypertensive rat models has shown improved LV systolic and diastolic function, which may be due to LV angiogenesis and a reduction of wall collagen deposition area [24].

Several researchers have described changes such as increased LV posterior wall thickness and ventricular septal hypertrophy in response to dexamethasone administration to premature neonates [9–11]. Our results do not show any significant change in the septal and LV dimensions, possibly because our cumulative dose of dexamethasone was substantially lower than the doses used in these studies. Similar results were reported by Sehgal et al., who used a cumulative dexamethasone dose of 0.89 mg/kg [22], which is a very similar dose range to that in our study.

From the PDA perspective, 60% of the cohort had PDA prior to their dexamethasone course. This then dropped to 39% after the completion of the course, but was not statistically significant ($p = 0.453$). Specific PDA-related echocardiographic parameters were not further

investigated in our present study. Sehgal et al. showed significant ductal constriction post dexamethasone use, along with improvements in metrics of pulmonary over circulation [22]. There have been some other studies that have reported ductal closure with steroids [25,26]. However, a future prospective study to analyze the effects of steroid on ductal parameters would be interesting.

Given that our study period witnessed two different dose regimes, we had the opportunity to explore a dose response relationship between steroids and right heart performance. We did not see a significant interaction between the dose and the RV systolic function parameters. Furthermore, our study explored the role of these changes in predicting respiratory outcomes. Our exploratory analysis showed that the changes in echocardiographic parameters could not predict successful extubation, days on oxygen, days on mechanical ventilation, or the development of CPHTN.

Our study's limitations include a small sample size and a single institution's experience, which may limit the generalizability of the findings. In addition, we did not include a long-term follow-up later in infancy to evaluate the patient's outcomes beyond discharge. The two different dosing regimens may have reduced the significance of some of the cardiac markers. A larger multi-center prospective study that includes advanced echocardiographic assessment up to 24–26 months of corrected age would be valuable. We acknowledge that there are technical limitations to echocardiographic measures of PVR, which may not have allowed us to capture the intricate and subtle physiological changes in this unique population. We did not examine the effect on diastolic cardiac function. Future studies utilizing novel echocardiographic techniques such as speckle tracking and strain analysis are warranted. However, this is the first study to longitudinally examine the effect of steroids on cardiorespiratory physiology, RV hemodynamics, and LV systolic function using advanced imaging techniques, as well as explore the dose–response relationship between steroids and cardiac systolic performance. Our findings reflect that low-dose dexamethasone (mean cumulative dose 0.98 mg/kg) used in premature neonates at risk of BPD has a positive cardio-pulmonary effect.

5. Conclusions

In conclusion, the use of postnatal dexamethasone for the prevention/treatment of CLD in premature neonates resulted in the expected improvements in respiratory status along with significant improvements in the echocardiographic measures of right heart systolic performance. This change appeared to be independent of respiratory improvement. There was also improvement in LV systolic function performance, as measured by TDI, without any adverse effect on LV wall thickness. There was a longitudinal reduction in the eccentricity index, but no statistically significant reduction in PVR was demonstrated in this cohort. While the >1 mg/kg dose allowed a higher chance of extubation, different dose ranges did not have a significant relationship with changes in the echocardiographic parameters.

Author Contributions: Conceptualization, S.B.; data curation, J.L., A.S., T.A. and S.B.; formal analysis, M.R.M.; methodology, J.L. and S.B.; supervision, S.B.; validation, R.L. and M.R.M.; writing—original draft, J.L. and S.B.; writing—review and editing, A.D.L.H., R.L. and M.R.M. All authors have read and agreed to the published version of the manuscript.

Funding: This research received no external funding.

Institutional Review Board Statement: The study was conducted in accordance with the Declaration of Helsinki and approved by the Institutional Review Board of Western University (The Western University Health Science Research Ethics Board; REB 113654; date of approval 16 July 2019).

Informed Consent Statement: Informed consent was obtained from all subjects involved in the study.

Data Availability Statement: Data are available upon request. Please contact the corresponding author.

Acknowledgments: We acknowledge the contribution of the participants and their families, without whom this work would not have been possible. We thank the NICU team and the Neonatal Hemodynamics Team for their cooperation and help in study conduct.

Conflicts of Interest: The authors declare no conflict of interest.

References

1. Schmidt, A.R.; Ramamoorthy, C. Bronchopulmonary dysplasia. *Pediatr. Anesth.* **2022**, *32*, 174–180. [CrossRef] [PubMed]
2. Halliday, H.L. Update on Postnatal Steroids. *Neonatology* **2017**, *111*, 415–422. [CrossRef] [PubMed]
3. Halliday, H.L.; Ehrenkranz, R.A.; Doyle, L.W. Early (<8 days) postnatal corticosteroids for preventing chronic lung disease in preterm infants. *Cochrane Database Syst. Rev.* **2014**, *5*, CD001146.
4. Halliday, H.L.; Ehrenkranz, R.A.; Doyle, L.W. Late (>7 days) postnatal corticosteroids for chronic lung disease in preterm infants. *Cochrane Database Syst. Rev.* **2014**, *5*, CD001145.
5. Ramaswamy, V.V.; Bandyopadhyay, T.; Nanda, D.; Bandiya, P.; Ahmed, J.; Garg, A.; Roehr, C.C.; Nangia, S. Assessment of Postnatal Corticosteroids for the Prevention of Bronchopulmonary Dysplasia in Preterm Neonates: A Systematic Review and Network Meta-analysis. *JAMA Pediatr.* **2021**, *175*, e206826. [CrossRef] [PubMed]
6. Doyle, L.W. Postnatal Corticosteroids to Prevent or Treat Bronchopulmonary Dysplasia. *Neonatology* **2021**, *118*, 244–251. [CrossRef]
7. Hillman, N.H.; Jobe, A.H. Preterm lung and brain responses to mechanical ventilation and corticosteroids. *J. Perinatol.* **2023**, *43*, 1222–1229. [CrossRef]
8. Lemyre, B.; Dunn, M.; Thebaud, B. Postnatal corticosteroids to prevent or treat bronchopulmonary dysplasia in preterm infants. *Paediatr. Child Health* **2020**, *25*, 322–331. [CrossRef]
9. Werner, J.C.; Sicard, R.E.; Hansen, T.W.; Solomon, E.; Cowett, R.M.; Oh, W. Hypertrophic cardiomyopathy associated with dexamethasone therapy for bronchopulmonary dysplasia. *J. Pediatr.* **1992**, *120 Pt 1*, 286–291. [CrossRef]
10. Skelton, R.; Gill, A.B.; Parsons, J.M. Cardiac effects of short course dexamethasone in preterm infants. *Arch. Dis. Child Fetal Neonatal Ed.* **1998**, *78*, F133–F137. [CrossRef]
11. Zecca, E.; Papacci, P.; Maggio, L.; Gallini, F.; Elia, S.; De Rosa, G.; Romagnoli, C. Cardiac adverse effects of early dexamethasone treatment in preterm infants: A randomized clinical trial. *J. Clin. Pharmacol.* **2001**, *41*, 1075–1081. [CrossRef] [PubMed]
12. Bensky, A.S.; Kothadia, J.M.; Covitz, W. Cardiac effects of dexamethasone in very low birth weight infants. *Pediatrics* **1996**, *97 Pt 1*, 818–821. [CrossRef]
13. de Vries, W.B.; Karemaker, R.; Mooy, N.F.; Strengers, J.L.; Kemperman, H.; Baerts, W.; Veen, S.; Visser, G.H.A.; Heijnen, C.J.; van Bel, F. Cardiovascular follow-up at school age after perinatal glucocorticoid exposure in prematurely born children: Perinatal glucocorticoid therapy and cardiovascular follow-up. *Arch. Pediatr. Adolesc. Med.* **2008**, *162*, 738–744. [CrossRef] [PubMed]
14. Wong, I.H.; Digby, A.M.; Warren, A.E.; Pepelassis, D.; Vincer, M.; Chen, R.P. Dexamethasone given to premature infants and cardiac diastolic function in early childhood. *J. Pediatr.* **2011**, *159*, 227–231. [CrossRef] [PubMed]
15. Marinelli, K.A.; Burke, G.S.; Herson, V.C. Effects of dexamethasone on blood pressure in premature infants with bronchopulmonary dysplasia. *J. Pediatr.* **1997**, *130*, 594–602. [CrossRef] [PubMed]
16. Slaughter, J.L.; Pakrashi, T.; Jones, D.E.; South, A.P.; Shah, T.A. Echocardiographic detection of pulmonary hypertension in extremely low birth weight infants with bronchopulmonary dysplasia requiring prolonged positive pressure ventilation. *J. Perinatol.* **2011**, *31*, 635–640. [CrossRef]
17. Mourani, P.M.; Abman, S.H. Pulmonary vascular disease in bronchopulmonary dysplasia: Pulmonary hypertension and beyond. *Curr. Opin. Pediatr.* **2013**, *25*, 329–337. [CrossRef]
18. Krishnan, U.; Rosenzweig, E.B. Pulmonary hypertension in chronic lung disease of infancy. *Curr. Opin. Pediatr.* **2015**, *27*, 177–183. [CrossRef]
19. Lai, W.W.; Geva, T.; Shirali, G.S.; Frommelt, P.C.; Humes, R.A.; Brook, M.M.; Pignatelli, R.H.; Rychik, J. Guidelines and standards for performance of a pediatric echocardiogram: A report from the Task Force of the Pediatric Council of the American Society of Echocardiography. *J. Am. Soc. Echocardiogr.* **2006**, *19*, 1413–1430. [CrossRef]
20. Doyle, L.W.; Ford, G.W.; Davis, N.M.; Callanan, C. Antenatal corticosteroid therapy and blood pressure at 14 years of age in preterm children. *Clin. Sci.* **2000**, *98*, 137–142. [CrossRef]
21. Evans, N. Cardiovascular effects of dexamethasone in the preterm infant. *Arch. Dis. Child Fetal Neonatal Ed.* **1994**, *70*, F25–F30. [CrossRef] [PubMed]
22. Sehgal, A.; Nold, M.F.; Roberts, C.T.; Menahem, S. Cardiorespiratory adaptation to low-dose dexamethasone for lung disease in extremely preterm infants: A prospective echocardiographic study. *J. Physiol.* **2022**, *600*, 4361–4373. [CrossRef] [PubMed]
23. Barreto-Chaves, M.L.; Heimann, A.; Fau-Krieger, J.E.; Krieger, J.E. Stimulatory effect of dexamethasone on angiotensin-converting enzyme in neonatal rat cardiac myocytes. *Braz. J. Med Biol. Res.* **2000**, *33*, 661–664. [CrossRef] [PubMed]
24. Duchatsch, F.; Tardelli, L.P.; Herrera, N.A.; Ruiz, T.F.R.; Vicentini, C.A.; Okoshi, K.; Santos, C.F.; Amaral, S.L. Dexamethasone and Training-Induced Cardiac Remodeling Improve Cardiac Function and Arterial Pressure in Spontaneously Hypertensive Rats. *J. Cardiovasc. Pharmacol. Ther.* **2021**, *26*, 189–199. [CrossRef]

25. Morales, P.; Rastogi, A.; Bez, M.L.; Akintorin, S.M.; Pyati, S.; Andes, S.M.; Pildes, R. Effect of dexamethasone therapy on the neonatal ductus arteriosus. *Pediatr. Cardiol.* **1998**, *19*, 225–229. [CrossRef]
26. Heyman, E.; Ohlsson, A.; Shennan, A.T.; Heilbut, M.; Coceani, F. Closure of patent ductus arteriosus after treatment with dexamethasone. *Acta Paediatr. Scand.* **1990**, *79*, 698–700. [CrossRef]

applied sciences

MDPI

Article

A Multicenter, Retrospective, Matched, Comparison Study of Clinical Efficacy and Cost-Effectiveness of Caterpillar Arterial Embolization Device versus Fibered Coils in Arterial Embolization

Megan J. Sue [1], Thanh T. Luong [1], Jonathan Park [2], Peng-Xu Ding [1], Frank Hao [1], Navid Eghbalieh [1,3] and Edward Wolfgang Lee [1,4,*]

[1] Division of Interventional Radiology, Department of Radiology, UCLA Medical Center, David Geffen School of Medicine at University of California, Los Angeles, CA 90095, USA; msue@mednet.ucla.edu (M.J.S.); ttluong@health.ucsd.edu (T.T.L.); jieru375@sina.com (P.-X.D.); frankhao@mednet.ucla.edu (F.H.); navide123@yahoo.com (N.E.)
[2] Torrance Memorial Medical Center, Torrance, CA 90505, USA; jonathan.park09@gmail.com
[3] Providence Holy Cross Medical Center, Mission Hills, CA 91345, USA
[4] Division of Liver and Pancreas Transplantation, Department of Surgery, David Geffen School of Medicine at University of California, Los Angeles, CA 90095, USA
* Correspondence: edwardlee@mednet.ucla.edu; Tel.: +1-310-267-8771

Abstract: Background: The purpose of this study was to evaluate and compare the clinical effectiveness and costs of using the Caterpillar Arterial Embolization Device (Caterpillar) and fibered coils in arterial embolization cases. Methods: In this multicenter retrospective study, demographic, laboratory, and procedural data were collected on a total of 48 patients between February 2020 and September 2020. Data were collected on 16 Caterpillar placements and matched with 32 controls who underwent coil embolization of the same vessel with a similar size. Clinical and procedural outcomes including type and size of vessels, time to vessel occlusion, fluoroscopy time, total procedure time, and costs were analyzed and compared. Results: Relative time to occlusion was significantly decreased in the Caterpillar group compared to the controls (57 $\pm$ 34 s vs. 11 min 44 s $\pm$ 8 min 13 s, $p = 0.00001611$). Fluoroscopy time (6.9 $\pm$ 15 min vs. 19.2 $\pm$ 14, $p = 0.017$) and total procedure time (81.0 $\pm$ 36 min vs. 111.5 $\pm$ 49 min, $p = 0.015$) were significantly reduced compared to the coil group. Lastly, overall cost of embolic materials was 1050 $\pm$ 0 USD for the Caterpillar group compared to 2312.75 $\pm$ 1382.84 USD in the coil group ($p = 0.000532$). Conclusion: The Caterpillar embolic devices appear safe and effective in arterial occlusion. Compared to fibered coils, the Caterpillar device results in decreased time to vessel occlusion, decreased fluoroscopy and procedural time, and decreased costs, making the Caterpillar an appealing choice for arterial embolization.

Keywords: embolization; vascular plug; coils; cost analysis

Citation: Sue, M.J.; Luong, T.T.; Park, J.; Ding, P.-X.; Hao, F.; Eghbalieh, N.; Lee, E.W. A Multicenter, Retrospective, Matched, Comparison Study of Clinical Efficacy and Cost-Effectiveness of Caterpillar Arterial Embolization Device versus Fibered Coils in Arterial Embolization. *Appl. Sci.* **2022**, *12*, 5262. https://doi.org/10.3390/app12105262

Academic Editor: Julio Garcia Flores

Received: 25 April 2022
Accepted: 17 May 2022
Published: 23 May 2022

1. Introduction

Embolization is a mainstay of all interventional radiology practices with procedures encompassing the arterial and venous circulatory systems and lymphatic system [1]. The ubiquitous nature and widespread need for embolic procedures has led to great innovations in available embolic devices. Currently, there are three major types of embolic devices available: liquid, particles, and metallic devices (coils or plugs). Often, operators choose to use different embolic agents in order to achieve the desired occlusive result. These decisions are based on the anatomy, pathology, and accessibility of the lesion, as well as operator ability and preference [2]. Metallic embolic devices such as coils, Amplatzer vascular plugs (AVPs), microvascular plugs (MVPs), and Caterpillars have been used in a wide range of embolization procedures [1,3–10]. When selective embolization is required, metallic

devices such as coils and plugs are often used due to these devices being controllable to achieve precise deployment and rapid occlusion of the target vessel [5].

Coils are the oldest and most commonly used metallic embolic materials. Coils come in multiple configurations and are widely available and relatively inexpensive [7]. However, multiple coils are often needed to achieve complete occlusion, necessitating a relatively long-segment landing zone, increased costs, procedure time, and radiation dose [7,9,11]. In multiple studies of pulmonary arteriovenous malformations (PAVMs), the use of coils alone was not sufficient and caused a higher rate of both PAVM persistence, re-perfusion, and recanalization of the treated vessel compared to an AVP, often requiring repeat interventions [8–10,12]. Several risk factors for recanalization of a PAVM when using coils are proximal coil placement, oversizing, and using too few coils. This suggests that the choice of embolic device can be a significant factor in determining overall procedure success [11].

The AVP was first developed in order to address many of the issues with coils. The AVP was designed to reduce the number of required embolic devices; a single AVP can replace multiple coils, decreasing procedure and radiation time, as well as associated costs, while achieving better control in high-flow vessels [1,5]. However, the device is stiff and requires a minimum catheter size of 4Fr for deployment [2]. This significantly limits its utility in distal and small vessels. In addition, the time to complete occlusion for both coils and AVPs can be a limiting factor. Multiple studies reported occlusion times ranging from 1 to 20 min, with thrombosis occurring gradually over time [6,11]. The MVP consists of a detachable and re-sheathable soft nitinol skeleton with a PTFE coating. It is deployed through a microcatheter. This allows for precise and near-immediate embolization of extremely tortuous or small vessels and addresses some of the shortcomings of an AVP without sacrificing functionality [7]. Using an MVP limits both the number of "judgement calls" in deciding the size, number, and packing density of the coils [11]. However, the MVP itself does have several disadvantages as it requires precise sizing, a straight landing zone, and suboptimal radio-opacities [2]. Under-sizing of the device is particularly dangerous as it can lead to partial occlusion of the vessel, as well as increased risk of device migration [5].

Compared to coils or other plugs, the Caterpillar Arterial Embolization (Caterpillar) device is a newer metallic embolic device, composed of two sets of opposing nitinol fibers for stability and thrombosis with a proximal polyurethane and polyethylene occlusion membrane for rapid occlusion [1]. Initial experience with the Caterpillar device suggests an advantage in terms of improved flexibility, deployment accuracy, and rapid occlusion [1]. However, these characteristics of Caterpillar devices have not been fully investigated, and, to date, there has not been a study comparing the Caterpillar device to other metallic embolic, nor are there any studies featuring a cost analysis comparing the two device types.

The purpose of this retrospective, matched study is to compare the technical success, clinical efficacy, safety (including complication rate), procedure time, and cost of the Caterpillar device and fibered endovascular coils in various arterial embolization procedures. Our primary hypothesis is to prove that the Caterpillar device can occlude the target arteries faster than coils.

2. Materials and Methods

2.1. Patient Selection and Demographic Information

This retrospective study was approved by the institutional review board (IRB#21-000278). Data were collected from three academic hospitals. Medical records for 48 patients including demographic, medical, and procedural information between February 2020 and September 2020 were obtained: 16 Caterpillar and 32 fibered coil deployments were 1:2 matched for embolized vessel type and size. For each Caterpillar device deployed, two patients who underwent coil embolization of the same vessel with a similar size (within 1 mm as measured intra-procedurally) were selected to serve as controls. Additional information was acquired on the procedure type, time to vessel occlusion, vessel size, fluoroscopy time, procedure time, and cost. All data were statistically analyzed.

2.2. Laboratory Assessement

We obtained pre-procedure values for international normalized ratio (INR) and platelet counts when available in the electronic medical record. The data were analyzed for the overall dataset, as well as in two subgroups: for the Caterpillar device group and for the matched coil-embolized control group.

2.3. Technical Aspects

Data were collected on several technical factors for each procedure. The time to occlusion was calculated for each device by analyzing the saved images from each case. The time of the first appearance of the embolic device on the images was recorded and compared with the final post-occlusion angiographic run. These times were subtracted in order to determine the time between the deployment of the embolic device and the time until the vessel was satisfactorily occluded, termed "time to occlusion". Fluoroscopic time was chosen as a surrogate for radiation dose; it was measured in minutes and obtained from the dose reports for each case. The total procedure time was recorded by our IR technologists at the time of initial needle access time to the completion of the case in the procedure report.

2.4. Statistical Analysis

Continuous variables were reported as the mean ± standard deviation. The Student's *t*-test was used to compare the differences in continuous variables. *p*-Values <0.05 were regarded as statistically significant. All statistical analyses were performed using SPSS software version 22.0 (SPSS, Chicago, IL, USA).

3. Results

3.1. Patient Demographics

The study population consisted of 48 patients: 35 males and 13 females, ranging in age from 34–88 years (mean ± SD 62.2 ± 15 years) (Table 1). During the study period, 16 Caterpillar devices were deployed (Figure 1A,B). and two matched controls with coil deployment (Figure 1C,D) were obtained for each Caterpillar device deployed. These two groups were not significantly different in age. Various vessels were embolized, including the gastroduodenal artery (GDA, *n* = 24), splenic artery (*n* = 9), mesenteric artery branches (*n* = 9), and internal iliac artery branches (*n* = 6).

Table 1. Patient demographics and baseline clinical characteristics of the procedures.

	Caterpillars (*n* = 16)	**Fibered Coils (*n* = 32)**	***p*-Value**
Age (years)	64 ± 13	58 ± 15	0.063
Sex (male), *N* (%)	13 (81.2)	22 (68.8)	0.625
Platelet count	155.3 ± 95	130.4 ± 89	0.393
INR	1.22 ± 0.2	1.33 ± 0.5	0.410
Procedures performed			
Y90 mapping	7 (43.7)	16 (50.0)	0.786
GI bleeding	4 (25.0)	6 (18.75)	0.822
Pre-op splenic embo	3 (18.8)	6 (18.75)	0.999
Pelvic trauma	2 (12.5)	4 (12.5)	1.000
Embolic materials used			
Caterpillar Micro Arterial Embolization Device	8		
Caterpillar Arterial Embolization Device	8		
Interlock coils		32	
Concerto coils		4	
Tornado coils		4	
Average number of embolic materials used	**1.0 ± 0.0**	**5.2 ± 2.0**	**0.0001**

Table 1. *Cont.*

	Caterpillars (n = 16)	Fibered Coils (n = 32)	p-Value
Arteries embolized			
Gastroduodenal	8	16	1.000
Splenic	3	6	1.000
Mesenteric branches	3	6	1.000
Internal iliac branches	2	4	1.000
Size of arteries			
Overall (mm)	3.2 ± 1.0	3.2 ± 1.0	1.000
>2 mm	10 (62.5)	20 (62.5)	1.000
<2 mm	6 (37.5)	12 (37.5)	1.000

Data are presented as the mean ± SD as appropriate. INR = international normalized ratio; GI = gastrointestinal; op = operative.

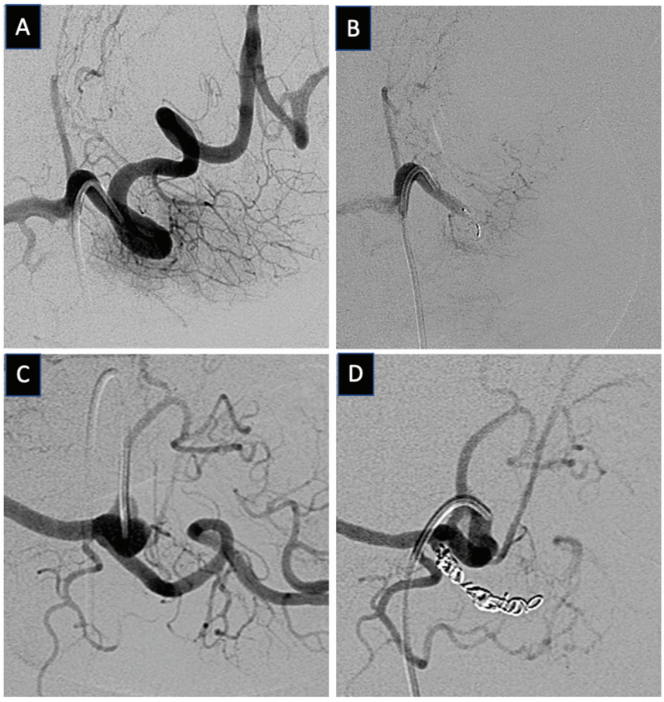

Figure 1. Selective angiographic images during the splenic artery embolization procedures: (**A**) pre-embolization and (**B**) post-embolization angiogram using Caterpillar Arterial Embolization Device; (**C**) pre-embolization and (**D**) post-embolization angiogram using fibered embolization coils.

3.2. Laboratory Assessement

Pre-procedure laboratory values were collected on all patients (Table 1). In the study population, the mean ± SD platelet count was 138.7 ± 91 × 10^3 platelets/μL among all patients. Platelet count was 155.3 ± 95 × 10^3 platelets/μL for the Caterpillar group and 130.4 ± 89 × 10^3 platelets/μL for the coil group. These values were not significantly different from one another (p = 0.39). INR values were also collected. For the entire cohort, the mean ± SD INR was 1.30 ± 0.4. In the Caterpillar group, the mean ± SD INR was 1.22 ± 0.2, while it was 1.33 ± 0.5 for the coil group. These values were not significantly different from one another (p = 0.41).

3.3. Time to Occluson

The relative time to occlusion (RTO) for each vessel was calculated by subtracting the time of the initial device deployment from the time of the post-embolization angiography to confirm complete occlusion of the target vessel (Table 2). For the Caterpillar group, the mean ± SD RTO was 57 ± 34 s. In contrast, the mean RTO for the coil groups was 11 min 44 s ± 8 min 13 s for matched sized vessels. The RTO was significantly shorter in the Caterpillar group compared to the coil group (p = 0.00001611).

Table 2. Comparison of embolization outcomes.

	Caterpillars (n = 16)	**Fibered Coils (n = 32)**	**p-Value**
Relative time to occlusion (RTO)			
Overall RTO	0 min 57 s ± 0 min 34 s	11 min 44 s ± 8 min 13 s	**0.000016**
RTO for >2 mm	0 min 50 s ± 0 min 34 s	12 min 54 s ± 8 min 46 s	**0.000011**
RTO for <2 mm	1 min 16 s ± 0 min 29 s	9 min 49 s ± 7 min 09 s	**0.000825**
Embolization related time			
Radiation time	19.2 ± 14 min	30.7 ± 15 min	**0.017**
Procedure time	81.0 ± 36 min	111.5 ± 49 min	**0.015**
Embolic material cost in USD			
Overall	1050 ± 0	2312.75 ± 1382.84	**0.000532**
Arteries >2 mm	1050 ± 0	2622.64 ± 1446.52	**0.000601**
Arteries <2 mm	1050 ± 0	1442.25 ± 721.67	**0.001**

Data are presented as the mean ± SD as appropriate.

The RTO was analyzed in subgroups. The larger vessel subgroup (>2 mm) RTO for the Caterpillar group was 50 ± 34 s compared to 12 min 54 s ± 8 min 46 s in the coil group, which was statistically different (p = 0.000011). When analyzing the smaller vessel subgroup (<2 mm), the RTO for the Caterpillar group was 1 min 16 s ± 29 s compared to 9 min 49 s ± 7 min 9 s in the coil group, which was also statistically different (p = 0.001).

3.4. Radiation and Procedure Time

Fluoroscopy time was chosen as a surrogate for the relative radiation dose (Table 2). The Caterpillar group had a significantly lower fluoroscopy mean ± SD time at 19.2 ± 14 min compared to the coil group (30.7 ± 15 min, p = 0.017). Procedure time was estimated by subtracting the end of procedure time by the initial needle time recorded (Table 2). The mean ± SD procedure time for the Caterpillar group was 81.0 ± 36 min, compared to the mean ± SD procedure time for the coil group of 111.5 ± 49 min. This value was significantly lower in the Caterpillar group (p = 0.015).

3.5. Cost Analysis

The average embolic material cost per procedure (AEMC) was analyzed using the institutional cost for all embolic materials used in each case (Table 2). The AEMC for the Caterpillar group was 1050 ± 0 USD compared to 2312.75 ± 1382.84 USD in the coil group (p = 0.000532), representing a 120% increase in cost. This cost difference was even higher in the larger vessel subgroup. AEMC in the Caterpillar group in vessels >2 mm was 1050 ± 0 USD compared to 2622.64 ± 1446.52 USD in the coil group (p = 0.000601), representing a 150% increase in cost. In vessels <2 mm, the AEMC in the Caterpillar group was 1050 ± 0 USD compared to 1442.25 ± 721.67 USD in the coil group (p = 0.001), representing a 43% increase in cost.

4. Discussion

The ability to accurately and safely deploy an embolization device is a cornerstone of a successful embolization procedure. While many embolic agents are available, they are often limited in their ability to achieve distal control and immediate occlusion, not re-sheathable, and difficult to place in tortuous or small target vessels. The Caterpillar Arterial Embolization Device (Caterpillar) appears to address many of these limitations. The Caterpillar with its dual nitinol fibers and occlusion membrane allows for accurate placement and improves occlusion timing. However, no clinical comparison studies have been performed to evaluate their embolic efficacy. In this study, we compared the embolic effects of the Caterpillar to the fibered endovascular coils in a variety of arterial embolic procedures. Overall, the Caterpillar device demonstrated a significantly shorter relative time to occlusion, significantly decreased cost, and potentially decreased radiation and procedure time compared to the fibered coil embolization in arterial procedures.

As the primary outcome, the Caterpillar embolization procedures were found to have a significantly reduced relative time to complete vessel occlusion in all procedures compared to fibered coil embolization procedures in our matched cohort. In all procedures, the Caterpillar achieved an overall 92% reduction in occlusion time from an average of 12 min to 1 min. This was due to (1) the decrease in the number of devices (one Caterpillar per procedure compared to multiple fibered coils) required for complete vessel occlusion, and (2) the proprietary occlusive membrane that is a part of the Caterpillar. This reduction in occlusion time was further analyzed in subgroups based on the vessel size (>2 or <2 mm). In the larger vessel group (2.1 to 5.1 mm), a similar reduction in occlusion time in the Caterpillar group was observed as expected, as many coils (up to 11) were needed in some cases. Similar findings were noted in the small vessel group (1.3 to 2 mm). The average occlusion time was significantly reduced in the Caterpillar group by 84% (from 9 min 49 s in the coil group to 1 min 56 s in Caterpillar group). Even though embolizing small vessels did not require as many coils or as much procedure time, more time was still needed for occlusion compared to a single device occlusion with Caterpillar. Future studies with a larger number of procedures with various vessel sizes should be performed to confirm these findings.

Shorter vascular occlusion times also translated to decreased overall procedure times. In addition to saving procedure time and radiation dose by simply requiring fewer devices (less time to open packages and deploy coils), using fewer embolic devices reduces procedure time by decreasing the number of "judgement calls" required by the operator (for example, determining the size, number, and packing density of coils). Ref. [12] In our study, mean procedure times were significantly shorter in the Caterpillar patients (81.0 $\pm$ 36 min), compared to the mean procedure time for the control group of 111.5 $\pm$ 49 min. Fluoroscopy time was chosen as the surrogate for relative radiation dose. The Caterpillar group had a significantly lower mean fluoroscopy time at 19.2 $\pm$ 14 min compared to the control group at 30.7 $\pm$ 15 min. Saving radiation dose for both the patient and the operator has a significant clinical impact for both parties, decreasing both deterministic and stochastic radiation effects. However, we believe that the overall procedure time or radiation time assessment is not an accurate assessment, as there are many other factors involved in increasing the procedure or radiation time such as the anatomical complexity of the target vessels for embolization, operators' experience, additional time spent on other parts of the procedure such as additional angiograms during Y90 mapping, or multiple catheter and wire exchanges. Hence, although the embolic deployment time is somewhat related to the overall procedure and radiation time, it is not truly correlative in some cases.

Perhaps one of the most important implications of our study is cost. Overall, the embolic device cost was significantly reduced in the Caterpillar group compared to the coil group by 54%. In subgroup analysis, coil embolization in larger vessels (>2 mm) would cost 150% more than Caterpillar embolization. This significant decrease in cost allows for better utilization of resources and cost efficiency. This is a small part of cost saving as the Caterpillar group also had significant time savings in embolization, which can translate to

less room time. In summary, it is more cost-effective to use Caterpillar than fibered coils in the embolization of selective vessel sizes.

Several limitations existed for this retrospective study, which relied on electronic medical records as its primary information source. However, only objective data, such as time and laboratory values, were collected, and all information was collated by two reviewers, limiting the risk of misclassification bias. In addition, the study was limited by its small sample size (16 Caterpillars and 32 matched controls). As the use of the device becomes more widespread, this concern may be addressed in a future study with a larger cohort. Additionally, inconsistent documentation may have affected the analysis of data from three institutions. Lastly, as mentioned above, the true effects on the procedure time and radiation time are not fully reliable as they were indirectly related to vessel occlusion time. Other procedural and anatomical factors can affect the procedure and radiation time. Hence, only relative outcomes of these parameters should be considered.

In conclusion, this is the first reported study comparing the efficacy and cost-effectiveness of the Caterpillar device (or any vascular plug) to conventional coils in terms of time to occlusion, as well as radiation and procedure time. Overall, the use of the Caterpillar devices allowed for accurate placement and rapid occlusion of the target vessel in every case in which they were used. Compared to coil embolization, the Caterpillar device demonstrated a significant decrease in time to vessel occlusion, relative radiation and procedure time, and embolic device cost.

Author Contributions: Conceptualization, E.W.L., T.T.L. and P.-X.D.; methodology, E.W.L., T.T.L. and P.-X.D.; validation, E.W.L., M.J.S., J.P., F.H. and N.E.; formal analysis, E.W.L., M.J.S. and J.P.; investigation, E.W.L., M.J.S., J.P., P.-X.D. and N.E.; writing—original draft preparation, M.J.S. and E.W.L.; writing—review and editing, M.J.S., T.T.L., J.P., P.-X.D., F.H., N.E. and E.W.L.; supervision, E.W.L.; funding acquisition, E.W.L. All authors have read and agreed to the published version of the manuscript.

Funding: This research received no external funding.

Institutional Review Board Statement: The retrospective clinical study was approved by the Institutional Review Board (or Ethics Committee) of the University of California, Los Angeles (IRB#21-000278, approved on 23 March 2021).

Informed Consent Statement: This study received a waiver of informed consent; the UCLA IRB waived the requirement for informed consent under 45 CFR 46.116(f) for the entire study.

Data Availability Statement: The data presented in this study are available on request from the corresponding author. The data are not publicly available due to privacy restrictions and HIPAA compliance.

Conflicts of Interest: E.W.L. has received consulting and research support from BD, consulting from Boston Scientifics Co., and consulting from Cook Medical; N.E. has received consulting from Boston Scientific Co.

References

1. Sweigert, J.; Lee, E.W. Caterpillar Mechanical Embolization Device: A New Vascular Plug. *J. Vasc. Interv. Radiol.* **2021**, *32*, 927–929. [CrossRef]
2. Giurazza, F.; Corvino, F.; Cavaglia, E.; Cangiano, G.; Amodio, F.; De Magistris, G.; Frauenfelder, G.; Guarnieri, G.; Muto, M.; Niola, R. Arterial embolizations with microvascular plug in extracranial and intracranial districts: Technical results. *Radiol. Med.* **2018**, *123*, 236–243. [CrossRef]
3. Conrad, M.B.; Ishaque, B.M.; Surman, A.M.; Kerlan, R.K., Jr.; Hope, M.D.; Dickey, M.A.; Hetts, S.W.; Wilson, M.W. Intraprocedural Safety and Technical Success of the MVP Micro Vascular Plug for Embolization of Pulmonary Arteriovenous Malformations. *J. Vasc. Interv. Radiol.* **2015**, *26*, 1735–1739. [CrossRef] [PubMed]
4. Hao, F.; Powell, D.; Weintraub, J.; Sheynzon, V. Pediatric Gastroduodenal Embolization with a Microvascular Plug. *Cardiovasc. Intero. Radiol.* **2016**, *39*, 788–790. [CrossRef]
5. Mahdjoub, E.; Tavolaro, S.; Parrot, A.; Cornelis, F.; Khalil, A.; Carette, M.F. Pulmonary Arteriovenous Malformations: Safety and Efficacy of Microvascular Plugs. *AJR Am. J. Roentgenol.* **2018**, *211*, 1135–1143. [CrossRef]
6. Pellerin, O.; Caruba, T.; Kandounakis, Y.; Novelli, L.; Pineau, J.; Prognon, P.; Sapoval, M. Embolization of the internal iliac artery: Cost-effectiveness of two different techniques. *Cardiovasc. Interv. Radiol.* **2008**, *31*, 1088–1093. [CrossRef] [PubMed]

7. Pellerin, O.; Maleux, G.; Dean, C.; Pernot, S.; Golzarian, J.; Sapoval, M. Microvascular plug: A new embolic material for hepatic arterial skeletonization. *Cardiovasc. Interv. Radiol.* **2014**, *37*, 1597–1601. [CrossRef]
8. Remy-Jardin, M.; Dumont, P.; Brillet, P.Y.; Dupuis, P.; Duhamel, A.; Remy, J. Pulmonary arteriovenous malformations treated with embolotherapy: Helical CT evaluation of long-term effectiveness after 2–21-year follow-up. *Radiology* **2006**, *239*, 576–585. [CrossRef]
9. Tau, N.; Atar, E.; Mei-Zahav, M.; Bachar, G.N.; Dagan, T.; Birk, E.; Bruckheimer, E. Amplatzer Vascular Plugs Versus Coils for Embolization of Pulmonary Arteriovenous Malformations in Patients with Hereditary Hemorrhagic Telangiectasia. *Cardiovasc. Intero. Radiol.* **2016**, *39*, 1110–1114. [CrossRef]
10. Woodward, C.S.; Pyeritz, R.E.; Chittams, J.L.; Trerotola, S.O. Treated pulmonary arteriovenous malformations: Patterns of persistence and associated retreatment success. *Radiology* **2013**, *269*, 919–926. [CrossRef]
11. Carlson, A.P.; Abbas, M.; Hall, P.; Taylor, C. Use of a Polytetrafluoroethylene-Coated Vascular Plug for Focal Intracranial Parent Vessel Sacrifice for Fusiform Aneurysm Treatment. *Oper. Neurosurg.* **2017**, *13*, 596–602. [CrossRef] [PubMed]
12. Stein, E.J.; Chittams, J.L.; Miller, M.; Trerotola, S.O. Persistence in Coil-Embolized Pulmonary Arteriovenous Malformations with Feeding Artery Diameters of 3 mm or Less: A Retrospective Single-Center Observational Study. *J. Vasc. Interv. Radiol.* **2017**, *28*, 442–449. [CrossRef]

applied sciences

MDPI

Review

Designing the Optimal Procedure: Role of CT Scan in the Planning of Transcatheter Structural Heart Interventions

Simone Circhetta [1], Edoardo Nobile [1], Aurelio De Filippis [1], Luisa Vicchio [1], Annunziata Nusca [1,*], Domenico De Stefano [2], Francesco Piccirillo [1], Valeria Cammalleri [1], Fabio Mangiacapra [1], Elisabetta Ricottini [1], Rosetta Melfi [1], Raffaele Rinaldi [1], Carlo Cosimo Quattrocchi [2], Francesco Grigioni [1] and Gian Paolo Ussia [1]

[1] Unit of Cardiac Sciences, Department of Medicine, Campus Bio-Medico University, 00128 Rome, Italy
[2] Unit of Diagnostic Imaging, Department of Medicine, Campus Bio-Medico University, 00128 Rome, Italy
* Correspondence: a.nusca@policlinicocampus.it

Abstract: Computed tomography (CT) scanning has recently assumed a first-pillar role in the preoperative planning of patients undergoing transcatheter structural heart procedures (e.g., transcatheter aortic valve implantation, TAVI; MitraClip; Triclip; left atrial appendage occlusion, LAAO). A careful preprocedural assessment is crucial for achieving the best possible result, and, currently, CT represents the paramount technique to obtain morphological data on cardiac and vessel structures, thus allowing to choose the most appropriate vascular approach, the type and size of devices, and all the required steps to meet procedural expectations. The image reconstruction accuracy also provides information to predict potential complications such as misplacements and leakages. This review aims to describe the role of CT in the decision-making approach of patients undergoing structural heart interventions and expand the clinicians' understanding of the benefits and drawbacks of this imaging technique.

Keywords: structural heart interventions; cardiac computed tomography; TAVI; MitraClip; Triclip; left appendage occlusion

Citation: Circhetta, S.; Nobile, E.; De Filippis, A.; Vicchio, L.; Nusca, A.; De Stefano, D.; Piccirillo, F.; Cammalleri, V.; Mangiacapra, F.; Ricottini, E.; et al. Designing the Optimal Procedure: Role of CT Scan in the Planning of Transcatheter Structural Heart Interventions. *Appl. Sci.* **2023**, *13*, 1589. https://doi.org/10.3390/app13031589

Academic Editor: Julio Garcia Flores

Received: 10 December 2022
Revised: 19 January 2023
Accepted: 21 January 2023
Published: 26 January 2023

1. Introduction

In recent years, cardiac computed tomography (CT) has become a useful tool for morphological cardiac imaging and has complemented echocardiography for evaluating structural heart diseases [1]. Due to its high spatial resolution, CT provides relevant morphologic information concerning chamber size, myocardial mass, and vascular and valvular structures [2,3]. In this regard, CT can determine the presence of disease and estimate the significance of dysfunction. Furthermore, it allows the morphological evaluation of other organs, by scanning through different planes, identifying potential related diseases worthy to be considered [4–9]. For these reasons, CT has become crucial for the heart team to decide on the intervention's suitability, both surgical and, even more, percutaneous [10]. Furthermore, as demonstrated by our group, CT is very useful for a better assessment of valves' morphology in order to provide a proper preinterventional planning [11–13]. In transcatheter heart valvular interventions (THVI), CT is also capable of providing accurate measurements for vascular access and device choice, assisting with landing zone characterization, defining patient-specific risk, and potentially reducing cardiac and peripheral procedural complications [14]. Thus, this review aims to retrace the main fields of CT application in structural heart diseases and related transcatheter interventions by demonstrating that this kind of imaging technology has become a cornerstone for clinicians and interventional cardiologists in the decision-making approach and management of complications.

2. Computed Tomography and Aortic Valve

2.1. Anatomy of the Aortic Valve

The three sinuses of Valsalva, the aortic leaflets, or cusps and the three fibrous interleaflet triangles compose the aortic root, including the aortic valve. The first correspond to the luminal surface of the three bulges of the aortic root, which support their respective valvular leaflets. The right and left sinuses house the corresponding coronary arteries (right and left), while the third sinus does not. Because of this, the third sinus is usually described as the noncoronary sinus [15].

The leaflets include the free edge, the closing edge attached to the aortic root, the lunulae, the belly, and the leaflet attachments or hinges. The hinges of each cusp join with those of the other two at the level of the sinotubular junction and run in parallel for a short stretch, forming the three aortic valve commissures. On the other side, the three interleaflet triangles are formed, owing to the semilunar fashion of the aortic leaflets' attachment to the wall of the aortic root. Each triangle represents a triangular region between the attachments of two adjacent leaflets and sinuses of Valsalva. The superior attachment of aortic leaflets (thus, the acute angles of the interleaflet triangles) is represented by the sinotubular junction, which demarcates the aortic root from ascending aorta, whereas the inferior boundary is demarcated by the ventricular–aortic junction. In detail, the peripheral attachments of the three aortic leaflets join to create a "crown-like" annular ring. The crown's base is represented by a virtual ring formed by joining the inferior attachment points (nadir) of the leaflets within the left ventricle (Figure 1a,b). The semilunar hinges then cross another true ring, the anatomic ventricular–aortic junction [16].

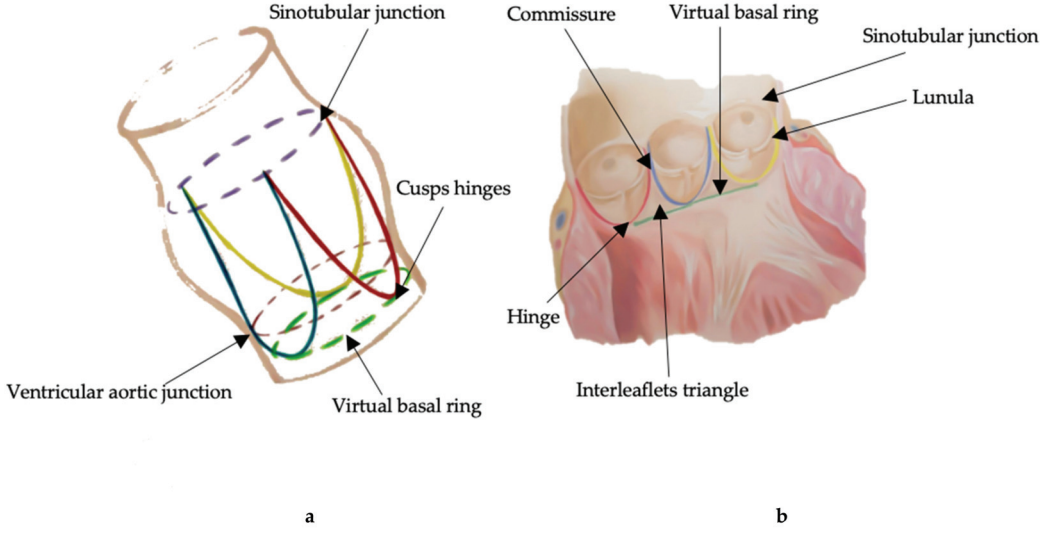

Figure 1. (**a**) Schematic representation of aortic valve anatomy. The dotted blue line indicates the sinotubular junction, the dotted green one depicts the virtual basal ring, and the dotted red one shows the ventricular aortic junction. (**b**) Graphic representation of an opened aortic root with its anatomical components.

2.2. Aortic Stenosis and TAVI (Transcatheter Aortic Valve Implantation) Indication

Aortic stenosis (AS) is the most prevalent valvular heart disease in Europe and the second most common in the United States. The progression of aortic stenosis depends on the severity of the condition at baseline [17]. Mean aortic valve gradients increased an average of 4, 6, and 10 mmHg/year in elderly patients with mild, moderate, and severe AS, respectively. Other factors that were associated with a faster hemodynamic progression included advanced aortic valve calcification, severe chronic renal failure, and anemia [18].

Without treatment, the average survival is only 2–3 years, with an increased risk of sudden death [18].

Transcatheter aortic valve implantation (TAVI) is a procedure that is now being recommended in older patients (≥75 years) or in those who are high risk (STSPROM/EuroSCORE II > 8%) or unsuitable for surgery. However, its indications are rapidly growing and progressively extending to younger patients with lower surgical risk [19]. Regarding aortic regurgitation, due to the difficult sealing and grasping of valves caused by the absence of calcium spots and the probable coexistence of dilated aortic root or ascending aorta, no clear recommendations exist, and the use of TAVI has been largely off-label [20–22].

2.3. CT Assessment of the Aortic Valve for Transcatheter Procedures

Multidetector computed tomography (MDCT) is considered crucial for the assessment of aortic valve defects (stenosis and regurgitation) and the preprocedural planning of TAVI [23].

On the technical side, TAVI CT assessment comprises two scans: an EKG-synchronized computed tomographic angiography (CTA) of the heart and aortic root, followed by a high-pitch non-EKG-synchronized CT multislice (CTM) for the evaluation of the access vessels. The two scans are combined into a complete protocol with a single contrast bolus through a peripheral vein. The amount of contrast medium should be calibrated to its concentration, patient's BMI, and kidney function (three thresholds should be considered: ≥60 mL/min/body surface area (BSA), 30–59 mL/min/BSA and <30 mL/min/BSA). Furthermore, for high-quality studies, according to the Cardiovascular Computed Tomography Society (SCCT), imaging should cover the entire cardiac cycle, and ALARA principles (as low as reasonably achievable) should be followed [24]. This means that the radiation dose that a patient could receive will vary depending on their weight or body mass index (BMI): 100 kV for patients with a BMI of 30 or less (or weight of 90 kg or less) to 120 kV for patients with a BMI of more than 30 kg (or weight more than 90 kg). Three scans are necessary to obtain useful parameters: the first is a basal one without contrast employed to calculate calcium scoring; a second one is used for cardiac evaluation with the administration of iodine contrast agent (after retrospective ECG synchronization); the last one should be extended from clavicles to the thigh's proximal portion in order to evaluate femoral and axillary accesses [24,25].

CT is almost universally accepted as a standard of care since its use has demonstrated a positive impact on clinical decision-making, favoring better post-TAVI clinical outcomes (Table 1) [26]. Therefore, Corcione et al. proposed a CT-based score called TAVI CT score, including the presence of nodular subvalvular calcium, the elliptical index (defined as the ratio of minimum aortic valve annulus diameter to maximum aortic valve annulus diameter), the aortic isthmus angle, the aorta ventricle angle, the presence of bicuspid valve, the coronary height, the detection of iliofemoral calcification, the access size, and the type of planned access, to predict outcomes. Notably, an increased risk of vascular complications was associated with higher scores [27]. Additionally, in a subanalysis of the WIN-TAVI registry, Spaziano et al. found that moderate or severe left ventricle outflow tract (LVOT) calcification detected by CT scan was an independent predictor of 1-year mortality or stroke [28]. The authors also reported that new pacemaker implantation (PMI) was independently associated with calcium volume of the right coronary cusp. In contrast, a protective effect on the same outcome was observed with the calcium volume of the noncoronary cusp. Lastly, according to this study, severe calcification of the noncoronary/right-coronary commissure can independently predict new atrial fibrillation onset [28]. In a study by Gama et al., it was demonstrated that membranous septum length measured at CT showed strong discriminatory ability for PMI [29]. Furthermore, Gegenava et al. highlighted that MDCT-derived global left ventricular longitudinal strain was a powerful predictor of all-cause mortality. As shown with the Kaplan–Meier curves, MDCT-derived LV GLS > −14% was related to higher cumulative rates of all-cause mortality than MDCT-derived LV GLS ≤−14% [30]. In the following paragraphs, we discuss all specific

parameters obtained using CT that are considered of interest in the preprocedural planning for aortic valve replacement.

2.3.1. Peripheral Access

Femoral access is the preferred access for TAVI. MDCT imaging identifies patients with complex vasculature anatomies, which may impact the decision to use an alternative vascular approach (i.e., transapical, transaxillary, or direct aortic) [31]. Vessel size and diameters, degree of calcification, vessel tortuosity, and high-risk features can be properly identified by CT through multiple projections (Figure 2a,b).

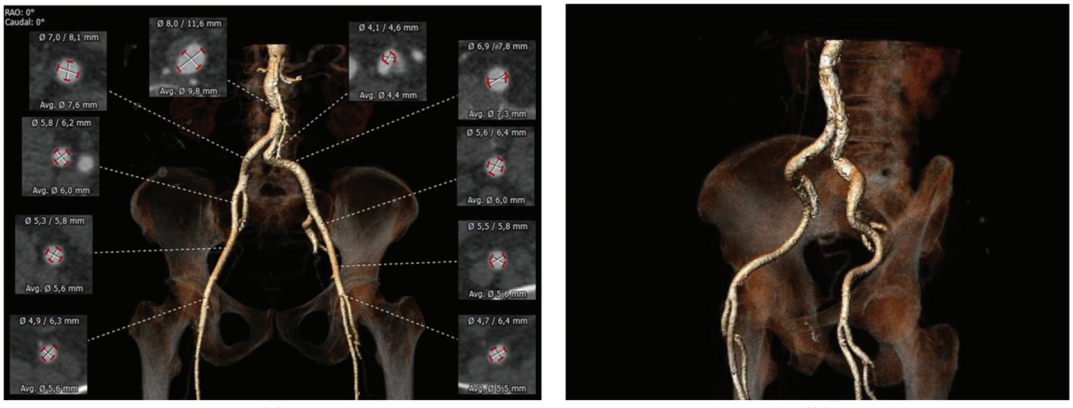

Figure 2. (**a**) Preoperative measurements of peripheral accesses for TAVI feasibility. (**b**) Preoperative femoral and iliac courses evaluation.

In a prospective study of 130 patients undergoing TAVI, Hayashida et al. found that vascular complications and 30-day mortality were associated with a sheath-to-femoral artery ratio (SFAR) of 1.05 or higher [32]. Later, Okuyama et al. proposed a change in this cut-off value, believing that this was too strict, providing high sensitivity but poor specificity, and 1.12 may be more appropriate (Table 1) [33].

Interestingly, the most recent valve delivery systems have a size ranging between 14 and 20 Fr, depending on the specific prosthesis valve type and size. While some years ago, a minimal lumen of femoral arteries of 6.0–6.5 mm was required, currently, with reduced delivery profiles, TAVI might also be indicated in patients with peripheral vessels as small as 5.0 mm [34].

2.3.2. Aortic Annulus

The aortic annulus for implanting percutaneous prostheses is not directly visible. It is a virtual ring that passes over a plane via the basal insertions (nadir) of the aortic valve cusps. It has an oval shape that varies during the cardiac cycle, even in patients with severe calcific AS. While the size of the aortic annulus was initially determined almost exclusively via two-dimensional transesophageal echocardiography (TEE), it has been proven that the aortic annulus is a dynamic measure during the cardiac cycle. Thus, 2D imaging could not be precise enough, and only 3D imaging can display a correct measurement. Furthermore, compared with a two-dimensional assessment of the annulus, MDCT-based measures have been proven to be highly reproducible and provide a deeper understanding of annular geometry [35]. Jurenkak et al. found that, during the cardiac cycle, the aortic root varies its shape, suggesting that an MDCT evaluation during the early systole phase is the best choice for TAVI planning [36].

Annular dimension can be quantified with multiple methods: cubic spline interpolation, polygon, attenuation/Hounsfield-unit-based contour detection, and freehand contour.

ECG-synchronized, ideally multiphasic, dataset should be used for proper measurement, identifying the reconstruction phase with the largest annular dimensions, thus ensuring accurate device sizing [24]. MDCT sizes the aortic annulus using annular area and perimeter measurements. In the Pivotal Trial of Medtronic Corevalve and the PARTNER 3 trial, it was demonstrated that annulus sizing based on CT measurements reduces the risk of complications such as paravalvular leakages. Moreover, the aortic annulus perimeter or cross-sectional area is superior to the annulus diameter for reducing the likelihood of paravalvular aortic regurgitation (PAR) [37,38] (Figure 3).

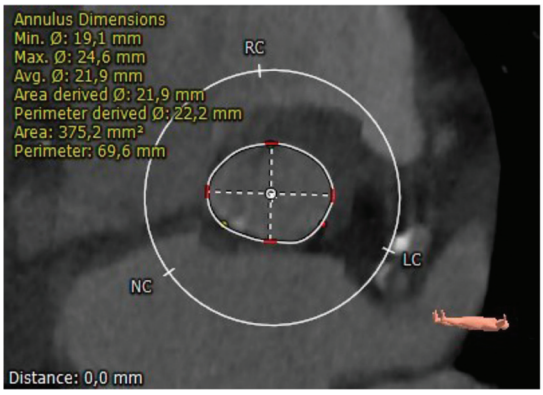

Figure 3. CT measurements of perimeter and area of aortic annulus.

Another goal of current CT sizing algorithms is to calculate a certain degree of oversizing of the transcatheter heart valve (THV) to avoid the post-implantation occurrence of paravalvular leaks (PVLs). It depends on the type of THV and the measurement used (perimeter/area). Self-expandable devices need more oversizing than balloon-expandable prostheses. Conversely, severe oversizing using balloon-expandable devices might increase the annular damage. Additionally, a 10 per cent perimeter oversize does not equal a 10 per cent area oversize, but it is closer to 20 per cent [39].

2.3.3. Aortic Leaflets

Three major parameters regarding aortic leaflets should be carefully considered during the preprocedural planning for TAVI: the number of cusps, the degree of leaflet calcification, and the height of the leaflets to the coronary ostia. MDCT has been proven to be superior to trans thoracic echocardiogram to discriminate aortic valvular morphology and the exact location and quantification of calcifications [40] (Figure 4a,b).

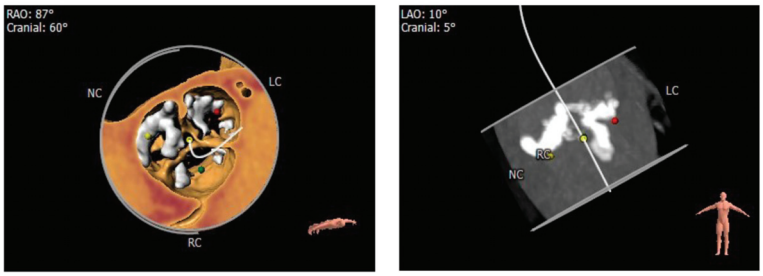

(**a**) (**b**)

Figure 4. (**a**) Calcium degree and morphology evaluation of the aortic valve by CT. (**b**) LAO–cranial view for calcium location assessment.

The bicuspid aortic valve (BAV) is an important risk factor for premature aortic stenosis and challenging anatomy for percutaneous interventions. Thus, patients with bicuspid valves were excluded in the largest trials regarding TAVI due to complex anatomic features (i.e., more calcified, and asymmetrical leaflets, annular eccentricity, and associated aortic dilation). However, in recent years, the interest in this topic has rapidly grown, and the first data appear to be quite satisfactory [41]. BAV has historically been diagnosed with echocardiography that, compared with pathologic analyses obtained from cardiac surgery, can detect this kind of valve morphology in a range between 54 and 93%. Nevertheless, CT was found to be superior to transthoracic echocardiography, especially in patients with extensively calcified aortic valves [42] (Figure 5). In fact, taking into account echocardiographic and tomographic images of fifty patients with AS plus probable bicuspid aortic valve and comparing with surgical findings, Tanaka et al. found that CT data were not significantly different from the intraoperative ones, but the echocardiographic were [42].

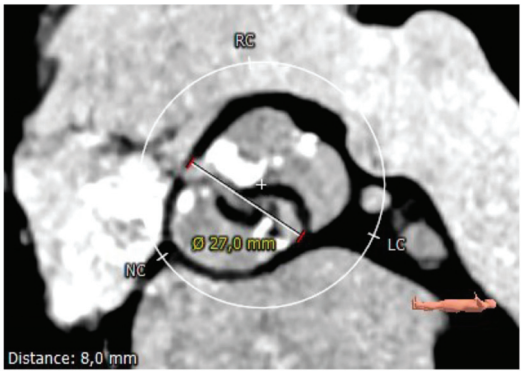

Figure 5. CT image of bicuspid valve.

MDCT images should assess several anatomical aspects in the setting of bicuspid aortic valves: the location of raphe by reviewing the commissures symmetry from the basal plane to the sinotubular junction, the specific morphology according to the Sievert classification, the extent of leaflet asymmetry, the degree of calcification, and the length and width of the raphe into the lumen. Indeed, more paravalvular regurgitation due to incomplete valve expansion could be associated with longer calcified raphe and calcium impingement > 4 mm [43].

Quantifying aortic valve calcification by noncontrast CT (CT-AVC) has demonstrated good accuracy in defining the valvular calcification burden (location, extent, and severity), demonstrating satisfactory concordance with echocardiography, and providing incremental prognostic information. CT-AVC has been reported to correlate significantly with peak velocity, mean gradient, and the aortic valvular area measured by echocardiography [44]. AVC is typically assessed by analyzing 1.5–3 mm slice thicknesses CT scans using prospective or retrospective electrocardiogram (ECG) gating and at lower tube current than contrast-enhanced CT studies, thus resulting in a low radiation dose of approximately 1 mSv. AVC can be measured by numerous methods, including Agatston, mass, and volumetric scores. Among these, the first method is more frequently employed.

Electron-beam and multidetector row CT studies demonstrate that the severity of AVC is a robust prognostic predictor in asymptomatic patients with severe AS (Table 1) [45]. Therefore, worse outcomes have been experienced by asymptomatic patients with severe AS and high calcium scores compared with those with low scores [46]. Moreover, preoperatively AVC assessment is crucial for TAVI because it has been demonstrated to negatively affect procedural success and outcomes given the greater presence of paravalvular regurgitation, conduction abnormalities, aortic annulus rupture, coronary ostia occlusion, and stroke. Furthermore, Leber et al. found that, in an analysis of 68 patients undergoing

TAVI, calcium score significantly correlated with 30-day major adverse cardiac events (MACE) and 1-year mortality and with the incidence and severity of post-procedural aortic regurgitation. Patients with calcium scores > 750 experienced a significantly lower 1-year survival rate than those with <750 [47]. Haensig et al. confirmed these findings in a series of 120 patients receiving an Edwards SAPIEN prosthesis via a transapical approach [48].

Extensive calcification of the aortic cusps also represents a risk factor for obstruction of the left main coronary artery during THV deployment [31]. Additionally, Lee et al. found that subjects with at least mild–moderate post-procedural aortic regurgitation had higher AVC scores than patients with no PAR on follow-up [49]. Unbehaun et al. evaluated the amount of calcifications of the aortic landing zone, including the left ventricle outflow tract (LVOT), aortic annulus, and valvular cusps in 307 patients undergoing transapical TAVI, using a semiquantitative (4-point scale) and quantitative (Agatston calcium score) CT method. They found that an increased risk of PAR was strongly related to each 100-unit increment of the Agatston calcium score. Furthermore, a higher risk of AR was reported in patients with asymmetric cusp calcification and severe calcification of the landing zone [50]. Interestingly, Feuchtner et al. recently showed that paravalvular AR increased with the protruding rather than the "adherent" calcifications of the aortic valve and root [51].

2.3.4. Coronary Ostia

MDCT is crucial to identify the distance from the annulus/leaflet hinge point to the left main and right coronary ostia and the length of the corresponding coronary cusp (Figure 6a,b). Multiplanar, three-dimensional techniques allow better visualization and assessment of these complex structures and their relationships. For this reason, CT represents the preprocedural imaging gold standard for the evaluation of the risk of coronary occlusion. Even if there is no threshold value contraindicating the procedure, an increased risk of coronary occlusion was reported in patients with a coronary ostial height from the annulus < 12 mm and a sinus of Valsalva mean diameter < 30 mm. To ensure reproducibility, the height of the coronary ostia perpendicular to the plane of the annulus should be measured with an electronic caliper from the plane of the ring to the bottom of the ostium. No recommendations exist as to whether these measurements should be performed in systole or diastole [24].

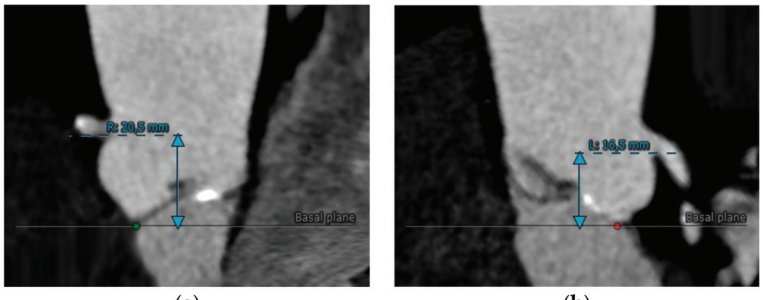

(**a**) (**b**)

Figure 6. (**a**) Right and (**b**) left coronary ostia height assessment by CT images.

Ribeiro et al. found that coronary occlusion most commonly affects the left coronary (88.6 per cent) and occurs more commonly in women and following balloon expandable TAVI. In a systematic review, several parameters were found to be possible predictors of procedural complications: a low-lying coronary ostium < 10 to 12 mm from the basal leaflet insertion to the coronary ostium as measured by MDCT, mean sinus of Valsalva diameter of <30 mm, and sinus of Valsalva diameter/annular diameter ratio of <1.25. Furthermore, according to this analysis, women appear to be more subjected to coronary occlusion because of smaller aortic root dimensions and lower coronary ostial height [52]. Probably, significantly oversized THV or aortic root dissection, the displacement of native bulky aortic

leaflets, impingement of the coronary ostia by the THV support structure, the embolization of calcium, thrombus, etc., are the mechanisms underlying coronary obstruction.

2.3.5. Sinotubular Junction (STJ) and Proximal Aorta

An inaccurate measure of the sinotubular junction and its degree of calcification may be associated with the incidence of prosthesis–patient mismatch (PPM) [53]. Small and severely calcified sinotubular junctions may also predispose to several complications: THV embolization, aortic root rupture during implantation of the THV, and balloon migration. In addition, using longer balloon-expandable valves, the sinotubular junction could be damaged with a transcatheter device.

The accuracy of MDCT imaging of the sinotubular junction depends on the measurement method. Compared with axial methods, double-oblique imaging yields similar findings to planimetry, and measurements obtained by double-oblique imaging are generally smaller, as was demonstrated in a study of patients with thoracic aortic aneurysms [54]. The height of the sinotubular junction should be measured perpendicular to the ring's plane using an electronic caliper from the annulus to its lowest point [24] (Figure 7a,b).

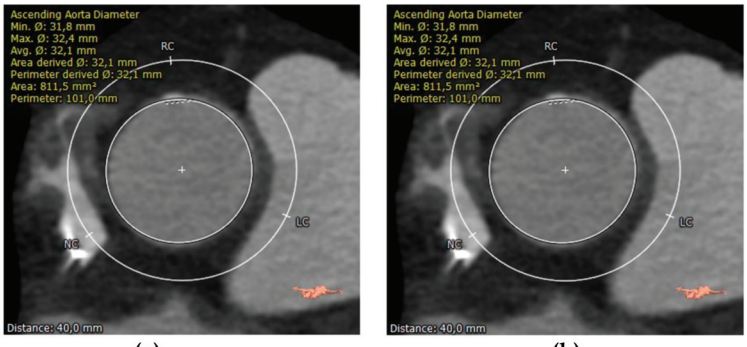

Figure 7. (**a**) Sinotubular junction and (**b**) proximal ascending aorta evaluated by CT for TAVI.

2.3.6. Left Ventricular Outflow Tract (LVOT) and Septum

Both self-expandable and balloon-expandable THVs extend their lower extremity into the left ventricular outflow tract (LVOT). A careful assessment of this region should be performed to minimize complications (Figure 8a,b).

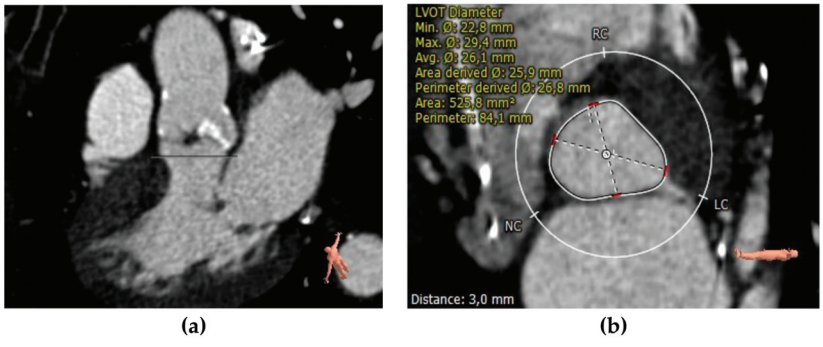

Figure 8. (**a**) LVOT calcium degree evaluation. (**b**) Preoperative LVOT measurements.

The proper seating of the THV and the risk of spontaneous repositioning after deployment can be affected by marked upper septal hypertrophy protruding in LVOT. Furthermore, prominent septal hypertrophy is associated with atrioventricular blocks and

the need for post-TAVI PMI [55]. Accordingly, Jilaihawi et al. showed that MDCT-based measurements of septal thickness predict the post-TAVI occurrence of AV blocks [56]. Septal hypertrophy causing significant LVOT obstruction is a contraindication to TAVI; however, as demonstrated by Moreno et al., proper modifications to THVs can allow successful implantation in this kind of patients [57]. Notably, Stolzmann et al. found that echocardiography tends to overestimate interventricular septum thickness compared with MDCT (up to 2.2 mm) [58] (Table 1).

Table 1. Main studies investigating the predictive role of CT-derived variables on related outcomes.

Study	CT-Derived Variable	Predicted Outcomes
Corcione et al. [27]	Valvular calcium score, elliptical index, aortic isthmus angle, aorta-ventricle angle, bicuspid valve, coronaries height, ilio-femoral calcifications, access size, type of planned access	Vascular complications
Spaziano et al. [28]	Left ventricle outflow tract calcium score	1-year mortality and stroke
Gama et al. [29]	Membranous septum length	Pacemaker implantation
Gegenava et al. [30]	Left ventricle global longitudinal strain	All-cause mortality
Hayashida et al. [32]	Sheath-to-femoral artery ratio > 1.05	Vascular complications and 30-day mortality
Okuyama et al. [33]	Sheath-to-femoral artery ratio > 1.12	Vascular complications and 30-day mortality
Rosenhek et al. [46]	Aortic calcium score	Paravalvular regurgitation, conduction abnormalities, aortic annulus rupture, coronary ostia occlusion and stroke
Leber et al. [47]	Aortic calcium score	30-day major adverse cardiac events, 1-year mortality and post-procedural aortic regurgitation
Haensig et al. [48]	Aortic calcium score	30-day major adverse cardiac events, 1-year mortality and post-procedural aortic regurgitation
Lee et al. [49]	Aortic calcium score	Para-aortic regurgitation
Unbehaun et al. [50]	Aortic calcium score	Para aortic regurgitation
Ribeiro et al. [52]	Low coronary ostium <10 to 12 mm, mean sinus of Valsalva diameter < 30 mm, sinus of Valsalva diameter/annular diameter ratio < 1.25	Coronary occlusion
Jilahawi et al. [56]	Septal thickness	Atrioventricular blocks

Furthermore, the risk of significative residual aortic regurgitation and second valve implantation can be affected by moderate or severe LVOT calcification. In this regard, Okuno et al. proposed a specific classification based on the severity of LVOT calcification: mild was detected in the presence of one nodule extending <5 mm in any dimension and covering <10% of the perimeter of the LVOT; moderate was documented in the presence of two nodules or one extending >5 mm in any direction or covering >10% of the perimeter of the LVOT; and severe was considered in the case of multiple nodules of single focus

extending >10 mm in length or covering >20% of the perimeter of the LVOT. Additionally, patients with moderate or severe LVOT calcification and treated with earlier-generation THVs suffered from an increased risk of annular rupture. The difference was not statistically significant among patients treated with newer generation prosthetic valves. Concordantly, it was observed that patients with moderate or severe LVOT calcification have an increased risk of death for all-cause mortality at one year [59].

3. Computed Tomography and Mitral Valve

3.1. Anatomy of the Mitral Valve

The mitral valve (MV) apparatus is composed of different parts: valvular annulus, two leaflets, chordae tendineae, and papillary muscles (Figure 9a,b).

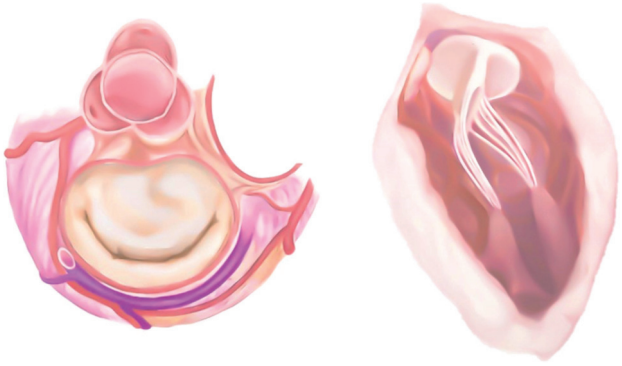

(**a**) (**b**)

Figure 9. (**a**) Transverse and (**b**) sagittal planes of the mitral valve.

The MV annulus has a saddle shape. Its anterior flat portion, thus, the superior "horn", is connected by collagen fibers with the aortic annulus at the level of the noncoronary and the left aortic valve cusps. This fibrous part is called the aortomitral junction [60]. The posterior part of the mitral annulus includes the low saddle points in proximity to the lateral and medial commissures and the posterior saddle horn. This posterior part of the annulus is in continuity with the flexible, less fibrotic endocardium and may be subject to dilation. For this reason, it follows the myocardial contraction and relaxation, accentuating saddle height and decreasing circumferential area [61]. Notably, the MV annulus is surrounded by critical vascular structures, particularly by the coronary sinus (CS) posteriorly and the left circumflex artery laterally.

The anterolateral and posteromedial commissures separate the anterior and the posterior MV leaflets. The two MV leaflets are significantly different in size. The anterior leaflet, during systole, configures the posterior part of the left ventricular outflow tract, occupies one-third of the annulus, and is longer than the posterior leaflet, which sticks to two-thirds of the annulus. The posterior leaflet typically has two indentations which divide it into three individual scallops: a P1 lateral scallop (adjacent to the left atrial appendage), a larger central P2, and a medial P3 scallop according to Carpentier's classification. Contrarywise, the anterior leaflet is not anatomically divided into scallops, but its segments are referred to as A1, A2, and A3, corresponding to P1–3 [60].

The subvalvular apparatus of the MV includes chordae tendineae and papillary muscles. The primary cords anchor to the free edges of the leaflets, the secondary ones to the ventricular surface of the leaflets, and the tertiary ones originate from the left ventricular wall or muscle trabeculae at the posterior leaflet of the VM. Their function is to maintain, during systole, both leaflets in a position that allows their coaptation in systole without protrusion into the left atrium [62,63]. As far as the papillary muscles are concerned, the

anterolateral muscle arises from the apical-lateral third of the left ventricle. In contrast, the posteromedial muscle derives from the middle of the lower wall of the left ventricle. From their apex, the papillary cords take origin [64]. Their vascularization is important to understand some complications of infarction: notably, the left anterior descending and diagonal or marginal coronary branches feed the anterolateral papillary muscle; instead, in most cases, only one coronary artery (depending on the dominance, circumflex or right coronary artery) feeds the posteromedial papillary muscle. The different vascularization allows us to understand the susceptibility of the latter to ischemia and rupture.

3.2. Mitral Regurgitation and Transcatheter Interventions

Mitral regurgitation (MR) is the most common valvular pathological condition in the Western world [65]. It can be classified as primary or secondary. Therefore, a primary valve defect such as a flail or prolapse causes a primary MR. Secondary MR is due to the incomplete coaptation of the valve leaflets caused by the malposition of the subvalvular apparatus; it can be both ischemic and not [66].

Today, surgery remains the standard gold treatment for symptomatic MR patients. However, in recent years, transcatheter mitral valve surgery (TMVI) has emerged as a safe option for patients with high surgical risk [67]. According to the latest ESC 2021 guidelines on valvulopathies, transcatheter mitral valve repair can be considered in patients with chronic mitral regurgitation, symptomatic, with high surgical risk or inoperable, carefully avoiding futile treatments (IIA for secondary mitral regurgitation and IIB for primary mitral regurgitation) [19].

Recently, various techniques for the transcatheter mitral valve have been devised, often with reference to pre-existing surgical techniques. The MitraClip NT® System (Abbott Vascular, Santa Clara, CA, USA) is a repair system that conceptually emulates the "edge-to-edge" repair described by Maisano et al. [68]. It consists of a clip that hooks the two mitral leaflets simultaneously, reducing the width of the regurgitant orifice. Several randomized trials demonstrated the benefit of MitraClip in reducing mortality and hospitalization rate in patients with primary and functional MR [69–71]. Some other devices have been designed for the percutaneous treatment of MR, such as the Cardioband System® (Valtech Cardio, Or Yehuda, Israel) and the CARILLON Mitral Contour System® (Cardiac Dimensions, Inc., Kirkland, WA, USA), which mimic annuloplasty procedures. Unlike the MitraClip system, the latter technique can only be used for secondary etiology [72]. Finally, great interest revolves around transcatheter mitral valve replacement (TMVR); however, the growth of this technique, due to the complex anatomy of the mitral valve apparatus, the heterogeneity of pathology, and mitral annular dynamism, is undoubtedly slower than the explosive development of TAVI. As anticipated, several devices have been developed for this purpose, each with a different valve-anchoring mechanism (e.g., native flap engagement, mitral annulus clamping, apical tether, mitral annulus clamping, radial force, outer anchorage, flaps annular, subannular mitral annulus).

3.3. CT Assessment of the Mitral Apparatus for Transcatheter Procedures

Imaging modalities are necessary to provide information on mitral valve anatomy complexity and obtain a detailed plan for transcatheter procedures. Although echocardiography has represented the gold standard for pre- and post-treatment grading, diagnosis, and monitoring, MDCT has become widespread for interventional planning in patients who are candidates for TMVI. It allows rapid image acquisition time and wide availability, excellent spatial resolution, allowing high-quality 2D and 3D reconstructions of the entire mitral apparatus at any moment of the cardiac cycle, high reproducibility and relative operator independence, visualization, quantification of calcifications, and a complete view of the heart in its entirety and the chest wall [72]. CT provides relevant information on mitral leaflet pathology. Compared with echocardiography, CT provided the highest accuracy in identifying prolapse (sensitivity of 96%; specificity of 93%) [73].

Furthermore, cardiac CT is an excellent technique for diagnosing annular disjunction, a remodeling process associated with mitral valve prolapse, since observation of the entire cardiac cycle allows us to evaluate not only the degree of disjunction but also the dynamics of the ring [74]. In the context of secondary or functional MR, CT also provides essential information regarding the geometry of the valve and the remodeling process (including flap tenting heights and coaptation depth). Knowing that these data are essential for docking the device, CT provides details on the anatomy of the left ventricle, which is also crucial in assessing feasibility. A ventricular diameter greater than 70 mm is often considered an exclusion criterion for transcatheter procedures [75].

Exact measurements of the mitral annulus are critical for choosing the correct device size and, consequently, for an effective TMVI procedure [76]. Equally important is the understanding of the modifications of the annulus during the various phases of the cardiac cycle (modifications that vary according to the type of etiology of the insufficiency); based on this, the landing zone and the type of device are decided [77]. It appears evident that the annulus is larger in patients with mitral regurgitation than in controls, with a greater remodeling in an anterior–posterior, rather than lateral, direction [76]. Furthermore, in functional MR, the annulus reduces movement compared to primary MR [78]. According to Palmisano et al., some annular geometry changes in patients with severe mitral regurgitation were detected using CT. They demonstrated that the mitral valve annulus was larger in patients with severe MR, especially in patients with prolapse (Carpentier type II). It is curious how, in these patients, the largest dimensions were found in the systolic phase, unlike controls in which the largest area is found in the early diastolic phase [79].

3.3.1. Annulus Sizing

Measurement of the mitral annulus is of primary importance since inaccurate sizing has devastating consequences. Moreover, given the complex mitral annulus 3D shape, collecting annular sizing could be challenging [80]. A direct calculation method involves tracing the edges of the annulus on conventional two-, three-, four-chamber, and short-axis views along the posterior mitral leaflet insertion and fibrous continuity. However, this method is time-consuming and can lead to an oversized device, increasing the risk of left ventricular outflow tract obstruction (LVOT). Blanke et al. developed a more straightforward method that assumes assimilating the mitral annulus to a planar D shape; given these premises, the two fibrous trigones are connected along a virtually straight line, effectively excluding the anterior horn [81]. Since the dimensions of the mitral annulus change during the cardiac cycle, the calculations are performed in the cardiac cycle phase in which the annulus is larger. Area and perimeter are the most used measures. However, other parameters are developed, such as the trigone–trigone distance; the intercommissural distance, which corresponds to the maximum diameter of the annulus parallel to the trigone–trigone distance; the septum-lateral distance, which corresponds to the maximum diameter of the annulus perpendicular to the IC. It must be emphasized that each device refers to different parameters for sizing [79].

3.3.2. Predicting LVOT Obstruction

The LVOT lies between the mitro-aortic continuity and the interventricular septum. The placement of a transcatheter mitral valve prosthesis could extend and narrow the LVOT (neo-LVOT) due to anterior deflection of the AML [82]. Indeed, LVOT obstruction is a significant cause of mortality and morbidity following TMV replacement procedures (TMVR) [83]. CT can predict the size of anticipated neo-LVOT, thus predicting potential obstruction. A recent study demonstrated that a CT neo-LVOT area measuring 1.7 cm^2 or smaller predicts LVOT obstruction with a sensitivity of 96% and a specificity of 92% [84]. Notably, the neo-LVOT size is also dynamic; for this reason, it is usually measured throughout systole.

Notably, LVOT changes the cardiac cycle; therefore, this measurement is made in systole. Several device- and patient-specific factors could influence the size of the neo-

LVOT. The former include stent protrusion, flare, and skirt size [85]. A more ventricular position of the mitral prosthesis, defined as a ventriculo-atrial offset of 80:20 (i.e., 80% of the device is positioned on the ventricular side and the remaining 20% on the atrial side), increases the risk of neo-LVOT obstruction. On the other hand, patient-specific characteristics include aortomitral angle, basal septal thickness, and anterior mitral leaflet length. The aortomitral angle is defined as the internal angle between the central axis of the mitral and aortic annulus; in particular, the risk of obstruction increases when the measurement of this angle approaches or exceeds 90°. Another factor influencing the risk of obstruction is the thickness of the interventricular septum, particularly a value greater than 14 mm [86]. Finally, longer anterior leaflet lengths (>30 mm) are associated with the possibility of neo-LVOT obstruction [87]. All these parameters should be carefully evaluated before proceeding with percutaneous mitral valve replacement to reduce complications and improve procedure success.

3.3.3. Landing Zone

CT provides information about the potential landing zone, defined as the site where the mitral prosthetic device should be deployed. It varies according to the device used and the specific mitral defect (functional MRI or mitral prolapse). As mentioned, a landing zone of 80/20 should be achieved. This means that, after deployment, about 80% of the device should be located on the ventricular side, whereas the remaining 20% on the atrial side. However, many factors may affect landing zone definition, such as the presence of mitral annulus (MAC) calcification, annular disjunction, and atrioventricular platform (abnormal atrial displacement of the mitral valve leaflet hinge point). In those devices that are anchored by friction and radial force, the MAC in the landing zone is essential [80]. Hence, CT accurately estimates gravity, density, and magnitude. Furthermore, an atrioventricular shelf of the LV myocardium can often be found near the junction point of the posterior mitral leaflet in patients with basal myocardial remodeling [88]. The presence of this shelf is more relevant for those mitral devices that use the inferolateral basal myocardium for anchoring. Finally, in these patients, the measurements must be performed in the physiological position [80].

3.3.4. Mitral Anulus Calcification

MAC is crucial when considering TMVI; it has been demonstrated to be an independent predictor of an elevated mean diastolic gradient after the MitraClip procedure [89]. It also contraindicates the use of some valve replacement devices. CT is the gold standard for its diagnosis and characterization, demonstrating a higher diagnostic performance than MRI and echocardiography. Degenerative annular mitral calcification (MAC) is a common finding in the elderly, with an incidence of about 6% [87]. It is the consequence of a progressive calcification of the fibrous part of the mitral annulus. Although typically confined to the posterior border of the annulus, its extension may circumferentially involve the annulus. Another cause of MAC is caseous calcification of the mitral annulus (CCMA). CCMA has a different territory of distribution (typically the area close to the posterior mitral leaflet) and a different composition (with calcium disposition only in the periphery and a central zone of variable attenuation without contrast enhancement). Therefore, CT can accurately describe these formations and the exact distinction between MAC and CCMA [90].

3.3.5. Vascular Structures

Preprocedural planning for TMVI includes careful evaluation of surrounding vascular structures using CT. Therefore, a fundamental part of the evaluation concerns the course and patency of the circumflex artery (Cx) due to its proximity to the posterior mitral annulus. When this distance is too short, some transcatheter procedures are contraindicated due to the risk of vessel closure during the fixation of the device. The distance between these two structures should be measured on multiple views to avoid the risk of dissection, closure, or perforation of the coronary sinus (CS) during or after the procedure [91,92]. In particular,

the relationship between the distance and angle between these two structures and the procedural success of patients undergoing transcatheter annuloplasty with the Carillon device has been demonstrated [93]. Consistently, a distance of CS to Cx of <8.6 mm in the distal device landing zone has been shown to be predictive of complications on the circumflex artery [94].

3.4. Other Potential Use of CT in Transcatheter Mitral Valve Interventions

Choosing the optimal approach for TVMI is also essential in procedural planning, and CT plays a crucial role in this context. Thus, in patients undergoing a transapical procedure, CT can be used to understand which intercostal space is close to the apex of the left ventricle and could allow the device to be deployed perpendicular to the mitral annulus, thus avoiding obstruction, perivalvular leaks, and canting [80]. Although most mitral procedures require intraprocedural transesophageal echocardiography guidance, CT can determine the optimal site for the septal puncture in those with the transseptal approach. Although there are no specific guidelines, it is preferred to puncture the inferoposterior section to obtain good coaxiality to the mitral annulus [95]. Moreover, it is very useful to calculate the distance from the puncture site to the mitral valve.

CT is also helpful in determining the optimal fluoroscopic viewing angle of the mitral annulus for device deployment, which should be perpendicular to the mitral annulus (coplanar angle) [80]. Knowledge of this angle is fundamental for interventionists for accurate coaxial device positioning. Indeed, any change from this fluoroscopic angle can translate into inaccurate deployment, potentially increasing procedural complications.

In patients undergoing mitral valve-in-valve (VIV), CT can identify patients at higher risk of complications, providing information on the pre-existing prosthesis and thus predicting the risk of LVOT obstruction [90].

Finally, CT has a role in the follow-up of patients undergoing TMVI, especially in assessing the presence of any subclinical thrombosis. Although the clinical significance of the latter is not yet known, CT can diagnose this complication by highlighting it as a thickening of the hypodense flap with the decreased movement of the prosthetic flaps [96]. CT also has a role in predicting the risk of mitral stenosis after the MitraClip procedure. In a study by Kaewkes et al., annulus diameters (both anteroposterior and medial–lateral), annulus area, and mitral valve orifice area were inversely associated with transvalvular gradients [97].

4. Computed Tomography and Tricuspid Valve

4.1. Anatomy of the Tricuspid Valve

The tricuspid valve (TV) is the heart's largest and most anterior valve, with a mean orifice area of 8 cm^2 [98]. Its functional anatomy comprises four main parts: annulus, leaflets, chords, and papillary muscles (Figure 10).

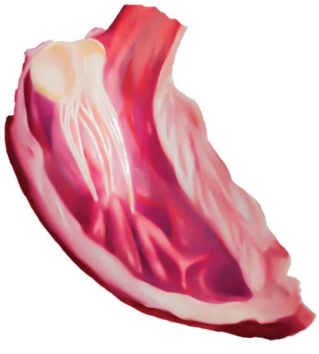

Figure 10. Graphic representation of tricuspid valve anatomy.

Even upon surgical inspection, the annulus is slim and difficult to identify; it has a nonplanar D shape and forms a 45-degree angle to the sagittal plane. Moreover, its structure changes during the various phases of the cardiac cycle, reaching an increase of 30% during the early phase of diastole [99]. The leaflets broadly vary among individuals. Three flaps (anterior, medial, and septal) are distinguishable in 54% of cases, but four or more flaps are often present. The anterior leaflet is the most extensive and mobile, while the posterior is the shortest in the circumferential plane. The septal leaflet is the shortest in the radial plane and the least mobile [100]. The tendinous cords are redundant, ranging from 17 to 36 [101]. Accessorial cords arise from the right ventricular free wall. The chordal insertion in the TV is variable and consists of rough zone chords, free edge chords, deep chords, basal chords (the most common type), and fan-shaped chords (which are attached mainly to the commissures) [11]. The cords emerging from the anterior papillary muscle attach to the anterior and posterior leaflets. In contrast, from the posterior papillary muscle, which can be bifid, the cords depart for the posterior and septal leaflets. The septal papillary muscle, usually smaller than the previous ones, instead supplies the cords for the anterior and septal leaflets [101]. Other anatomical structures are fundamental in all procedures performed on TV and in the right ventricle (RV). The noncoronary aortic valve cusp, the atrioventricular nodule, and the bundle of cords are in proximity to the anteroseptal commissure. Moreover, the coronary sinus is anatomically close to the posterior septal commissure, while the right coronary artery is close to the TV annulus [98,102].

4.2. Tricuspid Regurgitation and Transcatheter Interventions

Tricuspid valve disease has consistently been underestimated. However, in recent years there has been important progress in percutaneous repair techniques, which has shifted the focus to this pathology. An important study in Olmsted County reported an age- and sex-adjusted prevalence of 0.55% of greater or equal to moderate tricuspid regurgitation (TR), mostly women [102]. The mortality of those patients was significantly higher than that of the matched cases with trivial TR [102]. Similar findings were reported by another large cohort study, where long-term, higher functional TR severity was associated with considerably worse survival independently of baseline characteristics [103]. The development and successful results of transcatheter aortic valve implantation, followed by transcatheter therapies for mitral valve disease, have also opened many opportunities for transcatheter treatment of TR [104]. For this reason, the need to develop adequate imaging techniques for preoperative planning in this type of procedure has become increasingly urgent.

4.3. CT Assessment of the Tricuspid Apparatus for Transcatheter Procedures

The multiphasic, contrast-enhanced, retrospective cardiac-gated CT acquisition enables multiplanar reconstruction of the entire heart silhouette, including the proximal main vessels, allowing a comprehensive understanding of the right heart anatomy (Figure 11) [105].

The amounts of contrast and radiation required have been considerably reduced with the new CT scanners, as well as the duration of the acquisition phase. It is also possible to perform more precise reconstructions even in elevated heart rates, such as atrial fibrillation, a widespread pathology in patients with significant TR [106]. Notably, a dedicated protocol for tricuspid valve CT acquisition is necessary; it requires opacification of the right heart cavities by a monophasic or biphasic injection with a mixture of saline and contrast in different percentages and following bolus tracking in the right ventricle or the pulmonary artery [107].

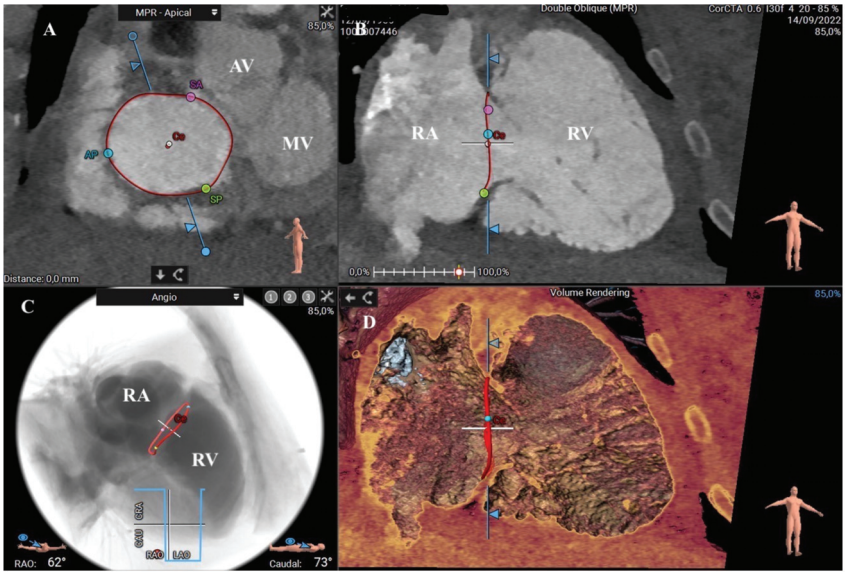

Figure 11. CT assessment of the tricuspid annulus using a semiautomated software-based approach (3mensio Structural Heart; Pie Medical Imaging, Maastricht, The Netherlands): (**A**) Transverse plane (short-axis) at level of tricuspid annulus that is delineated by the red line. The centroid of the tricuspid valve (Ce) and the three main commissures (SA: septal anterior, SP: septal posterior, AP: anteroposterior) are identified according to specific anatomical landmarks. (**B**) Coronal plane (long axis) at level of the anteroposterior diameter of the tricuspid annulus. (**C**) Fluoroscopic and angiographic simulation showing the three-dimensional position of the tricuspid annulus and commissures within the right heart chambers. (**D**) Three-dimensional recontraction by the volume rendering of the right chambers showing the geometrical spatial relationship of the tricuspid annulus and surrounding structures. RA: right atrium; RV: right ventricle; MV: mitral valve; AV: aortic valve.

The comprehensive assessment of the right heart and the adjacent anatomical structures, which the tricuspid defect could significantly remodel, provides an appropriate evaluation for TR severity, patients' clinical risk stratification, anatomical suitability for tricuspid interventions, and preprocedural planning in patients undergoing TV therapies [105]. Specifically, several fundamental parameters might be obtained by CT imaging in order to design the optimal procedure and achieve the highest success rate during transcatheter tricuspid valve interventions (TTVI), such as dimensions and morphology of the TV annulus, location of commissures, tethering parameters, anatomical regurgitant orifice area, right atrium (RA) and RV dimensions, surrounding structures, device landing zone, and vascular access routes [11]. Using multiplanar reconstruction, tricuspid cross-sectional area, perimeter, septolateral (SL), and anteroposterior (AP) diameters can be obtained by a short-axis view on the annular level. The SL diameter refers to the maximal distance in septal to the lateral direction (that corresponds to the anulus measurement in the four-chamber view at the transthoracic echocardiography), whereas the AP diameter is orthogonal to the previous one. Due to the complex saddle-shaped structure of the tricuspid annulus, a 2D approach does not precisely address the valvular anatomy. Therefore, 3D semiautomated software can help in this setting [108]. Moreover, dimensions are usually obtained both at end-systole and mid-diastole because of the dynamic variability in annular size. Interestingly, in a study by Praz et al., there was a good correspondence between TEE and CT for tricuspid annulus sizing and valve area in patients with severe TR [109]. Finally, distances between commissures (anteroseptal, posteroseptal, and anteroposterior) and distances between the centrum of the TV and commissures can also be measured [12].

The leaflet tethering is another important parameter to consider in TTVI planning. In a study by Van Rosendael et al. [110], in patients with TR $\geq$ 3+, CT exhibited greater tricuspid annulus and RV dimensions and marked tethering of the anterior and septal tricuspid leaflets compared to those with mild valvular defects. Of note, the grade of functional TR was independently correlated with the anteroposterior annulus diameter. The features of leaflet tethering, including tenting height, angle, and area, can be obtained with CT scan and compared to the ones visualized with echocardiography. The edge-to-edge repair using the Triclip (Abbott Vascular, Santa Clara, CA, USA) or PASCAL systems (Edwards Lifesciences, Irvine, CA, USA) allows bringing the TV leaflets closer, thus reducing the grade of regurgitation. The role of CT in the edge-to-edge repair is less important than the other techniques, even if viable information about the coaptation gap, annulus, and right chamber remodeling can be obtained [111].

Moreover, as described for the mitral valve, measuring the anatomical regurgitant orifice area (AROA) by CT is also feasible. It may be an additional grading tool for TR severity in patients with contradictory echocardiographic parameters [112]. Notably, this flow-independent parameter of TR severity provided by CT has been reported to strongly correlate with the 3D measurement of vena contracta (thus with three-dimensional assessment of the narrowest flow region of the tricuspid regurgitant volume), using transesophageal echocardiography [108]. The dimensions of the RV and RA are also crucial for evaluating the anatomic feasibility of transcatheter therapies. RA must allocate the delivery catheter and be large enough for various maneuvers during the procedure [11]. Furthermore, with the promising results of the trials regarding transcatheter TV replacement, assessing the right chambers is more important than ever. Some valves are used in high-risk patients, such as NaviGate bio prosthesis (NaviGate Cardiac Structures, Lake Forest) or EVOQUE valve (Edwards Lifesciences). In this setting, RV volume, the distance between the RV apex and the tricuspid annular plane, the location of the papillary muscles, the moderator band, and the presence of prominent trabeculae must be assessed with regard to the protrusion of the prosthesis into the RV, most notably to avoid RV outflow tract obstruction [111].

Tricuspid valve replacement is also challenging due to the lack of calcifications at the level of the tricuspid annulus [113]. The Melody prosthesis (Medtronic, Minneapolis) is usually used in transcatheter tricuspid valve-in-valve and valve-in-ring procedures. In this setting, 3D CT measurement of the effective inner diameters of the ring is fundamental to bypass the differences reported in the nominal size documented by surgical report [114]. Annuloplasty devices, such as Cardioband™ (Valtech Cardio, OrYehuda, Israel), use a transfemoral ring or suture-based approach to reduce the diameter in cases where annular dilation is the major pathophysiological mechanism. Therefore, in this type of transcatheter repair procedures, it is also essential to evaluate the structures surrounding the tricuspid annulus, particularly the course of the right coronary artery, that could be damaged. The vessel course in relation to the annulus is variable. An RCA course at the annular level was shown in 65% of patients, a superior (i.e., atrial) course in 10%, and a crossing course in 25% [115]. Finally, measurement of the inferior vena cava plays a role in some interventional procedures aiming to reduce TR. In the heterotopic implantation of valves in the caval veins, balloon-expandable transcatheter aortic valve prostheses such as Sapien XT (Edwards Lifesciences) are placed to reduce blood backflow and prevention of venous congestion. Other systems, such as the TricValve system (P&F, Vienna) or the Tricento (NVT AG, Muri), are deployed top-down from the superior to the inferior vena cava, improving pressure's profile in the right atrium. In these procedures, it is of crucial importance to calculate the distance between the junction plane of the inferior vena cava, the right atrium, and the first hepatic vein to avoid hepatic vein obstruction [12].

5. CT and Left Atrial Appendage

5.1. Anatomy of Left Atrial Appendage (LAA)

The left atrial appendage (LAA) is a finger-like projection from the body of the left atrium (LA). The junction is well defined by the presence of an orifice [116]. It is located on the anterior wall of the LA, and it extends to the lateral part of it, with the tip directed anterosuperiorly, with overlapping on the right ventricular outflow tract or the pulmonary trunk and the left main coronary vessel or the circumflex artery. The appendage overlies the atrioventricular groove and the left phrenic nerve courses over its covering fibrous pericardium [116]. Its orifice is usually elliptical, sometimes round, triangular, or water-drop shaped. The left ridge divides the orifice from the left pulmonary veins, whereas the muscular wall of the LA vestibule stands between the orifice and the mitral annulus [116]. LAA varies in size and shape; however, it is usually classified into four main types: "chicken wing" (the most common), "cactus" (30%), "windsock", and "cauliflower". The last one is the rarest but most associated with embolic events; it has a short overall length but a variable number of lobes without a dominant one [117]. Oppositely, the "chicken wing" shape is composed of a more prominent lobe that folds back on itself after it emerges from the orifice and could have secondary lobes [117]. The "cactus" shape has a dominant central lobe and secondary lobes emerging from it superiorly and inferiorly [118]. Finally, the "windsock" has a prominent lobe with multiple secondary and tertiary lobes with many variations in terms of localization [119].

5.2. Left Atrial Appendage Closure (LAAC)

In atrial fibrillation (AF), the LAA loses its contraction capability and undergoes a remodeling process that transforms it into a static pouch, with an increased risk of stagnation and thrombosis [120]. The risk of thrombosis is also higher in patients with left ventricular dysfunction and elevated left ventricular end-diastolic pressures, even without AF [121]. Traditionally, oral anticoagulation therapy has been the cornerstone of therapy for stroke prevention in patients with nonvalvular AF [122]. However, in some frailty patients, the increased bleeding risk associated with anticoagulation therapy might overcome the benefit of stroke prevention. Percutaneous left atrial appendage closure (LAAC) is a validated procedure that excludes the appendage with the use of dedicated devices. Two main devices are currently used in clinical practice: the Watchman (Boston Scientific), a parachute-shaped nitinol device with a permeable membrane over the atrial side and fixation barbs to secure it between the LAA walls, and the Amulet device, a self-expanding flexible nitinol mesh with a distal lobe, keeping hooks, and a proximal disk for sealing the LAA orifice. Both these devices have reported high post-procedural and long-term success rates of LAAC [123–125].

5.3. CT Assessment in LAA Transcatheter Closure

Multimodality imaging is essential for LAAC. MDCT allows a great resolution of LAA due to its minimal motion [126]. For patients in sinus rhythm, prospective electrocardiographic (ECG) gating is necessary by identifying either atrial systole/ventricular diastole or atrial diastole/ventricular systole. For patients in AF, retrospective ECG gating may be required, and the optimal reconstruction phase depends on the ventricular rate [127].

Computed tomography is particularly important in three phases regarding patients undergoing LAAC: the preprocedural exclusion of LA thrombosis, the preprocedural planning, taking into account LAA morphology and dimensions, and the surveillance after the procedure [126]. CT can easily exclude thrombi in the LAA, even if transesophageal echocardiography (TEE) remains the gold standard. A major strength of computed tomography is the high capability to exclude LAA thrombosis (96–100%) [128]. Delayed imaging allows the differentiation between the slow-flow sluggish and the thrombi; thus, the filling defect that persists after one minute of contrast injection is more suggestive of a real thrombus [129].

In the preprocedural planning of LAAC, the MDCT helps acquire information about LAA shape, size, and surrounding structures. Few studies compared computed tomography, transesophageal echocardiography, and angiography for LAA assessment. Most of them are retrospective, single-center studies, reporting larger dimensions with CT than 2D/3D-TEE and angiography. Rajwani et al. found that in 73 Watchman implantations, 2D-TEE and MDCT maximum diameter agreed on device size only in 25.4% of cases, mainly due to significative eccentricity of the orifice [130]. Notably, the LAAC device size choice depends on these measurements [126]. Computed tomography allows for determining LAA ostia and landing zones (the LAA zone where the LAAO device will ideally seat) and providing the minimum LAA diameter, maximum diameter, perimeter, and area. These measurements should be assessed at maximal LAA diastole or mid to late left ventricular systole, corresponding to maximum LAA end-diastolic filling. In this phase, the LAA is largest, thus reducing the risk of device undersizing and subsequent peri-device leaks. In a study by Wang et al., the CT-detected diameter of the LAA ostium calculated from the perimeter resulted in the best parameter for sizing the LAA occluder device [131]. It is essential to point out that different devices require different modalities of LAA ostium measurement [126]. For the Watchman, the landing zone is measured from the circumflex artery inferiorly to a superior point that is established at 1–2 cm within the left upper superior pulmonary vein ridge. For the Amplatzer Cardiac Plug (ACP) or the Amulet (second-generation ACP), the landing zone is usually placed 10 mm and 12–15 mm inward of the LAA orifice, respectively [126]. Once the LAA orifice diameters have been established, the LAA's depth must also be determined in the CT sagittal and coronal views. It is measured from the central point of the orifice to the apex of the main lobe, and the chosen device should have the same diameter as the LAA depth [126]. From a technical view, the assessment of the LAA shape is a valuable aid in predicting the level of difficulty of device implantation. The "chicken wing" shape is usually considered to be the most complicated, particularly in case of a proximal and sharp bend. "Cactus" and "cauliflower" shapes may be challenging compared with the "wind-sock" shape (Figure 12) [126].

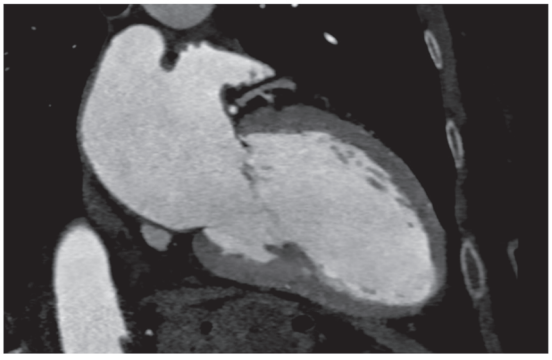

Figure 12. CT imaging for the assessment of left atrial appendage's conformation. Example of "chicken wing" shape.

Finally, MDCT has an important role in post-procedural follow-up, which can be performed 1–6 months after the device implantation. The primary role of computed tomography in this context is the exclusion of device-associated thrombus, post-implant device orientation, pericardial effusion, and peri-device leaks. Jaguszewski et al. found that CT detected leaks in 62% of cases in patients implanted with ACP, whereas TEE revealed only 36% [132]. A perpendicular position of the lobe in relation to the LAA neck has been reported to be a good predictor of the absence of residual leakage after the procedure; moreover, device compression of more than 10% is associated with complete sealing [133].

6. Conclusions

CT is a crucial imaging tool for structural cardiac disease interventions. Due to its high temporal and spatial resolution, cardiac CT has become fundamental for the preprocedural planning of THVI, allowing precise device sizing and vascular access assessment, helping with landing zone characterization, and reducing procedural complications. Ongoing indications for preprocedural computed tomography in cardiac interventional procedures include transcatheter aortic valve implantation, percutaneous interventions of the mitral, tricuspid, pulmonary valves, and left atrial appendage occlusion. The role of multimodality imaging will undoubtedly continue to grow because of the development of new software technologies that will allow integration of CT with other techniques [134–136], such as fluoroscopy in the catheterization laboratory. These advances will improve accuracy and safety in planning and guiding these interventions while reducing the dose of contrast volume, radiation exposure, and procedural duration.

Author Contributions: Conceptualization, A.N. and S.C.; validation, F.G., G.P.U.; writing—original draft preparation, A.N., S.C., E.N., A.D.F., L.V.; writing—review and editing, A.N., D.D.S.; visualization, F.P., V.C., F.M., E.R., R.M., R.R., C.C.Q.; supervision, G.P.U., F.G. All authors have read and agreed to the published version of the manuscript.

Funding: This research received no external funding.

Institutional Review Board Statement: Not applicable.

Informed Consent Statement: Not applicable.

Data Availability Statement: Not applicable.

Conflicts of Interest: The authors declare no conflict of interest.

References

1. Schoenhagen, P.; Numburi, U.; Halliburton, S.S.; Aulbach, P.; Von Roden, M.; Desai, M.Y.; Rodriguez, L.L.; Kapadia, S.R.; Tuzcu, E.M.; Lytle, B.W. Three-dimensional imaging in the context of minimally invasive and transcatheter cardiovascular interventions using multi-detector computed tomography: From pre-operative planning to intra-operative guidance. *Eur. Hear. J.* **2010**, *31*, 2727–2740. [CrossRef] [PubMed]
2. Boxt, L.M.; Lipton, M.J.; Kwong, R.Y.; Rybicki, F.; E Clouse, M. Computed tomography for assessment of cardiac chambers, valves, myocardium and pericardium. *Cardiol. Clin.* **2003**, *21*, 561–585. [CrossRef]
3. Ecabert, O.; Peters, J.; Schramm, H.; Lorenz, C.; von Berg, J.; Walker, M.J.; Vembar, M.; Olszewski, M.E.; Subramanyan, K.; Lavi, G.; et al. Automatic Model-Based Segmentation of the Heart in CT Images. *IEEE Trans. Med. Imaging* **2008**, *27*, 1189–1201. [CrossRef] [PubMed]
4. Hu, S.; Hoffman, E.; Reinhardt, J. Automatic lung segmentation for accurate quantitation of volumetric X-ray CT images. *IEEE Trans. Med. Imaging* **2001**, *20*, 490–498. [CrossRef] [PubMed]
5. Bae, K.T.; Giger, M.L.; Chen, C.; Kahn, C.E. Automatic segmentation of liver structure in CT images. *Med. Phys.* **1993**, *20*, 71–78. [CrossRef] [PubMed]
6. Mir, A.; Hanmandlu, M.; Tandon, S. Texture analysis of CT images. *IEEE Eng. Med. Biol. Mag.* **1995**, *14*, 781–786. [CrossRef]
7. Yang, X.; He, X.; Zhao, J.; Zhang, Y.; Zhang, S.; Xie, P. COVID-CT-Dataset: A CT Scan Dataset about COVID-19. *Mach. Learn.* **2020**. [CrossRef]
8. Sarma, A.; Heilbrun, M.E.; Conner, K.E.; Stevens, S.M.; Woller, S.C.; Elliott, C.G. Radiation and Chest CT Scan Examinations. *Chest* **2012**, *142*, 750–760. [CrossRef]
9. O'Connor, J.F.; Cohen, J.O. Computerized tomography (CAT scan, CT scan) in orthopaedic surgery. *JBJS* **1978**, *60*, 1096–1098. [CrossRef]
10. Patel, K.P.; Vandermolen, S.; Herrey, A.S.; Cheasty, E.; Menezes, L.; Moon, J.C.; Pugliese, F.; Treibel, T.A. Cardiac Computed Tomography: Application in Valvular Heart Disease. *Front. Cardiovasc. Med.* **2022**, *9*, 849540. [CrossRef]
11. Cammalleri, V.; Carpenito, M.; Bono, M.C.; Mega, S.; Ussia, G.P.; Grigioni, F. Transcatheter Tricuspid Valve Therapy: From Anatomy to Intervention. *Front. Cardiovasc. Med.* **2021**, *8*, 778445. [CrossRef] [PubMed]
12. Cammalleri, V.; Carpenito, M.; De Stefano, D.; Ussia, G.P.; Bono, M.C.; Mega, S.; Nusca, A.; Cocco, N.; Nobile, E.; De Filippis, A.; et al. Novel Computed Tomography Variables for Assessing Tricuspid Valve Morphology: Results from the TRIMA (Tricuspid Regurgitation IMAging) Study. *J. Clin. Med.* **2022**, *11*, 2825. [CrossRef] [PubMed]
13. Cammalleri, V.; Mega, S.; Ussia, G.P.; Grigioni, F. Mitral and Tricuspid Valves Percutaneous Repair in Patients with Advanced Heart Failure. *Hear. Fail. Clin.* **2021**, *17*, 607–618. [CrossRef] [PubMed]
14. Hell, M.M.; Achenbach, S. CT support of cardiac structural interventions. *Br. J. Radiol.* **2019**, *92*, 20180707. [CrossRef] [PubMed]

15. Piazza, N.; de Jaegere, P.; Schultz, C.; Becker, A.E.; Serruys, P.W.; Anderson, R.H. Anatomy of the Aortic Valvar Complex and Its Implications for Transcatheter Implantation of the Aortic Valve. *Circ. Cardiovasc. Interv.* **2008**, *1*, 74–81. [CrossRef] [PubMed]
16. Katsi, V.; Magkas, N.; Antonopoulos, A.; Trantalis, G.; Toutouzas, K.; Tousoulis, D. Aortic valve: Anatomy and structure and the role of vasculature in the degenerative process. *Acta Cardiol.* **2020**, *76*, 335–348. [CrossRef] [PubMed]
17. Kearney, L.; Ord, M.; Buxton, B.; Matalanis, G.; Patel, S.; Burrell, L.; Srivastava, P. Progression of aortic stenosis in elderly patients over long-term follow up. *Int. J. Cardiol.* **2012**, *167*, 1226–1231. [CrossRef]
18. Vahanian, A.; Beyersdorf, F.; Praz, F.; Milojevic, M.; Baldus, S.; Bauersachs, J.; Capodanno, D.; Conradi, L.; De Bonis, M.; De Paulis, R.; et al. *Multimodality Imaging for Transcatheter Aortic Valve Replacement*, 1st ed.; Springer: London, UK, 2014. [CrossRef]
19. Vahanian, A.; Beyersdorf, F.; Praz, F.; Milojevic, M.; Baldus, S.; Bauersachs, J.; Capodanno, D.; Conradi, L.; De Bonis, M.; De Paulis, R.; et al. 2021 ESC/EACTS Guidelines for the management of valvular heart disease. *Eur. Hear. J.* **2021**, *43*, 561–632. [CrossRef]
20. Tagliari, A.P.; Saadi, R.P.; Saadi, E.K. Transcatheter Aortic Valve Implantation for Pure Native Aortic Regurgitation: The Last Frontier. *J. Clin. Med.* **2022**, *11*, 5181. [CrossRef]
21. Nusca, A.; Bressi, E.; Colaiori, I.; Miglionico, M.; Di Sciascio, G. Antiplatelet therapy in valvular and structural heart disease interventions. *Cardiovasc. Diagn. Ther.* **2018**, *8*, 678–693. [CrossRef]
22. Ricottini, E.; Nusca, A.; Ussia, G.P.; Grigioni, F. Antithrombotic treatment for valve prostheses: Which drug, which dose, and when? *Prog. Cardiovasc. Dis.* **2022**, *72*, 4–14. [CrossRef]
23. Holmes, D.R.; Mack, M.J.; Kaul, S.; Agnihotri, A.; Alexander, K.P.; Bailey, S.R.; Calhoon, J.H.; Carabello, B.A.; Desai, M.Y.; Edwards, F.H.; et al. 2012 ACCF/AATS/SCAI/STS Expert Consensus Document on Transcatheter Aortic Valve Replacement. *J. Am. Coll. Cardiol.* **2012**, *59*, 1200–1254. [CrossRef]
24. Blanke, P.; Weir-McCall, J.R.; Achenbach, S.; Delgado, V.; Hausleiter, J.; Jilaihawi, H.; Marwan, M.; Norgaard, B.L.; Piazza, N.; Schoenhagen, P.; et al. Computed tomography imaging in the context of transcatheter aortic valve implantation (TAVI) / transcatheter aortic valve replacement (TAVR): An expert consensus document of the Society of Cardiovascular Computed Tomography. *J. Cardiovasc. Comput. Tomogr.* **2019**, *13*, 1–20. [CrossRef] [PubMed]
25. Chiocchi, M.; Ricci, F.; Pasqualetto, M.; D'errico, F.; Benelli, L.; Pugliese, L.; Cavallo, A.U.; Forcina, M.; Presicce, M.; De Stasio, V.; et al. Role of computed tomography in transcatheter aortic valve implantation and valve-in-valve implantation: Complete review of preprocedural and postprocedural imaging. *J. Cardiovasc. Med.* **2020**, *21*, 182–191. [CrossRef] [PubMed]
26. Binder, R.K.; Webb, J.G.; Willson, A.B.; Urena, M.; Hansson, N.C.; Norgaard, B.L.; Pibarot, P.; Barbanti, M.; Larose, E.; Freeman, M.; et al. The Impact of Integration of a Multidetector Computed Tomography Annulus Area Sizing Algorithm on Outcomes of Transcatheter Aortic Valve Replacement. *J. Am. Coll. Cardiol.* **2013**, *62*, 431–438. [CrossRef] [PubMed]
27. Corcione, N.; Morello, A.; Ferraro, P.; Cimmino, M.; Albanese, M.; Pepe, M.; Nestola, P.L.; Giordano, S.; Bardi, L.; Biondi-Zoccai, G.; et al. TAVI-CT score to evaluate the anatomic risk in patients undergoing transcatheter aortic valve implantation. *Sci. Rep.* **2022**, *12*, 1–9. [CrossRef]
28. Spaziano, M.; Chieffo, A.; Watanabe, Y.; Chandrasekhar, J.; Sartori, S.; Lefèvre, T.; Petronio, A.S.; Presbitero, P.; Tchetche, D.; Iadanza, A.; et al. Computed tomography predictors of mortality, stroke and conduction disturbances in women undergoing TAVR: A sub-analysis of the WIN-TAVI registry. *J. Cardiovasc. Comput. Tomogr.* **2018**, *12*, 338–343. [CrossRef]
29. Gama, F.; Teles, R.; Oliveira, A.; Brizido, C.; Goncalves, P.; Brito, J.; Ferreira, A.; Abecasis, J.; Almeida, M.; Mendes, M. Predicting pacemaker implantation after TAVR with procedural CT. *Eur. Hear. J.* **2020**, *41*, ehaa946.0192. [CrossRef]
30. Gegenava, T.; van der Bijl, P.; Hirasawa, K.; Vollema, E.M.; van Rosendael, A.; van der Kley, F.; de Weger, A.; Hautemann, D.J.; Reiber, J.H.; Marsan, N.A.; et al. Feature tracking computed tomography-derived left ventricular global longitudinal strain in patients with aortic stenosis: A comparative analysis with echocardiographic measurements. *J. Cardiovasc. Comput. Tomogr.* **2019**, *14*, 240–245. [CrossRef]
31. Masson, J.-B.; Kovac, J.; Schuler, G.; Ye, J.; Cheung, A.; Kapadia, S.; Tuzcu, M.E.; Kodali, S.; Leon, M.B.; Webb, J.G. Transcatheter Aortic Valve Implantation: Review of the Nature, Management, and Avoidance of Procedural Complications. *JACC: Cardiovasc. Interv.* **2009**, *2*, 811–820. [CrossRef]
32. Hayashida, K.; Lefèvre, T.; Chevalier, B.; Hovasse, T.; Romano, M.; Garot, P.; Mylotte, D.; Uribe, J.; Farge, A.; Donzeau-Gouge, P.; et al. Transfemoral Aortic Valve Implantation: New Criteria to Predict Vascular Complications. *JACC: Cardiovasc. Interv.* **2011**, *4*, 851–858. [CrossRef] [PubMed]
33. Okuyama, K.; Jilaihawi, H.; Kashif, M.; Takahashi, N.; Chakravarty, T.; Pokhrel, H.; Patel, J.; Forrester, J.S.; Nakamura, M.; Cheng, W.; et al. Transfemoral Access Assessment for Transcatheter Aortic Valve Replacement: Evidence-based application of computed tomography over invasive angiography. *Circ. Cardiovasc. Imaging* **2015**, *8*, e001995. [CrossRef] [PubMed]
34. Reardon, M.J.; Van Mieghem, N.M.; Popma, J.J.; Kleiman, N.S.; Søndergaard, L.; Mumtaz, M.; Adams, D.H.; Deeb, G.M.; Maini, B.; Gada, H.; et al. Surgical or Transcatheter Aortic-Valve Replacement in Intermediate-Risk Patients. *N. Engl. J. Med.* **2017**, *376*, 1321–1331. [CrossRef] [PubMed]
35. Lehmkuhl, L.; Foldyna, B.; Haensig, M.; Von Aspern, K.; Lücke, C.; Andres, C.; Grothoff, M.; Riese, F.; Nitzsche, S.; Holzhey, D.; et al. Role of preprocedural computed tomography in transcatheter aortic valve implantation. *Fortschr. Geb. Rontgenstr. Nuklearmed.* **2013**, *185*, 941–949. [CrossRef]
36. Jurencak, T.; Turek, J.; Kietselaer, B.L.J.H.; Mihl, C.; Kok, M.; Van Ommen, V.G.V.A.; Van Garsse, L.A.F.M.; Nijssen, E.C.; Wildberger, J.E.; Das, M. MDCT evaluation of aortic root and aortic valve prior to TAVI. What is the optimal imaging time point in the cardiac cycle? *Eur. Radiol.* **2015**, *25*, 1975–1983. [CrossRef]

37. Adams, D.H.; Popma, J.J.; Reardon, M.J.; Yakubov, S.J.; Coselli, J.S.; Deeb, G.M.; Gleason, T.G.; Buchbinder, M.; Hermiller, J., Jr.; Kleiman, N.S.; et al. Transcatheter Aortic-Valve Replacement with a Self-Expanding Prosthesis. *N. Engl. J. Med.* **2014**, *370*, 1790–1798. [CrossRef]
38. Mack, M.J.; Leon, M.B.; Thourani, V.H.; Makkar, R.; Kodali, S.K.; Russo, M.; Kapadia, S.R.; Malaisrie, S.C.; Cohen, D.J.; Pibarot, P.; et al. Transcatheter Aortic-Valve Replacement with a Balloon-Expandable Valve in Low-Risk Patients. *N. Engl. J. Med.* **2019**, *380*, 1695–1705. [CrossRef]
39. Mylotte, D.; Dorfmeister, M.; Elhmidi, Y.; Mazzitelli, D.; Bleiziffer, S.; Wagner, A.; Noterdaeme, T.; Lange, R.; Piazza, N. Erroneous Measurement of the Aortic Annular Diameter Using 2-Dimensional Echocardiography Resulting in Inappropriate CoreValve Size Selection: A retrospective comparison with multislice computed tomography. *JACC: Cardiovasc. Interv.* **2014**, *7*, 652–661. [CrossRef]
40. Helmy, S.M.; Karim, S.A. Multimodality imaging in aortic stenosis. *Hear. Views* **2022**, *23*, 22. [CrossRef]
41. Vincent, F.; Ternacle, J.; Denimal, T.; Shen, M.; Redfors, B.; Delhaye, C.; Simonato, M.; Debry, N.; Verdier, B.; Shahim, B.; et al. Transcatheter Aortic Valve Replacement in Bicuspid Aortic Valve Stenosis. *Circulation* **2021**, *143*, 1043–1061. [CrossRef]
42. Tanaka, R.; Yoshioka, K.; Niinuma, H.; Ohsawa, S.; Okabayashi, H.; Ehara, S. Diagnostic Value of Cardiac CT in the Evaluation of Bicuspid Aortic Stenosis: Comparison With Echocardiography and Operative Findings. *Am. J. Roentgenol.* **2010**, *195*, 895–899. [CrossRef] [PubMed]
43. Popma, J.J.; Ramadan, R. CT Imaging of Bicuspid Aortic Valve Disease for TAVR ∗. *JACC: Cardiovasc. Imaging* **2016**, *9*, 1159–1163. [CrossRef] [PubMed]
44. Doris, M.K.; Jenkins, W.; Robson, P.; Pawade, T.; Andrews, J.P.; Bing, R.; Cartlidge, T.; Shah, A.; Pickering, A.; Williams, M.C.; et al. Computed tomography aortic valve calcium scoring for the assessment of aortic stenosis progression. *Heart* **2020**, *106*, 1906–1913. [CrossRef]
45. Feuchtner, G.M.; Müller, S.; Grander, W.; Alber, H.F.; Bartel, T.; Friedrich, G.J.; Reinthaler, M.; Pachinger, O.; Nedden, D.Z.; Dichtl, W. Aortic valve calcification as quantified with multislice computed tomography predicts short-term clinical outcome in patients with asymptomatic aortic stenosis. *J. Hear. Valve Dis.* **2006**, *15*, 494–498.
46. Rosenhek, R.; Binder, T.; Porenta, G.; Lang, I.; Christ, G.; Schemper, M.; Maurer, G.; Baumgartner, H. Predictors of Outcome in Severe, Asymptomatic Aortic Stenosis. *New Engl. J. Med.* **2000**, *343*, 611–617. [CrossRef] [PubMed]
47. Leber, A.W.; Kasel, M.; Ischinger, T.; Ebersberger, U.H.; Antoni, D.; Schmidt, M.; Riess, G.; Renz, V.; Huber, A.; Helmberger, T.; et al. Aortic valve calcium score as a predictor for outcome after TAVI using the CoreValve revalving system. *Int. J. Cardiol.* **2011**, *166*, 652–657. [CrossRef]
48. Haensig, M.; Lehmkuhl, L.; Rastan, A.J.; Kempfert, J.; Mukherjee, C.; Gutberlet, M.; Holzhey, D.; Mohr, F.W. Aortic valve calcium scoring is a predictor of significant paravalvular aortic insufficiency in transapical-aortic valve implantation. *Eur. J. Cardio-Thoracic Surg.* **2012**, *41*, 1234–1241. [CrossRef]
49. Lee, J.A.; Singh, T.; Ben Dor, I.; Torguson, R.; Okubagzi, P.; Satler, L.; Goldstein, S.; Taylor, A.; Weigold, W.G.; Pichard, A.; et al. AAortic valve calcium score by computed tomography in predicting perivalvular aortic insufficiency post transcatheter aortic valve implantation (TAVI). *J. Am. Coll. Cardiol.* **2012**, *59*, E1962. [CrossRef]
50. Unbehaun, A.; Pasic, M.; Dreysse, S.; Drews, T.; Kukucka, M.; Mladenow, A.; Ivanitskaja-Kühn, E.; Hetzer, R.; Buz, S. Transapical Aortic Valve Implantation: Incidence and predictors of paravalvular leakage and transvalvular regurgitation in a series of 358 patients. *J. Am. Coll. Cardiol.* **2012**, *59*, 211–221. [CrossRef]
51. Feuchtner, G.; Plank, F.; Bartel, T.; Mueller, S.; Leipsic, J.; Schachner, T.; Müller, L.; Friedrich, G.; Klauser, A.; Grimm, M.; et al. Prediction of Paravalvular Regurgitation After Transcatheter Aortic Valve Implantation by Computed Tomography: Value of Aortic Valve and Annular Calcification. *Ann. Thorac. Surg.* **2013**, *96*, 1574–1580. [CrossRef]
52. Ribeiro, H.B.; Nombela-Franco, L.; Urena, M.; Mok, M.; Pasian, S.; Doyle, D.; DeLarochellière, R.; Côté, M.; Laflamme, L.; DeLarochellière, H.; et al. Coronary Obstruction Following Transcatheter Aortic Valve Implantation: A systematic review. *JACC: Cardiovasc. Interv.* **2013**, *6*, 452–461. [CrossRef] [PubMed]
53. Jilaihawi, H.; Chin, D.; Spyt, T.; Jeilan, M.; Vasa-Nicotera, M.; Bence, J.; Logtens, E.; Kovac, J. Prosthesis-patient mismatch after transcatheter aortic valve implantation with the Medtronic-Corevalve bioprosthesis. *Eur. Heart J.* **2009**, *31*, 857–864. [CrossRef] [PubMed]
54. Delgado, V.; Ng, A.C.T.; Shanks, M.; Van Der Kley, F.; Schuijf, J.D.; Van De Veire, N.R.L.; Kroft, L.; De Roos, A.; Schalij, M.J.; Bax, J.J. Transcatheter aortic valve implantation: Role of multimodality cardiac imaging. *Expert Rev. Cardiovasc. Ther.* **2010**, *8*, 113–123. [CrossRef]
55. Piazza, N.; Nuis, R.-J.; Tzikas, A.; Otten, A.; Onuma, Y.; García-García, H.; Schultz, C.; van Domburg, R.; van Es, G.-A.; van Geuns, R.; et al. Persistent conduction abnormalities and requirements for pacemaking six months after transcatheter aortic valve implantation. *Eurointervention* **2010**, *6*, 475–484. [CrossRef] [PubMed]
56. Jilaihawi, H.; Chin, D.; Vasa-Nicotera, M.; Jeilan, M.; Spyt, T.; Ng, G.A.; Bence, J.; Logtens, E.; Kovac, J. Predictors for permanent pacemaker requirement after transcatheter aortic valve implantation with the CoreValve bioprosthesis. *Am. Hear. J.* **2009**, *157*, 860–866. [CrossRef] [PubMed]
57. Moreno, R.; Calvo, L.; García, E.; Dobarro, D. Severe septal hypertrophy: Is it necessarily a contraindication for the transcatheter implantation of an Edwards-Sapien prosthesis? *Rev. Esp. Cardiol.* **2010**, *63*, 241–242. [CrossRef] [PubMed]

58. Stolzmann, P.; Scheffel, H.; Trindade, P.T.; Plass, A.R.; Husmann, L.; Leschka, S.; Genoni, M.; Marincek, B.; Kaufmann, P.A.; Alkadhi, H. Left Ventricular and Left Atrial Dimensions and Volumes: Comparison between dual-source CT and echo-cardiography. *Investig. Radiol.* **2008**, *43*, 284–289. [CrossRef] [PubMed]
59. Okuno, T.; Asami, M.; Heg, D.; Lanz, J.; Praz, F.; Hagemeyer, D.; Brugger, N.; Gräni, C.; Huber, A.; Spirito, A.; et al. Impact of Left Ventricular Outflow Tract Calcification on Procedural Outcomes After Transcatheter Aortic Valve Replacement. *JACC: Cardiovasc. Interv.* **2020**, *13*, 1789–1799. [CrossRef]
60. Maréchaux, S.; Illman, J.E.; Huynh, J.; Michelena, H.I.; Nkomo, V.T.; Tribouilloy, C. Functional anatomy and pathophysiologic principles in mitral regurgitation: Non-invasive assessment. *Prog. Cardiovasc. Dis.* **2017**, *60*, 289–304. [CrossRef]
61. Komoda, T.; Hetzer, R.; Oellinger, J.; Siniawski, H.; Hofmeister, J.; Hübler, M.; Felix, R.; Uyama, C.; Maeta, H. Mitral Annular Flexibility. *J. Card. Surg.* **1997**, *12*, 102–109. [CrossRef]
62. Millington-Sanders, C.; Meir, A.; Lawrence, L.; Stolinski, C. Structure of chordae tendineae in the left ventricle of the human heart. *J. Anat.* **1998**, *192*, 573–581. [CrossRef] [PubMed]
63. Ranganathan, N.; Lam, J.H.C.; Wigle, E.D.; Silver, M.D. Morphology of the Human Mitral Valve. *Circulation* **1970**, *41*, 459–467. [CrossRef] [PubMed]
64. Lam, J.H.C.; Ranganathan, N.; Wigle, E.D.; Silver, M.D. Morphology of the Human Mitral Valve. *Circulation* **1970**, *41*, 449–458. [CrossRef] [PubMed]
65. Nkomo, V.T.; Gardin, J.M.; Skelton, T.N.; Gottdiener, J.S.; Scott, C.G.; Enriquez-Sarano, M. Burden of valvular heart diseases: A population-based study. *Lancet* **2006**, *368*, 1005–1011. [CrossRef] [PubMed]
66. Delgado, V.; Tops, L.F.; Schuijf, J.D.; de Roos, A.; Brugada, J.; Schalij, M.J.; Thomas, J.D.; Bax, J.J. Assessment of Mitral Valve Anatomy and Geometry With Multislice Computed Tomography. *JACC: Cardiovasc. Imaging* **2009**, *2*, 556–565. [CrossRef]
67. Regueiro, A.; Granada, J.F.; Dagenais, F.; Rodés-Cabau, J. Transcatheter Mitral Valve Replacement. *J. Am. Coll. Cardiol.* **2017**, *69*, 2175–2192. [CrossRef]
68. Maisano, F.; Torracca, L.; Oppizzi, M.; Stefano, P.; D'Addario, G.; La Canna, G.; Zogno, M.; Alfieri, O. The edge-to-edge technique: A simplified method to correct mitral insufficiency1. *Eur. J. Cardio-Thoracic Surg.* **1998**, *13*, 240–246. [CrossRef] [PubMed]
69. Feldman, T.; Foster, E.; Glower, D.D.; Kar, S.; Rinaldi, M.J.; Fail, P.S.; Smalling, R.W.; Siegel, R.; Rose, G.A.; Engeron, E.; et al. Percutaneous Repair or Surgery for Mitral Regurgitation. *New Engl. J. Med.* **2011**, *364*, 1395–1406. [CrossRef]
70. Feldman, T.; Lim, S.; Fail, P.; Whisenant, B.; Rinaldi, M.; Grayburn, P.; Smalling, R.; Foster, E.; Weissman, N.; Kar, S. Everest ii realism—a continued access study to evaluate the safety and effectiveness of the mitraclip device: Analysis of results through 1 year. *J. Am. Coll. Cardiol.* **2015**, *65*, A1983. [CrossRef]
71. Stone, G.W.; Lindenfeld, J.; Abraham, W.T.; Kar, S.; Lim, D.S.; Mishell, J.M.; Whisenant, B.; Grayburn, P.A.; Rinaldi, M.; Kapadia, S.R.; et al. Transcatheter Mitral-Valve Repair in Patients with Heart Failure. *N. Engl. J. Med.* **2018**, *379*, 2307–2318. [CrossRef]
72. Faggioni, L.; Gabelloni, M.; Accogli, S.; Angelillis, M.; Costa, G.; Spontoni, P.; Petronio, A.S.; Caramella, D. Preprocedural planning of transcatheter mitral valve interventions by multidetector CT: What the radiologist needs to know. *Eur. J. Radiol. Open* **2018**, *5*, 131–140. [CrossRef] [PubMed]
73. Feuchtner, G.M.; Alkadhi, H.; Karlo, C.; Sarwar, A.; Meier, A.; Dichtl, W.; Leschka, S.; Blankstein, R.; Gruenenfelder, J.; Stolzmann, P.; et al. Cardiac CT Angiography for the Diagnosis of Mitral Valve Prolapse: Comparison with Echocardiography. *Radiology* **2010**, *254*, 374–383. [CrossRef] [PubMed]
74. Lee, A.P.-W.; Jin, C.-N.; Fan, Y.; Wong, R.H.; Underwood, M.J.; Wan, S. Functional Implication of Mitral Annular Disjunction in Mitral Valve Prolapse. *JACC: Cardiovasc. Imaging* **2017**, *10*, 1424–1433. [CrossRef] [PubMed]
75. Ewe, S.H.; Klautz, R.J.; Schalij, M.J.; Delgado, V. Role of computed tomography imaging for transcatheter valvular repair/insertion. *Int. J. Cardiovasc. Imaging* **2011**, *27*, 1179–1193. [CrossRef]
76. Naoum, C.; Leipsic, J.; Cheung, A.; Ye, J.; Bilbey, N.; Mak, G.; Berger, A.; Dvir, D.; Arepalli, C.; Grewal, J.; et al. Mitral Annular Dimensions and Geometry in Patients With Functional Mitral Regurgitation and Mitral Valve Prolapse. *JACC: Cardiovasc. Imaging* **2016**, *9*, 269–280. [CrossRef]
77. Nishimura, R.A.; Bonow, R.O. Percutaneous Repair of Secondary Mitral Regurgitation—A Tale of Two Trials. *New Engl. J. Med.* **2018**, *379*, 2374–2376. [CrossRef]
78. E van Wijngaarden, S.; Kamperidis, V.; Regeer, M.V.; Palmen, M.; Schalij, M.J.; Klautz, R.J.; Bax, J.J.; Marsan, N.A.; Delgado, V. Three-dimensional assessment of mitral valve annulus dynamics and impact on quantification of mitral regurgitation. *Eur. Hear. J. Cardiovasc. Imaging* **2017**, *19*, 176–184. [CrossRef]
79. Palmisano, A.; Nicoletti, V.; Colantoni, C.; Monti, C.B.; Pannone, L.; Vignale, D.; Darvizeh, F.; Agricola, E.; Schaffino, S.; De Cobelli, F.; et al. Dynamic changes of mitral valve annulus geometry at preprocedural CT: Relationship with functional classes of regurgitation. *Eur. Radiol. Exp.* **2021**, *5*, 1–12. [CrossRef]
80. Ranganath, P.; Moore, A.; Guerrero, M.; Collins, J.; Foley, T.; Williamson, E.; Rajiah, P. CT for Pre- and Postprocedural Evaluation of Transcatheter Mitral Valve Replacement. *Radiographics* **2020**, *40*, 1528–1553. [CrossRef]
81. Blanke, P.; Dvir, D.; Cheung, A.; Ye, J.; Levine, R.A.; Precious, B.; Berger, A.; Stub, D.; Hague, C.; Murphy, D.; et al. A simplified D-shaped model of the mitral annulus to facilitate CT-based sizing before transcatheter mitral valve implantation. *J. Cardiovasc. Comput. Tomogr.* **2014**, *8*, 459–467. [CrossRef]

82. Blanke, P.; Naoum, C.; Webb, J.; Dvir, D.; Hahn, R.T.; Grayburn, P.; Moss, R.R.; Reisman, M.; Piazza, N.; Leipsic, J. Multimodality Imaging in the Context of Transcatheter Mitral Valve Replacement. *JACC: Cardiovasc. Imaging* **2015**, *8*, 1191–1208. [CrossRef] [PubMed]
83. Wang, D.D.; Eng, M.H.; Greenbaum, A.; Myers, E.; Forbes, M.; Karabon, P.; Pantelic, M.; Song, T.; Nadig, J.; Guerrero, M.; et al. Validating a prediction modeling tool for left ventricular outflow tract (LVOT) obstruction after transcatheter mitral valve replacement (TMVR). *Catheter. Cardiovasc. Interv.* **2017**, *92*, 379–387. [CrossRef]
84. Yoon, S.-H.; Bleiziffer, S.; Latib, A.; Eschenbach, L.; Ancona, M.; Vincent, F.; Kim, W.-K.; Unbehaum, A.; Asami, M.; Dhoble, A.; et al. Predictors of Left Ventricular Outflow Tract Obstruction After Transcatheter Mitral Valve Replacement. *JACC: Cardiovasc. Interv.* **2019**, *12*, 182–193. [CrossRef] [PubMed]
85. Guerrero, M.; Salinger, M.; Pursnani, A.; Pearson, P.; Lampert, M.; Levisay, J.; Russell, H.; Feldman, T. Transseptal transcatheter mitral valve-in-valve: A step by step guide from preprocedural planning to postprocedural care. *Catheter. Cardiovasc. Interv.* **2017**, *92*, E185–E196. [CrossRef]
86. Gersh, B.J.; Maron, B.J.; Bonow, R.O.; Dearani, J.A.; Fifer, M.A.; Link, M.S.; Naidu, S.S.; Nishimura, R.A.; Ommen, S.R.; Rakowski, H.; et al. 2011 ACCF/AHA Guideline for the Diagnosis and Treatment of Hypertrophic Cardiomyopathy. *Circulation* **2011**, *124*, e783–e831. [CrossRef]
87. Babaliaros, V.C.; Greenbaum, A.B.; Khan, J.M.; Rogers, T.; Wang, D.D.; Eng, M.H.; O'Neill, W.W.; Paone, G.; Thourani, V.H.; Lerakis, S.; et al. Intentional Percutaneous Laceration of the Anterior Mitral Leaflet to Prevent Outflow Obstruction During Transcatheter Mitral Valve Replacement. *JACC: Cardiovasc. Interv.* **2017**, *10*, 798–809. [CrossRef]
88. Faletra, F.F.; Leo, L.A.; Paiocchi, V.L.; Caretta, A.; Viani, G.M.; Schlossbauer, S.A.; Demertzis, S.; Ho, S.Y. Anatomy of mitral annulus insights from non-invasive imaging techniques. *Eur. Hear. J. Cardiovasc. Imaging* **2019**, *20*, 843–857. [CrossRef]
89. Thaden, J.J.; Malouf, J.F.; Nkomo, V.T.; Pislaru, S.V.; Holmes, D.R.; Reeder, G.S.; Rihal, C.S.; Eleid, M.F. Mitral Valve Anatomic Predictors of Hemodynamic Success With Transcatheter Mitral Valve Repair. *J. Am. Hear. Assoc.* **2018**, *7*, e007315. [CrossRef] [PubMed]
90. Grover, R.; Ohana, M.; Arepalli, C.D.; Sellers, S.L.; Mooney, J.; Kueh, S.-H.; Kim, U.; Blanke, P.; Leipsic, J.A. Role of MDCT Imaging in Planning Mitral Valve Intervention. *Curr. Cardiol. Rep.* **2018**, *20*, 16. [CrossRef] [PubMed]
91. Natarajan, N.; Patel, P.; Bartel, T.; Kapadia, S.; Navia, J.; Stewart, W.; Tuzcu, E.M.; Schoenhagen, P. Peri-procedural imaging for transcatheter mitral valve replacement. *Cardiovasc. Diagn. Ther.* **2016**, *6*, 144–159. [CrossRef]
92. Storz, C.; Mangold, S.; Mueller, K.A.; Lausberg, H.; Gatidis, S.; Heber, S.D.; Schlett, C.L.; Nikolaou, K.; Bamberg, F. Cardiac CT for Guiding Mitral Valve Interventions. *Curr. Cardiovasc. Imaging Rep.* **2017**, *10*, 1–10. [CrossRef]
93. Rottländer, D.; Ballof, J.; Gödde, M.; Degen, H.; Ögütcü, A.; Alektorov, K.; Chatrou, M.; Heintzen, M.P.; Haude, M. CT-Angiography to predict outcome after indirect mitral annuloplasty in patients with functional mitral regurgitation. *Catheter. Cardiovasc. Interv.* **2020**, *97*, 495–502. [CrossRef]
94. Rottländer, D.; Gödde, M.; Degen, H.; Ögütcü, A.; Saal, M.; Haude, M. Procedural planning of CS -based indirect mitral annuloplasty using CT-angiography. *Catheter. Cardiovasc. Interv.* **2021**, *98*, 1393–1401. [CrossRef] [PubMed]
95. Urena, M.; Himbert, D.; Brochet, E.; Carrasco, J.L.; Iung, B.; Nataf, P.; Vahanian, A. Transseptal Transcatheter Mitral Valve Replacement Using Balloon-Expandable Transcatheter Heart Valves. *JACC: Cardiovasc. Interv.* **2017**, *10*, 1905–1919. [CrossRef] [PubMed]
96. Hosoba, S.; Mori, M.; Goto, Y.; Fukumoto, Y.; Shimura, T.; Yamamoto, M. Hypo-attenuated leaflet thickening in surgically-implanted mitral bioprosthesis. *J. Cardiothorac. Surg.* **2020**, *15*, 74–77. [CrossRef] [PubMed]
97. Kaewkes, D.; Patel, V.; Ochiai, T.; Flint, N.; Ahmad, Y.; Kim, I.; Koseki, K.; Sharma, R.; Joseph, J.; Yoon, S.-H.; et al. Usefulness of Computed Tomography to Predict Mitral Stenosis After Transcatheter Mitral Valve Edge-to-Edge Repair. *Am. J. Cardiol.* **2021**, *153*, 109–118. [CrossRef] [PubMed]
98. Dahou, A.; Levin, D.; Reisman, M.; Hahn, R.T. Anatomy and Physiology of the Tricuspid Valve. *JACC: Cardiovasc. Imaging* **2019**, *12*, 458–468. [CrossRef] [PubMed]
99. Taramasso, M.; Pozzoli, A.; Basso, C.; Thiene, G.; Denti, P.; Kuwata, S.; Nietlispach, F.; Alfieri, O.; Hahn, R.T.; Nickenig, G.; et al. Compare and contrast tricuspid and mitral valve anatomy: Interventional perspectives for transcatheter tricuspid valve therapies. *Eurointervention* **2018**, *13*, 1889–1898. [CrossRef]
100. Mangieri, A.; Sticchi, A.; Gohar, A.; Regazzoli, D.; Fazzari, F.; Pini, D.; Pellegrino, M.; Pagliaro, B.; Loiacono, F.; Chiarito, M.; et al. Percutaneous Tricuspid Valve Repair. *Rev. Cardiovasc. Med.* **2022**, *23*, 220. [CrossRef]
101. Oliveira, D.C.; Oliveira, C.G. The Forgotten, Not Studied or Not Valorized Tricuspid Valve: The Transcatheter Revolution Is Coming. *Cardiol. Res.* **2019**, *10*, 199–206. [CrossRef]
102. Topilsky, Y.; Maltais, S.; Medina-Inojosa, J.; Oguz, D.; Michelena, H.; Maalouf, J.; Mahoney, D.W.; Enriquez-Sarano, M. Burden of Tricuspid Regurgitation in Patients Diagnosed in the Community Setting. *JACC Cardiovasc. Imaging* **2019**, *12*, 433–442. [CrossRef]
103. Benfari, G.; Antoine, C.; Miller, W.L.; Thapa, P.; Topilsky, Y.; Rossi, A.; Michelena, H.I.; Pislaru, S.; Enriquez-Sarano, M. Excess Mortality Associated With Functional Tricuspid Regurgitation Complicating Heart Failure With Reduced Ejection Fraction. *Circulation* **2019**, *140*, 196–206. [CrossRef] [PubMed]
104. Praz, F.; Muraru, D.; Kreidel, F.; Lurz, P.; Hahn, R.T.; Delgado, V.; Senni, M.; von Bardeleben, R.S.; Nickenig, G.; Hausleiter, J.; et al. Transcatheter treatment for tricuspid valve disease. *Eurointervention* **2021**, *17*, 791–808. [CrossRef] [PubMed]

105. Hashimoto, G.; Fukui, M.; Sorajja, P.; Cavalcante, J.L. Essential roles for CT and MRI in timing of therapy in tricuspid regurgitation. *Prog. Cardiovasc. Dis.* **2019**, *62*, 459–462. [CrossRef] [PubMed]
106. Lewis, M.A.; Pascoal, A.; Keevil, S.F.; Lewis, C.A. Selecting a CT scanner for cardiac imaging: The heart of the matter. *Br. J. Radiol.* **2016**, *89*, 20160376. [CrossRef] [PubMed]
107. Pulerwitz, T.C.; Khalique, O.K.; Leb, J.; Hahn, R.T.; Nazif, T.; Leon, M.B.; George, I.; Vahl, T.P.; D'Souza, B.; Bapat, V.N.; et al. Optimizing Cardiac CT Protocols for Comprehensive Acquisition Prior to Percutaneous MV and TV Repair/Replacement. *JACC: Cardiovasc. Imaging* **2020**, *13*, 836–850. [CrossRef]
108. Lopes, B.B.; Sorajja, P.; Hashimoto, G.; Fukui, M.; Bapat, V.N.; Du, Y.; Bae, R.; Schwartz, R.S.; Stanberry, L.I.; Enriquez-Sarano, M.; et al. Tricuspid Anatomic Regurgitant Orifice Area by Functional DSCT. *JACC: Cardiovasc. Imaging* **2021**, *14*, 1669–1672. [CrossRef]
109. Praz, F.; Khalique, O.K.; Macedo, L.G.D.R.; Pulerwitz, T.C.; Jantz, J.; Wu, I.Y.; Kantor, A.; Patel, A.; Vahl, T.; Bapat, V.; et al. Comparison between Three-Dimensional Echocardiography and Computed Tomography for Comprehensive Tricuspid Annulus and Valve Assessment in Severe Tricuspid Regurgitation: Implications for Tricuspid Regurgitation Grading and Transcatheter Therapies. *J. Am. Soc. Echocardiogr.* **2018**, *31*, 1190–1202.e3. [CrossRef]
110. van Rosendael, P.J.; Joyce, E.; Katsanos, S.; Debonnaire, P.; Kamperidis, V.; van der Kley, F.; Schalij, M.J.; Bax, J.J.; Marsan, N.A.; Delgado, V. Tricuspid valve remodelling in functional tricuspid regurgitation: Multidetector row computed tomography insights. *Eur. Hear. J. Cardiovasc. Imaging* **2015**, *17*, 96–105. [CrossRef]
111. Hell, M.M.; Emrich, T.; Kreidel, F.; Kreitner, K.-F.; Schoepf, U.J.; Münzel, T.; von Bardeleben, R.S. Computed tomography imaging needs for novel transcatheter tricuspid valve repair and replacement therapies. *Eur. Hear. J. Cardiovasc. Imaging* **2020**, *22*, 601–610. [CrossRef]
112. Hahn, R.T.; Thomas, J.D.; Khalique, O.K.; Cavalcante, J.L.; Praz, F.; Zoghbi, W.A. Imaging Assessment of Tricuspid Regurgitation Severity. *JACC: Cardiovasc. Imaging* **2019**, *12*, 469–490. [CrossRef] [PubMed]
113. Fukuda, S.; Saracino, G.; Matsumura, Y.; Daimon, M.; Tran, H.; Greenberg, N.L.; Hozumi, T.; Yoshikawa, J.; Thomas, J.D.; Shiota, T. Three-Dimensional Geometry of the Tricuspid Annulus in Healthy Subjects and in Patients With Functional Tricuspid Regurgitation. *Circulation* **2006**, *114*, I492–I498. [CrossRef] [PubMed]
114. McElhinney, D.B.; Cabalka, A.K.; Aboulhosn, J.A.; Eicken, A.; Boudjemline, Y.; Schubert, S.; Himbert, D.; Asnes, J.D.; Salizzoni, S.; Bocks, M.L.; et al. Transcatheter Tricuspid Valve-in-Valve Implantation for the Treatment of Dysfunctional Surgical Bioprosthetic Valves: An International, Multicenter Registry Study. *Circulation* **2016**, *133*, 1582–1593. [CrossRef] [PubMed]
115. van Rosendael, P.J.; Kamperidis, V.; Kong, W.K.; van Rosendael, A.R.; van der Kley, F.; Marsan, N.A.; Delgado, V.; Bax, J.J. Computed tomography for planning transcatheter tricuspid valve therapy. *Eur. Hear. J.* **2016**, *38*, 665–674. [CrossRef] [PubMed]
116. Delgado, V.; Di Biase, L.; Leung, M.; Romero, J.; Tops, L.F.; Casadei, B.; Marrouche, N.; Bax, J.J. Structure and Function of the Left Atrium and Left Atrial Appendage. *J. Am. Coll. Cardiol.* **2017**, *70*, 3157–3172. [CrossRef] [PubMed]
117. Di Biase, L.; Santangeli, P.; Anselmino, M.; Mohanty, P.; Salvetti, I.; Gili, S.; Horton, R.; Sanchez, J.E.; Bai, R.; Mohanty, S.; et al. Does the Left Atrial Appendage Morphology Correlate With the Risk of Stroke in Patients With Atrial Fibrillation? *J. Am. Coll. Cardiol.* **2012**, *60*, 531–538. [CrossRef] [PubMed]
118. Karim, N.; Ho, S.Y.; Nicol, E.; Li, W.; Zemrak, F.; Markides, V.; Reddy, V.; Wong, T. The left atrial appendage in humans: Structure, physiology, and pathogenesis. *Eur.* **2019**, *22*, 5–18. [CrossRef]
119. Romero, J.; Natale, A.; Di Biase, L. Left Atrial Appendage Morphology and Physiology: "The Missing Piece in the Puzzle". *J. Cardiovasc. Electrophysiol.* **2015**, *26*, 928–933. [CrossRef]
120. Shirani, J.; Alaeddini, J. Structural Remodeling of the Left Atrial Appendage in Patients with Chronic Non-Valvular Atrial Fibrillation. *Cardiovasc. Pathol.* **2000**, *9*, 95–101. [CrossRef]
121. Vigna, C.; Russo, A.; De Rito, V.; Perna, G.; Villella, A.; Testa, M.; Sollazzo, V.; Fanelli, R.; Loperfido, F. Frequency of left atrial thrombi by transesophageal echocardiography in idiopathic and in ischemic dilated cardiomyopathy. *Am. J. Cardiol.* **1992**, *70*, 1500–1501. [CrossRef]
122. Crandall, M.A.; Bradley, D.J.; Packer, D.L.; Asirvatham, S.J. Contemporary Management of Atrial Fibrillation: Update on Anticoagulation and Invasive Management Strategies. *Mayo Clin. Proc.* **2009**, *84*, 643–662. [CrossRef] [PubMed]
123. Fountain, R.B.; Holmes, D.R.; Chandrasekaran, K.; Packer, D.; Asirvatham, S.; Van Tassel, R.; Turi, Z. The PROTECT AF (WATCHMAN Left Atrial Appendage System for Embolic PROTECTion in Patients with Atrial Fibrillation) Trial. *Am. Hear. J.* **2006**, *151*, 956–961. [CrossRef]
124. Holmes, D.R.; Reddy, V.Y.; Turi, Z.G.; Doshi, S.K.; Sievert, H.; Buchbinder, M.; Mullin, C.M.; Sick, P. Percutaneous closure of the left atrial appendage versus warfarin therapy for prevention of stroke in patients with atrial fibrillation: A randomised non-inferiority trial. *Lancet* **2009**, *374*, 534–542. [CrossRef]
125. Galea, R.; De Marco, F.; Meneveau, N.; Aminian, A.; Anselme, F.; Gräni, C.; Huber, A.T.; Teiger, E.; Iriart, X.; Bosombo, F.B.; et al. Amulet or Watchman Device for Percutaneous Left Atrial Appendage Closure: Primary Results of the SWISS-APERO Randomized Clinical Trial. *Circulation* **2022**, *145*, 724–738. [CrossRef] [PubMed]
126. Prakash, R.; Saw, J. Imaging for percutaneous left atrial appendage closure. *Catheter. Cardiovasc. Interv.* **2016**, *92*, 437–450. [CrossRef]
127. Oda, S.; Honda, K.; Yoshimura, A.; Katahira, K.; Noda, K.; Oshima, S.; Yuki, H.; Kidoh, M.; Utsunomiya, D.; Nakaura, T.; et al. 256-Slice coronary computed tomographic angiography in patients with atrial fibrillation: Optimal reconstruction phase and image quality. *Eur. Radiol.* **2015**, *26*, 55–63. [CrossRef] [PubMed]

128. Martinez, M.W.; Kirsch, J.; Williamson, E.E.; Syed, I.S.; Feng, D.; Ommen, S.; Packer, D.L.; Brady, P.A. Utility of Nongated Multidetector Computed Tomography for Detection of Left Atrial Thrombus in Patients Undergoing Catheter Ablation of Atrial Fibrillation. *JACC: Cardiovasc. Imaging* **2009**, *2*, 69–76. [CrossRef]
129. Hur, J.; Kim, Y.J.; Lee, H.-J.; Nam, J.E.; Hong, Y.; Kim, H.Y.; Lee, J.W.; Choi, B.W. Cardioembolic Stroke: Dual-Energy Cardiac CT for Differentiation of Left Atrial Appendage Thrombus and Circulatory Stasis. *Radiology* **2012**, *263*, 688–695. [CrossRef]
130. Rajwani, A.; Nelson, A.J.; Shirazi, M.G.; Disney, P.J.S.; Teo, K.S.L.; Wong, D.T.L.; Young, G.D.; Worthley, S.G. CT sizing for left atrial appendage closure is associated with favourable outcomes for procedural safety. *Eur. Hear. J. Cardiovasc. Imaging* **2016**, *18*, 1361–1368. [CrossRef]
131. Wang, Y.; Di Biase, L.; Horton, R.P.; Nguyen, T.; Morhanty, P.; Natale, A. Left Atrial Appendage Studied by Computed Tomography to Help Planning for Appendage Closure Device Placement. *J. Cardiovasc. Electrophysiol.* **2010**, *21*, 973–982. [CrossRef]
132. Jaguszewski, M.; Manes, C.; Puippe, G.; Salzberg, S.; Müller, M.; Falk, V.; Lüscher, T.; Luft, A.; Alkadhi, H.; Landmesser, U. Cardiac CT and echocardiographic evaluation of peri-device flow after percutaneous left atrial appendage closure using the AMPLATZER cardiac plug device. *Catheter. Cardiovasc. Interv.* **2014**, *85*, 306–312. [CrossRef] [PubMed]
133. Clemente, A.; Avogliero, F.; Berti, S.; Paradossi, U.; Jamagidze, G.; Rezzaghi, M.; Della Latta, D.; Chiappino, D. Multimodality imaging in preoperative assessment of left atrial appendage transcatheter occlusion with the Amplatzer Cardiac Plug. *Eur. Hear. J. Cardiovasc. Imaging* **2015**, *16*, 1276–1287. [CrossRef] [PubMed]
134. Diwakar, M.; Tripathi, A.; Joshi, K.; Sharma, A.; Singh, P.; Memoria, M.; Kumar, N. A comparative review: Medical image fusion using SWT and DWT. *Mater. Today: Proc.* **2020**, *37*, 3411–3416. [CrossRef]
135. Diwakar, M.; Tripathi, A.; Joshi, K.; Memoria, M.; Singh, P.; Kumar, N. Latest trends on heart disease prediction using machine learning and image fusion. *Mater. Today: Proc.* **2020**, *37*, 3213–3218. [CrossRef]
136. Joshi, K.; Kumar, M.; Tripathi, A.; Kumar, A.; Sehgal, J.; Barthwal, A. *Latest Trends in Multi-Modality Medical Image Fusion: A Generic Review*; Springer: Singapore, 2022; Volume 434, pp. 663–671. [CrossRef]

applied sciences

MDPI

Review

Beyond the Calcium Score: What Additional Information from a CT Scan Can Assist in Cardiovascular Risk Assessment?

Federico Bernardini [1], Martina Gelfusa [1], Mihail Celeski [1], Federica Coletti [1], Annunziata Nusca [1,*], Domenico De Stefano [2], Francesco Piccirillo [1], Fabio Mangiacapra [1], Paolo Gallo [1], Valeria Cammalleri [1], Nino Cocco [1], Raffaele Rinaldi [1], Carlo Cosimo Quattrocchi [2], Gian Paolo Ussia [1] and Francesco Grigioni [1]

[1] Unit of Cardiac Sciences, Department of Medicine, Campus Bio-Medico University of Rome, 00128 Rome, Italy
[2] Unit of Diagnostic Imaging, Department of Medicine, Campus Bio-Medico University of Rome, 00128 Rome, Italy
* Correspondence: a.nusca@policlinicocampus.it

Abstract: Coronary artery disease (CAD) still represents a leading cause of mortality worldwide. Early identification of patients at the highest risk of CAD is crucial to prevent acute adverse events and reduce morbidity and mortality. The coronary artery calcium (CAC) score is a reliable cardiovascular (CV) risk index with an independent prognostic value. Guidelines recommend using it as a risk enhancer in individuals with low or moderate CV risk. However, other computed tomography (CT) measurable parameters have recently been proposed as CV risk markers. Increasing evidence demonstrates the association between epicardial fat volume and coronary atherosclerosis in chronic and acute coronary syndromes. Furthermore, other parameters obtainable from CT, such as aortic stiffness, liver fat, aortic calcium, and myocardial scarring, are under investigation. This review aims to describe all CT potential in atherosclerosis detection and cardiovascular risk assessment beyond the CAC, trying to understand how to integrate CT parameters with traditional risk factors and to improve clinicians' ability to detect CAD early, allowing appropriate therapies promptly.

Keywords: cardiac computed tomography (CCT); cardiovascular (CV) risk; coronary artery calcium (CAC) score; epicardial adipose tissue (EAT); coronary atherosclerosis

Citation: Bernardini, F.; Gelfusa, M.; Celeski, M.; Coletti, F.; Nusca, A.; De Stefano, D.; Piccirillo, F.; Mangiacapra, F.; Gallo, P.; Cammalleri, V.; et al. Beyond the Calcium Score: What Additional Information from a CT Scan Can Assist in Cardiovascular Risk Assessment? *Appl. Sci.* **2023**, *13*, 241. https://doi.org/10.3390/app13010241

Academic Editor: Julio Garcia Flores

Received: 30 November 2022
Revised: 20 December 2022
Accepted: 23 December 2022
Published: 25 December 2022

Coronary artery disease (CAD) still represents the first cause of death worldwide, and its prevention (primary and secondary) has become a current health priority [1].

Estimating total cardiovascular (CV) risk is essential because it allows recognizing patients who could benefit most from prevention models [2]. In apparently healthy individuals, CV risk is composed of multiple risk factors (smoking habits, hypertension, diabetes mellitus, obesity, dyslipidemia, and family history of cardiovascular diseases) that interplay synergistically [3]. Therefore, various score systems including these CV risk factors have been developed for global risk estimation; the most used is the systematic coronary risk evaluation (SCORE) model and two variants for patients aged 40 to 69 (SCORE2) and for individuals over 70 (SCORE-OP) [4]. However, these scores have several limitations and do not allow for establishing the patient's absolute risk of developing coronary atherosclerosis.

Cardiovascular risk estimation has been improved in the last decade using imaging techniques, mainly looking for subclinical atherosclerotic disease [3]. Cardiac computed tomography angiography (CCTA) provides information on the presence and extension of coronary stenoses and plaque burden and morphology. Moreover, the coronary artery calcium (CAC) score has emerged as a marker of subclinical coronary disease in apparently healthy individuals. However, according to existing models, its predictive value is lower in patients with high or very low total CV risk [5]. Finally, epicardial fat volume, aortic stiffness, liver fat, aortic calcium, and myocardial scarring might be potential markers for the early detection of atherosclerosis and consequent CAD.

In this background, this review aims to describe all cardiac CT potential in atherosclerosis detection and CV risk assessment, focusing on the more traditional tools and emerging parameters under investigation. We also sought to provide information on integrating CT parameters with traditional risk factors to improve clinicians' ability to detect CAD promptly.

Five reviewers shortlisted studies and abstracts about CT-scan and cardiovascular risk assessment, excluding those that were not pertinent to the topic. Studies designed as randomized controlled trials, non-randomized trials, descriptive, and qualitative were included. The electronic search was performed on MEDLINE (pub-med) and conducted in English. The software used for the bibliography management was MENDELEY. Keywords and abbreviations were used for the concept of reduction/avoiding.

1. Current Role of CCTA in Clinical Practice and Guidelines

1.1. Chronic Coronary Syndromes

CCTA constitutes a first-line non-invasive tool in the diagnostic process of patients with stable chronic coronary syndromes (CCS). Nevertheless, its role in this category of patients went through a significant evolution. Indeed, the 2012 American Heart Association/American College of Cardiology (AHA/ACC) guidelines for the diagnosis and management of patients with stable ischemic heart disease (SIHD) reported that CCTA should be used as a first-line test for risk assessment only in patients with SIHD who were unable to exercise to an adequate workload (class IIa) [6]. The 2016 United Kingdom (UK) guidelines of National Institute for Health and Care Excellence (NICE) [7] recommend CCTA as the first-line diagnostic test in patients with atypical and typical angina (or electrocardiogram abnormalities suggestive of CAD in the absence of symptoms). More recently, the 2019 European Society of Cardiology (ESC) guidelines recommend CCTA (class IB) in suitable patients with low-to-intermediate clinical probability of CCS (Table 1) [8]. Indeed, the PROMISE trial demonstrated that CCTA is superior to functional testing in predicting cardiovascular events in patients with chest pain suspicious for coronary artery disease and reduces the rate of coronary angiography showing non-significant coronary artery disease [9]. Moreover, the SCOT-HEART trial in the same group of patients confirmed that using CCTA in addition to standard care resulted in a lower risk of death for CAD and reduced incidence of non-fatal myocardial infarction [10].

1.2. Acute Chest Pain

In the emergency department setting, CCTA may help rule out acute coronary syndrome (ACS) in patients with low-to-intermediate pre-test probability (PTP) due to its high negative predictive value. The 2014 American Heart Association/American College of Cardiology (AHA/ACC) guideline for the management of patients with non-ST-elevation acute coronary syndrome does not provide specific recommendations about CCTA [11]. However, CCTA is described as a more rapid and cost-effective diagnostic exam than stress myocardial perfusion imaging in low-risk patients with chest pain. In front of low-to-moderate risk of CAD and unconvincing results with cardiac troponin and/or electrocardiogram (ECG), the most recent European Society of Cardiology (ESC) guidelines for the management of acute coronary syndromes in patients presenting without persistent ST-segment elevation propose CCTA (Class IA) as a substitute to coronarography for ruling out ACS [12]. Furthermore, these recommendations advise performing CCTA (Class IB) for patients with persistent suspicion of ACS who have no return of chest pain, normal troponin values, and without electrocardiographic alterations before choosing an invasive strategy (Table 1) [12].

1.3. Plaque Burden

Several studies highlighted the optimal negative predictive value of CCTA, reporting annualized event rates ranging from 0.02% to 0.3% for short [13], intermediate [14], and long-term [15] outcomes in patients with normal CCTA. Contrarywise, the CONFIRM

(Coronary CT Angiography Evaluation for Clinical Outcomes: An InteRnational Multicenter) registry indicated a strong association between the extension and distribution of atherosclerotic plaques detected by CCTA and long-term prognosis, suggesting as the CCTA plaque burden might represent a significant predictor of patient outcomes [16].

Table 1. ESC and AHA/ACC guidelines recommendations about CCTA application in chronic coronary syndromes (CCS), acute coronary syndromes (ACS), and cardiovascular prevention.

Chronic Coronary Syndromes (CCS)	
ESC 2019	**AHA/ACC 2012**
Non-invasive functional imaging for myocardial ischemic or CCTA is recommended as the initial test to diagnose CAD in symptomatic patients in whom obstructive CAD cannot be excluded by clinical assessment alone **(I-B)**	CCTA can be useful as a first-line test for risk assessment in patients with SIHD who are unable to exercise to an adequate workload regardless of interpretability of ECG **(IIa-C)**
It is recommended that selection of the initial non-invasive diagnostic test is done based on the clinical likelihood of CAD and other patient characteristics that influence test performance, local expertise, and the availability of tests. **(I-C)**	CCTA may be reasonable for risk assessment in patients with SIHD who are able to exercise to an adequate workload but have an uninterpretable ECG **(IIb-B)**
CCTA should be considered as an alternative to invasive angiography if another non-invasive test is equivocal or non-diagnostic. **(IIa-C)**	CCTA can be useful for risk assessment in patients with SIHD who have an indeterminate result from functional testing **(IIa-C)**
Acute Coronary Syndromes (ACS)	
ESC 2020 (NSTEMI)	**AHA/ACC 2021 (chest pain)**
CCTA is recommended as an alternative to ICA to exclude ACS when there is a low-to-intermediate likelihood of CAD and when cardiac troponin and/or ECG are normal or inconclusive **(I-A)**	For intermediate-risk patients with acute chest pain and no known CAD eligible for diagnostic testing after a negative or inconclusive evaluation for ACS, CCTA is useful for exclusion of atherosclerotic plaque and obstructive CAD **(I-A)**
In patients with no recurrence of chest pain, normal ECG findings, and normal levels of cardiac troponin (preferably high sensitivity), but still with a suspected ACS, a non-invasive stress test (preferably with imaging) for inducible ischaemia or CCTA is recommended before deciding on an invasive approach. **(I-B)**	For intermediate-risk patients with acute chest pain with evidence of previous mildly abnormal stress test results, CCTA is reasonable for diagnosing obstructive CAD **(IIa-C)**
CardiovascularPrevention	
ESC 2021	**AHA/ACC 2019**
Coronary artery calcium (CAC) scoring can reclassify CVD risk in addition to conventional risk factors, and may be considered in men and women with calculated risks around decision thresholds	In intermediate-risk (7.5–20% 10-year ASCVD risk) adults or selected borderline-risk (5–7.5% 10-year ASCVD risk) adults in whom a coronary artery calcium score is measured for the purpose of making a treatment decision: -CAC scoring is zero → it is reasonable to withhold statin therapy and reassess in 5 to 10 years, as long as higher-risk conditions are absent (e.g., diabetes, family history of premature CAD, cigarette smoking); -CAC score is 1 to 99 → it is reasonable to initiate statin therapy for patients >55 years of age; -CAC score is 100 or higher → it is reasonable to initiate statin therapy **(IIa-B)**

CCS: chronic coronary syndromes; **CCTA:** coronary computed tomography angiography; **CAD:** coronary artery disease; **SIHD:** stable ischemic heart disease; **ECG:** electrocardiogram; **ACS:** acute coronary syndromes; **CVD:** cardiovascular disease; **ICA:** invasive coronary angiography; **CAC:** coronary artery calcium; **ASCVD**: atherosclerotic cardiovascular disease.

Several studies demonstrated how patients might be stratified across a risk continuum beyond a simple classification based on the presence of stenoses [17,18]. Indeed, in comparison to people without detectable plaques, the recognition of non-obstructive CAD on CCTA, which is typically undetected by stress test methodologies, has been related to an

adjusted hazard ratio for major adverse cardiac events (MACEs) among 1.6 and 7.1. [19]. Multiple studies showed that the number of segments involved is one of the best predictors of outcome, surpassing scores that only consider segments with mild or moderate stenosis [14,18]. Bittencourt et al. demonstrated that patients with nonobstructive CAD involving >4 coronary segments had a similar rate of cardiovascular death or myocardial infarction (MI) as those who had obstructive disease with ≤4 diseased segments [17]. The type of vessel involved also influences the prognosis of these patients. According to Weir-McCall et al., non-obstructive left main coronary artery disease, contrary to patients with CAD not including left main, was found to be related with a superior rate of plaque advancement and increased prevalence of high-risk plaques across the coronary artery tree. This implies that non-obstructive left main illness may serve as a potential indicator of a CAD category that is aggressive and may profit from a more aggressive therapy strategy [20].

Notably, plaque burden assessment by CCTA can be semi-quantitative, by counting the number of segments involved by atherosclerosis (segment involvement score (SIS), segment stenosis score (SSS), or CT-adapted Leaman score) [21] or quantitative through plaque burden using automated or semi-automated softwares [22].

In addition, numerous longitudinal trials have evaluated the function of quantitative coronary computed tomography (QCCTA) in the development of CAD across succedent CCTA studies in terms of disease advancement. Variations in QCCTA markers served as potential predictors for the progression of atherosclerotic plaque in the PARADIGM registry [22].

1.4. Plaque Morphology

Although the risk of plaque rupture is proportional to the extent of stenosis, it has been reported that nonobstructive lesions with typical features of plaque composition represent the majority of culprit lesions in ACS. Chang et al. realized a nested case-control study within a cohort of 25,251 patients undergoing CCTA with a follow-up of 3.4 years. ACS and non-event patients without prior CAD were matched for risk factors and CCTA-rated obstructive (≥50%) CAD [23]. Thus, separate core laboratories performed a blinded assessment of coronary lesions detected by CCTA, quantifying the percent stenosis diameter (SD), the percent plaque burden (PB), the plaque volume (PV) by composition (calcified, fibrous, fibrofatty, and necrotic core), and identifying high-risk plaques (HRP) (Figures 1 and 2). Notably, HRP was reported in 52% of ACS patients. Moreover, the authors reported higher PB and fibrofatty and necrotic PV in patients with ACS than non-event patients, regardless of stenosis severity [23].

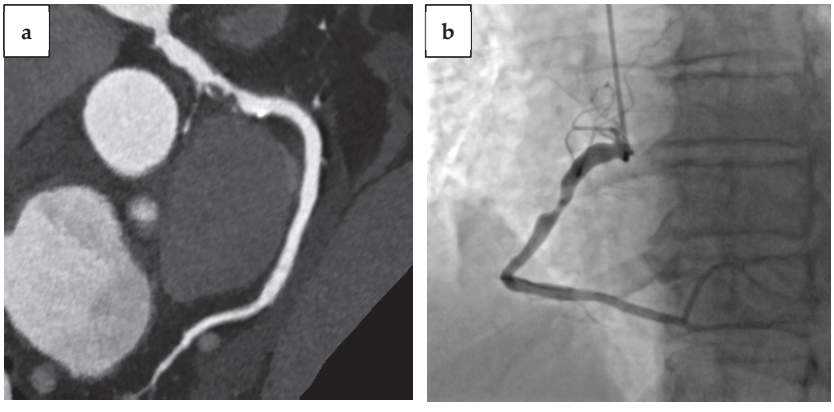

Figure 1. Right coronary artery unstable plaque: (**a**) Coronary computed tomography angiography (CCTA) assessment; (**b**) invasive coronary angiography (ICA) assessment.

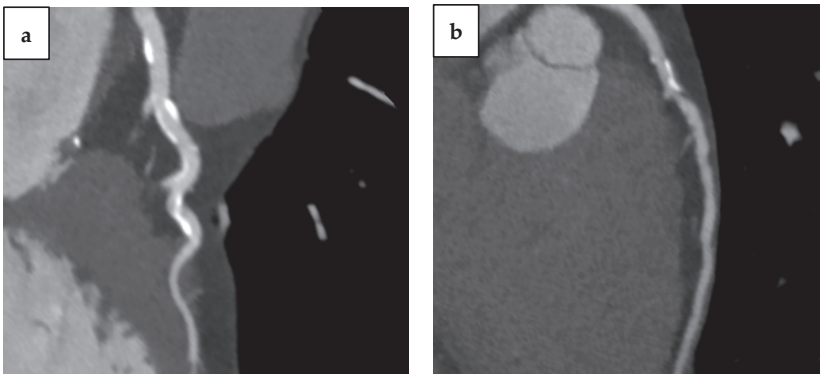

Figure 2. Coronary artery stable plaques: (**a**) calcific plaque; (**b**) fibro-calcific plaque.

From a histopathological perspective, a vulnerable plaque is defined by a thin fibrous cap, a large necrotic core, the presence of positive remodeling (PR) (remodeling index > 1.1), perivascular inflammation, and spotty calcifications. Moreover, recent studies have reported a specific attenuation pattern of atherosclerotic plaques on coronary CT images called "napkin ring sign" (NRS) [24]. It is described as a plaque core with low CT attenuation surrounded by a rim-like area of higher CT attenuation. The pathophysiology of this finding remains unclear, even if it may be linked to various high-risk characteristics such as contrast enhancement of the vasa vasorum, intraplaque hemorrhage, microcalcifications, or even healed ruptures [19]. Interestingly, Maurovich-Horvat et al., in a study involving heart donors, found that the detection of NRS at CCTA had high specificity and positive predictive value for the presence of advanced lesions [25].

Furthermore, Nakazato et al. evaluated coronary plaque characteristics with both CCTA and optical coherence tomography (OCT) [26]. They showed that PR and the presence of low-attenuation plaques (LAP) detected by CCTA are associated with thin cap fibroatheroma (TCFA) and higher macrophage infiltration evaluated by OCT. Concordantly, Hoffman et al. described a higher prevalence of remodeling in unstable plaques than in stable plaques [27]. Finally, in a sub-analysis of the NXT (HeartFlowNXT: HeartFlow Analysis of Coronary Blood Flow Using Coronary CT Angiography) study, CCTA, invasive angiography, and fractional flow reserve (FFR) were acquired for 383 lesions in patients with stable coronary syndromes [28]. The study revealed that LAP detected on CCTA significantly correlated with the presence of ischemia identified by FFR.

It has also been shown that the evaluation of plaque morphology with the detection of high-risk characteristics by CCTA is a useful method for forecasting future negative outcomes and the advancement of CAD. Motoyama et al., in a large longitudinal study, reported that both PR and LAP were strong predictors of future ACS events [29]. A sub-analysis of the SCOT-HEART trial revealed that the presence of adverse coronary plaque features confers a 3-fold increased risk of cardiovascular death or nonfatal MI [30]. Therefore, the Coronary Artery Disease Reporting and Data System (CAD-RADS) recommendations advise mentioning the existence of susceptible plaque whenever there are two or more high-risk criteria present (Figure 3) [31].

However, the image quality may be affected by artifacts invalidating the estimation of plaque morphology [32,33]. The most common are the motion and blooming artifacts, cause of severity overestimation of calcific plaques. The use of de-blooming algorithms and 3D reconstruction models allow us to overcome these limits ensuring a better CT-based analysis [34].

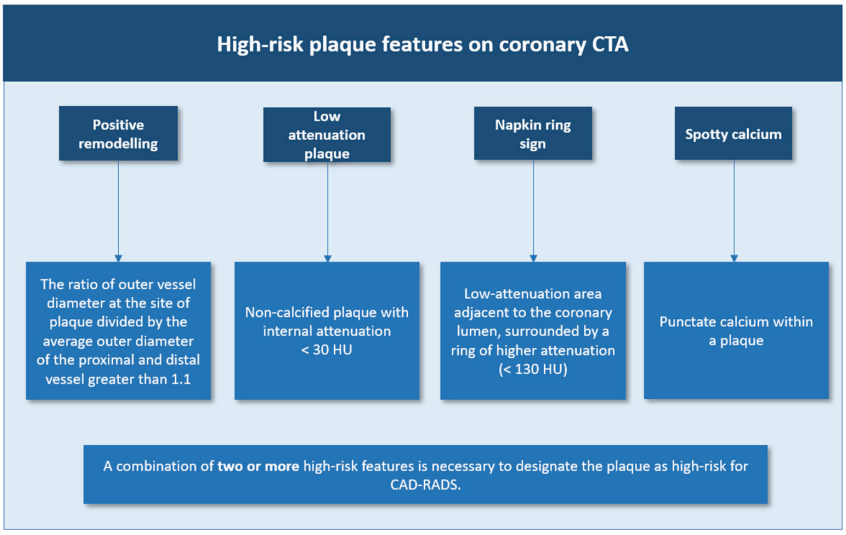

Figure 3. Vulnerable plaque features according to Coronary Artery Disease Reporting and Data System (CAD-RADS) guidelines.

1.5. CCTA in Previous Coronary Revascularization

The role of CCTA is still debated in patients previously revascularized with stents. The effectiveness of CCTA ≥64 slices for diagnosing coronary in-stent restenosis (ISR) and the effect of specific procedural aspects on diagnostic accuracy were examined in a recent meta-analysis that included 35 trials and 4131 stents [35]. This meta-analysis showed that CCTA could provide precise information about ISR lesions and that assessing these lesions could help identify changes over time. This is particularly important because patients with ISR may finally be suitable for non-invasive angiographic follow-up using CCTA. Nevertheless, in this context, CCTA has only been observed to have a high sensitivity in a few instances. For example, in stents with a diameter of >3 mm compared to those with lower diameters (94% vs. 89%), for stents with metal struts < 100 μm compared to thickening stents (96% vs. 84%), and for simple stents compared to stents implanted on bifurcations (95% vs. 88%) [19].

On the other hand, the role of CCTA in the evaluation of coronary artery bypass grafts (CABG) is more defined. A recent meta-analysis including 1975 patients and 5364 grafts revealed the excellent diagnostic performance of CCTA in the identification of graft stenosis or occlusion compared with invasive coronary angiography, with a sensitivity of 96%, a specificity of 96%, and a negative predictive value of 99% [36]. CCTA could also be used to assess the disease progression of native nongrafted vessels in patients with recurrent angina after CABG. Although these segments are often massively calcified and challenging to assess with CCTA, several studies, such as that of de Graaf et al., showed acceptable diagnostic accuracy for the detection of new coronary stenosis, with sensitivity and specificity of 83–100% and 77–100%, respectively [37].

2. Coronary Artery Calcium Score

To stratify cardiovascular risk, forecast patient outcomes, and direct preventative therapy, coronary artery calcium (CAC) scoring has become a widespread and efficient method. At this time, CAC score is advised to estimate the likelihood of developing cardiovascular diseases and mortality CAD-related in asymptomatic individuals [38]. Additionally, the CAC score is used to reclassify CV risk in other subgroups and to aid in developing primary prevention decisions such as statin therapy [19]. More recently, CT calcium scoring has become fundamental also in other clinical settings, such as allowing flow-independent

assessments of aortic stenosis severity when echocardiography measurements are discordant, pre-procedural planning of transcatheter aortic and mitral valve intervention, and in determining the etiology of cardiomyopathies [39].

2.1. Imaging Acquisition, Reconstruction, and Quantification of CAC

For CAC assessment, acquisition and reconstruction settings are standardized. Data are usually acquired using prospective electrocardiographic triggering in late diastole, with a section thickness of 2.5 mm, a section interval of 1 mm and without contrast material administration, using 120 kV tube voltage [38].

Electron-beam computed tomography (EBCT) and multi-detector computed tomography (MDCT) have been the main CT methods for CAC measurements, using fast scan speeds to reduce motion artifacts, with MDCT being associated with improved spatial resolution and largely replacing EBCT in practice [40].

Section thickness in the axial soft-tissue window and axial lung window settings for reconstruction is set to 2.5 mm. The CAC score is then determined using vendor-provided software, often measured with the use of the Agatston method, with calcification typically being defined as high attenuation (130 HU) and an area $\geq$ 1 mm [38,41]. The overall plaque area and a cofactor based on the attenuation of the plaque calcium in Hounsfield units are combined to get the Agatston score [38,42,43]. The area of the lesion (Ai) is multiplied by a weighting factor (wi) based on the maximal CT number (CTmax) in the segment of interest to determine the calcium score for each desired segment (CSi): CSi = wi x Ai, where wi is 1 if 130 HUCTmax <200 HU, 2 if 200 HU $\leq$ CTmax < 300 HU, 3 if 300 HU $\leq$ CTmax < 400 HU, 4 if 400 HU $\leq$ CTmax. Agatston score for each artery, each calcification, or the entire heart, also known as total calcium score (TCS), is calculated by summing the respective values for the regions of interest [41,43].

The Agatston score can be reported either as an absolute value with predetermined cut-offs or as a percentile compared to age-, sex-, and ethnicity-matched individuals using the Multi-Ethnic Study of Atherosclerosis (MESA) database [44]. As an alternative to total plaque burden, the following description of the total Agatston calcium score and the corresponding risk category is suitable: no coronary calcium, 1–9: minimal, 10–99: mild, 100–399: moderate, and $\geq$400: severe (Figure 4) [45]. However, the absolute measurement strategy outperformed the age-gender-ethnicity method, according to the MESA trial, even though both approaches produced effective risk categorization. In that study, even the lowest CAC (Agatston score of 1–10) was associated with a 3-fold increased risk of CAD than patients with an Agatston score of 0, and a score greater than 100 was associated with a 10-fold increased risk [44].

Another method for CAC assessment was developed based on volume scoring that represents the volume of the calcification; this score has become popular due to its relative resistance to slight variations in noise and its robust interscan reproducibility [46]. It is expressed with the product between the volume of one voxel and the number of voxels in the volume dataset related to the calcification. Nevertheless, there are several limits including the overestimation of the CAC grade in areas of strong attenuation and the vulnerability to partial volume averaging of this method. Another scoring system is the mass score, which is derived using the plaque volume, plaque attenuation, and a calibration factor that considers the water attenuation. Even though it is an up-and-coming method based on the measurement of a true mineral mass of calcium hydroxyapatite in the plaques, it requires complex postprocessing, and limited supporting data have been available so far [41,46]. Finally, Brown et al. proposed another score for clinical use, the calcium coverage score, defined as the percentage of coronary arteries affected by calcified plaque, which was highly associated with coronary heart disease events and provided information about cardiovascular occurrence beyond the calcium burden defined by the Agatston or calcium mass score [47].

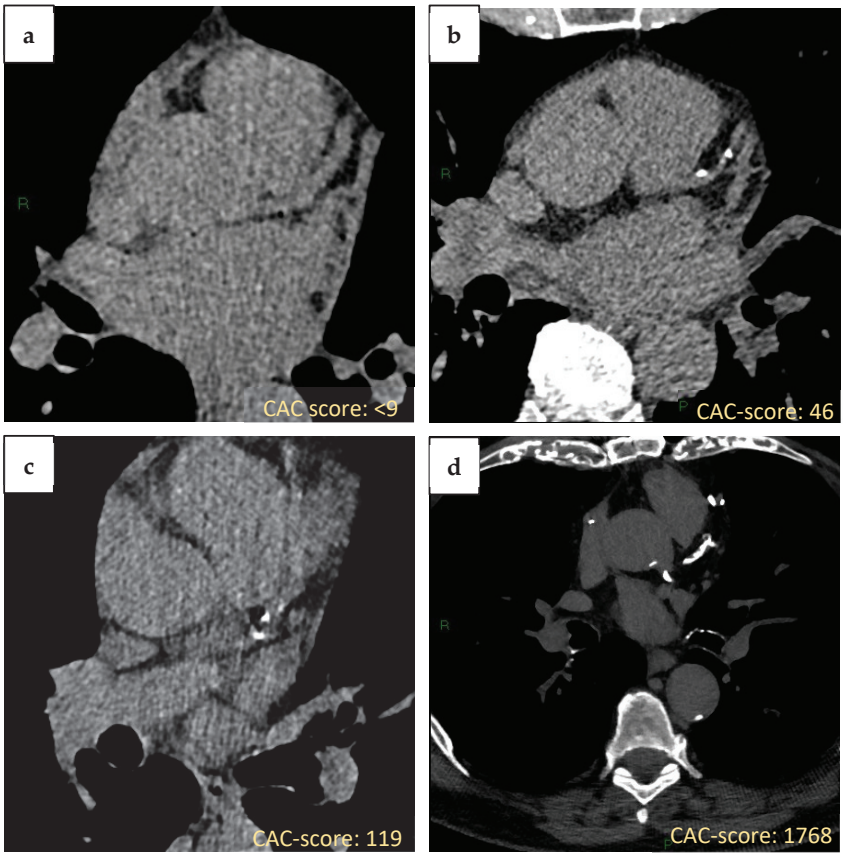

Figure 4. Coronary artery calcium (CAC) score assessment through cardiac computed tomography (CCT) stratified for risk category: (**a**) minimal risk, CAC score <9; (**b**) mild risk, CAC score 46; (**c**) moderate risk, CAC score 119; (**d**) severe risk, CAC score 1768.

2.2. Pathophysiological Mechanisms of Calcium Deposition

When foamy macrophages rich with lipids and vascular smooth muscle cells (VSMCs) start gathering in the coronary arteries, the atherosclerotic process begins. This provokes thickening of the tunica intima which is followed by an increase in free cholesterol, acellular remains and in the final stages of fibroatheroma, an almost total lack of extracellular matrix [48]. The earliest calcified components are made up of membrane-bound matrix vesicles that are actively calcifying, which are produced by apoptotic VSMCs [49]. Then, the coronary arteries calcification becomes an active pathogenic process, with ectopic bone production being the base of the process [50]. Notably, VSMCs usually express proteins that inhibit calcification. However, in the setting of atherosclerosis, the expression of some of these inhibitors (such as matrix Gla protein) is downregulated, contributing to a loss of homeostatic inhibition of calcification. On the other hand, transcription factors such as Msx2, Runx2, Sox9, Cbfa1, and bone morphogenetic proteins (BMPs) significantly increase the expression by VSMCs and macrophages of chondrocyte, osteoblastic, and osteoclastic-associated proteins facilitating the calcification process [51,52].

Only in histologic sections can these microcalcifications be identified, not with conventional imaging methods. When these minute calcium deposits consolidate, bigger calcium granules form that can be seen using common imaging methods such as CCTA. When macrocalcifications further aggregate, they could potentially form a large calcification

fragment that extends from the necrotic core to the collagen-rich matrix resulting in the formation of calcified plaque that may protrude into the lumen or media [48].

Inflammation, promoted by apolipoproteins and oxidized phospholipids in the artery wall, and oxidative stress are also essential in the vascular calcification process [53,54]. Furthermore, it has been estimated that conventional risk factors account for 40% of the variability of coronary calcification [55]. Indeed, CAC is strongly connected with low-density lipoprotein (LDL) cholesterol in young asymptomatic men [56]. Furthermore, glucose has been reported to promote vascular cell calcification, while insulin inhibits the same process [57]. In this regard, an increased coronary calcification has been demonstrated in diabetics, especially those with type II diabetes [58].

2.3. Prognostic Value of CAC and Risk Assessment

2.3.1. Asymptomatic Subjects

The most recent data suggest that, in addition to the established cardiac risk factors, the use of CAC is independently predictive of prognosis. Therefore, the rate of MACEs rises proportionally with increasing severity of coronary calcifications categorized by the Agatston calcium score [59,60]. While individuals with CAC levels $\geq$ 1000 have a mortality rate comparable to high-risk secondary prevention patients, asymptomatic subjects with 0 coronary calcium show a persistently very low risk throughout multiple studies [61,62].

CAC has also been demonstrated to further stratify patients who were assessed as intermediate risk using the Framingham Risk Score alone [63]. CAC score was independently predictive of ischemic outcomes above and beyond historical risk variables in univariable and multivariable models estimating CAD occurrence at 4.3 years of follow-up [64]. Other research has demonstrated that the incremental risk prediction value of CAC extended to both younger and older individuals, diabetic patients, smokers, and the elderly [65].

Furthermore, CAC may determine whether asymptomatic people might benefit from statin or aspirin as primary preventive therapy [66]. According to current recommendations for statin therapy, it is reasonable to assess CAC in patients with an intermediate risk of developing atherosclerotic cardiovascular disease [4]. However, none of the guidelines proposes management based on calcium score because of insufficient support from randomized clinical trials.

2.3.2. Symptomatic Patients

Recent European guidelines for the diagnosis and treatment of CCS state that CCTA is appropriate as a first-line diagnostic test for the evaluation of patients with no history of CAD, atypical or typical angina symptoms, or symptoms that are equivalent to angina, as well as patients who have undergone inconclusive stress testing. Three milestone multicenter studies which compared the accuracy of CCTA with ICA for the identification of obstructive coronary stenosis consistently reported high sensitivity values ranging from 85% to 95%, with a negative predictive value of almost 100% [67,68].

In this setting, CAC may raise estimates of the clinical likelihood of obstructive CAD (such as a coronary stenosis > 50%) together with sex, age, and symptoms. As a result of employing the CAC score in the pre-test estimate of the likelihood of CAD, more than half of symptomatic individuals were reclassified into a reduced risk category for obstructive CAD [69]. However, current evidence does not yet support its use as a diagnostic tool to rule out obstructive CAD because it does not provide precise information on the severity of coronary stenoses [8].

2.3.3. Role of CAC in Specific Subgroups

It is essential to mention the role of CCTA and CAC in some specific subgroups of patients at higher risk of developing ischemic events, such as those with diabetes, older age, and chronic renal insufficiency.

Patients with diabetes more frequently develop calcified and extensive CAD, presenting as silent ischemia, and greater plaque progression in terms of disease load and ad-

verse plaque characteristics than patients without diabetes. Therefore, Perrone-Filardi et al. reported higher mortality in diabetic patients than in nondiabetic patients for any degree of CAC [45]. Accordingly, a recent meta-analysis reported that the rise in CAC score is substantially linked to an elevated risk for all-cause mortality and/or fatal and non-fatal CV events in asymptomatic diabetics [70]. In addition, evaluation of CAC may help identify diabetic subjects who are more likely to have inducible ischemia and may be utilized as a strategy for preselecting people before functional imaging [45].

Few studies have examined the predictive significance of CAC in the elderly (>75 years). A recent study found that women are more at risk than men for cardiovascular and all-cause mortality, with CAC scores and percentiles being highly predictive of these outcomes among older persons. In contrast, relatively low-risk older individuals have low coronary artery calcium scores of 0 to 9 or 25th percentile [71].

Dialysis patients experience a faster progression of CAC, which is correlated with age, the length of dialysis, the etiology of chronic renal failure, changes in mineral metabolism, and the use and dosage of calcium-based phosphate binders. According to reports, the level of CAC in dialysis patients is related to cardiovascular outcomes [72]. However, further information is required to determine the potential practical application of the CAC score for further risk categorization of this subgroup [39].

2.3.4. CAC and Progression of Coronary Atherosclerosis

Calcium deposition within atherosclerotic plaques progresses by an average of 15 to 25% per year. Thus, the progression of CAC scores over time has been reported in several studies and associated with worse prognosis, as well as its regression due to specific anti-atherosclerotic therapies such as statins, has been associated with improved outcomes [44,73,74].

Previous studies have shown that CAC progression has been associated with a higher risk for MI and all-cause mortality [75–77]. Conversely, the Cooper Center Longitudinal Study (CCLS trial) found no additional predictive value of CAC progression compared with the single CAC measurement on cardiovascular outcomes [77]. Likewise, Lehmann et al. observed that CAC progression adds only weakly to risk prediction models for CAD, solely for those patients reporting a significant increase in CAC between baseline and 5-year follow-up (from 1 to 399 to CAC $\geq$ 400), who demonstrated a nearly 2-fold increase in cardiovascular events than subjects in which CAC remained below 400 [78]. Therefore, a second CAC scan may be beneficial in the presence of CAC > 0 to determine if and when CAC values tend to exceed the high-risk threshold of CAC $\geq$ 400 [78].

2.4. Emerging Technologies

Different technologies are emerging to overcome CAC's current limitations and offer better tools and methods for clinical decision-making. CAC scoring non-gated CT scans, dual-energy CT and virtual non-contrast imaging, and artificial intelligence for automatic CAC scoring show great potential [38]. Regarding non-gated-CT scan, the 2016 Society of Cardiovascular Computed Tomography (SCCT) and the Society of Thoracic Radiology (STR) guidelines recommended its use in the evaluation of CAC even in patients without known CAD for better prognostic stratification [79]. Furthermore, CT-derived FFR has been shown, together with other CT-derived hemodynamic parameters (wall shear stress and axial plaque stress) [80], to improve the specificity and accuracy of CCTA in several clinical trials, especially when assessing intermediate stenoses and may improve the selection of patients who are most likely to benefit from coronary angiography and revascularization [81]. On the other hand, computed tomography perfusion (CTP) imaging may be useful when the value of FFR is in the gray area (for example, 0.74–0.85) or when FFR cannot be calculated due to technical reasons. They allow to integrate the morphological data with hemodynamic risk indexes leading to better plaque evaluation. Integrating these analyses also with ECG-derived electromechanical parameters able to predict myocardial ischemia, we could

get complex models based on multimodal data analysis achieving a patient-specific risk assessment [82–84].

The combination with electromechanical models [85] could allow to overcome the limit of the CT-derived FFR overestimation in patients with concomitant coronary microvascular dysfunction, improving diagnostic accuracy [86–88].

Furthermore, integrating anatomical and functional imaging or hybrid imaging such as single positron emission computed tomography (SPECT)/CCTA may improve the selection of candidates for invasive procedures in patients with uncertain results with one of the two techniques [89].

However, further studies are requested to obtain strong evidence about the cost-effectiveness, the prognostic value of these technologies and their role in clinical decision-making [19,90].

3. Epicardial Adipose Tissue

The epicardial adipose tissue (EAT) is a metabolically active organ recently associated with heart failure and atrial fibrillation and classified as an independent risk factor for subclinical coronary artery disease [91,92]. For this reason, in the last years, some evidence suggests as the assessment of EAT using CCTA might represent an additional tool to quantify patients' cardiovascular risk.

3.1. Anatomy and Functions of Epicardial Adipose Tissue

The intrathoracic adipose tissue surrounding the heart can be divided into epicardial adipose tissue (EAT) and pericardial fat (PF). The PF is located between the pericardial visceral and parietal layers; it derives from the primitive thoracic mesenchyme and is supplied by branches of the internal thoracic artery [93]. On the other hand, EAT is placed between the pericardial visceral layer and the myocardial muscle covering about 80% of the cardiac surface; it originates from the splanchnopleuric mesoderm and is vascularized by branches of coronary arteries. Lastly, the portion of the EAT immediately contiguous with the adventitial layer of coronary arteries is called pericoronary adipose tissue (PCAT) [94].

The EAT is microscopically composed of different cells, including adipocytes, resident monocytes, immune cells, and nerve cells [95]. Interestingly, no muscle fascia between EAT and myocardium is present, allowing direct communication between these two organs through paracrine and vasocrine mechanisms [93]. Physiologically, EAT plays a protective role for the heart. It acts as a local energy store and provides free fatty acids to the myocardial tissue in times of high demand [96]. It also releases adipokines with anti-inflammatory, antioxidant, and vasodilator functions (adiponectin and adrenomedullin) [97]. In addition, the EAT offers mechanical support preventing coronary artery torsion during cardiac contraction, exerts a thermoregulatory function [96] and acts as an immune organ [98].

However, in pathological conditions, EAT becomes pro-arrhythmogenic and pro-atherogenic. Indeed, in patients who have CAD, EAT shows pro-inflammatory features with an increased concentration of inflammatory M1 macrophages than anti-inflammatory M2 macrophages [99], higher production of interleukin-6 (IL-6), interleukin-1 (IL-1), and tumor necrosis factor-alpha (TNF-a) associated with reduced production of adiponectin and adrenomedullin, and an elevated concentration of reactive oxygen species (ROS) [100].

The mechanisms of EAT dysfunction might translate into atherosclerotic plaque development are not entirely known. However, it has been proposed that macrophages, together with T- and B-lymphocytes, are triggered by the Toll-like receptor (TLR) binding that stimulates nuclear factor-κB (NF-κB) and JUNN-terminal kinase (JNK) [101,102]. The activation of these two molecules leads to increased interleukin production, such as IL-6, facilitating endothelial cell permeability and monocyte adhesion [103]. The entire process is powered by the increased ROS levels that further favor endothelial dysfunction and interleukin secretion [100].

3.2. Quantification of Epicardial Adipose Tissue Using CCTA

A trustworthy quantification of EAT can be obtained using different non-invasive techniques. EAT thickness could be measured by transthoracic echocardiography on the free wall of the right ventricle [104]. However, CCTA is considered the most validated and reproducible technique for its quantification, given the higher spatial resolution compared to magnetic resonance (MR) and allowing for simultaneous evaluation of CAD [105].

In detail, quantification of EAT by CCTA envisages the measure of density (Hounsfield units), volume (cm^3), and thickness (mm). Epicardial fat density ranges from −190 to −30 Hounsfield units (HU) [106]. Measurements of thickness may be achieved in the horizontal long-axis plane, in the basal short-axis plane, and over the right ventricular free wall [107]. Regarding volume quantification, manual segmentation of EAT is the most widespread method. The operator manually draws EAT contours every 15 mm within a region of interest that usually includes the anterosuperior mediastinum at the pulmonary trunk level, the left main trunk, the left anterior descending and circumflex arteries in proximal segments, the posterior mediastinum, and the inferior diaphragmatic surface. (Figure 5a–c) Different software can be used to optimize and speed up this process [108]. The advantages of CT volumetric quantification are the high definition and reproducibility, whereas the main limitation is the need for a long segmentation time for an accurate measurement [109]. EAT can also be measured during coronary CT in the interval between contrast administration and angiographic acquisition and does not require specific acquisition [108].

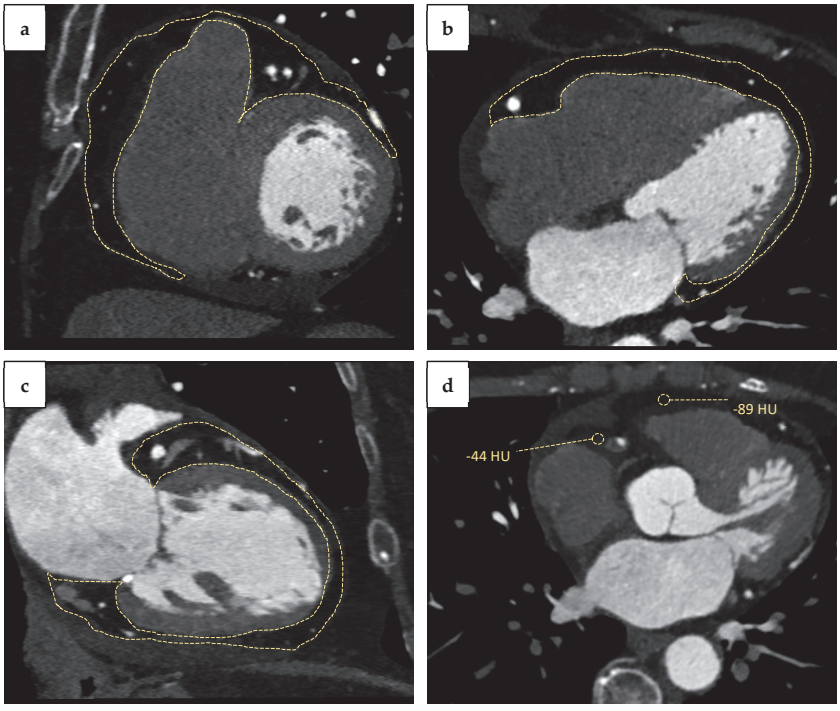

Figure 5. Cardiac computed tomography angiography (CCTA) assessment of epicardial adipose tissue (EAT) and peri-coronary adipose tissue (PCAT): (**a**) EAT in short-axis view; (**b**) EAT in four-chamber view; (**c**) EAT in two-chamber view (dashed line); (**d**) peri-coronary adipose tissue (PCAT) radiodensity (−44 HU) compared with radiodensity of EAT surrounding free left ventricle wall (−89 HU).

3.3. Epicardial Fat Volume and Atherosclerosis Progression

Recent studies have demonstrated that EAT volume is associated with the development and progression of atherosclerotic plaques. Therefore, previous studies reported greater EAT volumes in patients with angiographic evidence of coronary stenoses than those without [110,111]. Similarly, Gitsioudis et al., enrolling patients with intermediate CAD risk undergoing cardiac CT with contextual EAT volume quantification, showed a higher EAT volume in patients with coronary stenosis >50% compared with those with <50%. Moreover, the multivariate regression analysis revealed an independent association between coronary stenosis severity, plaque burden, and EAT volume [112].

Notably, EAT volume is also associated with atherosclerosis progression and, more specifically, with the development of high-risk plaques. In this regard, Alexopoulos et al. demonstrated that EAT was higher in patients with mixed/non-calcified plaques than those with calcified lesions [113]. The same evidence was reported by Tsuyoshi et al., that quantified epicardial fat volume in 1308 patients with symptomatic CAD and a zero-calcium score. EAT was greater in patients with obstructive atherosclerotic plaques than no plaque and even more in those with vulnerable plaque than no plaque [114]. Similarly, a recent meta-analysis by Nerlekar et al. confirmed the association between EAT volume and high-risk plaques [115]. Otsuka et al. found that EAT volume in ACS patients was significantly higher than in those suffering from CCS [116]. Finally, Yamashita et al. demonstrated a significant positive correlation between EAT volume and necrotic plaque detected using intravascular ultrasound imaging (IVUS) and a negative correlation between EAT volume and fibrous plaque [117].

Several studies also reported a direct relationship between EAT and CAC score. Iwasaki et al. demonstrated increased CAC in patients with EAT volume >100 cm^3 than in those with EAT volume <100 cm^3, with a higher incidence of CAD in the same group [118]. These results were confirmed in the study conducted by Cosson et al., where EAT volume was independently associated with CAC $\geq$ 100 AU (per 10 cm^3 increase: OR 1.11 (1.02–1.20)) [119].

Another measurable parameter derived from EAT assessment and associated with a worse prognosis is fat radiodensity. Franssens et al. demonstrated in 140 patients undergoing CT-scan that one standard deviation lower EAT attenuation (5 HU) was associated with 1.9 and 1.07 higher odds (for men and women respectively) of being in higher CAC class (0, 1 to 100, 101 to 400, and >400) [120]. Similarly, Goeller et al. quantified both EAT volume and density in 456 asymptomatic patients; EAT volume resulted lowest in patients without coronary calcium and higher in patients with severe atherosclerosis, while EAT density resulted lower in patients with high coronary calcium and increased occurrence of adverse clinical events [121].

Finally, all this evidence allows identifying EAT volume as a predictor of MACEs. For example, Eisenberg et al. quantify EAT volume in asymptomatic patients from the EISNER (Early Identification of Subclinical Atherosclerosis by Noninvasive Imaging Research) trial, showing its association with increased risk of MACE after 14 $\pm$ 3 years of follow-up. It was also demonstrated that MACE risk progressively increased with EAT volume $\geq$ 113 cm^3 and CAC $\geq$ 100 AU [122]. Thus, Fuller et al. revealed that patients with CAD who died from sudden cardiac death had significantly higher EAT thickness [123]. Moreover, in the Heinz Nixdorf Recall Study, the incidence of coronary events increased directly with EAT quartiles, with a doubling of EAT volume associated with a 1.5-fold risk of coronary events independently from other traditional CV risk factors [124].

3.4. Pericoronary Fat: Marker of Coronary Artery Stenosis Severity

Another CT-measurable parameter associated with CAD severity is the pericoronary fat (Figure 5d). In this regard, a study conducted by Gorter et al. evaluated in 128 symptomatic patients undergoing percutaneous coronary intervention (PCI) the EAT volume and the pericoronary fat. Patients with low BMI and multivessel coronary disease had increased values of both CT parameters compared to patients without CAD [125]. Likewise, Balcer

et al. analyzed PCAT volume in 46 patients with acute MI undergoing coronary-CT angiography, demonstrating higher values around culprit lesions than non-culprit ones [126]. Furthermore, Ma et al. reported a raised pericoronary adipose tissue mean attenuation (PCATMA) in arteries with CT-measured plaques, particularly in non-calcified/mixed plaques [127]. Interestingly, PCATMA was also associated with in-stent restenosis. Thus, Nogic et al. enrolled 151 patients undergoing CT-scan for suspected CAD, treated with stent implantation within three months and that repeated coronary angiography after a maximum of five years for any reason. The study demonstrated that patients with ISR had a significantly increased lesion-specific PCATMA at baseline compared with patients without stent hyperplasia [128].

3.5. Effective Therapies in the Reduction of Epicardial Fat

Recent studies have shown several drugs' efficacy in reducing EAT thickness and volume. Thanks to their pleiotropic effects, statins have been reported to reduce epicardial fat metabolic activity, thickness, and attenuation [129]. In this setting, atorvastatin provided better results than pravastatin [130]. Furthermore, metformin also reduced EAT thickness after three months of treatment in diabetic patients [131]; similar results were reported for liraglutide, semaglutide, and dulaglutide [132,133]. Correspondingly, sodium-glucose cotransporter 2 (SGLT-2) inhibitors (dapagliflozin and empagliflozin) demonstrated a reduced EAT volume in CAD patients after six months of treatment [134]. Notwithstanding, further studies are needed to evaluate how the well-known cardiovascular benefit of all these drugs might be related to the attenuation of EAT thickness and volume.

4. Additional CT-Measurable Parameters for Cardiovascular Risk Stratification

4.1. Aortic Calcium

The assessment of extra coronary calcifications, such as aortic valve calcification, mitral annular calcification, and thoracic aortic calcium (TAC), can improve cardiovascular risk stratification beyond the CAC score. Notably, non-contrast cardiac CT estimates coronary and extra coronary calcifications with the same scans without additional scanning or radiation.

Different methods for evaluating TAC have been reported. The simplest one is just identifying the presence or absence of aortic calcium, recording TAC in a binary fashion. Alternatively, TAC can be expressed with the Agatston method, similar to CAC [135]. Several studies demonstrated a correlation between TAC and cardiovascular events. In the Multi-Ethnic Study of Atherosclerosis (MESA), Budoff et al. demonstrated that TAC predicted future cardiovascular events over risk factors and CAC, but only in women [136]. Another study by Santos et al. showed that the presence of TAC was associated with all-cause mortality. This relationship was independent of conventional cardiovascular risk factors and the presence of CAC. Accordingly, Allison et al. showed that multisite calcifications, including thoracic aortic calcifications, predict total mortality [137].

Furthermore, previous studies have reported a close relationship between TAC and CAC. Rivera et al. analyzed a cohort from the MESA and demonstrated that TAC is significantly associated with CAC incidence and progression [138]. Previously, Kuller and colleagues showed that the presence of TAC and carotid plaques in postmenopausal women is significantly related to CAC [139].

4.2. Liver Fat

Cardiac CT scans used for CAC scoring can also identify both epicardial and liver fat (LF) without any modifications to the scan protocol; this latter is identified as a decreased liver attenuation [140]. The attenuation measurement obtained with CT is more reliable than that obtained with echocardiography or cardiac magnetic resonance (CMR), especially in a homogeneous and non-hypervascular parenchymal organ [141]. Cardiac CT generally does not include the whole liver in the scans. However, it has been demonstrated that

the attenuation measurement of two or three sites of the liver reflects that of the whole liver [142].

LF is considered a marker of cardio-metabolic health because it is closely associated with non-alcoholic fatty liver disease (NAFLD), which is correlated to metabolic syndrome and CV disease [143,144]. Indeed, it has been shown that patients with NAFLD have an increased risk of developing atherosclerotic disease [144]. In this regard, NAFLD has been independently associated with increased carotid intima-media thickness (CIMT) and CAC, both measures of atherosclerosis severity [145]. In addition, the ROMICAT II trial demonstrated that high-risk plaque features evaluated by CCTA (positive remodeling, napkin-ring sign, spotty calcification, low attenuation) were more frequent in patients with NAFLD compared with patients without NAFLD [146]. Furthermore, Wolff et al. investigated the relationship between LF, traditional cardiovascular risk factors and subclinical coronary artery disease [147]. The authors found that LF was associated with all traditional cardiovascular risk factors, specifically to waist circumference, diastolic blood pressure, HDL cholesterol and diabetes mellitus. Additionally, a greater volume of LF was associated with a higher burden of subclinical CAD, regardless of the presence of other cardiovascular risk factors [147].

Several mechanisms have been proposed to motivate the relationship between LF and CAD. Firstly, the fatty liver excretes high levels of substances that damage the cardiovascular system, such as coagulation factors, very low-density lipoproteins, and C-reactive protein. Additionally, LF is closely linked to insulin resistance and pro-inflammatory status [148,149]. All this evidence suggests that LF, measured with CT, can be valid for a comprehensive cardiovascular risk assessment together with other CT parameters.

4.3. Myocardial Scar

An emerging application of non-contrast cardiac CT in detecting myocardial scars due to an occult MI has recently been demonstrated. The 10-year mortality related to unrecognized MI is estimated to be 45–50% [150]. Therefore, recognizing occult MI is crucial to identify that subgroup of patients who could benefit from intensive medical treatments, coronary revascularization procedures, or implantable cardioverter defibrillator implantation. The evidence of an occult MI also has prognostic value since it is considered a predictor of MACE recurrence and cardiac death.

The areas of old MI appear hypo-attenuated due to fatty replacement on non-contrast cardiac CT or pre-contrast cardiac CT [151]. Specifically, myocardial fat associated with an old MI appears on CT as an area of subendocardial hypoattenuation following the culprit coronary artery [152,153]. In this regard, Ichikawa et al. showed that left ventricle myocardial fat can be observed at least after three years from the MI with a subendocardial location [154]. Furthermore, in patients with old MI the different CT attenuation between normal and necrotic myocardium is more significant compared to patients with acute MI, suggesting that cardiac CT may help differentiate between recent and old MI [155]. Another interesting study evaluated the ability of non-contrast cardiac CT to identify chronic MI in patients with evidence of no-reversible perfusion alterations on nuclear myocardial imaging [156]. Sixty-two patients with non-reversible perfusion defects underwent CAC scanning and MI was identified as a hypo-attenuation area on CT. The study showed that non-contrast cardiac CT was able to identify prior MI in 57 patients, with a sensitivity of 92% [156].

Furthermore, the delayed enhancement cardiac CT, which shares a similar pathophysiological basis with delayed enhancement cardiac magnetic resonance, provides more specific information in this context. A delayed phase CT scan is generally performed 5–15 min after CCTA with the administration of an additional contrast medium. Iodinated contrast is an extracellular contrast agent with late washout from areas of abnormal myocardium, such as fibrosis or scar [157]. Therefore, cardiac CT with delayed enhancement can be used to identify myocardial scar or fibrosis in both ischemic and non-ischemic cardiopathy, similar to CMR with late gadolinium enhancement, which is actually the

gold standard for tissue characterization. Compared with CMR, cardiac CT has some advantages, such as higher availability and shorter examination time. It can also be helpful in patients with CMR contraindications (i.e., claustrophobia and metallic implants).

Several studies demonstrated that contrast-enhanced cardiac CT allows the identification and quantification of MI, showing a good agreement with CMR [158–160]. Specifically, two different contrast-enhancement patterns can be observed in case of MI: early hypo-enhancement, which is correlated to the microvascular obstruction in acute MI, and delayed hyper-enhancement, which is typical of chronic MI. Therefore, the ability of cardiac CT to characterize ischemic myocardium can be helpful in the clinical reality to stratify cardiovascular risk and also to manage clinical decisions. In addition, delayed enhancement cardiac CT may facilitate, in patients with acute chest pain and elevated cardiac biomarkers, the differentiation of myocarditis and ACS through the detection of the characteristic mid-wall or subepicardial delayed enhancement and the absence of significant coronary stenosis in patients with myocarditis. Indeed, Palmisano et al. demonstrated in patients with acute chest pain and elevated cardiac troponin with negative triple rule out (TRO) CT scan that late contrast enhancement CT can increase the diagnostic rate identifying myocarditis, myocardial infarction with non-obstructed coronary artery (MINOCA) and Takotsubo cardiomyopathy [161].

For instance, Bouleti et al. demonstrated that delayed phase cardiac CT could be a valid alternative to delayed enhancement CMR in detecting inflammatory segments in patients with acute myocarditis, with a diagnostic accuracy of 95% [162]. Furthermore, Esposito et al. showed that cardiac CT with delayed enhancement also provides a three-dimensional characterization of myocardial scars associated with ventricular tachycardias. This information may help to plan electrophysiological procedures such as electro-anatomic mapping and arrhythmias radiofrequency catheter ablation [163].

Lastly, delayed enhancement cardiac CT can be used to measure an index of diffuse myocardial fibrosis, which is named myocardial extracellular volume fraction (ECV) [164]. ECV can be estimated using the following method obtained from cardiac CT: ECV = (1–hematocrit) $\times$ (ΔHULV myocardium/ΔHULV blood), where ΔHU is the change in HU attenuation pre-contrast and in the delayed phase CT (HU delayed phase – HU pre-contrast) [157]. The measurement of ECV with cardiac CT can be helpful in the setting of non-ischemic cardiomyopathies, such as hypertrophic cardiomyopathy, cardiac amyloidosis, dilated cardiomyopathy, and sarcoidosis. Hence, several studies demonstrated that mean ECV values obtained with delayed phase cardiac CT are significantly higher in patients with hypertrophic cardiomyopathy, cardiac amyloidosis and dilated cardiomyopathy compared to healthy subjects [165,166]. In these patients, delayed enhancement cardiac CT also assesses the identification of myocardial fibrosis areas with various delayed enhancement patterns (transmural, subepicardial, subendocardial, or mid myocardial).

5. Limits of CCTA

There are several limits of the CCTA. Respiratory motion artifacts are a frequent issue in image acquisition that can reduce image quality. The presence of arrhythmias or other technological factors might also cause problems with electrocardiographic gating during picture acquisition. In some cases, there may be technical problems such as partial exclusion of the coronary arteries from the field of vision [41,90]. Besides that, coronary artery motion artifacts, non-coronary calcium (for instance calcified thoracic lymph nodes, pleural or pericardial calcifications, mitral annular calcification), and artifacts from adjacent metallic prostheses are potential issues that can cause CAC calculation and other CT parameters assessment to be inaccurate [38]. Moreover, radiation exposure is also a limiting factor. However, radiation doses may be further reduced using low tube potential (<100 kVp) and high-pitch helical acquisition, when appropriate, and consequent heart rate lowering [167].

6. Conclusions

CCTA is a first-line investigation tool approved by the current AHA and ESC guidelines for detecting coronary stenosis in chronic and acute coronary syndromes [6,8]. Moreover, through CAC scoring assessment, it is also recommended in asymptomatic patients for cardiovascular risk stratification [4]. Recently, CCTA's role as a predictor of plaque burden has been emerging, and other measurable parameters are being evaluated. Beyond CAC, EAT volume is the more promising, associated with atherosclerosis progression, development of high-risk plaques, and increased MACEs [110–123]. The others are aortic calcium [137] (able to improve CV risk stratification exceeding CAC score), liver fat [144] (a marker of cardio-metabolic health and atherosclerosis development) and myocardial scar [155] (an indicator of worst prognosis in patients with myocardial infarction). In the future, these novel CCTA applications allow a better prognostic stratification and early detection of patients at risk of developing severe atherosclerosis and adverse clinical events. Notwithstanding the need for further studies, their use in clinical practice might also guide optimal primary and secondary prevention strategies.

Author Contributions: Conceptualization, A.N. and F.B.; validation, F.G. and G.P.U.; writing, A.N., F.B., F.C., M.G. and M.C.; review and editing, A.N., N.C., R.R. and D.D.S.; visualization, F.P., F.M., P.G. and V.C.; supervision, F.G., G.P.U. and C.C.Q. All authors have read and agreed to the published version of the manuscript.

Funding: This research received no external funding.

Conflicts of Interest: The authors declare no conflict of interest.

References

1. Ralapanawa, U.; Sivakanesan, R. Epidemiology and the Magnitude of Coronary Artery Disease and Acute Coronary Syndrome: A Narrative Review. *J. Epidemiol. Glob. Health* **2021**, *11*, 169–177. [CrossRef] [PubMed]
2. Mach, F.; Baigent, C.; Catapano, A.L.; Koskinas, K.C.; Casula, M.; Badimon, L.; Chapman, M.J.; De Backer, G.G.; Delgado, V.; Ference, B.A.; et al. 2019 ESC/EAS Guidelines for the Management of Dyslipidaemias: Lipid Modification to Reduce Cardiovascular Risk. *Eur. Heart J.* **2020**, *41*, 111–188. [CrossRef] [PubMed]
3. Liew, S.M.; Lee, W.K.; Khoo, E.M.; Ismail, I.Z.; Ambigapathy, S.; Omar, M.; Suleiman, S.Z.; Saaban, J.; Mohd Zaidi, N.F.; Yusoff, H. Can Doctors and Patients Correctly Estimate Cardiovascular Risk? A Cross-Sectional Study in Primary Care. *BMJ Open* **2018**, *8*, e017711. [CrossRef]
4. Visseren, F.L.J.; Mach, F.; Smulders, Y.M.; Carballo, D.; Koskinas, K.C.; Bäck, M.; Benetos, A.; Biffi, A.; Boavida, J.-M.; Capodanno, D.; et al. 2021 ESC Guidelines on Cardiovascular Disease Prevention in Clinical Practice. *Eur. Heart J.* **2021**, *42*, 3227–3337. [CrossRef] [PubMed]
5. Volume-, J.E. New Insights in Cardiovascular Risk Estimation and Stratification. *e-J. Cardiol. Pract.* **2022**, *22*, 1–9.
6. Fihn, S.D.; Gardin, J.M.; Abrams, J.; Berra, K.; Blankenship, J.C.; Dallas, A.P.; Douglas, P.S.; Foody, J.M.; Gerber, T.C.; Hinderliter, A.L.; et al. 2012 ACCF/AHA/ACP/AATS/PCNA/SCAI/STS Guideline for the Diagnosis and Management of Patients with Stable Ischemic Heart Disease. *Circulation* **2012**, *126*, e354–e471. [CrossRef]
7. National Institute for Health and Care Excellence (NICE). *Putting NICE Guidance into Practice Resource Impact Report: Hypercholesterolaemia and Mixed*; National Institute for Health and Care Excellence (NICE): London, UK, 2016.
8. Knuuti, J.; Wijns, W.; Saraste, A.; Capodanno, D.; Barbato, E.; Funck-Brentano, C.; Prescott, E.; Storey, R.F.; Deaton, C.; Cuisset, T.; et al. 2019 ESC Guidelines for the Diagnosis and Management of Chronic Coronary Syndromes. *Eur. Heart J.* **2020**, *41*, 407–477. [CrossRef]
9. Douglas, P.S.; Hoffmann, U.; Patel, M.R.; Mark, D.B.; Al-Khalidi, H.R.; Cavanaugh, B.; Cole, J.; Dolor, R.J.; Fordyce, C.B.; Huang, M.; et al. Outcomes of Anatomical versus Functional Testing for Coronary Artery Disease. *N. Engl. J. Med.* **2015**, *372*, 1291–1300. [CrossRef]
10. The SCOT-HEART Investigators. Coronary CT Angiography and 5-Year Risk of Myocardial Infarction. *N. Engl. J. Med.* **2018**, *379*, 924–933. [CrossRef]
11. Amsterdam, E.A.; Wenger, N.K.; Brindis, R.G.; Casey, D.E.; Ganiats, T.G.; Holmes, D.R.; Jaffe, A.S.; Jneid, H.; Kelly, R.F.; Kontos, M.C.; et al. 2014 AHA/ACC Guideline for the Management of Patients with Non–ST-Elevation Acute Coronary Syndromes. *J. Am. Coll. Cardiol.* **2014**, *64*, e139–e228. [CrossRef]

12. Collet, J.-P.; Thiele, H.; Barbato, E.; Barthélémy, O.; Bauersachs, J.; Bhatt, D.L.; Dendale, P.; Dorobantu, M.; Edvardsen, T.; Folliguet, T.; et al. 2020 ESC Guidelines for the Management of Acute Coronary Syndromes in Patients Presenting without Persistent ST-Segment Elevation. *Eur. Heart J.* **2021**, *42*, 1289–1367. [CrossRef] [PubMed]
13. Hadamitzky, M.; Distler, R.; Meyer, T.; Hein, F.; Kastrati, A.; Martinoff, S.; Schömig, A.; Hausleiter, J. Prognostic Value of Coronary Computed Tomographic Angiography in Comparison with Calcium Scoring and Clinical Risk Scores. *Circ. Cardiovasc. Imaging* **2011**, *4*, 16–23. [CrossRef] [PubMed]
14. Andreini, D.; Pontone, G.; Mushtaq, S.; Bartorelli, A.L.; Bertella, E.; Antonioli, L.; Formenti, A.; Cortinovis, S.; Veglia, F.; Annoni, A.; et al. A Long-Term Prognostic Value of Coronary CT Angiography in Suspected Coronary Artery Disease. *JACC Cardiovasc. Imaging* **2012**, *5*, 690–701. [CrossRef] [PubMed]
15. Finck, T.; Hardenberg, J.; Will, A.; Hendrich, E.; Haller, B.; Martinoff, S.; Hausleiter, J.; Hadamitzky, M. 10-Year Follow-Up after Coronary Computed Tomography Angiography in Patients with Suspected Coronary Artery Disease. *JACC Cardiovasc. Imaging* **2019**, *12*, 1330–1338. [CrossRef] [PubMed]
16. Al-Mallah, M.H.; Qureshi, W.; Lin, F.Y.; Achenbach, S.; Berman, D.S.; Budoff, M.J.; Callister, T.Q.; Chang, H.-J.; Cademartiri, F.; Chinnaiyan, K.; et al. Does Coronary CT Angiography Improve Risk Stratification over Coronary Calcium Scoring in Symptomatic Patients with Suspected Coronary Artery Disease? Results from the Prospective Multicenter International CONFIRM Registry. *Eur. Heart J.—Cardiovasc. Imaging* **2014**, *15*, 267–274. [CrossRef]
17. Bittencourt, M.S.; Hulten, E.; Ghoshhajra, B.; O'Leary, D.; Christman, M.P.; Montana, P.; Truong, Q.A.; Steigner, M.; Murthy, V.L.; Rybicki, F.J.; et al. Prognostic Value of Nonobstructive and Obstructive Coronary Artery Disease Detected by Coronary Computed Tomography Angiography to Identify Cardiovascular Events. *Circ. Cardiovasc. Imaging* **2014**, *7*, 282–291. [CrossRef]
18. Hadamitzky, M.; Taubert, S.; Deseive, S.; Byrne, R.A.; Martinoff, S.; Schomig, A.; Hausleiter, J. Prognostic Value of Coronary Computed Tomography Angiography during 5 Years of Follow-up in Patients with Suspected Coronary Artery Disease. *Eur. Heart J.* **2013**, *34*, 3277–3285. [CrossRef]
19. Pontone, G.; Rossi, A.; Guglielmo, M.; Dweck, M.R.; Gaemperli, O.; Nieman, K.; Pugliese, F.; Maurovich-Horvat, P.; Gimelli, A.; Cosyns, B.; et al. Clinical Applications of Cardiac Computed Tomography: A Consensus Paper of the European Association of Cardiovascular Imaging—Part I. *Eur. Heart J.—Cardiovasc. Imaging* **2022**, *23*, 299–314. [CrossRef]
20. Weir-McCall, J.R.; Villines, T.C.; Shaw, L.J.; Abbara, S.; Ferencik, M.; Nieman, K.; Achenbach, S.; Nicol, E. Highlights of the Twelfth Annual Scientific Meeting of the Society of Cardiovascular Computed Tomography. *J. Cardiovasc. Comput. Tomogr.* **2018**, *12*, 3–7. [CrossRef]
21. Min, J.K.; Shaw, L.J.; Devereux, R.B.; Okin, P.M.; Weinsaft, J.W.; Russo, D.J.; Lippolis, N.J.; Berman, D.S.; Callister, T.Q. Prognostic Value of Multidetector Coronary Computed Tomographic Angiography for Prediction of All-Cause Mortality. *J. Am. Coll. Cardiol.* **2007**, *50*, 1161–1170. [CrossRef]
22. Lee, S.-E.; Chang, H.-J.; Sung, J.M.; Park, H.-B.; Heo, R.; Rizvi, A.; Lin, F.Y.; Kumar, A.; Hadamitzky, M.; Kim, Y.J.; et al. Effects of Statins on Coronary Atherosclerotic Plaques. *JACC Cardiovasc. Imaging* **2018**, *11*, 1475–1484. [CrossRef] [PubMed]
23. Chang, H.-J.; Lin, F.Y.; Lee, S.-E.; Andreini, D.; Bax, J.; Cademartiri, F.; Chinnaiyan, K.; Chow, B.J.W.; Conte, E.; Cury, R.C.; et al. Coronary Atherosclerotic Precursors of Acute Coronary Syndromes. *J. Am. Coll. Cardiol.* **2018**, *71*, 2511–2522. [CrossRef] [PubMed]
24. Maurovich-Horvat, P.; Hoffmann, U.; Vorpahl, M.; Nakano, M.; Virmani, R.; Alkadhi, H. The Napkin-Ring Sign: CT Signature of High-Risk Coronary Plaques? *JACC Cardiovasc. Imaging* **2010**, *3*, 440–444. [CrossRef] [PubMed]
25. Maurovich-Horvat, P.; Schlett, C.L.; Alkadhi, H.; Nakano, M.; Otsuka, F.; Stolzmann, P.; Scheffel, H.; Ferencik, M.; Kriegel, M.F.; Seifarth, H.; et al. The Napkin-Ring Sign Indicates Advanced Atherosclerotic Lesions in Coronary CT Angiography. *JACC Cardiovasc. Imaging* **2012**, *5*, 1243–1252. [CrossRef] [PubMed]
26. Nakazato, R.; Otake, H.; Konishi, A.; Iwasaki, M.; Koo, B.-K.; Fukuya, H.; Shinke, T.; Hirata, K.-i.; Leipsic, J.; Berman, D.S.; et al. Atherosclerotic Plaque Characterization by CT Angiography for Identification of High-Risk Coronary Artery Lesions: A Comparison to Optical Coherence Tomography. *Eur. Heart J.—Cardiovasc. Imaging* **2015**, *16*, 373–379. [CrossRef] [PubMed]
27. Hoffmann, U.; Moselewski, F.; Nieman, K.; Jang, I.-K.; Ferencik, M.; Rahman, A.M.; Cury, R.C.; Abbara, S.; Joneidi-Jafari, H.; Achenbach, S.; et al. Noninvasive Assessment of Plaque Morphology and Composition in Culprit and Stable Lesions in Acute Coronary Syndrome and Stable Lesions in Stable Angina by Multidetector Computed Tomography. *J. Am. Coll. Cardiol.* **2006**, *47*, 1655–1662. [CrossRef]
28. Ahmadi, A.; Leipsic, J.; Øvrehus, K.A.; Gaur, S.; Bagiella, E.; Ko, B.; Dey, D.; LaRocca, G.; Jensen, J.M.; Bøtker, H.E.; et al. Lesion-Specific and Vessel-Related Determinants of Fractional Flow Reserve beyond Coronary Artery Stenosis. *JACC Cardiovasc. Imaging* **2018**, *11*, 521–530. [CrossRef]
29. Motoyama, S.; Ito, H.; Sarai, M.; Kondo, T.; Kawai, H.; Nagahara, Y.; Harigaya, H.; Kan, S.; Anno, H.; Takahashi, H.; et al. Plaque Characterization by Coronary Computed Tomography Angiography and the Likelihood of Acute Coronary Events in Mid-Term Follow-Up. *J. Am. Coll. Cardiol.* **2015**, *66*, 337–346. [CrossRef]
30. Williams, M.C.; Moss, A.J.; Dweck, M.; Adamson, P.D.; Alam, S.; Hunter, A.; Shah, A.S.V.; Pawade, T.; Weir-McCall, J.R.; Roditi, G.; et al. Coronary Artery Plaque Characteristics Associated with Adverse Outcomes in the SCOT-HEART Study. *J. Am. Coll. Cardiol.* **2019**, *73*, 291–301. [CrossRef]

31. Cury, R.C.; Abbara, S.; Achenbach, S.; Agatston, A.; Berman, D.S.; Budoff, M.J.; Dill, K.E.; Jacobs, J.E.; Maroules, C.D.; Rubin, G.D.; et al. CAD-RADSTM Coronary Artery Disease—Reporting and Data System. An Expert Consensus Document of the Society of Cardiovascular Computed Tomography (SCCT), the American College of Radiology (ACR) and the North American Society for Cardiovascular Imaging (NASCI). *J. Cardiovasc. Comput. Tomogr.* **2016**, *10*, 269–281. [CrossRef]
32. Kalisz, K.; Buethe, J.; Saboo, S.S.; Abbara, S.; Halliburton, S.; Rajiah, P. Artifacts at Cardiac CT: Physics and Solutions. *RadioGraphics* **2016**, *36*, 2064–2083. [CrossRef] [PubMed]
33. Liu, H.; Wingert, A.; Wang, J.; Zhang, J.; Wang, X.; Sun, J.; Chen, F.; Khalid, S.G.; Jiang, J.; Zheng, D. Extraction of Coronary Atherosclerotic Plaques from Computed Tomography Imaging: A Review of Recent Methods. *Front. Cardiovasc. Med.* **2021**, *8*, 597568. [CrossRef] [PubMed]
34. Liu, H.; Wingert, A.; Wang, X.; Zhang, J.; Sun, J.; Chen, F.; Khalid, S.G.; Gong, Y.; Xia, L.; Jiang, J.; et al. Consistency in Geometry among Coronary Atherosclerotic Plaques Extracted from Computed Tomography Angiography. *Front. Physiol.* **2021**, *12*, 715265. [CrossRef] [PubMed]
35. Dai, T.; Wang, J.; Hu, P. Diagnostic Performance of Computed Tomography Angiography in the Detection of Coronary Artery In-Stent Restenosis: Evidence from an Updated Meta-Analysis. *Eur. Radiol.* **2018**, *28*, 1373–1382. [CrossRef] [PubMed]
36. Chan, M.; Ridley, L.; Dunn, D.J.; Tian, D.H.; Liou, K.; Ozdirik, J.; Cheruvu, C.; Cao, C. A Systematic Review and Meta-Analysis of Multidetector Computed Tomography in the Assessment of Coronary Artery Bypass Grafts. *Int. J. Cardiol.* **2016**, *221*, 898–905. [CrossRef]
37. De Graaf, F.R.; van Velzen, J.E.; Witkowska, A.J.; Schuijf, J.D.; van der Bijl, N.; Kroft, L.J.; de Roos, A.; Reiber, J.H.C.; Bax, J.J.; de Grooth, G.J.; et al. Diagnostic Performance of 320-Slice Multidetector Computed Tomography Coronary Angiography in Patients after Coronary Artery Bypass Grafting. *Eur. Radiol.* **2011**, *21*, 2285–2296. [CrossRef]
38. Gupta, A.; Bera, K.; Kikano, E.; Pierce, J.D.; Gan, J.; Rajdev, M.; Ciancibello, L.M.; Gupta, A.; Rajagopalan, S.; Gilkeson, R.C. Coronary Artery Calcium Scoring: Current Status and Future Directions. *RadioGraphics* **2022**, *42*, 947–967. [CrossRef]
39. Greenland, P.; Bonow, R.O.; Brundage, B.H.; Budoff, M.J.; Eisenberg, M.J.; Grundy, S.M.; Lauer, M.S.; Post, W.S.; Raggi, P.; Redberg, R.F.; et al. ACCF/AHA 2007 Clinical Expert Consensus Document on Coronary Artery Calcium Scoring by Computed Tomography in Global Cardiovascular Risk Assessment and in Evaluation of Patients with Chest Pain. *Circulation* **2007**, *115*, 402–426. [CrossRef]
40. Shah, N.R.; Coulter, S.A. An Evidence-Based Guide for Coronary Calcium Scoring in Asymptomatic Patients without Coronary Heart Disease. *Tex. Heart Inst. J.* **2012**, *39*, 240–242.
41. McCollough, C.H.; Ulzheimer, S.; Halliburton, S.S.; Shanneik, K.; White, R.D.; Kalender, W.A. Coronary Artery Calcium: A Multi-Institutional, Multimanufacturer International Standard for Quantification at Cardiac CT. *Radiology* **2007**, *243*, 527–538. [CrossRef]
42. Sandfort, V.; Bluemke, D.A. CT Calcium Scoring. History, Current Status and Outlook. *Diagn. Interv. Imaging* **2017**, *98*, 3–10. [CrossRef] [PubMed]
43. Agatston, A.S.; Janowitz, W.R.; Hildner, F.J.; Zusmer, N.R.; Viamonte, M.; Detrano, R. Quantification of Coronary Artery Calcium Using Ultrafast Computed Tomography. *J. Am. Coll. Cardiol.* **1990**, *15*, 827–832. [CrossRef] [PubMed]
44. Budoff, M.J.; Nasir, K.; McClelland, R.L.; Detrano, R.; Wong, N.; Blumenthal, R.S.; Kondos, G.; Kronmal, R.A. Coronary Calcium Predicts Events Better with Absolute Calcium Scores Than Age-Sex-Race/Ethnicity Percentiles. *J. Am. Coll. Cardiol.* **2009**, *53*, 345–352. [CrossRef] [PubMed]
45. Perrone-Filardi, P.; Achenbach, S.; Mohlenkamp, S.; Reiner, Z.; Sambuceti, G.; Schuijf, J.D.; Van der Wall, E.; Kaufmann, P.A.; Knuuti, J.; Schroeder, S.; et al. Cardiac Computed Tomography and Myocardial Perfusion Scintigraphy for Risk Stratification in Asymptomatic Individuals without Known Cardiovascular Disease: A Position Statement of the Working Group on Nuclear Cardiology and Cardiac CT of the European Soci. *Eur. Heart J.* **2011**, *32*, 1986–1993. [CrossRef] [PubMed]
46. Callister, T.Q.; Cooil, B.; Raya, S.P.; Lippolis, N.J.; Russo, D.J.; Raggi, P. Coronary Artery Disease: Improved Reproducibility of Calcium Scoring with an Electron-Beam CT Volumetric Method. *Radiology* **1998**, *208*, 807–814. [CrossRef]
47. Brown, E.R.; Kronmal, R.A.; Bluemke, D.A.; Guerci, A.D.; Carr, J.J.; Goldin, J.; Detrano, R. Coronary Calcium Coverage Score: Determination, Correlates, and Predictive Accuracy in the Multi-Ethnic Study of Atherosclerosis. *Radiology* **2008**, *247*, 669–675. [CrossRef]
48. Shekar, C.; Budoff, M. Calcification of the Heart: Mechanisms and Therapeutic Avenues. *Expert Rev. Cardiovasc. Ther.* **2018**, *16*, 527–536. [CrossRef]
49. Proudfoot, D.; Shanahan, C.M. Biology of Calcification in Vascular Cells: Intima versus Media. *Herz* **2001**, *26*, 245–251. [CrossRef]
50. Tintut, Y.; Alfonso, Z.; Saini, T.; Radcliff, K.; Watson, K.; Boström, K.; Demer, L.L. Multilineage Potential of Cells from the Artery Wall. *Circulation* **2003**, *108*, 2505–2510. [CrossRef]
51. Tyson, K.L.; Reynolds, J.L.; McNair, R.; Zhang, Q.; Weissberg, P.L.; Shanahan, C.M. Osteo/Chondrocytic Transcription Factors and Their Target Genes Exhibit Distinct Patterns of Expression in Human Arterial Calcification. *Arterioscler. Thromb. Vasc. Biol.* **2003**, *23*, 489–494. [CrossRef]
52. Nusca, A.; Viscusi, M.M.; Piccirillo, F.; De Filippis, A.; Nenna, A.; Spadaccio, C.; Nappi, F.; Chello, C.; Mangiacapra, F.; Grigioni, F.; et al. In Stent Neo-Atherosclerosis: Pathophysiology, Clinical Implications, Prevention, and Therapeutic Approaches. *Life* **2022**, *12*, 393. [CrossRef] [PubMed]

53. Bear, M.; Butcher, M.; Shaughnessy, S.G. Oxidized Low-Density Lipoprotein Acts Synergistically with β-Glycerophosphate to Induce Osteoblast Differentiation in Primary Cultures of Vascular Smooth Muscle Cells. *J. Cell. Biochem.* **2008**, *105*, 185–193. [CrossRef] [PubMed]
54. Piccirillo, F.; Carpenito, M.; Verolino, G.; Chello, C.; Nusca, A.; Lusini, M.; Spadaccio, C.; Nappi, F.; Di Sciascio, G.; Nenna, A. Changes of the Coronary Arteries and Cardiac Microvasculature with Aging: Implications for Translational Research and Clinical Practice. *Mech. Ageing Dev.* **2019**, *184*, 111161. [CrossRef] [PubMed]
55. Maher, J.E.; Raz, J.A.; Bielak, L.F.; Sheecly, P.F.; Schwartz, R.S.; Peyser, P.A. Potential of Quantity of Coronary Artery Calcification to Identify New Risk Factors for Asymptomatic Atherosclerosis. *Am. J. Epidemiol.* **1996**, *144*, 943–953. [CrossRef] [PubMed]
56. Taylor, A.J.; Feuerstein, I.; Wong, H.; Barko, W.; Brazaitis, M.; O'Malley, P.G. Do Conventional Risk Factors Predict Subclinical Coronary Artery Disease? Results from the Prospective Army Coronary Calcium Project. *Am. Heart J.* **2001**, *141*, 463–468. [CrossRef] [PubMed]
57. Chen, N.X.; Duan, D.; O'Neill, K.D.; Moe, S.M. High Glucose Increases the Expression of Cbfa1 and BMP-2 and Enhances the Calcification of Vascular Smooth Muscle Cells. *Nephrol. Dial. Transplant.* **2006**, *21*, 3435–3442. [CrossRef]
58. Burke, A.P.; Farb, A.; Malcom, G.T.; Liang, Y.; Smialek, J.; Virmani, R. Effect of Risk Factors on the Mechanism of Acute Thrombosis and Sudden Coronary Death in Women. *Circulation* **1998**, *97*, 2110–2116. [CrossRef]
59. Erbel, R.; Möhlenkamp, S.; Moebus, S.; Schmermund, A.; Lehmann, N.; Stang, A.; Dragano, N.; Grönemeyer, D.; Seibel, R.; Kälsch, H.; et al. Coronary Risk Stratification, Discrimination, and Reclassification Improvement Based on Quantification of Subclinical Coronary Atherosclerosis. *J. Am. Coll. Cardiol.* **2010**, *56*, 1397–1406. [CrossRef]
60. Vliegenthart, R.; Oudkerk, M.; Hofman, A.; Oei, H.-H.S.; van Dijck, W.; van Rooij, F.J.A.; Witteman, J.C.M. Coronary Calcification Improves Cardiovascular Risk Prediction in the Elderly. *Circulation* **2005**, *112*, 572–577. [CrossRef]
61. Sarwar, A.; Shaw, L.J.; Shapiro, M.D.; Blankstein, R.; Hoffman, U.; Cury, R.C.; Abbara, S.; Brady, T.J.; Budoff, M.J.; Blumenthal, R.S.; et al. Diagnostic and Prognostic Value of Absence of Coronary Artery Calcification. *JACC Cardiovasc. Imaging* **2009**, *2*, 675–688. [CrossRef]
62. Peng, A.W.; Mirbolouk, M.; Orimoloye, O.A.; Osei, A.D.; Dardari, Z.; Dzaye, O.; Budoff, M.J.; Shaw, L.; Miedema, M.D.; Rumberger, J.; et al. Long-Term All-Cause and Cause-Specific Mortality in Asymptomatic Patients with CAC $\geq$ 1000. *JACC Cardiovasc. Imaging* **2020**, *13*, 83–93. [CrossRef] [PubMed]
63. Greenland, P. Coronary Artery Calcium Score Combined with Framingham Score for Risk Prediction in Asymptomatic Individuals. *JAMA* **2004**, *291*, 210. [CrossRef] [PubMed]
64. Arad, Y.; Goodman, K.J.; Roth, M.; Newstein, D.; Guerci, A.D. Coronary Calcification, Coronary Disease Risk Factors, C-Reactive Protein, and Atherosclerotic Cardiovascular Disease Events. *J. Am. Coll. Cardiol.* **2005**, *46*, 158–165. [CrossRef] [PubMed]
65. Greenland, P.; Blaha, M.J.; Budoff, M.J.; Erbel, R.; Watson, K.E. Coronary Calcium Score and Cardiovascular Risk. *J. Am. Coll. Cardiol.* **2018**, *72*, 434–447. [CrossRef]
66. Ajufo, E.; Ayers, C.R.; Vigen, R.; Joshi, P.H.; Rohatgi, A.; de Lemos, J.A.; Khera, A. Value of Coronary Artery Calcium Scanning in Association with the Net Benefit of Aspirin in Primary Prevention of Atherosclerotic Cardiovascular Disease. *JAMA Cardiol.* **2021**, *6*, 179. [CrossRef]
67. Budoff, M.J.; Dowe, D.; Jollis, J.G.; Gitter, M.; Sutherland, J.; Halamert, E.; Scherer, M.; Bellinger, R.; Martin, A.; Benton, R.; et al. Diagnostic Performance of 64-Multidetector Row Coronary Computed Tomographic Angiography for Evaluation of Coronary Artery Stenosis in Individuals without Known Coronary Artery Disease. *J. Am. Coll. Cardiol.* **2008**, *52*, 1724–1732. [CrossRef]
68. Meijboom, W.B.; van Mieghem, C.A.G.; Mollet, N.R.; Pugliese, F.; Weustink, A.C.; van Pelt, N.; Cademartiri, F.; Nieman, K.; Boersma, E.; de Jaegere, P.; et al. 64-Slice Computed Tomography Coronary Angiography in Patients with High, Intermediate, or Low Pretest Probability of Significant Coronary Artery Disease. *J. Am. Coll. Cardiol.* **2007**, *50*, 1469–1475. [CrossRef]
69. Winther, S.; Schmidt, S.E.; Mayrhofer, T.; Bøtker, H.E.; Hoffmann, U.; Douglas, P.S.; Wijns, W.; Bax, J.; Nissen, L.; Lynggaard, V.; et al. Incorporating Coronary Calcification into Pre-Test Assessment of the Likelihood of Coronary Artery Disease. *J. Am. Coll. Cardiol.* **2020**, *76*, 2421–2432. [CrossRef]
70. Sow, M.A.; Magne, J.; Salle, L.; Nobecourt, E.; Preux, P.-M.; Aboyans, V. Prevalence, Determinants and Prognostic Value of High Coronary Artery Calcium Score in Asymptomatic Patients with Diabetes: A Systematic Review and Meta-Analysis. *J. Diabetes Complicat.* **2022**, *36*, 108237. [CrossRef]
71. Wang, F.M.; Rozanski, A.; Arnson, Y.; Budoff, M.J.; Miedema, M.D.; Nasir, K.; Shaw, L.J.; Rumberger, J.A.; Blumenthal, R.S.; Matsushita, K.; et al. Cardiovascular and All-Cause Mortality Risk by Coronary Artery Calcium Scores and Percentiles among Older Adult Males and Females. *Am. J. Med.* **2021**, *134*, 341–350. [CrossRef]
72. Block, G.A.; Raggi, P.; Bellasi, A.; Kooienga, L.; Spiegel, D.M. Mortality Effect of Coronary Calcification and Phosphate Binder Choice in Incident Hemodialysis Patients. *Kidney Int.* **2007**, *71*, 438–441. [CrossRef] [PubMed]
73. Gassett, A.J.; Sheppard, L.; McClelland, R.L.; Olives, C.; Kronmal, R.; Blaha, M.J.; Budoff, M.; Kaufman, J.D. Risk Factors for Long-Term Coronary Artery Calcium Progression in the Multi-Ethnic Study of Atherosclerosis. *J. Am. Heart Assoc.* **2015**, *4*, e001726. [CrossRef] [PubMed]
74. Schindler, T.H.; Cadenas, J.; Facta, A.D.; Li, Y.; Olschewski, M.; Sayre, J.; Goldin, J.; Schelbert, H.R. Improvement in Coronary Endothelial Function Is Independently Associated with a Slowed Progression of Coronary Artery Calcification in Type 2 Diabetes Mellitus. *Eur. Heart J.* **2009**, *30*, 3064–3073. [CrossRef] [PubMed]

75. Raggi, P.; Callister, T.Q.; Shaw, L.J. Progression of Coronary Artery Calcium and Risk of First Myocardial Infarction in Patients Receiving Cholesterol-Lowering Therapy. *Arterioscler. Thromb. Vasc. Biol.* **2004**, *24*, 1272–1277. [CrossRef]
76. Budoff, M.J.; Young, R.; Lopez, V.A.; Kronmal, R.A.; Nasir, K.; Blumenthal, R.S.; Detrano, R.C.; Bild, D.E.; Guerci, A.D.; Liu, K.; et al. Progression of Coronary Calcium and Incident Coronary Heart Disease Events. *J. Am. Coll. Cardiol.* **2013**, *61*, 1231–1239. [CrossRef]
77. Radford, N.B.; DeFina, L.F.; Barlow, C.E.; Lakoski, S.G.; Leonard, D.; Paixao, A.R.M.; Khera, A.; Levine, B.D. Progression of CAC Score and Risk of Incident CVD. *JACC Cardiovasc. Imaging* **2016**, *9*, 1420–1429. [CrossRef]
78. Lehmann, N.; Erbel, R.; Mahabadi, A.A.; Rauwolf, M.; Möhlenkamp, S.; Moebus, S.; Kälsch, H.; Budde, T.; Schmermund, A.; Stang, A.; et al. Value of Progression of Coronary Artery Calcification for Risk Prediction of Coronary and Cardiovascular Events. *Circulation* **2018**, *137*, 665–679. [CrossRef]
79. Hecht, H.S.; Cronin, P.; Blaha, M.J.; Budoff, M.J.; Kazerooni, E.A.; Narula, J.; Yankelevitz, D.; Abbara, S. 2016 SCCT/STR Guidelines for Coronary Artery Calcium Scoring of Noncontrast Noncardiac Chest CT Scans: A Report of the Society of Cardiovascular Computed Tomography and Society of Thoracic Radiology. *J. Cardiovasc. Comput. Tomogr.* **2017**, *11*, 74–84. [CrossRef]
80. Zang, Y.; Dai, L.; Zhang, Y.; Xia, L. One-Dimensional Simulation of Transmural Heterogeneity of Cardiac Cellular Electromechanics. *Comput. Cardiol.* **2011**, *38*, 65–68.
81. Huang, A.L.; Maggiore, P.L.; Brown, R.A.; Turaga, M.; Reid, A.B.; Merkur, J.; Blanke, P.; Leipsic, J.A. CT-Derived Fractional Flow Reserve (FFR CT): From Gatekeeping to Roadmapping. *Can. Assoc. Radiol. J.* **2020**, *71*, 201–207. [CrossRef]
82. Zhao, X.; Zhang, J.; Gong, Y.; Xu, L.; Liu, H.; Wei, S.; Wu, Y.; Cha, G.; Wei, H.; Mao, J.; et al. Reliable Detection of Myocardial Ischemia Using Machine Learning Based on Temporal-Spatial Characteristics of Electrocardiogram and Vectorcardiogram. *Front. Physiol.* **2022**, *13*, 854191. [CrossRef] [PubMed]
83. He, J.; Tse, G.; Korantzopoulos, P.; Letsas, K.P.; Ali-Hasan-Al-Saegh, S.; Kamel, H.; Li, G.; Lip, G.Y.H.; Liu, T. P-Wave Indices and Risk of Ischemic Stroke. *Stroke* **2017**, *48*, 2066–2072. [CrossRef] [PubMed]
84. Tse, G.; Wong, C.W.; Gong, M.Q.; Meng, L.; Letsas, K.P.; Li, G.P.; Whittaker, P.; Bhardwaj, A.; Sawant, A.C.; Wu, W.K.; et al. Meta-Analysis of T-Wave Indices for Risk Stratification in Myocardial Infarction. *J. Geriatr. Cardiol.* **2017**, *14*, 776–779. [PubMed]
85. Dou, J.; Xia, L.; Deng, D.; Zang, Y.; Shou, G.; Bustos, C.; Tu, W.; Liu, F.; Crozier, S. A Study of Mechanical Optimization Strategy for Cardiac Resynchronization Therapy Based on an Electromechanical Model. *Comput. Math. Methods Med.* **2012**, *2012*, 948781. [CrossRef]
86. Geng, Y.; Wu, X.; Liu, H.; Zheng, D.; Xia, L. Index of Microcirculatory Resistance: State-of-the-Art and Potential Applications in Computational Simulation of Coronary Artery Disease. *J. Zhejiang Univ. B* **2022**, *23*, 123–140. [CrossRef]
87. Geng, Y.; Liu, H.; Wang, X.; Zhang, J.; Gong, Y.; Zheng, D.; Jiang, J.; Xia, L. Effect of Microcirculatory Dysfunction on Coronary Hemodynamics: A Pilot Study Based on Computational Fluid Dynamics Simulation. *Comput. Biol. Med.* **2022**, *146*, 105583. [CrossRef]
88. Yeung, C.; Baranchuk, A.; Tse, G.; Liu, T. The Importance of Measuring Coronary Blood Flow for Clinical Decision Making. *Curr. Cardiol. Rev.* **2019**, *15*, 320–321. [CrossRef]
89. Rizvi, A.; Han, D.; Danad, I.; Ó Hartaigh, B.; Lee, J.H.; Gransar, H.; Stuijfzand, W.J.; Roudsari, H.M.; Park, M.W.; Szymonifka, J.; et al. Diagnostic Performance of Hybrid Cardiac Imaging Methods for Assessment of Obstructive Coronary Artery Disease Compared with Stand-Alone Coronary Computed Tomography Angiography. *JACC Cardiovasc. Imaging* **2018**, *11*, 589–599. [CrossRef]
90. Hyafil, F.; Jaber, W.A.; Neglia, D. Highlights of the 14th International Conference on Nuclear Cardiology and Cardiac Computed Tomography. *Eur. Heart J.—Cardiovasc. Imaging* **2019**, *21*, 1–9. [CrossRef]
91. Le Jemtel, T.H.; Samson, R.; Ayinapudi, K.; Singh, T.; Oparil, S. Epicardial Adipose Tissue and Cardiovascular Disease. *Curr. Hypertens. Rep.* **2019**, *21*, 36. [CrossRef]
92. Sacks, H.S.; Fain, J.N. Human Epicardial Adipose Tissue: A Review. *Am. Heart J.* **2007**, *153*, 907–917. [CrossRef] [PubMed]
93. Iacobellis, G.; Corradi, D.; Sharma, A.M. Epicardial Adipose Tissue: Anatomic, Biomolecular and Clinical Relationships with the Heart. *Nat. Clin. Pract. Cardiovasc. Med.* **2005**, *2*, 536–543. [CrossRef] [PubMed]
94. Antonopoulos, A.S.; Sanna, F.; Sabharwal, N.; Thomas, S.; Oikonomou, E.K.; Herdman, L.; Margaritis, M.; Shirodaria, C.; Kampoli, A.-M.; Akoumianakis, I.; et al. Detecting Human Coronary Inflammation by Imaging Perivascular Fat. *Sci. Transl. Med.* **2017**, *9*, eaal2658. [CrossRef] [PubMed]
95. Mazurek, T.; Zhang, L.; Zalewski, A.; Mannion, J.D.; Diehl, J.T.; Arafat, H.; Sarov-Blat, L.; O'Brien, S.; Keiper, E.A.; Johnson, A.G.; et al. Human Epicardial Adipose Tissue Is a Source of Inflammatory Mediators. *Circulation* **2003**, *108*, 2460–2466. [CrossRef]
96. Rabkin, S.W. Epicardial Fat: Properties, Function and Relationship to Obesity. *Obes. Rev.* **2007**, *8*, 253–261. [CrossRef]
97. Lin, A.; Dey, D.; Wong, D.T.L.; Nerlekar, N. Perivascular Adipose Tissue and Coronary Atherosclerosis: From Biology to Imaging Phenotyping. *Curr. Atheroscler. Rep.* **2019**, *21*, 47. [CrossRef]
98. Chechi, K.; Richard, D. Thermogenic Potential and Physiological Relevance of Human Epicardial Adipose Tissue. *Int. J. Obes. Suppl.* **2015**, *5*, S28–S34. [CrossRef]
99. Hirata, Y.; Tabata, M.; Kurobe, H.; Motoki, T.; Akaike, M.; Nishio, C.; Higashida, M.; Mikasa, H.; Nakaya, Y.; Takanashi, S.; et al. Coronary Atherosclerosis Is Associated with Macrophage Polarization in Epicardial Adipose Tissue. *J. Am. Coll. Cardiol.* **2011**, *58*, 248–255. [CrossRef]

100. Demir, B.; Demir, E.; Acıksarı, G.; Uygun, T.; Utku, I.K.; Gedikbasi, A.; Caglar, I.M.; Pirhan, O.; Tureli, H.O.; Oflar, E.; et al. The Association between the Epicardial Adipose Tissue Thickness and Oxidative Stress Parameters in Isolated Metabolic Syndrome Patients: A Multimarker Approach. *Int. J. Endocrinol.* **2014**, *2014*, 954045. [CrossRef]
101. Baker, A.R.; Harte, A.L.; Howell, N.; Pritlove, D.C.; Ranasinghe, A.M.; da Silva, N.F.; Youssef, E.M.; Khunti, K.; Davies, M.J.; Bonser, R.S.; et al. Epicardial Adipose Tissue as a Source of Nuclear Factor-KB and c-Jun N-Terminal Kinase Mediated Inflammation in Patients with Coronary Artery Disease. *J. Clin. Endocrinol. Metab.* **2009**, *94*, 261–267. [CrossRef]
102. Nusca, A.; Piccirillo, F.; Bernardini, F.; De Filippis, A.; Coletti, F.; Mangiacapra, F.; Ricottini, E.; Melfi, R.; Gallo, P.; Cammalleri, V.; et al. Glycaemic Control in Patients Undergoing Percutaneous Coronary Intervention: What Is the Role for the Novel Antidiabetic Agents? A Comprehensive Review of Basic Science and Clinical Data. *Int. J. Mol. Sci.* **2022**, *23*, 7261. [CrossRef] [PubMed]
103. Montazerifar, F.; Bolouri, A.; Paghalea, R.S.; Mahani, M.K.; Karajibani, M. Obesity, Serum Resistin and Leptin Levels Linked to Coronary Artery Disease. *Arq. Bras. Cardiol.* **2016**, *107*, 348–353. [CrossRef] [PubMed]
104. Yafei, S.; Elsewy, F.; Youssef, E.; Ayman, M.; Elshafei, M.; Abayazeed, R. Echocardiographic Association of Epicardial Fat with Carotid Intima–Media Thickness in Patients with Type 2 Diabetes. *Diabetes Vasc. Dis. Res.* **2019**, *16*, 378–384. [CrossRef] [PubMed]
105. Militello, C.; Rundo, L.; Toia, P.; Conti, V.; Russo, G.; Filorizzo, C.; Maffei, E.; Cademartiri, F.; La Grutta, L.; Midiri, M.; et al. A Semi-Automatic Approach for Epicardial Adipose Tissue Segmentation and Quantification on Cardiac CT Scans. *Comput. Biol. Med.* **2019**, *114*, 103424. [CrossRef] [PubMed]
106. Mancio, J.; Azevedo, D.; Saraiva, F.; Azevedo, A.I.; Pires-Morais, G.; Leite-Moreira, A.; Falcao-Pires, I.; Lunet, N.; Bettencourt, N. Epicardial Adipose Tissue Volume Assessed by Computed Tomography and Coronary Artery Disease: A Systematic Review and Meta-Analysis. *Eur. Heart J.—Cardiovasc. Imaging* **2018**, *19*, 490–497. [CrossRef]
107. Wang, T.-D.; Lee, W.-J.; Shih, F.-Y.; Huang, C.-H.; Chang, Y.-C.; Chen, W.-J.; Lee, Y.-T.; Chen, M.-F. Relations of Epicardial Adipose Tissue Measured by Multidetector Computed Tomography to Components of the Metabolic Syndrome Are Region-Specific and Independent of Anthropometric Indexes and Intraabdominal Visceral Fat. *J. Clin. Endocrinol. Metab.* **2009**, *94*, 662–669. [CrossRef] [PubMed]
108. La Grutta, L.; Toia, P.; Farruggia, A.; Albano, D.; Grassedonio, E.; Palmeri, A.; Maffei, E.; Galia, M.; Vitabile, S.; Cademartiri, F.; et al. Quantification of Epicardial Adipose Tissue in Coronary Calcium Score and CT Coronary Angiography Image Data Sets: Comparison of Attenuation Values, Thickness and Volumes. *Br. J. Radiol.* **2016**, *89*, 20150773. [CrossRef]
109. Spearman, J.V.; Renker, M.; Schoepf, U.J.; Krazinski, A.W.; Herbert, T.L.; De Cecco, C.N.; Nietert, P.J.; Meinel, F.G. Prognostic Value of Epicardial Fat Volume Measurements by Computed Tomography: A Systematic Review of the Literature. *Eur. Radiol.* **2015**, *25*, 3372–3381. [CrossRef]
110. Bastarrika, G.; Broncano, J.; Schoepf, U.J.; Schwarz, F.; Lee, Y.S.; Abro, J.A.; Costello, P.; Zwerner, P.L. Relationship between Coronary Artery Disease and Epicardial Adipose Tissue Quantification at Cardiac CT. *Acad. Radiol.* **2010**, *17*, 727–734. [CrossRef]
111. Yu, W.; Liu, B.; Zhang, F.; Wang, J.; Shao, X.; Yang, X.; Shi, Y.; Wang, B.; Xu, Y.; Wang, Y. Association of Epicardial Fat Volume with Increased Risk of Obstructive Coronary Artery Disease in Chinese Patients with Suspected Coronary Artery Disease. *J. Am. Heart Assoc.* **2021**, *10*, e018080. [CrossRef]
112. Gitsioudis, G.; Schmahl, C.; Missiou, A.; Voss, A.; Schüssler, A.; Abdel-Aty, H.; Buss, S.J.; Mueller, D.; Vembar, M.; Bryant, M.; et al. Epicardial Adipose Tissue Is Associated with Plaque Burden and Composition and Provides Incremental Value for the Prediction of Cardiac Outcome. A Clinical Cardiac Computed Tomography Angiography Study. *PLoS ONE* **2016**, *11*, e0155120. [CrossRef] [PubMed]
113. Alexopoulos, N.; McLean, D.S.; Janik, M.; Arepalli, C.D.; Stillman, A.E.; Raggi, P. Epicardial Adipose Tissue and Coronary Artery Plaque Characteristics. *Atherosclerosis* **2010**, *210*, 150–154. [CrossRef] [PubMed]
114. Ito, T.; Suzuki, Y.; Ehara, M.; Matsuo, H.; Teramoto, T.; Terashima, M.; Nasu, K.; Kinoshita, Y.; Tsuchikane, E.; Suzuki, T.; et al. Impact of Epicardial Fat Volume on Coronary Artery Disease in Symptomatic Patients with a Zero Calcium Score. *Int. J. Cardiol.* **2013**, *167*, 2852–2858. [CrossRef] [PubMed]
115. Nerlekar, N.; Brown, A.J.; Muthalaly, R.G.; Talman, A.; Hettige, T.; Cameron, J.D.; Wong, D.T.L. Association of Epicardial Adipose Tissue and High-Risk Plaque Characteristics: A Systematic Review and Meta-Analysis. *J. Am. Heart Assoc.* **2017**, *6*, e006379. [CrossRef]
116. Otsuka, K.; Ishikawa, H.; Yamaura, H.; Shirasawa, K.; Kasayuki, N. Epicardial Adipose Tissue Volume Is Associated with Low-Attenuation Plaque Volume in Subjects with or without Increased Visceral Fat: A 3-Vessel Coronary Artery Analysis with CT Angiography. *Eur. Heart J.* **2021**, *42*. [CrossRef]
117. Yamashita, K.; Yamamoto, M.H.; Igawa, W.; Ono, M.; Kido, T.; Ebara, S.; Okabe, T.; Saito, S.; Amemiya, K.; Isomura, N.; et al. Association of Epicardial Adipose Tissue Volume and Total Coronary Plaque Burden in Patients with Coronary Artery Disease. *Int. Heart J.* **2018**, *59*, 1219–1226. [CrossRef]
118. Iwasaki, K.; Matsumoto, T.; Aono, H.; Furukawa, H.; Samukawa, M. Relationship between Epicardial Fat Measured by 64-Multidetector Computed Tomography and Coronary Artery Disease. *Clin. Cardiol.* **2011**, *34*, 166–171. [CrossRef]
119. Cosson, E.; Nguyen, M.T.; Rezgani, I.; Berkane, N.; Pinto, S.; Bihan, H.; Tatulashvili, S.; Taher, M.; Sal, M.; Soussan, M.; et al. Epicardial Adipose Tissue Volume and Myocardial Ischemia in Asymptomatic People Living with Diabetes: A Cross-Sectional Study. *Cardiovasc. Diabetol.* **2021**, *20*, 224. [CrossRef]

120. Franssens, B.T.; Nathoe, H.M.; Visseren, F.L.J.; van der Graaf, Y.; Leiner, T.; Algra, A.; van der Graaf, Y.; Grobbee, D.E.; Rutten, G.E.H.M.; Visseren, F.L.J.; et al. Relation of Epicardial Adipose Tissue Radiodensity to Coronary Artery Calcium on Cardiac Computed Tomography in Patients at High Risk for Cardiovascular Disease. *Am. J. Cardiol.* **2017**, *119*, 1359–1365. [CrossRef]
121. Goeller, M.; Achenbach, S.; Marwan, M.; Doris, M.K.; Cadet, S.; Commandeur, F.; Chen, X.; Slomka, P.J.; Gransar, H.; Cao, J.J.; et al. Epicardial Adipose Tissue Density and Volume Are Related to Subclinical Atherosclerosis, Inflammation and Major Adverse Cardiac Events in Asymptomatic Subjects. *J. Cardiovasc. Comput. Tomogr.* **2018**, *12*, 67–73. [CrossRef]
122. Eisenberg, E.; McElhinney, P.A.; Commandeur, F.; Chen, X.; Cadet, S.; Goeller, M.; Razipour, A.; Gransar, H.; Cantu, S.; Miller, R.J.H.; et al. Deep Learning–Based Quantification of Epicardial Adipose Tissue Volume and Attenuation Predicts Major Adverse Cardiovascular Events in Asymptomatic Subjects. *Circ. Cardiovasc. Imaging* **2020**, *13*, e009829. [CrossRef] [PubMed]
123. Fuller, B.; Garland, J.; Anne, S.; Beh, R.; McNevin, D.; Tse, R. Increased Epicardial Fat Thickness in Sudden Death From Stable Coronary Artery Atherosclerosis. *Am. J. Forensic Med. Pathol.* **2017**, *38*, 162–166. [CrossRef] [PubMed]
124. Mahabadi, A.A.; Berg, M.H.; Lehmann, N.; Kälsch, H.; Bauer, M.; Kara, K.; Dragano, N.; Moebus, S.; Jöckel, K.-H.; Erbel, R.; et al. Association of Epicardial Fat with Cardiovascular Risk Factors and Incident Myocardial Infarction in the General Population. *J. Am. Coll. Cardiol.* **2013**, *61*, 1388–1395. [CrossRef] [PubMed]
125. Gorter, P.M.; de Vos, A.M.; van der Graaf, Y.; Stella, P.R.; Doevendans, P.A.; Meijs, M.F.L.; Prokop, M.; Visseren, F.L.J. Relation of Epicardial and Pericoronary Fat to Coronary Atherosclerosis and Coronary Artery Calcium in Patients Undergoing Coronary Angiography. *Am. J. Cardiol.* **2008**, *102*, 380–385. [CrossRef] [PubMed]
126. Balcer, B.; Dykun, I.; Schlosser, T.; Forsting, M.; Rassaf, T.; Mahabadi, A.A. Pericoronary Fat Volume but Not Attenuation Differentiates Culprit Lesions in Patients with Myocardial Infarction. *Atherosclerosis* **2018**, *276*, 182–188. [CrossRef] [PubMed]
127. Ma, R.; van Assen, M.; Ties, D.; Pelgrim, G.J.; van Dijk, R.; Sidorenkov, G.; van Ooijen, P.M.A.; van der Harst, P.; Vliegenthart, R. Focal Pericoronary Adipose Tissue Attenuation Is Related to Plaque Presence, Plaque Type, and Stenosis Severity in Coronary CTA. *Eur. Radiol.* **2021**, *31*, 7251–7261. [CrossRef]
128. Nogic, J.; Kim, J.; Layland, J.; Chan, J.; Cheng, K.; Wong, D.; Brown, A. TCT-241 Pericoronary Adipose Tissue Is a Predictor of In-Stent Restenosis and Stent Failure in Patients Undergoing Coronary Artery Stent Insertion. *J. Am. Coll. Cardiol.* **2021**, *78*, B98. [CrossRef]
129. Kang, J.; Kim, Y.-C.; Park, J.J.; Kim, S.; Kang, S.-H.; Cho, Y.J.; Yoon, Y.E.; Oh, I.-Y.; Yoon, C.-H.; Suh, J.-W.; et al. Increased Epicardial Adipose Tissue Thickness Is a Predictor of New-Onset Diabetes Mellitus in Patients with Coronary Artery Disease Treated with High-Intensity Statins. *Cardiovasc. Diabetol.* **2018**, *17*, 10. [CrossRef]
130. Raggi, P.; Gadiyaram, V.; Zhang, C.; Chen, Z.; Lopaschuk, G.; Stillman, A.E. Statins Reduce Epicardial Adipose Tissue Attenuation Independent of Lipid Lowering: A Potential Pleiotropic Effect. *J. Am. Heart Assoc.* **2019**, *8*, e013104. [CrossRef]
131. Ziyrek, M.; Kahraman, S.; Ozdemir, E.; Dogan, A. Metformin Monotherapy Significantly Decreases Epicardial Adipose Tissue Thickness in Newly Diagnosed Type 2 Diabetes Patients. *Rev. Port. Cardiol.* **2019**, *38*, 419–423. [CrossRef]
132. Iacobellis, G.; Villasante Fricke, A.C. Effects of Semaglutide Versus Dulaglutide on Epicardial Fat Thickness in Subjects with Type 2 Diabetes and Obesity. *J. Endocr. Soc.* **2020**, *4*, bvz042. [CrossRef] [PubMed]
133. Iacobellis, G.; Mohseni, M.; Bianco, S.D.; Banga, P.K. Liraglutide Causes Large and Rapid Epicardial Fat Reduction. *Obesity* **2017**, *25*, 311–316. [CrossRef] [PubMed]
134. Sato, T.; Aizawa, Y.; Yuasa, S.; Kishi, S.; Fuse, K.; Fujita, S.; Ikeda, Y.; Kitazawa, H.; Takahashi, M.; Sato, M.; et al. The Effect of Dapagliflozin Treatment on Epicardial Adipose Tissue Volume. *Cardiovasc. Diabetol.* **2018**, *17*, 6. [CrossRef] [PubMed]
135. Desai, M.Y.; Cremer, P.C.; Schoenhagen, P. Thoracic Aortic Calcification. *JACC Cardiovasc. Imaging* **2018**, *11*, 1012–1026. [CrossRef]
136. Budoff, M.J.; Nasir, K.; Katz, R.; Takasu, J.; Carr, J.J.; Wong, N.D.; Allison, M.; Lima, J.A.C.; Detrano, R.; Blumenthal, R.S.; et al. Thoracic Aortic Calcification and Coronary Heart Disease Events: The Multi-Ethnic Study of Atherosclerosis (MESA). *Atherosclerosis* **2011**, *215*, 196–202. [CrossRef]
137. Allison, M.A.; Hsi, S.; Wassel, C.L.; Morgan, C.; Ix, J.H.; Wright, C.M.; Criqui, M.H. Calcified Atherosclerosis in Different Vascular Beds and the Risk of Mortality. *Arterioscler. Thromb. Vasc. Biol.* **2012**, *32*, 140–146. [CrossRef]
138. Rivera, J.J.; Nasir, K.; Katz, R.; Takasu, J.; Allison, M.; Wong, N.D.; Barr, R.G.; Carr, J.J.; Blumenthal, R.S.; Budoff, M.J. Relationship of Thoracic Aortic Calcium to Coronary Calcium and Its Progression (from the Multi-Ethnic Study of Atherosclerosis [MESA]). *Am. J. Cardiol.* **2009**, *103*, 1562–1567. [CrossRef]
139. El-Saed, A.; Sekikawa, A.; Edmundowicz, D.; Evans, R.W.; Sutton-Tyrrell, K.; Kadowaki, T.; Choo, J.; Takamiya, T.; Kuller, L.H. Coronary Calcification Is More Predictive of Carotid Intimal Medial Thickness in Black Compared to White Middle Aged Men. *Atherosclerosis* **2008**, *196*, 913–918. [CrossRef]
140. Kodama, Y.; Ng, C.S.; Wu, T.T.; Ayers, G.D.; Curley, S.A.; Abdalla, E.K.; Vauthey, J.N.; Charnsangavej, C. Comparison of CT Methods for Determining the Fat Content of the Liver. *Am. J. Roentgenol.* **2007**, *188*, 1307–1312. [CrossRef]
141. Cademartiri, F.; Sverzellati, N.; Guaricci, A.I.; Maffei, E. Fat and Cardiovascular Risk: The Role of Cardiac CT. *Eur. Heart J.—Cardiovasc. Imaging* **2016**, *17*, 1368–1369. [CrossRef]
142. Bos, D.; Leening, M.J.G. Leveraging the Coronary Calcium Scan beyond the Coronary Calcium Score. *Eur. Radiol.* **2018**, *28*, 3082–3087. [CrossRef] [PubMed]

143. Yki-Järvinen, H. Non-Alcoholic Fatty Liver Disease as a Cause and a Consequence of Metabolic Syndrome. *Lancet Diabetes Endocrinol.* **2014**, *2*, 901–910. [CrossRef] [PubMed]
144. Stahl, E.P.; Dhindsa, D.S.; Lee, S.K.; Sandesara, P.B.; Chalasani, N.P.; Sperling, L.S. Nonalcoholic Fatty Liver Disease and the Heart. *J. Am. Coll. Cardiol.* **2019**, *73*, 948–963. [CrossRef] [PubMed]
145. Sung, K.-C.; Wild, S.H.; Kwag, H.J.; Byrne, C.D. Fatty Liver, Insulin Resistance, and Features of Metabolic Syndrome. *Diabetes Care* **2012**, *35*, 2359–2364. [CrossRef]
146. Puchner, S.B.; Lu, M.T.; Mayrhofer, T.; Liu, T.; Pursnani, A.; Ghoshhajra, B.B.; Truong, Q.A.; Wiviott, S.D.; Fleg, J.L.; Hoffmann, U.; et al. High-Risk Coronary Plaque at Coronary CT Angiography Is Associated with Nonalcoholic Fatty Liver Disease, Independent of Coronary Plaque and Stenosis Burden: Results from the ROMICAT II Trial. *Radiology* **2015**, *274*, 693–701. [CrossRef]
147. Wolff, L.; Bos, D.; Murad, S.D.; Franco, O.H.; Krestin, G.P.; Hofman, A.; Vernooij, M.W.; van der Lugt, A. Liver Fat Is Related to Cardiovascular Risk Factors and Subclinical Vascular Disease: The Rotterdam Study. *Eur. Heart J.—Cardiovasc. Imaging* **2016**, *17*, 1361–1367. [CrossRef]
148. Kotronen, A.; Yki-Järvinen, H. Fatty Liver. *Arterioscler. Thromb. Vasc. Biol.* **2008**, *28*, 27–38. [CrossRef]
149. Al Rifai, M.; Silverman, M.G.; Nasir, K.; Budoff, M.J.; Blankstein, R.; Szklo, M.; Katz, R.; Blumenthal, R.S.; Blaha, M.J. The Association of Nonalcoholic Fatty Liver Disease, Obesity, and Metabolic Syndrome, with Systemic Inflammation and Subclinical Atherosclerosis: The Multi-Ethnic Study of Atherosclerosis (MESA). *Atherosclerosis* **2015**, *239*, 629–633. [CrossRef]
150. Kannel, W.B.; Abbott, R.D. Incidence and Prognosis of Unrecognized Myocardial Infarction. *N. Engl. J. Med.* **1984**, *311*, 1144–1147. [CrossRef]
151. Madaj, P.; Budoff, M.J. Risk Stratification of Non-Contrast CT beyond the Coronary Calcium Scan. *J. Cardiovasc. Comput. Tomogr.* **2012**, *6*, 301–307. [CrossRef]
152. Kimura, F.; Matsuo, Y.; Nakajima, T.; Nishikawa, T.; Kawamura, S.; Sannohe, S.; Hagiwara, N.; Sakai, F. Myocardial Fat at Cardiac Imaging: How Can We Differentiate Pathologic from Physiologic Fatty Infiltration? *RadioGraphics* **2010**, *30*, 1587–1602. [CrossRef] [PubMed]
153. Zafar, H.M.; Litt, H.I.; Torigian, D.A. CT Imaging Features and Frequency of Left Ventricular Myocardial Fat in Patients with CT Findings of Chronic Left Ventricular Myocardial Infarction. *Clin. Radiol.* **2008**, *63*, 256–262. [CrossRef] [PubMed]
154. Ichikawa, Y.; Kitagawa, K.; Chino, S.; Ishida, M.; Matsuoka, K.; Tanigawa, T.; Nakamura, T.; Hirano, T.; Takeda, K.; Sakuma, H. Adipose Tissue Detected by Multislice Computed Tomography in Patients after Myocardial Infarction. *JACC Cardiovasc. Imaging* **2009**, *2*, 548–555. [CrossRef] [PubMed]
155. Nieman, K.; Cury, R.C.; Ferencik, M.; Nomura, C.H.; Abbara, S.; Hoffmann, U.; Gold, H.K.; Jang, I.-K.; Brady, T.J. Differentiation of Recent and Chronic Myocardial Infarction by Cardiac Computed Tomography. *Am. J. Cardiol.* **2006**, *98*, 303–308. [CrossRef]
156. Gupta, M.; Kadakia, J.; Hacioglu, Y.; Ahmadi, N.; Patel, A.; Choi, T.; Yamada, G.; Budoff, M. Non-Contrast Cardiac Computed Tomography Can Accurately Detect Chronic Myocardial Infarction: Validation Study. *J. Nucl. Cardiol.* **2011**, *18*, 96–103. [CrossRef]
157. Ko, S.M.; Hwang, S.H.; Lee, H.-J. Role of Cardiac Computed Tomography in the Diagnosis of Left Ventricular Myocardial Diseases. *J. Cardiovasc. Imaging* **2019**, *27*, 73. [CrossRef]
158. Lardo, A.C.; Cordeiro, M.A.S.; Silva, C.; Amado, L.C.; George, R.T.; Saliaris, A.P.; Schuleri, K.H.; Fernandes, V.R.; Zviman, M.; Nazarian, S.; et al. Contrast-Enhanced Multidetector Computed Tomography Viability Imaging after Myocardial Infarction. *Circulation* **2006**, *113*, 394–404. [CrossRef]
159. Mahnken, A.H.; Koos, R.; Katoh, M.; Wildberger, J.E.; Spuentrup, E.; Buecker, A.; Günther, R.W.; Kühl, H.P. Assessment of Myocardial Viability in Reperfused Acute Myocardial Infarction Using 16-Slice Computed Tomography in Comparison to Magnetic Resonance Imaging. *J. Am. Coll. Cardiol.* **2005**, *45*, 2042–2047. [CrossRef]
160. Gerber, B.L.; Belge, B.; Legros, G.J.; Lim, P.; Poncelet, A.; Pasquet, A.; Gisellu, G.; Coche, E.; Vanoverschelde, J.-L.J. Characterization of Acute and Chronic Myocardial Infarcts by Multidetector Computed Tomography. *Circulation* **2006**, *113*, 823–833. [CrossRef]
161. Palmisano, A.; Vignale, D.; Tadic, M.; Moroni, F.; De Stefano, D.; Gatti, M.; Boccia, E.; Faletti, R.; Oppizzi, M.; Peretto, G.; et al. Myocardial Late Contrast Enhancement CT in Troponin-Positive Acute Chest Pain Syndrome. *Radiology* **2022**, *302*, 545–553. [CrossRef]
162. Bouleti, C.; Baudry, G.; Iung, B.; Arangalage, D.; Abtan, J.; Ducrocq, G.; Steg, P.-G.; Vahanian, A.; Henry-Feugeas, M.-C.; Pasi, N.; et al. Usefulness of Late Iodine Enhancement on Spectral CT in Acute Myocarditis. *JACC Cardiovasc. Imaging* **2017**, *10*, 826–827. [CrossRef] [PubMed]
163. Esposito, A.; Palmisano, A.; Antunes, S.; Maccabelli, G.; Colantoni, C.; Rancoita, P.M.V.; Baratto, F.; Di Serio, C.; Rizzo, G.; De Cobelli, F.; et al. Cardiac CT with Delayed Enhancement in the Characterization of Ventricular Tachycardia Structural Substrate. *JACC Cardiovasc. Imaging* **2016**, *9*, 822–832. [CrossRef] [PubMed]
164. Treibel, T.A.; Fontana, M.; Steeden, J.A.; Nasis, A.; Yeung, J.; White, S.K.; Sivarajan, S.; Punwani, S.; Pugliese, F.; Taylor, S.A.; et al. Automatic Quantification of the Myocardial Extracellular Volume by Cardiac Computed Tomography: Synthetic ECV by CCT. *J. Cardiovasc. Comput. Tomogr.* **2017**, *11*, 221–226. [CrossRef] [PubMed]
165. Lee, H.-J.; Im, D.J.; Youn, J.-C.; Chang, S.; Suh, Y.J.; Hong, Y.J.; Kim, Y.J.; Hur, J.; Choi, B.W. Myocardial Extracellular Volume Fraction with Dual-Energy Equilibrium Contrast-Enhanced Cardiac CT in Nonischemic Cardiomyopathy: A Prospective Comparison with Cardiac MR Imaging. *Radiology* **2016**, *280*, 49–57. [CrossRef] [PubMed]

166. Treibel, T.A.; Bandula, S.; Fontana, M.; White, S.K.; Gilbertson, J.A.; Herrey, A.S.; Gillmore, J.D.; Punwani, S.; Hawkins, P.N.; Taylor, S.A.; et al. Extracellular Volume Quantification by Dynamic Equilibrium Cardiac Computed Tomography in Cardiac Amyloidosis. *J. Cardiovasc. Comput. Tomogr.* **2015**, *9*, 585–592. [CrossRef]
167. Richards, C.E.; Obaid, D.R. Low-Dose Radiation Advances in Coronary Computed Tomography Angiography in the Diagnosis of Coronary Artery Disease. *Curr. Cardiol. Rev.* **2019**, *15*, 304–315. [CrossRef]

applied sciences

MDPI

Review

Translational Echocardiography: The Dog as a Clinical Research Model of Cardiac Dysfunction

Cesar Augusto Flores Dueñas [1,*], Ignacio Alonso Cordero Yañez [2], Roberto Mujica González [3], José Carlomán Herrera Ramírez [1], Martín Francisco Montaño Gómez [1], Soila Maribel Gaxiola Camacho [4] and Issa Carolina García Reynoso [1]

[1] Veterinary Sciences Research Institute, Autonomous University of Baja California, Mexicali 21360, Baja California, Mexico
[2] CVET, Veterinary Cardiology Services, Santiago 7910484, Chile
[3] Albeitar Veterinary Hospital, Guadalajara 45640, Jalisco, Mexico
[4] Veterinary Medicine and Zootechnics School, Autonomous University of Sinaloa, Culiacan 80260, Sinaloa, Mexico
* Correspondence: augusto.flores@uabc.edu.mx

Abstract: Heart disease is a major contributor to mortality and disability on a global scale. Hence, there is a need for research to improve non-invasive diagnostic techniques. Diseases in dogs with characteristics very similar to those of human pathologies hold promise as a source of data for evaluating and developing echocardiographic techniques and devices. Methods: We conducted a structured literature search from June 2022 to January 2023 to evaluate the relevance of dogs as a translational model for echocardiographic clinical research. We searched various academic databases, including PubMed Central (PMC), Core, DIGITAL.CSIC, DOAB, DOAJ, EBSCO host, Elsevier B.V, Redib, Scopus, and Web of Science, available through the Academic Information System of the Autonomous University of Baja California. Results: Out of the 243 articles initially screened, we identified 119 relevant articles that met our inclusion criteria for further analysis. This review is an introduction to the canine model by analyzing the cardiovascular anatomical similarities between the two species, the pathophysiological overlaps in some diseases, the parallels in echocardiographic techniques in dogs compared to humans, and the suitability of dogs with a naturally occurring cardiac disease as a model for translational clinical research compared to other animal species. Conclusions: This review emphasizes the importance of canine patients as an ideal cardiac disease symmetrical clinical model since they share common heart diseases with humans. Furthermore, dogs have a shorter lifespan, leading to the relatively rapid evolution of these diseases, which makes studying these pathologies and developing echocardiographic techniques more feasible. The results strongly indicate the need for interdisciplinary collaboration and translational medical research to create innovative echocardiographic technologies and improve the connection between veterinary and human cardiac imaging research.

Keywords: translational echocardiography; multidisciplinary cardiology; multidisciplinary echocardiography; comparative cardiology; comparative echocardiography; translational research; disease model

Citation: Flores Dueñas, C.A.; Cordero Yañez, I.A.; González, R.M.; Herrera Ramírez, J.C.; Montaño Gómez, M.F.; Gaxiola Camacho, S.M.; García Reynoso, I.C. Translational Echocardiography: The Dog as a Clinical Research Model of Cardiac Dysfunction. *Appl. Sci.* **2023**, *13*, 4437. https://doi.org/10.3390/app13074437

Academic Editor: Julio Garcia Flores

Received: 30 January 2023
Revised: 14 March 2023
Accepted: 15 March 2023
Published: 31 March 2023

1. Introduction

Cardiac disease is a critical global health issue affecting humans and animals, specifically domestic dogs [1,2]. Naturally occurring cardiac diseases with morphology and presentation similar to human pathologies are common in veterinary clinical settings. In addition, the similarities in cardiac diseases between humans and dogs are numerous [3]. The similarities offer a unique opportunity to obtain necessary information, and serve as a basis for clinical and research explorations of vast importance for developing improvements in diagnostic echocardiography techniques.

This review focuses on the characteristics of the most prevalent dog pathologies that are symmetrical to human cardiac pathologies in terms of pathophysiology and advanced cardiac ultrasound imaging techniques. Collaboration across disciplines can reveal new diagnostic strategies, primarily in echocardiography and therapeutics, that help approach and combat cardiovascular pathologies whose knowledge can be transferred between species. Although the use of animals in experimental research is becoming increasingly obsolete [4], clinical research is a rapidly expanding field in veterinary medicine. Furthermore, the rapid growth and short lifespan of the canine patient make it possible to study the behavior of cardiovascular diseases in a shorter period, which is advantageous for investigating the evolution of relevant pathologies.

Cardiac imaging is today an indispensable tool for diagnosis and patient evolution monitoring. In cardiology, ultrasound has broad clinical applications due to its ability to provide high-quality images, detailed descriptions, and quantifications of the cardiovascular system. An ultrasound of the heart allows the observation of mechanical, structural, and hemodynamic pathophysiological phenomena in cardiac diseases in a non-invasive manner. The improvement and evolution of diagnostic imaging would not have been possible without animal studies [5]. Current clinical veterinary cardiology uses practically the same echocardiographic techniques as human cardiology, including the most advanced techniques. In this review article, we will refer to transthoracic echocardiography (TTE).

2. Review Methodology

After conducting an in-depth analysis, the authors have identified four main topics and 23 subtopics that are essential to understanding the significance of dogs as a clinical model. By delving into these topics, readers can gain a comprehensive perspective on the importance of using dogs in clinical research. The present review was conducted in four steps based on the methodology proposed by [6]. Figure 1 shows the flowchart of the review process employed in this present work.

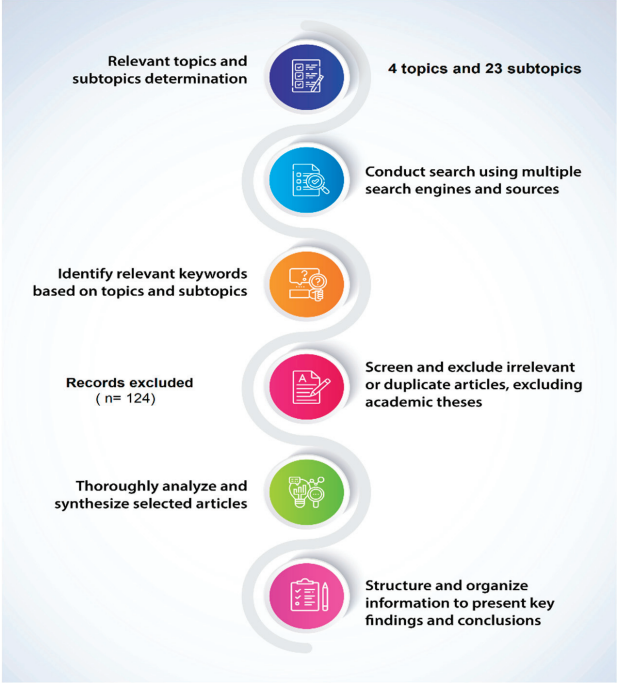

Figure 1. Review process workflow.

Step 1. Conducting the search. The search was conducted using a comprehensive information search program that utilizes multiple search engines and information sources such as PubMed Central (PMC), Core, DIGI-TAL.CSIC, DOAB, DOAJ, EBSCO host, Elsevier B.V, Redib, Scopus, and Web of Science, available through the Academic Information System of the Autonomous University of Baja California.

Step 2. Identification of keywords. The authors identified relevant keywords based on the four topics and 23 subtopics proposed by the authors included in this review.

Step 3. Selection and analysis of academic information and articles. In this process, the authors screened and excluded irrelevant or duplicate articles. In this analysis, academic theses were excluded.

Step 4. Documentation and synthesis of results. The selected articles were thoroughly analyzed and synthesized, with the information structured and organized to clearly present the key findings and conclusions.

3. Cardiac Anatomical Similarities between the Human and the Dog

The cardiac anatomy of dogs and humans share many similar features [3,7], as shown in Figure 2. In larger mammals such as canines, the heart is usually located ventral to the mediastinum [7,8]. Compared to humans, a dog's heart has a less pronounced left hemithorax orientation, and the long axis of the heart has a more ventral orientation. The base of the heart reaches approximately, the dorsal plane adjacent to the first rib and slopes to a variable degree in a craniodorsal direction [7,9]. Dogs have an ovoid cardiac structure [8]. This differs slightly from human anatomy, where the heart has a trapezoidal shape and, like its canine counterpart, an acute apex. In both species, the apexes of the heart consist solely of the left ventricular cavities and structures [7,9–11].

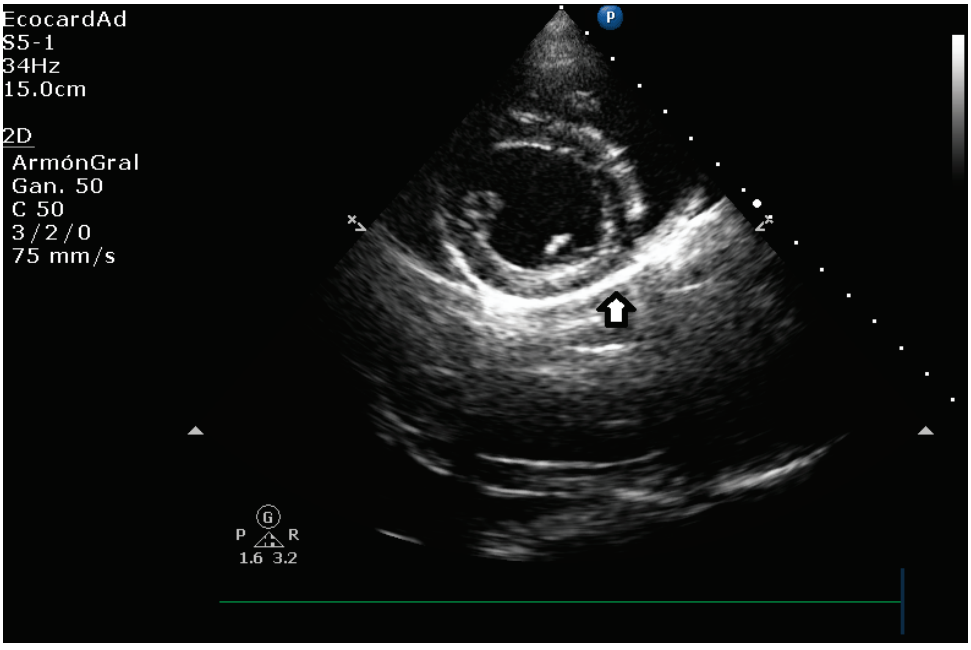

Figure 2. Right parasternal short axis view in the canine patient, showing pericardium as a hyperechoic line surrounding myocardium.

A dog's mean heart mass weight to body weight ratio is 0.9 to 2.2% of its body weight [10,11]. These measurements are likely to vary by breed. It has been reported that a human's mean heart mass weight to body weight ratio is 5 g per kilogram [11].

The pericardium surrounds the heart in humans and dogs, creating the pericardial cavity. The pericardium is attached to the diaphragm and sternum at the base of the heart. However, both species have different degrees of attachment to the diaphragm [8,12,13]. Humans have a firm and broad extension to the central tendinous aponeurosis of the diaphragm. On the other hand, dogs have a phrenopericardial ligament attached to the pericardium and, externally, a thin layer of mediastinal pleura attached to the pericardium, allowing the heart to be kept centered in the thorax [11].

The basic structure of the pericardium is very similar between the two species, but there are distinct differences [14–16]. Unlike other large mammals, where the thickness of the pericardial wall increases with heart size, humans have a thicker pericardium than animals with similar heart sizes [11]. In the human heart, the thickness of the pericardium is 2 mm or less [17], whereas the thickness of the pericardium in the dog is considerably thinner (0.18-0.20 mm) [11]. The normal pericardial fluid volume in most dogs is between 0.5 and 2.5 mL, and some dogs may have up to 15 mL, compared to volumes of 20–60 mL in adult human hearts [11–13].

3.1. Auricular Anatomical Coincidences

Similar to humans, the right and left atria of the adult dog heart are separated by the interatrial septum a muscular wall that extends from the base of the heart to the atrioventricular valves. The interatrial septum is composed of two layers: the muscular layer, which is continuous with the myocardium of the atria, and the membranous layer, which is a thin fibrous membrane that covers the muscular layer [7,11]. The cardiac base receives all the great vessels. It is generally cranially oriented and in mammals, including dogs, the orientation of the cardiac base is primarily determined by the animal's posture [9,13]. Recent studies suggest that cardiac orientation also varies with age and other factors, such as body size and physical activity [18]. Additionally, advances in imaging technology have allowed for more detailed visualization and understanding of the complex anatomical structures of the heart [19]. Symmetrically to humans, during fetal development, the human heart is structured to allow blood to flow directly from the right to left atrium, bypassing the lungs. This occurs via the foramen ovale, which is a small opening in the interatrial septum. The foramen ovale has a valve-like flap on the left atrial side, which prevents blood from flowing back into the right atrium when the left atrium contracts. Once the newborn begins to breathe air, the pulmonary circulation is established, and the foramen ovale usually closes, becoming a small depression in the interatrial septum known as the fossa ovalis [11,19]. In adults, the fossa ovalis is a slight depression on the right atrial side of the interatrial wall [13,19]. Dogs have more posterior fossa ovalis than humans [7].

In large mammals, the venous sinus is integrated into the right atrium and marked by the sinoatrial node. Dogs have the same atrial architecture, which includes the venous sinus, crista terminalis, fossa ovalis, and Eustachian valves (inferior vena cava and coronary sinus valves) [9,13]. Normally, there is an anterior (cranial or superior) and a posterior (caudal or inferior) vena cava. The location of the vena cava ostia entering the atrium may vary in some mammals [7,11,19]. Specifically, the inferior and superior vena cava ostia enter almost at right angles in animal models of large mammals, whereas in humans, they enter the atrium almost in line [9,11]. The inferior vena cava in domestic animals is usually long (>5 cm) in contrast to its short length in humans (1–3 cm) [7,11]. In most species, the coronary sinus ostium is located in the posterior wall of the right atrium, but its location may vary slightly. There are also considerable species differences in the number of pulmonary veins entering the left atrium. In human hearts, there are four [9,20,21] or occasionally five pulmonary veins, whereas in dog hearts, there are five or six [11]. In large mammals, the atria are separated from the ventricles by a fibrous tissue called the cardiac skeleton. The cardiac or fibrous skeleton is composed of dense connective tissue and consists of four fibrous rings that encircle the four heart valves - the mitral valve, tricuspid valve, aortic valve, and pulmonary valve. These rings provide support for the heart valves and help to maintain their proper position. In addition to the fibrous

rings, the cardiac skeleton also contains fibrous tissue that forms a barrier between the atria and ventricles. This barrier prevents the electrical signals that control the heart's contraction from spreading between the atria and ventricles, ensuring that the heart beats in a coordinated manner. The fibrous skeleton also serves as an attachment site for the heart's muscle fibers and for the connective tissue that surrounds the heart [11,22].

3.2. Ventricular Chambers in Both Species

With characteristics common to the human heart, the ventricles are the main ejection chambers of the heart. Therefore, their walls are much more muscular than the atria, making this normal function more efficient. Since the wall thickness of the right ventricle corresponds to approximately one-third of that of the left ventricle, the structure results in lower systolic pressure. The left ventricle exhibits a greater degree of muscularity compared to the right ventricle. This is because the left ventricle has to generate high pressure to propel blood through the systemic circulation, which comprises a larger network of blood vessels compared to the pulmonary circulation. In fact, systemic circulation has a resistance that is usually more than four times higher than pulmonary circulation, necessitating a greater contractile force in the left ventricular wall. To achieve efficient contraction of the heart, trabeculae are interlaced between the walls of both ventricles, primarily near the apex, thereby reinforcing the walls and increasing the force of systolic contraction. This intricate network of trabeculae, known as the trabecular network, plays a crucial role in maintaining the structural integrity and functionality of the heart [11,13]. Larger mammalian hearts have less ventricular trabeculation than normal adult human hearts, and the trabeculations are usually thicker than human hearts as a compensatory contractile phenomenon [7,9,11]. In dogs, the walls of the ventricles are attached to papillary muscles that support the atrioventricular valves.

The heart of a large mammalian animal, such as a dog, has three papillary muscles in the right ventricle and two in the left ventricle, similar to human anatomy. However, variations occur in individuals and species [7,8,11]. There are at least two chordae tendineae per papillary muscle to ensure redundancy. Both ventricles are traversed by fibrous or muscular bands containing Purkinje fibers. The dog's right ventricle usually has a prominent moderator band [7]. Species differ significantly in the origin and insertion of the band, as well as in its structure. In the dog, the septal wall near the base of the anterior papillary muscle extends into the lumen through one or more branched muscle filaments. Dogs' left and right ventricles are also structurally symmetrical to human chambers. At the opening of the septal leaflet of the mitral valve, the dog's left ventricle physiologically divides into an inflow and outflow region, exhibiting a conical structure [11,19].

3.3. Similarities in Cardiac Valves

The dog heart has four cardiac valves with structures and locations similar to humans. As illustrated in Figure 3, its transthoracic echocardiographic appearance and other cardiac structures are similar to that of humans. The heart has two atrioventricular valves and two semilunar valves situated between the ventricles and the outflow tracts of the pulmonary artery and aorta on either side. These valves play a critical role in regulating the flow of blood through the heart. The fibrous leaflets of the atrioventricular valves are connected to the papillary muscles of each ventricle by the chordae tendineae. This connection is essential in preventing atrial valve prolapse during ventricular contraction. On the other hand, the closure of the pulmonary, semilunar, and aortic valves does not involve chordae tendineae but instead relies on pressure gradients to facilitate their proper functioning [11,19].

In both dogs and humans, the tricuspid valve separates the right atrium from the right ventricle and is almost symmetric in structure. The right ventricle has three papillary muscles associated with it. In some cases, the anterosuperior and inferior leaflets of the tricuspid valve may appear to have only two leaflets in certain canine patients due to the fusion of their commissures [11]. Variations in the number of papillary muscles have been observed not only between different mammalian species but also among individuals

within the same species. These variations are important to consider when evaluating cardiac function and diagnosing any abnormalities or pathologies. The left atrium and left ventricle are separated by the bicuspid valve, which typically has two leaflets-anterior or septal and posterior or parietal. However, it has been reported in humans that the mitral valve may have multiple leaflets, with some individuals exhibiting significant variations in the number and morphologic variability of the mitral valve leaflets [23]. This anatomical variation is relatively rare, but it is important to be aware of it when evaluating mitral valve function or performing interventions on the valve. In both humans and dogs, there is a fibrous connection between the mitral and aortic valves that extends from the central fibrous body to the left fibrous trigone. This fibrous continuum is important for maintaining the structural integrity of the heart and for the proper functioning of the valves [7]. There are variations in the annulus fibrosus that support the mitral valve and its leaflets among different species. In humans, there is an annular segment at the base of the mural cusp. However, this segment can be difficult to identify in some breeds of dogs [11]. The semilunar pulmonary valve has a similar appearance to the aortic valve but is thinner. Unlike the aortic valve, there are no coronary ostia located behind the cusps of the pulmonary valve [7].

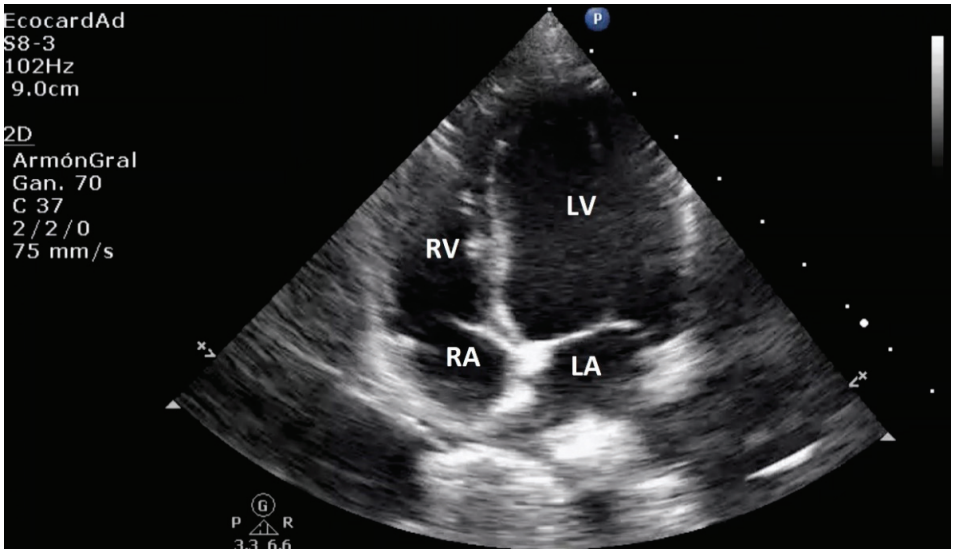

Figure 3. Right parasternal 4 chamber apical view demonstrates left and right ventricle, left and right atrium, and atrioventricular valve.

3.4. The Coronary System

In mammals, the intrinsic circulatory system consists of two main coronary arteries [7]; the coronary sinus is an essential pathway that connects the coronary veins to the right atrium. It is a complex network of tributary veins that returns deoxygenated coronary blood to the right atrium. Positioned posterior to the coronary sulcus, the coronary system has an orifice located in the medial and anterior area of the inferior vena cava's orifice. It is located immediately above the atrioventricular junction. A semicircular valve, known as the valve of Thebesius, guards the orifice of the coronary sinus, which is always located in the morphologic right atrium in a healthy individual [24]; The perfusion areas of large mammals differ between and within species; similar differences have also been described in humans. Dogs usually receive most of their myocardial supply from the left coronary artery, whereas in roughly 90% of human cases, the right coronary artery is dominant [11]. Normal human hearts show little development of coronary collateral circulation [25]. In contrast,

canine hearts present extensive coronary collateral networks located almost exclusively on the epicardial surface [11,26].

4. Myxomatous Mitral Valve Disease in Dogs as a Clinical Model in the Study of the Pathology in Humans

Myxomatous degeneration of the heart valves (MDMV) or myxomatous mitral valve disease (MMVD), which occurs in both canine and human patients, is a non-inflammatory pathology with a continuous progression of the valvular structure caused by a defect in the mechanical integrity of the leaflets as a result of altered synthesis and remodeling, and the continuous wear they receive as part of the disease mechanism. The presence of bulky and thickened valve leaflets is some of the most characteristic morphological abnormalities detectable by echocardiography (Figure 4). In addition, this pathology affects valvular and chordae tendineae integrity, which likewise shows thickening, elongation, and instability, and may rupture [27–29].

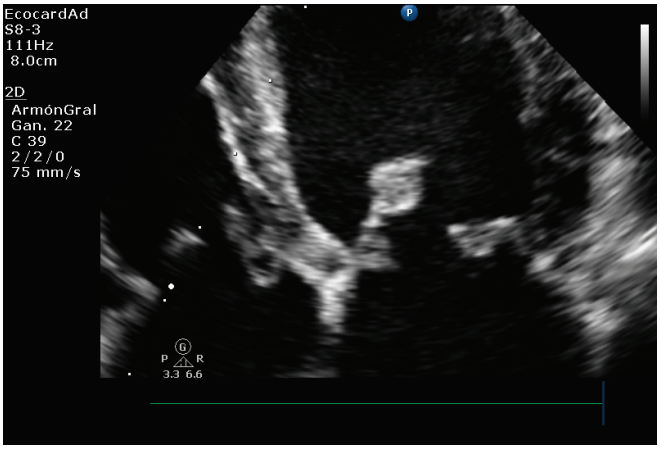

Figure 4. Myxomatous mitral valve degeneration in the canine patient's left apical 4-chamber view.

One of the main objectives of this review is to highlight the potential value of natural MMVD in the dog as a model for interdisciplinary echocardiographic clinical research.

5. (MDMV) Comparative Pathology and Pathophysiology

The mitral valve structure undergoes severe and repeated mechanical stress during systole, the pressure generated by the contracting left ventricle causes the valve leaflets to close, resulting in mechanical stress on the valve structure. The fibroblasts and myofibroblasts in the valve tissue respond to this stress by synthesizing and remodeling the extracellular matrix, which is the network of proteins and other molecules that provide support and structure to the valve tissue. This remodeling process involves the deposition of new extracellular matrix components, such as collagen and elastin, and the breakdown of old or damaged components. During diastole, the pressure in the left atrium decreases, and the valve leaflets open, resulting in flexion of the valve structure. The smooth muscle cells and interstitial cells in the valve tissue respond to this mechanical stress by contracting and relaxing, respectively, to help maintain the valve's shape and function. Furthermore, the endothelial cells that line the inner surface of the valve leaflets experience shear stress from the blood flow. These cells respond to this stress by releasing signaling molecules that regulate cell behavior and extracellular matrix synthesis, helping to maintain the valve's integrity and function [30,31]. The above occurs when the heart valves open and close more than three billion times in the half-life of a human adult and more than half a billion times in the half-life of a canine.

The mitral apparatus experiences the cardiac apparatus's most significant transvalvular pressure gradient [30]. During the contractile phase, the leaflets endure high degrees of tension and rapid mechanics of movement and stretching, constant tension, and, after complete closure, an extreme increase in tension and stiffness to avoid further deformation of the leaflets, and prevent the mitral regurgitation caused by the straightening of the collagen fibers within the leaflets [32,33].

The macroscopic and histological structures of the human and canine leaflets are similar [34,35] and are designed to withstand repeated stresses due to the specialized structure of the inner layers of the mitral leaflets [30,34,35]. The mitral valve is closely related to the fibrous skeleton of the heart, and the mitral annulus, in particular, is an important component of the fibrous skeleton that helps to maintain the shape and function of the valve [30,36]. The valvular annulus is the ring-like structure that supports the mitral valve and connects it to the heart's muscular wall. It serves as an anchor for the valve's leaflets, chordae tendineae, and papillary muscles, allowing for the proper opening and closing of the valve during the cardiac cycle. The shape of the valvular annulus is not flat but rather saddle-shaped, with a higher curvature at the anterior and posterior ends and a lower curvature at the lateral ends. This shape reduces the stress on the chordae tendineae and leaflets during systole when the valve is closed, as it allows for the distribution of the mechanical forces evenly across the valve. The saddle-shaped annulus also enables the valve to open and close more efficiently, reducing the strain on the valve and its components [30,37,38]. Other similarities of the mitral valve structure in dogs and humans include the continuity of the anterior leaflet with the aortic valve cusps at the aortic root and a branched network of chordae tendineae that connects to the anterior and posterior papillary muscle [19].

The mitral apparatus, which is present in both humans and dogs, consists of layers of extracellular matrix and connective tissue. The specialized innermost regions include a spongy region made of an extracellular proteoglycan matrix and a fibrous region composed of collagen that extends to the chordae tendineae. Valvular interstitial cells are also present in the valve [30,39–41]. Valvular interstitial cells are crucial for maintaining the structure and function of the mitral valve. They regulate the composition of the spongiosa and fibrosa to ensure proper balance between synthesis and degradation of extracellular matrix components. This helps maintain the integrity of the valve. The spongiosa, which is rich in proteoglycans, allows for absorption of large forces and stresses during closure. The leaflets of the valve are further reinforced by layers of collagen and elastin, which provide the necessary tensile strength during closure [30,39,42].

Some forms of mitral valve disease in humans and dogs involve the thickening of the leaflets and nodular growths along their edges, resulting in valvular insufficiency. Additionally, the expansion of the spongiosa and loss and disorganization of the collagen fibers in the fibrosa layer can lead to the rupture of the chordae tendineae [30,39] (Figure 5a,b).

Myxomatous mitral valve regurgitation is the most common type of valvular heart disease, affecting 0.6–2.4% of the population, and is the leading indication for surgical repair of the mitral valve in humans [30,43,44]. This condition is also known as myxomatous mitral valve disease or mitral valve prolapse syndrome. Understanding the pathophysiological mechanisms of this valvular lesion is crucial to manage this disease. Analyzing echocardiographic changes during the disease can help provide a better understanding of the disease and help stratify the risk in different populations of patients with this pathology.

The timely diagnosis of mitral valve prolapse syndrome and the determination of the ideal moment for its surgical correction is an essential factor in clinical cardiology. Chronic mitral regurgitation, due to the increasing average age of the population and the higher prevalence of myxomatous disease in the human population, occurs as frequently as aortic stenosis. Moderate or severe mitral regurgitation is found in 1.7% of the population worldwide and up to 9.3% of geriatric patients older than 75 years [44–46]. Echocardiographic techniques are the main tool for the evaluation of mitral regurgitation. In the current medical environment, echocardiography is more important than ever for diagnosing valvular

pathology that causes mitral regurgitation phenomena of varying severity and determining the timing of medical or surgical intervention. Important clinical indicators related to the stage of mitral regurgitation include patient symptoms, echocardiographic findings, and hemodynamic indicators, allowing cardiologists and cardiac surgeons to conduct a comprehensive assessment for optimal clinical outcomes [44].

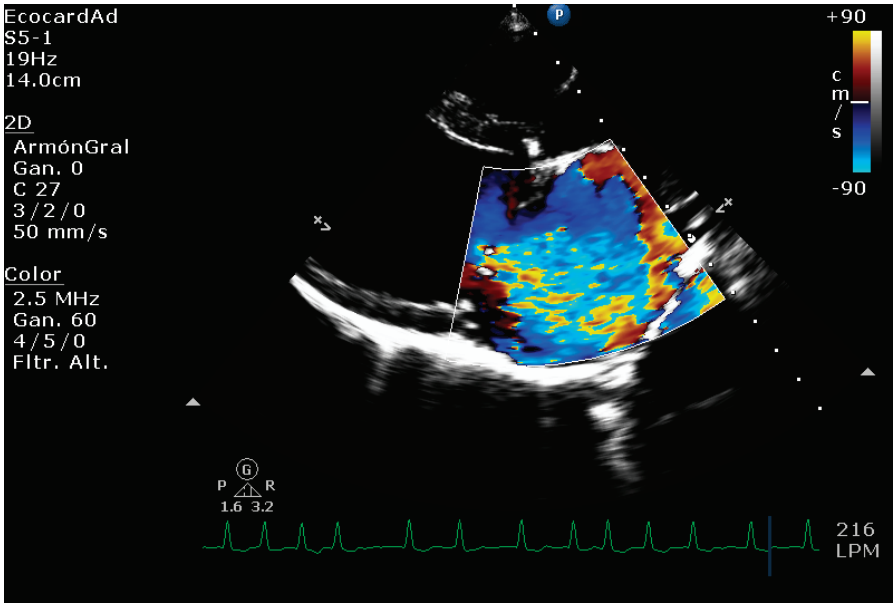

(**a**)

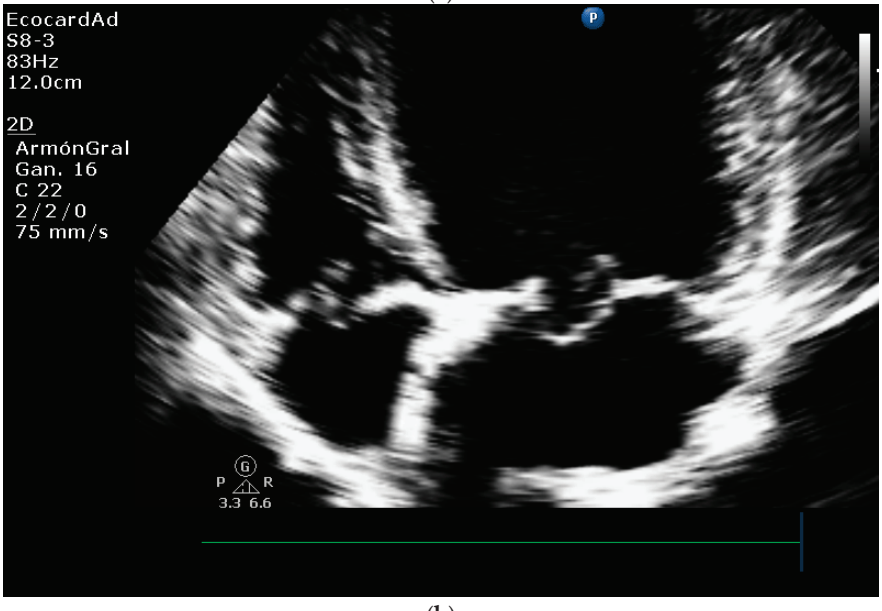

(**b**)

Figure 5. (**a**) Mitral insufficiency and (**b**) Septal leaflet prolapse associated with Myxomatous degeneration in a canine patient.

5.1. Mitral Valve Disease Epidemiology

Mitral regurgitation is a common valvular heart disease affecting millions of people worldwide. It is the third most common form of valvular heart disease, and its prevalence is estimated to be between 3–5% in the general population. Mitral valve prolapse is the most common mitral valve pathology, accounting for 2% to 3% of the total population [45]. The chronic degenerative nature of this pathology and the increased life expectancy probably contribute to these presentation rates [46]. Degenerative myxomatous mitral valve disease is dogs' most prevalent form of heart disease. In the same way, being a degenerative phenomenon, it is more present in geriatric patients [30,47].

Degenerative myxomatous mitral valve disease is commonly observed in other small dog breeds with less than 15 kg of body weight, such as Miniature Poodles, Miniature Schnauzers, and Chihuahuas [48–52]. In fact, this pathology accounts for a substantial proportion of all heart disease cases in dogs, amounting to around 75% of cardiac clinical cases [51].

Mitral valve prolapse is a condition commonly observed in Cavalier King Charles Spaniels, characterized by the failure of the left atrioventricular valve to close properly due to the accumulation of abnormal myxomatous material and nodular changes on the valve leaflets. This condition is prevalent in a significant percentage of Cavalier King Charles Spaniels, ranging from 11.4–44.95%, and is often accompanied by age and sex-dependent heart murmurs. This degenerative valve disease is similar to myxomatous valvular degeneration, also known as valvular endocardiosis. Although tricuspid valve involvement is less frequent, it can still occur. What makes Mitral valve prolapse in Cavalier King Charles Spaniels unique is that it tends to occur at a younger age, with almost 19% of dogs under one year of age exhibiting heart murmurs, and likely more than 50% of dogs over five years of age displaying murmurs [50,51].

Degenerative mitral valve disease is a prevalent cardiac condition affecting dogs and humans, characterized by progressive degeneration of the mitral valve leading to mitral regurgitation. The clinical presentation varies in both species and can range from mild asymptomatic regurgitation to severe mitral insufficiency with congestive heart failure [52]. In dogs, valvular degeneration, mitral regurgitation, eccentric cardiac hypertrophy, systolic dysfunction, left heart failure, and congestive heart failure are the clinical consequences of severe Degenerative mitral valve disease. In addition. Cardiac mortality within six years of diagnosis of mitral valve disease is 11% in dogs [53,54]. Although surgical repair is associated with better outcomes, it is not widely available due to its high cost and the limited number of veterinary medical units that perform the procedure. Therefore, medical treatment with loop diuretics, Angiotensin-converting enzyme inhibitors, aldosterone receptor inhibitors, and inodilators or positive inotropes is the standard of care for dogs with severe mitral regurgitation and secondary congestive pulmonary edema [30,54,55].

The clinical course of Degenerative mitral valve disease in dogs begins with mild asymptomatic mitral regurgitation, progresses to varying degrees of mitral insufficiency with eccentric left ventricular hypertrophy and atrial enlargement, and commonly escalates later to severe mitral insufficiency with clinical signs of congestive pulmonary edema, typically occurring during the relatively short adult lifespan of the dog compared to humans [30].

5.2. Canine Myxomatous Mitral Valve Disease. Comparative Transthoracic Echocardiography with Human Mitral Valve Prolapse

Many diagnostic methods exist for evaluating mitral valve disease in human and small animal medicine. Transthoracic echocardiography is a basic and primary test for establishing both species' diagnosis and prognostic profile of mitral valve disease. TTE enables clinicians to identify mitral valve lesions, classify the extent and type of regurgitation, evaluate the severity of cardiac remodeling, assess myocardial function, and measure left ventricular filling pressures and pulmonary artery pressure, providing a comprehensive evaluation of cardiac health [56–58]. Various types of ultrasound imaging technologies are

available and frequently employed in veterinary and human cardiology. These include traditional methods such as two-dimensional (2D) Doppler echocardiography, M-mode, color Doppler, pulse wave (PW), continuous wave (CW), as well as newer and more advanced techniques such as tissue Doppler (TDI), two-dimensional speckle tracking echocardiography (STE), and strain and strain rate ultrasound. These echocardiographic techniques in parallel settings can assess and monitor regional and global myocardial function and stratify the severity and progression of mitral valve pathology [59–61]. While the evaluation of mitral regurgitation and chronic heart failure severity in dogs with mitral disease shares similarities with that in human patients, veterinary cardiologists prioritize assessing the extent of cardiac remodeling and dysfunction as a result of mitral regurgitation.

5.3. Comparative Assessment of Mitral Regurgitation Severity

In order to assess the severity of a valvular defect, color flow and continuous wave signals of mitral regurgitation jets (CW) are utilized in both humans and animals. Still, a more quantitative approach is required on both species to determine mitral regurgitation severity. This quantitative assessment is commonly used in humans to grade the severity of mitral regurgitation [61]. Although a quantitative assessment of mitral regurgitation (MR) is commonly used to grade the severity of MR in human patients, it is seldom utilized in veterinary medicine. This is because the practical application of this method is limited in dogs, and defining the location of effective regurgitant orifice area (EROA) and the flow convergence shape in canine patients with mitral regurgitation can be challenging [60].

5.4. Mitral Regurgitation Quantification in the Canine Model

The Proximal Isovelocity Surface Area (PISA) method is a widely accepted gold standard for quantifying the extent of mitral regurgitation jet in humans [60,61]. While a clinical study has shown that this method is repeatable and reproducible in awake dogs [62], it is less practical and requires several precautions to obtain optimal flow convergence images in dogs with mitral disease [63,64]. Therefore, in veterinary practice, the use of PISA should be employed with caution, taking into account the potential limitations and technical challenges associated with its application. The severity of mitral regurgitation in dogs can be determined by the regurgitation fraction (RF) obtained through the proximal isovelocity surface area (PISA) method. Several studies have demonstrated that RF is closely associated with the severity of degenerative valve disease and other important echocardiographic indicators, such as the ratio of the left atrium to the aorta (LA/Ao) and pulmonary artery systolic pressure [62,65]. A different clinical study found that PISA quantification of mitral regurgitation showed a wide range of RF, which is why it is not routinely performed in cardiologic evaluation in dogs [62].

The severity of mitral regurgitation can be semi-quantified using color-flow Doppler to measure the mitral regurgitant maximum jet area (MRA) ratio in relation to the left atrial area (LAA). This method has been validated in dogs and demonstrates a strong correlation with Doppler-derived regurgitant volume and effective regurgitant orifice area, making it a reliable tool for assessing mitral regurgitation severity [66,67]. In human medicine, mitral regurgitation has been widely studied, and there are several stratification scales and widely disseminated echocardiographic evaluation guidelines [61,68,69]. In the same way, as in TTE studies of canine patients, the characteristics and changes in mitral structure and morphology and signs of valvular remodeling are evaluated. Doppler technology is also useful for assessing mitral regurgitation qualitatively, semi-qualitatively, and quantitatively.

Most of the echocardiographic variables used in the human patient have been studied in domestic canine medicine; in the same way, these methods require extensive training to obtain repeatable results in the measurements and avoid measurement variability in the generation of erroneous results [70]. Color flow imaging of the mitral regurgitation jet area is the most commonly used technique for assessing the severity of mitral regurgitation in dogs. The former method is not used in humans, as it is not considered reliable for determining the severity of mitral insufficiency [68,69]. This method has become widespread in the

domestic canine patient because it is easy to perform; however, some studies have indicated that the correlation of the jet area with the severity of mitral regurgitation is poor, as well as its reproducibility [67]. One of the most commonly used semiqualitative techniques in veterinary TTE is the measurement of the effective regurgitant orifice or the width of the vena contracta. This method, compared with other qualitative methods, is equally useful for evaluating eccentric and central jets. However, it is unreliable in multiple jets as it depends on the geometry of the regurgitant orifice [69]. A study in dogs with Mitral Myxomatous Degeneration reported that vena contracta and E-vel correlated strongly with mitral regurgitant fraction reported in cardiac MRI studies.

However, E-vel had superior repeatability, being more reliable in dogs [71]. Among quantitative methods, proximal isovelocity surface area assessment is one of the most widely used methods to evaluate the effective regurgitant orifice area and regurgitant volume. However, its reliability in eccentric jets has been questioned [69,72]. Another important fact is that echocardiographic dynamic behavior and variability of mitral regurgitation in patients with mitral valve prolapse has been described in dogs, which should be considered an inherent limitation of the proximal isovelocity surface [73]. Different authors have described real-time three-dimensional echocardiography as a useful tool to evaluate the effective area of the regurgitant orifice in dogs with MMVD [73,74]. The above technique is not widely used due to the need for highly trained personnel and high equipment costs for its implementation in clinical veterinary practice. Other quantitative methods based on spectral Doppler for assessing effective regurgitant orifice areas and regurgitant volumes, such as the mitral inflow method and systolic volume requirement, are impractical in veterinary medicine, and humans are not recommended as a first-choice method for quantifying the severity of mitral regurgitation [68,69,71].

The clinical stage classification of canine patients with MMVD should be based on ACVIM guidelines, which recommend using LA/Ao and LVIDDn to determine the degree of cardiac remodeling [55]. A study involving 558 dogs with MMVD found that LA/Ao > 1.7 was the most significant prognostic index among the echocardiographic indices currently used in veterinary cardiology [75]. Recently, a specific score, the proposed MINE score, relies on four distinct echocardiographic indicators [70]: (1) the left atrium to aorta (LA/Ao) ratio is determined from the right parasternal short-axis view [76]; (2) the left ventricular end-diastolic diameter is adjusted for body weight to obtain a normalized value. This approach allows for a more accurate interpretation of the data, since the size of the left ventricle can vary significantly based on the size of the animal (LVIDDN), obtained in M-mode and in the right parasternal short-axis projection [77]; (3) the left ventricular shortening fraction (FS) is obtained in M-mode obtained in the right parasternal short-axis window [77]; and (4) the maximum velocity of the E-wave transmitral flow (E-vel) is commonly obtained using pulsed Doppler imaging in the left apical four-chamber projection [78]. The above protocol has been proposed as a staging tool for the severity of myxomatous mitral valve disease in dogs. For the purpose of evaluating left-sided cardiac remodeling, left ventricular dynamics, and left ventricular filling pressure, the authors of this study selected four key echocardiographic variables [70]. These variables include LA/Ao and LVIDDN for the assessment of left cardiac remodeling, FS for left ventricular function, and E-vel for evaluating left ventricular filling pressure, all of which are echocardiographic variables evaluated in the mentioned study. The MINE scores have prognostic value in dogs with myxomatous mitral valve disease.

5.5. Left Heart Remodeling Assessment and LA Evaluation

Chronic, hemodynamically significant mitral regurgitation can lead to volume overload of the left atrium (LA) and left ventricle (LV), resulting in the enlargement of both chambers of the heart. To assess the severity of LA and LV remodeling, several indicators can be evaluated, including the LA-to-aortic root ratio (LA/Ao), indexed LA diameter, LV end-diastolic internal dimension to aortic root ratio (LVID/Ao), and LV internal dimension at end-diastole (nLVID). These parameters can provide valuable information about the

degree of cardiac remodeling and guide management decisions for patients with chronic mitral regurgitation [36].

Estimating the diameter of the left atrium (LA) is a highly reliable indicator of prognostic outcomes in dogs with mitral valve disease (MMVD) [54]. It also enables the decision to initiate medication in dogs with preclinical MMVD and to estimate the risk for the development of left-sided congestive heart failure (CHF) [79]. When evaluating dogs with MMVD, assessments of left atrial and left ventricular chamber dimensions can aid clinicians in predicting the likelihood of disease progression and the risk of developing congestive heart failure [79,80]. The extent of left atrial enlargement is significantly associated with the progression of congestive heart failure and the survival rates of both symptomatic and asymptomatic dogs with MMVD [57,65].

5.6. Comparative Left Ventricle Assessment

Systematic left ventricle evaluation provides important information to assess the severity and progression of degenerative mitral valve disease. The mechanisms involved in LV remodeling and enlargement resulting from mitral regurgitation are a set of complex mechanical wear and tear mechanisms and cellular and structural responses to that stress [81], leading to a progressive increase in end-diastolic and end-systolic volume. Research in canine patients identified an allometric relationship between body weight and LV end-systolic diameter (LVID) and LV end-diastolic diameter (LVIDd) in the M-mode approximation [82], which now allows prediction intervals to be determined for a wide range of canine patients' body weights. It was standardized that using the dimensions of the LVIDd in M-mode divided by the body weight of the dog raised to the power of 0.294 ($BW^{0.294}$) should be found in the reference values of $\leq$1.85, in addition to the LVID values obtained in M-mode divided by the body weight of the dog raised to the power of 0.315 ($BW^{0.315}$) must be in the cutoff point of $\leq$1.26; values greater than these indicate LV enlargement in the canine patient. There are scenarios where the systolic function can be affected in dogs with MMVD [82]. However, the evaluation of systolic function in dogs presents challenges in its assessment due to the change in ventricular load conditions. With disease progression, mitral regurgitation results in a gradual increase in preload and a slight decrease in afterload. There is a significant impact on all non-invasive indicators of cardiac function as a result of these changes. A hyperdynamic ventricle commonly increases fractional shortening and ejection fraction, reducing its sensitivity for detecting LV dysfunction in patients with this pathology [83]. With this pathology, increased left ventricular dimensions at the end of systole could indicate a decrease in systolic function. Considering the relationship between this measurement and patient weight, an allometrically scaled LVID > 1.26 suggests an increase in LVIDs, which may indicate LV systolic dysfunction in patients with MMVD [82].

5.7. Key Main Useful Echocardiographic Considerations for the Approach of Mitral Endocardiosis in Canine Patients

5.7.1. Evaluation of the Regurgitant Area

It corresponds to a semi-quantitative analysis that evaluates the route of the regurgitant flow. For example, in the left apical four-chamber or right parasternal four-chamber view, the color Doppler mode will allow us to obtain its area, called the regurgitant jet area (Figure 6), and compare it with the area of the left atrium.

This technique is a reliable diagnostic approach with good repeatability and reproducibility when performed by a trained clinician. It can be used to assess the severity of mitral regurgitation by measuring the regurgitant volume and calculating the regurgitant fraction. A regurgitant fraction of less than 30% indicates mild mitral regurgitation, while a regurgitant fraction between 30% and 70% indicates moderate regurgitation. A regurgitant fraction greater than 70% indicates severe regurgitation. However, it is important to note that this method has limitations. The accuracy of the measurements is influenced by factors such as systolic blood pressure, left atrial pressure, jet direction, the frequency of the

transducer, and the gain level. Clinicians should be aware of these limitations and use their clinical judgment when interpreting the results. In some cases, additional diagnostic tests or assessments may be necessary to fully evaluate the severity of mitral regurgitation [84,85].

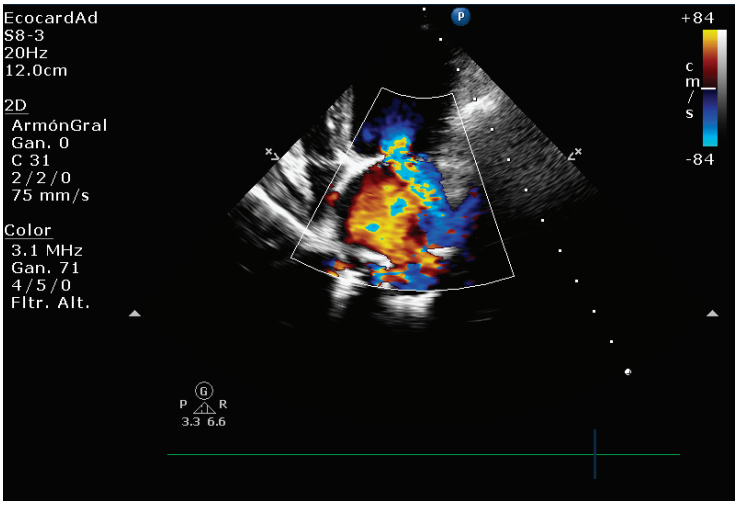

Figure 6. Severe mitral regurgitation in the canine patient.

5.7.2. Presence of Vena Contracta

The vena contracta is a simple and reproducible method. It is defined as the narrowest area of the regurgitant jet, immediately below the anatomical orifice, as shown in Figure 7. The width correlates with the size of the regurgitant orifice. It is measured in the parasternal long axis or apical planes, moving the color baseline in the direction of the jet up to a Nyquist velocity that identifies the narrowest area of the jet (40–70 cm/s). Other methods must be used for intermediate values or multiple jets [54,85,86].

5.7.3. Degree of Myxomatous Degeneration

Nodules appear at the free edges of the leaflets with myxomatous degeneration, along with the thickening of the chordae tendineae, as shown in Figure 8. The nodules can fuse as they enlarge, resulting in a generalized mitral valve thickening. A rupture of the chordae tendineae can cause the valve to lose its support, further aggravating regurgitation. These abnormalities have different consequences depending on their deformation, retraction of valve leaflets, and chordae tendineae condition [82,84,85,87–89]. The mitral valve leaflets appear remodeled and thickened in a two-dimensional mode, with an irregular nodular appearance.

5.7.4. Mitral Valve Prolapse

It is characterized by the movement of one or two leaflets beyond the annular plane of the mitral valve in systole. When the chordae tendineae rupture, all or part of the affected leaflet usually prolapses into the left atrium in systole. The severity of the prolapse correlates with the stage of mitral regurgitation. The rupture of the chordae tendineae corresponds to a relevant situation since they determine the final systolic position and tension of the mitral valve leaflets, and contribute to the systolic closure of the mitral valve. Myxomatous degeneration can lead to chordae tendineae rupture, aggravating pre-existing mitral regurgitation [84,85,87,88].

Primary rupture of the chordae tendineae can lead to a complete loss of tension in one of the leaflets, which generates a movement that shows the dance of the chordae tendineae, known as “flail”. This event leads to an abrupt worsening of mitral valve regurgitation,

which in the worst case, will cause acute congestive heart failure (CHF). Ruptured chordae tendineae can be seen using traditional two-dimensional TTE, as shown in Figure 9 [84,85].

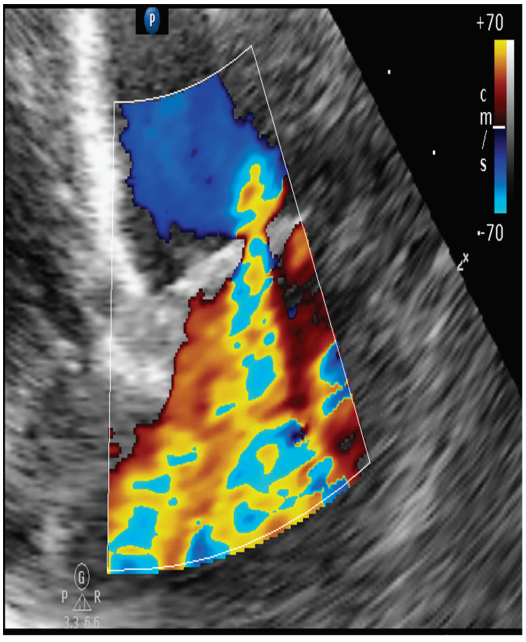

Figure 7. Mitral regurgitation due to myxomatous degeneration with severe regurgitation. The presence of vena contracta that demonstrates greater severity is associated with non-coaptation of the valve leaflets.

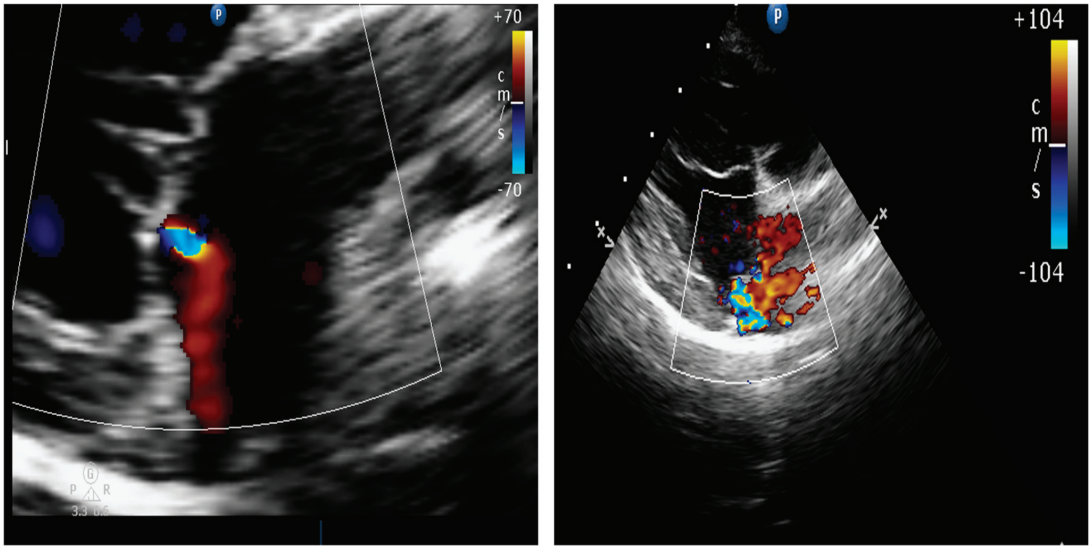

Figure 8. Mitral regurgitation in dogs due to myxomatous degeneration. Different degrees of valvular degeneration.

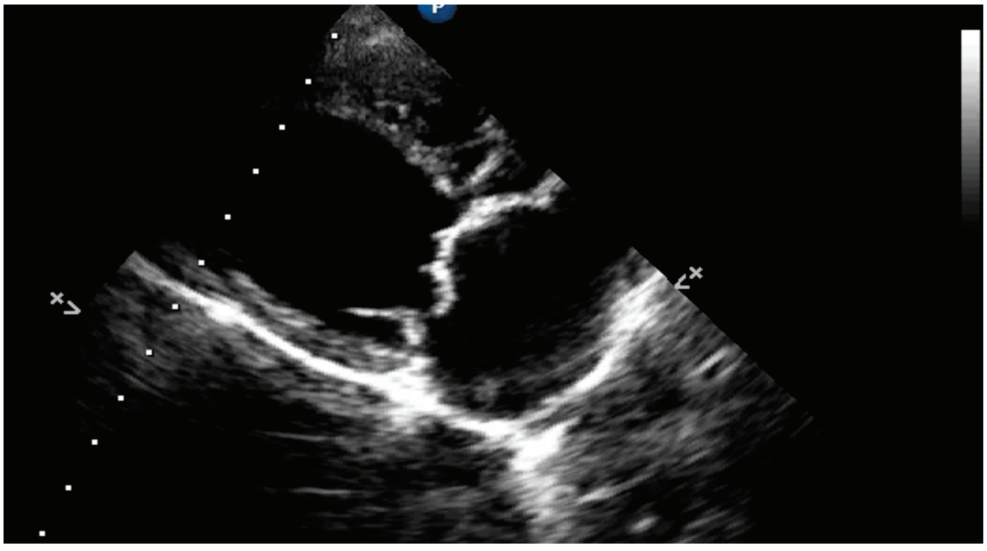

Figure 9. The presence of mitral valve septal leaflet prolapse is associated with tendinous chord rupture in the canine patient.

5.7.5. Vmax Wave E

The maximum velocity of the E wave is influenced by atrial filling (preload) and the diastolic properties of the left ventricle, as shown in Figure 10. The maximum velocity of wave E tends to increase with preload, but only up to a certain point. The relaxation rate of the left ventricle decreases earlier in the development of congestive heart failure [54,67,85,90,91].

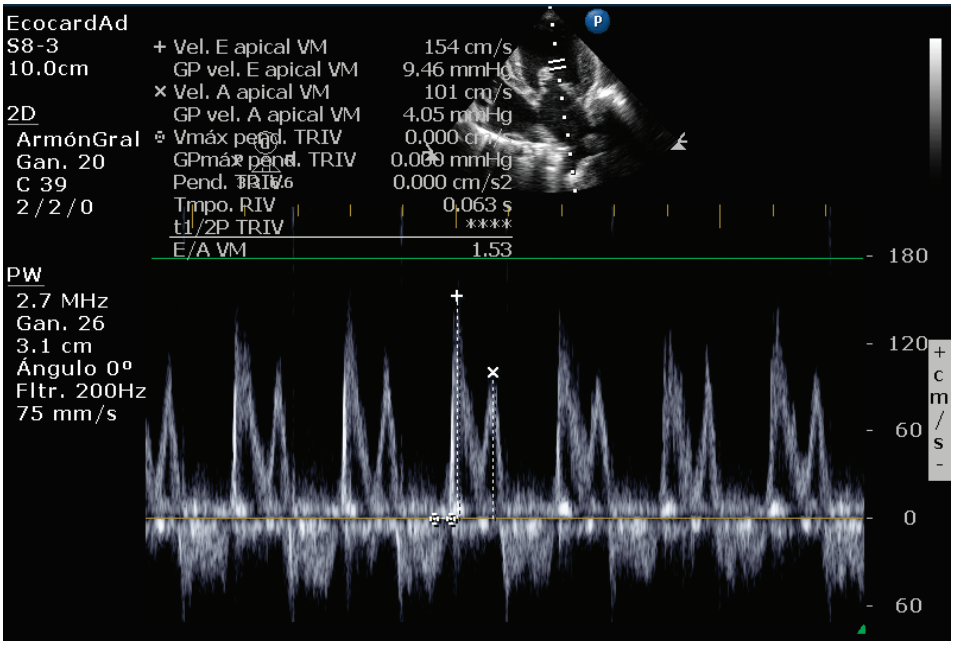

Figure 10. Transmitral Doppler shows increased E-wave velocity in a dog.

An E wave peak velocity greater than 1.2 m/s is associated with increased intra-atrial pressure; we can attribute the responsibility of pulmonary edema to the presence of congestive heart failure with values higher than these.

5.7.6. E-Wave Deceleration Time

The literature review revealed that TDE is the parameter with the highest correlation with pulmonary capillary pressure in mitral regurgitation patients with systolic dysfunction. Values below 80 cm/sec are recognized as diminished [85,91,92].

5.7.7. E/IVRT Ratio

An IVRT cutoff value < 45 ms and E/IVRT > 2.5 large diastolic filling pressures are seen as decisive in considering the possibility of congestive heart failure, as shown in Figure 11 [54,67,85,90,91,93].

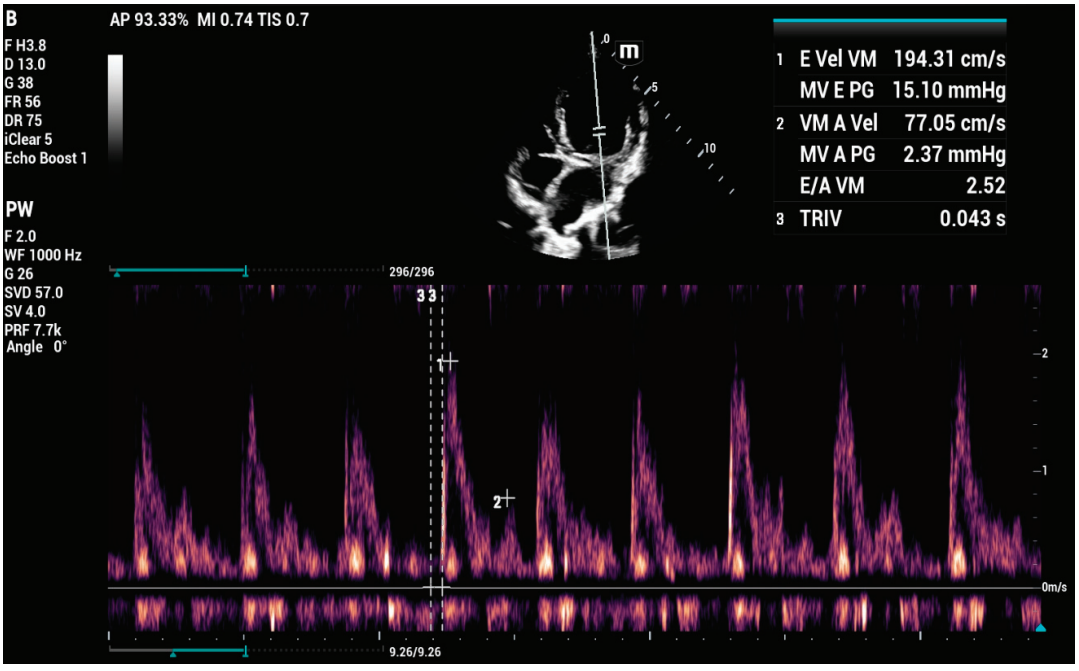

Figure 11. Increased E/IVRT ratio in a canine patient showing a restrictive pattern with mitral valve insufficiency and cardiogenic pulmonary edema.

5.7.8. E/é Ratio of the Mitral Annulus

An E/e ratio > 11.5 in the case of patients with mitral valve insufficiency suggests an increase in the pressure of the pulmonary capillary above physiological levels, as shown in Figure 12. It generates the possibility of presenting congestive heart failure. A cardiogenic origin can be established in patients with pulmonary edema [53,67,85,90,91,93–95].

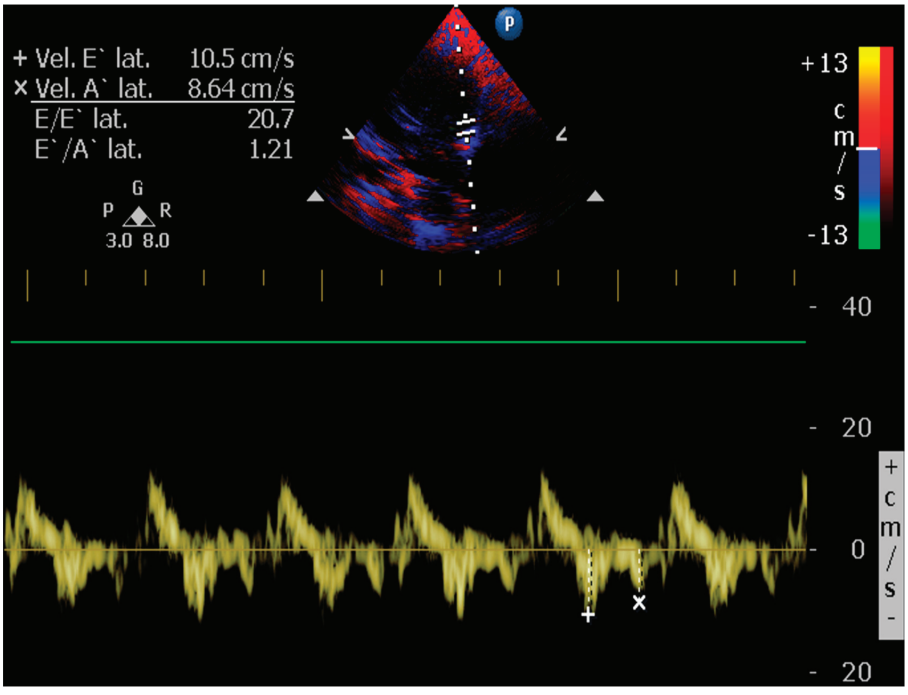

Figure 12. Altered E/e ratio in a canine patient with congestive heart failure.

6. Dilated Cardiomyopathy (DCM), a Human and Canine Common Disease

Cardiomyopathies are cardiac muscle disorders that could lead to mechanical and electrical heart malfunctions [96,97]. Cardiovascular disease is the fourth most common cause of death in dogs [98] and one of the most prevalent causes of death in humans [99]. Dilated cardiomyopathy (DCM) is the second most prevalent form of heart disease in domestic canines, accounting for 10% of heart disease in this species [97]. It is estimated to be the third most common hereditary heart disease in humans, affecting 35 patients in every 100,000, according to data that are considered underestimated [96].

Due to the similarities of DCM in humans and dogs regarding phenotypic characteristics and pathology progression, studies have suggested that canine MCD may act as a model for this pathology in humans. The above may apply to other fields, such as comparative clinical imaging research [100]. The scientific observation of the clinical course of this disease in the dog can guide improvements in clinical care and echocardiographic techniques in both canine and human patients.

Animal models of dilated cardiomyopathy are a useful research area because they can provide relevant information on the disease's cellular, structural, and hemodynamic progression, which is essential in improving treatment regimens [101], interventional procedures, and diagnostic imaging techniques. While there are many animal models in which dilated cardiomyopathy is induced, naturally occurring cases in dogs are particularly valuable concerning the disease's natural progression, especially when the underlying mechanisms are similar in dogs and people [96]. In addition to providing a potential natural model for human DCM in canines, it is potentially useful for studying new strategies and technologies for echocardiographic diagnosis in humans.

A significant association exists between dilated cardiomyopathy and congestive heart failure in dogs characterized by enlargement and impaired left ventricle contraction [96,102]. It is possible to classify dilated cardiomyopathy into three major stages [96]. At stage one, the heart appears normal, with no clinical evidence of cardiac disease, and often includes

dogs genetically predisposed to this pathology [96]. Stage two, classified as the preclinical or occult phase, involves morphologic and electrical changes in the heart, but with no overt clinical symptoms. Finally, stage three includes clinical signs of congestive heart failure [96].

The ideal standard approach for diagnosing DCM is based on 24 h echocardiographic and electrocardiographic (ECG) evaluations and monitoring the clinical presentation and patient progress [103]. In addition to a color Doppler echocardiographic evaluation, an electrocardiogram should also be performed simultaneously. The basic protocol includes all measurements performed in triplicate for volume and, ideally, five sequential cardiac cycles for M-mode testing [96]. Congenital or acquired heart disease other than DCM may also cause volume overload, systolic dysfunction, or both, and must be distinguished as a differential diagnosis in the dog. Volume overload in dogs can be caused by pathologies such as patent ductus arteriosus, ventricular septal defect, mitral valve dysplasia, and the myxomatous degeneration of the mitral valve [102].

6.1. Echocardiographic Measurements on DCM

Experience and clinical evidence point to TTE as a sensitive and specific medical resource in diagnosing dilated cardiomyopathy in dogs with congestive heart failure due to heart failure with reduced ejection fraction [104].

6.1.1. Measurement of Left Ventricular Volume by Simpson's Method of Disks and Left Ventricular M-Mode

M-mode echocardiography is widely used in canine cardiology. Its one-dimensional nature limits the spatial information it provides, and the technique is based on geometric assumptions, which may vary according to the heart disease conditions, as shown in Figure 13 [102,103]. The American Society of Echocardiography recommends against using linear measurements to calculate left ventricular volume in the human patient and suggests that the biplanar Simpson's disk method (SMOD) is more suitable for this purpose [100]. Similarly, in a clinical study in dogs, the SMOD method was more sensitive than M-mode for detecting the presence of early echocardiographic changes, as shown in Figure 14a,b [96], and these results recommend that SMOD reference values should be used as a priority in the detection of early changes [103].

LV volume using the SMOD method is calculated in the right parasternal four-chamber long-axis view and in the left apical four-chamber view (in this technique, the aorta should not be visualized in either of these views), and it is important to trace the endocardial border in each image used. The image frame used to measure end-diastolic volume is selected by referencing the frames related to the onset of the QRS complex signaled by the synchronous electrocardiographic trace when the mitral valve is closed and the volume is at its peak. When measuring end-systolic volume in the heart, cardiologists choose the final frame just prior to the opening of the mitral valve. This is often the frame that follows the end of the T wave on an ECG and corresponds to a point in the cardiac cycle where volume is at its minimum. By selecting this specific frame, clinicians can obtain an accurate assessment of the heart's function. The right parasternal and left apical views should be measured, and larger volumes should be used, reducing the possibility of volume underestimation. It is important to note that the natural tendency for apical shortening in the heart can result in an underestimation of end-systolic and end-diastolic volumes. This phenomenon can complicate the interpretation of echocardiographic data [96].

The SMOD formula is a commonly used method to estimate left ventricular volume. This formula is based on tracing the endocardial border through the mitral valve annulus and measuring the longitudinal axis of the left ventricle. The left ventricular cavity is then divided into 20 disks of equal height to calculate the volume of the left ventricle. The cross-sectional area of each disk is determined by measuring the diameters of the left ventricle from two orthogonal views, which allows for a more accurate calculation of left ventricular volumes, and the end-diastolic (EDV) and end-systolic (ESV) volumes should be calculated

by the sum of the stacked disks, which is determined by the software of the current echocardiography equipment. The quantified volumes can be normalized concerning body surface area to obtain volume indices (EDV-I and ESV-I). Current guidelines indicate that an ESV-I greater than 80 mL/m^2 indicates systolic dysfunction [96,102]. Ejection fraction (EF) is calculated similarly to fractional shortening, but volume measurements are determined using the formula presented below:

$$EF = (EDV - ESV)/EDVEF = EDV - ESV/EDV$$

Ejection fraction (EF) considers radial and longitudinal cardiac variations, and dogs with ejection fraction less than 40% are considered to have reduced contractile capacity [102].

6.1.2. E-Point to Septal Separation or EPSS: An Echocardiographic Parameter for Accurate Assessment of Left Ventricular Performance

The separation between the E point and the septum should be measured in the right parasternal long axis or the parasternal short axis at the level of the tip of the mitral septal leaflet. The separation between the E point and septum refers to the distance between the mitral septal leaflet's peak early diastolic motion (E point) and the interventricular septum. A recent study in dogs evaluated EPSS as a technique for detecting occult dilated cardiomyopathy in Doberman canine patients. It demonstrated that EPSS greater than 6.5 mm is a valuable additional variable for diagnosing DCM. Incorporating the E point in the septal separation (EPSS) measurement, in addition to M-mode measurements, can enhance the sensitivity and specificity of cardiac evaluations, comparable to volume measurements obtained using the Simpson's biplane method of disk summation or SMOD [96], as seen in Figure 15.

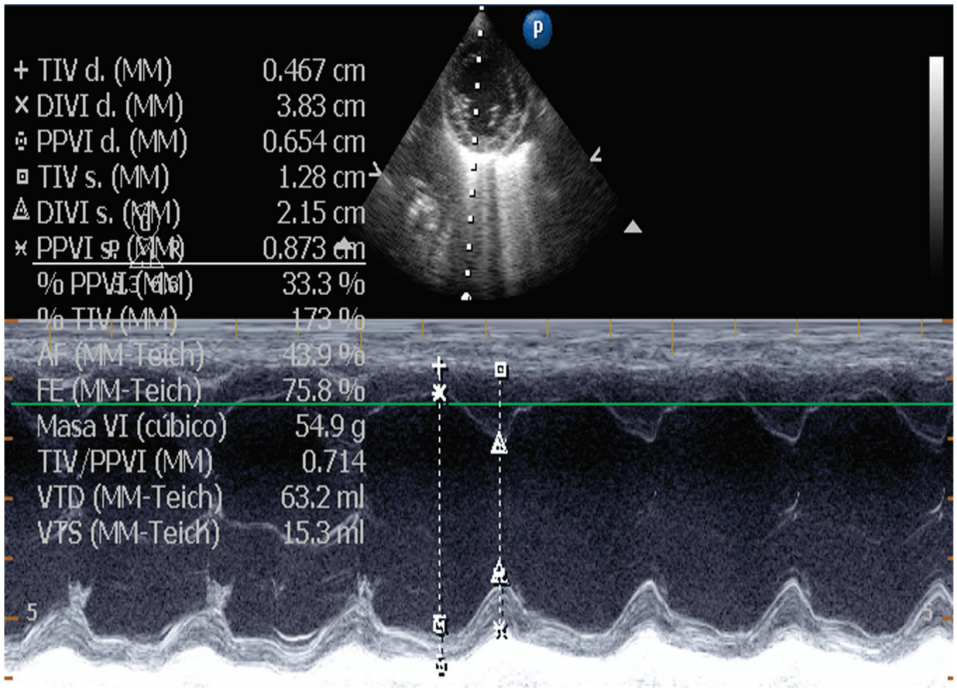

Figure 13. Left ventricular M-mode measurements in a dog.

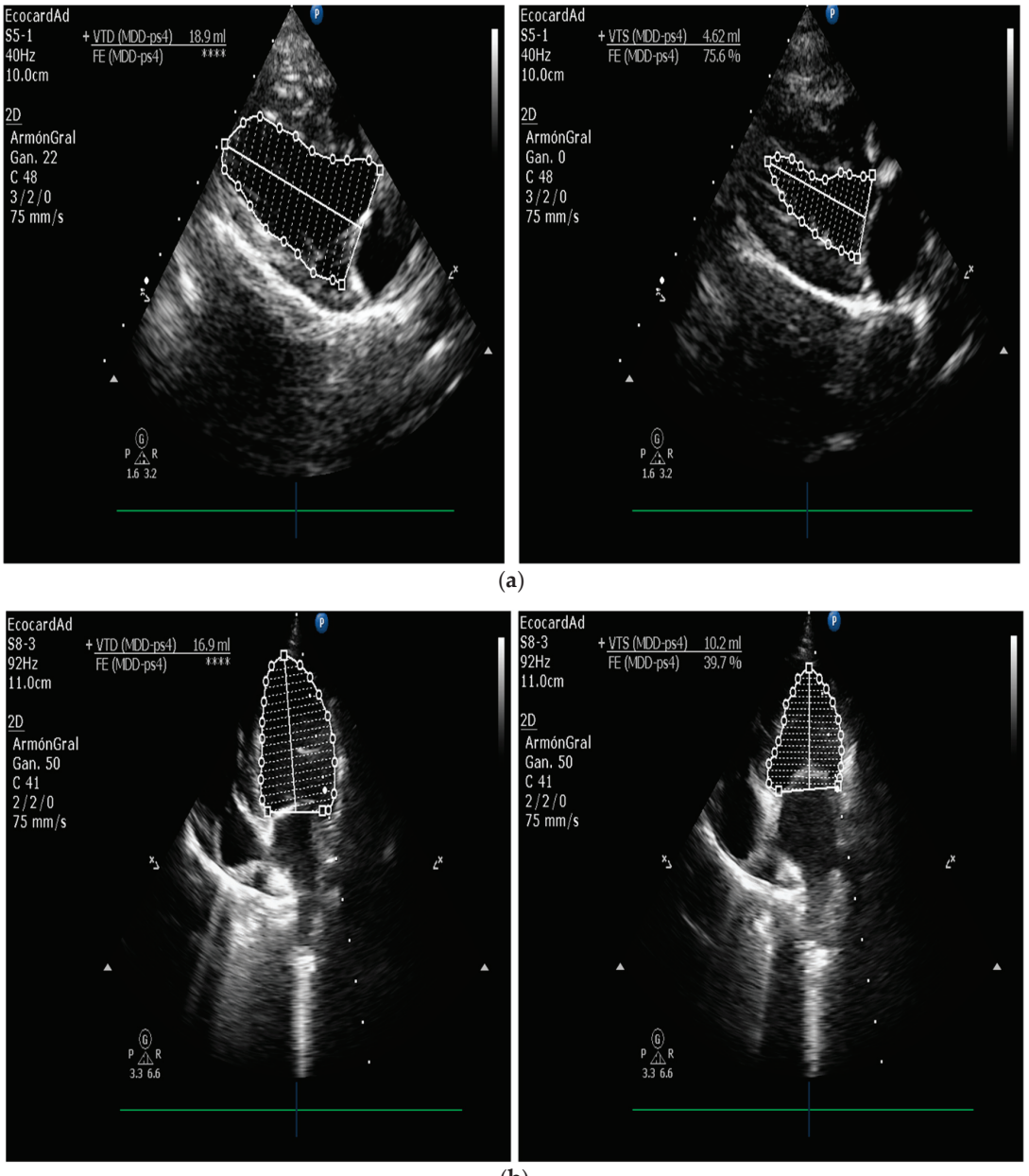

Figure 14. (**a**,**b**). Left ventricular volume by Simpson's method of canine disk patient.

6.1.3. Sphericity Index (SI)

Assessing the left ventricle's geometric shape or sphericity can be achieved by comparing the diastolic length. This measurement can be obtained from the right or left parasternal long axis views, as well as the apical four-chamber view acquired at end-diastole using the SMOD technique. However, it is crucial to exercise caution when measuring the apical LVIDd in M-mode to avoid any potential measurement-shortening. The Sphericity Index

is calculated by dividing the LV diastolic length by the left ventricular diastolic width at diastole. A Sphericity Index value less than 1.65 indicates increased sphericity and is considered abnormal according to the European Society of Veterinary Cardiology guidelines [45]. A study in dogs concluded that a value less than 1.65 is also the best cutoff point for identifying occult DCM in Doberman canine patients. However, it has been found that the sensitivity and specificity of SI, when used as the sole measure, is not sufficiently robust (sensitivity 86.8%, specificity 87.6%) compared to other standard volume estimates such as SMOD and EPSS. Due to the above points, its inclusion as a recommended parameter in standard monitoring protocols for dogs is not highly recommended, as shown in Figure 16a,b [96].

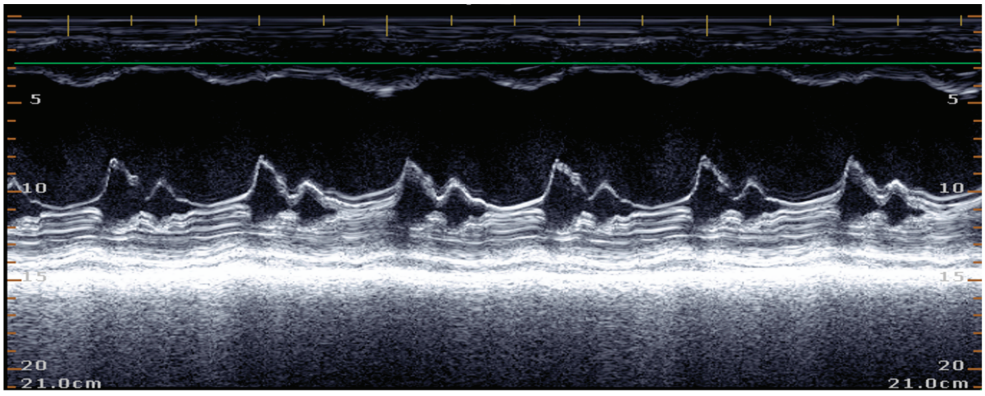

Figure 15. Increased mitral septal separation in a canine patient with DCM.

6.1.4. Tissue Doppler and Speckle Tracking

Tissue Doppler imaging comprises several techniques such as tissue velocity imaging (TVI), strain, and strain rate imaging. Tissue velocity imaging allows for the assessment of the myocardial wall's early (a') and late (a') diastolic (e') and systolic (s') velocities using either pulsed wave or color Doppler myocardial echography [105].

TVI has demonstrated to be a promising technique for detecting early myocardial dysfunction in dogs with cardiomyopathy [105,106]. One study involving canine patients with either occult or overt dilated cardiomyopathy (DCM) demonstrated that the mitral annular velocities measured by pulsed-wave tissue velocity imaging were reduced in both systolic and diastolic phases [107]. In addition, a singular study investigated the systolic and diastolic tissue velocity imaging as well as strain parameters in canines diagnosed with Idiopathic Dilated Cardiomyopathy across different breeds [108].

In echocardiography, the assessment of myocardial deformation involves measuring the displacement and velocity of cardiac tissue during both systole and diastole. Strain refers to a dimensionless index of deformation that quantifies the percentage change in the length of a myocardial segment in the radial, circumferential, or longitudinal direction relative to the baseline measurement [109]. In contrast to tissue velocity imaging (TVI), strain and strain rate imaging are minimally influenced by the motion of the heart and tethering effects in adjacent segments. This overcomes the limitations of TVI and provides more accurate results. In human patients, these measurements have demonstrated high sensitivity in detecting myocardial diseases [110].

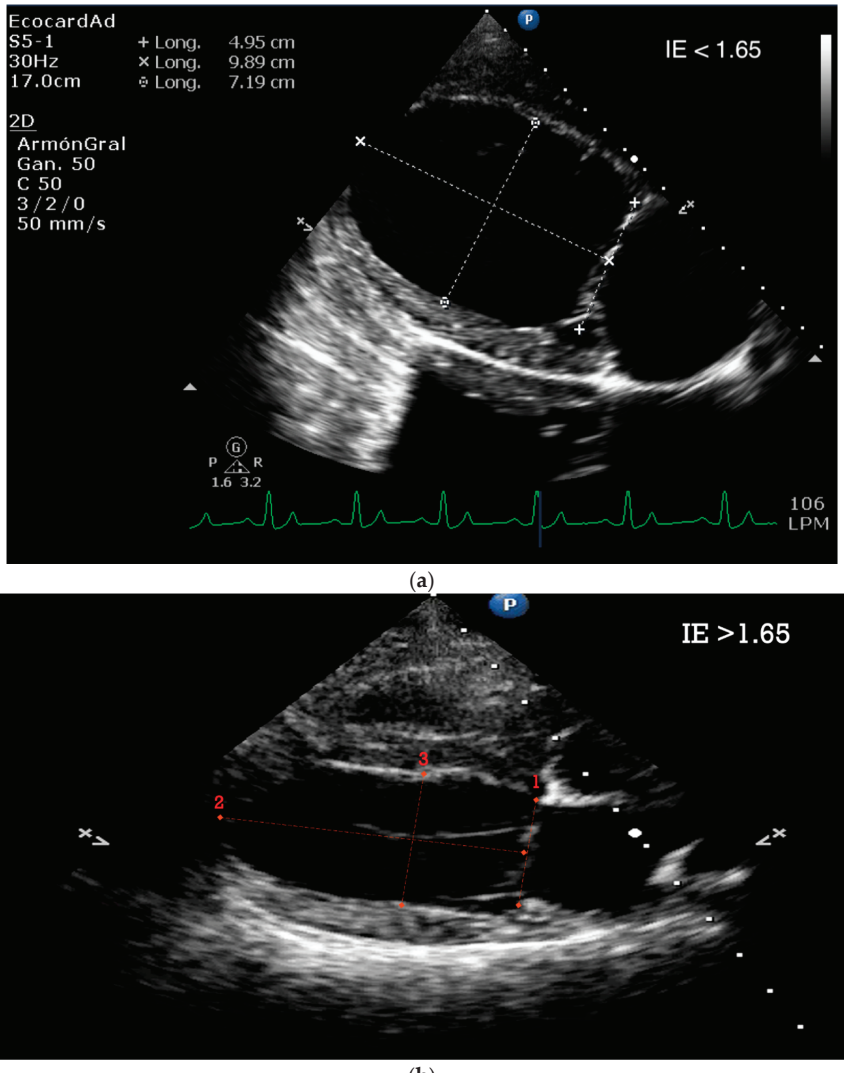

Figure 16. (**a**). Decreased Sphericity Index in canine patient. (**b**). Normal Sphericity Index in the canine patient.

7. Canine Patients with Naturally Occurring Cardiac Diseases—Learning from a Potential Echocardiography Research Model

Dogs have been an essential model for cardiology research since the beginning of experimental physiology in the nineteenth century, allowing the understanding of various mechanisms involved in the electrophysiological and mechanical functioning of the human heart [111]. Dogs' most common cardiovascular diseases, myxomatous mitral valve degeneration (MVDM) and primary dilated cardiomyopathy (CMD), have an incidence of approximately 10% in daily canine veterinary clinical practice. In addition, the relatively short life span of dogs (12–14 years, depending on the breed) and the rapid evolution of these diseases turn the canine patient into a relevant clinical model for the comparative study of these same pathologies in humans [55,112].

In dogs, MVDM is the most common cardiovascular disease and has been associated with canine geriatric patients of certain dog breeds. In humans, its estimated prevalence is 2 to 3% of all cardiac diseases. The molecular and degenerative mechanisms involved in the evolution of the disease appear to be common in both species. For example, the migration of endothelial cells towards the interstitial tissue, stripping the valve's surface, characterizes the myxomatous degeneration of valve tissue in humans and canines [30].

For its part, CMD is the second most common cardiovascular disease in dogs. It develops from a preclinical or hidden phase, without obvious symptoms, up to a clinical-stage marked by congestive heart failure due to systolic dysfunction, severe arrhythmias, syncope, and even sudden death. In both canines and humans, it is associated with several genetic, inflammatory, and hemodynamic factors that cause a decrease in the contractile capacity of the myocardium and an increase in the internal diameter of the cardiac chambers [104,112].

Although murine models, mice, and rats have been used to study acute myocardial infarction and arterial hypertension, they have not been used to study these chronic diseases. In addition, these models face practical, technical, and scientific limitations inherent to the use of these species, for example: (a) The cardiovascular characteristics derived from their size, weight, and high metabolic rate make them very different from the human heart, especially in heart rate, oxygen consumption by the myocardium, contractility or inotropy, and response to drugs. (b) The difficult handling of these species makes them prone to stress during handling, with consequent cardiovascular physiological effects of elevated serum catecholamine levels. The tendency to develop arterial hypertension due to its management in the laboratory setting has made the murine model one of the most widely used models for the study of this condition, reaching the point of using hypertension induction methods that, in some cases, collide with important bioethical considerations regarding current scientific research. For example, arterial hypertension may be induced in rats that are semi-drowning in swimming pools which they cannot leave, meaning they must swim to survive, or hypertension may be induced by a combination of unilateral nephrectomy and a 10% sodium chloride solution orogastric tube [113]. (c) The need for aggressive manual or chemical containment employing sedation/anesthesia for clinical, electrocardiographic, and echocardiographic examination with the logical alterations of the cardiovascular variables to be evaluated, induced by the stress of handling or by the drugs used in the anesthetic plan. (d) The size of the murine models' hearts makes it difficult to obtain valid echocardiographic measurements, requiring special training for the staff, high-frequency ultrasound probes, and special adaptations of the software used for study interpretation. All of the above to make its implementation viable [114].

On the other hand, the dog, in its evolutionary process of more than 10,000 years accompanying the human being, has managed to adapt to its handling in such a way that, with minimum manual restraint (or sometimes without it), it tends to behave as an adequate clinical model, allowing painless procedures such as blood pressure measurement, electrocardiography, and echocardiography to be carried out without significant alterations, which will enable the evaluation of chronic diseases such as VMVD and CMD [111]. Furthermore, imaging acquisitions are ideal in cardiovascular disease animal models when performed with awake and cooperative animals, routinely performed in the dog during the follow-up of its cardiac pathology [5].

Echocardiography has become a systematic study in evaluating dogs' cardiovascular diseases because it is a minimally invasive procedure and is easily tolerated by dogs. Furthermore, the values obtained are reliable and repeatable since there is equipment adapted to the dogs' size and weight and computerized cardiology programs (software) adapted for the species, which correlate these values to the weight or body surface area of the patient, thus avoiding errors related to the variability of size, weight, and conformation of the thorax according to different breeds of dogs [101].

Currently, there are studies on dogs that show intervals or reference values, indexed to weight, breed, and even physical activity, for most of the normal echocardiographic

parameters for measuring size, contractility, and ejection of the cardiac chambers, degree of deformation of the walls, and the morphometric comparison of the various structures that make up the heart [115]. Likewise, canine echocardiography in its different modes (B, M, color or spectral Doppler, Tissue) allows us to evaluate the thickness, motility, and degree of competence of the heart valves, as well as the direction and speed of transvalvular blood flow, and calculate pressure gradients, the stage stenosis of the valves, or post- stenotic dilatations, among other parameters, in a reliable and repeatable way. This provides valuable information about the different stages through which dogs affected by these two diseases pass, allowing extrapolation of some of these findings to human pathology. Likewise, the relatively high incidence and prevalence in the population of these two canine diseases will enable the use of naturally affected patients as study models to evaluate both their evolution and the hemodynamic consequences derived from them, as well as the reaction to treatments [116].

Another advantage of using canine patients naturally affected by cardiac diseases as a comparative model in clinical imaging research is that these patients are diagnosed early in the course of the disease. Appropriate treatment is usually prescribed, allowing for the stable course of these pathologies in many cases, periodic evaluations of its evolution, and the determination of the effect of treatment on the disease and the survival period. Recently published studies, the EPIC study [79] and the BESST study [117], established an increase of up to 15 months in the preclinical stage of MMVD or Stage B2 in dogs (according to ACVIM consensus guidelines for the diagnosis and treatment of myxomatous mitral valve disease in dogs), allowing an adequate quality of life until the outcome of death or euthanasia associated with heart disease. This advantage enables a proper echocardiographic approach to these pathologies and an evaluation of the variations induced by current treatment.

Finally, the ideal animal model for studying human cardiac pathologies does not exist. However, the canine model appears to be appropriate for studying some chronic cardiac pathologies due to similarities in the neuroendocrine control of cardiac function, function, and expression of ion channels, hemodynamics, and even pharmacodynamics, in addition to the previously mentioned species and diseases. This is not the case for conditions with an acute and hyperacute course, such as myocardial infarction, since the coronary irrigation of the left ventricular myocardium in dogs is done through several collaterals of the main left coronary artery, compensating for the temporary ischemia of the infarcted tissue, modifying the course and intensity of the disease [111].

8. Conclusions

In cardiovascular research, animal models are essential for testing mechanistic hypotheses and insights and are relevant in translational research, the evaluation of medical procedures, and the development of imaging technologies.

There are many similarities between human and canine cardiac patients, including the cardiac anatomical structure, pathophysiological processes of some common myocardial and valvular diseases, and echocardiographic techniques used by both species, as shown in Table 1. Due to their remarkable similarity to the human heart, dogs are ideal models for studying ventricular function in heart failure models and improving echocardiographic assessment techniques and devices.

The present review proposes the canine patient with natural heart disease as a model for the clinical investigation of cardiac pathologies that are symmetric with those of the human patient. This is an excellent option in a current scenario, where continuous follow-up of cardiac disease in the dog is common, using technologies that allow for the measuring and monitoring of its evolution. In addition, the dog presents a particularity that we seek to point out; its short relative lifespan allows observing the behavior of these diseases in shorter periods than its human counterpart. Additionally, the current advanced veterinary cardiology and the highly manageable dog in the clinical context allow cardiac ultrasound studies without sedation or anesthesia, which is an advantage over other animal models. Observations from clinical echocardiography on dogs could improve our understanding

of cardiac disease, and canine models of human cardiac pathologies could supplement existing preclinical animal models.

Table 1. Comparison of Transthoracic Echocardiographic Techniques in Humans and Canines.

Technique	
Echocardiographic positioning	**Dogs** are usually imaged in right and left lateral position. The **human** patient should be supine or left lateral decubitus. This will bring the heart away from the sternum.
Normal Basic Echocardiographic Views	**Human:** Parasternal long axis, parasternal short axis, apical four chamber, apical four-chamber view, subxiphoid (subcostal), suprasternal view, and IVC views. **Canines:** Four-chamber right-sided parasternal long-axis view, five-chamber right-sided parasternal long-axis view, right-sided short-axis view of the left ventricle at the level of the papillary muscles, right-sided short-axis view at the level of the left atrium and aorta.
Quantitative assessment of mitral regurgitation	Commonly used in human patients, but seldom utilized in canine patients and practical application is limited (defining EROA and flow convergence shape can be challenging) [60].
Flow convergence area measurement by PISA	A standard gold method in **humans**, not routinely performed in cardiologic evaluation in **dogs** (PISA quantification showed a wide range of RF in a clinical study) [61,62].
Color flow imaging of the mitral regurgitation jet area	The most commonly used technique for assessing severity in **dogs**. The former method is not used in **humans** as it is not considered reliable for determining the severity of mitral insufficiency.
Measurement of Left Ventricular Volume	M-mode echocardiography is widely used in **canine** cardiology, but its utility is debated. American Society of Echocardiography recommends against using linear measurements in the **human** patient. SMOD is recommended [100,102,103].
Quantification of the severity of left ventricular remodeling	**Canine:** AI: Ao ratio, AI diameter indexed to weight, VI: Ao ratio, the normalized internal diameter of the VI at the end of normal diastole. Widely used. **Human:** Cardiovascular magnetic resonance is the gold standard and more accurate than echocardiography [118,119].

Our review has certain limitations. Narrative reviews are susceptible to selection bias, which is a disadvantage of this review genre. However, due to the novelty of the subject and the limited number of articles on the significance of using canine patients as a clinical model in echocardiographic translational research, other types of review systems may not be suitable. Our study provides a starting point for future investigations into the relevance of evaluating other echocardiographic techniques, such as transesophageal echocardiography and interventional imaging, in this topic. These areas should be the subject of future reviews to further advance our understanding of the topic.

This work does not propose using the canine patient as an experimental research model, which we believe will become increasingly obsolete due to its bioethical implications, but rather in the context of designing new echocardiographic technologies using interdisciplinary work and comparative and translational medical research. These comparisons could lead to the discovery of new echocardiographic diagnostic strategies to improve existing techniques and technologies, many of which could be tested on the dog. In addition, canine cardiac patients may provide clinically relevant models for relevant cardiovascular diseases of the heart in humans, and serve as a crucial link between preclinical echocardiographic research in naturally occurring disease models in dogs and clinical trials in human medicine. In this collaborative work, patients of both species could benefit from this combined interdisciplinary research effort.

Veterinary hospitals can provide excellent diagnostic and long-term medical care for canine pets, a basis for clinically relevant veterinary clinical trials. Translational research in canine patients with naturally occurring cardiac disease could strengthen the link between veterinary and human cardiac imaging research and feedback on the knowledge gained between the two disciplines.

Author Contributions: Conceptualization, C.A.F.D. and I.A.C.Y.; writing—original draft preparation, C.A.F.D., I.A.C.Y., R.M.G., J.C.H.R., M.F.M.G., S.M.G.C. and I.C.G.R.; writing—review and editing, C.A.F.D. and I.A.C.Y.; supervision, C.A.F.D.; project administration, C.A.F.D. All authors have read and agreed to the published version of the manuscript.

Funding: This research received no external funding.

Institutional Review Board Statement: Not applicable.

Informed Consent Statement: Not applicable.

Data Availability Statement: Not applicable.

Acknowledgments: The authors gratefully acknowledge Fernanda Reyna, Sergio Quintero, Efren Valenzuela, and the faculty and administrative personnel of the Veterinary Sciences Research Institute, Autonomous University of Baja California.

Conflicts of Interest: The authors declare no conflict of interest.

References

1. Roth, G.A.; Mensah, G.A.; Fuster, V. The Global Burden of Cardiovascular Diseases and Risks. *J. Am. Coll. Cardiol.* **2020**, *76*, 2980–2981. [CrossRef] [PubMed]
2. Gaar-Humphreys, K.R.; Spanjersberg, T.C.F.; Santarelli, G.; Grinwis, G.C.M.; Szatmári, V.; Roelen, B.A.J.; Vink, A.; van Tintelen, J.P.; Asselbergs, F.W.; Fieten, H.; et al. Genetic Basis of Dilated Cardiomyopathy in Dogs and Its Potential as a Bidirectional Model. *Animals* **2022**, *12*, 1679. [CrossRef] [PubMed]
3. Camacho, P.; Fan, H.; Liu, Z.; He, J.Q. Large Mammalian Animal Models of Heart Disease. *J. Cardiovasc. Dev. Dis.* **2016**, *3*, 30. [CrossRef] [PubMed]
4. Löwa, A.; Jevtić, M.; Gorreja, F.; Hedtrich, S. Alternatives to animal testing in basic and preclinical research of atopic dermatitis. *Exp. Dermatol.* **2018**, *27*, 476–483. [CrossRef]
5. Santos, A.; Fernández-Friera, L.; Villalba, M.; López-Melgar, B.; España, S.; Mateo, J.; Mota, R.A.; Jiménez-Borreguero, J.; Ruiz-Cabello, J. Cardiovascular imaging: What have we learned from animal models? *Front. Pharmacol.* **2015**, *6*, 227. [CrossRef]
6. Demiris, G.; Oliver, D.P.; Washington, K.T. Defining and analyzing the problem. In *Behavioral Intervention Research in Hospice and Palliative Care*; Elsevier: Amsterdam, The Netherlands, 2019; pp. 27–39.
7. Getty, R. General heart and blood vessels. In *Sisson and Grossman's: The Anatomy of the Domestic Animals*, 5th ed.; Sisson, S., Grossman, J.D., Getty, R., Eds.; Saunders: Philadelphia, PA, USA, 1975; pp. 164–175.
8. Michaelsson, M.; Ho, S.Y. *Congenital Heart Malformations in Mammals: An Illustrated Text*; Imperial College Press: River Edge, NJ, USA; London, UK, 2000.
9. Crick, S.J.; Sheppard, M.N.; Ho, S.Y.; Gebstein, L.; Anderson, R.H. Anatomy of the pig heart: Comparisons with normal human cardiac structure. *J. Anat.* **1998**, *193*, 105–119. [CrossRef]
10. Queiroz, L.L.; Moura, L.R.; Moura, V.M.B.D. Morphometric assessment of canine heart without macroscopically visible changes caused by cardiac disease. *Ciênc. Anim. Bras.* **2018**, *19*, e43748. [CrossRef]
11. Hill, A.J.; Laizzo, P.A. Comparative cardiac anatomy. In *Handbook of Cardiac Anatomy, Physiology, and Devices*; Iaizzo, P., Ed.; Humana Press: Totowa, NJ, USA, 2009. [CrossRef]
12. Rodriguez, E.R.; Tan, C.D. Structure and Anatomy of the Human Pericardium. *Prog. Cardiovasc. Dis.* **2017**, *59*, 327–340. [CrossRef]
13. Evans, H.E. The heart and arteries. In *Miller's Anatomy of the Dog*, 3rd ed.; Miller, M.E., Evans, H.E., Eds.; Saunders: Philadelphia, PA, USA, 1993; pp. 586–602.
14. Holt, J.P. The normal pericardium. *Am. J. Cardiol.* **1970**, *26*, 455–465. [CrossRef]
15. Naimark, W.A.; Lee, J.M.; Limeback, H.; Cheung, D.T. Correlation of structure and viscoelastic properties in the pericardia of four mammalian species. *Am. J. Physiol.* **1992**, *263*, H1095–H1106. [CrossRef]
16. Spodick, D.H. *The Pericardium: A Comprehensive Textbook*; Dekker: New York, NY, USA, 1997.
17. Czum, J.M.; Silas, A.M.; Althoen, M.C. Evaluation of the Pericardium with CT and MR. *ISRN Cardiol.* **2014**, *2014*, 174908. [CrossRef] [PubMed]
18. Jakovljevic, D.G. Physical activity and cardiovascular aging: Physiological and molecular insights. *Exp. Gerontol.* **2018**, *109*, 67–74. [CrossRef]
19. Singh, B. *Dyce, Sack, and Wensing's Textbook of Veterinary Anatomy*, 5th ed.; Elsevier: St. Louis, MO, USA, 2017.
20. Walmsley, R. Anatomy of human mitral valve in adult cadaver and comparative anatomy of the valve. *Br. Heart J.* **1978**, *40*, 351–366. [CrossRef] [PubMed]
21. Tarniceriu, C.C.; Hurjui, L.L.; Tanase, D.M.; Nedelcu, A.H.; Gradinaru, I.; Ursaru, M.; Stefan Rudeanu, A.; Delianu, C.; Lozneanu, L. The Pulmonary Venous Return from Normal to Pathological—Clinical Correlations and Review of Literature. *Medicina* **2021**, *57*, 293. [CrossRef] [PubMed]
22. Pettersson, G.B.; Hussain, S.T.; Ramankutty, R.M.; Lytle, B.W.; Blackstone, E.H. Reconstruction of fibrous skeleton: Technique, pitfalls and results. *Multimed. Man. Cardiothorac. Surg.* **2014**, *2014*, mmu004. [CrossRef]

23. Krawczyk-Ożóg, A.; Hołda, M.K.; Sorysz, D.; Koziej, M.; Siudak, Z.; Dudek, D.; Klimek-Piotrowska, W. Morphologic variability of the mitral valve leaflets. *J. Thorac. Cardiovasc. Surg.* **2017**, *154*, 1927–1935. [CrossRef] [PubMed]
24. Chen, Y.A.; Nguyen, E.T.; Dennie, C.; Wald, R.M.; Crean, A.M.; Yoo, S.J.; Jimenez-Juan, L. Computed tomography and magnetic resonance imaging of the coronary sinus: Anatomic variants and congenital anomalies. *Insights Imaging* **2014**, *5*, 547–557. [CrossRef]
25. Bigler, M.R.; Seiler, C. The Human Coronary Collateral Circulation, Its Extracardiac Anastomoses and Their Therapeutic Promotion. *Int. J. Mol. Sci.* **2019**, *20*, 3726. [CrossRef]
26. Teunissen, P.F.; Horrevoets, A.J.; van Royen, N. The coronary collateral circulation: Genetic and environmental determinants in experimental models and humans. *J. Mol. Cell. Cardiol.* **2012**, *52*, 897–904. [CrossRef]
27. Palmisano, A.; Nicoletti, V.; Colantoni, C.; Monti, C.B.; Pannone, L.; Vignale, D.; Darvizeh, F.; Agricola, E.; Schaffino, S.; De Cobelli, F.; et al. Dynamic changes of mitral valve annulus geometry at preprocedural CT: Relationship with functional classes of regurgitation. *Eur. Radiol. Exp.* **2021**, *5*, 34. [CrossRef]
28. Coutinho, G.F.; Antunes, M.J. Current status of the treatment of degenerative mitral valve regurgitation. *Rev. Port. Cardiol.* **2021**, *40*, 293–304. [CrossRef] [PubMed]
29. Neto, F.L.; Marques, L.C.; Aiello, V.D. Myxomatous degeneration of the mitral valve. *Autops. Case Rep.* **2018**, *8*, e2018058. [CrossRef] [PubMed]
30. Oyama, M.A.; Elliott, C.; Loughran, K.A.; Kossar, A.P.; Castillero, E.; Levy, R.J.; Ferrari, G. Comparative pathology of human and canine myxomatous mitral valve degeneration: 5HT and TGF-β mechanisms. *Cardiovasc. Pathol.* **2020**, *46*, 107196. [CrossRef] [PubMed]
31. Merryman, W.D.; Youn, I.; Lukoff, H.D.; Krueger, P.M.; Guilak, F.; Hopkins, R.A.; Sacks, M.S. Correlation between heart valve interstitial cell stiffness and transvalvular pressure: Implications for collagen biosynthesis. *Am. J. Physiol. Heart Circ. Physiol.* **2006**, *290*, H224–H231. [CrossRef] [PubMed]
32. Sacks, M.S.; He, Z.; Baijens, L.; Wanant, S.; Shah, P.; Sugimoto, H.; Yoganathan, A.P. Surface strains in the anterior leaflet of the functioning mitral valve. *Ann. Biomed. Eng.* **2002**, *30*, 1281–1290. [CrossRef]
33. McCarthy, K.P.; Ring, L.; Rana, B.S. Anatomy of the mitral valve: Understanding the mitral valve complex in mitral regurgitation. *Eur. J. Echocardiogr.* **2010**, *11*, i3–i9. [CrossRef]
34. Fox, P.R. Pathology of myxomatous mitral valve disease in the dog. *J. Vet. Cardiol.* **2012**, *14*, 103–126. [CrossRef]
35. Markby, G.; Summers, K.M.; MacRae, V.E.; Del-Pozo, J.; Corcoran, B.M. Myxomatous degeneration of the canine mitral valve: From gross changes to molecular events. *J. Comp. Pathol.* **2017**, *156*, 371–383. [CrossRef]
36. Saremi, F.; Sánchez-Quintana, D.; Mori, S.; Muresian, H.; Spicer, D.E.; Hassani, C.; Anderson, R.H. Fibrous skeleton of the heart: Anatomic overview and evaluation of pathologic conditions with CT and MR imaging. *RadioGraphics* **2017**, *37*, 1330–1351. [CrossRef]
37. Jimenez, J.H.; Soerensen, D.D.; Zhaoming, H.; He, S.; Yoganathan, A.P. Effects of a saddle shaped annulus on mitral valve function and chordal force distribution: An in vitro study. *Ann. Biomed. Eng.* **2003**, *31*, 1171–1181. [CrossRef]
38. Padala, M.; Hutchison, R.A.; Croft, L.R.; Jimenez, J.H.; Gorman, R.C.; Gorman, J.H. Saddle shape of the mitral annulus reduces systolic strains on the P2 segment of the posterior mitral leaflet. *Ann. Thorac. Surg.* **2009**, *88*, 1499–1504. [CrossRef] [PubMed]
39. Connell, P.S.; Han, R.I.; Grande-Allen, K.J. Differentiating the aging of the mitral valve from human and canine myxomatous degeneration. *J. Vet. Cardiol.* **2012**, *14*, 31–45. [CrossRef] [PubMed]
40. Aupperle, H.; Disatian, S. Pathology, protein expression and signaling in myxomatous mitral valve degeneration: Comparison of dogs and humans. *J. Vet. Cardiol.* **2012**, *14*, 59–71. [CrossRef] [PubMed]
41. Combs, M.D.; Yutzey, K.E. Heart valve development: Regulatory networks in development and disease. *Circ. Res.* **2009**, *105*, 408–421. [CrossRef]
42. Ayoub, S.; Ferrari, G.; Gorman, R.C.; Gorman, J.H.; Schoen, F.J.; Sacks, M.S. Heart valve biomechanics and underlying mechanobiology. *Comp. Physiol.* **2016**, *6*, 1743–1780.
43. Nkomo, V.T.; Gardin, J.M.; Skelton, T.N.; Gottdiener, J.S.; Scott, C.G.; EnriquezSarano, M. Burden of valvular heart diseases: A population-based study. *Lancet* **2006**, *368*, 1005–1011. [CrossRef]
44. Marechaux, S.; Illman, J.E.; Huynh, J.; Michelena, H.I.; Nkomo, V.T.; Tribouilloy, C. Functional anatomy and pathophysiologic principles in mitral regurgitation: Non-invasive assessment. *Prog. Cardiovasc. Dis.* **2017**, *60*, 289–304. [CrossRef]
45. Aluru, J.S.; Barsouk, A.; Saginala, K.; Rawla, P.; Barsouk, A. Valvular Heart Disease Epidemiology. *Med. Sci.* **2022**, *10*, 32. [CrossRef]
46. Iung, B.; Vahanian, A. Epidemiology of valvular heart disease in the adult. *Nat. Rev. Cardiol.* **2011**, *8*, 162–172. [CrossRef]
47. Borgarelli, M.; Buchanan, J.W. Historical review, epidemiology and natural history of degenerative mitral valve disease. *J. Vet. Cardiol.* **2012**, *14*, 93–101. [CrossRef]
48. Parker, H.G.; Kilroy-Glynn, P. Myxomatous mitral valve disease in dogs: Does size matter? *J. Vet. Cardiol.* **2012**, *14*, 19–29. [CrossRef] [PubMed]
49. Lewis, T.W.; Wiles, B.M.; Llewellyn-Zaidi, A.M.; Evans, K.M.; O'Neill, D.G. Longevity and mortality in Kennel Club registered dog breeds in the UK in 2014. *Canine. Genet. Epidemiol.* **2018**, *5*, 10. [CrossRef] [PubMed]
50. Bagardi, M.; Bionda, A.; Locatelli, C.; Cortellari, M.; Frattini, S.; Negro, A.; Crepaldi, P.; Brambilla, P.G. Echocardiographic Evaluation of the Mitral Valve in Cavalier King Charles Spaniels. *Animals* **2020**, *10*, 1454. [CrossRef] [PubMed]

51. Hyun, C. Mitral valve prolapse in Cavalier King Charles spaniel: A review and case study. *J. Vet. Sci.* **2005**, *6*, 67–73. [CrossRef]
52. Enriquez-Sarano, M.; Michelena, H.I. Mitral regurgitation in the 21st century. *Prog. Cardiovasc. Dis.* **2017**, *60*, 285–288. [CrossRef]
53. Atkins, C.; Bonagura, J.; Ettinger, S.; Fox, P.; Gordon, S.; Haggstrom, J.; Hamlin, R.; Keene, B.; Luis-Fuentes, V.; Stepien, R. Guidelines for the diagnosis and treatment of canine chronic valvular heart disease. *J. Vet. Intern. Med.* **2009**, *23*, 1142–1150. [CrossRef]
54. Borgarelli, M.; Crosara, S.; Lamb, K.; Savarino, P.; La Rosa, G.; Tarducci, A.; Haggstrom, J. Survival characteristics and prognostic variables of dogs with preclinical chronic degenerative mitral valve disease attributable to myxomatous degeneration. *J. Vet. Intern. Med.* **2012**, *26*, 69–75. [CrossRef]
55. Keene, B.W.; Atkins, C.E.; Bonagura, J.D.; Fox, P.R.; Häggström, J.; Fuentes, V.L.; Oyama, M.A.; Rush, J.E.; Stepien, R.; Uechi, M. ACVIM consensus guidelines for the diagnosis and treatment of myxomatous mitral valve disease in dogs. *J. Vet. Intern. Med.* **2019**, *33*, 1127–1140. [CrossRef]
56. Boon, J.A. Acquired heart disease: Mitral insufficiency. In *Manual of Veterinary Echocardiography*, 1st ed.; Boon, J.A., Ed.; Williams and Wilkins: Baltimore, MD, USA, 1998; pp. 261–286.
57. Serres, F.; Chetboul, V.; Tissier, R.; Poujol, L.; Gouni, V.; Carlos Sampedrano CPouchelon, J.L. Comparison of 3 ultrasound methods for quantifying left ventricular systolic function: Correlation with disease severity and prognostic value in dogs with mitral valve disease. *J. Vet. Intern. Med.* **2008**, *22*, 566–577. [CrossRef]
58. Bonagura, J.D.; Schober, K.E. Can ventricular function be assessed by echocardiography in chronic canine mitral valve disease? *J. Small Anim. Pract.* **2009**, *50*, 12–24. [CrossRef]
59. Chetboul, V. Advanced techniques in echocardiography in small animals. *Vet. Clin. Small Anim. Pract.* **2010**, *40*, 529–543. [CrossRef] [PubMed]
60. Suh, S.-I.; Lu, T.-L.; Choi, R.; Hyun, C. Echocardiographic Features in Canine Myxomatous Mitral Valve Disease: An Animal Model for Human Mitral Valve Prolapse. In Proceedings of the Advanced Concepts in Endocarditis-2021, Virtual, 25 August 2021. [CrossRef]
61. Lancellotti, P.; Tribouilloy, C.; Hagendorff, A.; Popescu, B.A.; Edvardsen, T.; Pierard, L.A.; Badano, L.; Zamorano, J.L. Scientific document Committee of the European Association of cardiovascular imaging: Recommendations for the echocardiographic assessment of native valvular regurgitation: An executive summary from the European Association of Cardiovascular Imaging. *Eur. Heart J. Cardiovasc. Imaging* **2013**, *14*, 611–644. [CrossRef] [PubMed]
62. Gouni, V.; Serres, F.J.; Pouchelon, J.L.; Tissier, R.; Lefebvre, H.P.; Nicolle, A.P.; Sampedrano, C.C.; Chetboul, V. Quantification of mitral valve regurgitation in dogs with degenerative mitral valve disease by use of the proximal isovelocity surface area method. *J. Am. Vet. Med. Assoc.* **2007**, *231*, 399–406. [CrossRef]
63. Zoghbi, W.A.; Enriquez-Sarano, M.; Foster, E.; Grayburn, P.A.; Kraft, C.D.; Levine, R.A.; Nihoyannopoulos, P.; Otto, C.M.; Quinones, M.A.; Rakowski, H.; et al. Recommendations for evaluation of the severity of native valvular regurgitation with two-dimensional and Doppler echocardiography. *J. Am. Soc. Echocardiogr.* **2003**, *16*, 777–802. [CrossRef]
64. Chetboul, V.; Tissier, R. Echocardiographic assessment of canine degenerative mitral valve disease. *J. Vet. Cardiol.* **2012**, *14*, 127–148. [CrossRef] [PubMed]
65. Chetboul, V.; Serres, F.; Tissier, R.; Lefebvre, H.P.; Sampedrano, C.C.; Gouni, V.; Poujol, L.; Hawa, G.; Pouchelon, J.L. Association of plasma N-terminal pro-B-type natriuretic peptide concentration with mitral regurgitation severity and outcome in dogs with asymptomatic degenerative mitral valve disease. *J. Vet. Intern. Med.* **2009**, *23*, 984–994. [CrossRef]
66. Muzzi, R.A.; de Araújo, R.B.; Muzzi, L.A.; Pena, J.L.; Silva, E.F. Regurgitant jet area by Doppler color flow mapping: Quantitative assessment of mitral regurgitation severity in dogs. *J. Vet. Cardiol.* **2003**, *5*, 33–38. [CrossRef]
67. Sargent, J.; Muzzi, R.; Mukherjee, R.; Somarathne, S.; Schranz, K.; Stephenson, H.; Connolly, D.; Brodbelt, D.; Fuentes, V.L. Echocardiographic predictors of survival in dogs with myxomatous mitral valve disease. *J. Vet. Cardiol.* **2015**, *17*, 1–12. [CrossRef]
68. Grayburn, P.A.; Weissman, N.J.; Zamorano, J.L. Quantitation of mitral regurgitation. *Circulation* **2012**, *126*, 2005–2017. [CrossRef]
69. Zoghbi, W.A.; Adams, D.; Bonow, R.O.; Enriquez-Sarano, M.; Foster, E.; Grayburn, P.A.; Hahn, R.T.; Han, Y.; Hung, J.; Lang, R.M.; et al. Recommendations for non-invasive evaluation of native Valvular regurgitation: A report from the American Society of Echocardiography developed in collaboration with the Society for Cardiovascular Magnetic Resonance. *J. Am. Soc. Echocardiogr.* **2017**, *30*, 303–371. [CrossRef]
70. Vezzosi, T.; Grosso, G.; Tognetti, R.; Meucci, V.; Patata, V.; Marchesotti, F.; Domenech, O. The Mitral INsufficiency Echocardiographic score: A severity classification of myxomatous mitral valve disease in dogs. *J. Vet. Intern. Med.* **2021**, *35*, 1238–1244. [CrossRef] [PubMed]
71. Sargent, J.; Connolly, D.J.; Watts, V.; Mõtsküla, P.; Volk, H.A.; Lamb, C.R.; Luis Fuentes, V. Assessment of mitral regurgitation in dogs: Comparison of results of echocardiography with magnetic resonance imaging. *J. Small Anim. Pract.* **2015**, *56*, 641–650. [CrossRef] [PubMed]
72. Biner, S.; Rafique, A.; Rafii, F.; Tolstrup, K.; Noorani, O.; Shiota, T.; Gurudevan, S.; Siegel, R.J. Reproducibility of proximal isovelocity surface area, vena contracta, and regurgitant jet area for assessment of mitral regurgitation severity. *JACC Cardiovasc. Imaging* **2010**, *3*, 235–243. [CrossRef] [PubMed]
73. Paiva, R.M.; Garcia-Guasch, L.; Manubens, J.; Montoya-Alonso, J.A. Proximal isovelocity surface area variability during systole in dogs with mitral valve prolapse. *J. Vet. Cardiol.* **2011**, *13*, 267–270. [CrossRef]

74. Tidholm, A.; Bodegård-Westling, A.; Höglund, K.; Häggström, J.; Ljungvall, I. Real-time 3-dimensional echocardiographic assessment of effective regurgitant orifice area in dogs with myxomatous mitral valve disease. *J. Vet. Intern. Med.* **2017**, *31*, 303–310. [CrossRef]
75. Borgarelli, M.; Savarino, P.; Crosara, S.; Santilli, R.A.; Chiavegato, D.; Poggi, M.; Bellino, C.; La Rosa, G.; Zanatta, R.; Haggstrom, J.; et al. Survival characteristics and prognostic variables of dogs with mitral regurgitation attributable to myxomatous valve disease. *J. Vet. Intern. Med.* **2008**, *22*, 120–128. [CrossRef]
76. Hansson, K.; Häggström, J.; Kvart, C.; Lord, P. Left atrial to aortic root indices using two-dimensional and M-mode echocardiography in cavalier King Charles spaniels with and without left atrial enlargement. *Vet. Radiol. Ultrasound* **2002**, *43*, 568–575. [CrossRef]
77. Cornell, C.C.; Kittleson, M.D.; Torre, P.D.; Häggström, J.; Lombard, C.W.; Pedersen, H.D.; Vollmar, A.; Wey, A. Allometric scaling of M-mode cardiac measurements in normal adult dogs. *J. Vet. Intern. Med.* **2004**, *18*, 311–321. [CrossRef]
78. Schober, K.E.; Hart, T.M.; Stern, J.A.; Li, X.; Samii, V.F.; Zekas, L.J.; Scansen, B.A.; Bonagura, J.D. Detection of congestive heart failure in dogs by Doppler echocardiography. *J. Vet. Intern. Med.* **2010**, *24*, 1358–1368. [CrossRef]
79. Boswood, A.; Häggström, J.; Gordon, S.G.; Wess, G.; Stepien, R.L.; Oyama, M.A.; Keene, B.W.; Bonagura, J.; MacDonald, K.A.; Patteson, M.; et al. Effect of pimobendan in dogs with preclinical myxomatous mitral valve disease and cardiomegaly: The EPIC study—A randomized clinical trial. *J. Vet. Intern. Med.* **2016**, *30*, 1765–1779. [CrossRef]
80. Reynolds, C.A.; Brown, D.C.; Rush, J.E.; Fox, P.R.; Nguyenba, T.P.; Lehmkuhl, L.B.; Gordon, S.G.; Kellihan, H.B.; Stepien, R.L.; Lefbom, B.K.; et al. Prediction of first onset of congestive heart failure in dogs with degenerative mitral valve disease: The PREDICT cohort study. *J. Vet. Cardiol.* **2012**, *14*, 193–202. [CrossRef] [PubMed]
81. Dillon, A.R.; Dell'Italia, L.J.; Tillson, M.; Killingsworth, C.; Denney, T.; Hathcock, J.; Botzman, L. Left ventricular remodeling in preclinical experimental mitral regurgitation of dogs. *J. Vet. Cardiol.* **2012**, *14*, 73–92. [CrossRef]
82. Menciotti, G.; Borgarelli, M. Review of Diagnostic and Therapeutic Approach to Canine Myxomatous Mitral Valve Disease. *Vet. Sci.* **2017**, *4*, 47. [CrossRef]
83. McGinley, J.C.; Berretta, R.M.; Chaudhary, K.; Rossman, E.; Bratinov, G.D.; Gaughan, J.P.; Houser, S.; Margulies, K.B. Impaired contractile reserve in severe mitral valve regurgitation with a preserved ejection fraction. *Eur. J. Heart Fail.* **2007**, *9*, 857–864. [CrossRef]
84. Baron Toaldo, M.; Romito, G.; Guglielmini, C.; Diana, A.; Pelle, N.G.; Contiero, B.; Cipone, M. Prognostic value of echocardiographic indices of left atrial morphology and function in dogs with myxomatous mitral valve disease. *J. Vet. Intern. Med.* **2018**, *32*, 914–921. [CrossRef] [PubMed]
85. Lancellotti, P.; Pibarot, P.; Chambers, J.; La Canna, G.; Pepi, M.; Dulgheru, R.; Dweck, M.; Delgado, V.; Garbi, M.; Vannan, M.A.; et al. Multi-modality imaging assessment of native valvular regurgitation: An EACVI and ESC council of valvular heart disease position paper. *Eur. Heart J. Cardiovasc. Imaging* **2022**, *23*, e171–e232. [CrossRef] [PubMed]
86. Di Marcello, M.; Terzo, E.; Locatelli, C.; Palermo, V.; Sala, E.; Dall'Aglio, E.; Bussadori, C.M.; Spalla, I.; Brambilla, P.G. Assessment of mitral regurgitation severity by Doppler color flow mapping of the vena contracta in dogs. *J. Vet. Intern. Med.* **2014**, *28*, 1206–1213. [CrossRef] [PubMed]
87. Pedersen, H.D.; Häggström, J. Mitral valve prolapse in the dog: A model of mitral valve prolapse in man. *Cardiovasc. Res.* **2000**, *47*, 234–243. [CrossRef] [PubMed]
88. Nakamura, K.; Osuga, T.; Morishita, K.; Suzuki, S.; Morita, T.; Yokoyama, N.; Ohta, H.; Yamasaki, M.; Takiguchi, M. Prognostic value of left atrial function in dogs with chronic mitral valvular heart disease. *J. Vet. Intern. Med.* **2014**, *28*, 1746–1752. [CrossRef] [PubMed]
89. Wesselowski, S.; Borgarelli, M.; Menciotti, G.; Abbott, J. Echocardiographic anatomy of the mitral valve in healthy dogs and dogs with myxomatous mitral valve disease. *J. Vet. Cardiol.* **2015**, *17*, 97–106. [CrossRef]
90. Hezzell, M.J.; Boswood, A.; Moonarmart, W.; Elliott, J. Selected echocardiographic variables change more rapidly in dogs that die from myxomatous mitral valve disease. *J. Vet. Cardiol.* **2012**, *14*, 269–279. [CrossRef] [PubMed]
91. Kim, Y.H.; Choi, G.J.; Park, C. Rate of left ventricular pressure change by Doppler echocardiography in dogs with chronic mitral valve disease at different stages of congestive heart failure. *Vet. Radiol. Ultrasound* **2018**, *59*, 758–766. [CrossRef] [PubMed]
92. Chetboul, V.; Bussadori, C.; De Madron, É. *Clinical Echocardiography of the Dog and Cat*; Elsevier: Amsterdam, The Netherlands, 2016; pp. 127–138.
93. Kim, H.T.; Han, S.M.; Song, W.J.; Kim, B.; Choi, M.; Yoon, J.; Youn, H.Y. Retrospective study of degenerative mitral valve disease in small-breed dogs: Survival and prognostic variables. *J. Vet. Sci.* **2017**, *18*, 369–376. [CrossRef] [PubMed]
94. Kim, J.H.; Park, H.M. Usefulness of conventional and tissue Doppler echocardiography to predict congestive heart failure in dogs with myxomatous mitral valve disease. *J. Vet. Intern. Med.* **2015**, *29*, 132–140. [CrossRef] [PubMed]
95. Santos, M.; Rivero, J.; McCullough, S.D.; West, E.; Opotowsky, A.R.; Waxman, A.B.; Systrom, D.M.; Shah, A.M. E/e' Ratio in Patients with Unexplained Dyspnea: Lack of Accuracy in Estimating Left Ventricular Filling Pressure. *Circ. Heart Fail.* **2015**, *8*, 749–756. [CrossRef]
96. Simpson, S.; Kordtomeikel, K.; Wong, S.; Bennison, S.; El-Gendy, S.A.; Cobb, M.; Rutland, C.S. Diagnosis, Prognosis, Management, Treatment, Research and Advances in Canine Dilated Cardiomyopathy. In *Canine Genetics, Health and Medicine*; Rutland, C., Ed.; IntechOpen: London, UK, 2021; Available online: https://www.intechopen.com/chapters/76601 (accessed on 17 November 2022). [CrossRef]

97. Egenvall, A.; Bonnett, B.N.; Häggström, J. Heart Disease as a Cause of Death in Insured Swedish Dogs Younger than 10 Years of Age. *J. Vet. Intern. Med.* **2006**, *20*, 894–903. [CrossRef] [PubMed]
98. Fleming, J.M.; Creevy, K.E.; Promislow, D.E. Mortality in north american dogs from 1984 to 2004: An investigation into age-, size-, and breed-related causes of death. *J. Vet. Intern. Med.* **2011**, *25*, 187–198. [CrossRef]
99. Mathers, C.D.; Loncar, D. Projections of global mortality and burden of disease from 2002 to 2030. *PLoS Med.* **2006**, *3*, e442. [CrossRef]
100. Mausberg, T.B.; Wess, G.; Simak, J.; Keller, L.; Drögemüller, M.; Drögemüller, C.; Webster, M.T.; Stephenson, H.; Dukes-McEwan, J.; Leeb, T. A locus on chromosome 5 is associated with dilated cardiomyopathy in Doberman Pinschers. *PLoS ONE* **2011**, *6*, e20042. [CrossRef]
101. Dixon, J.A.; Spinale, F.G. Large animal models of heart failure: A critical link in the translation of basic science to clinical practice. *Circ Heart Fail.* **2009**, *2*, 262–271. [CrossRef]
102. Wess, G.; Domenech, O.; Dukes-McEwan, J.; Häggström, J.; Gordon, S. European Society of Veterinary Cardiology screening guidelines for dilated cardiomyopathy in Doberman Pinschers. *J. Vet. Cardiol.* **2017**, *19*, 405–415. [CrossRef] [PubMed]
103. Wess, G.; Schulze, A.; Butz, V.; Simak, J.; Killich, M.; Keller, L.J.; Maeurer, J.; Hartmann, K. Prevalence of dilated cardiomyopathy in doberman pinschers in various age groups. *J. Vet. Intern. Med.* **2010**, *24*, 533–538. [CrossRef] [PubMed]
104. Bonagura, J.D.; Visser, L.C. Echocardiographic assessment of dilated cardiomyopathy in dogs. *J. Vet. Cardiol.* **2022**, *40*, 15–50. [CrossRef] [PubMed]
105. Wess, G.; Killich, M.; Hartmann, K. Comparison of pulsed wave and color Doppler myocardial velocity imaging in healthy dogs. *J. Vet. Intern. Med.* **2010**, *24*, 360–366. [CrossRef]
106. Chetboul, V.; Carlos, C.; Blot, S.; Thibaud, J.L.; Escriou, C.; Tissier, R.; Retortillo, J.L.; Pouchelon, J.L. Tissue Doppler assessment of diastolic and systolic alterations of radial and longitudinal left ventricular motions in Golden Retrievers during the preclinical phase of cardiomyopathy associated with muscular dystrophy. *Am. J. Vet. Res.* **2004**, *65*, 1335–1341. [CrossRef]
107. O'Sullivan, M.L.; O'Grady, M.R.; Minors, S.L. Assessment of diastolic function by Doppler echocardiography in normal Doberman Pinschers and Doberman Pinschers with dilated cardiomyopathy. *J. Vet. Intern. Med.* **2007**, *21*, 81–91. [CrossRef]
108. Chetboul, V.; Gouni, V.; Sampedrano, C.C.; Tissier, R.; Serres, F.; Pouchelon, J.L. Assessment of regional systolic and diastolic myocardial function using tissue Doppler and strain imaging in dogs with dilated cardiomyopathy. *J. Vet. Intern. Med.* **2007**, *21*, 719–730. [CrossRef]
109. Klaeboe, L.G.; Edvardsen, T. Echocardiographic assessment of left ventricular systolic function. *J. Echocardiogr.* **2019**, *17*, 10–16. [CrossRef]
110. Dandel, M.; Hetzer, R. Echocardiographic strain and strain rate imaging–clinical applications. *Int. J. Cardiol.* **2009**, *132*, 11–24. [CrossRef]
111. Loen, V.; Vos, M.A.; van der Heyden, M.A.G. The canine chronic atrioventricular block model in cardiovascular preclinical drug research. *Br. J. Pharmacol.* **2022**, *179*, 859–881. [CrossRef]
112. Japp, A.G.; Gulati, A.; Cook, S.A.; Cowie, M.R.; Prasad, S.K. The Diagnosis and Evaluation of Dilated Cardiomyopathy. *J. Am. Coll. Cardiol.* **2016**, *67*, 2996–3010. [CrossRef] [PubMed]
113. Romero Borges, R.; Valido Díaz, A.; Bernal Llerenas, T.; Fimia Duarte, R.; Iannacone, R. Biomodel of arterial hypertension in Wistar rats administered 10% saline solution. *Biotempo* **2018**, *15*, 75–82.
114. Zaragoza, C.; Gomez-Guerrero, C.; Martin-Ventura, J.L.; Blanco-Colio, L.; Lavin, B.; Mallavia, B.; Tarin, C.; Mas, S.; Ortiz, A.; Egido, J. Animal models of cardiovascular diseases. *J. Biomed. Biotechnol.* **2011**, *2011*, 497841. [CrossRef] [PubMed]
115. Esser, L.C.; Borkovec, M.; Bauer, A.; Häggström, J.; Wess, G. Left ventricular M-mode prediction intervals in 7651 dogs: Population-wide and selected breed -specific values. *J. Vet. Intern. Med.* **2020**, *34*, 2242–2252. [CrossRef]
116. de Madron, É. Normal Views: 2D, TM, Spectral, and Color Doppler. In *Clinical Echocardiography of the Dog and Cat*; Chetboul, V., Bussadori, C., de Madron, É, Eds.; Elsevier Publishing: St. Louis, MO, USA, 2016.
117. Coffman, M.; Guillot, E.; Blondel, T.; Garelli-Paar, C.; Feng, S.; Heartsill, S.; Atkins, C.E. Clinical efficacy of a benazepril and spironolactone combination in dogs with congestive heart failure due to myxomatous mitral valve disease: The BEnazepril Spironolactone STudy (BESST). *J. Vet. Intern. Med.* **2021**, *35*, 1673–1687. [CrossRef]
118. Bellenger, N.G.; Burgess, M.I.; Ray, S.G.; Lahiri, A.; Coats, A.J.; Cleland, J.G.; Pennell, D.J. Comparison of left ventricular ejection fraction and volumes in heart failure by echocardiography, radionuclide ventriculography and cardiovascular magnetic resonance. Are they interchangeable? *Eur. Heart J.* **2000**, *21*, 1387–1396. [CrossRef]
119. Grothues, F.; Smith, G.C.; Moon, J.C.; Bellenger, N.G.; Collins, P.; Klein, H.U.; Pennell, D.J. Comparison of interstudy reproducibility of cardiovascular magnetic resonance with two-dimensional echocardiography in normal subjects and in patients with heart failure or left ventricular hypertrophy. *Am. J. Cardiol.* **2002**, *90*, 29–34. [CrossRef]

applied sciences

MDPI

Review

Impact of LGE-MRI in Arrhythmia Ablation

Paz Garre [1,2], Sara Vázquez-Calvo [1,2], Elisenda Ferro [3,4], Till Althoff [1,2] and Ivo Roca-Luque [1,2,5,*]

[1] Institut Clinic Cardiovascular, Hospital Clínic, Universitat de Barcelona, 08036 Barcelona, Spain
[2] Institut d'Investigacions Biomèdiques August Pi i Sunyer (IDIBAPS), 08036 Barcelona, Spain
[3] Medtronic Iberica, 08970 Sant Joan Despí, Spain
[4] Fundació Clínic per a la Recerca Biomèdica (FCRB), 08036 Barcelona, Spain
[5] Centro de Investigación Biomédica en Red de Enfermedades Cardiovasculares (CIBERCV), 28029 Madrid, Spain
* Correspondence: iroca@clinic.cat

Abstract: The use of late gadolinium enhancement magnetic resonance imaging (LGE-MRI) in arrhythmia ablation is increasing due to the capacity to detect, quantify and characterize cardiac fibrosis both in atrium and ventricle. Catheter ablation has become a standard treatment for arrhythmias, and LGE-MRI has demonstrated to be a useful tool to plan and guide ablation. Furthermore, recent studies have proved the usefulness in substrate analysis and postablation evaluation. This review will analyze the application and the current role of LGE-MRI to improve strategies for the two main cardiac arrhythmias: Atrial fibrillation and ventricular tachycardia.

Keywords: cardiac magnetic resonance; late gadolinium enhancement; atrial fibrillation; ventricular tachycardia; ablation; fibrosis; electroanatomical mapping

Citation: Garre, P.; Vázquez-Calvo, S.; Ferro, E.; Althoff, T.; Roca-Luque, I. Impact of LGE-MRI in Arrhythmia Ablation. *Appl. Sci.* **2023**, *13*, 3862. https://doi.org/10.3390/app13063862

Academic Editor: Julio Garcia Flores

Received: 31 January 2023
Revised: 6 March 2023
Accepted: 9 March 2023
Published: 17 March 2023

1. Introduction

Magnetic resonance imaging (MRI) has become a cornerstone of the diagnostic and prognostic evaluation of patients with cardiac arrhythmias. It is widely used for qualitative and quantitative evaluation of cardiac conditions and support diagnosis, monitoring disease progression and treatment planning [1]. Nowadays, late gadolinium enhancement (LGE) MRI is being used to detect and quantify cardiac fibrosis in both ventricular and atrial arrhythmias [2–6].

Atrial fibrillation (AF) is the most prevalent sustained cardiac arrhythmia, being observed in up to 2% of the general population and in over 5–10% of the elderly population (>70 years of age). In this sense, due to the ageing of society and demographic changes, the overall prevalence is expected to increase even further [7]. Atrial fibrillation is associated with a fivefold risk of stroke and a threefold incidence of congestive heart failure and doubles the risk of mortality and dementia [8]. Isolation of the pulmonary veins (PV) by catheter ablation has emerged as a first-line therapy for patients with symptomatic AF not responding to pharmaceutical treatment [9]. PVI has achieved high success in paroxysmal atrial fibrillation. Nevertheless, in persistent AF, there is still a high rate of recurrence. A very recent study (ERASE AF) demonstrated that ablation of extra PV areas with low voltage detected with mapping catheters is helpful in these patients. In this sense, MRI could play a role in detecting these areas with LGE.

Ventricular tachycardia (VT) is the most frequent etiology of sudden cardiovascular death (SCD) [10]. In patients with structural heart disease, VT is frequent and catheter ablation has become a standard treatment [11,12], being the main mechanism responsible for a re-entrant circuit [13–15]. In this sense, there is an area of slow conduction of intermediate tissue (so called border zone (BZ)) inside the core scar connecting regions of healthy tissue. These areas of slow conduction are referred to as conducting channels (CCs) which can be rigorously defined during ablation procedures using electroanatomical maps (EAMs) [15–18]. On the other hand, MRI allows the depiction of the BZ, healthy tissue and

core scar, identifying also CCs. A great concordance between EAMs and images obtained by MRI has been reported. Moreover, in a recent study [19] MRI has been carried out post mortem in cases of sudden cardiac death to research cardiac morphological alterations. Despite advancements in ablation technology and better understanding of arrhythmic substrates, VT recurrence rates are still high [20–23]. For this reason, there is a clinical need to improve the characterization of the VT substrate and the efficacy of VT ablation. In this context, LGE-MRI may play an important role.

The objective of this review is to analyse the application of LGE-MRI to improve ablation strategies for the two main cardiac arrhythmias: AF and VT.

2. Use of LGE-MRI for the Detection of Fibrosis

2.1. Principles of LGE

LGE-MRI for the detection of myocardial fibrosis was already described in the late 1990s. Its validation was firstly performed with a canine model with controlled myocardial infarction and LGE-MRI was compared with histology [24]. Contrast agents that use mainly gadolinium are able to diffuse freely into the interstitium but are unable to pass through intact cell membranes, leading to their accumulation in the extracellular space.

Fibrosis replacement produces an expansion of extracellular space so there is an increase in the volume of the distribution of gadolinium. More important, there is a prolonged washout of the gadolinium due the decreased number of capillary vessels in the scar tissue [25,26]. Regarding T1 sequence, gadolinium contrast agents decrease the T1 relaxation time of adjacent tissue. Therefore, LGE enhancement produces an increased signal intensity in T1-weighted MRI images. In addition, other diseases related to the expansion of the extracellular space can be shown by LGE, such as oedema and inflammation formation. Given the lack of specificity for fibrotic tissue detection, the lesion assessment can be challenging [27].

2.2. Protocol of Image Acquisition and LGE Analysis

To date, there is no agreement on the best standardized way to acquire MRI images for the detection of myocardial fibrosis [28–31]. Either 3T or 1.5 scanners can be used to acquire postcontrast images applying fast 3D gradient echo series with fat suppression and ECG gating. Subsequent inversion recovery sequences are used to nullify the signal of healthy myocardium and improve signal intensity and T1 contrast. The optimum inversion time (TI) that suppress healthy tissue (typically 250–300 ms) is initially determined empirically. Scar areas will thus appear hyperenhanced relative to healthy myocardium. Adjustment of TI values during acquisition may be necessary to accommodate incremental T1 values of the normal tissue owing to gadolinium washout. For this reason, ECG gating is important to limit motion artifacts and the MRI acquisition window is limited to less to 20% of the RR interval. For patients with AF, cardioversion is often recommended prior to the study to improve image quality [30,32]. Finally, in some patients another limiting factor could be the need for long breath-holds. To solve that limitation, free-breathing 3D navigators can be used that suppress respiratory artefacts through respiratory gating. Typical LGE-MRI sequences result in a voxel size of $1.25 \times 1.25 \times 2.5$ mm with scan times of 10–15 min, depending on heart rate and breathing patterns.

Regarding myocardial fibrosis, to obtain high-quality LGE-MRI images to evaluate it, the time delay between contrast injection and image acquisition is crucial, as the LGE amount depends on wash-in and washout kinetics. Despite there being no official consensus, usually LGE-MRI acquisition is performed 15–25 min (atrium) or 7–15 min (ventricle) after gadolinium contrast agent injection. The time delay may even be adjusted for each patient due to individual perfusion (cardiovascular function) and washout kinetics (renal function).

In our centre, the acquisition of ventricle images is performed 10–15 min after an intravenous gadolinium injection, and 20 min in the atrium.

2.3. Image Acquisition for Patients with Cardiac Devices

Most patients scheduled for VT ablation are individuals with established cardiomyopathy who carry an implantable cardioverter defibrillator (ICD) implanted for primary or secondary prevention. This issue represents a major limitation for MRI because of security and also because of hyperintense image artefacts that can be caused by the device.

Regarding safety, several studies have shown an extremely low risk of device-related complications in patients who undergo cardiac MRI, not only in MRI conditional devices, but also in the case of theoretical MRI nonconditional devices. With adequate intraprocedural programming of the device, MRI is safe in patients with MRI nonconditional devices [33–35]. In this sense, the main issue with patients with cardiac devices is the quality of MRI images due to the possible artefacts related to the ICD. Artefacts can occur when metallic ICD components distort the magnetic field [36,37] making it difficult to obtain clear images using LGE-MRI. The effect of ICD artefacts are most prominent in the anterior wall, and in patients with left sided devices, in the anterior and apical left ventricle. Some studies have suggested that limited spectral bandwidth of the inversion pulse used in LGE-MRI is the primary cause of device-related artefacts [38,39]. To avoid those artefacts, particular wideband MRI sequences have been recently developed, increasing the bandwidth of the inversion and excitation pulses. Therefore, the use of wideband sequences can minimize device-related artefacts and, subsequently, overcome the image artefact, making LGE-MRI robust for myocardial characterization [33,40,41]. Many centres including ours are now applying these wideband sequences, avoiding device-related artefacts and achieving high quality images, even in areas closed to the ICD. In fact, our group has recently proved a strong correlation between wideband LGE-MRI and electroanatomical maps [42]. In this study [42] the accuracy of wideband sequences to detect CCs previously located in EAMs was analysed for 13 patients with an ICD and a wideband sequence. The accuracy of CCs identified was 85.1% and the positive predicting value was 92.5%.

3. Image Post-Processing (Pre-Procedural)

3.1. Image Processing: Segmentation and Fibrosis Detection

Post-processing is necessary to acquire a 3D anatomical reconstruction of the chamber of interest and to identify, analyse and evaluate the scarring tissue. To acquire this 3D anatomical segmentation, there is a great deal of established open-source and commercial software for image post-processing.

The two steps required to achieve this 3D anatomical structure are segmentation of the anatomical chamber (LA and/or RA and PPVV in the case of AF and LV and/or RV in the case of VT) and detection of fibrotic and scarring areas inside the segmented anatomical structure.

I. Segmentation of anatomical structures

Accurate segmentation is required for scar analysis and fibrosis visualization. The segmentation process was performed manually. Clinicians or engineers segment the atrial wall or the myocardium manually: An accurate slice-by-slice 2D tracing of the LA wall and endocardial and epicardial myocardium to confine the region of interest (ROI) while avoiding anatomical structures (aortic ring, valves, papillary muscles, etc.), the blood pool, fat, etc. Currently, the different segmentation software programs have semiautomatic tools available. Therefore, the manual process may be used after this automatic segmentation to refine the results.

II. Detection of fibrotic tissue

Once the anatomy is properly segmented, the fibrotic regions (LGE) can be assessed qualitatively by visual assessment or quantitatively by using different thresholding techniques. To apply thresholding techniques, different approaches with different algorithms have been improved for the detection of arrhythmogenic areas. To date, there is limited reproducibility across centres because there is no single standardized method for LGE image analysis.

Obtaining a consistent internal reference for normalization and validated signal intensity thresholds that can accurately differentiate between healthy and scar tissue are crucial for quantifying LGE. The reason is that T1-weighted imaging relies on signal intensity contrast instead of directly measured absolute values.

Different methods have been validated for atrial fibrosis quantification (Table 1) [29–31,43–47]. Each method uses distinct internal references and thresholds. As an internal reference, the mean signal intensity of the blood pool is used extensively by numerous groups. Our group has recently validated a method quantifying signal intensity ratios using the mean signal intensity of the left atrial (LA) blood pool as a reference (signal intensity of each given voxel/mean signal intensity of the blood) [29]. The atrium thresholds to characterize healthy myocardium (signal intensity ratio $\leq$ 1.2) and fibrotic tissue (signal intensity ratio > 1.32) were derived from distinct cohorts including both young healthy individuals and post-AF ablation patients. Subsequently these cut-offs were verified in various studies in comparison with voltage mapping during ablation procedures and they were correlated with clinical endpoints [6,48,49] (Figure 1).

Table 1. LGE-MRI post-processing defining thresholds for fibrosis analysis.

	Reference	Model	n	Reference for Normalization	Defined Thresholds
Atrial Fibrosis	Peters et al., 2007 [31]	Human	23	LA blood pool signal intensity	"Minimum threshold which eliminates most left atrial blood pool pixels"
	Oakes et al., 2009 [30]	Human	81	Normal tissue	Mean signal intensity (normal tissue) + (2–4) SD
	Khurram et al., 2014 [47]	Human	75	Mean LA blood pool signal intensity	Fixed IIR threshold: upper limit of normal > 0.97 and dense scar > 1.6
	Harrison et al., 2014 [43]	Animal	16	Mean LA blood pool signal intensity	"2.3 SD for LGE post ablation and 3.3 SD for LGE chronically"
	Dewire et al., 2014 [46]	Human	60	Mean LA blood pool signal intensity	Universal threshold (abnormal myocardium: IIR > 0.97 and <1.61; dense scar: IIR > 1.61)
	Harrison et al., 2015 [44]	Human	20	Mean LA blood pool signal intensity	No universal threshold. Visualization of signal intensities in SD from reference
	Benito el al., 2017 [29]	Human	40	Mean LA blood pool signal intensity	Fixed IIR threshold: upper limit of normal = 1.2 and dense scar > 1.32
	Kurose et al., 2020 [45]	Human	30	Healthy atrial wall	>2 SDs above the mean of healthy left atrium wall
LV Fibrosis	Amado et al., 2004 [50]	Animal	13	Healthy myocardial segment	Mean signal intensity (noninfarcted myocardium region) + (1–6 SD)
	Yan et al., 2006 [51]	Human	144	Healthy myocardial segment	BZ: 2–3 SDs and scar > 3 SDs above remote myocardium
	Andreu et al., 2011 [52]	Human	12	Maximal myocardial signal	Scar > 60% of maximal signal intensity
	Fernandez-Armenta et al., 2013 [53]	Human	21	Maximal myocardial signal	Healthy tissue < 40%, BZ: 40–60% and scar > 60% of maximal signal intensity
	Cochet et al., 2013 [54]	Human	9	Maximal myocardial signal	BZ: 35–50% and scar > 50% of maximal signal intensity

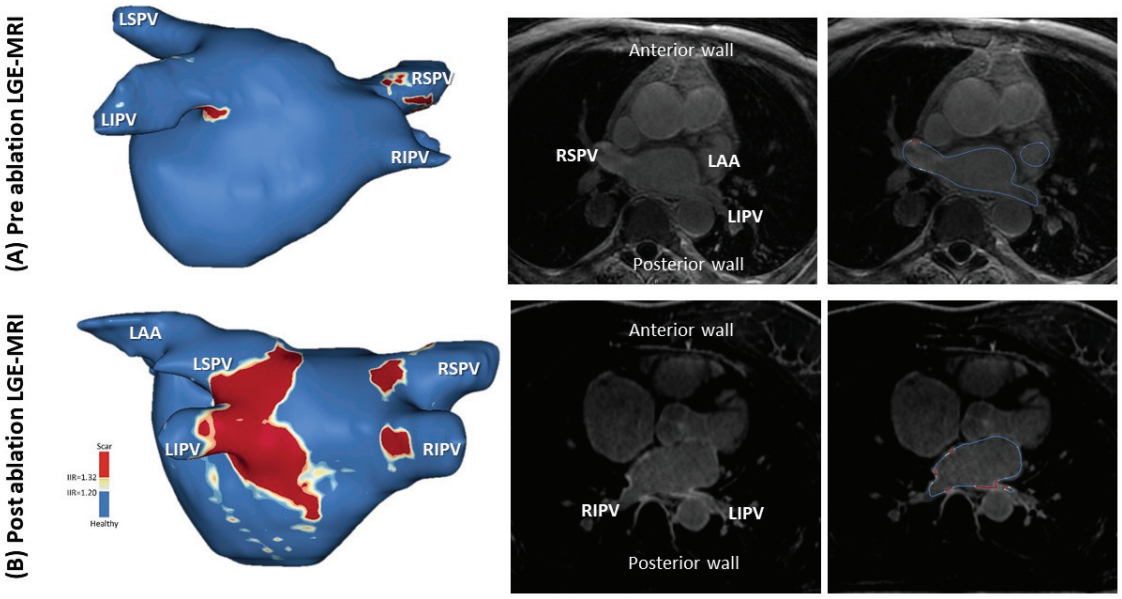

Figure 1. Postero-anterior view of three-dimensional left atrium reconstruction of LGE-MRI. 3D-LGE-LA reconstruction includes colour-coding based on image intensity ratios with thresholds for border zone (yellow 1.2–1.32) and dense scar (red > 1.32). (**A**) First line corresponds to preprocedural LGE-MRI and (**B**) second corresponds to a post-ablation LGE-MRI (3 months after PVI). LAA = left atrial appendage; LIPV = left inferior pulmonary vein; LSPV = left superior pulmonary vein; RIPV = right inferior pulmonary vein; RSPV = right superior pulmonary vein.

The most interesting approaches to detect and quantify fibrosis in LGE-MRI of the left atrial wall are carefully benchmarked by Pontecorboli et al. [2]. This review provides a critical analysis of the different methods to detect and quantify fibrosis in LGE-MRI, stating their advantages and limitations.

Likewise, for ventricular fibrosis quantification, various thresholds and methods have been verified (Table 1) [50–54]. Table 1 summarizes the main studies defining thresholds for LV. The most commonly used approach is the full width at half maximum (FWHM), which is a fixed thresholding method in which a fixed intensity threshold is defined as half of the maximum intensity of a user-selected hyperenhanced region. Another method is to define remote "healthy" myocardial segments as an internal reference for normalization. Another common method is the fixed-model approach, whereby intensities are thresholded to a fixed number of standard deviations (SD) from the mean intensity of the nulled myocardium or blood pool [55]. This is known as the n-SD method.

Our group study found that the correlation with EAM voltage mapping was reached with the thresholds of <40% as healthy tissue and >60% as a dense scar of the maximum signal intensity (Figure 2).

3.2. Deep Learning-Based Methods

With the development of artificial intelligence techniques, the application of deep learning to fibrosis and substrate visualization has also been studied, leading to the development of a fully automated key for LGE-MRI segmentation. An increasing number of various deep learning models using convolutional neural networks (for example, U-Net [56]) have demonstrated encouraging results in the segmentation of cardiac substructures. Goodfellow et al. 2016 [57] mathematically detail these deep neural networks.

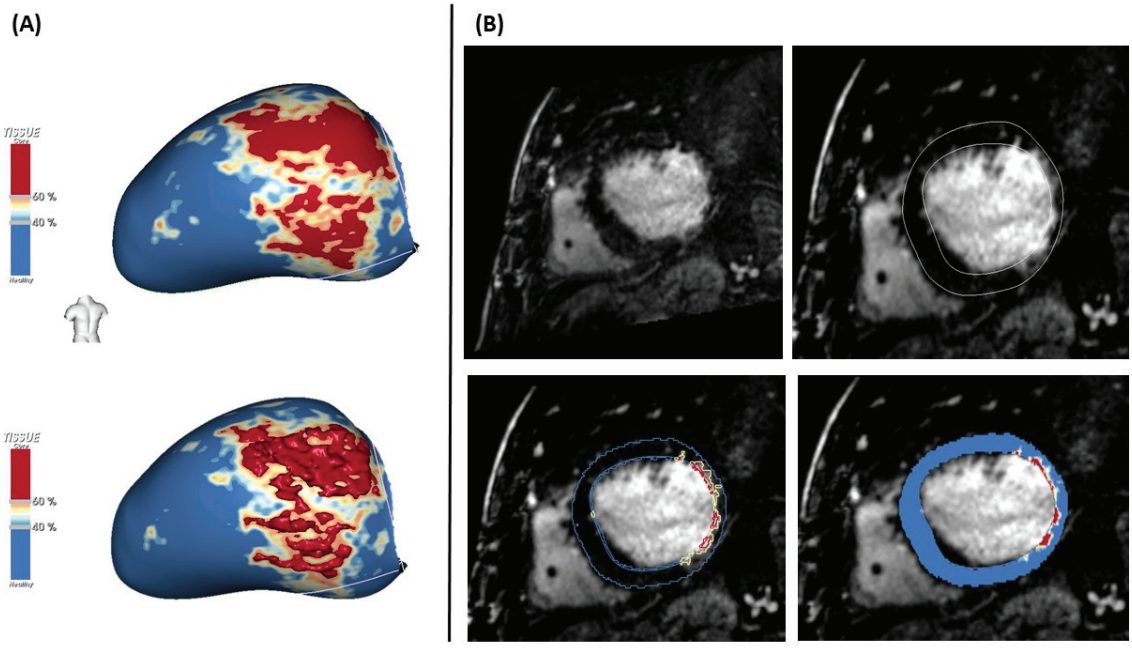

Figure 2. (**A**) Three-dimensional left ventricle reconstruction of LGE-MRI. LGE-based colour-coding is used to differentiate LV dense scar (red > 60% of maximum signal intensity) from border zone (yellow, 40–60% of maximum signal intensity) and healthy tissue (blue < 40%). (**B**) Raw images of LGE-MRI in a patient with chronic MI. Semiautomatic segmentation of epicardium and endocardium with detection of dense scar and border zone is shown.

4. Use of the Processed LGE-MRI for Ablation Procedures

LGE-MRI in VT or AF ablation procedures has proved to be an important tool to plan and guide ablation. Regarding planification, LGE-MRI allows us to perform a preprocedural assessment of cardiac anatomy and myocardial scar (location of conducting channels in the case of VT and PPVV gaps in AF), to decide the optimal access approach (especially in VT where both endocardial and epicardial approaches can be selected) and exclude intracardiac thrombus. In addition, 3D-LGE-MRI reconstruction can be visualized side by side or merged with electroanatomical maps during the procedure. In VT ablation, for example, MRI-aided ablation has demonstrated a lower need for RF delivery, higher noninducibility rates after substrate ablation, and a higher VT recurrence-free survival [58].

4.1. Determination of the Optimal Access Approach

In VT ablation, the location of the myocardial fibrosis is important for determining and designing ablation access: An epicardial approach for patients with epicardial or transmural scars and an endocardial approach for those without epicardial or transmural scars. In addition, LGE-MRI accurately defines intramural scarring, which is a major determinant of VT ablation failure [59]. For this specific case, ablation techniques such as septal alcholization [60], bipolar ablation or ablation using needle ablation catheters can be chosen to enhance outcomes [61].

4.2. Exclusion of Intracardiac Thrombus

In recent years, DE-MRI has been well validated as an accurate technique for the detection of left thrombi [62,63]. It is important in both VT and AF ablation to determine the presence of thrombus because patients with heart failure are at increased risk for thromboembolic events.

4.3. Integration of LGE-MRI and Electroanatomical Map (EAM) during Ablation

Several electroanatomical advanced mapping systems that display bipolar voltage maps and activation maps on a 3D reconstruction of the intracardiac chamber of interest have become available over the past few decades. Each system uses a different technology to generate a 3D image, record electrograms, and localize the electrode catheter in space. Current ablation techniques are heavily reliant on EAM systems (Carto (New York, NY, USA), Biosense Webster, Inc. (Irvine, CA, USA); NAVX (Paris, France), St Jude Medical (Saint Paul, MN, USA); Rhythmia Mapping, Boston Scientific Inc., (Boston, MA, USA).

Electroanatomical systems have been validated for anatomical and electrical accuracy in the atria as well as the ventricles [64–66]. However, there is an important limitation: the 3-dimensional reconstructions from catheters can provide inaccurate data on scar characteristics and could under- or overestimate the extent of scarring and arrhythmogenic substrate. This is due to different reasons: the influence of the electrode size, interelectrode spacing, angle of the incoming wavefront to the mapping catheter [60,67], and contact of the catheter with tissue (especially for those without a contact force sensor). Henceforth, EAMs can hardly be considered the gold standard of substrate definition. Moreover, it must be considered that low voltage detected in the EAM is not always equivalent to fibrosis and vice versa. Fibrosis distribution and fibrosis architecture and the possibility of far-field detection of the healthy tissue in the border of the fibrosis could affect the amplitude of the electrogram detected in the EAM.

Integration of imaging data into EAM systems provides more information about the arrhythmogenic substrate. Therefore, it is possible to merge the EAM with the 3D LGE-MRI reconstruction. Successful integration (with high accuracy) between EAM and MRI has been demonstrated in several studies [53,66,68].

For the merging process, landmarks in both the 3D reconstruction and EAM must be placed (one or more, depending on the system). The selected points to be used as the landmarks or fiducials must be in an identifiable and distinguishable place in the mapped anatomies (for example, the mitroaortic union, LV apex, the ostium of the pulmonary veins, etc.) with a certain angulation that enables them to be placed in the same direction. Once these points are selected, the estimated corresponding location of this endocardial point is marked on the imported 3D MRI surface reconstruction, thus creating a 'landmark pair'. At this point, the navigation system superimposes the 3D MRI surface reconstruction onto the real-time electroanatomic map with different algorithms, depending on each system (visual alignment, surface registration, etc.). Once the integration is completed, the user is able to navigate with the catheters over the 3D MRI reconstruction, visualizing and localizing the scar and the fibrotic tissue.

4.4. LGE-MRI for AF Ablation

The use of LGE-MRI for the assessment of fibrosis in the atrium has not become routine clinical practice. This is because the wall thickness of the atrium is lower than 1 mm, which is near the limit of spatial resolution of MRI, and due to less extensive and more diffuse fibrosis in comparison with the fibrosis in the ventricle. Nevertheless, recent improvements have been developed in MRI acquisition, including 3D navigated inversion recovery sequences to enhance signal-to-noise ratios and resolution, allowing valid atrium characterization [30,69]. These advances are now making LGE-MRI a widely accepted tool for assessing lesions, stratifying risks and selecting appropriate patients for AF ablation in many specialized centres [3].

Many other studies since then have tried to identify LGE-MRI predictors of recurrence after PVI ablation, and the degree of atrial fibrosis was confirmed to be an important predictor. In a retrospective study including patients undergoing AF ablation, there was an observed 45% increased risk of recurrence for each 10% increase in atrial fibrosis at the 5-year follow-up [70]. These data were supported by findings from another cohort of 165 patients. Patients with an amount of LGE less than 35% had favourable ablation outcomes regardless of AF persistence at baseline, whereas those with LGE greater than

35% had a higher rate of AF recurrence in the first year of follow-up after ablation [71]. In the DECAAF multicentre study [72], 260 patients who underwent PVI were included, and the extent of fibrosis in the LA was categorized as 1 (<10% of the atrial wall), 2 (>10% to <20%), 3 (>20% to <30%) and 4 (>30%). Recurrent arrhythmia during follow-up was direct and graded: from 15% in the stage I group to 51% in the stage IV group. In a subsequent randomized study, catheter ablation of left atrial fibrosis was proposed [73]. The benefit of ablation of these areas could not be demonstrated by this study. This result was supported by other randomized trials, where MRI fibrosis ablation plus PVI was not more effective than PVI alone [74].

Another important potential use of LGE-MRI is to guide repeated ablation procedures, as most cases of AF recurrence after PVI ablation are associated with areas of incomplete ablation or gaps around the pulmonary veins [49,75] (Figure 3). Some studies indicate that those gaps can be identified by LGE-MRI with high accuracy [6,48,49,76]. Badger et al. 2010 [75] demonstrated that LGE-MRI is able to confirm a PVI gap with very high predictive values. Bisbal et al. 2014 [6] showed for the first time that the elimination of gaps detected by LGE MRI generates a reisolation of PPVV in the majority of cases. In this particular study, the LGE-MRI reconstruction was merged with the EAM, so the operator was blinded to electrical information, only isolating gaps localized in the MRI. Reisolation was acquired in 95.6% of the reconnected PVs. In addition to guiding redo procedures, gap detection by LGE-MRI has been considered a predictor of AF recurrence. Linhart et al. 2018 [69] found that the relative gap length calculated as the absolute gap length divided by total length of the ablation line measured during MRI at 3 months of follow-up was a marker predicting AF recurrence 1 year after PVI.

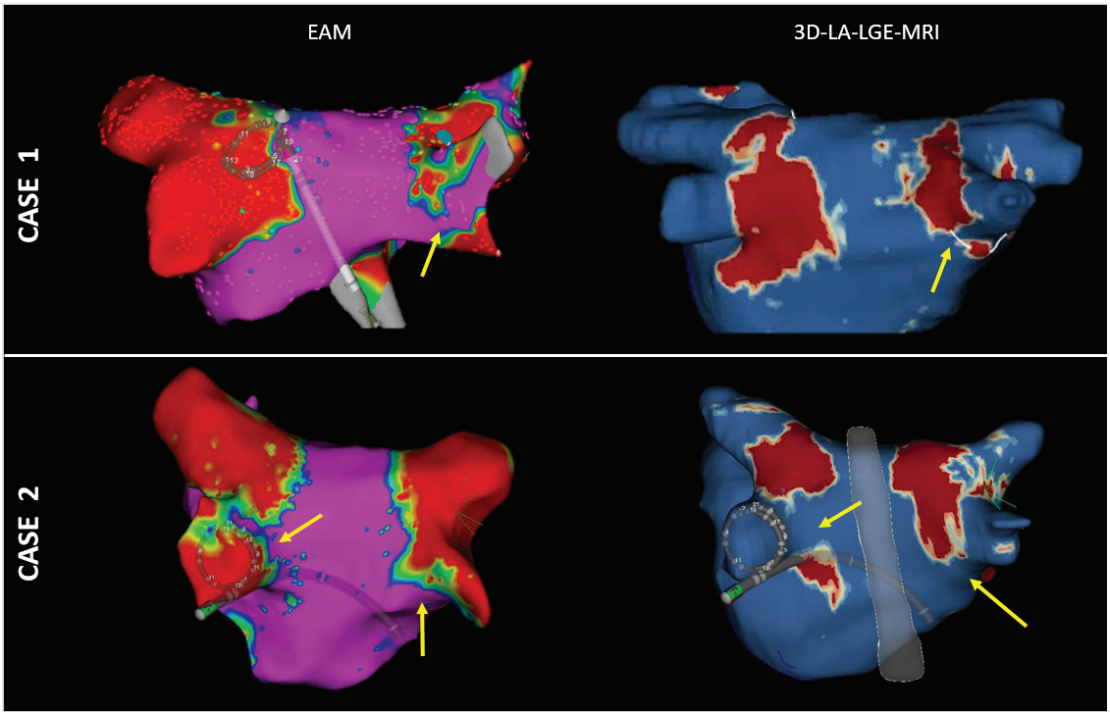

Figure 3. Agreement between EAM voltage map and LGE-MRI gap localisation. From (**left**) to (**right**), voltage map with gaps localised during a repeated ablation intervention. Right, gaps localised at the same region by prior LGE-MRI 3 months post first ablation. Yellow arrows indicate detected EAM gaps and LGE-MRI discontinuities, respectively.

4.5. LGE-MRI for VT Ablation

The use of LGE-MRI in patients undergoing VT ablation is increasing, especially for the preprocedural assessment of the cardiac anatomy and myocardial scarring and for intraprocedural integration.

On the one hand, the use of LGE-MRI provides accurate knowledge of the arrhythmic substrate, including the critical VT isthmuses, the BZ areas and CCs, supporting ablation strategies [52,54,58,77]. The identification of these specific areas has been very useful in cases of ischaemic cardiomyopathy [52,54,58,77]. Moreover, LGE-MRI is also very helpful in cases of nonischaemic cardiomyopathy (NICM). In this sense, some studies have demonstrated that the location of scar in NICM, is also useful for the ablation procedure [78]. This is because the ablation technique and the type of tachycardia is related to the location of scar tissue. Similarly, the effectiveness of using MRI for selecting the appropriate ablation technique was demonstrated in a study involving 80 patients with both NICM and ischemic cardiomyopathy (ICM). In that study, the epicardial or endocardial access was chosen based on MRI. In addition, in case of the intramural substrate, the distance of the scar to the right and left endocardium was used to decided how to approach this substrate [79]. Figure 4 shows an example of the correspondence of LGE-MRI 3D reconstruction with an EAM map.

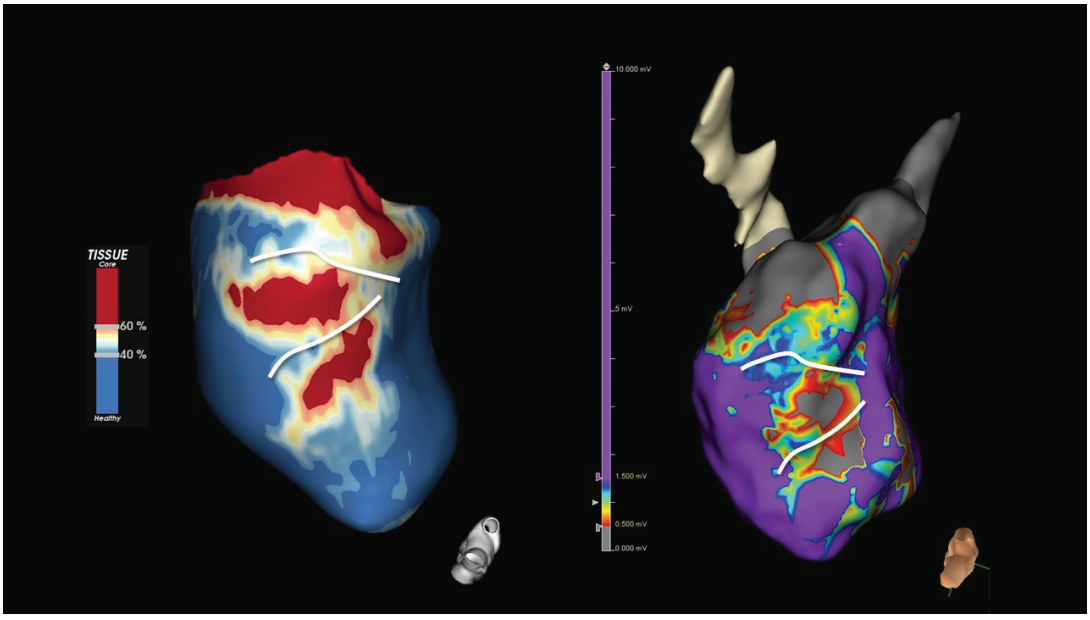

Figure 4. Example of correlation of the 3D-VI reconstruction from LGE-MRI with electroanatomical voltage map. From left to right: LGE-MRI map (colour-coding: blue: healthy tissue, yellow: border zone and red: core scar) with two clear conducting channels (white line); and electroanatomical map high density voltage map showing septal scar (colour-coding: purple: healthy tissue, red: border zone and grey: core scar), with conducting channels at the same region as compared to the LGE-MRI.

On the other hand, in relation to EAMs, studies have not only demonstrated the feasibility of integration during the ablation procedure and a good correlation between 3D-LV reconstruction and EAMs [52,79,80], but have also shown that the scars in MRI scans were larger compared to those detected by EAMs. Moreover, some VT isthmuses were found in regions identified as scar by MRI, but were nonvisible in EAMs [65]. These kinds of studies underscore the value of integrating LGE and EAM for comprehensive scar characterization, particularly in the context of defining infarct BZs, nontransmural scars, and small subepicardial scars [65]. This role of preprocedural MRI to aid procedural access

has also been related to a lower VT recurrence rate, improving the ablation results. A study in patients with ischemic heart disease and epicardial substrate identified prior to ablation by MRI showed that those patients that underwent ablation with epicardial access had better results in terms of VT recurrence, compared to patients who underwent exclusively the endocardial approach [80].

Finally, there is a clear role of MRI in predicting the risk of VT recurrence, even without integration images into the EAM. In a study by Quinto et al. [81], 110 patients who underwent VT ablation with preprocedural LGE-MRI were analysed, identifying MRI-related factors that were clearly linked to a higher rate of VT recurrence, such as mass of border zone and total scar, septal substrate or midmural and transmural CCs. Similarly, in a smaller study [82], scar area was also linked to clinical outcomes, such as VT recurrence. Another study [83] involving 25 non ischemic patients, also verified that the extension of septal LGE was associated with a higher rate of VT recurrence.

5. Conclusions

LGE-MRI constitutes the gold standard for noninvasive characterization of arrhythmogenic myocardial substrate in AF and VT. Its usefulness in both preprocedural planning, substrate analysis and post-ablation evaluation has been proved, even though more technological developments are needed to implement it into routine practice.

6. Limitations

Some limitations need to be addressed. First, consistent methodological and analytical standards defining fibrotic tissue characterization are needed to achieve reproducibility of results between centres. The use of the same values and methods to define fibrotic tissue, will promote the implementation in clinical practice. Second, there is also no homogenous method for integrating MRI-3D into the navigation system. Each group used different structures for merging (pulmonary veins, right ventricle, aortic roof, pulmonary artery, etc.). A more standardized method for using MRI to facilitate ablation would be beneficial for increasing its practical use. In the area of VT ablation, the assessment of ablation lesions has been investigated in small series [28,84,85]. More research is required to confirm and evaluate the usefulness of LGE-MRI in the evaluation of ventricular ablation lesions. Finally, despite new MRI scans, spatial resolution could be insufficient to detect small areas of fibrosis in the atrium wall due to its thickness. In the same line, some types of interstitial fibrosis could be underdetected with conventional LGE, and T1 mapping needs to be improved for clinical practice.

Author Contributions: Conceptualization: P.G., S.V.-C. and E.F., writing: P.G.; review: S.V.-C. and E.F.; and supervision: T.A. and I.R.-L. All authors have read and agreed to the published version of the manuscript.

Funding: This study was supported by Hospital Clinic de Barcelona/Instituto de Salud Carlos III (ISCIII) PI20/00693/CB16/11/00354.

Institutional Review Board Statement: Not applicable.

Informed Consent Statement: Not applicable.

Data Availability Statement: Not applicable.

Conflicts of Interest: I.R.-L. have served as consultants for Boston Scientific and Abbott Medical. T.A. has received research grants for investigator-initiated trials from Biosense Webster.

References

1. Kim, H.W.; Farzaneh-Far, A.; Kim, R.J. Cardiovascular magnetic resonance in patients with myocardial infarction. *J. Am. Coll. Cardiol.* **2009**, *55*, 1–16. [CrossRef] [PubMed]
2. Pontecorboli, G.; Figueras i Ventura, R.M.; Carlosena, A.; Benito, E.; Prat-Gonzales, S.; Padeletti, L.; Mont, L. Use of delayed-enhancement magnetic resonance imaging for fibrosis detection in the atria: A review. *Europace* **2017**, *19*, 180–189. [CrossRef] [PubMed]

3. Hindricks, G.; Potpara, T.; Dagres, N.; Arbelo, E.; Bax, J.J.; Blomstrom-Lundqvist, C.; Boriani, G.; Castella, M.; Dan, G.A.; Dilaveris, P.E.; et al. ESC guidelines for the diagnosis and management of atrial fibrillation developed in collaboration with the European Association of Cardio-Thoracic Surgery (EACTS). *Eur. Heart J.* **2021**, *42*, 373–498. [CrossRef] [PubMed]
4. Cronin, E.M.; Bogun, F.M.; Maury, P.; Peichl, P.; Chen, M.; Namboodiri, N.; Aguinaga, L.; Leite, L.R.; Al-Khatib, S.; Anter, E.; et al. 2019 HRS/EHRA/APHRS/LAHRS expert consensus statement on catheter ablation of ventricular arrhythmias: Executive summary. *Europace* **2020**, *22*, 450–495. [CrossRef]
5. Berruezo, A.; Penela, D.; Jáuregui, B.; Soto-Iglesias, D. The role of imaging in catheter ablation of ventricular arrhythmias. *Pacing Clin. Electrophysiol.* **2021**, *44*, 1115–1125. [CrossRef]
6. Bisbal, F.; Guiu, E.; Cabanas-Grandío, P.; Berruezo, A.; Prat-Gonzalez, S.; Vidal, B.; Garrido, C.; Andreu, D.; Fernandez-Armenta, J.; Tolosana, J.M.; et al. CMR-guided approach to localize and ablate gaps in repeat AF ablation procedure. *JACC Cardiovasc. Imaging* **2014**, *7*, 653–663. [CrossRef]
7. Feinberg, W.M.; Blackshear, J.L.; Laupacis, A.; Kronmal, R.; Hart, R.G. Prevalence, age distribution and gender of patients with atrial fibrillation: Analysis and implications. *Arch. Intern. Med.* **1995**, *155*, 469–473. [CrossRef]
8. January, C.T.; Wann, L.; Alpert, J.S.; Calkins, H.; Cigarroa, J.E.; Cleveland, J.C., Jr.; Conti, J.B.; Ellinor, P.T.; Ezekowitz, M.D.; Field, M.E.; et al. AHA/ACC/HRS guideline for the management of patients with atrial fibrillation: Executive summary: A report of the American College of Cardiology/American Heart Association Task Force on Practice Guidelines and the Heart Rhythm Society. *J. Am. Coll. Cardiol.* **2014**, *64*, 2246–2280. [CrossRef]
9. Calkins, H.; Kuck, K.H.; Cappato, R.; Brugada, J.; Camm, A.J.; Chen, S.A. 2012 HRS/EHRA/ECAS expert consensus statement on catheter and surgical ablation of atrial fibrillation: Recommendations for patient selection, procedural techniques, patient management and follow-up, definitions, endpoints, and research trial design. *Europace* **2012**, *14*, 528–606. [CrossRef]
10. John, R.M.; Tedrow, U.B.; Koplan, B.A.; Albert, C.M.; Epstein, L.M.; Sweeney, M.O.; Miller, A.L.; Michaud, G.; Stevenson, W. Ventricular arrhythmias and sudden cardiac death. *Lancet* **2012**, *380*, 1520–1529. [CrossRef]
11. Tung, R.; Vaseghi, M.; Frankel, D.S.; Vergara, P.; Di Biase, L.; Nagashima, K.; Yu, R.; Vangala, S.; Tseng, C.-H.; Choi, E.-K.; et al. Freedom from recurrent ventricular tachycardia after catheter ablation is associated with improved survival in patients with structural heart disease: An International VT Ablation Center Collaborative Group study. *Heart Rhythm* **2015**, *12*, 1997–2007. [CrossRef]
12. Dukkipati, S.R.; Koruth, J.S.; Chouddry, S.; Miller, M.A.; Whang, W.; Reddy, V.Y. Catheter ablation of ventricular. *J. Am. Coll. Cardiol.* **2017**, *70*, 2924–2941. [CrossRef]
13. De Bakker, J.M.T.; Van Capelle, F.J.L.; Janse, M.J.; Wilde, A.A.M.; Coronel, R.; Becker, A.E.; Dingemans, K.P.; van Hemel, N.M.; Hauer, R.N. Reentry as a cause of ventricular tachycardia in patients with chronic ischemic heart disease: Electrophysiologic and anatomic correlation. *Circulation* **1988**, *77*, 589–606. [CrossRef]
14. Harada, T.; Stevenson, W.G.; Kocovic, D.Z.; Friedman, P.L. Catheter ablation of ventricular tachycardia after myocardial infarction: Relation of endocardial sinus rhythm late potentials to the reentry circuit. *J. Am. Coll. Cardiol.* **1997**, *30*, 1015–1023. [CrossRef]
15. Mountantonakis, S.E.; Park, R.E.; Frankel, D.S.; Hutchinson, M.D.; Dixit, S.; Cooper, J.; Callans, D.; Marchlinski, F.E.; Gerstenfeld, E.P. Relationship between voltage map "channels" and the location of critical isthmus sites in patients with post-infarction cardiomyopathy and ventricular tachycardia. *J. Am. Coll. Cardiol.* **2013**, *61*, 2088–2095. [CrossRef]
16. Bogun, F.; Marine, J.E.; Oral, H.; Pelosi, F.; Morady, F. Relative timing of isolated potentials during post-infarction ventricular tachycardia and sinus rhythm. *J. Interv. Card. Electrophysiol.* **2004**, *10*, 65–72. [CrossRef]
17. Arenal, A.; Glez-Torrecilla, E.; Ortiz, M.; Villacastín, J.; Fdez-Portales, J.; Sousa, E.; del Castillo, S.; de Isla, L.P.; Jimenez, J.; Almendral, J. Ablation of electrograms with an isolated, delayed component as treatment of unmappable monomorphic ventricular tachycardias in patients with structural heart disease. *J. Am. Coll. Cardiol.* **2003**, *41*, 81–92. [CrossRef]
18. Bogun, F.; Good, E.; Reich, S.; Elmouchi, D.; Igic, P.; Lemola, K.; Tschopp, D.; Jongnarangsin, K.; Oral, H.; Chugh, A.; et al. Isolated potentials during sinus rhythm and pace-mapping within scars as guides for ablation of post-infarction ventricular tachycardia. *J. Am. Coll. Cardiol.* **2006**, *47*, 2013–2019. [CrossRef]
19. Bertozzi, G.; Cafarelli, F.P.; Ferrara, M.; Di Fazio, N.; Guglielmi, G.; Cipolloni, L.; Manetti, F.; La Russa, R.; Fineschi, V. Sudden Cardiac Death and Ex-Situ Post-Mortem Cardiac Magnetic Resonance Imaging: A Morphological Study Based on Diagnostic Correlation Methodology. *Diagnostics* **2022**, *12*, 218. [CrossRef]
20. Aziz, Z.; Shatz, D.; Raiman, M.; Upadhyay, G.A.; Beaser, A.D.; Besser, S.A. Targeted ablation of ventricular tachycardia guided by wavefront discontinuities during sinus rhythm: A new functional substrate mapping strategy. *Circulation* **2019**, *140*, 1383–1397. [CrossRef]
21. Willems, S.; Tilz, R.R.; Steven, D.; Kääb, S.; Wegscheider, K.; Gellér, L.; Meyer, C.; Heeger, C.-H.; Metzner, A.; Sinner, M.F.; et al. Preventive or deferred ablation of ventricular tachycardia in patients with ischemic cardiomyopathy and implantable defibrillator (Berlin VT): A multicenter randomized trial. *Circulation* **2020**, *2020*, 1057–1067. [CrossRef] [PubMed]
22. Hadjis, A.; Frontera, A.; Rosario, L.; Bisceglia, C.; Bognoni, L.; Foppoli, L.; Lipartiti, F.; Paglino, G.; Radinovic, A.; Tsitsinakis, G.; et al. Complete electroanatomic imaging of the diastolic pathway is associated with improved. *Circ. Arrhythm. Electrophysiol.* **2020**, *2020*, 927–937. [CrossRef]
23. Quinto, L.; Sanchez-Somonte, P.; Alarcón, F.; Garre, P.; Castillo, À.; San Antonio, R. Ventricular tachycardia burden reduction after substrate ablation: Predictors of recurrence. *Heart Rhythm* **2021**, *18*, 896–904. [CrossRef] [PubMed]

24. Kim, R.J.; Fieno, D.S.; Parrish, T.B.; Harris, K.; Chen, E.-L.; Simonetti, O.; Bundy, J.; Finn, J.P.; Klocke, F.J.; Judd, R.M. Relationship of MRI delayed contrast enhancement to irreversible injury, infarct age, and contractile function. *Circulation* **1999**, *100*, 1992–2002. [CrossRef]
25. Bing, R.; Dweck, M.R. Myocardial fibrosis: Why image, how to image and clinical implications. *Heart* **2019**, *105*, 1832–1840. [CrossRef]
26. Mewton, N.; Liu, C.Y.; Croisille, P. Assessment of myocardial fibrosis with cardiovascular magnetic resonance. *J. Am. Coll. Cardiol.* **2011**, *57*, 891–903. [CrossRef]
27. Kiuchi, K.; Fukuzawa, K.; Nogami, M.; Watanabe, Y.; Takami, M.; Izawa, Y.; Negi, N.; Kyotani, K.; Mori, S.; Hirata, K.-I. Visualization of intensive atrial inflammation and fibrosis after cryoballoon ablation: PET/MRI and LGE-MRI analysis. *J. Arrhythm.* **2021**, *37*, 52–59. [CrossRef]
28. Dickfeld, T.; Kato, R.; Zviman, M.; Lai, S.; Meininger, G.; Lardo, A.C.; Roguin, A.; Blumke, D.; Berger, R.; Calkins, H.; et al. Characterization of radiofrequency ablation lesions with gadolinium-enhanced cardiovascular magnetic resonance imaging. *J. Am. Coll. Cardiol.* **2006**, *47*, 370–378. [CrossRef]
29. Benito, E.M.; Carlosena-Remirez, A.; Guasch, E. Left atrial fibrosis quantification by late gadolinium-enhanced magnetic resonance: A new method to standardize the thresholds for reproducibility. *Europace* **2017**, *19*, 1272–1279. [CrossRef]
30. Oakes, R.S.; Badger, T.J.; Kholmovski, E.G. Detection and quantification of left atrial structural remodeling with delayed-enhancement magnetic resonance imaging in patients with atrial fibrillation. *Circulation* **2009**, *119*, 1758–1767. [CrossRef]
31. Peters, D.C.; Wylie, J.V.; Hauser, T.H.; Kissinger, K.V.; Botnar, R.M.; Essebag, V.; Josephson, M.E.; Manning, W.J. Detection of pulmonary vein and left atrial scar after catheter ablation with three-dimensional navigator-gated delayed enhancement MR imaging: Initial experience. *Radiology* **2007**, *243*, 690–695. [CrossRef]
32. Vijayakumar, S.; Kholmovski, E.; McGann, C.; Marrouche, N.F. Dependence of contrast to noise ratio between ablation scar and other tissues on patient heart rate and flip angle for late gadolinium enhancement imaging of the left atrium. *J. Cardiovasc. Magn. Reson.* **2012**, *14* (Suppl. S1), O107. [CrossRef]
33. Do, D.H.; Eyvazian, V.; Bayoneta, A.J.; Hu, P.; Finn, J.P.; Bradfield, J.S. Cardiac magnetic resonance imaging using wideband sequences in patients with non-conditional cardiac implanted electronic devices. *Heart Rhythm* **2018**, *15*, 218–225. [CrossRef]
34. Seewoster, T.; Lobe, S.; Hilbert, S.; Bollmann, A.; Sommer, P.; Lindemann, F.; Bacevičius, J.; Schöne, K.; Richter, S.; Döring, M.; et al. Cardiovascular magnetic resonance imaging in patients with cardiac implantable electronic devices: Best practice and real-world experience. *Europace* **2019**, *19*, 818–823. [CrossRef]
35. Flett, A.S.; Hasleton, J.; Cook, C.; Hausenloy, D.; Quarta, G.; Ariti, C.; Muthurangu, V.; Moon, J.C. Evaluation of techniques for the quantification of myocardial scar of differing etiology using cardiac magnetic resonance. *JACC Cardiovasc. Imaging* **2011**, *4*, 150–156. [CrossRef]
36. Dickfeld, T.; Tian, J.; Ahmad, G.; Jimenez, A.; Turgeman, A.; Kuk, R.; Peters, M.; Saliaris, A.; Saba, M.; Shorofsky, S.; et al. MRI-guided ventricular tachycardia ablation: Integration of late gadoliniumenhanced 3D scar in patients with implantable cardioverterdefibrillators. *Circ. Arrhythm. Electrophysiol.* **2011**, *4*, 172–184. [CrossRef]
37. Sasaki, T.; Hansford, R.; Zviman, M.M. Quantitative assessment of artifacts on cardiac magnetic resonance imaging of patients with pacemakers and implantable cardioverter-defibrillators. *Circ. Cardiovasc. Imaging* **2011**, *4*, 662–670. [CrossRef]
38. Rashid, S.; Rapacchi, S.; Shivkumar, K.; Plotnik, A.; Finn, J.P.; Hu, P. Modified wideband three-dimensional late gadolinium enhancement MRI for patients with implantable cardiac devices. *Magn. Reson. Med.* **2016**, *75*, 572–584. [CrossRef]
39. Rashid, S.; Rapacchi, S.; Vaseghi, M. Improved late gadolinium enhancement MR imaging for patients with implanted cardiac devices. *Radiology* **2014**, *270*, 269–274. [CrossRef]
40. Bhuva, A.N.; Kellman, P.; Graham, A.; Ramlall, M.; Boubertakh, R.; Feuchter, P.; Hawkins, A.; Lowe, M.; Lambiase, P.D.; Sekhri, N.; et al. Clinical impact of cardiovascular magnetic resonance with optimized myocardial scar detection in patients with cardiac implantable devices. *Int. J. Cardiol.* **2019**, *15*, 72–78. [CrossRef]
41. Hilbert, S.; Weber, A.; Nehrke, K.; Bornert, P.; Schnackenburg, B.; Oebel, S. Artefact-free late gadolinium enhancement imaging in patients with implanted cardiac devices using a modified broadband sequence: Current strategies and results from a real-world patient cohort. *Europace* **2018**, *20*, 801–807. [CrossRef] [PubMed]
42. Roca-Luque, I.; Van Breukelen, A.; Alarcon, F.; Garre, P.; Tolosana, J.M.; Borras, R. Ventricular scar channel entrances identified by new wideband cardiac magnetic resonance sequence to guide ventricular tachycardia ablation in patients with cardiac defibrillators. *Europace* **2020**, *22*, 598–606. [CrossRef] [PubMed]
43. James, L.H.; Henrik, K.J.; Sarah, A.P.; Amedeo, C.; Anne, K.G.; Lars, Ø.B.; Steen, F.; Pedersen, J.F.; Bentzon, C.K.; Rashed, K.; et al. Cardiac magnetic resonance and electroanatomical mapping of acute and chronic atrial ablation injury: A histological validation study. *Eur. Heart J.* **2014**, *35*, 1486–1495. [CrossRef]
44. Harrison, J.L.; Sohns, C.; Linton, N.W.; Karim, R.; Williams, S.E.; Rhode, K.S.; Gill, J.; Cooklin, M.; Rinaldi, C.A.; Wright, M.; et al. Repeat left atrial catheter ablation: Cardiac magnetic resonance prediction of endocardial voltage and gaps in ablation lesion sets. *Circ. Arrhythm. Electrophysiol.* **2015**, *8*, 270–278. [CrossRef] [PubMed]
45. Kurose, J.; Kiuchi, K.; Fukuzawa, K. Lesion characteristics between cryoballoon ablation and radiofrequency ablation with a contact-force sensing catheter: Late-gadolinium enhancement magnetic resonance imaging assessment. *J. Cardiovasc. Electrophysiol.* **2020**, *31*, 2572–2581. [CrossRef]

46. Dewire, J.; Khurram, I.M.; Pashakhanloo, F.; Spragg, D.; Marine, J.E.; Berger, R.D. The association of pre-existing left atrial fibrosis with clinical variables in patients referred for catheter ablation of atrial fibrillation. *Clin. Med. Insights Cardiol.* **2014**, *8* (Suppl. S1), 25–30. [CrossRef]
47. Khurram, I.M.; Beinart, R.; Zipunnikov, V.; Dewire, J.; Yarmohammadi, H.; Sasaki, T.; Spragg, D.D.; Marine, J.E.; Berger, R.D.; Halperin, H.R.; et al. Magnetic resonance image intensity ratio, a normalized measure to enable interpatient comparability of left atrial fibrosis. *Heart Rhythm* **2014**, *11*, 85–92. [CrossRef]
48. Quinto, L.; Cozzari, J.; Benito, E.; Alarcón, F.; Bisbal, F.; Trotta, O.; Caixal, G.; Antonio, R.S.; Garre, P.; Prat-Gonzalez, S.; et al. Magnetic resonance guided re-ablation for atrial fibrillation is associated with a lower recurrence rate: A case-control study. *Europace* **2020**, *22*, 1805–1811. [CrossRef]
49. Fochler, F.; Yamaguchi, T.; Kheirkahan, M. Late gadolinium enhancement magnetic resonance imaging guided treatment of post atrial fibrillation ablation recurrent arrhythmia. *Circ. Arrhythm. Electrophysiol.* **2019**, *12*, e007174. [CrossRef]
50. Amado, L.; Gerber, B.; Gupta, S.; Rettmann, D.; Szarf, G.; Schock, R.; Nasir, K.; Kraitchman, D.; Lima, J. Accurate and objective infarct sizing by contrastenhanced magnetic resonance imaging in a canine myocardial infarction model. *J. Am. Coll. Cardiol.* **2004**, *44*, 2383–2389. [CrossRef]
51. Yan, A.T.; Shayne, A.J.; Brown, K.A.; Gupta, S.N.; Chan, C.W.; Luu, T.M.; Di Carli, M.F.; Reynolds, H.G.; Stevenson, W.G.; Kwong, R.Y. Characterization of the peri-infarct zone by contrast-enhanced cardiac magnetic resonance imaging is a powerful predictor of postmyocardial infarction mortality. *Circulation* **2006**, *114*, 32–39. [CrossRef]
52. Andreu, D.; Berruezo, A.; Ortiz-Pérez, J.T.; Silva, E.; Mont, L.; Borràs, R.; de Caralt, T.M.; Perea, R.J.; Fernández-Armenta, J.; Zeljko, H.; et al. Integration of 3D electroanatomic maps and magnetic resonance scar characterization into the navigation system to guide ventricular tachycardia ablation. *Circ. Arrhythm. Electrophysiol.* **2011**, *4*, 674–683. [CrossRef]
53. Fernandez-Armenta, J.; Berruezo, A.; Andreu, D. Threedimensional architecture of scar and conducting channels based on high resolution ce-CMR: Insights for ventricular tachycardia ablation. *Circ. Arrhythm. Electrophysiol.* **2013**, *6*, 528–537. [CrossRef]
54. Cochet, H.; Komatsu, Y.; Sacher, F. Integration of merged delayed-enhanced magnetic resonance imaging and multidetector computed tomography for the guidance of ventricular tachycardia ablation: A pilot study. *J. Cardiovasc. Electrophysiol.* **2013**, *24*, 419–426. [CrossRef]
55. Roca-Luque, I.; Rivas-Gándara, N.; Francisco-Pascual, J.; Rodriguez-Sanchez, J.; Cuellar-Calabria, H.; Rodriguez-Palomares, J.; García-Del Blanco, B.; Pérez-Rodon, J.; Santos-Ortega, A.; Rosés-Noguer, F.; et al. Preprocedural imaging to guide transcoronary ethanol ablation for refractory septal ventricular tachycardia. *J. Cardiovasc. Electrophysiol.* **2019**, *30*, 448–456. [CrossRef]
56. Ronneberger, O.; Fischer, P.; Brox, T. U-Net: Convolutional networks for biomedical image segmentation. In *Medical Image Computing and Computer-Assisted Intervention—MICCAI 2015*; Lecture Notes in Computer Science; Navab, N., Hornegger, J., Wells, W., Frangi, A., Eds.; Springer: Cham, Switzerland, 2015; Volume 9351, pp. 234–241. [CrossRef]
57. Goodfellow, I.; Bengio, Y.; Courville, A. *Deep Learning*; MIT Press: Cambridge, MA, USA, 2016.
58. Gupta, S.; Desjardins, B.; Baman, T.; Ilg, K.; Good, E.; Crawford, T.; Oral, H.; Pelosi, F.; Chugh, A.; Morady, F.; et al. Delayed-enhanced MR scar imaging and intraprocedural registration into an electroanatomical mapping system in post-infarction patients. *JACC Cardiovasc. Imaging* **2012**, *5*, 207–210. [CrossRef]
59. Bogun, F.M.; Desjardins, B.; Good, E.; Gupta, S.; Crawford, T.; Oral, H.; Ebinger, M.; Pelosi, F.; Chugh, A.; Jongnarangsin, K.; et al. Delayed-enhanced magnetic resonance imaging in nonischemic cardiomyopathy: Utility for identifying the ventricular arrhythmia substrate. *J. Am. Coll. Cardiol.* **2009**, *53*, 1138–1145. [CrossRef]
60. Takigawa, M.; Relan, J.; Martin, R.; Kim, S.; Kitamura, T.; Frontera, A.; Cheniti, G.; Vlachos, K.; Massoullié, G.; Martin, C.A.; et al. Effect of bipolar electrode orientation on local electrogram properties. *Heart Rhythm* **2018**, *15*, 1853–1861. [CrossRef]
61. Kumar, S.; Tedrow, U.B.; Stevenson, W.G. Adjunctive interventional techniques when percutaneous catheter ablation for drug refractory ventricular arrhythmias fail: A contemporary review. *Circ. Arrhythm. Electrophysiol.* **2017**, *10*, e003676. [CrossRef]
62. Weinsaft, J.W.; Kim, H.W.; Shah, D.J.; Klem, I.; Crowley, A.L.; Brosnan, R.; James, O.G.; Patel, M.R.; Heitner, J.; Parker, M.; et al. Detection of left ventricular thrombus by delayed-enhancement cardiovascular magnetic resonance prevalence and markers in patients with systolic dysfunction. *J. Am. Coll. Cardiol.* **2008**, *52*, 148–157. [CrossRef]
63. Weinsaft, J.W.; Kim, R.J.; Ross, M.; Krauser, D.; Manoushagian, S.; LaBounty, T.M.; Cham, M.D.; Min, J.K.; Healy, K.; Wang, Y.; et al. Contrast-enhanced anatomic imaging as compared to contrast enhanced tissue characterization for detection of left ventricular thrombus. *JACC Cardiovasc. Imaging* **2009**, *2*, 969–979. [CrossRef] [PubMed]
64. Stevenson, W.G.; Delacretaz, E.; Friedman, P.L. Identification and ablation of macroreentrant ventricular tachycardia with the CARTO electroanatomical mapping system. *Pacing Clin. Electrophysiol.* **1998**, *21*, 1448. [CrossRef] [PubMed]
65. Marchlinski, F.E.; Callans, D.J.; Gottlieb, C.D.; Zado, E. Linear ablation lesions for control of un-mappable ventricular tachycardia in patients with ischemic and nonischemic cardiomyopathy. *Circulation* **2000**, *101*, 1288. [CrossRef] [PubMed]
66. Wijnmaalen, A.P.; van der Geest, R.J.; van Huls van Taxis, C.F.B.; Siebelink, H.M.J.; Kroft, L.J.M.; Bax, J.J.; Reiber, J.H.; Schalij, M.J.; Zeppenfeld, K. Head-to-head comparison of contrast-enhanced magnetic resonance imaging and electroanatomical voltage mapping to assess post-infarct scar characteristics in patients with ventricular tachycardias: Real-time image integration and reversed registration. *Eur. Heart J.* **2011**, *32*, 104–114. [CrossRef]
67. Vázquez-Calvo, S.; Garre, P.; Sánchez-Somonte, P. Orthogonal high density mapping with VT isthmus analysis vs. pure substrate VT ablation: A case-control study. *Front. Cardiovasc. Med.* **2022**, *9*, 912335. [CrossRef]

68. Yamashita, S.; Sacher, F.; Mahida, S.; Berte, B.; Lim, H.S.; Komatsu, Y.; Amraoui, S.; Denis, A.; Derval, N.; Laurent, F.; et al. Role of high-resolution image integration to visualize left phrenic nerve and coronary arteries during epicardial ventricular tachycardia ablation. *Circ. Arrhythm. Electrophysiol.* **2015**, *8*, 371–380. [CrossRef]
69. Linhart, M.; Alarcon, F.; Borras, R. Delayed gadolinium enhancement magnetic resonance imaging detected anatomic gap length in wide circumferential pulmonary vein ablation lesions is associated with recurrence of atrial fibrillation. *Circ. Arrhythm. Electrophysiol.* **2018**, *11*, e006659. [CrossRef]
70. Chelu, M.G.; King, J.B.; Kholmovski, E.G.; Ma, J.; Gal, P.; Marashly, Q.; AlJuaid, M.A.; Kaur, G.; Silver, M.A.; Johnson, K.A.; et al. Atrial fibrosis by late gadolinium enhancement magnetic resonance imaging and catheter ablation of atrial fibrillation: 5-year follow-up data. *J. Am. Heart Assoc.* **2018**, *7*, e006313. [CrossRef]
71. Khurram, I.M.; Habibi, M.; Gucuk Ipek, E.; Chrispin, J.; Yang, E.; Fukumoto, K.; Dewire, J.; Spragg, D.D.; Marine, J.E.; Berger, R.D.; et al. Left atrial LGE and arrhythmia recurrence following pulmonary vein isolation for paroxysmal and persistent AF. *JACC Cardiovasc. Imaging* **2016**, *9*, 142–148. [CrossRef]
72. Marrouche, N.F.; Wilber, D.; Hindricks, G.; Jais, P.; Akoum, N.; Marchlinski, F.; Kholmovski, E.; Burgon, N.; Hu, N.; Mont, L.; et al. Association of atrial tissue fibrosis identified by delayed enhancement MRI and atrial fibrillation catheter ablation: The DECAAF study. *JAMA* **2014**, *311*, 498–506. [CrossRef]
73. Marrouche, N.F.; Wazni, O.; McGann, C.; Greene, T.; Dean, J.M.; Dagher, L.; Kholmovski, E.; Mansour, M.; Marchlinski, F.; Wilber, D.; et al. Effect of MRI-Guided Fibrosis Ablation vs Conventional Catheter Ablation on Atrial Arrhythmia Recurrence in Patients with Persistent Atrial Fibrillation: The DECAAF II Randomized Clinical Trial. *JAMA* **2022**, *327*, 2296–2305. [CrossRef]
74. Bisbal, F.; Benito, E.; Teis, A.; Alarcón, F.; Sarrias, A.; Caixal, G.; Villuendas, R.; Garre, P.; Soto, N.; Cozzari, J.; et al. Magnetic Resonance Imaging-Guided Fibrosis Ablation for the Treatment of Atrial Fibrillation: The ALICIA Trial. *Circ. Arrhythm. Electrophysiol.* **2020**, *13*, e008707. [CrossRef]
75. Badger, T.J.; Daccarett, M.; Akoum, N.W. Evaluation of left atrial lesions after initial and repeat atrial fibrillation ablation: Lessons learned from delayed-enhancement MRI in repeat ablation procedures. *Circ. Arrhythm. Electrophysiol.* **2010**, *3*, 249–259. [CrossRef]
76. Chubb, H.; Aziz, S.; Karim, R. Optimization of late gadolinium enhancement cardiovascular magnetic resonance imaging of post-ablation atrial scar: A cross-over study. *J. Cardiovasc. Magn. Reson.* **2018**, *20*, 30. [CrossRef]
77. Desjardins, B.; Crawford, T.; Good, E.; Oral, H.; Chugh, A.; Pelosi, F.; Morady, F.; Bogun, F. Infarct architecture and characteristics on delayed enhanced magnetic resonance imaging and electroanatomic mapping in patients with postinfarction ventricular arrhythmia. *Heart Rhythm* **2009**, *6*, 644–651. [CrossRef]
78. Piers, S.R.D.; Tao, Q.; De Riva Silva, M.; Siebelink, H.M.; Schalij, M.J.; Van Der Geest, R.J.; Zeppenfeld, K. CMR-based identification of critical isthmus sites of ischemic and nonischemic ventricular tachycardia. *JACC Cardiovasc. Imaging* **2014**, *7*, 774–784. [CrossRef]
79. Andreu, D.; Ortiz-Perez, J.T.; Boussy, T.; Fernandez-Armenta, J.; Caralt, T.M.; Perea, R.J. Usefulness of contrast-enhanced cardiac magnetic resonance in identifying the ventricular arrhythmia substrate and the approach needed for ablation. *Eur. Heart. J.* **2014**, *35*, 1316–1326. [CrossRef]
80. Acosta, J.; Fernández-Armenta, J.; Penela, D.; Andreu, D.; Borras, R.; Vassanelli, F.; Korshunov, V.; Perea, R.J.; de Caralt, T.M.; Ortiz, J.T.; et al. Infarct transmurality as a criterion for first-line endo-epicardial substrate-guided ventricular tachycardia ablation in ischemic cardiomyopathy. *Heart Rhythm* **2016**, *13*, 85–95. [CrossRef]
81. Quinto, L.; Sanchez, P.; Alarco, F.; Garre, P.; Zaraket, F.; Prat-gonzalez, S. Cardiac magnetic resonance to predict recurrences after ventricular tachycardia ablation: Septal involvement, transmural channels, and left ventricular mass. *Europace* **2021**, *23*, 1437–1445. [CrossRef]
82. Ávila, P.; Pérez-David, E.; Izquierdo, M.; Rojas-González, A.; Sánchez-Gómez, J.M.; Ledesma-Carbayo, M.J. Scar extension measured by magnetic resonancebased nal intensity mapping predicts ventricular tachycardia recurrence after substrate ablation in patients with previous myocardial infarction. *JACC Clin. Electrophysiol.* **2015**, *1*, 353–365. [CrossRef]
83. Nishimura, T.; Patel, H.N.; Wang, S.; Upadhyay, G.A.; Smith, H.L.; Ozcan, C. Prognostic value of cardiac magnetic resonance septal late gadolinium enhancement patterns for periaortic ventricular tachycardia ablation: Heterogeneity of the anteroseptal substrate in nonischemic cardiomyopathy. *Heart Rhythm* **2021**, *18*, 579–588. [CrossRef] [PubMed]
84. Ghafoori, E.; Kholmovski, E.; Thomas, S.; Silvernagel, J.; Nathan, A.; Nan, H. Characterization of gadolinium contrast enhancement of radiofrequency ablation lesions in predicting edema and chronic lesion size. *Circ. Arrhythm. Electrophysiol.* **2017**, *10*, e005599. [CrossRef] [PubMed]
85. Dabbagh, G.S.; Ghannam, M.; Siontis, K.C.; Attili, A.; Cochet, H.; Jais, P.; Eng, M.J.; Latchamsetty, R.; Jongnarangsin, K.; Morady, F.; et al. Magnetic resonance mapping of cathter ablation lesions after postinfarction ventricular tachycardia ablation. *JACC Cardiovasc. Imaging* **2021**, *14*, 588–598. [CrossRef]

applied sciences

MDPI

Review

Cardiac Nuclear Imaging Findings in Atypical Variants of Takotsubo Cardiomyopathy

Maria Silvia De Feo [1], Miriam Conte [1], Viviana Frantellizzi [1,*], Luca Filippi [2], Laura Evangelista [3,4], Maria Ricci [5] and Giuseppe De Vincentis [1]

[1] Department of Radiological Sciences, Oncology and Anatomo Pathology, Sapienza, University of Rome, 00161 Rome, Italy
[2] Nuclear Medicine Unit, Department of Oncohaematology, Fondazione PTV Policlinico Tor Vergata University Hospital, 00133 Roma, Italy
[3] Department of Biomedical Sciences, Humanitas University, Via Rita Levi Montalcini 4, 20072 Pieve Emanuele, Italy
[4] IRCCS Humanitas Research Hospital, Via Manzoni 56, 20089 Rozzano, Italy
[5] Nuclear Medicine Unit, Cardarelli Hospital, 86100 Campobasso, Italy
* Correspondence: viviana.frantellizzi@uniroma1.it

Abstract: Background: In addition to the typical form resembling the classical Japanese octopus trap, atypical variants of Takotsubo cardiomyopathy (TTC) sparing the left ventricular apex have emerged over the years. The aim of this systematic review is to provide a comprehensive overview of the cardiac nuclear imaging findings in atypical variants. Methods: This systematic review was performed according to the Preferred Reporting Items for Systematic Reviews and Meta-analyses (PRISMA) guidelines. The literature research was carried out online on the Pubmed, Scopus, Central (Cochrane Library), and Web Of Science databases. Results: A total of 14 articles were ultimately selected. Myocardial perfusion scintigraphy was performed in nine studies, followed by 123I-mIBG scintigraphy, 123I-BMIPP scintigraphy, and 18F-FDG PET. In seven cases, a single cardiac nuclear imaging technique was performed, while in the remaining five and two cases, two and three different imaging modalities were, respectively, used. The most common atypical variant of our selection was the midventricular form, followed by reverse/inverted/basal TTC, with only a single case reported of a focal pattern. Conclusions: As the reason why TTC variants occur is still not clear, a deeper understanding of the current knowledge could be the basis for providing more insights into this fascinating disorder and its uncommon manifestations.

Keywords: takotsubo; 123I-mIBG; 123I-BMIPP; 18F-FDG PET; cardiac nuclear imaging; TTC; myocardial perfusion scintigraphy

Citation: De Feo, M.S.; Conte, M.; Frantellizzi, V.; Filippi, L.; Evangelista, L.; Ricci, M.; De Vincentis, G. Cardiac Nuclear Imaging Findings in Atypical Variants of Takotsubo Cardiomyopathy. *Appl. Sci.* **2024**, *14*, 487. https://doi.org/10.3390/app14020487

Academic Editor: Julio Garcia Flores

Received: 28 July 2023
Revised: 25 September 2023
Accepted: 3 January 2024
Published: 5 January 2024

1. Introduction

Takotsubo cardiomyopathy (TTC) was first described in Japanese literature over three decades ago. The name derives from the Japanese term for the typical octopus (tako) trapping pot (tsubo), a fishermen's amphora with a narrow neck and a round bottom, resembling the characteristic end-systolic shape assumed by the left ventricle in the most common variant of the disease [1]. Following the first description, initial reports in the 1990s were mainly from Japan, but have rapidly increased from almost every country since 2000 [2]. TTC has emerged over the years as an important cause of an acute reversible cardiac condition related to transient left ventricular systolic dysfunction with a segmental distribution extending beyond single epicardial coronary artery territories [3], often accompanied by the ballooning of the involved segments, in the absence of significant obstructive coronary artery disease (CAD) [4]. The prevalence of TTC is currently estimated at 1–2% of all patients presenting with symptoms of acute coronary syndrome (ACS) [5,6]. According to the literature data, the incidence is 5.2/100,000 in females and

0.6/100,000 in males [7,8]. Up to 90% of TC patients are women and 80% are over the age of 50 years; the mean age is 67 years, as reported in the International Takotsubo Registry [9]. Although the mechanisms underlying TTC are not fully understood, with several postulated hypotheses existing, including transient multivessel epicardial coronary spasm and microvascular dysfunction [10], a link to sudden stressors and high catecholamine levels has been established [11–13]. The interaction between adrenergic hyperactivation and cardiovascular system response to the peak of catecholamines plays a central role in the pathophysiology of TTC. The large majority of patients diagnosed with TC have experienced either significant emotional, physical, or environmental stress [3,14–16], suggesting how the release of large quantities of norepinephrine from the sympathetic nervous system and epinephrine from the adrenal medulla could be a major mechanism underlying this syndrome [17,18]. Stressors vary widely among reports of TTC cases and include natural disasters to weddings and surprise parties, from surgery and anesthesia to thyrotoxicosis [19] and sepsis, from the postpartum period [20,21] to COVID-19 infection [22], from subarachnoid hemorrhage and stroke to pancreatitis and cholecystitis, from pheochromocytoma to neoplasm and cancer-related therapies, and so on [23]. The reaction to stressors depends on individual factors influencing both catecholamine production and myocyte and microvascular response to sympathetic stimulation [24], with estrogen deficiency, genetic factors, and neurologic and psychiatric disorders being predisposing factors to mental and physical triggers [25–29]. Despite the clinical presentation usually mimicking ACS [30], with patients often presenting with chest pain, followed by dyspnea and syncope [31], having electrocardiographic abnormalities (ST-segment elevation, ST-segment depression, T-wave negative conversion, and QT prolongation) [32] and showing a mild elevation of myocardionecrosis enzyme levels, as well as the marked elevation of brain natriuretic peptide (BNP) and N-terminal pro-BNP [33–36], TTC is formally considered a benign self-limiting state presenting a favorable prognosis [37] and it is generally characterized by a temporary impairment with complete recovery within 3 weeks. However, complications including lethal ventricular arrhythmia, pump failure, outflow tract obstruction, cardiac rupture, and systemic embolization may occur in the acute phase and cause morbidity and mortality. The overlapping of clinical features between TTC and ACS makes particularly critical the early distinction of the two entities, which is of primary importance due to their completely different management. Several diagnostic criteria have been developed following the first proposal by Abe et al. in 2003 [38], but no consensus has yet been reached. The diagnostic criteria issued by the Takotsubo Cardiomyopathy Study Group (TCSG) are commonly followed in Japan [39]. Internationally, the 2008 Revised Mayo Clinic Criteria, based on the presence of transient left ventricle systolic dysfunction, absence of obstructive coronary disease, new electrocardiographic abnormalities or modest elevation in troponin, and absence of pheochromocytoma or myocarditis, are the most widely used [5]. However, certain limitations to the above-mentioned criteria have been recently addressed in the International Takotsubo diagnostic criteria [40]. Specifically, a diagnosis of TTC should not be excluded in the presence of significant CAD, in line with data from the International Takotsubo Registry reporting a rate of coexistence of CAD higher than expected (15.3%) [9]; in the presence of pheochromocytoma, as it can cause TC-like syndrome via catecholamine storm, being a secondary cause of TC [41]; and in the presence of wall motion abnormalities in the distribution of a single coronary artery, considering that rarely a focal subtype of TTC may involve only single coronary artery distribution, typically the anterolateral wall [42]. To predict the probability of diagnosing TTC and to differentiate it from ACS in the acute setting, the Inter Tak Diagnostic Score has been developed [43]. Based on this score, patients with non-ST elevation and a high score (>70 points), reflecting a high probability of TTC, should undergo an echocardiogram to provide an immediate assessment of the regional wall motion abnormalities, to assess right ventricle involvement and to evaluate TTC complications [44–46]. In clinical practice, an early coronary angiography is generally performed without delay within 48 h of the onset of symptoms [47] in patients with acute chest pain, ST-segment elevation, and elevated

cardiac enzymes [48]. Left ventriculography, performed simultaneously with coronary angiography, helps confirm the diagnosis and identify the subtype of TTC [49]. Among non-invasive imaging techniques, both cardiovascular magnetic resonance (CMR) imaging and coronary computed tomography (CT) angiography have been proposed in TTC diagnostic algorithms [50]. In this scenario, cardiac nuclear imaging may represent a further non-invasive diagnostic and prognostic option able to provide additional pathophysiological details thanks to its functional nature. In a recent systematic review, Nayar et al. summarized the current literature, from perfusion and metabolic studies to sympathetic innervation imaging, underlining their role in improving diagnostic accuracy, providing prognostic information, and appreciating TTC pathophysiology [51]. However, at present, cardiac nuclear imaging is not included in the main diagnostic criteria [39]. To date, the term 'takotsubo' is widely used in recognition of Sato et al., who first described it in 1990 [52,53], but a consensus has not been reached, leading to variable nomenclature in the literature including acute stress-induced cardiomyopathy, broken-heart syndrome [54], apical ballooning syndrome, or ampulla cardiomyopathy [55], with no term properly describing the heterogeneous ventricular appearance of this syndrome [56]. The typical form, accounting for 80% of all cases, affects the left ventricle apex with end-systolic hypercontraction and the narrowing of basal segments associated with akinesia of the mid and apical segments, resulting in the apical ballooning form of the classical Japanese octopus trap [57]. However, atypical forms of TTC sparing the left ventricular apex have been described in the literature [58,59]. The midventricular form with a hawk's beak appearance [60,61], often referred to as "midventricular ballooning syndrome" is the most common atypical form (4–40%), presenting with midventricular dilation and akinesia in end-systole and hyperkinetic basal and apical segments. The basal or reverse or inverted type, showing basal dyskinesia with midventricular and apical sparing, as well as the focal type, represent less common atypical variants, occurring in 2.2% and 1.5% of subjects, respectively [9,62]. Right ventricle-isolated involvement and biventricular forms have also been observed [63,64]. The prevalence of such atypical forms has previously been considered rare, but the reported number of TTC variants has continuously increased during recent years [65–69], so that the expression "transient left ventricular dysfunction syndrome" (TLVDS), not including any reference to the specific shape taken by the left ventricle, has been proposed as a new and more appropriate definition for TTC [70]. Dealing with the uncommon presentations of a still not fully understood disorder represents a further challenge. To our knowledge, there are only a few reports involving cardiac nuclear imaging in atypical variants of TTC [71,72]. The aim of this systematic review was to provide a comprehensive overview of the cardiac nuclear imaging findings in atypical variants of TTC by using a systematic approach to identify and collect published studies on this topic. A focus was put on the potential contribution of nuclear medicine for a more complete understanding of the atypical variants of this fascinating disorder.

2. Materials and Methods

2.1. Search Strategy and Study Selection

This systematic review was performed according to the Preferred Reporting Items for Systematic Reviews and Meta-analyses (PRISMA) guidelines [73]. The literature research was carried out online on Pubmed, Scopus, Central (Cochrane Library), and Web Of Science databases with a search strategy based on the following keywords: "Reverse" OR "Inverted" OR "Basal" OR "Midventricular" OR "Focal" OR "Atypical Takotsubo" AND "Nuclear Medicine". The search included all papers published until May 2023. English language was mandatory for inclusion. Eligible articles had to focus on the role of cardiac nuclear imaging in patients with atypical variants of TTC. Publications concerning the typical apical form were excluded, as well as reviews, animal studies, and articles not performing nuclear imaging studies. In addition to retrospective analysis and prospective studies, case reports, case series, letters to the editor, and interesting images were included. The reference lists of suitable studies were carefully checked to identify any additional relevant literature.

2.2. Data Extraction and Methodological Quality Assessment

Data extraction included authors, location, year of publication, type of study, sample size, gender and age, type of atypical variant of TTC, type of nuclear medicine study, and relevance of imaging findings in the acute phase and during follow-up. The methodological quality assessment was performed through the Critical Appraisal Skills Programme (CASP) [74]. Both data extraction and critical appraisal were independently performed by two reviewers. Disagreements and discrepancies were resolved by unanimous approval after discussion among researchers.

3. Results

3.1. Search Results

A total of 104 articles were found and thus screened by examining each abstract in order to identify suitable studies. A total of 14 articles were ultimately selected for the qualitative analysis of this systematic review. The detailed study selection flow chart, showing the search strategy and the applied selection criteria, is presented in Figure 1.

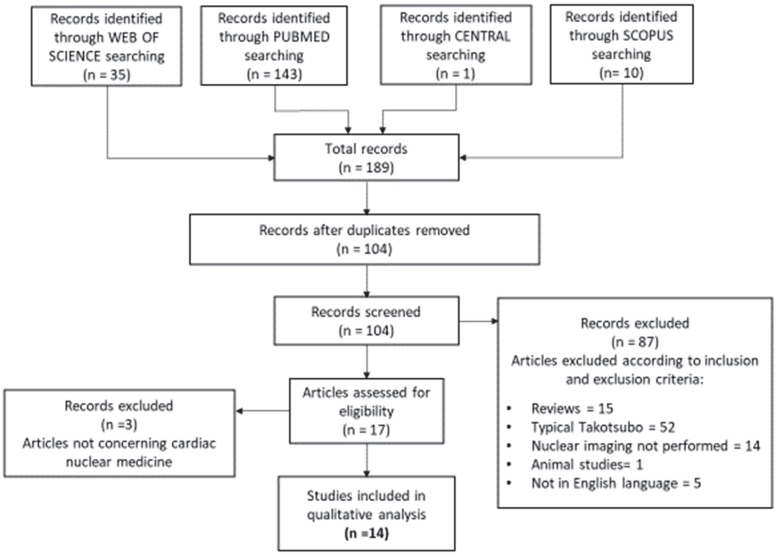

Figure 1. PRISMA flow chart.

3.2. Methodological Quality

The critical appraisal only involved the retrospective studies by Kurowski et al. [70] and Cimarelli et al. [71] and the prospective study by Miyajima and colleagues [75] (Figure 2). Case reports and case series were not considered as a part of this process. All the analyzed studies satisfied at least 8 of the 11 domains but showed high risk in two domains. One of the major concerns with the selected papers was represented by the lack of a reference standard, as the diagnosis of TTC is based on specific diagnostic algorithms rather than a single test. In addition, the absence of an adequate follow-up limited the evaluation of patients' outcomes in one study. Finally, it was found there was a level of high concern of the applicability in evaluating the possibilities of the application of the reported results. However, cumulatively, the quality appraisal result was quite good.

	1. Was there a clear question for the study to address?	2. Was there a comparison with an appropriate reference standard?	3. Did all patients get the diagnostic test and reference standard?	4. Could the results of the test have been influenced by the results of the reference standard?	5. Is the disease status of the tested population clearly described?	6. Were the methods for performing the test described in sufficient detail?	7. What are the results?	8. How sure are we about the results? Consequences and cost of alternatives performed?	9. Can the results be applied to your patients/the population of interest?	10. Can the test be applied to your patient or population of interest?	11. Were all outcomes important to the individual or population considered?	12. What would be the impact of using this test on your patients/population?
Kurowski et al. 2007	☺	☺	☺	☹	☺	☺	☺	?	☹	☺	☺	It may help in the identification of atypical variants through the correlation between location of perfusion/metabolism defects and wall motion abnormalities.
Cimarelli et al. 2010	☺	☺	☺	☹	☺	☺	☺	☺	☹	☺	☺	It may underline the role of nuclear imaging in the setting of patho-physiological mechanisms of TTC
Miyajima et al. 2022	☺	☺	☺	☹	☺	☺	☺	☺	☹	☺	☺	It may indicate a reversible disorder of the myocardial cell membrane, mitochondria, and microcirculation.

☺ Low risk; ? Unknown; ☹ High risk

Figure 2. CASP diagnostic checklist: tabular representation of quality assessment results [70,71,75].

3.3. Analysis of the Evidence

The 14 selected papers were published from 2004 to 2021. Most of the studies were conducted by authors from Japan (n = 7), followed by researchers from France (n = 3) and Italy (n = 2), with the remaining two studies performed in the USA and in Germany. Only two retrospective studies and one prospective study were found according to the selection criteria. The majority of the selected studies were case reports involving one or two patients. Letters to the editor (n = 3) and interesting images (n = 2) were also included. The total number of patients was 37. It is worth specifying that this number is not the sum of the subjects involved in the selected papers but represents the result of a further selection carefully performed for each single publication to include only patients with atypical variants of TTC, since four studies also included subjects with the typical apical form. For completeness, we should also underline that the study by Kurowski et al. [70] does not specify whether all 13 of their subjects with atypical variants were submitted to cardiac nuclear imaging, so the total number of 37 could be slightly overstated. Subjects were mostly women (30 females, 7 males). As concerning cardiac nuclear imaging, myocardial perfusion scintigraphy was performed in nine studies, specifically with technetium-99m (99mTc) sestamibi in four papers, with thallium-201 (201Tl) in an additional four studies and with 201Tl or 99mTc-tetrofosmin in the remaining one, followed by I-123-meta-iodobenzyl-guanidine (123I-mIBG) myocardial scintigraphy (n = 7), I-123-beta-metyl-iodophenyl pentadecanoic acid (123I-BMIPP) myocardial scintigraphy (n = 4), and fluorine-18-fluoro-2-deoxyglucose (18F-FDG) positron emission tomography (PET) (n = 3). In most cases (n = 7), a single cardiac nuclear imaging technique was performed, while in the remaining five and two studies, two and three different imaging modalities were, respectively, used. According to the literature data, the most common atypical variant of our selection of studies was the midventricular form (n = 8), followed by reverse/inverted/basal TTC (n = 5), with only a single case report of a focal pattern. The scintigraphic follow-up data concerning atypical variants are available in a minority of publications (n = 3), while in the case report by Cadeddu et al. [76], 123I-mIBG scintigraphy was not performed in the acute phase. The main characteristics of the included studies are reported in Table 1. The cardiac nuclear imaging findings of the selected papers for each type of atypical variant of TTC are described in detail in the following paragraphs.

3.3.1. Cardiac Nuclear Imaging Findings in Midventricular TTC

In 2008, Cimarelli and colleagues [72], analyzed imaging patterns obtained with 99mTc-tetrofosmin gated-single photon emission computed tomography (G-SPECT), 123I-mIBG SPECT, and 18F-FDG gated-positron emission tomography (G-PET) of an 83-year-old

woman with typical TTC and a 67-year-old woman with transient midventricular ballooning. In the patient with the atypical variant of TTC, despite the myocardial perfusion images revealing no defects, the analysis of the left ventricular motion and thickness showed severe midventricular hypokinesia associated with a decreased left ventricular ejection fraction (LVEF) measured by G-SPECT. Moreover, the authors revealed a similar pattern of 123I-mIBG and 18F-FDG uptake, with defects related to left ventricular dysfunction. Following this case report, a retrospective study involving a total of 18 patients, of whom 5 subjects had midventricular TTC, was published in 2009 [71]. Myocardial perfusion imaging with 99mTc-tetrofosmin or 201-Tl was performed on three out of five subjects in the sub-acute phase and revealed the absence of perfusion defects, associated with a severe midventricular hypokinesis with preserved apical and basal function. 123I-mIBG SPECT and 18F-FDG G-PET were performed in one and in all five patients, respectively. Hypocontractile but normally perfused segments were characterized by a severe decrease in both 123I-mIBG and 18F-FDG uptake, with a large topographic overlapping of the metabolic defects and innervation abnormalities on the qualitative analysis. Previously, in 2007, Kurowski and coworkers [70] retrospectively analyzed 35 patients with TLVDS, of whom 13 had atypical midventricular TTC. The myocardial perfusion 99mTc-sestamibi scintigraphy and 18F-FDG PET studies showed a strong correlation between the location of the wall motion abnormality and myocardial perfusion/metabolism defects. In particular, myocardial glucose metabolism was revealed to be affected to a greater extent than perfusion, leading to an inverse mismatch typical for the appearance of postischemic stunned myocardium. A case of transient midventricular akinesia in a 67-year-old woman without a history of heart disease was reported in 2008 by Moriya et al. [77]. During the acute phase, decreased uptake was seen in the 123I-BMIPP myocardial scintigraphy. The main finding in the acute phase was the discrepancy of the uptake between the mid region and apex, which reduced during the course. On the other hand, the decreased uptake revealed on the 123I-mIBG scintigraphy in the mid portion during the acute phase persisted through 3 and 6 months later. Similarly, the washout map showed an increased washout in the mid to basal portion of the inferior and lateral wall during the acute phase and increased the washout in the mid portion of the anterolateral wall in images taken 3 and 6 months later, suggesting how the abnormal findings of the 123I-mIBG persisted for 6 months even though the left ventricle contraction was recovered. The above-described findings concerning 123I-BMIPP scintigraphy are in line with a previous case report of a 51-year-old Japanese man published in 2007 by Yoshikawa and colleagues [78], who revealed a decreased uptake in the mid ventricle corresponding to the midventricular akinetic region, which normalized at 4 months after discharge. 99mTc-sestamibi scintigraphy, also performed by the authors on the fifth day, showed no perfusion defects. Similarly, normal 201Tl uptake was revealed on early images performed on the third day of admission in an 87-year-old woman diagnosed with a midventricular variant of TTC, as reported by Yoshida and coworkers [79] a year later. After a coronary angiogram showed no organic stenosis, a ventriculogram revealed akinesis in the middle portion of the left ventricle and transthoracic echocardiography (TTE) confirmed the abovementioned finding, 201Tl scintigraphy and 123I-mIBG scintigraphy were performed to exclude a possible previous myocardial injury by Nagai et al. [80], who published an interesting image in 2014. The mismatch images obtained by subtracting the 201Tl images showing no defects from the corresponding 123-I BMIPP images showing metabolic abnormalities revealed a ring-shaped defect on the polar maps in this 74-year-old woman with mid-ventricular ballooning syndrome. In 2012, Arao et al. [81] also reported a "doughnut-like" circular uptake reduction on bull's eye imaging in 123I-mIBG scintigraphy performed on the sixth day in an 83-year-old woman referred to their institution. The involved area coincided with the ballooning region demonstrated through left ventriculography but not with any epicardial coronary artery territory.

3.3.2. Cardiac Nuclear Imaging Findings in Basal/Inverted/Reverse TTC

Three out of five papers concerning basal/inverted/reverse TTC were performed using 123I-mIBG scintigraphy as a single cardiac nuclear imaging technique. In 2011, Cadeddu and colleagues [76] published a rare case of dobutamine-induced inverted TTC, which occurred with an atypical presentation including no chest pain, no ECG abnormalities, and a lack of increase in cardiac troponin. A 48-year-old female patient was referred to their echo laboratory due to a long history of atypical precordial chest pain. During a dobutamine/atropine stress echocardiogram, hypokinesia of the mid-basal anterior wall was noted and the test was interrupted. The recovery images showed a progressive worsening of the kinetic pattern with akinesia of all the left ventricular mid-basal segments and severe impairment of the global systolic function (LVEF = 25%). 123I-mIBG myocardial scintigraphy performed two months later showed decreased uptake in the whole left ventricle with increased washout in late images. A few years later, an interesting image by Humbert et al. [82] highlighted the dual role of 123I-mIBG scintigraphy in TTC through the case of a 41-year-old woman showing ischemic stroke and cardiogenic pulmonary edema a few hours after hysterectomy due to endometriosis. TTE showed a low LVEF at 25% with thrombi in the left ventricle. CMR performed a few days later revealed apical hyperkinesis and basal hypokinesis, as well as no late gadolinium enhancement. 123I-mIBG scintigraphy confirmed the presence of the acute dysfunction of the myocardial sympathetic nerve endings and revealed decreased uptake in the hypokinetic basal segments, sparing the apex, suggesting an atypical pattern of TTC. The whole-body planar scintigraphy performed 24 h after injection showed a high uptake of the right adrenal mass consistent with the presence of a pheochromocytoma, a possible endogenous cause of adrenergic stress related cardiomyopathy. In this case, 123I-mIBG allowed for the final diagnosis of inverted stress-related cardiomyopathy secondary to pheochromocytoma. Following this paper, a year later, Ceccacci and colleagues [83] reported the case of a 40-year-old woman admitted to the Emergency Department for syncope associated with severe oppressive pain in the epigastric region. According to the Mayo Clinic criteria, the absence of coronary lesions, the presence of dyskinesia of the basal and middle segments, as well as the absence of myocarditis as confirmed by CMR, strongly suggested the diagnosis of inverted takotsubo cardiomyopathy which was confirmed through 123I-mIBG scintigraphy revealing increased adrenergic receptor activity in the apex, with simultaneous reduction in the basal region (See Figure 3). Myocardial scintigraphy with 99mTc-sestamibi was performed as a single cardiac nuclear imaging modality to assess the left ventricular perfusion in the remaining two publications. A fixed midventricular and basal circumferential area of hypoperfusion and hypokinesis with preservation of the ventricular apex was revealed during a rest–stress dipyridamole Tc-99m sestamibi myocardial perfusion G-SPECT by Davis and coworkers [84] in a 49-year-old black male admitted to the intensive care unit with acute respiratory failure with anoxic encephalopathy and elevated cardiac biomarkers. In this case, as the anatomical distribution of the specific perfusion defects did not appear to represent obstructive epicardial coronary pathology, immediate coronary angiography was not performed and a final diagnosis of atypical stress-induced cardiomyopathy was made. In a recent study published in 2021, Miyajima et al. [75] prospectively enrolled 20 patients with typical TTC and 8 patients (6 females, 2 males) with reverse TTC and assessed the minimum percentage uptake (min-%-uptake), extent score (ES), and summed rest score (SRS) at acute and chronic phases through myocardial perfusion scintigraphy with 99mTc-sestamibi. In the group of subjects with reverse TTC, the imaging procedure was performed within a few days after admission in the acute phase and approximately one month after admission in the chronic phase. The analysis revealed that the min-%-uptake, ES, and SRS were mild to moderately reduced in the acute phase and were normalized with progression from acute to chronic phase in both TTC groups, suggesting how reversible disorders such as microcirculation, myocardial cell membrane, and mitochondria may be involved in the pathophysiology.

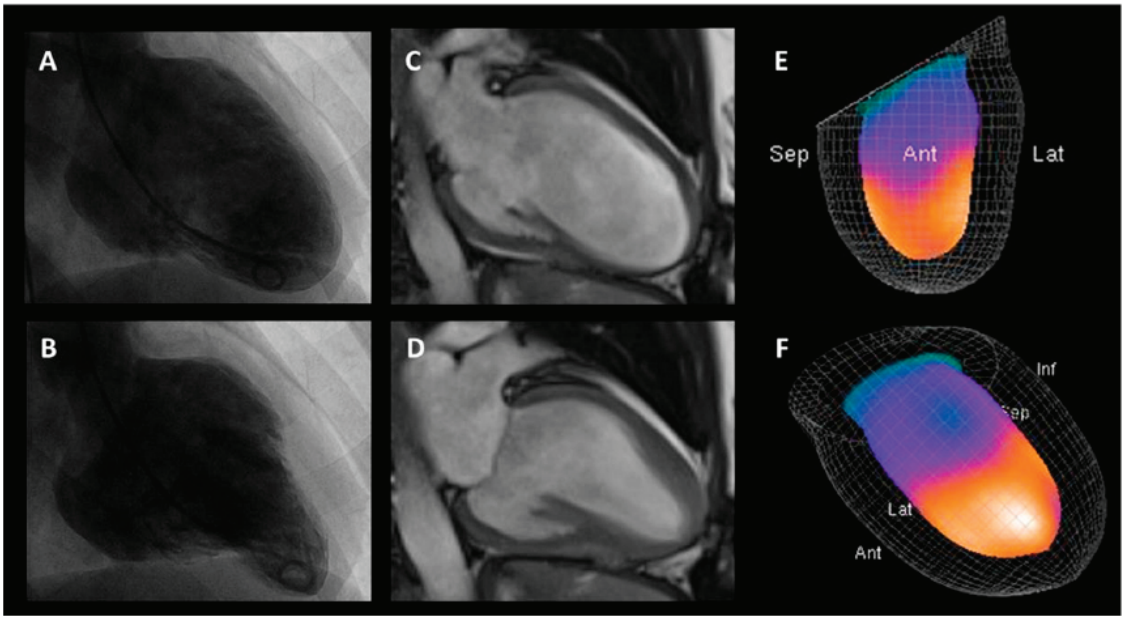

Figure 3. A case of inverted/reverse/basal TTC. Left ventriculography ((**A**): diastolic phase; ((**B**): systolic phase) and cardiac magnetic resonance imaging ((**C**): diastolic phase; (**D**): systolic phase) show a depressed systolic function with dyskinesia of the basal and middle segments (Figure: (**A**–**D**)) and hyperkinesia of apex and para-apical areas (Figure: (**A**–**D**)). Figure (**E**,**F**) show an increased adrenergic receptor activity in the apical side of the left ventricle, with simultaneous reduction in the basal region to the 123I-mIBG scintigraphy [83].

3.3.3. Cardiac Nuclear Imaging Findings in Focal TTC

In 2004, the case of a 64-year-old man was published by Suzuki et al. [85]. He was a heavy drinker admitted due to hypokalemia-related myopathy and suffered a cardiopulmonary arrest lasting approximately 5 min on the fifth hospital day. 201Tl perfusion scintigraphy, performed on the tenth day, showed no perfusion defects, while 123I-BMIPP scintigraphy, performed on the fourteenth hospital day, revealed decreased uptake in the anterior and septal regions of the left ventricle in agreement with the anteroseptal area of left ventricular wall motion abnormality. Cardiac nuclear imaging contributed to formulating the possible diagnosis of an atypical focal form of TTC.

Table 1. Characteristics of included studies.

Source, Year, Location, Type of Study	Number of Patients, Sex, Age	TTC Variant	Cardiac Nuclear Imaging Technique	Time from Acute Event to First Imaging/Follow Up	Tracer Uptake in Involved Segments during the Acute Phase/at Follow-Up
Suzuki et al., 2004, Japan, case report [85]	1 M, 64 y	focal	- 201Tl SPECT - 123I-BMIPP SPECT	- 10 days/NP - 14 days/NP	- normal/NP - reduced/NP
Yoshikawa et al., 2007, Japan, letter to the editor [78]	1 M, 51 y	midventricular	- 99mTc-sestamibi-SPECT - 123I-BMIPP SPECT	- 5 days/NP - 5 days/4 months	- normal/NP - reduced/normalized
Kurowski et al., 2007, Germany, retrospective study [70]	12 F and 1 M, 70.4 y ± 10.2 y	midventricular	- 99mTc-sestamibi SPECT - 18F-FDG PET	2 to 6 days (mean 4)/NP	- mildly reduced/NP - severely reduced/NP
Yoshida et al., 2009, Japan, letter to the editor [79]	1 F, 87 y	midventricular	201Tl SPECT	3 days/NP	normal/NP
Moriya et al., 2009, Japan, case report [77]	1 F, 67 y	midventricular	- 123I-BMIPP SPECT - 123I-mIBG SPECT	- NA/3 and 6 months - NA/3 and 6 months	- reduced/normalized - reduced/reduced
Cimarelli et al., 2008, France, case report [72]	1 F, 67 y	midventricular	- 99mTc-tetrofosmin G-SPECT - 123I-mIBG SPECT - 18F-FDG G-PET	- 4 days/NP - 6 days/NP - 8 days/NP	- normal/NP - absent/NP - markedly reduced/NP
Cimarelli et al., 2010, France, retrospective study [71]	4 F and 1 M, median age 67 y (range: 13–87 y) *	midventricular	- 99mTc-tetrofosmin/201Tl G-SPECT (n = 3) - 123I-mIBG SPECT (n = 1) - 18F-FDG G-PET (n = 5)	- 10.4 days (range: 5–15) * /NP - 11.6 days (range: 4–20) * /NA - 8.9 days (range: 3–20) * /NA	- normal/NP - reduced/NA - reduced/NA

Table 1. *Cont.*

Source, Year, Location, Type of Study	Number of Patients, Sex, Age	TTC Variant	Cardiac Nuclear Imaging Technique	Time from Acute Event to First Imaging/Follow Up	Tracer Uptake in Involved Segments during the Acute Phase/at Follow-Up
Davis et al., 2009, USA, case report [84]	1 M, 49 y	reverse/inverted/basal	99mTc-sestamibi SPECT	NA/NP	reduced/NP
Cadeddu et al., 2011, Italy, case report [76]	1 F, 48 y	reverse/inverted/basal	123I-mIBG SPECT	NP/2 months	NP/reduced
Arao et al., 2013, Japan, letter to the editor [81]	1 F, 83 y	midventricular	123I-mIBG SPECT	6 days/NP	reduced/NP
Nagai et al., 2014, Japan, image focus [80]	1 F, 74 y	midventricular	- 201Tl SPECT - 123I-BMIPP SPECT	NA/NP	- normal/NP - reduced/NP
Humbert et al., 2015, France, interesting image [82]	1 F, 41 y	reverse/inverted/basal TTC secondary to pheochromocytoma	123I-mIBG SPECT	NA/NP	reduced/NP
Ceccacci et al., 2016, Italy, case report [83]	1 F, 40 y	reverse/inverted/basal	123I-mIBG SPECT	NA/NP	reduced/NP
Miyajima et al., 2022, Japan, prospective study [75]	6 F and 2 M, 58y [44–83]	reverse/inverted/basal	99mTc-sestamibi SPECT	3.0 [2.0–3.0] days/35 [24–46] days	mild to moderately reduced/normalized

Abbreviations: y: years; F: female; M: male; NA: not applicable; NP: not performed; *: data reflecting the total cohort including patients with typical TTC.

4. Discussion and Limitations

Different studies have shown a decreased tracer uptake at myocardial perfusion imaging during the acute phase of TTC, and its gradual improvement in the subacute and chronic phases [86,87]. However, most literature data show normal myocardial perfusion during the subacute phase of TTC in hypo-contractile ventricular segments reflecting preserved coronary blood flow and blood flow reserve [88–90]. The association between normal perfusion and reduced metabolism is commonly known as inverse flow–metabolism mismatch and it is considered the metabolic state of stunned myocardium [91]. According to these findings, stunned myocardium mediated by catecholamine oversecretion seems to play a crucial role in TTC, with transient coronary microvascular dysfunction representing a potentially associated phenomenon secondary to acute catecholamine release, rather than the primary causative mechanism of the disease. Cardiac autonomic innervation is a complex system. To preserve homeostasis, the stress-activated post-ganglionic sympathetic nerve releases norepinephrine into the synaptic cleft, producing a wide range of cardiac effects on the heart rate, blood pressure, and contractility through the interaction with a post-synaptic adrenergic receptor (AR). However, during the acute phase of TTC, high circulating levels of epinephrine and norepinephrine may cause catecholamine toxicity in myocardial cells. Animal studies have suggested that acute catecholamine overload may lead to a stunning of the myocardium [92] and have a negative inotropic action with apical ballooning in rats [93], due to a shift to an inhibitory signal mediated by ß2 AR, particularly abundant in the apical region [94]. In addition to the highest density of ß-AR, the mammalian left ventricular apex shows the lowest density of sympathetic innervation, a combination making it particularly sensitive and vulnerable to exaggerated sympathetic stimulation than the mid and basal segments [95,96]. The description of the variant forms of TTC sparing the apex might be explained by the interindividual differences in the distribution of sympathetic receptors in the left ventricle, as speculated by Kurowsky et al. [70], as well as by Cimarelli and coworkers in the case series published in 2008 and a year later in a retrospective study [71,72]. However, as a case of both typical and atypical TTC occurring in the same patient at different periods was reported [97], probably, the pathogenesis of TTC variants cannot be explained only by the individual distribution of AR in the myocardium [81]. The reason atypical variants occur and whether they resemble basic pathophysiology with TTC simply affecting different left ventricular regions still remains a matter of speculation. In this background, cardiac nuclear imaging may improve the current knowledge of the atypical manifestations of this fascinating and still mysterious disease.

Given the hypothesis of enhanced catecholamine release secondary to exaggerated sympathetic stimulation as the central causative mechanism of TTC, 123I-mIBG scintigraphy seems to be the most specific diagnostic imaging tool [98,99]. 123I-mIBG, a structural analog of norepinephrine reflecting sympathetic neuron integrity and function, represents an extremely useful imaging tool for detecting abnormalities in the myocardial adrenergic

nervous system and for studying the causes and effects of cardiac sympathetic hyperactivity [100–102]. In patients with TTC, the increased levels of plasma catecholamines inhibit neuronal norepinephrine uptake by presynaptic sympathetic endings [103], resulting in reduced signal in the involved segments of the left ventricle on 123I-mIBG scintigraphy [99,104]. In 2005, Ito et al. [89] observed the same discrepancies between long-chain fatty acid uptake assessed through 123I-BMIPP scintigraphy and cardiac innervation on 123I-mIBG scintigraphy, suggesting the existence of sympathetic nerve control on cardiac metabolism. Similarly, a large correlation between the location and extent of 123I-mIBG defects and reduced glucose metabolism is reported in the literature, suggesting that catecholamine-mediated myocardial insulin resistance as well as the inhibited intracellular translocation of glucose transporters (GLUT-4) by calcium overload may be responsible for the transient reduced 18F-FDG uptake in the hypokinetic areas [105,106]. In addition, catecholamines exert a large vasoconstrictor effect potentially causing transient multivessel epicardial coronary spasm and microvascular dysfunction [107–111].

Cardiac nuclear imaging findings in atypical variants of TTC reflect literature data published for the typical apical form, but with different distribution patterns of uptake defects. In particular, the analysis of the selected papers showed normal perfusion in most publications, with a mild reduction reported only in a minority of papers [70–84], always followed by complete normalization on follow-up studies when performed [75–77]. Perfusion G-SPECT confirmed the presence of motion and thickness abnormalities, associated with a reduction in LVEF during the acute phase, in accordance with echocardiographic findings [72]. Concerning the evaluation of sympathetic innervation, 123I-mIBG scintigraphy always revealed a marked reduction in tracer uptake in the involved area during the acute phase [72], reflecting the central role of abnormal myocardial adrenergic nervous system activation in the pathogenesis of the disease and non-invasively contributing to the final diagnosis of atypical TTC [81,83]. Moreover, in one case, it was extremely useful in identifying a pheochromocytoma as a secondary cause of TLVDS [82]. As discussed above, sympathetic nervous system dysfunction may be the mechanism underlying the metabolic alterations revealed through both 123I-BMIPP scintigraphy [80] and 18F-FDG PET [70–72]. The transient nature of all these defects is always confirmed in follow-up studies [78], with a possible delay in the recovery of sympathetic function with respect to metabolic defects [76,77]. However, these data are scarce and difficult to compare as the time occurring from the onset of symptoms to cardiac nuclear imaging in both acute phase and during follow-up is extremely variable.

A mention of some additional limitations and drawbacks is needed. First of all, it is worth highlighting that the number of selected studies is quite limited. Both the rare occurrence of uncommon forms of TTC and the non-inclusion of cardiac nuclear imaging in the diagnostic pathway could be possible explanations for the low number of publications on this topic. Moreover, one of the major concerns in the analyzed literature is represented by the type of published papers, as the vast majority of them are single case reports or case series involving no more than two patients. We can speculate that the paucity of both retrospective analyses and prospective studies concerning cardiac nuclear imaging in TTC in general and atypical TTC variants in particular may represent the main obstacle preventing it from being included in the current diagnostic algorithms. An additional non-negligible limitation of most papers is represented by the lack of follow-up imaging, particularly useful for corroborating the transient nature of nuclear imaging findings.

5. Conclusions

Following the first reports from Japan, interest in TTC has spread worldwide, fueled by its fascinating and still not fully understood pathogenesis. Over the years, cardiac nuclear imaging has not only provided complementary diagnostic and prognostic information in a non-invasive manner, but has contributed to the pathophysiological understanding of TTC by assessing myocardial perfusion, innervation abnormalities as well as metabolic alterations in both the acute and chronic phases of the disease. According to the available

data, it is possible to suppose that typical and atypical TTC resemble basic pathophysiology, so that the disease should no longer be regarded as an apical ballooning syndrome, but rather a transient left ventricular dysfunction showing different phenotypes. The present review could be the starting point for systematically investigating both the diagnostic role and the prognostic contribution of cardiac nuclear imaging in uncommon TTC forms. Moreover, since the reason why atypical variants occur is still not clear, we believe that a deep understanding of the current knowledge on this topic may be the basis for the development of cardiac nuclear imaging tracers with more and more specific targets in the myocardium, able to provide more insights into the less common manifestations of this fascinating disorder.

Author Contributions: Conceptualization, G.D.V. and V.F.; methodology, M.S.D.F. and M.C.; validation, M.R. and L.F.; formal analysis, V.F.; investigation, M.S.D.F.; data curation, M.C.; writing—original draft preparation, M.S.D.F.; supervision, L.E., V.F. and G.D.V. All authors have read and agreed to the published version of the manuscript.

Funding: This research received no external funding.

Institutional Review Board Statement: Not applicable.

Informed Consent Statement: Not applicable.

Data Availability Statement: Not applicable.

Conflicts of Interest: The authors declare no conflict of interest.

References

1. Fernández-Pérez, G.C.; Aguilar-Arjona, J.A.; de la Fuente, G.T.; Samartín, M.; Ghioldi, A.; Arias, J.C.; Sánchez-González, J. Takotsubo cardiomyopathy: Assessment with cardiac MRI. *Am. J. Roentgenol.* **2010**, *195*, W139–W145. [CrossRef] [PubMed]
2. Sharkey, S.W.; Lesser, J.R.; Zenovich, A.G.; Maron, M.S.; Lindberg, J.; Longe, T.F.; Maron, B.J. Acute and reversible cardiomyopathy provoked by stress in women from the United States. *Circulation* **2005**, *111*, 472–479. [CrossRef] [PubMed]
3. Ghadri, J.-R.; Wittstein, I.S.; Prasad, A.; Sharkey, S.; Dote, K.; Akashi, Y.J.; Cammann, V.L.; Crea, F.; Galiuto, L.; Desmet, W.; et al. International Expert Consensus Document on Takotsubo Syndrome (Part I): Clinical Characteristics, Diagnostic Criteria, and Pathophysiology. *Eur. Heart J.* **2018**, *39*, 2032–2046. [CrossRef] [PubMed]
4. Murthy, A.; Arora, J.; Singh, A.; Gedela, M.; Karnati, P.; Nappi, A. Takotsubo Cardiomyopathy: Typical and Atypical Variants, A Two-Year Retrospective Cohort Study. *Cardiol. Res.* **2014**, *5*, 139–144. [CrossRef] [PubMed]
5. Prasad, A.; Lerman, A.; Rihal, C.S. Apical ballooning syndrome (Tako-Tsubo or stress cardiomyopathy): A mimic of acute myocardial infarction. *Am. Heart J.* **2008**, *155*, 408–417. [CrossRef]
6. Tsuchihashi, K.; Ueshima, K.; Uchida, T.; Oh-Mura, N.; Kimura, K.; Owa, M.; Yoshiyama, M.; Miyazaki, S.; Haze, K.; Ogawa, H.; et al. Transient left ventricular apical ballooning without coronary artery stenosis: A novel heart syndrome mimicking acute myocardial infarction. Angina Pectoris-Myocardial Infarction Investigations in Japan. *J. Am. Coll. Cardiol.* **2001**, *38*, 11–18. [CrossRef]
7. Agarwal, S.; Bean, M.G.; Hata, J.S.; Castresana, M.R. Perioperative Takotsubo Cardiomyopathy: A Systematic Review of Published Cases. *Semin. Cardiothorac. Vasc. Anesthesia* **2017**, *21*, 277–290. [CrossRef]
8. Natale, E.; Mistrulli, R. Takotsubo syndrome: More frequent in women, more dangerous in men. *Eur. Heart J. Suppl.* **2023**, *25*, B119–B122. [CrossRef]
9. Templin, C.; Ghadri, J.R.; Diekmann, J.; Napp, L.C.; Bataiosu, D.R.; Jaguszewski, M.; Cammann, V.L.; Sarcon, A.; Geyer, V.; Neumann, C.A.; et al. Clinical Features and Outcomes of Takotsubo (Stress) Cardiomyopathy. *N. Engl. J. Med.* **2015**, *373*, 929–938. [CrossRef]
10. Rivero, F.; Cuesta, J.; García-Guimaraes, M.; Bastante, T.; Alvarado, T.; Antuña, P.; Alfonso, F. Time-Related Microcirculatory Dysfunction in Patients With Takotsubo Cardiomyopathy. *JAMA Cardiol.* **2017**, *2*, 699–700. [CrossRef]
11. Amin, H.Z.; Pradipta, A. Takotsubo Cardiomyopathy: A Brief Review. *J. Med. Life* **2020**, *13*, 3–7. [CrossRef] [PubMed]
12. Boyd, B.M.; Solh, T.M. Takotsubo cardiomyopathy: Review of broken heart syndrome. *J. Am. Acad. Physician Assist.* **2020**, *33*, 24–29. [CrossRef] [PubMed]
13. Matta, A.G.; Carrié, D. Epidemiology, Pathophysiology, Diagnosis, and Principles of Management of Takotsubo Cardiomyopathy: A Review. *Experiment* **2023**, *29*, e939020. [CrossRef] [PubMed]
14. de Chazal, H.M.; Del Buono, M.G.; Keyser-Marcus, L.; Ma, L.; Moeller, F.G.; Berrocal, D.; Abbate, A. Stress Cardiomyopathy Diagnosis and Treatment: JACC State-of-the-Art Review. *J. Am. Coll. Cardiol.* **2018**, *72*, 1955–1971. [CrossRef]

15. Dias, A.; Gil, I.J.N.; Santoro, F.; Madias, J.E.; Pelliccia, F.; Brunetti, N.D.; Salmoirago-Blotcher, E.; Sharkey, S.W.; Eitel, I.; Akashi, Y.J.; et al. Takotsubo syndrome: State-of-the-art review by an expert panel—Part 1. *Cardiovasc. Revascularization Med.* **2019**, *20*, 70–79. [CrossRef]
16. Dias, A.; Gil, I.J.N.; Santoro, F.; Madias, J.E.; Pelliccia, F.; Brunetti, N.D.; Salmoirago-Blotcher, E.; Sharkey, S.W.; Eitel, I.; Akashi, Y.J.; et al. Takotsubo syndrome: State-of-the-art review by an expert panel—Part 2. *Cardiovasc. Revascularization Med.* **2019**, *20*, 153–166. [CrossRef]
17. Wittstein, I.S.; Thiemann, D.R.; Lima, J.A.C.; Baughman, K.L.; Schulman, S.P.; Gerstenblith, G.; Wu, K.C.; Rade, J.J.; Bivalacqua, T.J.; Champion, H.C. Neurohumoral features of myocardial stunning due to sudden emotional stress. *N. Engl. J. Med.* **2005**, *352*, 539–548. [CrossRef]
18. Akashi, Y.J.; Goldstein, D.S.; Barbaro, G.; Ueyama, T. Takotsubo cardiomyopathy: A new form of acute, reversible heart failure. *Circulation* **2008**, *118*, 2754–2762. [CrossRef]
19. Miyazaki, S.; Kamiishi, T.; Hosokawa, N.; Komura, M.; Konagai, H.; Sagai, H.; Takamoto, T. Reversible left ventricular dysfunction "takotsubo" cardiomyopathy associated with hyperthyroidism. *Jpn. Heart J.* **2004**, *45*, 889–894. [CrossRef]
20. Ruiz, S.; Martinez-Marin, M.; Luque, P.; Nassar, N.; Oros, D. Takotsubo cardiomyopathy after cesarean section: A case report and literature review. *J. Obstet. Gynaecol. Res.* **2017**, *43*, 392–396. [CrossRef]
21. Citro, R.; Giudice, R.; Mirra, M.; Petta, R.; Baldi, C.; Bossone, E.; Piscione, F. Is Tako-tsubo syndrome in the postpartum period a clinical entity different from peripartum cardiomyopathy? *J. Cardiovasc. Med.* **2013**, *14*, 568–575. [CrossRef] [PubMed]
22. Titus, A.; Sattar, Y.; Patel, N.; Taha, A.; Sandhyavenu, H.; Gonuguntla, K.; Thyagaturu, H.; Almas, T.; Balla, S. In-Hospital Outcomes of Takotsubo Cardiomyopathy During the COVID-19 Pandemic: Propensity Matched National Cohort. *Curr. Probl. Cardiol.* **2023**, *48*, 101598. [CrossRef] [PubMed]
23. Manabe, O.; Naya, M.; Oyama-Manabe, N.; Koyanagawa, K.; Tamaki, N. The role of multimodality imaging in takotsubo cardiomyopathy. *J. Nucl. Cardiol.* **2019**, *26*, 1602–1616. [CrossRef] [PubMed]
24. Wittstein, I.S. The Sympathetic Nervous System in the Pathogenesis of Takotsubo Syndrome. *Heart Fail. Clin.* **2016**, *12*, 485–498. [CrossRef] [PubMed]
25. Anderson, J.L.; Horne, B.D.; Le, V.T.; Bair, T.L.; Min, D.B.; Minder, C.M.; Dhar, R.; Mason, S.; Muhlestein, J.B.; Knowlton, K.U. Spectrum of radionuclide perfusion study abnormalities in takotsubo cardiomyopathy. *J. Nucl. Cardiol.* **2022**, *29*, 1034–1046. [CrossRef]
26. Moscatelli, S.; Montecucco, F.; Carbone, F.; Valbusa, A.; Massobrio, L.; Porto, I.; Brunelli, C.; Rosa, G.M. An Emerging Cardiovascular Disease: Takotsubo Syndrome. *BioMed Res. Int.* **2019**, *2019*, 6571045. [CrossRef]
27. Pelliccia, F.; Kaski, J.C.; Crea, F.; Camici, P.G. Pathophysiology of Takotsubo Syndrome. *Circulation* **2017**, *135*, 2426–2441. [CrossRef]
28. Galiuto, L.; De Caterina, A.R.; Porfidia, A.; Paraggio, L.; Barchetta, S.; Locorotondo, G.; Rebuzzi, A.G.; Crea, F. Reversible coronary microvascular dysfunction: A common pathogenetic mechanism in Apical Ballooning or Tako-Tsubo Syndrome. *Eur. Heart J.* **2010**, *31*, 1319–1327. [CrossRef]
29. Patel, S.M.; Lerman, A.; Lennon, R.J.; Prasad, A. Impaired coronary microvascular reactivity in women with apical ballooning syndrome (Takotsubo/stress cardiomyopathy). *Eur. Heart J. Acute Cardiovasc. Care* **2013**, *2*, 147–152. [CrossRef]
30. Buchmann, S.J.; Lehmann, D.; Stevens, C.E. Takotsubo Cardiomyopathy—Acute Cardiac Dysfunction Associated With Neurological and Psychiatric Disorders. *Front. Neurol.* **2019**, *10*, 917. [CrossRef]
31. Mejía-Rentería, H.D.; Núñez-Gil, I.J. Takotsubo syndrome: Advances in the understanding and management of an enigmatic stress cardiomyopathy. *World J. Cardiol.* **2016**, *8*, 413–424. [CrossRef] [PubMed]
32. Namgung, J. Electrocardiographic Findings in Takotsubo Cardiomyopathy: ECG Evolution and Its Difference from the ECG of Acute Coronary Syndrome. *Clin. Med. Insights Cardiol.* **2014**, *8*, 29–34. [CrossRef] [PubMed]
33. Priya, S.; Nagpal, P.; Aggarwal, T.; Huynh, J.; Khandelwal, K.; Khandelwal, A. Review of multi-modality imaging update and diagnostic work up of Takotsubo cardiomyopathy. *Clin. Imaging* **2021**, *80*, 334–347. [CrossRef] [PubMed]
34. Ahmed, K.A.; Madhavan, M.; Prasad, A. Brain natriuretic peptide in apical ballooning syndrome (Takotsubo/stress cardiomyopathy): Comparison with acute myocardial infarction. *Coron. Artery Dis.* **2012**, *23*, 259–264. [CrossRef] [PubMed]
35. Gopalakrishnan, P.; Zaidi, R.; Sardar, M.R. Takotsubo cardiomyopathy: Pathophysiology and role of cardiac biomarkers in differential diagnosis. *World J. Cardiol.* **2017**, *9*, 723–730. [CrossRef] [PubMed]
36. Budnik, M.; Kochanowski, J.; Piatkowski, R.; Wojtera, K.; Peller, M.; Gaska, M.; Glowacka, P.; Karolczak, P.; Ochijewicz, D.; Opolski, G. Simple markers can distinguish Takotsubo cardiomyopathy from ST segment elevation myocardial infarction. *Int. J. Cardiol.* **2016**, *219*, 417–420. [CrossRef]
37. Sharkey, S.W.; Windenburg, D.C.; Lesser, J.R.; Maron, M.S.; Hauser, R.G.; Lesser, J.N.; Haas, T.S.; Hodges, J.S.; Maron, B.J. Natural history and expansive clinical profile of stress (tako-tsubo) cardiomyopathy. *J. Am. Coll. Cardiol.* **2010**, *55*, 333–341. [CrossRef]
38. Abe, Y.; Kondo, M.; Matsuoka, R.; Araki, M.; Dohyama, K.; Tanio, H. Assessment of clinical features in transient left ventricular apical ballooning. *J. Am. Coll. Cardiol.* **2003**, *41*, 737–742. [CrossRef]
39. Kawai, S.; Kitabatake, A.; Tomoike, H. Takotsubo cardiomyopathy study group guidelines for diagnosis of takotsubo (ampulla) cardiomyopathy. *Circ. J.* **2007**, *71*, 990–992. [CrossRef]
40. Bybee, K.A.; Prasad, A. Stress-related cardiomyopathy syndromes. *Circulation* **2008**, *118*, 397–409. [CrossRef]

41. de Souza, F.; Gismondi, R.A.O.C.; Neto, S.H.C.; de Mattos, M.A. Tako-tsubo-like cardiomyopathy and extra-adrenal pheochromocytoma: Case report and literature review. *Clin. Res. Cardiol.* **2008**, *97*, 397–401. [CrossRef] [PubMed]
42. Kato, K.; Kitahara, H.; Fujimoto, Y.; Sakai, Y.; Ishibashi, I.; Himi, T.; Kobayashi, Y. Prevalence and Clinical Features of Focal Takotsubo Cardiomyopathy. *Circ. J.* **2016**, *80*, 1824–1829. [CrossRef] [PubMed]
43. Ghadri, J.R.; Cammann, V.L.; Jurisic, S.; Seifert, B.; Napp, L.C.; Diekmann, J.; Bataiosu, D.R.; D'Ascenzo, F.; Ding, K.J.; Sarcon, A.; et al. A novel clinical score (InterTAK Diagnostic Score) to differentiate takotsubo syndrome from acute coronary syndrome: Results from the International Takotsubo Registry. *Eur. J. Heart Fail.* **2017**, *19*, 1036–1042. [CrossRef] [PubMed]
44. Citro, R.; Lyon, A.R.; Meimoun, P.; Omerovic, E.; Redfors, B.; Buck, T.; Lerakis, S.; Parodi, G.; Silverio, A.; Eitel, I.; et al. Standard and advanced echocardiography in takotsubo (stress) cardiomyopathy: Clinical and prognostic implications. *J. Am. Soc. Echocardiogr.* **2015**, *28*, 57–74. [CrossRef] [PubMed]
45. Citro, R.; Okura, H.; Ghadri, J.R.; Izumi, C.; Meimoun, P.; Izumo, M.; Dawson, D.; Kaji, S.; Eitel, I.; Kagiyama, N.; et al. Multimodality imaging in takotsubo syndrome: A joint consensus document of the European Association of Cardiovascular Imaging (EACVI) and the Japanese Society of Echocardiography (JSE). *J. Echocardiogr.* **2020**, *18*, 199–224. [CrossRef] [PubMed]
46. Izumo, M.; Nalawadi, S.; Shiota, M.; Das, J.; Dohad, S.; Kuwahara, E.; Fukuoka, Y.; Siegel, R.J.; Shiota, T.; Lai, D.T.; et al. Mechanisms of acute mitral regurgitation in patients with takotsubo cardiomyopathy: An echocardio-graphic study. *Circ. Cardiovasc. Imaging* **2011**, *4*, 392–398. [CrossRef] [PubMed]
47. Bossone, E.; Lyon, A.; Citro, R.; Athanasiadis, A.; Meimoun, P.; Parodi, G.; Cimarelli, S.; Omerovic, E.; Ferrara, F.; Limongelli, G.; et al. Takotsubo cardiomyopathy: An integrated multi-imaging approach. *Eur. Heart J. Cardiovasc. Imaging* **2014**, *15*, 366–377. [CrossRef]
48. Lüscher, T.F.; Templin, C. Is takotsubo syndrome a microvascular acute coronary syndrome? Towards of a new definition. *Eur. Heart J.* **2016**, *37*, 2816–2820. [CrossRef]
49. Hirose, K.; Moriya, M.; Ishiwata, S.; Ohno, M. A case of Takotsubo cardiomyopathy that was confirmed by cardiac catheterization at all three times of onset. *J. Cardiol. Cases* **2015**, *12*, 152–155. [CrossRef]
50. Ghadri, J.-R.; Wittstein, I.S.; Prasad, A.; Sharkey, S.; Dote, K.; Akashi, Y.J.; Cammann, V.L.; Crea, F.; Galiuto, L.; Desmet, W.; et al. International Expert Consensus Document on Takotsubo Syndrome (Part II): Diagnostic Workup, Outcome, and Management. *Eur. Heart J.* **2018**, *39*, 2047–2062. [CrossRef]
51. Nayar, J.; John, K.; Philip, A.; George, L.; George, A.; Lal, A.; Mishra, A. A Review of Nuclear Imaging in Takotsubo Cardiomyopathy. *Life* **2022**, *12*, 1476. [CrossRef]
52. Sato, H.T.H.; Uchida, T. Takotsubo type cardiomyopathy due to multivessel spasm. In *Clinical Aspect of Myocardial Injury: From Ischemia to Heart Failure*; Kodama, K., Haze, K., Hon, M., Eds.; Kagakuhyouronsya Co.: Tokyo, Japan, 1990; pp. 56–64. (In Japanese)
53. Sato, H. Tako-tsubo-like left ventricular dysfunction due to multivessel coronary spasm. In *Clinical Aspect of Myocardial Injury: From Ischemia to Heart Failure*; Kagakuhyoronsha Publishing Co.: Tokyo, Japan, 1990.
54. Brandspiegel, H.Z.; Marinchak, R.A.; Rials, S.J.; Kowey, P.R. A broken heart. *Circulation* **1998**, *98*, 1349. [CrossRef] [PubMed]
55. Matta, A.; Delmas, C.; Campelo-Parada, F.; Lhermusier, T.; Bouisset, F.; Elbaz, M.; Nader, V.; Blanco, S.; Roncalli, J.; Carrié, D. Takotsubo cardiomyopathy. *Rev. Cardiovasc. Med.* **2022**, *23*, 38. [CrossRef] [PubMed]
56. Sharkey, S.W.; Lesser, J.R.; Maron, M.S.; Maron, B.J. Why not just call it tako-tsubo cardiomyopathy: A discussion of nomenclature. *J. Am. Coll. Cardiol.* **2011**, *57*, 1496–1497. [CrossRef] [PubMed]
57. Eitel, I.; von Knobelsdorff-Brenkenhoff, F.; Bernhardt, P.; Carbone, I.; Muellerleile, K.; Aldrovandi, A.; Francone, M.; Desch, S.; Gutberlet, M.; Strohm, O.; et al. Clinical characteristics and cardiovascular magnetic resonance findings in stress (takotsubo) cardiomyopathy. *JAMA* **2011**, *306*, 277–286. [CrossRef]
58. Di Filippo, C.; Bacchi, B.; Di Mario, C. Novel Aspects of Classification, Prognosis and Therapy in Takotsubo Syndrome. *Eur. Cardiol. Rev.* **2019**, *14*, 191–196. [CrossRef]
59. Gupta, S.; Gupta, M.M. Takotsubo syndrome. *Indian Heart J.* **2018**, *70*, 165–174. [CrossRef]
60. Matta, A.; Roncalli, J.; Elbaz, M.; Lhermusier, T.; Campelo-Parada, F.; Bouisset, F.; Elenizi, K.; Nader, V.; Carrié, D. Mid-Ventricular Takotsubo Cardiomyopathy with Hawk's Beak Appearance: A Case Report. *Am. J. Case Rep.* **2020**, *21*, e919563. [CrossRef]
61. Roncalli, J.; Carrie, D.; Fauvel, J.-M.; Losordo, D.W. A "hawk's beak" to identify the new transient midventricular Tako-Tsubo syndrome. *Int. J. Cardiol.* **2008**, *127*, e179–e180. [CrossRef]
62. Ennezat, P.V.; Pesenti-Rossi, D.; Aubert, J.M.; Rachenne, V.; Bauchart, J.J.; Auffray, J.L.; Logeart, D.; Cohen-Solal, A.; Asseman, P. Transient left ventricular basal dysfunction without coronary stenosis in acute cerebral disorders: A novel heart syndrome (inverted takotsubo). *Echocardiography* **2005**, *22*, 599–602. [CrossRef]
63. Sumida, H.; Morihisa, K.; Katahira, K.; Sugiyama, S.; Kishi, T.; Oshima, S. Isolated Right Ventricular Stress (Takotsubo) Cardiomyopathy. *Intern. Med.* **2017**, *56*, 2159–2164. [CrossRef] [PubMed]
64. Elesber, A.A.; Prasad, A.; Bybee, K.A.; Valeti, U.; Motiei, A.; Lerman, A.; Chandrasekaran, K.; Rihal, C.S. Transient cardiac apical ballooning syndrome: Prevalence and clinical implications of right ventricular involvement. *J. Am. Coll. Cardiol.* **2006**, *47*, 1082–1083. [CrossRef] [PubMed]
65. Van de Walle, S.O.; Gevaert, S.A.; Gheeraert, P.J.; De Pauw, M.; Gillebert, T.C. Transient stress-induced cardiomyopathy with an "inverted takotsubo" contractile pattern. *Mayo Clin. Proc.* **2006**, *81*, 1499–1502. [CrossRef] [PubMed]

66. Yasu, T.; Tone, K.; Kubo, N.; Saito, M. Transient mid-ventricular ballooning cardiomyopathy: A new entity of Takotsubo cardiomyopathy. *Int. J. Cardiol.* **2006**, *110*, 100–101. [CrossRef]
67. Aubert, J.M.; Ennezat, P.V.; Tricot, O.; Darchis, J.; Bauchart, J.J.; Auffray, J.L.; Lesenne, M.; Van Belle, E.; Goldstein, P.; Asseman, P. Mid-ventricular ballooning heart syndrome. *Echocardiography* **2007**, *24*, 329–334. [CrossRef]
68. Tamura, A.; Kawano, Y.; Watanabe, T.; Aso, T.; Abe, Y.; Yano, S.; Kadota, J. A report of 2 cases of transient mid-ventricular ballooning. *Int. J. Cardiol.* **2007**, *122*, e10–e12. [CrossRef]
69. Sanchez-Recalde, A.; Iborra, C.; Costero, O.; Moreno, R.; de Sá, E.L.; Sobrino, J.A.; López-Sendón, J.L. Isolated left ventricular basal ballooning in young women: "Inverted Takotsubo" pattern related to catecholamine-toxicity. *Am. J. Cardiol.* **2007**, *100*, 1496–1497. [CrossRef]
70. Kurowski, V.; Kaiser, A.; von Hof, K.; Killermann, D.P.; Mayer, B.; Hartmann, F.; Schunkert, H.; Radke, P.W. Apical and midventricular transient left ventricular dysfunction syndrome (tako-tsubo cardiomyopathy) frequency, mechanisms, and prognosis. *Chest* **2007**, *132*, 809–816. [CrossRef]
71. Cimarelli, S.; Sauer, F.; Morel, O.; Ohlmann, P.; Constantinesco, A.; Imperiale, A. Transient left ventricular dysfunction syndrome: Patho-physiological bases through nuclear medicine imaging. *Int. J. Cardiol.* **2010**, *144*, 212–218. [CrossRef]
72. Cimarelli, S.; Imperiale, A.; Ben-Sellem, D.; Rischner, J.; Detour, J.; Morel, O.; Ohlmann, P.; Constantinesco, A. Nuclear medicine imaging of takotsubo cardiomyopathy: Typical form and midventricular ballooning syndrome. *J. Nucl. Cardiol.* **2008**, *15*, 137–141. [CrossRef]
73. Liberati, A.; Altman, D.G.; Tetzlaff, J.; Mulrow, C.; Gøtzsche, P.C.; Ioannidis, J.P.A.; Clarke, M.; Devereaux, P.J.; Kleijnen, J.; Moher, D. The PRISMA statement for reporting systematic reviews and meta-analyses of studies that evaluate health care interventions: Explanation and elaboration. *PLoS Med.* **2009**, *6*, e1000100. [CrossRef] [PubMed]
74. Singh, J. Critical appraisal skills programme. *J. Pharmacol. Pharmacother.* **2013**, *4*, 76–77. [CrossRef]
75. Miyajima, K.; Tawarahara, K.; Saito, N. Serial changes of myocardial perfusion imaging in takotsubo and reverse takotsubo cardiomyopathy. *J. Nucl. Cardiol.* **2022**, *29*, 2599–2611. [CrossRef] [PubMed]
76. Cadeddu, C.; Nocco, S.; Cadeddu, F.; Deidda, M.; Bassareo, P.; Serra, A.; Piga, M.; Mercuro, G. Inverted takotsubo cardiomyopathy induced by dobutamine stress echocardiography with atypical presentation. *Case Rep. Cardiol.* **2011**, *2011*, 413645. [CrossRef] [PubMed]
77. Moriya, M.; Naito, K.; Takahashi, M.; Ozoe, A.; Manabe, T.; Hosaka, H.; Suzuki, M. A case of transient mid-ventricular akinesia (a variant form of Takotsubo cardiomyopathy) followed with I-123-beta-metyl-iodophenyl pentadecanoic acid and I-123-meta-iodobenzyl-guanidine myocardial scintigraphy. *J. Cardiol.* **2009**, *53*, 140–145. [CrossRef] [PubMed]
78. Yoshikawa, M.; Yamamoto, T.; Shirakabe, A.; Ohno, T.; Tanaka, K. Myocardial scintigraphy in a patient with transient mid-ventricular ballooning cardiomyopathy: Case report. *Int. J. Cardiol.* **2007**, *119*, e8–e10. [CrossRef] [PubMed]
79. Yoshida, T.; Hibino, T.; Fujimaki, T.; Oguri, M.; Kato, K.; Yajima, K.; Ohte, N.; Yokoi, K.; Kimura, G. Transient mid-ventricular ballooning syndrome complicated by syncope: A variant of tako-tsubo cardiomyopathy. *Int. J. Cardiol.* **2009**, *135*, e20–e23. [CrossRef]
80. Nagai, T.; Konishi, T.; Arakawa, J.; Hisadome, H.; Tabata, H. Synchronicity of echocardiography and cardiac nuclear medicine in mid-ventricular ballooning syndrome: Paired 'ring signs' on polar maps. *Eur. Heart J. Cardiovasc. Imaging* **2014**, *15*, 947. [CrossRef]
81. Arao, K.; Ako, J.; Momomura, S.-I. Transient mid-ventricular ballooning: Insights from 123I-metaiodobenzylguanidine (MIBG) scintigraphy. *Int. J. Cardiol.* **2013**, *164*, e15–e16. [CrossRef]
82. Humbert, O.; Stamboul, K.; Gudjoncik, A.; Kanoun, S.; Richard, C.; Cochet, A.; Cottin, Y. Dual Diagnostic Role of 123I-MIBG Scintigraphy in Inverted-Takotsubo Pattern Cardiomyopathy. *Clin. Nucl. Med.* **2015**, *40*, 816–818. [CrossRef]
83. Ceccacci, A.; Mancone, M.; Calcagno, S.; De Vincentis, G.; Sardella, G.; Fedele, F. Role of MIBG scintigraphy in reverse Tako-tsubo cardiomyopathy: Confirming a pathophysiologic hypothesis. *Int. J. Cardiol.* **2016**, *223*, 54–55. [CrossRef] [PubMed]
84. Davis, M.; Hardebeck, C. Reverse Takotsubo syndrome diagnosed with Tc-99m SPECT perfusion study. *J. Nucl. Cardiol.* **2009**, *16*, 999–1002. [CrossRef] [PubMed]
85. Suzuki, K.; Osada, N.; Akasi, Y.J.; Suzuki, N.; Sakakibara, M.; Miyake, F.; Maki, F.; Takahashi, Y. An atypical case of "takotsubo cardiomyopathy" during alcohol withdrawal: Abnormality in the transient left ventricular wall motion and a remarkable elevation in the ST segment. *Intern. Med.* **2004**, *43*, 300–305. [CrossRef] [PubMed]
86. Ito, K.; Sugihara, H.; Kawasaki, T.; Yuba, T.; Doue, T.; Tanabe, T.; Adachi, Y.; Katoh, S.; Azuma, A.; Nakagawa, M. Assessment of ampulla (Takotsubo) cardiomyopathy with coronary angiography, two-dimensional echocardiography and 99mTc-tetrofosmin myocardial single photon emission computed tomography. *Ann. Nucl. Med.* **2001**, *15*, 351–355. [CrossRef] [PubMed]
87. Ito, K.; Sugihara, H.; Katoh, S.; Azuma, A.; Nakagawa, M. Assessment of Takotsubo (ampulla) cardiomyopathy using 99mTc-tetrofosmin myocardial SPECT—Comparison with acute coronary syndrom. *Ann. Nucl. Med.* **2003**, *17*, 115–122. [CrossRef] [PubMed]
88. Bybee, K.A.; Murphy, J.; Prasad, A.; Wright, R.S.; Lerman, A.; Rihal, C.S.; Chareonthaitawee, P. Acute impairment of regional myocardial glucose uptake in the apical ballooning (takotsubo) syndrome. *J. Nucl. Cardiol.* **2006**, *13*, 244–250. [CrossRef] [PubMed]
89. Fro, K.; Sugihara, H.; Kinoshita, N.; Azuma, A.; Matsubara, H. Assessment of Takotsubo cardiomyopathy (transient left ventricular apical ballooning) using99mTc-tetrofosmin,123I-BMIPP,123I-MIBG and99mTc-PYP myocardial SPECT. *Ann. Nucl. Med.* **2005**, *19*, 435–445. [CrossRef]

90. Obunai, K.; Misra, D.; Vantosh, A.; Bergmann, S.R. Metabolic evidence of myocardial stunning in takotsubo cardiomyopathy: A positron emission tomography study. *J. Nucl. Cardiol.* **2005**, *12*, 742–744. [CrossRef]
91. Perrone-Filardi, P.; Bacharach, S.L.; Dilsizian, V.; Marin-Neto, J.; Maurea, S.; Arrighi, J.A.; Bonow, R.O. Clinical significance of reduced regional myocardial glucose uptake in regions with normal blood flow in patients with chronic coronary artery disease. *J. Am. Coll. Cardiol.* **1994**, *23*, 608–616. [CrossRef]
92. Ueyama, T.; Hano, T.; Kasamatsu, K.; Yamamoto, K.; Tsuruo, Y.; Nishio, I. Estrogen attenuates the emotional stress-induced cardiac responses in the animal model of tako-tsubo (ampulla) cardiomyopathy. *J. Cardiovasc. Pharmacol.* **2003**, *42*, S117–S120. [CrossRef]
93. Paur, H.; Wright, P.T.; Sikkel, M.B.; Tranter, M.H.; Mansfield, C.; O'Gara, P.; Stuckey, D.J.; Nikolaev, V.O.; Diakonov, I.; Pannell, L.; et al. High levels of circulating epinephrine trigger apical cardiodepression in a β2 -adrenergic receptor/Gi –dependent manner: A new model of Takotsubo cardiomyopathy. *Circulation* **2012**, *126*, 697–706. [CrossRef] [PubMed]
94. Lyon, A.R.; Rees, P.S.C.; Prasad, S.; Poole-Wilson, P.A.; Harding, S.E. Stress (Takotsubo) cardiomyopathy—A novel pathophysiological hypothesis to explain catecholamine-induced acute myocardial stunning. *Nat. Clin. Pract. Cardiovasc. Med.* **2008**, *5*, 22–29. [CrossRef] [PubMed]
95. Mori, H.; Ishikawa, S.; Kojima, S.; Hayashi, J.; Watanabe, Y.; I E Hoffman, J.; Okino, H. Increased responsiveness of left ventricular apical myocardium to adrenergic stimuli. *Cardiovasc. Res.* **1993**, *27*, 192–198. [CrossRef] [PubMed]
96. Kawano, H.; Okada, R.; Yano, K. Histological study on the distribution of autonomic nerves in the human heart. *Heart Vessel.* **2003**, *18*, 32–39. [CrossRef] [PubMed]
97. Ghadri, J.R.; Jaguszewski, M.; Corti, R.; Lüscher, T.F.; Templin, C. Different wall motion patterns of three consecutive episodes of takotsubo cardiomyopathy in the same patient. *Int. J. Cardiol.* **2012**, *160*, e25–e27. [CrossRef] [PubMed]
98. Akashi, Y.J.; Nakazawa, K.; Sakakibara, M.; Miyake, F.; Musha, H.; Sasaka, K. 123I-MIBG myocardial scintigraphy in patients with 'takotsubo' cardiomyopathy. *J. Nucl. Med.* **2004**, *45*, 1121–1127. [PubMed]
99. Burgdorf, C.; von Hof, K.; Schunkert, H.; Kurowski, V. Regional alterations in myocardial sympathetic innervation in patients with transient left-ventricular apical ballooning (Tako-Tsubo cardiomyopathy). *J. Nucl. Cardiol.* **2008**, *15*, 65–72. [CrossRef]
100. Pontico, M.; Brunotti, G.; Conte, M.; Corica, F.; Cosma, L.; De Angelis, C.; De Feo, M.S.; Lazri, J.; Matto, A.; Montebello, M.; et al. The prognostic value of 123I-mIBG SPECT cardiac imaging in heart failure patients: A systematic review. *J. Nucl. Cardiol.* **2022**, *29*, 1799–1809. [CrossRef]
101. Verschure, D.; Poel, E.; De Vincentis, G.; Frantellizzi, V.; Nakajima, K.; Gheysens, O.; de Groot, J.R.; Verberne, H.J. The relation between cardiac 123I-*m*IBG scintigraphy and functional response 1 year after CRT implantation. *Eur. Heart J. Cardiovasc. Imaging* **2021**, *22*, 49–57. [CrossRef]
102. De Vincentis, G.; Frantellizzi, V.; Fedele, F.; Farcomeni, A.; Scarparo, P.; Salvi, N.; Fegatelli, D.A.; Mancone, M.; Verschure, D.O.; Verberne, H.J. Role of cardiac 123I-mIBG imaging in predicting arrhythmic events in stable chronic heart failure patients with an ICD. *J. Nucl. Cardiol.* **2019**, *26*, 1188–1196. [CrossRef]
103. Knuuti, J.; Sipola, P. Is it time for cardiac innervation imaging? *Q. J. Nucl. Med. Mol. Imaging* **2005**, *49*, 97–105. [PubMed]
104. De Vincentis, G.; Frantellizzi, V. The 123I-mIBG heart/mediastinum ratio: Moving from 2D to 3D imaging. *J. Nucl. Cardiol.* **2021**, *28*, 2578–2580. [CrossRef] [PubMed]
105. Deibert, D.C.; Defronzo, R.A. Epinephrine-induced insulin resistance in man. *J. Clin. Investig.* **1980**, *65*, 717–721. [CrossRef] [PubMed]
106. Shepherd, P.R.; Kahn, B.B. Glucose transporters and insulin action—Implications for insulin resistance and diabetes mellitus. *N. Engl. J. Med.* **1999**, *341*, 248–257. [CrossRef] [PubMed]
107. A Cohen, R.; Shepherd, J.T.; Vanhoutte, P.M. Prejunctional and postjunctional actions of endogenous norepinephrine at the sympathetic neuroeffector junction in canine coronary arteries. *Circ. Res.* **1983**, *52*, 16–25. [CrossRef] [PubMed]
108. Meimoun, P.; Malaquin, D.; Sayah, S.; Benali, T.; Luycx-Bore, A.; Levy, F.; Zemir, H.; Tribouilloy, C. The coronary flow reserve is transiently impaired in tako-tsubo cardiomyopathy: A prospective study using serial doppler transthoracic echocardiography. *J. Am. Soc. Echocardiogr.* **2008**, *21*, 72–77. [CrossRef] [PubMed]
109. Vitale, C.; MC Rosano, G.; Kaski, J.C. Role of Coronary Microvascular Dysfunction in Takotsubo Cardiomyopathy. *Circ. J.* **2016**, *80*, 299–305. [CrossRef]
110. Elesber, A.; Lerman, A.; Bybee, K.A.; Murphy, J.G.; Barsness, G.; Singh, M.; Rihal, C.S.; Prasad, A. Myocardial perfusion in apical ballooning syndrome: Correlate of myocardial injury. *Am. Heart J.* **2006**, *152*, 469.e9–469.e13. [CrossRef]
111. Kume, T.; Akasaka, T.; Kawamoto, T.; Yoshitani, H.; Watanabe, N.; Neishi, Y.; Wada, N.; Yoshida, K. Assessment of coronary microcirculation in patients with takotsubo-like left ventricular dysfunction. *Circ. J.* **2005**, *69*, 934–939. [CrossRef]

applied sciences

MDPI

Review

Assessment of Cardiovascular Disease in Autosomal Dominant Polycystic Kidney Disease

Antonietta Gigante *, Adolfo Marco Perrotta, Francesca Tinti , Eleonora Assanto, Maurizio Muscaritoli, Silvia Lai † and Rosario Cianci †

Department of Translational and Precision Medicine, Sapienza University of Rome, 00185 Rome, Italy; silvia.lai@uniroma1.it (S.L.)

* Correspondence: antonietta.gigante@uniroma1.it

† These authors contributed equally to this work.

Abstract: Autosomal dominant polycystic kidney disease (ADPKD) is an inherited kidney disease which leads to progressive kidney failure. About 5–10% of patients requiring renal replacement therapy are affected by ADPKD. Cardiovascular diseases are the main causes of morbidity and mortality in these patients with ADPKD; arterial hypertension (AH) is the first symptom with a very early onset. Anyway, some other cardiovascular abnormalities have been reported in ADPKD regardless of the presence of AH. With this background, we conducted a systematic review, collecting all randomized controlled trials (RCTs) and quasi-RCTs found on the main databases; we evaluated the evidence about different imaging techniques to grade the cardiovascular risk in a very early stage of disease. This review aims to describe all cardiovascular assessments in ADPKD patients to improve clinicians' ability to discover cardiovascular involvement early, allowing appropriate therapies promptly.

Keywords: autosomal dominant polycystic kidney disease; left ventricular hypertrophy; heart rate variability; cardiovascular risk; flow-mediated dilation; carotid intima–media thickness; pulse wave velocity

Citation: Gigante, A.; Perrotta, A.M.; Tinti, F.; Assanto, E.; Muscaritoli, M.; Lai, S.; Cianci, R. Assessment of Cardiovascular Disease in Autosomal Dominant Polycystic Kidney Disease. *Appl. Sci.* **2023**, *13*, 7175. https://doi.org/10.3390/app13127175

Academic Editor: Julio Garcia Flores

Received: 17 May 2023
Revised: 9 June 2023
Accepted: 14 June 2023
Published: 15 June 2023

1. Introduction

Autosomal dominant polycystic kidney disease (ADPKD) is a heterogeneous genetic disorder included in ciliopathies. The cystic dilatation of renal tubules and the progressive destruction of renal parenchyma leads to end-stage renal disease (ESRD) in half of affected patients aged 50 to 60 years. Thus, ADPKD is the fourth most common cause of renal replacement therapy worldwide, with an estimated prevalence between 1:1000 and 1:2500. ADPKD is characterized by the age-dependent growth of kidney cysts, and it is mainly caused by mutations in the PKD1 and PKD2 genes encoding for polycystin 1 (PC1) and polycystin 2 (PC2), which regulate differentiation, proliferation, survival, apoptosis, and autophagy [1]. More recently identified genes such as GANAB (encoding glucosidase II subunit α (GIIα)), PMM2, DNAJB11, ALG9, and IFT140 are also responsible for the development of cysts.

Mutations in PC1 and PC2, transmembranes glicoproteins that are colocalized to the primary cilium of the kidney tubular epithelial cells, cause lower intracellular levels of calcium and increased intracellular cyclic adenosine monophosphate, with aberrant cell proliferation and fluid secretion into cysts. ADPKD is a systemic disease that may involve different organs, showing high phenotypic variability [2].

The advances in knowledge of multiple molecular pathways underlying the pathophysiology of ADPKD involve the understanding of multiple mechanisms associated with extrarenal manifestations, including cardiac manifestations.

Cardiovascular disease is a major cause of morbidity and mortality in patients with ADPKD, and cardiac-related death in these patients is estimated to be 1.6- to 3.2-fold higher

compared to the general population, with 33% of deaths mainly due to ischemic heart disease and congestive heart failure [2].

Beyond the classic cardiovascular complications characterized by heart failure and coronary artery disease, well known in chronic kidney disease (CKD), ADPKD itself results in a genetically defined increased risk of cardiovascular complications.

Arterial hypertension (AH), a common finding in these patients, often occurs before the onset of renal failure and is associated with the most rapid progression to ESRD, with an increased cardiovascular risk.

The frequency of AH is increased at young age and is more frequent in patients with mutations in *PKD1* than in *PKD2* and in polycystic patients with hypertensive parents.

Early diagnosis is facilitated by the self-measurement of blood pressure or ambulatory BP monitoring (ABPM), particularly in those patients with masked hypertension who do not show a normal BP decrease at night-time (non-dippers) [3].

The pathogenesis of AH in ADPKD is not fully elucidated, but specific mechanisms such as the activation of the renin–angiotensin–aldosterone system (RAAS), impaired nitric oxide (NO)-related vasorelaxation, increased sympathetic nerve activity, increased plasma endothelin-1 concentrations, and insulin resistance have been revealed.

Sodium overload is also characteristic of ADPKD patients, and sodium-sensitive hypertension is described, associated with increased total kidney volume [3].

Left ventricular hypertrophy, a powerful, independent risk factor for cardiovascular morbidity and mortality, frequently occurs in patients with ADPKD. Both AH and left ventricular hypertrophy have important roles in cardiovascular complications in these individuals. The effect of cyst enlargement on renal vessels with parenchyma ischemia explains the activation of RAAS, which plays an important role in the development of hypertension in ADPKD [3]. Altered intrarenal hemodynamics cause endothelial dysfunction, NO production, and the hyperactivation of the sympathetic nervous system (SNS). The RAAS is stimulated at an early stage of the disease, even before the appearance of hypertension and other clinical findings. Similarly, increased left ventricular mass indices and diastolic dysfunction are reported in ADPKD patients with well-preserved renal function before the development of AH. Endothelial dysfunction, inflammation, and accelerated atherosclerosis are early-stage changes in ADPKD patients [4]. Biventricular diastolic dysfunction, endothelial dysfunction, increased carotid intima–media thickness (IMT), and increased arterial stiffness are present even in young ADPKD patients with normal blood pressure and well-preserved renal function [5]. Over the years, many innovations have been reported in renal imaging with computed tomography (CT) or magnetic resonance imaging (MRI) to evaluate, in addition, to renal volume, intermediate volume or renal fibrotic and perfusion volume [6,7] with important prognostic implications for ADPKD patients.

Intracranial aneurysm (ICA) is one of the cardiovascular manifestations of ADPKD, but information about the natural history of ICA in ADPKD patients comes from small, single-center observational studies. These mainly describe an increased prevalence of asymptomatic ICA detected via magnetic resonance angiography (MRA), with 9–12% of patients demonstrating ICA, compared with ~2–3% of the general population. The prevalence is higher in ADPKD patients with a positive family history compared to ADPKD patients with a negative family history. Family history is recognized as the main risk factor for ICA rupture as well, which occurs at the average age of 40, almost 10 years earlier than in the general population [8].

Data from pre-symptomatic screening demonstrated that the majority of ICA localize in the anterior circulation of the circle of Willis, with nearly all being of a small size <7 mm, falling in the low-risk category for rupture.

Therefore, guidelines suggest to only perform screening for ICA in ADKPK patients with family or personal history of ICA rupture. All patients with ADPKD should receive counseling about the risk of ICA, considering the pros and cons of pre-symptomatic

screening and reserving diagnostic imaging for those individuals who remain anxious about their risk and individuals with high-risk professions [8,9].

Vascular disorders such as aneurysms and arterial dissections of large arteries, including aorta, coronary, and splenic arteries, are reported in ADPKD patients, representing an important cause of death. However, the prevalence of abdominal aortic aneurysms does not seem to be increased in patients with ADPKD.

Polycystin proteins have a role in epithelial cell/matrix interactions, and polycystin mutations are associated with collagen and extracellular matrix abnormalities. The high expression of PKD1 and 2 in the human adult vascular wall, particularly in the dense plaques of the smooth muscle cell, accounts for the risk of vascular wall modification. Characteristic phenotypes of some ADPKD patients showing arachnodactyly, high-arched palates, pectus deformities, joint laxity, flat feet, and positive thumb signs should alert clinicians toward an increased predisposition to vascular involvement [10].

There is no standard assessment suggested in these patients, and the clinical presentation of vascular disorders may be highly variable and mimic many common conditions. Given the high risk of complications in these patients, contrast-enhanced computed tomography should be considered when suggestive symptoms develop for differential diagnosis.

The other major extrarenal complications of ADPKD include hepatic and pancreatic cysts, colonic diverticula, dolichoectasias, abdominal wall hernias, cerebral and ascending thoracic aorta aneurysms, seminal vesicle cysts, and male infertility [2].

ADPKD is also associated with significant pain and discomfort, which may affect the quality of life of these patients. The quality of life (QOL) of patients with ADPKD could be associated with abdominal distention, pain, and anorexia caused by liver and kidney enlargement, even if other associated symptoms could also affect QOL such as sleep disturbance, heartburn, urinary tracts, fever, and hematuria [11].

Current treatment strategies include conservative therapy and reducing cyclic adenosine monophosphate levels, cell proliferation, and fluid secretion with somatostatin analogs and vasopressin V2 receptor antagonists that have been shown to slow the deterioration of renal function and the growth of renal and hepatic cysts [1].

A thorough clinical evaluation is essential to characterize the high cardiovascular risk in these patients through cardiovascular imaging to report important prognostic evaluations. Therefore, we conducted a systematic review of the current knowledge on cardiovascular assessment via imaging in ADPKD patients.

2. Methods

All randomized controlled trials (RCTs) and quasi-RCTs evaluating the current knowledge about imaging cardiovascular assessment in ADPKD patients were included.

1. Cochrane Renal Group's specialised register;
2. ClinicalTrial.gov (http://www.clinicaltrials.gov, accessed on 1 April 2023);
3. WHO International Clinical Trials Registry Platform (http://www.who.int/ictrp/en/, accessed on 1 April 2023);
4. MEDLINE.

We checked the reference lists of nephrology or cardiology textbooks, review articles, and relevant studies.

3. Results

The results of the research are summarized in Figure 1.

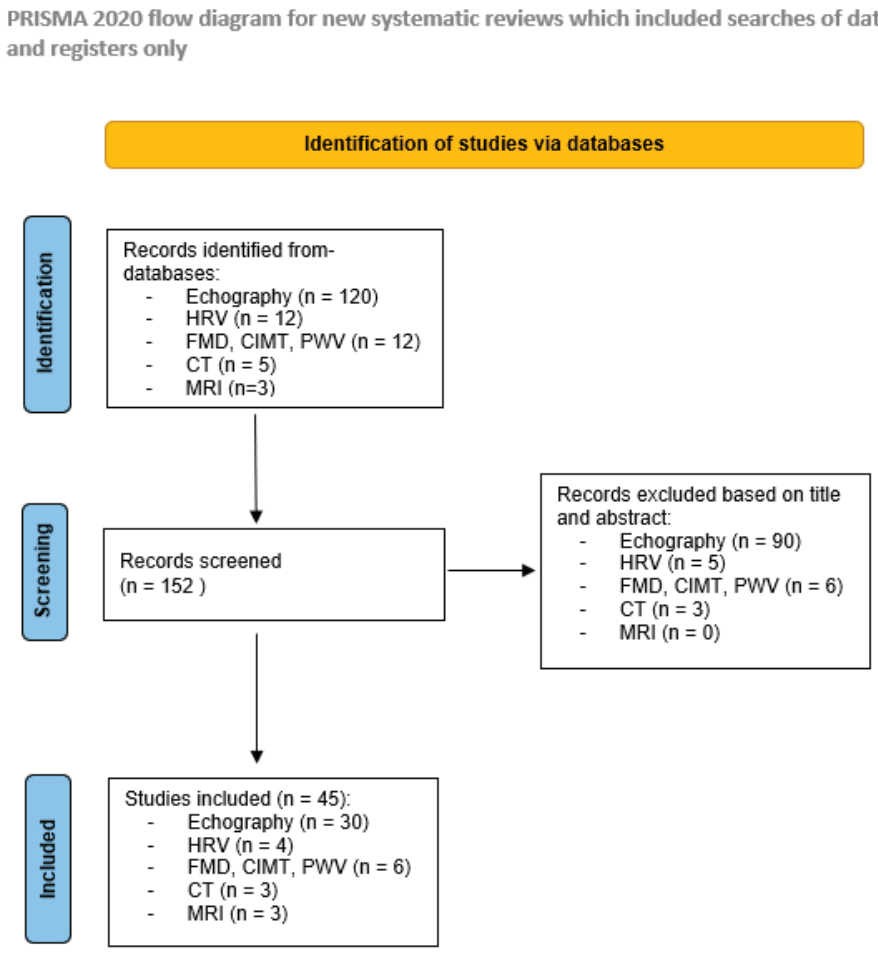

Figure 1. Abbrev.: HRV, heart rate variability; FMD, flow-mediated dilation; CIMT, carotid intima–media thickness; PWV, pulse wave velocity; CT, computed tomography; MRI, magnetic resonance imaging.

4. Echocardiography

Echocardiography findings in ADPKD patients have been well known for a long time [12–15]. Specific cardiac abnormalities related to mutations of PC1 and PC2 have not been reported, but all valvular apparatuses are involved in this condition; the most reported valvular defects are mitral valve prolapse, mitral incompetence, and tricuspid valve prolapse. Regardless of other possible causes, these abnormalities are more frequent in affected patients than in the general population [16–20]. According to the study by Lumiaho A. et al., mitral valve prolapse occurs in 26% of patients with PKD1, 14% of unaffected relatives, and 10% of control subjects [16].

Some observations report an increased incidence of large- and small-vessel aneurisms localized on ascendent aorta and coronary arteries [21,22]. These are specific experiences, not based on large studies; thus, is not possible to correlate ADPKD with a higher rate of aneurisms on these sites.

A matter to explore is the mechanism which leads to these abnormalities. It seems that cardiovascular disease is not totally related to kidney disease. An interesting study

conducted by Timio et al. on three cohorts of patients (affected individuals, non-affected familiars, and the general population) showed a higher prevalence of valvular abnormalities not only in affected people (3-fold higher than in healthy controls) but also in non-affected familiars (1.5-fold higher than in healthy controls) [23]. The mechanisms which underline these abnormalities are still unclear and probably need to be better understood to set up a specific prevention. We could suppose other pathogenetic pathway, different from the ones that cause kidney disease and cystic formation, involved in the changes in cardiac architecture.

4.1. Left Ventricular Hypertrophy and Molecular Mechanisms

Another debated issue is the prevalence of left ventricular hypertrophy (LVH) in ADPKD patients. Some authors consider LVH a consequence of early arterial hypertension onset. In any case, PC1 and PC2 are involved in several intracellular signaling pathways, which can influence cardiac function. PC-1 regulates mammalian target of rapamycin (mTOR) and PC-2 can influence B-cell lymphoma-2 (Bcl-2), leading to a down-regulation of mitophagy and apoptosis; both include pathways which can trigger hypertrophy in cardiac muscle [24–30]. Based on this hypothesis, PC-1 or PC-2 abnormalities in the heart could lead to an impairment in cardiac structure and function independently of kidney function or blood pressure. Different studies which investigate the prevalence of LVH among ADPKD patients underline that hypertrophy is more prevalent in young, affected patients than in the general population, regardless of the presence of AH [31–33]. Moreover, Pietrzak-Nowacka et al. [34] found higher left ventricular mass indexes (LVMIs) in male ADPKD patients (13%) than in the healthy group (2%) when comparing ADPKD patients and age- and sex-matched patients with essential hypertension [35]. Otherwise, not all the authors agree with this hypothesis, and this correlation is still uncertain; in fact, some studies do not show a higher incidence of LVH in ADPKD patients when compared with hypertensive patients [35]. A possible source of uncertainty was explained in the review conducted by Alam et al. [36]. In this study, the prevalence of LVH in ADPKD patients was 20–40% when assessed via echocardiography; when they took studies which assess LVH using MRI into consideration, the prevalence fell to 4%. These differences could be related to the imaging modality, variations in the parameters used to define LVH, or demographic differences in the study populations.

4.2. Novel Echographic Parameters for Cardiovascular Risk

Beyond the classical echocardiographic parameters, some studies show that PC1 and PC2 mutations are also related with novel risk factors and novel radiological markers [7]. In recent years, several studies have been focused on the correlation between epicardial adipose tissue and other possible cardiovascular risk factors. In three studies, ADPKD patients had more epicardial adipose tissue (EAT), associated with a higher risk of cardiovascular events [37,38]. EAT is considered a proper tissue with neuroendocrine functions, and its thickness is related with all the classical cardiovascular risk factors such as IMT and LVH.

In conclusion, the prevalence of cardiac abnormalities seems to be particularly high in ADPKD patients compared with the healthy population and hypertensive population.

An early assessment of these abnormalities is clinically relevant, considering the high rate of cardiovascular events in the ADPKD population. An adequate diagnostic pathway could improve therapeutic choices. Thus, we can suggest performing echocardiography in the affected patients, despite the presence of hypertension, to more accurately stratify the cardiovascular risk.

5. Heart Rate Variability (HRV)

In ADPKD patients, there is a dysregulation of the autonomic nervous system (ANS) [39]. The ANS is related to the cardiovascular system through heart rate control by the sympathetic and parasympathetic branches; catecholamines, released from the sympathetic nervous system, accelerate the heart rate. Additionally, contraction force and conduc-

tion are linked to sympathovagal balance, and changes in this equilibrium result in autonomic dysfunction.

The assessment of heart rate variability (HRV) reflects the influence of ANS (sympathetic and parasympathetic) on the cardiovascular system. Since cardiovascular complications are the main causes of death in patients at different stage of CKD, it is important to assess HRV as sign of cardiovascular impairment. HRV is defined as the variation in time intervals between consecutive heart beats over a period of observation (time of recording). Commonly using an Electrocardiographic Holter-Recording, this period can last 24 h or 5–10 min (a long or short time of recording, respectively), representing both the time domain and frequency domain able to evaluate global autonomic activity with the standard deviation of all normal-to-normal intervals (SDNN), sympathetic activity with low frequency (LF), parasympathetic activity with high frequency (HF), and sympathovagal balance with a sympathetic/parasympathetic ratio (LF/HF ratio) (Figure 2). Sympathovagal influence on the sinoatrial node (SA node) is indicated by HRV, an indirect index of cardiac neural control. The increased activation of the sympathetic system, mainly expressed by LF, causes a variation in heart rate and can promote hypertension, myocardial hypertrophy, and fibrosis, conditions associated with the risk of sudden cardiac death [40]. HRV and QT corrected for heart rate (QTc) interval evaluation can help in evaluating the arrhythmic risk and the autonomic dysfunction of patients [41]. In advanced CKD, regardless of the cause, the alteration of the autonomic system expressed by changes in HRV parameters represents a predictive factor for the rapid progression of CKD. In an observational study by the National Taiwan University Hospital conducted in 326 non-dialysis patients (median follow up period 2.02 years), a correlation between the late stage of CKD and low HRV was reported [42]. Among HRV parameters, SDNN, expressed as global autonomic function, LF (sympathetic system), HF (parasympathetic), and the LF/HF (sympathetic/parasympathetic) ratio were higher in early stages of CKD, while lower LF, HF, and LF/HF were correlated to late stages of CKD, which means a stronger compromission of ANS. Extremely lower LF and LF/HF were found in the rapid CKD progression group (diabetic and non-diabetic patients with worse values of serum creatinine, eGFR, proteinuria, albumin, hemoglobin, and HBA1c). Kidneys are directly innervated by the sympathetic nerve, which is one of the factors regulating the tubular and vascular function of glomeruli [42–44]. The pathogenetic mechanism of autonomic disfunction in ADPKD is not clear. Some hypotheses, such as uremic toxins, irregular erythropoietin secretion, and the overproduction of inflammatory mediators, are mentioned as causes of damage to autonomic kidney innervation. An imbalance between the sympathetic and parasympathetic system is also responsible for essential hypertension, which is the main feature of most ADPKD patients in the early stage of the disease. This is likely due to the presence and the enlargement of cysts in ADPKD, which cause an activation of the RAAS through renal arterial ischemia. A similar activation of RAAS is observed in bilateral atherosclerotic renal artery stenosis. RAAS activation causes autonomic disfunction with sympathetic prevalence [41]. Increased sympathetic tone is also caused by the reduction in baroreflex sensitivity due to high arterial stiffness related to elevated blood pressure. This process can be found in hypertensive and ADPKD patients with hypertension, because it is related to both these diseases. One study conducted on 65 patients evaluated the HRV in mild hypertensive patients with ADPKD (21 patients) versus patients with hypertension and organ damage (20 patients) and versus healthy controls (24 patients). HRV was more significantly reduced in ADPKD patients than in healthy controls, and the LF and LF/HF ratio were higher than in healthy controls. In hypertensive patients with organ damage, the same level of HRV abnormality was observed as in the ADPKD patients [41]. Since HRV variation is also detectable in young ADPKD patients without hypertension and/or CKD, it plays an important role as a predictive risk factor and therefore can be detected early in the disease course.

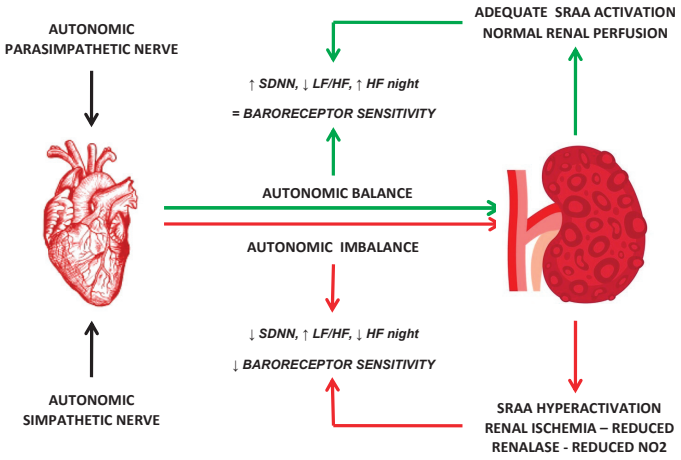

Figure 2. Autonomic dysfunction in autosomal dominant polycystic kidney disease. Abbreviations: SDNN: standard deviation of all sinus rhythm RR intervals; LF: low frequency, HF: high frequency, LF/HF: low frequency/high frequency, SRAA: systemic renin angiotensin aldosterone; NO: nitric oxide.

The evaluation of HRV can contribute to risk stratification by evaluating the imbalance of the sympathetic/parasympathetic system linked to cardiac complications such as coronary artery disease, arrhythmia events, and sudden cardiac death.

In conclusion, although no specific guidelines or standardized protocols for HRV measurement are available in ADPKD patients, it is an important, easy, and economic tool which contributes to the better assessment of cardiovascular risk in this cohort of patients.

6. Flow-Mediated Dilation (FMD), Carotid Intima–Media Thickness (IMT), and Pulse Wave Velocity (PWV)

Changes in endothelial function and increased carotid IMT and arterial stiffness are present in the early stages of the disease in young ADPKD patients and are associated with increased cardiovascular risk [5]. Endothelial cells produce more collagen and dysregulate matrix metalloproteinases as a consequence of the inflammatory status and stress factors present in ADPKD, which increase arterial stiffness. This is associated with uncontrolled arterial blood pressure and increases peripherical resistance, worsening hypertension and exposing patients to an increased rate of cardiovascular events and mortality [44].

A damaged endothelium loses its atheroprotective effect, as impaired vasomotion is responsible for the abnormal regulation of blood vessel tone [44,45]. When endothelial dysfunction occurs, the composition of the endothelial bilayer changes: the intima–media thickness is augmented and the amount of collagen is increased, worsening arterial stiffness. The pathogenetic process underlying endothelial dysfunction in ADPKD is still an object of debate, suggesting a role of the inflammatory status and vascular oxidative stress, as demonstrated by high levels of circulating NF-κB. Endothelial dysfunction is characterized by changes in the barrier permeability, which expose the vessels to aging and atherosclerosis, and by an altered vasodilatation/vasoconstriction ratio, mediated by the reduction in NO [5,45]. Endothelium dysfunction leads to the stiffness of the vessels increasing the peripherical arterial resistances, worsening arterial hypertension. Thus, endothelial dysfunction is a risk factor for cardiovascular events, such as stroke and coronary artery disease, with an increased mortality rate.

Some studies suggest that the activation of RAAS, mediated by the extension of cysts, can contribute to vascular dysfunction in addition to autonomic dysfunction [43].

In fact, the activation of RAAS, impaired NO-related vasorelaxation, increased sympathetic nerve activity, increased plasma endothelin-1 concentrations, and insulin resistance have also been observed [1,2].

Hyperaldosteronism contributes to the further growth of cysts, renal fibrosis, and the progression of cardiorenal disease. This effect is attributed to the aldosterone-induced target organ inflammation and fibrosis and the development of metabolic syndrome. The mechanisms by which aldosterone exerts its negative effect include oxidative stress and endothelial dysfunction through the decreased synthesis and release of NO, the production of reactive oxygen species mediated by nicotinamide-adenine-dinucleotide-phosphate-oxidase-dependent mechanisms, inflammation, and fluid retention, determining vascular remodeling, hypertrophy, and fibrosis. Furthermore, aldosterone also seems to be involved in the development of metabolic syndrome, dyslipidemia, endothelial dysfunction, and insulin resistance. The majority of these effects are mediated by the activation of the mineralocorticoid receptors that are expressed in cardiomyocytes, cardiac fibroblasts, and vascular smooth muscle cells, and they are mediated by the genomic and non-genomic effects of the hormone. The mechanisms by which aldosterone may contribute to insulin resistance include the increased degradation of insulin receptor substrates, the reduced transcription of the insulin receptor gene, interference with insulin signaling mechanisms, inflammation, reduced adiponectin production, and increased oxidative stress [4,43].

Moreover, experimental evidence suggests that PC1 and PC2 serve as mechanoreceptors in endothelial cells and smooth muscle cells, which sense the shear stress of the blood flow. The reduction in these glycoproteins may implicate an alteration in intracellular signaling, leading to reduced NO production. The reduction in NO may promote oxidative stress, vasoconstriction, hypoxia, and vascular remodeling, contributing to renal function decline and cardiovascular morbidity [44]. Increased oxidative stress and inflammation are other factors that contribute to the reduction in NO availability [44]. The evaluation of a possible therapy to improve endothelial-dependent vasodilatation is in progress, through the brachial infusion of dopamine in normotensive APDKD patients in order to restore NO bioavailability [44].

In fact, some authors showed that the stimulation of dopamine type 5 receptor on polycystin-deficient endothelial cells restores cilia length and shear-stress-induced calcium-dependent NO release, which suggests that stimulating dopamine receptors may have beneficial effects in ADPKD patients [44]. Studies over the past 2 decades have indicated the presence of an inflammatory component in ADPKD human and murine models [45].

NOXs are enzymes present in the vascular wall, and their primary task is to produce reactive oxygen species (ROS) superoxide, at physiologically low levels, in vascular cells. Some evidence showed overactive NOX systems in the initiation and progression of vascular disease via excessive ROS production by cells of the artery wall at levels that are cytotoxic. These ROS may lead to the activation of proinflammatory pathways; the depletion of antioxidants; and oxidative damage to proteins, lipids, and DNA. Among the NOX isoforms, NOX2 is believed to have the greatest implication in vascular disease. The overexpression of NOX2 in mice results in significantly increased superoxide production, and NOX2 knockout mice show significantly reduced ROS levels. Therefore, the increased activation of NOX2 could contribute to the diminished bioavailability of NO, and thus endothelial dysfunction and vascular cell hypertrophy. NOX2 upregulation could also explain the oxidative stress observed in patients with ADPKD, including endothelial dysfunction [4,45].

Due to the important role of the endothelium in the homeostasis of vessels, for example, in mediating vasodilatation related to shear stress (increasing or decreasing the speed of blood flow), in the regulation of inflammation, it is important to detect endothelial dysfunction.

Some non-invasive methods are used to detect endothelial disfunction. One of these methods is flow-mediated dilation (FMD) characterized by the evaluation of the diameter of the brachial artery before and after reactive hyperemia through the ultrasound technique.

FMD is realized through the measurement of the diameter of a peripheric artery, a usual brachial artery, with a linear ultrasound transducer. The diameter of the artery is valued on a specific position at rest (baseline), then after inflation, lasting 15 s, and consequently upon the deflation of a sphygmomanometer cuff, which simulates shear stress. FMD is generally calculated as FMD (%) = (Peak diameter – baseline diameter)/(baseline diameter) [43]. After this shear stress factor, endothelia should produce NO to stimulate vasodilatation and then reactive hyperemia. In ADPKD patients, there is endothelium dysfunction in the inflammatory state, with low NO available and increased arterial stiffness worsening flow-mediated vasodilatation [44–49].

A meta-analysis of 27 studies, including a total of 1967 ADPKD patients with preserved renal function (eGFR > 60/mL/min/1.73 m^2) compared to healthy controls, showed increased vascular stiffness and endothelial disfunction in patients with ADPKD. These damages were already present at the early stage of renal disease [46]. In particular, FMD was estimated to be significantly lower in ADPKD patients compared to healthy controls. ADPKD was also linked to significantly higher pulse wave velocity (PWV) and carotid IMT with the stiffening of large elastic arteries, contributing to cardiovascular dysfunction [46]. Carotid IMT is evaluated via the ultrasonographic technique as the distance between the lumen–intima and media–adventitia is 1–2 cm proximal to the carotid bulb.

The link between high IMT (intima–media thickness) and cardiovascular risk is well known. IMT represents the medial hypertrophy and thickening of smooth muscles and increases when the endothelium is damaged. An increased IMT contributes to the creation of a turbulent blood flow, which is a risk factor for atherosclerosis [3,5,36]. For these reasons, periodically valuating IMT, as a measure of endothelial dysfunction, is important to assess CV risk in ADPKD hypertensive and non-hypertensive patients.

Carotid IMT and FMD have also been used to assess endothelial dysfunction in a study conducted on 54 ADPKD patients, 20 of them being smokers, and 45 healthy controls, 19 of them being non-smokers. Healthy smokers and ADPKD non-smoker patients had similar values of FMD and CIMT. Smoker ADPKD patients had a higher IMT and lower FMD compared to ADPKD non-smoker patients [46]. The increased stiffening of large elastic arteries in ADPKD patients can be detected through a higher Carotid–Femoral PWV and Carotid–Radial PWV. Pulse Wave Velocity is non-invasively measured through a transcutaneous tonometer positioned at the carotid, brachial, radial, and femoral arteries [49]. At each site, two distinct waves are recorded: the first one reflects the left ventricular ejection and the second one is the reflected wave from peripheral segments. Pulse wave velocity is calculated as distance divided by time between the lowest part of the obtained waveforms. From these values, the Stiffness Index can be calculated [49]. One study on 55 ADPKD patients has shown that increased arterial stiffness is related to the occurrence of ESKD and cardiovascular complications (myocardial infarction, stroke, and cardiovascular interventions) in ADPKD, particularly in patients with multiple cardiovascular risk factors (obesity, hypertension, diabetes mellitus, smoking, and lipid abnormalities) [49]. The evaluation of arterial stiffness and endothelial disfunction is one of the main predictive factors of cardiovascular complications and renal disease progression in ADPKD patients. It can already be identified in the early stage of renal disease and even in not-yet hypertensive patients [44]. Increased arterial stiffness is found in people with CKD, and its etiology has an influence on the degree of arterial stiffness: in ADPKD patients, arterial stiffness develops earlier and the progression is more rapid than in patients at comparable stages of kidney disease [49]. Further studies and trials are necessary to evaluate the therapeutic implications of these parameters.

7. Computed Tomography

The study of the heart in ADPKD patients with CT is rarely performed because of the risk of contrast-induced nephropathy linked to the administration of contrast media in patients often affected by CKD. No randomized control trials or quasi-RCTs are available on heart CT scans in ADPKD patients.

Rare cardiac manifestations of ADPKD have been described beyond valvular abnormalities, in particular aortic aneurysm, coronary arterial aneurisms (CAAs) and dissections of coronary arteries (CADs). Different prevalence rates were reported by gender, patients' characteristics, and AH. The male gender is prevalent in CAAs, while patients diagnosed with CADs are mainly female. Presentation before 50 years of age is also a characteristic of these patients. The frequent concomitant presence of atherosclerosis and AH was described in CAA patients. The left anterior descending artery was most affected in CADs, while right coronary artery predominance was described in CAAs [50].

Coronary dissection showed female and left descending anterior artery predominance, with features similar to non-ADPKD patients, but the median diagnostic age was below the expected value (41 vs. 50 years old). Coronary aneurysms had male and right coronary artery predominance but a lower median diagnostic age (44 years old) and a higher rate of multiple vessel affection than that reported for non-ADPKD patients [50].

Diagnoses of coronary artery disease are primary made using coronary angiography, which allows contemporary diagnosis and treatment via coronary angioplasty.

Only one case of spontaneous coronary artery dissection (SCAD) underwent diagnosis via a coronary CT scan performed during a health check in a 59-year-old man. In this case, renal function was within the normal limits, and the CT scan helped in the diagnosis of SCAD [51]. Coronary artery dissection is a rare complication described in ADPKD patients, characterized by unstable angina, acute myocardial infarction, or even sudden cardiac death [50,52].

Only one more paper reported a CT angiogram of the chest revealing a Stanford type A and DeBakey type I aortic dissection involving the aortic valve and extending to the abdominal aorta with the coeliac, superior and inferior mesenteric, and left renal arteries arising from the false lumen [52]. The authors suggest that patients with ADPKD should be investigated for intracranial, coronary, and aortic vascular anomalies to prevent such devastating outcomes. A CT scan should only be used for the diagnosis of acute dissection.

8. Magnetic Resonance Imaging

Several studies reported the presence of LVH in patients affected by ADPKD. The prevalence ranges widely depending on age, gender, and hypertension, varying between 19 and 48% [16,53].

In the general population, the gold standard for the assessment of LV mass (LVM) is cardiac magnetic resonance imaging (MRI), but the evaluation of LVH and LVM is mainly performed via echocardiography. Cardiac MR more accurately determines left ventricular dimensions and the LV mass, enhancing information about the pattern of hypertrophy and myocardial fibrosis. In ADPKD patients, MRI is not usually performed for the evaluation of LVM.

One single study performed cardiac MRI for the assessment of LV mass and LVH, reporting significantly a lower prevalence value compared to echocardiographic studies [54]. Five hundred and forty-three hypertensive patients with GFR > 60 mL/min per 1.73 m^2 underwent the MR assessment of LVM before starting an intensive angiotensin blockade. The enrolled patients were younger than 50 years, with the satisfactory control of blood pressure and a high incidence of angiotensin-converting enzyme inhibitor (ACEi) administration. The prevalence of LVH was 0.93% using LVMI and 3.9% using non-indexed LV mass. The normal range of LVM via MR was lower than that reported via echocardiography, as described in previous studies comparing LVM indexes determined via cardiac MRI and echocardiography [54]. The indices of LVM were accounted for body size, reporting that LVMI demonstrated the strongest correlation in patients with ADPKD. Systolic blood pressure measured at office, serum creatinine, and urine albumin were directly associated with LVMI. Female gender was inversely associated, as expected, because of the relation between gender and body size. The authors suggest that aggressive blood pressure control and use of ACEi in patients with ADPKD was associated with decreased LVH. Left ventricular mass determined from cardiac MR appeared to be lower than that

determined via M-mode echocardiography; the greater accuracy of MRI should account for this discrepancy and may lead to different management options for patients [54–56].

Some authors also used MRI in ADPKD to evaluate pericardial effusion and found larger pericardial effusion thickness in ADPKD subjects compared to a population control matched for age, gender, and GFR. Liu et al. [55] used MRI, including ECG-gated cine MR of the aorta and heart, to evaluate pericardial effusion independently with three observers, measuring the maximum pericardial effusion thickness in diastole using electronic calipers. All MRI exams were obtained on a 1.5 T using a body array coil (Signa HDXT, GEHealthcare, Waukesha, WI, USA, or Magnetom Aera, Siemens Healthineers, Erlangen, Germany). Patients with ADPKD and a mean eGFR of 67 mL/min/1.73 m^2 demonstrated a significantly higher prevalence of pericardial effusion > 5 mm compared to matched controlled patients (21% in ADPKD patients, vs. 3% in control population). The occurrence of pericardial effusion was independent of heart failure, rheumatologic disease, increased fluid intake, or thyroid dysfunction. Pericardial effusion thickness significantly correlated with gender and right and left pleural effusion and negatively correlated with age. The retrospective measurement of pericardial effusion thickness was similar in MRI and echocardiography when echocardiographic images were retrospectively analyzed, but only two out of eight effusions seen on MRI were reported on the initial echocardiography reading performed when blinded to MRI results. The evidence of pleural and pericardial effusion on MRI highlights the need for further investigations in these patients to explain the pathophysiology.

Moreover, considering that intracranial aneurisms have a higher prevalence in ADPKD than in the general population [55], the current guidelines only suggest performing brain MRI in the subjects with a positive familiar history of subarachnoid hemorrhage (SAH) or kidney transplantation candidates [57].

9. Cardiopulmonary Exercise Testing (CPET)

Cardiopulmonary exercise testing (CPET), also referred to as a VO_2 (oxygen consumption) test, is a specialized type of stress test or exercise test that measures exercise ability. This test provides information about the heart and lung function to understand if patients' response to exercise is normal. CPET defines the maximum exercise capacity through the measurement of peak oxygen uptake (VO_2). Oxygen uptake ($V'O_2$), carbon dioxide production ($V'CO_2$), and minute ventilation (V'E) are determined. CPET consists of a steady-state resting period, then one minute of warm-up without a load, followed by a stepwise protocol in which the work rate is increased in 1 min intervals by increments of 10 Watt. The exercise test is considered maximal for a value of respiratory exchange ratio (RER) > 1.05. The Lactic Threshold (LT) is detected individually using the V-slope method [58]. Workload (W), LT, maximal oxygen consumption ($V'O_2max$), HR peak values, and BP are evaluated and compared with those obtained in a group of healthy subjects matched for age, height, weight, and gender. Oxygen uptake and ventilatory patterns obtained during the submaximal portion of CPET also give valuable information because of the possibility to evaluate the ability to perform activities of daily living during low-level exercise. CPET has become an important clinical tool to evaluate exercise capacity and to predict outcome in patients with heart failure and other cardiac conditions. It provides the assessment of the integrative exercise responses involving pulmonary, cardiovascular, and skeletal muscle systems, which are not adequately reflected through the measurement of individual organ system function. CPET is being used increasingly in a wide spectrum of clinical applications for the evaluation of undiagnosed exercise intolerance and for the objective determination of functional capacity and impairment [58].

Few studies assessed the role of CPET in ADPKD, showing reduced tolerance to stress and decreased anaerobic thresholds in patients with preserved kidney function [59,60]. VO_2 peak and anaerobic threshold are the major predictors of all-cause and cardiovascular disease, and in ADPKD patients, they are often out of the normal range. It is impor-

tant to confirm that exercise capacity is impaired in ADPKD with preserved kidney and cardiac function.

Therefore, early and non-invasive markers of cardiovascular risk and CPET should be performed in ADPKD patients, in the early stages of disease, despite the cost implication. Note that Parmar et al. [61] reported a case of subarachnoid hemorrhage from a ruptured berry aneurysm after stress testing in a patient with ADPKD.

10. Myocardial Scintigraphy

(99m) Tc-sestamibi myocardial perfusion imaging is frequently performed in conjunction with exercise or pharmacologic stress testing for the evaluation of coronary heart disease, but this method has never been used to evaluate the cardiovascular performance of ADPKD patients. Occasionally, incidental non-cardiac findings are detected upon review of the projectional images. In particular, a case of a patient with a history of ADPKD who was found to have a large abdominal photopenic area on the projectional images consistent with hepatic cysts was described [62].

Clinical Implications

Cardiovascular problems are a major cause of morbidity and mortality in ADPKD patients. Hypertension occurs in 50–70% of patients before the reduction in glomerular filtration at an earlier age than the general population, and it is associated with an increased rate of progression to ESRD [1,2]. Additionally, LVH occurs frequently and has important roles in cardiovascular complications in patients with ADPKD. Moreover, endothelial dysfunction, biventricular diastolic dysfunction, increased carotid intima–media thickness, and impaired coronary flow velocity reserve are present even in young ADPKD patients with normal blood pressure and well-preserved renal function [3,5,43]. Coronary and cerebral aneurysms and dissections represent a source of coronary syndromes and death in ADPKD. Clinical disparities may suggest a different mechanism of aneurysm formation compared to the population without ADPKD; in fact, the genetic mutations of ADPKD may predispose individuals to coronary abnormalities, especially aneurysms.

These findings suggest that cardiovascular involvement starts very early during ADPKD. Intracranial and extracranial aneurysms and cardiac valvular defects are other potential cardiovascular problems in patients with ADPKD. The early diagnosis and treatment of hypertension with drugs that block the renin–angiotensin–aldosterone system have the potential to decrease the cardiovascular complications and slow the progression of renal disease in ADPKD.

11. Conclusions

Cardiovascular involvement is prevalent in patients with ADPKD and represents the main cause of mortality. The main pathological findings are characterized by hypertension, LVH, aneurysms, cardiac valvular defects, aortic root dilation, and other cardiovascular manifestations. These abnormalities in clinical practice correlate with disease progression in ADPKD.

The main instrumental examination used for the assessment of cardiovascular disease in ADPKD is echocardiography, which is now performed early in all patients.

In addition, non-invasive, easy, economic diagnostic tests to assess cardiovascular risk, such as HRV, CPET, FMD, and PWD, are also performed to better assess high and early cardiovascular risk in ADPKD patients.

Most of the abnormalities are potentially subclinical. In fact, the early signs of the atherosclerosis process are characterized by endothelial dysfunction and high IMT, even in ADPKD with normal renal function and blood pressure. Understanding the association between ADPKD and increased cardiovascular risk leads to the establishment of an early and effective diagnostic assessment of cardiovascular changes to improve the time management of medications, to evaluate cardiovascular and kidney outcomes, and to improve the cardiovascular prognosis of ADPKD patients.

Author Contributions: Conceptualization, A.G. and S.L.; validation, E.A. and A.M.P.; writing, S.L., E.A., F.T. and A.M.P.; review and editing, A.G., S.L., R.C. and M.M.; visualization, A.G. and F.T.; supervision, S.L., R.C. and M.M. All authors have read and agreed to the published version of the manuscript.

Funding: This research received no external funding.

Institutional Review Board Statement: Not applicable.

Informed Consent Statement: Not applicable.

Data Availability Statement: Not applicable.

Conflicts of Interest: The authors declare no conflict of interest.

References

1. Capuano, I.; Buonanno, P.; Riccio, E.; Amicone, M.; Pisani, A. Therapeutic advances in ADPKD: The future awaits. *J. Nephrol.* **2022**, *35*, 397–415. [CrossRef] [PubMed]
2. Perrone, R.D.; Ruthazer, R.; Terrin, N.C. Survival after end-stage renal disease in autosomal dominant polycystic kidney disease: Contribution of extrarenal complications to mortality. *Am. J. Kidney Dis.* **2001**, *38*, 777–784. [CrossRef] [PubMed]
3. Ecder, T. Cardiovascular complications in autosomal dominant polycystic kidney disease. *Curr. Hypertens. Rev.* **2013**, *9*, 2–11. [CrossRef] [PubMed]
4. Lai, S.; Petramala, L.; Mastroluca, D.; Petraglia, E.; Di Gaeta, A.; Indino, E.; Panebianco, V.; Ciccariello, M.; Shahabadi, H.H.; Galani, A.; et al. Hyperaldosteronism and cardiovascular risk in patients with autosomal dominant polycystic kidney disease. *Medicine* **2016**, *95*, e4175. [CrossRef]
5. Ecder, T.; Schrier, R.W. Cardiovascular abnormalities in autosomal-dominant polycystic kidney disease. *Nat. Rev. Nephrol.* **2009**, *5*, 221–228. [CrossRef] [PubMed]
6. Caroli, A.; Antiga, L.; Conti, S.; Sonzogni, A.; Fasolini, G.; Ondei, P.; Perico, N.; Remuzzi, G.; Remuzzi, A. Intermediate volume on computed tomography imaging defines a fibrotic compartment that predicts glomerular filtration rate decline in autosomal dominant polycystic kidney disease patients. *Am. J. Pathol.* **2011**, *179*, 619–627. [CrossRef]
7. Lai, S.; Mastroluca, D.; Letizia, C.; Petramala, L.; Perrotta, A.M.; DiGaeta, A.; Ferrigno, L.; Ciccariello, M.; D'Angelo, A.R.; Panebianco, V. Magnetic resonance imaging 3T and total fibrotic volume in autosomal dominant polycystic kidney disease. *Intern. Med. J.* **2018**, *48*, 1505–1513. [CrossRef]
8. Haemmerli, J.; Morel, S.; Georges, M.; Haidar, F.; Chebib, F.T.; Morita, A.; Nozaki, K.; Tominaga, T.; Bervitskiy, A.V.; Rzaev, J.; et al. Characteristics and Distribution of Intracranial Aneurysms in Patients with Autosomal Dominant Polycystic Kidney Disease Compared with the General Population: A Meta-Analysis. *Kidney360* **2023**, *4*, e466–e475. [CrossRef]
9. Chapman, A.B.; Devuyst, O.; Eckardt, K.U.; Gansevoort, R.T.; Harris, T.; Horie, S.; Kasiske, B.L.; Odland, D.; Pei, Y.; Perrone, R.D.; et al. Conference Participants. Autosomal-dominant polycystic kidney disease (ADPKD): Executive summary from a Kidney Disease: Improving Global Outcomes (KDIGO) Controversies Conference. *Kidney Int.* **2015**, *88*, 17–27. [CrossRef]
10. Silverio, A.; Prota, C.; Di Maio, M.; Polito, M.V.; Cogliani, F.M.; Citro, R.; Gigantino, A.; Iesu, S.; Piscione, F. Aortic dissection in patients with autosomal dominant polycystic kidney disease: A series of two cases and a review of the literature. *Nephrology* **2015**, *20*, 229–235. [CrossRef]
11. Lai, S.; Mangiulli, M.; Perrotta, A.M.; Gigante, A.; Napoleoni, L.; Cipolloni, E.; Mitterhofer, A.P.; Gasperini, M.L.; Muscaritoli, M.; Cianci, R.; et al. Cardiovascular Risk and Quality of Life in Autosomal Dominant Polycystic Kidney Disease Patients on Therapy with Tolvaptan: A Pilot Study. *Curr. Vasc. Pharmacol.* **2021**, *19*, 556–564. [CrossRef]
12. Castiglioni, G.; Gibelli, G.; Milani, S.; Benelli, R.; Riegler, P.; Fasciolo, F.; Leone, M.A.; Scarpino, L.; Cantafio, S.; Conte, F. Cardiac valvular abnormalities in ADPKD. Preliminary results from the Italian Multicentric Study. *Contrib. Nephrol.* **1995**, *115*, 159–162.
13. Ivy, D.D.; Shaffer, E.M.; Johnson, A.M.; Kimberling, W.J.; Dobin, A.; Gabow, P.A. Cardiovascular abnormalities in children with autosomal dominant polycystic kidney disease. *J. Am. Soc. Nephrol.* **1995**, *5*, 2032–2036. [CrossRef]
14. Hossack, K.F.; Leddy, C.L.; Johnson, A.M.; Schrier, R.W.; Gabow, P.A. Echocardiographic findings in autosomal dominant polycystic kidney disease. *N. Engl. J. Med.* **1988**, *319*, 907–912. [CrossRef]
15. Ha, S.K.; Park, C.H.; Kna, J.S.; Lee, S.Y.; Lee, J.I.; Kim, S.J.; Seo, J.K.; Lee, H.Y.; Han, D.S. Extrarenal manifestations of autosomal dominant polycystic kidney disease. *Yonsei Med. J.* **1997**, *38*, 111–116. [CrossRef] [PubMed]
16. Lumiaho, A.; Ikäheimo, R.; Miettinen, R.; Niemitukia, L.; Laitinen, T.; Rantala, A.; Lampainen, E.; Laakso, M.; Hartikainen, J. Mitral valve prolapse and mitral regurgitation are common in patients with polycystic kidney disease type 1. *Am. J. Kidney Dis.* **2001**, *38*, 1208–1216. [CrossRef]
17. Varnero, S.; Becchi, G.; Bormida, R.; Martinengo, E.; Carozzi, S. Valvular prolapse in autosomal dominant polycystic kidney. *G. Ital. Di Cardiol.* **1992**, *22*, 825–828.
18. Chebib, F.T.; Hogan, M.C.; El-Zoghby, Z.M.; Irazabal, M.V.; Senum, S.R.; Heyer, C.M.; Madsen, C.D.; Cornec-Le Gall, E.; Behfar, A.; Harris, P.C.; et al. Autosomal Dominant Polycystic Kidney Patients May Be Predisposed to Various Cardiomyopathies. *Kidney Int. Rep.* **2017**, *2*, 913–923. [CrossRef]

19. Miyamoto, R.; Sekine, A.; Fujimaru, T.; Suwabe, T.; Mizuno, H.; Hasegawa, E.; Yamanouchi, M.; Chiga, M.; Mori, T.; Sohara, E.; et al. Echocardiographic Findings and Genotypes in Autosomal Dominant Polycystic Kidney Disease. *Kidney Dis.* **2021**, *8*, 246–252. [CrossRef] [PubMed]
20. Akpinar, T.S.; Kucukdagli, P.; Ozer, P.K.; Karaayvaz, E.B.; Ince, B.; Bakkaloglu, O.K.; Sarihan, I.; Medetalibeyoglu, A.; Altinkaynak, M.; Uzun, D.D.; et al. Subclinic arterial and left ventricular systolic impairment in autosomal dominant polycystic kidney disease with preserved renal functions. *Int. J. Cardiovasc. Imaging* **2022**, *38*, 271–278. [CrossRef]
21. Kang, Y.R.; Ahn, J.H.; Kim, K.H.; Choi, Y.M.; Choi, J.; Park, J.R. Multiple cardiovascular manifestations in a patient with autosomal dominant polycystic kidney disease. *J. Cardiovasc. Ultrasound* **2014**, *22*, 144–147. [CrossRef]
22. Elfanish, A.; Meissner, A.; Weidemann, A.; Christoph, A. Giant coronary aneurysm in a patient with autosomal dominant polycystic kidney disease. *Clin. Res. Cardiol.* **2021**, *110*, 148–150. [CrossRef] [PubMed]
23. Timio, M.; Monarca, C.; Pede, S.; Gentili, S.; Verdura, C.; Lolli, S. The spectrum of cardiovascular abnormalities in autosomal dominant polycystic kidney disease: A 10-year follow-up in a five-generation kindred. *Clin. Nephrol.* **1992**, *37*, 245–251.
24. Oto, O.A.; Edelstein, C.L. The Pathophysiology of Left Ventricular Hypertrophy, beyond Hypertension, in Autosomal Dominant Polycystic Kidney Disease. *Nephron*, 2022, *ahead of print*. [CrossRef]
25. Jin, X.; Rong, S.; Mei, C.; Chen, J.; Ye, C.; Chen, X. Ultrasonic characterization (integrated backscatter) of myocardial tissue in patients with autosomal dominant polycystic kidney disease. *Nephron Clin. Pract.* **2010**, *114*, c288–c294. [CrossRef] [PubMed]
26. Wanic-Kossowska, M.; Posnik, B.; Kobelski, M.; Pawliczak, E.; Pawlaczyk, K.; Hoppe, K.; Schwermer, K.; Sikorska, D. The polymorphism of the ACE gene affects left ventricular hypertrophy and causes disturbances in left ventricular systolic/diastolic function in patients with autosomal dominant polycystic kidney disease. *Sci. World J.* **2014**, *2014*, 707658. [CrossRef]
27. Valero, F.A.; Martinez-Vea, A.; Bardají, A.; Gutierrez, C.; Garcia, C.; Richart, C.; Oliver, J.A. Ambulatory blood pressure and left ventricular mass in normotensive patients with autosomal dominant polycystic kidney disease. *J. Am. Soc. Nephrol.* **1999**, *10*, 1020–1026. [CrossRef]
28. Martinez-Vea, A.; Bardají, A.; Gutierrez, C.; Garcia, C.; Peralta, C.; Aguilera, J.; Sanchez, P.; Vidiella, J.; Angelet, P.; Compte, T.; et al. Echocardiographic evaluation in patients with autosomal dominant polycystic kidney disease and end-stage renal disease. *Am. J. Kidney Dis.* **1999**, *34*, 264–272. [CrossRef]
29. Yildiz, A.; Sag, S.; Gul, C.B.; Güllülü, S.; Can, F.E.; Bedir, Ö.; Aydin, M.F.; Oruç, A.; Demirel, S.; Akgür, S.; et al. Morning blood pressure surge in early autosomal dominant polycystic kidney disease and its relation with left ventricular hypertrophy. *Ren. Fail.* **2021**, *43*, 223–230. [CrossRef] [PubMed]
30. Chen, H.; Watnick, T.; Hong, S.N.; Daly, B.; Li, Y.; Seliger, S.L. Left ventricular hypertrophy in a contemporary cohort of autosomal dominant polycystic kidney disease patients. *BMC Nephrol.* **2019**, *20*, 386. [CrossRef] [PubMed]
31. Bardají, A.; Vea, A.M.; Gutierrez, C.; Ridao, C.; Richart, C.; Oliver, J.A. Left ventricular mass and diastolic function in normotensive young adults with autosomal dominant polycystic kidney disease. *Am. J. Kidney Dis.* **1998**, *32*, 970–975. [CrossRef]
32. Zeier, M.; Geberth, S.; Schmidt, K.G.; Mandelbaum, A.; Ritz, E. Elevated blood pressure profile and left ventricular mass in children and young adults with autosomal dominant polycystic kidney disease. *J. Am. Soc. Nephrol.* **1993**, *3*, 1451–1457. [CrossRef] [PubMed]
33. Martinez-Vea, A.; Bardaj, A.; Gutierrez, C.; Garca, C.; Peralta, C.; Marcas, L.; Oliver, J.A. Exercise blood pressure, cardiac structure, and diastolic function in young normotensive patients with polycystic kidney disease: A prehypertensive state. *Am. J. Kidney Dis.* **2004**, *44*, 216–223. [CrossRef]
34. Pietrzak-Nowacka, M.; Safranow, K.; Czechowska, M.; Dutkiewicz, G.; Kornacewicz-Jach, Z.; Ciechanowski, K. Autosomal dominant polycystic kidney disease and hypertension are associated with left ventricular mass in a gender-dependent manner. *Kidney Blood Press. Res.* **2012**, *36*, 301–309. [CrossRef] [PubMed]
35. Harrap, S.B.; Davies, D.L.; Macnicol, A.M.; Dominiczak, A.F.; Fraser, R.; Wright, A.F.; Watson, M.L.; Briggs, J.D. Renal, cardiovascular and hormonal characteristics of young adults with autosomal dominant polycystic kidney disease. *Kidney Int.* **1991**, *40*, 501–508. [CrossRef] [PubMed]
36. Alam, A.; Perrone, R.D. Left ventricular hypertrophy in ADPKD: Changing demographics. *Curr. Hypertens. Rev.* **2013**, *9*, 27–31. [CrossRef]
37. Sag, S.; Yildiz, A.; Gullulu, S.; Gungoren, F.; Ozdemir, B.; Cegilli, E.; Oruc, A.; Ersoy, A.; Gullulu, M. Early atherosclerosis in normotensive patients with autosomal dominant polycystic kidney disease: The relation between epicardial adipose tissue thickness and carotid intima-media thickness. *Springerplus* **2016**, *5*, 211. [CrossRef]
38. Concistrè, A.; Petramala, L.; Scoccia, G.; Sciomer, S.; Bisogni, V.; Saracino, V.; Iannucci, G.; Lai, S.; Mastroluca, D.; Iacobellis, G.; et al. Epicardial Fat Thickness in Patients with Autosomal Dominant Polycystic Kidney Disease. *Cardiorenal Med.* **2018**, *8*, 199–207. [CrossRef]
39. Lai, S.; Mangiulli, M.; Perrotta, A.M.; Di Lazzaro Giraldi, G.; Testorio, M.; Rosato, E.; Cianci, R.; Gigante, A. Reduction in Heart Rate Variability in Autosomal Dominant Polycystic Kidney Disease. *Kidney Blood Press. Res.* **2019**, *44*, 1142–1148. [CrossRef]
40. Lai, S.; Bagordo, D.; Perrotta, A.M.; Gigante, A.; Gasperini, M.L.; Muscaritoli, M.; Mazzaferro, S.; Cianci, R. Autonomic dysfunction in kidney diseases. *Eur. Rev. Med. Pharmacol. Sci.* **2020**, *24*, 8458–8468. [CrossRef]
41. Lai, S.; Perrotta, A.M.; Bagordo, D.; Mazzaferro, S.; Menè, P.; Gigante, A.; Tinti, F.; Galani, A.; Cianci, R. Screening of QTc interval and global autonomic activity in autosomal dominant polycystic kidney disease and atherosclerotic renal artery stenosis hypertensive patients. *Eur. Rev. Med. Pharmacol. Sci.* **2021**, *25*, 6333–6338. [CrossRef]

42. Chou, Y.-H.; Huang, W.-L.; Chang, C.-H.; Yang, C.C.H.; Kuo, T.B.J.; Lin, S.-L.; Chiang, W.-C.; Chu, T.-S. Heart rate variability as a predictor of rapid renal function deterioration in chronic kidney disease patients. *Obs. Study Nephrol.* **2019**, *24*, 806–813. [CrossRef]
43. Nowak, K.L.; Wang, W.; Farmer-Bailey, H.; Gitomer, B.; Malaczewski, M.; Klawitter, J.; Jovanovich, A.; Chonchol, M. Vascular Dysfunction, Oxidative Stress, and Inflammation in Autosomal Dominant Polycystic Kidney Disease. *Clin. J. Am. Soc. Nephrol.* **2018**, *13*, 1493–1501. [CrossRef]
44. Bellos, I.; Kontzoglou, K.; Perrea, D.N. Markers of endothelial dysfunction and arterial stiffness in patients with early-stage autosomal dominant polycystic kidney disease: A meta-analysis Meta-Analysis. *Int. J. Clin. Pract.* **2021**, *75*, e13721. [CrossRef]
45. Lorthioir, A.; Joannidès, R.; Rémy-Jouet, I.; Fréguin-Bouilland, C.; Iacob, M.; Roche, C.; Monteil, C.; Lucas, D.; Renet, S.; Audrézet, M.P.; et al. Polycystin deficiency induces dopamine-reversible alterations in flow-mediated dilatation and vascular nitric oxide release in humans. *Kidney Int.* **2015**, *87*, 465–472. [CrossRef]
46. Kocaman, O.; Oflaz, H.; Yekeler, E.; Dursun, M.; Erdogan, D.; Demirel, S.; Alisir, S.; Turgut, F.; Mercanoglu, F.; Ecder, T. Endothelial dysfunction and increased carotid intima-media thickness in patients with autosomal dominant polycystic kidney disease. *Am. J. Kidney Dis.* **2004**, *43*, 854–860. [CrossRef]
47. Gul, C.B.; Yildiz, A.; Sag, S.; Oruc, A.; Ersoy, A.; Gullulu, S. The Effect of Smoking on Endothelial Dysfunction in Autosomal Dominant Polycystic Kidney Disease Patients with Preserved Renal Function. *Ren. Fail.* **2021**, *43*, 1124–1129. [CrossRef]
48. Nowak, K.L.; Farmer, H.; Cadnapaphornchai, M.A.; Gitomer, B.; Chonchol, M. Vascular dysfunction in children and young adults with autosomal dominant polycystic kidney disease. *Nephrol. Dial. Transplant.* **2017**, *32*, 342–347. [CrossRef] [PubMed]
49. Sági, B.; Késői, I.; Késői, B.; Vas, T.; Csiky, B.; Kovács, T.; Nagy, J. Arterial stiffness may predict renal and cardiovascular prognosis in autosomal-dominant polycystic kidney disease. *Physiol. Int.* **2018**, *105*, 145–156. [CrossRef] [PubMed]
50. Briosa Neves, J.; Brogueira Rodrigues, F.; António Lopes, J. Autosomal dominant polycystic kidney disease and coronary artery dissection or aneurysm: A systematic review. *Ren. Fail.* **2016**, *38*, 493–502. [CrossRef] [PubMed]
51. Lee, C.; Fang, C.; Huang, C.; Ng, S.-H.; Yip, H.-K.; Ko, S.-F. Computed Tomography Angiographic Demonstration of an Unexpected Left Main Coronary Artery Dissection in a Patient with Polycystic Kidney Disease. *J. Thorac. Imaging* **2011**, *26*, W4–W6. [CrossRef] [PubMed]
52. Hydoub, Y.M.; Alnuaimi, M.; Nour, S. Catastrophic extrarenal manifestation of autosomal dominant polycystic kidney disease: Lessons learnt. *BMJ Case Rep.* **2019**, *12*, e231944. [CrossRef] [PubMed]
53. Chapman, A.B.; Johnson, A.M.; Rainguet, S.; Hossack, K.; Gabow, P.; Schrier, R.W. Left ventricular hypertrophy in autosomal dominant polycystic kidney disease. *J. Am. Soc. Nephrol.* **1997**, *8*, 1292–1297. [CrossRef]
54. Perrone, R.D.; Abebe, K.Z.; Schrier, R.W.; Chapman, A.B.; Torres, V.E.; Bost, J.; Kaya, D.; Miskulin, D.C.; Steinman, T.I.; Braun, W.; et al. Cardiac magnetic resonance assessment of left ventricular mass in autosomal dominant polycystic kidney disease. *Clin. J. Am. Soc. Nephrol.* **2011**, *6*, 2508–2515. [CrossRef]
55. Liu, J.; Fujikura, K.; Dev, H.; Riyahi, S.; Blumenfeld, J.; Kim, J.; Rennert, H.; Prince, M.R. Pericardial Effusion on MRI in Autosomal Dominant Polycystic Kidney Disease. *J. Clin. Med.* **2022**, *11*, 1127. [CrossRef]
56. AlNuaimi, D.; AlKetbi, R.; AlFalahi, A.; AlBastaki, U.; Pierre-Jerome, C. Ruptured Berry Aneurysm as the initial presentation of Polycystic Kidney Disease: A case report and review of literature. *J. Radiol. Case Rep.* **2018**, *12*, 1–8. [CrossRef] [PubMed]
57. Capelli, I.; Zoli, M.; Righini, M.; Faccioli, L.; Aiello, V.; Spinardi, L.; Gori, D.; Friso, F.; Rustici, A.; Bortolotti, C.; et al. MR Brain Screening in ADPKD Patients: To Screen. or not to Screen? *Clin. Neuroradiol.* **2022**, *32*, 69–78. [CrossRef] [PubMed]
58. Albouaini, K.; Egred, M.; Alahmar, A.; Wright, D.J. Cardiopulmonary exercise testing and its application. *Postgrad. Med. J.* **2007**, *83*, 675–682. [CrossRef]
59. Reinecke, N.L.; Cunha, T.M.; Heilberg, I.P.; Higa, E.M.; Nishiura, J.L.; Neder, J.A.; Almeida, W.S.; Schor, N. Exercise capacity in polycystic kidney disease. *Am. J. Kidney Dis.* **2014**, *64*, 239–246. [CrossRef]
60. Lai, S.; Mastroluca, D.; Matino, S.; Panebianco, V.; Vitarelli, A.; Capotosto, L.; Turinese, I.; Marinelli, P.; Rossetti, M.; Galani, A.; et al. Early Markers of Cardiovascular Risk in Autosomal Dominant Polycystic Kidney Disease. *Kidney Blood Press. Res.* **2017**, *42*, 1290–1302. [CrossRef]
61. Parmar, M.S. Subarachnoid hemorrhage after exercise stress testing. Case Reports. *Can. J. Cardiol.* **2004**, *20*, 555–556. [PubMed]
62. Lyon, J.; Spaulding, J.; Zack, P.M. Large abdominal photopenic area on 99mTc-sestamibi myocardial perfusion imaging. *J. Nucl. Med. Technol.* **2012**, *40*, 281–282. [CrossRef] [PubMed]

MDPI
St. Alban-Anlage 66
4052 Basel
Switzerland
www.mdpi.com

Applied Sciences Editorial Office
E-mail: applsci@mdpi.com
www.mdpi.com/journal/applsci

Academic Open
Access Publishing

mdpi.com

ISBN 978-3-7258-0504-4